How Hot, How Deep, How Long: Constraints on the Tectono-Metamorphic Evolution of Granulite Terranes

Victor Emmanuel Guevara

Dissertation submitted to the Faculty of the
Virginia Polytechnic Institute and State University
in partial fulfillment of the requirements for the degree of

Doctor of Philosophy
In
Geosciences

Mark J. Caddick, Chair
James S. Beard
Michael Brown
Richard D. Law
James A. Spotila
Robert J. Tracy

April 17, 2017
Blacksburg, VA

Keywords: Metamorphism, Granulite, Archean, Ultrahigh Temperature

How Hot, How Deep, How Long: Constraints on the Tectono-Metamorphic Evolution of Granulite Terranes

Victor E. Guevara

ABSTRACT

Granulites are the dense, strong metamorphic rocks that are produced during high- (HT) to ultrahigh-temperature metamorphism (UHT) and partial melting of Earth's crust. Granulites are ubiquitous in exhumed Archean cratons and are thought to comprise much of Earth's stable lower crust. Understanding the mechanisms responsible for crustal heating in Archean terranes is thus paramount to understanding the stabilisation of early continental crust, and whether such mechanisms resemble modern tectonic processes. It is therefore important to quantify the pressure–temperature–time (*P–T–t)* paths of Archean granulites, as such paths can be diagnostic of heating mechanism. This dissertation explores: 1) novel approaches to reconstructing the *P–T–t* paths of granulites, and 2) what the deciphered *P–T–t* paths of rocks from two Archean granulite terranes reveal about Archean crustal heating. The first chapter shows how petrologic modelling at multiple scales from a texturally heterogeneous granulite can provide "snapshots" of the *P–T* path, which would be difficult to reconstruct otherwise. The remaining chapters are focused on reconstructing the *P–T–t* paths of two Archean granulite terranes: the Beartooth Mountains, and the Pikwitonei granulite domain (PGD). The second and third chapters present evidence for cryptic HT metamorphism of the Beartooth granulites at ~2.7 Ga characterized by rapid (< 1 Ma) exhumation at HT and fast cooling (~10-100 °C/Ma) in the middle crust. This suggests advective/conductive heating over short length-scales. In the fourth chapter, thermobarometric data suggest the western PGD experienced UHT decompression followed by cooling in the lower crust. High-precision zircon and monazite dates reveal apparently episodic crystallization over at least ~24 Ma. This episodicity could reflect multiple thermal cycles or the control of local reactions on zircon/monazite crystallization during cooling. High-spatial resolution petrochronology provides temporal constraints on prograde metamorphism. These data suggest metamorphism in the PGD was driven by a long-lived heat source over large length-scales near the base of the lithosphere. Disparities in the timescales, length-scales, and the depth and amount of heating between the terranes may suggest different crustal heating mechanisms in each, and that the late Archean Earth may have been tectonically diverse.

How Hot, How Deep, How Long: Constraints on the Tectono-Metamorphic Evolution of Granulite Terranes

Victor E. Guevara

GENERAL AUDIENCE ABSTRACT

Granulites are the dense and strong rocks that are produced during extreme heating, high- (HT) to ultrahigh-temperature (UHT) metamorphism, and partial melting of Earth's continental crust. Granulites are common in exhumed fragments of Earth's ancient, Archean (> 2.5 billion yrs old) crust and are thought to comprise much of Earth's stable lower crust. Understanding the mechanisms responsible for extreme heating of the crust is thus crucial to understanding how Earth's early continents were stabilised, and how plate tectonic processes have evolved through Earth history. Metamorphic rocks preserve a commonly cryptic record of the path(s) they took through the crust, which are controlled in part by the heating mechanism(s) and tectonic settings involved in their genesis. It is therefore important to quantify the pressure–temperature–time (*P–T–t)* paths of Archean granulites, as such paths may be diagnostic of particular crustal heating mechanisms. This dissertation explores: 1) novel approaches to reconstructing the pressure–temperature–time (*P–T–t)* paths of granulites, and 2) what the deciphered *P–T–t* paths of rocks from two Archean granulite terranes reveal about Archean crustal heating. The first chapter presents a novel way to reconstruct the *P–T* path of a texturally complex and heterogeneous rock, which reveals a more detailed history than conventional methods would. The second, third, and fourth chapters are focused on reconstructing the *P–T–t* paths of granulites from two Archean terranes that record HT/UHT metamorphism ~2.7 billion years ago: the Beartooth Mountains, and the Pikwitonei granulite domain (PGD). These studies show that crustal heating of the Beartooth granulites was brief (< 1 million years duration) and seems to have occurred over short length-scales in the middle crust, while crustal heating of the PGD was long-lived (> 24 million years duration) and occurred over large length-scales near the base of the crust. The disparities in the timescales, length-scales, and the depth and amount of heating between the two terranes may suggest different crustal heating mechanisms operated in each, and that the Earth may have been tectonically diverse ~2.7 billion years ago.

DEDICATION

This dissertation is dedicated to S.P. Guevara, who inspired in me a curiosity for the natural world and the tenacity and courage to chase my dreams.

"Often, Precambrian rock is collectively referred to as "the basement" – the basement of continents – as if that is all there is to say about it before setting up on top of it the wonders of the world."

– John McPhee, in *Rising from the Plains*

ACKNOWLEDGMENTS

There are many talented, generous, and genuinely kind people to thank who have contributed to the successful completion of the work presented in this document, and I apologize in advance to those who I have forgotten to acknowledge here. First and foremost I would like to thank my advisor, Mark Caddick, for being a good friend and amazing mentor over the years. I have learned too many things from working with you to list here, but I feel that I have grown substantially and learned the proper spelling of "modelling" and "behaviour", as well as the correct pronunciation of "basalt" and "H_2O" as a result. I also thank my good friend and colleague Besim Dragovic for keeping me laughing, and being humble and kind when times were tough. You have been essentially a co-advisor to me, and it has been great fun stopping into your office to chat about Archean granulites, politics, and various topics related to metamorphic geology. I am excited to continue our work together, both on Archean granulites and whatever future projects lay on the horizon.

I thank Bob Tracy, who has also mentored me throughout my PhD studies, for his wisdom and patience, despite my ineptitude on the microprobe. Committee members Jim Beard, Mike Brown, Rick Law, and Jim Spotila also deserve recognition for asking the tough questions – I would not be nearly as rigorous a scientist as I am today without our discussions over the years. Mike Brown has been particularly generous with his time, meeting me to chat over lunch at various conferences, and driving down to Blacksburg for my committee meetings. Scott Maclennan, Ethan Baxter, Blair Schoene, Andrew Kylander-Clark, and Chris Couëslan are thanked for collaborating on these projects with me. I also thank several folks who provided scientific mentorship prior to my arrival at Virginia Tech: Julie Baldwin, Dave West, Ray Coish, Will Amidon, Don Winston, Chris Koteas, and Rebecca Bendick have all played a role in generating my geological curiosity and development as a geoscientist.

Funding for this research was provided by: National Science Foundation, National Geographic Society Young Explorers Program, Geological Society of America, Earthscope Awards for Geochronology Student Research Program, Tobacco Root Geological Society, Colorado Scientific Society, the Virginia Tech Department of Geosciences, and a David R. Wones geological scholarship.

Thanks to my family for being supportive of my endeavors throughout my life. I thank my friends and fellow geoscience students (both at Virginia Tech and other institutions) for the companionship, support, and, in some cases, lab and field assistance, over the years. I especially acknowledge (in no particular order): Michelle Fame, Neal Auchter, Kristie Dorfler, Cailey Condit, Whitney Bausch, Liane Stevens, Calvin Mako, Jarek Trela, Jordie, Laura Hamm, Hector LaMadrid, Joe Cochran, Sarah Ulrich, Cody Mason, Nick Heaverlo, Jen Gorce, Philip Prince, Kirk Broadwell, Allie Nagurney, Emma Tulsky, Juliet Ryan-Davis, Chelsea Ward-Waller, Hanna Brooks, Matt Petroff, Sebastian Mergelsberg, and everyone else. Y'all are great.

ATTRIBUTIONS

Chapter 2 was published as "Guevara, V.E. and Caddick, M.J., 2016, Shooting at a moving target: phase equilibria modelling of high-temperature metamorphism. *Journal of Metamorphic Geology*, 34, 209-235." Copyright permission has been granted from John Wiley and Sons to reprint this article. ***VE Guevara*** was responsible for all microprobe and scanning electron microscope analysis, petrographic analysis, phase equilibria calculations, and manuscript preparation. *MJ Caddick* was responsible for assisting with phase equilibria calculations, petrographic interpretation, coding THERMOCALC dataset version 6 and updated solution models from White et al. (2014) for use in Perple_X, and assisted in manuscript preparation and presentation.

Chapter 3 was published as "Dragovic, B., Guevara, V.E., Caddick, M.J., Baxter, E.F., and Kylander-Clark, A.R.C., 2016, A pulse of cryptic granulite-facies metamorphism in the Archean Wyoming Craton revealed by Sm-Nd and U-Pb monazite geochronology. *Precambrian Research*, 283, 24-49." Copyright permission has been granted from Elsevier to reprint this article. ***VE Guevara*** was responsible for project conception, raising initial funding, field observations and interpretations, sample collection, petrographic analysis and interpretation, electron microprobe analyses, LA-ICP-MS analyses, grain imaging of monazite, U-Pb monazite geochronological analyses, phase equilibria modelling, assistance with interpretation of geochronologic data, and manuscript writing and preparation. *B Dragovic* was responsible for Sm-Nd garnet geochronology, diffusion model calculations of trace and major elements in garnet, calculation of melt loss effects on Sm-Nd garnet ages, manuscript writing and preparation, LA-ICPMS analyses, age resetting calculations, assistance with electron microprobe analyses, assistance with petrographic analyses, assistance with phase equilibria modelling, and assistance with field observations and sample collection. *MJ Caddick* was responsible for assistance with: diffusion modelling, petrographic interpretation, Sm-Nd garnet and U-Pb monazite geochronologic interpretation, field observations, sample collection, and manuscript preparation and presentation. *EF Baxter* was responsible for assistance with interpretation of Sm-Nd garnet geochronology. *ARC Kylander-Clark* was responsible for assistance with reduction and interpretation and U-Pb geochronologic data.

Chapter 4 is a revised manuscript that was resubmitted in April 2017 to *Journal of Metamorphic Geology* as "Guevara, V.E., Caddick, M.J., and Dragovic, B., 2017, Rapid high-temperature decompression recorded by Archean granulites of the Northern Wyoming Province." ***VE Guevara*** conceived the project, performed the electron microprobe analyses, phase equilibria calculations, petrographic interpretations, diffusion modelling calculations, and manuscript preparation. *MJ Caddick* developed the diffusion model codes and assisted with data interpretation of the phase equilibria and diffusion modelling. B. Dragovic assisted with data interpretation and manuscript preparation.

Chapter 5 is a manuscript in preparation for submission to *Journal of Petrology*, tentatively as "Guevara, V.E., Maclennan, S.A., Schoene, B., Caddick, M.J., Dragovic, B., Kylander-Clark, A.R.C., and Couëslan, C.G., Timescales of Archean ultrahigh-temperature metamorphic processes: integration of high-spatial resolution and high-precision U-Pb petrochronology." ***VE Guevara*** conceived the project and was responsible for obtaining project funding from

Earthscope AGeS, fieldwork/sample collection, petrographic analysis, electron microprobe analyses, phase equilibia modelling, locating zircon and monazite grains in thin section, grain imaging/X-ray mapping, grain separation and mounting, laser ablation split-stream analyses, sample preparation for ID-TIMS-TEA analyses, data interpretation, and manuscript preparation. *SA Maclennan* performed ID-TIMS zircon and monazite analyses, performed solution-ICPMS analyses of monazite and zircon, and assisted with sample preparation and grain dissolution, as well as data interpretation. *B. Schoene* assisted with sample preparation for ID-TIMS analyses and data interpretation. *MJ Caddick* and *B Dragovic* assisted with data interpretation, manuscript preparation and presenation, fieldwork, and sample collection. *ARC Kylander-Clark* was responsible for reduction and interpretation of laser ablation split-stream geochronologic data and manuscript preparation. *CG Couëslan* was responsible for assistance with fieldwork and sample collection, petrographic analyses, manuscript preparation, and interpretation of data in a regional context.

TABLE OF CONTENTS

Chapter 1: Introduction

1.1 INTRODUCTION

Granulites are the dense and relatively anhydrous metamorphic rocks that are produced during high-temperature (HT, > 750 °C) to ultrahigh-temperature metamorphism (UHT, > 900 °C) of Earth's continental crust. The refractory nature of granulites (resulting from the loss of partial melt) makes them exceptionally strong (e.g. Menegon *et al.*, 2011; Williams *et al.*, 2014) – indeed, granulites are thought to comprise much of Earth's stable cratonic lower crust (Bohlen & Mezger, 1989; Rudnick & Fountain, 1995; Brown, 2013). Crustal metamorphism is the result of heating due to plate tectonic processes on modern Earth, and considerable progress has been made in understanding the tectonic mechanisms responsible for crustal heating to HT/UHT conditions and granulite genesis (e.g. Caggianelli & Prosser, 2002; Clark *et al.*, 2011; Ague *et al.*, 2012; Gordon *et al.*, 2012; Brown, 2014; Pownall *et al.*, 2014; Dorfler *et al.*, 2015; Kelsey & Hand, 2015). However, the extreme thermal conditions of HT/UHT metamorphism limit the utility of many petrologic and geochronologic techniques when applied to HT/UHT metamorphic rocks. For example, rapid diffusion at HT/UHT conditions can make thermobarometry based on exchange reactions misleading (e.g. Frost & Chacko, 1989), or can render many commonly-used geochronologic techniques ineffective, as isotopic closure temperatures are exceeded (e.g. Bloch *et al.*, 2015; Kelsey & Hand, 2015). Moreover, the generation and subsequent loss of partial melt makes it difficult to accurately determine the reactive bulk composition from which apparently equilibrated mineral assemblages grew, thus complicating the application of thermodynamic modelling techniques (e.g. White *et al.*, 2001; White *et al.*, 2004; White & Powell, 2011; Korhonen *et al.*, 2014) and/or the interpretation of accessory phase geochronology (e.g. Harley *et al.*, 2007; Harley & Nandakumar, 2014; Taylor *et al.*, 2016). Therefore, in many cases, the pressure–temperature–time (*P–T–t*) histories of HT/UHT metamorphic rocks remain elusive: how hot did they get? At what depths were they buried to? Over what timescales were HT/UHT conditions sustained, and how rapidly did they cool to ambient geothermal gradients? What *P–T* paths do HT/UHT rocks record? This information is necessary to evaluate the geodynamic mechanisms for extreme crustal heating (e.g. Brown, 2014; Kelsey & Hand, 2015; Harley, 2016).

Many Archean cratons preserve evidence for at least one period of HT/UHT metamorphism, suggesting that extreme crustal heating and granulite formation is integral to the stabilization of continental crust, but the tectonic mechanisms for crustal heating on the Archean Earth are poorly understood. Indeed, whether or not modern plate tectonic processes operated at all on the Archean Earth remains a subject of vigorous debate (e.g. de Wit, 1998; Brown, 2015). Unequivocal evidence for subduction and collision, such as, for example, paired metamorphic belts, blueschists and eclogites, ophiolites, and fold-and-thrust belts/accretionary wedges, remain elusive in the Archean rock record (e.g. Brown, 2007b; Stern, 2007; Palin & White, 2016). Moreover, partial melting of a hotter Archean mantle may have produced a thicker and weaker oceanic lithosphere than on modern Earth, making subduction difficult to initiate (e.g. Korenaga, 2006; Stern, 2007; van Hunen & van den Berg, 2008; Herzberg *et al.*, 2010; Johnson *et al.*, 2014). A hotter mantle would also result in less efficient coupling between a convecting mantle and overlying lithosphere (e.g. O'Neill *et al.*, 2007). These inferences, as well as those from 'dome and keel' from Archean granite-greenstone terranes, have led to the idea that a form of vertical, gravity-driven, stagnant-lid tectonics ("sagduction") prevailed in the Archean (e.g. Bédard *et al.*, 2003; Bédard, 2006; van Hunen & Moyen, 2012; O'Neill & Debaille, 2014). However, others have suggested modern subduction-accretion style processes were operating in the Archean, based on: 1) map patterns suggestive of lateral terrane accretion (e.g. Kusky, 1998; Schoene *et al.*, 2008; Cutts *et al.*, 2015), 2) geochemical evidence from Hadean detrital zircons and their inclusion assemblages that suggest the presence of granitic crust and relatively "cold" geothermal gradients (e.g. Harrison *et al.*, 2008), 3) the similarities between modern arc rocks and middle to late Archean granitoids (e.g. Laurent *et al.*, 2014), and 4) geochemical constraints that suggest deep (>12-15 kbar melting pressure) melting of a metabasaltic source was required to produce the ubiquitous Archean tonalite-trondjhemite-granodiorite (TTG) suites (e.g. Moyen & Martin, 2012), though this latter point does not preclude sagduction as a mechanism for such melting (e.g. Martin *et al.*, 2014; Johnson *et al.*, 2016; Palin *et al.*, 2016). Geodynamic models suggest that the Earth transitioned from a stagnant-lid tectonic regime to a subduction-like regime at some point in the Neoarchean (3.0-2.5 Ga; Sizova *et al.*, 2010), when ambient mantle temperatures were starting to cool from their peak at > 200 °C above present-day (Herzberg *et al.*, 2010). The transition predicted by geodynamic models agrees with existing constraints from the Archean metamorphic record (e..g Brown, 2007b; Brown, 2014), which suggest a secular

change in the style of metamorphism near the Archean-Proterozoic boundary, which in turn may record a secular change in tectonic regime.

However, the Archean metamorphic record remains relatively underexplored, particularly with respect to reconstruction and quantification of the *P–T–t* paths and metamorphic durations recorded by Archean HT/UHT metamorphic rocks through field-based, empirical study. This is necessary to assess the tectonic mechanisms that led to extreme crustal heating in the Archean, and whether or not such processes resemble those associated with modern-style plate tectonic processes. The research presented in this dissertation explores: 1) novel approaches to applying petrologic and geochronologic techniques to 'reading' HT/UHT metamorphic rocks and reconstructing their *P–T–*t histories, and 2) reconstruction and quantification of the *P–T–t* paths of Neoarchean granulites from two contrasting terranes, and how these paths, in the context of field observations and regional geology, inform our understanding of crustal heating mechanisms in the Archean.

In Chapter 2, "*Shooting at a moving target: phase equilibria modelling of high-temperature metamorphism"*, which was published in *Journal of Metamorphic Geology* in March 2016, I investigate how thermodynamic modelling of mineral equilibria over different length-scales may be useful for elucidating the *P–T* paths of texturally and compositionally heterogeneous granulites, in which the effective bulk composition from which apparently equilibrated mineral assemblages grew likely evolved over substantially along the *P–T* path. I show that at the hand-specimen scale, an EBC can be identified and used to constrain the *P–T* conditions at which the 'whole rock' was last in equilibrium, in the presence of intergranular melt that has subsequently been lost or consumed. Smaller macrodomains (~cm scale) and microdomains (~mm scale) can be identified that represent subsequent evolution during and after melt channelization and loss, and *P–T* pseudosections can be calculated for the compositions of these domains. Using this approach, I show that a texturally complex hand-sample from the Gruf complex, Central Alps, experienced a *P–T* path characterized by near-isothermal decompression after attainment of peak UHT conditions. Additionally, I show how the use of different thermodynamic datasets in phase equilibria modelling can lead to different interpretations of the petrologic evolution of a rock.

In Chapter 3, "*A pulse of cryptic granulite-facies metamorphism in the Archean Wyoming Craton revealed by Sm-Nd garnet and U-Pb monazite geochronology"*, which was published in

Precambrian Research in September 2016, I present new Sm-Nd garnet and U-Pb monazite geochronology from granulite-facies metasediments from the northern Wyoming Province in the eastern Beartooth Mountains, MT and WY, USA. These granulites exist as km-scale xenoliths in a large, ~2.83-2.79 Ga calc-alkaline batholith known as the Long Lake Magmatic Complex (LLMC). Bulk Sm-Nd garnet dates, combined with preserved major and trace element zoning in garnet, suggest that HT metamorphism occurred at ~2.70–2.68 Ga, long after emplacement of the LLMC. U-Pb monazite dates suggest two phases of metamorphism at ~2.78 and 2.69–2.67 Ga. Field evidence suggests that HT metamorphism of the metasediments post-dated LLMC emplacement. Simple diffusion modelling of major and trace elements in garnet show that: 1) residence at HT conditions was brief (likely < 1 Ma), and 2) the high mean square of the weighted deviates (MSWDs) of Sm-Nd bulk garnet dates likely result from polyphase garnet growth during metamorphic events widely separated in time, in agreement with the U-Pb monazite dates. Phase equilibria modelling of LLMC tonalite indicates that the LLMC did not partially melt during this later HT event, and I postulate that relatively anhydrous conditions prevented wholesale recrystallization of the LLMC, leaving any evidence for this later HT event cryptic in the LLMC. I propose that potentially widespread but weakly-recorded metamorphism, as shown here, could be a phenomenon observed in other metamorphic terranes.

In Chapter 4, "*Rapid high-temperature decompression recorded by Archean granulites of the northern Wyoming Province"*, which was resubmitted in April 2017 to *Journal of Metamorphic* Geology, I use phase equilibria modelling to reconstruct segments of the *P–T* path followed by the Beartooth granulites studied in Chapter 3, and, in light of these new *P–T* path constraints, use a *P–T* path-dependent diffusion model of major element zonation in garnet (in addition to the simple model in Chapter 3 in which diffusion only occurred at a static temperature) to constrain the timescales of different segments of the *P–T* path. I show that these rocks followed a tight, clockwise *P–T* path characterized by near-isobaric heating, near-isothermal decompression by ~0.5–1 kbar after attainment of peak *P–T* conditions of ~6.5 kbar, 800 °C, followed by cooling and decompression. Path-dependent diffusion modelling suggests that HT decompression was brief, and that cooling rates were likely on the order of 10–100 °C/Ma. The exhumation and cooling rates derived here are similar to those in modern convergent margin settings characterized by thick crust and high topography. Substantial changes (>25 °C/kbar) in apparent geothermal gradient along the *P–T* path, as well as the rapid

HT decompression inferred here point to advective or conductive heating, and may require input of mafic melts. Though voluminous mafic magmas are not evident in the eastern Beartooth mountains, I propose that conductive or advective heating associated with mafic intrusions at greater depths in the crustal column than currently exposed is possible, consistent with ~2.7–2.67 Ga mafic magmatism elsewhere in the Wyoming Province, ~60–200 km away from the Beartooth granulites.

In Chapter 5, "*Timescales of Archean ultrahigh-temperature metamorphic processes: integration of high-spatial resolution and high-precision U-Pb petrochronology*", I combine quantitative thermobarometry and U-Pb monazite and zircon petrochronology using high-spatial resolution laser ablation split-stream inductively coupled mass spectrometry (LASS) and high-precision isotope dilution thermal ionization mass spectrometry + solution ICP-MS trace element analyses (ID-TIMS-TEA) on a combination of *in-situ* grains and separated grain fragments to place constraints on the timescales of ultrahigh temperature (UHT) metamorphism recorded by a pelite from the Archean Pikwitonei granulite domain located on the northwest edge of the Superior Province. Thermodynamic modelling combined with microstructural analysis and mineral composition constraints suggest that the rock records peak *P–T* conditions of ~960 °C, 8.5-9 kbar, and experienced a *P–T* path characterized by UHT decompression followed by near-isobaric cooling at ~7.5-8 kbar. *In-situ* LASS monazite ages provide important information on the prograde metamorphic history of the sample, showing multiple generations of monazite with trace element signatures consistent with growth after/during garnet growth and feldspar breakdown from >2700-2675 Ma. *In-situ* LASS zircon data could be interpreted to record a single episode of zircon growth due to the high age uncertainties of LASS spot dates, and similar REE chemistries. In contrast, the TIMS-TEA zircon data reveal a more complex zircon crystallization history, with at least five apparently distinct episodes of zircon growth over a ~24 Ma period from 2674–2650 Ma, with REE chemistry of grain fragments within each episode suggesting variable feldspar growth and dissolution during this period. TIMS analyses of monazite show a similar apparent episodicity. This could record zircon/monazite growth in response to dynamic petrologic processes within localized equilibrium domains such as zircon/monazite melt saturation in isolated melt pockets, fluxing of externally-derived melt, or different local effective bulk compositions leading to different reaction histories among chemically isolated domains during melt crystallization and slow cooling. This study highlights

how *in-situ* LASS and ID-TIMS-TEA can be used as complementary techniques to constrain the metamorphic histories of Archean rocks: the high-spatial resolution *in-situ* LASS technique allowed for sampling of a volumetrically small prograde monazite population, while high-precision ID-TIMS-TEA reveals a complex accessory phase crystallization history that is not apparent in the LASS data but yields important insight into the petrologic evolution. Collectively, the data suggest that HT conditions may have been sustained over a long duration (>50 Ma) in the Pikwitonei granulite domain, and could reflect either multiple heating and cooling episodes over this period, or a single, long-lived metamorphic cycle characterized by decompression at UHT conditions followed by near-isobaric cooling in the mid- to lower crust.

Finally, In Chapter 6, I summarize the major findings of the work presented here, highlight new questions raised as a result of this work, and outline potential future avenues of research. At the time of this writing, work is underway to address some of these questions and future avenues of research.

1.2 REFERENCES

Ague, J. J., Eckert, J. O., Chu, X., Baxter, E. F. & Chamberlain, C. P., 2012. Discovery of ultrahigh-temperature metamorphism in the Acadian orogen, Connecticut, USA. *Geology*.

Bédard, J. H., 2006. A catalytic delamination-driven model for coupled genesis of Archaean crust and sub-continental lithospheric mantle. *Geochimica Et Cosmochimica Acta*, **70**, 1188-1214.

Bédard, J. H., Brouillette, P., Madore, L. & Berclaz, A., 2003. Archaean cratonization and deformation in the northern Superior Province, Canada: an evaluation of plate tectonic versus vertical tectonic models. *Precambrian Research*, **127**, 61-87.

Bloch, E., Ganguly, J., Hervig, R. & Cheng, W., 2015. 176Lu–176Hf geochronology of garnet I: experimental determination of the diffusion kinetics of Lu3+ and Hf4+ in garnet, closure temperatures and geochronological implications. *Contributions to Mineralogy and Petrology*, **169**, 12.

Bohlen, S. R. & Mezger, K., 1989. Origin of Granulite Terranes and the Formation of the Lowermost continental Crust. *Science*, **244**, 326-329.

Brown, M., 2007. Metamorphic conditions in orogenic belts: A record of secular change. *International Geology Review*, **49**, 193-234.

Brown, M., 2013. Granite: From genesis to emplacement. *Geological Society of America Bulletin*, **125**, 1079-1113.

Brown, M., 2014. The contribution of metamorphic petrology to understanding lithosphere evolution and geodynamics. *Geoscience Frontiers*, **5**, 553-569.

Brown, M., 2015. Paleo- to Mesoarchean polymetamorphism in the Barberton Granite-Greenstone Belt, South Africa: Constraints from U-Pb monazite and Lu-Hf garnet geochronology on the tectonic processes that shaped the belt: Discussion. *Geological Society of America Bulletin*, **127**, 1550-1557.

Caggianelli, A. & Prosser, G., 2002. Modelling the thermal perturbation of the continental crust after intraplating of thick granitoid sheets: a comparison with the crustal sections in Calabria (Italy). *Geological Magazine*, **139**, 699-706.

Clark, C., Fitzsimons, I. C. W., Healy, D. & Harley, S. L., 2011. How Does the Continental Crust Get Really Hot? *Elements*, **7**, 235-240.

Cutts, K. A., Stevens, G. & Kisters, A., 2015. Reply to "Paleo- to Mesoarchean polymetamorphism in the Barberton granite-greenstone belt, South Africa: Constraints from U-Pb monazite and Lu-Hf garnet geochronology on the tectonic processes that shaped the belt: Discussion" by M. Brown. *Geological Society of America Bulletin*, **127**, 1558-1563.

de Wit, M. J., 1998. On Archean granites, greenstones, cratons and tectonics; does the evidence demand a verdict? *Precambrian Research*, **91**, 181-227.

Dorfler, K. M., Caddick, M. J. & Tracy, R. J., 2015. Thermodynamic Modeling of Crustal Melting Using Xenolith Analogs from the Cortlandt Complex, New York, USA. *Journal of Petrology*, **56**, 389–408.

Frost, B. R. & Chacko, T., 1989. The granulite uncertainty principle; limitations on thermobarometry in granulites. *Journal of Geology*, **97**, 435-450.

Gordon, S. M., Luffi, P., Hacker, B., Valley, J., Spicuzza, M., Kozdon, R., Kelemen, P., Ratshbacher, L. & Minaev, V., 2012. The thermal structure of continental crust in active orogens: insight from Miocene eclogite and granulite xenoliths of the Pamir Mountains. *Journal of Metamorphic Geology*, **30**, 413-434.

Harley, S. L., 2016. A matter of time: The importance of the duration of UHT metamorphism. *Journal of Mineralogical and Petrological Sciences*, **111**, 50-72.

Harley, S. L., Kelly, N. M. & Möller, A., 2007. Zircon Behaviour and the Thermal Histories of Mountain Chains. *Elements*, **3**, 25-30.

Harley, S. L. & Nandakumar, V., 2014. Accessory Mineral Behaviour in Granulite Migmatites: a Case Study from the Kerala Khondalite Belt, India. *Journal of Petrology*, **55**, 1965-2002.

Harrison, T. M., Schmitt, A. K., McCulloch, M. T. & Lovera, O. M., 2008. Early (≥ 4.5 Ga) formation of terrestrial crust: Lu–Hf, δ 18 O, and Ti thermometry results for Hadean zircons. *Earth and Planetary Science Letters*, **268**, 476-486.

Herzberg, C., Condie, K. & Korenaga, J., 2010. Thermal history of the Earth and its petrological expression. *Earth and Planetary Science Letters*, **292**, 79-88.

Johnson, T. E., Brown, M., Goodenough, K. M., Clark, C., Kinny, P. D. & White, R. W., 2016. Subduction or sagduction? Ambiguity in constraining the origin of ultramafic–mafic bodies in the Archean crust of NW Scotland. *Precambrian Research*, **283**, 89-105.

Johnson, T. E., Brown, M., Kaus, B. J. P. & VanTongeren, J. A., 2014. Delamination and recycling of Archaean crust caused by gravitational instabilities. *Nature Geoscience*, **7**, 47-52.

Kelsey, D. E. & Hand, M., 2015. On ultrahigh temperature crustal metamorphism: Phase equilibria, trace element thermometry, bulk composition, heat sources, timescales and tectonic settings. *Geoscience Frontiers*, **6**, 311-356.

Korenaga, J., 2006. Archean geodynamics and the thermal evolution of Earth. In: *Archean Geodynamics and Environments Geophys. Monogr. Ser.*, pp. 7-32, AGU, Washington, DC.

Korhonen, F. J., Clark, C., Brown, M. & Taylor, R. J. M., 2014. Taking the temperature of Earth's hottest crust. *Earth and Planetary Science Letters*, **408**, 341-354.

Kusky, T. M., 1998. Tectonic setting and terrane accretion of the Archean Zimbabwe craton. *Geology*, **26**, 163-166.

Laurent, O., Martin, H., Moyen, J. F. & Doucelance, R., 2014. The diversity and evolution of late-Archean granitoids: Evidence for the onset of "modern-style" plate tectonics between 3.0 and 2.5 Ga. *Lithos*, **205**, 208-235.

Martin, H., Moyen, J.-F., Guitreau, M., Blichert-Toft, J. & Le Pennec, J.-L., 2014. Why Archaean TTG cannot be generated by MORB melting in subduction zones. *Lithos*, **198**, 1-13.

Menegon, L., Nasipuri, P., Stunitz, H., Behrens, H. & Ravna, E., 2011. Dry and strong quartz during deformation of the lower crust in the presence of melt. *Journal of Geophysical Research-Solid Earth*, **116**.

Moyen, J.-F. & Martin, H., 2012. Forty years of TTG research. *Lithos*, **148**, 312-336.

O'Neill, C. & Debaille, V., 2014. The evolution of Hadean–Eoarchaean geodynamics. *Earth and Planetary Science Letters*, **406**, 49-58.

O'Neill, C., Jellinek, A. & Lenardic, A., 2007. Conditions for the onset of plate tectonics on terrestrial planets and moons. *Earth and Planetary Science Letters*, **261**, 20-32.

Palin, R. M. & White, R. W., 2016. Emergence of blueschists on Earth linked to secular changes in oceanic crust composition. *Nature Geoscience*, **9**, 60-64.

Palin, R. M., White, R. W. & Green, E. C., 2016. Partial melting of metabasic rocks and the generation of tonalitic–trondhjemitic–granodioritic (TTG) crust in the Archaean: Constraints from phase equilibrium modelling. *Precambrian Research*, **287**, 73-90.

Pownall, J. M., Hall, R., Armstrong, R. A. & Forster, M. A., 2014. Earth's youngest known ultrahigh-temperature granulites discovered on Seram, eastern Indonesia. *Geology*, **42**, 279-282.

Rudnick, R. L. & Fountain, D. M., 1995. Nature and composition of the continental crust - a lower crustal perspective. *Reviews of Geophysics*, **33**, 267-309.

Schoene, B., de Wit, M. J. & Bowring, S. A., 2008. Mesoarchean assembly and stabilization of the eastern Kaapvaal craton: A structural-thermochronological perspective. *Tectonics*, **27**.

Sizova, E., Gerya, T., Brown, M. & Perchuk, L. L., 2010. Subduction styles in the Precambrian; insight from numerical experiments. *Lithos (Oslo)*, **116**, 209-229.

Stern, R. J., 2007. When and how did plate tectonics begin? Theoretical and empirical considerations. *Chinese Science Bulletin*, **52**, 578-591.

Taylor, R. J. M., Kirkland, C. L. & Clark, C., 2016. Accessories after the facts: Constraining the timing, duration and conditions of high-temperature metamorphic processes. *Lithos*, **264**, 239-257.

van Hunen, J. & Moyen, J. F., 2012. Archean Subduction: Fact or Fiction? *Annual Review of Earth and Planetary Sciences, Vol 40*, **40**, 195-219.

van Hunen, J. & van den Berg, A. P., 2008. Plate tectonics on the early Earth: Limitations imposed by strength and buoyancy of subducted lithosphere. *Lithos*, **103**, 217-235.

White, R., Powell, R. & Halpin, J., 2004. Spatially-focussed melt formation in aluminous metapelites from Broken Hill, Australia. *Journal of Metamorphic Geology*, **22**, 825-845.

White, R., Powell, R. & Holland, T., 2001. Calculation of partial melting equilibria in the system Na2O–CaO–K2O–FeO–MgO–Al2O3–SiO2–H2O (NCKFMASH). *Journal of metamorphic Geology*, **19**, 139-153.

White, R. W. & Powell, R., 2011. On the interpretation of retrograde reaction textures in granulite facies rocks. *Journal of Metamorphic Geology*, **29**, 131-149.

Williams, M. L., Dumond, G., Mahan, K., Regan, S. & Holland, M., 2014. Garnet-forming reactions in felsic orthogneiss: Implications for densification and strengthening of the lower continental crust. *Earth and Planetary Science Letters*, **405**, 207-219.

Chapter 2. Shooting at a moving target: phase equilibria modelling of high-temperature metamorphism

V.E. Guevara[1] and M.J. Caddick[1]

Department of Geosciences, Virginia Polytechnic Institute and State University, Blacksburg, VA 24061, USA

Published March 2016 in *Journal of Metamorphic Geology,* 34, 209-235

2.1 ABSTRACT

Thermodynamic modeling and the calculation of *P–T* pseudosections are commonly employed for quantifying the *P–T* evolution of metamorphic rocks. A key assumption involved in interpreting a *P–T* pseudosection is that the bulk-rock composition used is representative of the effective bulk composition (EBC) from which apparently equilibrated mineral assemblages grew. Choosing an EBC can be difficult in cases where the rock has evolved significantly throughout the *P–T* history and has become domainal for whatever reason (e.g. loss of fluid and/or melt), particularly at suprasolidus conditions. During partial melting, melt migration may not only change the bulk composition by melt loss but also may generate local variations due to the variable consumption/loss of melt from domain to domain to create volumes of rock that were once internally equilibrated in the presence of a grain boundary melt, but which departed from equilibrium as inter-granular mobility was slowed by local reductions in melt volume. As well as careful consideration of an EBC, the results of thermodynamic modeling are highly dependent on the specific thermodynamic dataset and solution models used, as updates to these datasets may lead to substantially different calculated phase equilibria.

This contribution addresses: 1) how consideration of evolving EBCs at multiple scales of observation can be used to resolve the history of complex high-grade rocks, and 2) how use of different thermodynamic datasets and *a–x* models (i.e. THERMOCALC ds5.5 vs. ds6) can result in different interpretations of metamorphic evolution. This study investigates the evolution of a mineralogically heterogeneous and texturally complex hand sample of granulite from the Gruf Complex (Central Alps). At the hand-specimen scale an EBC can be identified and used to constrain the *P–T* conditions at which the 'whole-rock' was last in mutual equilibrium, in the presence of intergranular melt that has subsequently been lost or consumed. Smaller macrodomains (~cm scale) and microdomains (~mm scale) can be identified that represent subsequent evolution during and after melt channelization and loss, and *P–T* pseudosections can be calculated for the compositions of these domains. Using this approach reveals that the sample experienced a clockwise *P–T* path marked by near–isothermal decompression following attainment of peak UHT conditions (~960 ˚C, 8.5 kbar). The approach enables construction of a *P–T* history of a rock for which *P–T* pseudosections are otherwise difficult to interpret. Thermodynamic modeling using ds6 yields similar results to those stated above, but suggests: 1) near–isothermal decompression occurred over a wider *P* range (~0.5 kbar vs. 1.5 kbar), and 2) that not all microdomains record this part of the *P–T* evolution.

2.2 INTRODUCTION

A common objective in metamorphic studies is to accurately determine the pressure-temperature (*P–T*) paths recorded by rocks. Such *P–T* paths ultimately lead to a better understanding of many facets of the Earth system, including crustal architecture and rheology, geothermal gradients, and the flow of heat, mass, and fluids in the crust, all of which have profound implications for understanding global-scale geodynamic processes. Recent advances in petrologic techniques have resulted in increasing confidence in the *P–T* histories recorded by metamorphic rocks. In part this can be attributed to the advent of quantitative pressure–temperature–composition (*P–T–*

X) pseudosection modeling using internally consistent thermodynamic datasets and solution models, which have seen widespread application and development in studies of various tectonic settings (e.g. Powell *et al.*, 1998; Waters & Lovegrove, 2002; White & Powell, 2002; Harris *et al.*, 2004; Johnson & Brown, 2004; Konrad-Schmolke *et al.*, 2005; Štipska & Powell, 2005; Galli *et al.*, 2007; Spear & Pyle, 2010; Vorhies & Ague, 2011; Korhonen *et al.*, 2012; Yakymchuk *et al.*, 2015).

A key assumption involved in constructing and interpreting a *P–T* pseudosection is that the input rock composition is representative of the effective bulk composition (EBC) from which apparently equilibrated mineral assemblages and textures developed (e.g. Stüwe, 1997; Johnson & Brown, 2004), implying that a single chemical potential (μ) can be constrained for each component at any given *P* and *T*. During metamorphism, equilibrium between mineral grains is achieved over constantly evolving time- and length scales during progress through *P–T* space (e.g. Carlson, 2002; Powell *et al.*, 2005), with development of distinct textures representing a complex interplay between processes that act to reduce chemical potential (μ) gradients (e.g. mineral dissolution, mass transfer, crystal growth or re-equilibration) and processes that may maintain or increase μ gradients (e.g. changing *P* or *T*, or influx of material from a fluid). Equilibrium is typically efficiently maintained when fluid or melt along grain boundaries facilitates rapid intergranular transport (Guiraud *et al.*, 2001; Carlson, 2010), for example in the case of prograde dehydration and melting reactions. This implies that metamorphic rocks preserve limited μ gradients for many components, at least within localized domains (Korzhinskii, 1959; Thompson, 1959). Thus, segments of the prograde metamorphic evolution may be deduced with *P–T* pseudosections if the scale of these domains can be identified, with progressive fractionation of subsequently unreactive porphyroblast phases from the effective bulk composition commonly considered in this regard (e.g. Spear *et al.*, 1991; Marmo *et al.*, 2002; Caddick *et al.*, 2007; Konrad-Schmolke *et al.*, 2008). Accurate determination of *P–T* of equilibration is also subject to the assumption that original mineral growth compositions are preserved (Florence & Spear, 1991; Caddick *et al.*, 2010).

Granulite facies rocks have typically experienced extensive dehydration, partial melting, and subsequent fluid/melt extraction. Several lines of evidence suggest open-system melting and melt removal in natural examples, such as the preservation of high-grade, nominally anhydrous mineral assemblages, residual bulk compositions consistent with extraction of large volumes of

felsic melt, and structures suggestive of amalgamation of anatectic melt from a residual source (e.g. Sawyer, 1996; Brown & Solar, 1998; Solar & Brown, 2001; Brown, 2002; White & Powell, 2002; Baldwin *et al.*, 2005; Brown *et al.*, 2011; Kelsey & Hand, 2014). These combined processes of silicate melt and hydrous fluid extraction and/or consumption ultimately modify equilibration volumes, and domains of rock that were in equilibrium with each other in the presence of grain boundary fluid depart from equilibrium (over appropriate timescales) as intergranular mobility is slowed greatly by fluid loss or consumption (Guiraud *et al.*, 2001). For example, data from Carlson (2010) suggest that equilibration for 1 Myr at 800 ˚C will result in characteristic Al diffusion distances of 1–10 cm in the presence of hydrous fluid but only ~ 100 μm in an anhydrous rock.

This reduction of equilibration length scales is typically manifested by the formation of mineralogically, chemically, and texturally distinct domains at the sub-m to μm scale, evolving to progressively smaller domains as the ability of the system to flatten chemical potential gradients is reduced (e.g. White & Powell, 2002; Baldwin *et al.*, 2005; White & Powell, 2011). The evolution of residual rocks after fluid/melt loss may then be more effectively explored by thermodynamic modeling of local compositions of these distinct domains than by using a whole-rock composition. This approach relies upon identification of a volume of material in which mineralogical and textural development appears to have occurred locally, yet preserved chemical potential gradients are minimal. Though this is a difficult task, several studies have accomplished this with success (e.g. Harris *et al.*, 2004; Johnson *et al.*, 2004; Baldwin *et al.*, 2005; Nasipuri *et al.*, 2009; Belyanin *et al.*, 2012; Anderson *et al.*, 2013; Kelsey & Hand, 2014; Lanari *et al.*, 2014; Walsh *et al.*, 2014). Upon complete fluid/melt loss, equilibration is likely to become extremely sluggish, and the assumption of flattened chemical potential gradients across even μm-scale volumes of rock fails, rendering interpretations based on *P–T* pseudosections potentially misleading. Chemical potential (μ-μ) diagrams have been shown to yield additional useful constraints on metamorphic evolution in this case (White *et al.*, 2008; Stipska *et al.*, 2010; White & Powell, 2011; Baldwin *et al.*, 2015), but simple and effective methodologies for inferring equilibrium domains in the stages leading to this point are still lacking.

In addition to choosing an appropriate EBC, the results and interpretations of phase equilibria modeling may depend on the specific thermodynamic dataset and solution models used. Several internally-consistent thermodynamic datasets and corresponding solution models

have been developed (e.g. Berman, 1988; Holland & Powell, 1990, 1998; White *et al.*, 2000; Holland & Powell, 2003; White *et al.*, 2007; White *et al.*, 2014a). Updates to these datasets can lead to substantially different calculated phase equilibria, and therefore may lead the petrologist to a different interpretation of the metamorphic evolution of a given rock (Korhonen *et al.*, 2014).

The foregoing considerations have been frequently discussed, but their incorporation into methodologies for determining the *P–T* evolution of high-grade metamorphic rocks has proven challenging. This paper aims to address: 1) the question of how evolving equilibration domains can be accounted for with thermodynamic modeling, showing how multiple 'scales of observation' can be used to successfully resolve a relatively simple *P–T* history from a seemingly complex high-grade rock, and 2) how use of different thermodynamic datasets may lead to different interpretations of metamorphic evolution. To illustrate this, the evolution of a single, texturally and mineralogically complex and heterogeneous hand sample (Figs 2.1 & 2.2) that records ultrahigh temperature (UHT) metamorphism at > 900 ˚C (Galli *et al.*, 2011) is investigated. Following the above discussion, this contribution shows that an effective "whole-rock" bulk composition (over which chemical potentials were flattened) can be identified and used to determine the *P–T* conditions at which equilibration length scales were last at >cm scale, in the presence of melt that has subsequently been partially lost and/or channelized. Smaller macrodomains (cm-scale) and microdomains (mm- to sub-mm-scale) are identified that record evolution during or after this melt loss/channelization, and *P–T* pseudosections can be calculated for the compositions of these domains. These calculations, which are based on observations and measurements over three orders of magnitude in length scale (Fig. 2.3), reveal a heating–decompression history of the sample in question. However, this interpretation is dependent on the thermodynamic data used, with recalculation using a new dataset (ds6 of Holland and Powell (2011)) and re-parameterized solution models (White *et al.*, 2014b) yielding subtly but importantly different conclusions than calculations with THERMOCALC dataset ds5.5 (Holland & Powell, 1998) and older solution models (White *et al.*, 2007).

2.3 GEOLOGIC BACKGROUND

The Gruf Complex is a body of high-grade rocks approximately 10 x 20 km in size, located in the Central Alps at the southeastern margin of the Lepontine metamorphic dome (Fig. A1). It is bordered by the Chiavenna ophiolite and Tambo Nappe to the north, the 32-30 Ma Bergell

Pluton to the east, and the Novate granite and Adula Nappe to the south and west. The Gruf Complex is lithologically distinct from these various plutons and nappes and is dominantly comprised of migmatitic quartzofeldspathic gneisses and pelitic rocks that experienced peak metamorphic conditions in the upper amphibolite facies of ~700-750 °C, 6-8 kbar between 34 and 29 Ma (Galli *et al.*, 2011; Galli *et al.*, 2012). Rare boulders of Mg–Al-rich sapphirine bearing granulites were first discovered in two talus slopes by Cornelius (1916), and further investigated Bucher-Nurminen and Droop (1983). Galli (2010) mapped the area in detail, and found that these Mg–Al rich granulites occur as cm- to m-sized enclaves and schlieren both within the migmatitic orthogneisses and in charnockites. The sample analyzed in this study was collected from a large, m-size boulder in the main river of Val Codera by A. Galli (Figs 1 & S1). The charnockites form east–west striking sheet-like bodies separated from the surrounding quartzofeldspathic gneisses by ~50 cm thick shear zones (Galli *et al.*, 2011). Droop and Bucher-Nurminen (1984) suggested that the Gruf granulites reached peak metamorphic conditions at `>800°C, 10 kbar, followed by near–isothermal decompression and the formation of symplectitic coronae at 750°C, 5 kbar. More recent quantitative thermobarometry and phase equilibria modeling has suggested that granulites and charnockites from the Gruf complex record UHT peak *P–T* conditions of 920-960 °C, 8.5-9.5 kbar, and that symplectitic corona textures record conditions of 720-740°C, 7-7.5 kbar (Galli *et al.*, 2011; Oalmann *et al.*, 2013a).

The timing of UHT metamorphism and, consequently, the *P–T* evolution of the Gruf granulites, is controversial. Several workers attribute an Eocene age to the UHT metamorphism, suggesting that extreme crustal temperatures were achieved during Alpine orogenesis, with slab break–off and associated asthenospheric mantle upwelling providing additional heat for UHT metamorphism (Liati & Gebauer, 2003; Schmitz *et al.*, 2009; Möller *et al.*, 2012; Oalmann *et al.*, 2013a; Oalmann *et al.*, 2013b). Others suggest that UHT conditions were attained in the Permian due to mafic underplating during collapse of the Variscan orogen, with symplectitic coronae representing partial re-equilibration during Alpine orogenesis at *P–T* conditions similar to those of the upper-amphibolite facies gneisses of the Gruf complex and the rest of the Central Alps (Galli *et al.*, 2011; Galli *et al.*, 2012). *P–T* path-dependent garnet diffusion modeling by Galli *et al.* (2011) suggests rapid (1 Myr or less) heating and cooling to/from peak UHT conditions. Though peak *P–T* conditions of UHT metamorphism and conditions of symplectite formation are relatively well-established, there is little constraint on the *immediate* post-peak metamorphic

evolution of the Gruf granulites, which may shed light on the tectonic environment in which UHT conditions were achieved. This contribution aims to constrain the pre-peak, peak, and immediately post-peak metamorphic conditions from a single hand sample. The question of mono- or polycyclic metamorphism is not directly addressed here; instead this study is mainly focused on questioning the extent to which pseudosection methods can be applied to infer successive *P–T* conditions of equilibration in complex, residual, UHT granulites. In particular, formation of some of the lower-temperature symplectites described and interpreted by Galli et al. (2011) to represent a discrete, post-UHT metamorphic event are not investigated in this study.

2.4 METHODS

The thermodynamic modeling in this study uses input compositions derived from: 1) distinct domains visible in hand sample on the > cm scale ('macrodomains'); 2) a weighted sum of the macrodomain compositions to approximate a bulk (whole-rock) composition; and 3) local, textural domains on the mm to sub-mm scale ('microdomains'). Here, a macrodomain is defined as a distinct volume of rock for which mineralogical and textural homogeneity is apparent in hand sample. A microdomain is defined as an area of a thin section that displays evidence for localized mineral reaction at the grain scale. Three main macrodomains in the ~ 30 × 15 × 15 cm hand sample can be defined based primarily on the size and distribution of garnet porphyroblasts, and are discussed in the following section (Figs 2.1 & 2.2). At least one polished thin section was made for each macrodomain (Fig. 2.2). Petrographic study reveals several distinct mineral textures (microdomains) within each of the macrodomains.

Major element mineral compositions were determined through wavelength dispersive spectrometry (WDS) on a Cameca SX-50 electron probe microanalyzer at Virginia Tech. Operating conditions for spot analyses were a 15 kv accelerating voltage, 20 nA beam current, 40 s count time, and a beam diameter of < 5 μm. Representative analyses of petrologically important phases are shown in Table 2.1 and discussed below.

Representative pieces of each macrodomain were identified by eye and mechanically separated from each other (and from any leucosome veins/patches) for XRF analysis. Major element compositions were determined by X-ray fluorescence spectroscopy (XRF, Table 2.2a) using a Phillips 2404 XRF vacuum spectrometer at Franklin and Marshall College, USA, together with loss on ignition (LOI). FeO content was analyzed by Fe^{2+} titration.

Microdomain major element compositions were determined by thin section area analyses using a CAMSCAN Series II scanning electron microscope (SEM) fitted with a Bruker electron dispersive spectrometer (EDS) at Virginia Tech. EDS spectra of major elements were collected for pre-defined areas (typically between 0.25 and 4 mm^2) using a 15 kv accelerating voltage, 40 nA beam current, and 90 s counting time. Peak-height ratios of the resultant spectra were calibrated against both natural and synthetic standards to yield semi-quantitative compositional data, assuming that the 2D mapped area is appropriate for a 3D equilibration volume. Different areas were mapped for each texture of interest with this EDS method, so that the effective equilibration domain could be determined iteratively by calculating pseudosections for the composition of each area and comparing these with the observed texture. For example, choosing an inappropriate domain might result in in the absence of certain phases from the pseudosection that are present in the observed texture (e.g. sapphirine, sillimanite, spinel), or vice versa.

The relative mobility of each of the chemical components forming the preserved mineral assemblages probably varied dramatically at any given *P–T* condition during the rock's metamorphic evolution. Previous work shows that the relative intergranular transport rates of major mineral-forming species can vary with fluid availability and composition (e.g. Carlson, 2010; Carlson *et al.*, 2015) but that Al_2O_3 mobility is commonly rate limiting in texture development (e.g. Carmichael, 1969; Foster, 1999; Kelly *et al.*, 2013), and components such as H_2O can generally be modeled assuming open system behavior (e.g. Korzhinskii, 1959; Thompson, 1959; Walther & Orville, 1982). This implies that definition of a single domain boundary within which *all* species were effectively open to communication over the same time and length scale is impossible (i.e. mobile components such as H_2O and Na_2O may have been 'open' outside of this domain while species such as Al_2O_3 may have retained μ gradients below the scale of the domain at the time of its apparent equilibration). Calculated phase equilibria for numerous possible versions of a compositional domain for each texture thus only allow for a 'best compromise' composition that is most consistent with equilibration of the observed and calculated assemblages. Agreement between observation and model suggests that the chosen effective composition is appropriate, implying that the inferred equilibration domain is not substantially larger than the actual equilibration length scales of slowly diffusing species. This compromise is implicit in *all* constructed pseudosections, including those representing hand-specimen scale samples, which require the assumption that chemical potential gradients of each

species are negligible across the volume of interest but that closed system behavior is obeyed for all constrained components over the equilibration time- and length scales recorded (i.e. that metasomatism has not modified the sample during metamorphism). Major element microdomain bulk compositions determined via the SEM method described above are shown in Table 2.3a.

Initial *P–T* pseudosections (e.g. Figs 2.5-2.9, 2.11, 2.12, A2-A4) were constructed using Perple_X (version 6.6: Connolly, 2005) and dataset version 5.5 of Holland & Powell (1998) in the model system NCKFMASHTO, considering the following solution phase descriptions: biotite (Tajcmanova *et al.*, 2009), silicate melt (White *et al.*, 2007), cordierite, garnet, chlorite, and staurolite (Holland & Powell, 1998), feldspar (Holland & Powell, 2003), ilmenite–hematite (White *et al.*, 2000; hereafter referred to as ilmenite, or 'Ilm' in the phase diagrams in Figs 2.5-2.9, 2.11, 2.12), sapphirine (Taylor-Jones & Powell, 2010), spinel (White *et al.*, 2002), and white mica (Coggon & Holland, 2002). MnO was excluded because it would have little effect at the *P–T* conditions of interest here (White *et al.*, 2014b). *P–T* pseudosections for macrodomains were constructed using compositions determined by XRF, with titration providing a maximum constraint on Fe_2O_3 content and LOI providing a maximum constraint on *current* H_2O content. Since the primary granulite-facies assemblages are well preserved and the rock contains <5% leucosome, macrodomain compositions are interpreted to represent a residuum of a protolith that has been modified by melt loss. H_2O content for both macrodomains and microdomains was thus set so that the inferred equilibrium assemblage was stable as close as possible to the solidus without contravening petrographic observations, to represent equilibration in the presence of melt prior to melt loss/consumption (following e.g. Korhonen *et al.*, 2013; Diener *et al.*, 2014). Lower H_2O contents than those utilized here predict the stability of phases that appear to have been absent throughout the metamorphic history, as detailed in Fig. A3 and further discussed below. Fe_2O_3 content was estimated with T–M_{Fe2O3} diagrams, using constraints from the peak metamorphic assemblage and the titration results.

2.5 RESULTS AND INTERPRETATIONS

In the following section, the hand sample scale equilibration domains and associated results of thermodynamic modeling are first described (macrodomains C, F and CF highlighted in Fig. 2.1). A single hand sample scale bulk composition, estimated by combining the compositions of the macrodomains proportionally, is then investigated for inferring the earlier evolution. Finally, microdomains are addressed, in which equilibration appears to have been on approximately the

mm-scale. For each domain, textural, mineralogical, and chemical features are presented first, followed by the results and interpretations of thermodynamic modeling.

2.5.1 Macrodomains: petrography and mineral chemistry

The hand sample exhibits an unfoliated, massive texture (Fig. 2.1). The preservation of granulite facies assemblages indicates that the original protolith composition has been substantially modified by melt loss prior to cooling below the solidus (e.g. White & Powell, 2002). Thin (0.5-2 cm thick), randomly oriented leucocratic veins/patches comprise less than 5 vol. % of the rock and are interpreted to represent retained but channelized and possibly modified melt (Figs 2.1 & 2.2). Three macrodomains are visible in hand sample, based on the size and distribution of garnet porphyroblasts: a coarse-grained domain characterized by sparse garnet crystals as large as 10 mm in diameter (macrodomain C); a fine-grained domain characterized by closely spaced, <2 mm garnet crystals (macrodomain F); and a bimodal domain with closely spaced fine and coarse garnet crystals (macrodomain CF) (Fig. 2.1). Textural and compositional features common to each macrodomain are described in the following paragraph, while nuanced differences between macrodomains are described separately in the subsequent subsections below.

All macrodomains contain porphyroblastic garnet and orthopyroxene. Garnet is weakly zoned in CaO, with generally higher X_{grs} cores (~0.05-0.1), than rims (0.04-0.05; Table 2.1a). FeO, MgO, and MnO are relatively homogeneous throughout, except at crystal rims, where X_{alm} generally increases (from ~0.50 to ~0.55-0.60) and X_{pyr} generally decreases (from ~0.39-0.40 to 0.38-0.33; Table 2.1a). Porphyroblastic orthopyroxene is zoned, with low Al_2O_3 cores and rims (~5-6.5 wt.%) and the highest Al_2O_3 content (~7.5-9.9 wt.%) at annuli near the rims (Table 2.1b), as documented by Galli *et al.* (2011). Biotite occurs as inclusions in porphyroblastic garnet and orthopyroxene, as highly resorbed, primary flakes in the matrix, and as late grains that cross-cut or surround other minerals. Primary biotite contains ~4.5-5.3 wt. % TiO_2 (Table 2.1c) and is commonly separated from porphyroblastic minerals by a moat of cordierite. Late biotite forms unoriented, subhedral to euhedral flakes (or clusters of flakes) that commonly cross-cut and surround porphyroblastic orthopyroxene, garnet, and/or primary biotite (e.g. "retrogressed area" in Fig. 2.2; Fig. 2.4 a,b) and contain 2.2-4.1 wt.% TiO_2 (Table 2.1c). Clusters of fine-grained sillimanite with or without wormy intergrowths of spinel occur in the matrix near embayments in garnet and orthopyroxene porphyroblasts, surrounded by cordierite and/or plagioclase (Fig. 2.4a). Such embayments generally follow the shape of the sillimanite ± spinel clusters. Spinel

also occurs as inclusions in garnet, possibly reflecting breakdown/replacement of earlier-formed staurolite inclusions, prior to significant partial melting (Galli et al., 2011). Cordierite is found in the matrix of each macrodomain, surrounding garnet, orthopyroxene, and biotite. Symplectitic coronae of cordierite and lamellar orthopyroxene commonly surround resorbed, rounded garnet porphyroblasts (Fig 2.4b-d). Lamellar orthopyroxene contains similar Al_2O_3 contents to porphyroblastic cores and rims, and less than porphyroblastic annuli. Plagioclase occurs as inclusions in garnet and orthopyroxene and as coarse, anhedral, resorbed/ rounded grains in the matrix (such as that described for Microdomain 03-03 below), surrounded by late biotite and cordierite, or on the rim of resorbed garnet. Despite thorough searches with optical and electron microscopy, potassium feldspar was not observed in any of the macrodomains. Quartz occurs as coarse (up to ~1 mm diameter), rounded grains in the matrix exhibiting chessboard extinction (Fig. 2.4c; interpreted to be a prograde/peak phase) and as rounded inclusions in garnet and orthopyroxene (Fig. 2.4d; interpreted as a prograde phase). Finer-grained matrix intergrowths of quartz, cordierite, and plagioclase may be interpreted as crystallized melt (all three interpreted as retrograde phases in this textural setting). Rutile and ilmenite both occur as inclusions in garnet, orthopyroxene, and biotite, with ilmenite also occurring as subhedral to anhedral grains in the matrix. Late-forming minerals in all macrodomains include cordierite, biotite, plagioclase, lamellar orthopyroxene, quartz, sillimanite, spinel, and ilmenite.

Though *all* of the macrodomains exhibit the mineral occurrences and textures described above, subtle differences between each macrodomain are evident, with each macrodomain exhibiting features unique to it, as described in the following section. A 'macrodomain assemblage' can be defined for each macrodomain, representing the mineral assemblage inferred to have last equilibrated on the macrodomain scale. The term 'peak assemblage' is not used, as macrodomain and microdomain equilibration (and thus different equilibrium assemblages associated with each) both appear to have occurred close to the peak *T* (shown and described below). Table 2.2a shows bulk compositions of each macrodomain determined through XRF. Table 2.2b shows the bulk composition for each macrodomain used for thermodynamic modeling after adjusting H_2O and Fe_2O_3 content.

Macrodomain C

Macrodomain C is characterized by garnet porphyroblasts up to 10 mm in diameter (Figs 2.1 & 2.2). Retrograde biotite is abundant, enveloping garnet and orthopyroxene or occurring as

clusters in interstitial spaces between porphyroblasts ('retrogressed area' in Figs 2.2 & 2.4a,b). Primary biotite, containing up to 4.9 wt.% TiO_2, is much less abundant than retrograde biotite, which contains ~3.4 wt% TiO_2. Orthopyroxene porphyroblasts are up to 3 mm long and contain up to 9.8 wt.% Al_2O_3. Coarse-grained rutile (100-200 μm diameter) completely enveloped by ilmenite occurs as inclusions in late biotite. Based on these observations, the inferred macrodomain assemblage is garnet, orthopyroxene, biotite, plagioclase, quartz, ilmenite, and melt.

Macrodomain F

Macrodomain F is characterized by small (0.25-2 mm in diameter), closely spaced garnet porphyroblasts (Figs 2.2 & 2.4c). Porphyroblastic orthopyroxene occurs as large grains up to 2 mm in diameter and in some cases contains small inclusions of garnet (Fig. 2.4d). The highest analyzed Al_2O_3 content in porphyroblastic orthopyroxene is 9.9 wt.%. Primary biotite (TiO_2 content up to ~5 wt.%) is more common than in Macrodomain C. Retrograde biotite is rarer than in Macrodomain C, and is found in embayments of garnet and orthopyroxene porphyroblasts. Quartz sometimes occurs as symplectitic intergrowths with cordierite around garnet. Orthopyroxene mantles coarse-grained quartz and separates it from coronae of symplectitic cordierite and orthopyroxene around garnet (Fig. 2.4c). In some cases, plagioclase occurs with symplectitic orthopyroxene instead of cordierite on the rim of resorbed garnet (Fig. 2.4d). Coarse-grained rutile (up to ~250 μm diameter) occurs as subhedral to anhedral grains included in orthopyroxene, garnet, and primary biotite. Sillimanite occurs as fine-grained laths included in orthopyroxene and garnet. Rare sapphirine occurs as inclusions in garnet (early) as well as small grains surrounded by cordierite in embayments of resorbed porhpyroblastic orthopyroxene and garnet (late).

Based on these observations, the assemblage for macrodomain F is inferred to be garnet, orthopyroxene, biotite, plagioclase, quartz, ilmenite, and melt, as in macrodomain C. Sapphirine, spinel and/or sillimanite are not included in this assemblage because they occur only as inclusions in garnet and/or orthopyroxene, or in embayments in garnet, suggesting that their stability was either during garnet growth or due to more localized equilibration during garnet breakdown, described below in the microdomain section.

Macrodomain CF

Macrodomain CF is characterized by both large (up to 10 mm) and small (<2 mm) garnet porphyroblasts (Figs 2.1-2.2). Garnet also occurs as inclusions in porphyroblastic orthopyroxene. which is found as up to 3 mm long crystals with up to 9.3 wt.% Al_2O_3. Oriented needles of sillimanite within orthopyroxene may represent exsolution of Al_2O_3 upon cooling (Fig. 4f; Baldwin *et al.*, 2005); therefore the measured Al_2O_3 in orthopyroxene is taken to be a minimum. Primary biotite contains up to 5.3 wt.% TiO_2. Fine-grained quartz typically exhibits cuspate grain boundaries separated from other quartz grains by thin films of plagioclase, interpreted to represent thin films of relict melt that crystallized on grain boundaries. Sillimanite occurs as coarse (~500-800 μm long), prismatic laths surrounded by cordierite and in some cases intergrown with fine-grained spinel (Fig. 2.4e). Sillimanite also occurs as inclusions in orthopyroxene and garnet, as well as the aforementioned fine-grained clusters in garnet embayments (Fig. 2.4f). Sapphirine occurs as small (~200-300 μm diameter) resorbed grains in embayments of resorbed porphyroblastic garnet, with coronae of symplectitic spinel and/or plagioclase feldspar and/or cordierite. Spinel and sapphirine also occur as inclusions in garnet. Rutile is smaller (typically ~100 μm diameter) and less abundant than in macrodomain F, and occurs exclusively as tiny, rounded, randomly-oriented grains in garnet. Ilmenite occurs as inclusions in biotite, orthopyroxene, and garnet, as well as in the matrix. Based on these observations, the assemblage is interpreted to be garnet, orthopyroxene, biotite, plagioclase, sillimanite, melt, and possibly quartz. As in macrodomain F, phases that occur only as inclusions in porphyroblasts and/or in porphyroblast embayments were not included in this assemblage (e.g. sapphirine).

2.5.2 Macrodomains: thermodynamic modelling

P–T pseudosections for macrodomains C, F, and CF are shown in Figs 5, 6, and 7, respectively. In each, the inferred macrodomain assemblage (outlined by the brown dashed lines in Figs 2.5-2.7) is predicted to be stable above ~8.5 kbar, and at temperatures between ~920 °C and ~940 °C. Cordierite, spinel, and/or sapphirine are predicted to be stable at pressures less than 8.5 kbar in all cases. Isopleths of melt abundance are subvertical in each case (Fig. A2), and the observed assemblage of each macrodomain is predicted to be in equilibrium with as little as ~2 vol. % melt at the lower-*T* limits of the predicted macrodomain assemblage stability field, and up to ~25-30 vol. % melt at the upper-*T* limits. Predicted melt abundance is strongly dependent on the

chosen H_2O content of the bulk composition, with lower H_2O content resulting in lower predicted melt abundance and an elevated solidus. A pseudosection for Macrodomain F with lower H_2O content is shown in Fig. A3c, exhibiting an elevated solidus above which the macrodomain assemblage is stable, but predicting biotite breakdown to be coincident with production of potassium feldspar (Fig. A3d), inconsistent with our petrographic observations. Such rationale leads us to believe that the H_2O contents chosen for Figs 2.5–2.7 are appropriate.

Although rutile is present in each macrodomain as inclusions in garnet, orthopyroxene, and primary biotite (and thus was part of the assemblage during garnet and orthopyroxene growth), the pseudosections do not predict rutile stability with the macrodomain assemblages within the modeled *P–T* range. Similarly, the presence of spinel and sapphirine as inclusions in garnet also suggest that they were part of the assemblage during garnet growth, but they are not predicted to be in equilibrium with the macrodomain assemblage by the pseudosections.

The highest predicted biotite TiO_2 contents within the macrodomain assemblage field for macrodomains C and CF are lower than the highest measured TiO_2 contents (4.9 and 5.5 wt.% in C and CF respectively). The highest predicted TiO_2 in biotite within the macrodomain assemblage field for macrodomain F is approximately in agreement with the measured value (~5 wt.%). The predicted ranges of Al_2O_3 in orthopyroxene within the assemblage fields for macrodomains C and F are also lower than the measured values (9.8 and 9.9 wt.% respectively). For macrodomain CF, the predicted range of Al_2O_3 in orthopyroxene at the upper-*T* end of the assemblage field coincides roughly with the measured content (9.3 wt.%), however the presence of exsolved sillimanite needles in orthopyroxene suggest its measured Al_2O_3 content is a minimum, and that Al_2O_3 content was higher prior to cooling. All of the pseudosections predict decreasing garnet and increasing orthopyroxene abundances and increasing TiO_2 in biotite and Al_2O_3 in orthopyroxene with increasing temperature within the assemblage field. Further significant orthopyroxene growth and garnet breakdown could occur during decompression.

Integrated Bulk Composition

A *P–T* pseudosection for a composition approximating the whole rock is shown in Fig. 2.8. The composition was estimated by measuring the area of each macrodomain in Fig. 2.1 and combining their compositions proportionally, assuming that areal extent of each domain is an appropriate proxy for volumetric proportion. If equilibrium was ever attained on a scale larger than the macrodomains, modeling for this composition may reveal the approximate *P–T* of this

equilibration. Calculated intergranular diffusion distances of Al in a rock saturated in hydrous fluid or melt at 800-900 °C for the apparent metamorphic duration (1 Myr, Galli *et al.*, 2011) are ~1-10 cm (see Fig. 9 in Carlson (2010)); i.e. similar to or greater than distances between the macrodomains, thus implying that such hand sample scale equilibration may have been attained. The macrodomain assemblages all include garnet, orthopyroxene, biotite, plagioclase, quartz, and ilmenite (with CF also containing sillimanite), interpreted to be in equilibrium with melt, and thus this assemblage could represent the equilibrium assemblage on a scale larger than the macrodomains, prior to their development.

The topology shown in Fig. 2.8 is almost identical to the *P–T* pseudosections constructed for macrodomains C and F, with slight shifts in the predicted *P–T* stability of the macrodomain assemblage field, as well as the solidus. The macrodomain assemblage of garnet, orthopyroxene, biotite, plagioclase, quartz, and ilmenite (in equilibrium with melt) is stable at >8.5 kbar, ~740-940 °C. As in Figs 2.5–2.7, the pseudosection does not predict rutile stability with the inferred equilibrium assemblage within the modeled *P–T* range, despite the presence of rutile as inclusions in garnet, orthopyroxene, and primary biotite. Furthermore, spinel and sapphirine are not predicted to be in equilibrium with the observed assemblages. The maximum predicted TiO_2 in biotite and Al_2O_3 in orthopyroxene contents within this assemblage field are 4.7 wt.% and 9 wt.% respectively, broadly matching measured values. Decreasing garnet and increasing orthopyroxene contents are predicted to accompany heating or decompression. Cordierite is predicted to be stable at lower pressures than the macrodomain assemblage. Isopleths for melt abundance range from ~1-25 vol. % within the field of the macrodomain assemblage (Fig. A2).

Summary of thermodynamic modeling of macrodomains and the integrated bulk composition

Several common features between the pseudosections for each macrodomain and the integrated bulk composition provide constraints on the *P–T* path. In general, the highest *measured* Al_2O_3 in orthopyroxene and TiO_2 in biotite contents are higher than those *calculated* in the fields of the macrodomain assemblages, suggesting either our use of inappropriate thermodynamic data or that the highest Al orthopyroxene and Ti biotite may have formed from a different effective bulk composition, perhaps after equilibrium volumes shrank below the macrodomain scale (explored further below). An exception to this is TiO_2 in biotite in Macrodomain F, for which the measured contents agree with those predicted, suggesting that TiO_2-rich biotite in this macrodomain may record equilibration at the macrodomain scale. Although inclusions of rutile in orthopyroxene

and garnet lower the abundance of TiO_2 'available' for subsequent reactions, the effect of this on biotite TiO_2 content is negligible because: 1) the assemblage is continuously buffered by an ilmenite–hematite solution (both observed and predicted to be stable with the macrodomain assemblage) which buffered a_{TiO2} (Ghent & Stout, 1984); and 2) TiO_2 enrichment in biotite in this case is likely to result from preferential retention of TiO_2 during partial biotite breakdown rather than new biotite growth with increased TiO_2. This is supported by the pseudosections and by calibrated biotite thermometers (e.g. Henry *et al.*, 2005) which predict increasing TiO_2 content in biotite upon heating, as well as by pseudosection predictions of ilmenite growth during biotite breakdown with heating. The whole-rock pseudosection contoured for TiO_2 in biotite and Al_2O_3 in orthopyroxene suggests that the observed orthopyroxene zoning patterns (e.g. orthopyroxene with low Al_2O_3 cores and high Al_2O_3 annuli/rims; Galli et al. 2011) and textural features (e.g. primary, resorbed biotite with high TiO_2 content) can be explained by prograde heating at >8.5 kbar.

We propose that near the end of prograde heating, melt was channelized and extracted, eventually failing to be contiguously connected along grain boundaries and leading to reduction of equilibration volumes to the scale of macrodomains. Pseudosections for each macrodomain, as well as the whole-rock composition, predict that the macrodomain assemblage was in equilibrium with melt (Fig. A2), suggesting that at least some melt was retained in the rock. The presence of leucosome veins and patches visible at the hand sample scale show how melt was channelized (Figs 2.1 & 2.2). Equilibration volumes likely shrank to the macrodomain scale at the *P–T* conditions in which the macrodomain assemblage fields of Figs 5–7 intersect (~8.5-9 kbar, ~920-940 °C). At these conditions, the melt fraction predicted for the macrodomains varies significantly within a narrow temperature range, increasing from ~8 % to 30 % over ~ 35 ˚C upon continued biotite breakdown melting. It is noted here that: 1) the absolute melt abundance co-existing with the macrodomain is thus poorly defined, being very sensitive to both temperature of equilibration and the abundance of H_2O; and 2) reduction in initial H_2O content moves the solidus to higher temperature. The initial H_2O content was, however, constrained to best produce assemblages consistent with the observed textures. To demonstrate, a *P–T* pseudosection for macrodomain F with slightly reduced H_2O content (0.64 wt.%, or 2.23 mol.% vs. 0.80 wt.%, or 2.78 mol.%; shown in Fig. S3a,c) predicts stability of the macrodomain assemblage of biotite, plagioclase, quartz, orthopyroxene, garnet, ilmenite, and melt directly

above the solidus, but biotite breakdown is predicted to be coincident with the production of potassium feldspar (Fig. S3d). The presence of relict prograde biotite and the complete absence of potassium feldspar are inconsistent with this prediction. The *P–T* pseudosections shown in Figs 5-7 all predict biotite breakdown without necessarily producing potassium feldspar, implying that our chosen estimates for H_2O content of the macrodomains are appropriate. Upon further melt channelization/extraction, evidence (presented and discussed below) suggests that equilibration volumes decreased to the scale of microdomains, abandoning this macrodomain-scale equilibration.

Though it is emphasised here that the macrodomain and whole-rock bulk compositions are inappropriate for deducing the retrograde *P–T* evolution, several general aspects of the rock's history are illuminated in these pseudosections. The contours for garnet and orthopyroxene abundance in each pseudosection demonstrate that orthopyroxene growth at the expense of garnet (as indicated by garnet surrounded by and included in porphyroblastic orthopyroxene) can be explained by a clockwise *P–T* path. A counterclockwise *P–T* path would result in simultaneous orthopyroxene breakdown and garnet growth, which is not observed. Moreover, the presence of late cordierite, sapphirine, and spinel suggest a generally decompressional *P–T* path, though since there is no single field in which all are predicted to be stable (along with the macrodomain assemblage), it is most likely that these phases crystallized locally from smaller equilibrium volumes.

2.5.3 Microdomains: petrology and thermodynamic modelling

Three microdomains from within CF (Fig. 2.2) were chosen for additional thermodynamic modeling. The compositions determined by semi-quantitative SEM area analysis are shown in Table 2.3a, with the bulk compositions used in thermodynamic modeling, including adjusted H_2O and Fe_2O_3 contents, shown in Table 2.3b.

Microdomain 03-06

Microdomain 03-06 is characterized by a resorbed garnet porphyroblast with a cordierite corona, which is surrounded by biotite and porphyroblastic orthopyroxene (Fig. 2.9a,b). The corona contains resorbed, high-Ti primary biotite (~4.5-5.1 wt.% TiO_2), and when in contact with its outer margin, biotite and orthopyroxene are again commonly resorbed. Some biotite outside the corona appears to be texturally equilibrated and is interpreted as a retrograde phase. Sapphirine is

present in an embayment in the garnet porphyroblast, and is resorbed where in contact with cordierite. Late plagioclase is volumetrically minor and, where present, occurs as thin rims on resorbed biotite, interpreted to represent crystallized melt. Minor ilmenite is present as inclusions in garnet and in the cordierite corona. The last-stage equilibrium assemblage for this microdomain is thus inferred to be garnet, biotite, cordierite, ilmenite, sapphirine, and melt.

A compositional domain deemed most appropriate for modeling this texture is highlighted in Fig. 9 and its composition is given in Table 2.3. A pseudosection for this composition shows that the highest measured TiO_2 concentrations in biotite (~5.1 wt.% TiO_2; Table 2.1c) and inferred equilibrium assemblage were achieved at ~8.5 kbar, 950-970°C for this microdomain (Fig. 2.9d). Calculated phase proportions are useful for highlighting the growth and breakdown of different phases during *P–T* evolution (Fig. 2.10), and suggest that decompression (by ~0.5 kbar) can produce phase relationships observed in the texture (Fig. 2.10). This is consistent with resorption of garnet and sapphirine and replacement by cordierite, which is the dominant feature of the texture. Biotite growth is predicted along this decompression path, suggesting that much of the observed biotite resorption occurred on the preceding heating path to peak temperature. Melt is consumed along any near isothermal decompression path through the field of the inferred equilibrium assemblage (Fig. 2.10).

Eventual cooling results in production of a small amount of plagioclase feldspar upon melt crystallization, consistent with volumetrically minor retrograde plagioclase in the texture. However, it is likely that equilibration volumes shrunk throughout cooling as melt was consumed, and thus it may be inappropriate to use the same *P–T* pseudosection to infer a path to plagioclase stability.

Microdomain 03-04

Microdomain 03-04 is similar to microdomain 03-06 and is characterized by a resorbed and fractured garnet porphyroblast with a cordierite corona surrounded by biotite and resorbed porphyroblastic orthopyroxene, but lacks sapphirine and contains spinel and sillimanite inclusions in garnet (Fig. 2.11a,b). Where in contact with the cordierite corona, biotite and orthopyroxene are commonly resorbed, though some biotite appears texturally equilibrated. Resorbed, primary high-Ti (4.5-5.1 wt.% TiO_2; Table 2.1c) biotite also occurs within the cordierite corona, with some resorbed, optically continuous pieces separated by cordierite (e.g. close to labeled 'Bt_1' in Fig. 11a,b). Inclusions of sillimanite and spinel in garnet are typically

mantled by a rim of cordierite, with garnet Mg and Fe contents decreasing and increasing, respectively, at the interface with these inclusion assemblages (Table A1). This zoning pattern is also observed on the outer rims of the garnet, where it is in contact with its cordierite corona, and is thus likely the result of Fe–Mg exchange between garnet and cordierite. The cordierite surrounding sillimanite and spinel inclusions is therefore interpreted to represent retrograde reaction rather than a primary feature, possibly forming by one or a combination of the reactions: Gt + Sil + Qz è Crd, and Spl + Qtz è Crd. Ilmenite occurs as inclusions in garnet and in cordierite.

The equilbrium assemblage for this texture is inferred to be garnet, biotite, sillimanite, spinel, ilmenite, and melt, and is outlined in the pseudosection by the brown dashed line in Fig. 11d. The compositional domain chosen is shown in Fig. 11b, with a *P–T* pseudosection for this composition indicating conditions of ~8.5 kbar, 960-970°C (Fig. 2.11c,d) for the cordierite-absent peak assemblage. Calculated modal abundances of various phases are shown in Fig. A4. As in microdomain 03-06, decompression from ~8.5-8.0 kbar accompanied by slight cooling from peak *T* can produce the observed texture, resulting in the breakdown of garnet and sillimanite, and the appearance and growth of cordierite. Further decompression accompanied by slight cooling (~20 °C) would result in breakdown of garnet, spinel and sillimanite, consumption of melt, cordierite growth, and a small amount of late biotite growth, all consistent with observed phase relationships.

Microdomain 03-03

Microdomain 03-03 is quite different to previous examples, being characterized by a sillimanite cluster that is partly surrounded by resorbed plagioclase feldspar (Fig. 2.12a,b) that also contains rare spinel inclusions. Embayments in this plagioclase contain cordierite, locally surrounding sillimanite and spinel, and plagioclase is always separated from high-TiO_2 biotite (~4.7-5.3 wt.%; Table 2.1b) and resorbed porphyroblastic orthopyroxene by cordierite. Minor ilmenite occurs as small grains within both cordierite and plagioclase.

The compositional domain chosen for this texture and resultant *P–T* pseudosection are shown in. 12. The solidus is strongly dependent on initial H_2O content but here ranges between ~920 and 960 ˚C. Phase equilibria suggest that the inferred equilibrium assemblage of sillimanite, plagioclase feldspar, spinel, orthopyroxene, biotite, cordierite, and ilmenite was stable at ~960-980 ˚C at ~8-8.5kbar (field outlined in Fig. 2.12c). The TiO_2 content of biotite

within this assemblage field matches the measured range in the texture (~4.5-5.2 wt.%; Fig. 2.12c) and decompression through this field can again produce most of the textural relationships observed within this microdomain (Figs 2.12d & A5): cordierite and spinel grow, while orthopyroxene and sillimanite are consumed.

2.6 SUMMARY OF THERMODYNAMIC MODELING OF ALL DOMAINS

Results obtained with THERMOCALC ds5.5, as implemented in Perple_X, are summarized in Fig. 13a. Several of the assemblage fields discussed previously are small relative to likely uncertainties stemming from both thermodynamic and bulk compositional uncertainty (e.g. Angiboust *et al.*, 2012; Green, 2013; Palin *et al.*, 2015), so all field outlines in Fig. 2.13 have been expanded to $\sim \pm 0.25$ kbar and $\sim \pm 40$ ˚C to account for some of this uncertainty, emphasizing that while absolute *P–T* conditions of equilibration are not accurately known, the relative path recorded here is clear.

Thermodynamic modeling of the integrated bulk composition suggests that prograde heating can be broadly constrained by the stability of the macrodomain assemblage at T = ~700-930 °C, >8.5 kbar (Fig. 2.8), interpreted to reflect a large scale equilibrium assemblage at a point when melt was connected along most grain boundaries. Equilibration was reduced to the macrodomain scale at ~8.5-9 kbar, ~920-940 °C, as shown by overlapping equilibrium assemblage stabilities of each of the macrodomains. This initial isolation of cm-scale domains presumably records increasingly patchy melt connectivity due to progressive melt loss or channelization near the final stages of heating (e.g. Rosenberg & Handy, 2005; Yakymchuk & Brown, 2014). Pseudosection constraints suggest retention of between ~8 and 30 vol. % melt on the whole-rock scale, with the estimate depending on absolute peak T, bulk-composition uncertainty (primarily with regard to initial H_2O content) and thermodynamic uncertainty (Fig. A2). The low range of this estimate would be consistent with patchy melt distribution but higher melt fraction would probably imply larger-scale contiguous melt connectivity (e.g. Arzi, 1978; van der Molen & Paterson, 1979; Lejeune & Richet, 1995; Rosenberg & Handy, 2005).

Very closely spaced melt fraction isopleths in the macrodomain pseudosections (Fig. A2) suggest that each macrodomain volume may also have retained as little as ~8-10 vol. % melt, again within the range in which grain boundary melt would be expected to be discontinuously connected within the rock, and may have occurred in increasingly isolated pockets as melt was channelized, extracted or eventually consumed (subsequently equilibrating as the

microdomains). It is re-emphasised here that although choosing lower H_2O contents results in lower predicted melt abundances, predicted biotite breakdown and concurrent potassium feldspar production with lower H_2O content is inconsistent with petrographic observations (Fig. A3d).

The thermal peak was likely between 940 and 980 ˚C, revealed by the maximum *T* recorded by macrodomains (940 °C) and the *T* range recorded by the microdomains (950-980 °C), which effectively overlap within uncertainty (e.g. Palin *et al.*, 2015). This transition from macro- to microdomain equilibration is more clearly associated with high temperature decompression, possibly coincident with melt loss and/or channelization and likely during partial melt consumption, as revealed by microdomain pseudosections (Figs 2.10, A4, & A5). These pseudosections predict *local* equilibration with a high melt fraction (~15-30 vol. %) near the peak UHT conditions. This does not constitute a fraction of the whole rock, but rather of just the microdomain itself, again reflecting the channelization/patchy isolation of grain boundary melt. Patches of retrograde biotite throughout the rock provide additional evidence that melt was only locally present during later stages of the evolution, reacting with porphyroblastic phases upon cooling. The continued presence of melt in the microdomains allowed maintenance of chemical equilibrium over mm to sub-mm length scales during decompression, prior to cooling and significant melt consumption. It is envisioned that this equilibration was strongly localized, with melt-depleted zones concurrently experiencing equilibration length scales far shorter than those of the analyzed microdomains.

2.7 THERMODYNAMIC MODELING IN DS6

The preceding calculations were based upon modeling using a revision ("ds5.5") of the thermodynamic data of Holland & Powell (1998), with a selection of mineral solution models published since 1998. The release of a new internally consistent thermodynamic dataset (ds6; Holland & Powell, 2011) and corresponding updated *a–x* models for common phases in metapelites (White *et al.*, 2014a; White *et al.*, 2014b) provides an opportunity to compare pseudosections for the same rock made with the new (ds6) and old datasets (ds5.5). Use of the updated dataset and corresponding re-parameterized *a–x* models may result in substantially different predicted phase equilibria compared to those in a pseudosection constructed using the old dataset and solution models (Kelsey & Hand, 2014). For example, Korhonen *et al.* (2014) show that the predicted *P–T* stabilities for rutile, cordierite, orthopyroxene, and sapphirine are significantly different between ds6 and ds5.5 for the same rock. Petrologists commonly employ

forward modeling of phase equilibria to interpret the mineral compositions and textures in metamorphic rocks; therefore this study investigates how the use of ds6 may lead one to interpret the metamorphic evolution of a sample differently than when using ds5.5. In all cases, the input system compositions for ds6 calculations were identical to those for the pseudosections presented previously.

The ds6 pseudosections for macrodomains F and CF and the integrated whole-rock composition are shown in Fig. 2.14. The diagrams for macrodomains F, C (not shown), and the integrated whole-rock composition have similar overall topologies to their respective counterparts in ds5.5 (i.e. Figs 2.5-2.8) but shift stability of the observed macrodomain assemblages in each to a smaller range (7.7-9.7 kbar, ~ 800-920 °C). A significant difference between the ds5.5 and ds6 results is that rutile is predicted to be stable with the observed macrodomain assemblages at ~800-825 °C in the latter but absent from the entire explored *P–T* range in the former. Rutile is observed in each macrodomain as inclusions in garnet and orthopyroxene, and thus the predicted stability of rutile in equilibrium with the other phases in the macrodomain assemblage in the ds6 pseudosection for the integrated whole-rock composition may place somewhat tighter pressure constraints on the prograde heating path to UHT conditions.

The ds6 pseudosection for macrodomain CF (Fig. 2.14c) fails to predict the inferred macrodomain assemblage of garnet, orthopyroxene, biotite, plagioclase feldspar, sillimanite, quartz, and melt. This implies that either: 1) the assemblage is predicted to be stable outside of the explored *P–T* range (unlikely because orthopyroxene has a restricted predicted *P* range that overlaps with the predicted stability field of cordierite); 2) our interpretation of the macrodomain assemblage is incorrect; 3) the bulk composition is inappropriate; or 4) the initial H_2O and/or Fe_2O_3 content of CF requires further adjustment for the ds6 calculation. Our petrographic observations suggest the macrodomain assemblage must include orthopyroxene and exclude cordierite, and there is no field in the pseudosection where orthopyroxene is stable with the rest of the macrodomain assemblage (garnet, plagioclase feldspar, quartz, ilmenite, sillimanite, and melt) in the absence of cordierite. To calculate a pseudosection for macrodomain CF in which this inferred macrodomain assemblage is stable, (i.e., Fig. 2.14d), initial Fe_2O_3/FeO must be modified to an extremely high value of 1, substantially different from the bulk compositions used for modeling of the other macrodomains (in which Fe_2O_3/FeO = ~0.22, Table A2). It is unlikely

that macrodomain CF is substantially more oxidized than the other two macrodomains, as there are neither geochemical nor petrographic evidence to support such oxidation.

The ds6 pseudosections for the compositions of the microdomains are shown in Fig. 2.15. The inferred equilibrium assemblage of microdomain 03-06 (garnet + melt + biotite + cordierite + ilmenite + sapphirine) is predicted to be stable at ~910-950 °C, 6-7.8 kbar (Fig. 2.15a), a much wider *P* range and a *T* range shifted to lower *T* than calculated with ds5.5 (Fig. 2.11). Contours for calculated abundances of phases in the microdomain (not shown) are broadly similar to those in the pseudosection calculated using ds5.5 (Fig. 2.10) and would lead to a similar interpretation of garnet and sapphirine breakdown, melt consumption, and cordierite growth during decompression, albeit with substantially greater decompression at this stage (1.5 kbar rather than 0.5 kbar with ds5.5; shown by red star and dashed red arrow in Fig. 2.13b).

Two of the calculations (for microdomains 03-03 and 03-04) fail to predict the inferred equilibrium assemblage within those textures (Fig. 2.15b,c), again suggesting that: 1) H_2O and Fe_2O_3 contents need to be adjusted, 2) our interpretation of the equilibrium assemblages are incorrect, or 3) the equilibration volume observed for the minerals in the microdomain is substantially different than the one chosen. T–M_{H2O}, T–M_{Fe2O3}, and P–M_{Fe2O3} diagrams were calculated for microdomain 03-04 (Fig. A6, compositions used shown in Table A3), again failing to predict the inferred peak assemblage and showing that simply adjusting the H_2O and Fe_2O_3 content of the microdomain composition is insufficient to predict stability of the inferred equilibrium assemblage in ds6.

2.8 DISCUSSION AND CONCLUSIONS

2.8.1 Shooting at a moving target: evolving thermodynamic datasets

Fig. 13 shows the summary of our *P–T* path interpretations based on modeling of macrodomains and microdomains in ds5.5 and ds6. Though both inferred *P–T* paths have a roughly clockwise topology marked by near–isothermal decompression, there remain significant differences between the two interpretations. The stability of rutile in equilibrium with the inferred macrodomain assemblage (garnet, plagioclase, quartz, biotite, orthopyroxene, ilmenite, melt) in the integrated whole-rock composition pseudosection calculated using ds6 places a tight pressure constraint of ~9 kbar during prograde heating to UHT conditions, while there is no maximum pressure constraint on this part of the *P–T* path in ds5.5. The temperatures at which equilibration

volumes are interpreted to be reduced to the scale of macrodomains are lower (~900-915 °C) in ds6 than they are in ds5.5 (~920-940 °C), though overlapping within uncertainty. In both interpretations, the microdomains appear to record equilibria at lower pressures than the macrodomains, and the textures in the microdomains are interpreted to record evolution during decompression. While all three microdomains studied here are interpreted to record similar decompression paths using ds5.5, only one microdomain composition (03-06) predicts the inferred equilibrium assemblage to be stable using ds6, with a texture indicative of decompression. Therefore, one might interpret the microdomains when using ds5.5 as recording the same part of the *P–T* path, while an interpretation using ds6 might be that only some microdomains directly record this decompression. The interpreted decompression between macrodomains and microdomains in ds6 (~1 kbar) is greater than with ds5.5 (0-0.5 kbar), and the amount of decompression recorded within the microdomains is also significantly greater in ds6 (~1.5-2 kbar) than it is in ds5.5 (~0.5 kbar).

2.8.2 Shooting at a moving target: evolving equilibrium length scales during high-*T* metamorphism

Use of 'whole-rock' composition inputs for phase equilibria modeling is common practice, and has been applied with great success (e.g. Zeh *et al.*, 2004; Powell & Holland, 2008; Vorhies & Ague, 2011; Gordon *et al.*, 2012; Korhonen *et al.*, 2013). However, care needs to be taken when interpreting a pseudosection constructed for whole-rock compositions of texturally heterogeneous rocks that experienced melt loss (e.g. Baldwin *et al.*, 2005; White & Powell, 2011; Kelsey & Hand, 2014), as the whole-rock composition is merely indicative of the last time equilibrium was achieved at the whole-rock scale when connected intergranular fluids were present. Similarly, the macrodomains studied here appear to record equilibria only at a set of *P–T* conditions before effective equilibration volumes shrank below the cm scale upon partial melt loss, channelization or consumption (~900-940 °C, ~8.5-9 kbar; Fig. 13). Though contouring the whole-rock and macrodomain diagrams for mineral compositions and modal proportions fails to directly yield information on the peak *T* attained, such contours are still useful for comparison with observed zoning patterns in order to place constraints on the shape of the *P–T* path. For example, prograde heating in the integrated bulk composition pseudosection (Fig. 2.8) can produce the general mineralogical relationships observed on the whole-rock scale and changes in phase abundance would be consistent with observed textures, but absolute phase abundances

retrieved from the diagram are not expected to constrain *P–T* conditions due to both melt loss from and partial retrogression in this sample.

Phase equilibria modeling yields similar *P–T* paths for three distinct microdomains (when using ds5.5, Fig. 13a), involving near–isothermal decompression from peak temperatures achieved at ~8.5-9 kbar and ~960 °C (using ds5.5), and in general agreement with peak *P–T* estimates from previous studies (Galli *et al.*, 2011; Oalmann *et al.*, 2013a). Modeling of the microdomains in ds6 also results in a near-isothermal decompression path, but with a slightly different interpretation of the metamorphic evolution (as described above; Fig. 2.13b).

Regardless of whether ds5.5 or ds6 is used, metamorphic evolution is revealed in relative detail when modeling rock compositions at evolving equilibration length scales. Results suggest a clockwise *P–T* path, with 5 cm or larger equilibration scales at approximately 8.5-9 kbar, 900-940 °C (lower *P–T* in ds6, higher *P–T* in ds5.5). Peak *T* is seemingly best recorded within the microdomains (i.e. several mm equilibration scales) at ~7.5-8.5 kbar, 920-980 °C (again, lower *P–T* in ds6, higher *P–T* in ds5.5), though due to uncertainties and the apparently similar *T* recorded by macro- and microdomain equilibria, it may have been attained when equilibration volumes were still at the cm scale. Attainment of peak *T* was followed by near isothermal decompression, a part of the *P–T* path apparently only recorded by the microdomains.

2.8.3 Implications for UHT metamorphism in the Gruf complex

The timing and tectonic setting of UHT metamorphism in the Gruf complex has remained contentious: some argue that the UHT metamorphism was the result of mafic underplating during Permian orogenic collapse (Galli *et al.*, 2011; Galli *et al.*, 2012), while others suggest that UHT conditions were achieved during Eocene Alpine orogenesis (Droop & Bucher-Nurminen, 1984; Möller *et al.*, 2012; Oalmann *et al.*, 2013a). Though the timing of UHT metamorphism is outside the scope of this study, the morphology of *P–T* paths can be indicative of particular tectonic mechanisms and environments. The apparent *P–T* paths recorded by the whole-rock, macrodomains, and microdomains suggest heating to UHT conditions at lower crustal depths (~25-30 km), followed by near–isothermal decompression. This is initially suggestive of a cycle of crustal thickening, heating, and exhumation, characteristic of collisional orogenic settings (e.g. England & Thompson, 1984; Thompson & England, 1984). However, the inferred rapid (~1 Myr) heating-cooling timescales of UHT metamorphism based on garnet diffusion modeling (Galli *et al.*, 2011) suggests a different heating mechanism than simple burial and radioactive

heating in thickened orogenic crust, predicted to occur over timescales of 10^1-10^2 Myrs (e.g. England & Thompson, 1984; Thompson & England, 1984; Clark *et al.*, 2011). Additionally, the microdomains record only limited high-*T* decompression after peak *P–T* conditions (~0.5–2 kbar; smaller amount using ds5.5, larger amount using ds6), suggesting that decompression may have stopped at pressures between 8-6.5 kbar, with the rock stalling and cooling at mid-crustal depths after attainment of UHT conditions.

As Galli et al. (2011) identified, whole-rock pseudosections are inappropriate for inferring later stage metamorphic evolution of the Gruf Complex. The methodology employed here, however, reveals additional information about *P–T* conditions following extraction of partial melts, with models yielding appropriate mineral equilibria and compositions. The microdomains studied here appear to have formed during a distinctly different stage of the metamorphic history (i.e. decompression at UHT conditions) than the opx–crd and opx–spr symplectites that yielded ~720-740 °C, 7-7.5 kbar and ~800 ˚C, 5 kbar with multiphase thermobarometry in the Galli et al. (2011) and Droop and Bucher-Nurminen (1984) studies, respectively. These symplectites were interpreted by Galli et al. to represent re-equilibration during a second amphibolite-facies metamorphic event, and our data neither confirm nor dispute this.

The UHT *P–T* path derived here provides new constraints on the metamorphic evolution of the Gruf Complex that are mutually consistent with either 1) the interpretation that granulite metamorphism at ~280-260 Ma was due to mafic underplating during orogenic collapse and lithospheric thinning, and was followed by cooling during mid-crustal residence until Eocene (~31 Ma) upper-amphibolite facies metamorphism and exhumation (Galli et al., 2012); or 2) that metamorphism was driven by slab-breakoff and asthenospheric upwelling during a single stage, Alpine *P–T* path as envisioned by e.g. Oalmann *et al.* (2013a). Both tectonic scenarios involve a short-lived heat source at lower-crustal depths for UHT metamorphism, and are compatible with the *P–T* path derived here. Additional in-situ geochronology of phases that grew before or during UHT conditions, or crystallized from UHT partial melts (e.g. Oalmann *et al.*, 2011; Möller *et al.*, 2012; Möller *et al.*, 2013; Oalmann *et al.*, 2014), is required to further resolve the tectono-metamorphic evolution of the Gruf Complex, with particular value in geochronology on crystals for which trace element thermometry is also available (e.g. Baldwin & Brown, 2008; Kelsey & Hand, 2014; Oalmann *et al.*, 2014).

2.9 ACKNOWLEDGMENTS

The authors are grateful for the sample provided by A. Galli. J. Diener and T. Johnson are thanked for their critical and constructive reviews of earlier versions of this manuscript. We also thank A. Möller, J. Oalmann, A. Galli, M. Brown, R. Tracy, and B. Dragovic, for stimulating discussions regarding this work. M. Brown is also thanked for swift and thorough editorial handling. L. Fedele is thanked for assistance with the electron microprobe analyses and S. Mertzmann is thanked for XRF analyses. This work was funded by the Department of Geosciences at Virginia Tech and NSF award EAR-1447568 to Caddick.

2.10 REFERENCES

Anderson, J. R., Kelsey, D. E., Hand, M. & Collins, W. J., 2013. Conductively driven, high-thermal gradient metamorphism in the Anmatjira Range, Arunta region, central Australia. *Journal of Metamorphic Geology*, **31**, 1003-1026.

Angiboust, S., Langdon, R., Agard, P., Waters, D. & Chopin, C., 2012. Eclogitization of the Monviso ophiolite (W. Alps) and implications on subduction dynamics. *Journal of Metamorphic Geology*, **30**, 37-61.

Arzi, A. A., 1978. Critical phenomona in rheology of partially melted rocks. *Tectonophysics*, **44**, 173-184.

Baldwin, J. A. & Brown, M., 2008. Age and duration of ultrahigh-temperature metamorphism in the Anapolis-Itaucu Complex, Southern Brasilia Belt, central Brazil - constraints from U-Pb geochronology, mineral rare earth element chemistry and trace-element thermometry. *Journal of Metamorphic Geology*, **26**, 213-233.

Baldwin, J. A., Powell, R., Brown, M., Moraes, R. & Fuck, R. A., 2005. Modelling of mineral equilibria in ultrahigh-temperature metamorphic rocks from the Anapolis-Itaucu Complex, central Brazil. *Journal of Metamorphic Geology*, **23**, 511-531.

Baldwin, J. A., Powell, R., White, R. W. & Štípská, P., 2015. Using calculated chemical potential relationships to account for replacement of kyanite by symplectite in high pressure granulites. *Journal of Metamorphic Geology*, **33**, 311-330.

Bédard, J. H., 2006. A catalytic delamination-driven model for coupled genesis of Archaean crust and sub-continental lithospheric mantle. *Geochimica Et Cosmochimica Acta*, **70**, 1188-1214.

Bédard, J. H., Brouillette, P., Madore, L. & Berclaz, A., 2003. Archaean cratonization and deformation in the northern Superior Province, Canada: an evaluation of plate tectonic versus vertical tectonic models. *Precambrian Research*, **127**, 61-87.

Belyanin, G. A., Rajesh, H. M., Sajeev, K. & Van Reenen, D. D., 2012. Ultrahigh-temperature metamorphism from an unusual corundum plus orthopyroxene intergrowth bearing Al-Mg granulite from the Southern Marginal Zone, Limpopo Complex, South Africa. *Contributions to Mineralogy and Petrology*, **164**, 457-475.

Berman, R. G., 1988. Internally-Consistent Thermodynamic Data for Minerals in the System Na2O-K2O-CaO-MgO-FeO-Fe2O3-Al2O3-SiO2-TiO2-H2O-CO2. *Journal of Petrology*, **29**, 445-522.

Bohlen, S. R. & Mezger, K., 1989. Origin of Granulite Terranes and the Formation of the Lowermost continental Crust. *Science*, **244**, 326-329.

Brown, M., 2002. Retrograde processes in migmatites and granulites revisited. *Journal of Metamorphic Geology*, **20**, 25-40.

Brown, M., 2007. Metamorphic conditions in orogenic belts: A record of secular change. *International Geology Review*, **49**, 193-234.

Brown, M., 2013. Granite: From genesis to emplacement. *Geological Society of America Bulletin*, **125**, 1079-1113.

Brown, M., 2014. The contribution of metamorphic petrology to understanding lithosphere evolution and geodynamics. *Geoscience Frontiers*, **5**, 553-569.

Brown, M., 2015. Paleo- to Mesoarchean polymetamorphism in the Barberton Granite-Greenstone Belt, South Africa: Constraints from U-Pb monazite and Lu-Hf garnet

geochronology on the tectonic processes that shaped the belt: Discussion. *Geological Society of America Bulletin*, **127**, 1550-1557.

Brown, M., Korhonen, F. J. & Siddoway, C. S., 2011. Organizing Melt Flow through the Crust. *Elements*, **7**, 261-266.

Brown, M. & Solar, G. S., 1998. Granite ascent and emplacement during contractional deformation in convergent orogens. *Journal of Structural Geology*, **20**, 1365-1393.

Bucher-Nurminen, K. & Droop, G., 1983. The metamorphic evolution of garnet-cordierite-sillimanite-gneisses of the Gruf-Complex, Eastern Pennine Alps. *Contributions to Mineralogy and Petrology*, **84**, 215-227.

Caddick, M. J., Bickle, M. J., Harris, N. B. W., Holland, T. J. B., Horstwood, M. S. A. & Ahmad, T., 2007. Burial and exhumation history of a Lesser Himalayan schist: Recording the formation of an inverted metamorphic sequence in NW India. *Earth and Planetary Science Letters*, **264**, 375-390.

Caddick, M. J., Konopásek, J. & Thompson, A. B., 2010. Preservation of garnet growth zoning and the duration of prograde metamorphism. *Journal of Petrology*, **51**, 2327-2347.

Caggianelli, A. & Prosser, G., 2002. Modelling the thermal perturbation of the continental crust after intraplating of thick granitoid sheets: a comparison with the crustal sections in Calabria (Italy). *Geological Magazine*, **139**, 699-706.

Carlson, W. D., 2002. Scales of disequilibrium and rates of equilibration during metamorphism. *American Mineralogist*, **87**, 185-204.

Carlson, W. D., 2010. Dependence of reaction kinetics on H_2O activity as inferred from rates of intergranular diffusion of aluminium. *Journal of Metamorphic Geology*, **28**, 735-752.

Carlson, W. D., Hixon, J. D., Garber, J. M. & Bodnar, R. J., 2015. Controls on metamorphic equilibration: the importance of intergranular solubilities mediated by fluid composition. *Journal of Metamorphic Geology*, **33**, 123-146.

Carmichael, D. M., 1969. On the mechanism of prograde metamorphic reactions in quartz-bearing pelitic rocks. *Contributions to mineralogy and petrology*, **20**, 244-267.

Clark, C., Fitzsimons, I. C. W., Healy, D. & Harley, S. L., 2011. How Does the Continental Crust Get Really Hot? *Elements*, **7**, 235-240.

Coggon, R. & Holland, T. J. B., 2002. Mixing properties of phengitic micas and revised garnet-phengite thermobarometers. *Journal of Metamorphic Geology*, **20**, 683-696.

Connolly, J. A. D., 2005. Computation of phase equilibria by linear programming: A tool for geodynamic modeling and its application to subduction zone decarbonation. *Earth and Planetary Science Letters*, **236**, 524-541.

Cornelius, v. H. P., 1916. Ein alpines Vorkommen von Sapphirin. *Centralblatt für Mineralogie, Geologie und Paläontologie*, 265-269.

Cutts, K. A., Stevens, G. & Kisters, A., 2015. Reply to "Paleo- to Mesoarchean polymetamorphism in the Barberton granite-greenstone belt, South Africa: Constraints from U-Pb monazite and Lu-Hf garnet geochronology on the tectonic processes that shaped the belt: Discussion" by M. Brown. *Geological Society of America Bulletin*, **127**, 1558-1563.

de Wit, M. J., 1998. On Archean granites, greenstones, cratons and tectonics; does the evidence demand a verdict? *Precambrian Research*, **91**, 181-227.

Diener, J. F. A., White, R. W. & Hudson, T. J. M., 2014. Melt production, redistribution and accumulation in mid-crustal source rocks, with implications for crustal-scale melt transfer. *Lithos*, **200–201**, 212-225.

Dorfler, K. M., Caddick, M. J. & Tracy, R. J., 2015. Thermodynamic Modeling of Crustal Melting Using Xenolith Analogs from the Cortlandt Complex, New York, USA. *Journal of Petrology*, **56**, 389–408.

Droop, G. T. R. & Bucher-Nurminen, K., 1984. Reaction textures and metamorphic evolution of sapphirine-bearing granulites from the Gruf complex, Italian Central Alps. *Journal of Petrology*, **25**, 766-803.

England, P. C. & Thompson, A. B., 1984. Pressure-temperature-time paths of regional metamorphism I. Heat transfer during the evolution of regions of thickened continental crust. *Journal of Petrology*, **25**, 894-928.

Florence, F. P. & Spear, F. S., 1991. Effects of diffusional modification of garnet growth zoning on *P–T* path calculations. *Contributions to Mineralogy and Petrology*, **107**, 487-500.

Foster, C. T., 1999. Forward modeling of metamorphic textures. *The Canadian Mineralogist*, **37**, 415-429.

Frost, B. R. & Chacko, T., 1989. The granulite uncertainty principle; limitations on thermobarometry in granulites. *Journal of Geology*, **97**, 435-450.

Galli, A., 2010. *Tectono-metamorphic evolution of the Gruf Complex (Swiss and Italian Central Alps)*. Unpub. Ph.D dissertation Thesis, ETH Zürich.

Galli, A., Le Bayon, B., Schmidt, M. W., Burg, J.-P., Caddick, M. J. & Reusser, E., 2011. Granulites and charnockites of the Gruf Complex: evidence for Permian ultra-high temperature metamorphism in the Central Alps. *Lithos*, **124**, 17-45.

Galli, A., Le Bayon, B., Schmidt, M. W., Burg, J. P., Reusser, E., Sergeev, S. A. & Larionov, A., 2012. U-Pb zircon dating of the Gruf Complex: disclosing the late Variscan granulitic lower crust of Europe stranded in the Central Alps. *Contributions to Mineralogy and Petrology*, **163**, 353-378.

Galli, A., Manckelow, N. S., Reusser, E. & Caddick, M. J., 2007. Structural geology and petrography of the Naret region (northern Valle Maggia, N. Ticino, Switzerland). *Swiss Journal of Geoscience*, **100**, 53-70.

Ghent, E. & Stout, M., 1984. TiO2 activity in metamorphosed pelitic and basic rocks: principles and applications to metamorphism in southeastern Canadian Cordillera. *Contributions to Mineralogy and Petrology*, **86**, 248-255.

Gordon, S. M., Luffi, P., Hacker, B., Valley, J., Spicuzza, M., Kozdon, R., Kelemen, P., Ratshbacher, L. & Minaev, V., 2012. The thermal structure of continental crust in active orogens: insight from Miocene eclogite and granulite xenoliths of the Pamir Mountains. *Journal of Metamorphic Geology*, **30**, 413-434.

Green, E. C. R., White, R.W., Powell, R., 2013. Exploring Uncertainties in Phase Diagram Calculations via a Monte Carlo Method. In: *pre-Goldschmidt 2013 workshop "Applying phase equilibria modelling to rocks"*, Florence, Italy.

Guiraud, M., Powell, R. & Rebay, G., 2001. H_2O in metamorphism and unexpected behaviour in the preservation of metamorphic mineral assemblages. *Journal of Metamorphic Geology*, **19**, 445-454.

Harris, N. B. W., Caddick, M. J., Kosler, J., Goswami, S., Vance, D. & Tindle, A. G., 2004. The pressure-temperature-time path of migmatites from the Sikkim Himalaya. *Journal of Metamorphic Geology*, **22**, 249-264.

Harrison, T. M., Schmitt, A. K., McCulloch, M. T. & Lovera, O. M., 2008. Early (≥ 4.5 Ga) formation of terrestrial crust: Lu–Hf, δ 18 O, and Ti thermometry results for Hadean zircons. *Earth and Planetary Science Letters*, **268**, 476-486.

Henry, D. J., Guidotti, C. V. & Thomson, J. A., 2005. The Ti-saturation surface for low-to-medium pressure metapelitic biotites: Implications for geothermometry and Ti-substitution mechanisms. *American Mineralogist*, **90**, 316-328.

Herzberg, C., Condie, K. & Korenaga, J., 2010. Thermal history of the Earth and its petrological expression. *Earth and Planetary Science Letters*, **292**, 79-88.

Holland, T. & Powell, R., 2003. Activity-composition relations for phases in petrological calculations: an asymmetric multicomponent formulation. *Contributions to Mineralogy and Petrology*, **145**, 492-501.

Holland, T. J. B. & Powell, R., 1990. An enlarged and updated internally consistent thermodynamic dataset with uncertainties and correlations - the system K_2O-Na_2O-CaO-MgO-MnO-FeO-Fe_2O_3-Al_2O_3-TiO_2-SiO_2-C-H_2-O_2. *Journal of Metamorphic Geology*, **8**, 89-124.

Holland, T. J. B. & Powell, R., 1998. An internally consistent thermodynamic data set for phases of petrological interest. *Journal of Metamorphic Geology*, **16**, 309-343.

Holland, T. J. B. & Powell, R., 2011. An improved and extended internally consistent thermodynamic dataset for phases of petrological interest, involving a new equation of state for solids. *Journal of Metamorphic Geology*, **29**, 333-383.

Johnson, T., Brown, M., Gibson, R. & Wing, B., 2004. Spinel–cordierite symplectites replacing andalusite: evidence for melt-assisted diapirism in the Bushveld Complex, South Africa. *Journal of Metamorphic Geology*, **22**, 529-545.

Johnson, T. E. & Brown, M., 2004. Quantitative Constraints on Metamorphism in the Variscides of Southern Brittany – a Complementary Pseudosection Approach. *Journal of Petrology*, **45**, 1237-1259.

Johnson, T. E., Brown, M., Goodenough, K. M., Clark, C., Kinny, P. D. & White, R. W., 2016. Subduction or sagduction? Ambiguity in constraining the origin of ultramafic–mafic bodies in the Archean crust of NW Scotland. *Precambrian Research*, **283**, 89-105.

Johnson, T. E., Brown, M., Kaus, B. J. P. & VanTongeren, J. A., 2014. Delamination and recycling of Archaean crust caused by gravitational instabilities. *Nature Geoscience*, **7**, 47-52.

Kelly, E. D., Carlson, W. D. & Ketcham, R. A., 2013. Crystallization kinetics during regional metamorphism of porphyroblastic rocks. *Journal of Metamorphic Geology*, **31**, 963-979.

Kelsey, D. E. & Hand, M., 2014. On ultrahigh temperature crustal metamorphism: Phase equilibria, trace element thermometry, bulk composition, heat sources, timescales and tectonic settings. *Geoscience Frontiers*, **6**, 311-356.

Konrad-Schmolke, M., Handy, M. R., Babist, J. & O'Brien, P. J., 2005. Thermodynamic modelling of diffusion-controlled garnet growth. *Contributions to Mineralogy and Petrology*, **149**, 181-195.

Konrad-Schmolke, M., O'Brien, P. J., De Capitani, C. & Carswell, D. A., 2008. Garnet growth at high- and ultra-high pressure conditions and the effect of element fractionation on mineral modes and composition. *Lithos*, **103**, 309-332.

Korenaga, J., 2006. Archean geodynamics and the thermal evolution of Earth. In: *Archean Geodynamics and Environments Geophys. Monogr. Ser.*, pp. 7-32, AGU, Washington, DC.

Korhonen, F. J., Brown, M., Clark, C. & Bhattacharya, S., 2013. Osumilite-melt interactions in ultrahigh temperature granulites: phase equilibria modelling and implications for the *P*–

T-t evolution of the Eastern Ghats Province, India. *Journal of Metamorphic Geology*, **31**, 881-907.

Korhonen, F. J., Brown, M., Grove, M., Siddoway, C. S., Baxter, E. F. & Inglis, J. D., 2012. Separating metamorphic events in the Fosdick migmatite-granite complex, West Antarctica. *Journal of Metamorphic Geology*, **30**, 165-192.

Korhonen, F. J., Clark, C., Brown, M. & Taylor, R. J. M., 2014. Taking the temperature of Earth's hottest crust. *Earth and Planetary Science Letters*, **408**, 341-354.

Korzhinskii, D. S., 1959. *Physicochemical Basis of the Analysis of the Paragenesis of Minerals*. Published by Consultants Bureau, Inc., New York.

Kusky, T. M., 1998. Tectonic setting and terrane accretion of the Archean Zimbabwe craton. *Geology*, **26**, 163-166.

Lanari, P., Vidal, O., De Andrade, V., Dubacq, B., Lewin, E., Grosch, E. G. & Schwartz, S., 2014. XMapTools: A MATLAB (c)-based program for electron microprobe X-ray image processing and geothermobarometry. *Computers & Geosciences*, **62**, 227-240.

Laurent, O., Martin, H., Moyen, J. F. & Doucelance, R., 2014. The diversity and evolution of late-Archean granitoids: Evidence for the onset of "modern-style" plate tectonics between 3.0 and 2.5 Ga. *Lithos*, **205**, 208-235.

Lejeune, A.-M. & Richet, P., 1995. Rheology of crystal-bearing silicate melts: An experimental study at high viscosities. *Journal of Geophysical Research: Solid Earth*, **100**, 4215-4229.

Liati, A. & Gebauer, D., 2003. Geochronological constraints for the time of metamorphism in the Gruf Complex (Central Alps) and implications for the Adula-Cima Lunga nappe system. *Schweizerische Mineralogische Und Petrographische Mitteilungen*, **83**, 159-172.

Marmo, B. A., Clarke, G. L. & Powell, R., 2002. Fractionation of bulk rock composition due to porphyroblast growth: effects on eclogite facies mineral equilibria, Pam Peninsula, New Caledonia. *Journal of Metamorphic Geology*, **20**, 151-165.

Möller, A., Bousquet, R., Oalmann, J., Schmitz, S., Wilke, M., Nelson, D. R. & Schefer, S., 2012. In-situ monazite geochronology of UHT granulites from the Gruf Complex, Central Alps. *International Geological Congress, Abstracts*, **34**, 3828.

Möller, A., Savage, J., Oalmann, J. & Bousquet, R., 2013. Constraining the alpine history of the high grade Gruf Complex, Central Alps, by correlating deformation, U-Pb zircon geochronology and composition of felsic dikes and leucosomes. *Abstracts with Programs - Geological Society of America*, **45**, 509.

Moyen, J.-F. & Martin, H., 2012. Forty years of TTG research. *Lithos*, **148**, 312-336.

Nasipuri, P., Bhattacharya, A. & Das, S., 2009. Metamorphic reactions in dry and aluminous granulites: a Perple_X *P–T* pseudosection analysis of the influence of effective reaction volume. *Contributions to Mineralogy and Petrology*, **157**, 301-311.

O'Neill, C. & Debaille, V., 2014. The evolution of Hadean–Eoarchaean geodynamics. *Earth and Planetary Science Letters*, **406**, 49-58.

O'Neill, C., Jellinek, A. & Lenardic, A., 2007. Conditions for the onset of plate tectonics on terrestrial planets and moons. *Earth and Planetary Science Letters*, **261**, 20-32.

Oalmann, J., Möller, A. & Bosquet, R., 2013a. *P–T* modeling reveals juxtaposition of units within the Gruf Complex (Central Alps) during orogenesis. *Mineralogical Magazine*, **77**, 1873.

Oalmann, J., Möller, A. & Bosquet, R., 2013b. Petrological evidence for UHT metamorphism during orogenesis, Gruf complex, European Central Alps. *Geological Society of America Abstracts with Programs*, **45**, 662.

Oalmann, J., Möller, A. & Bousquet, R., 2011. In situ U-Pb dating of rutile in UHT granulites from the Gruf Complex, European Central Alps. *Mineralogical Magazine*, **75**, 1559.

Oalmann, J., Möller, A. & Bousquet, R., 2014. Linking zircon growth zones to *P–T* conditions; an example from the Gruf Complex, Central Alps. *Mineralogical Magazine*, **77**, 1844.

Palin, R. M., Weller, O. M., Waters, D. J. & Dyck, B., 2015. Quantifying geological uncertainty in metamorphic phase equilibria modelling; a Monte Carlo assessment and implications for tectonic interpretations. *Geoscience Frontiers*, **in press**, 1-17.

Palin, R. M. & White, R. W., 2016. Emergence of blueschists on Earth linked to secular changes in oceanic crust composition. *Nature Geoscience*, **9**, 60-64.

Powell, R., Guiraud, M. & White, R. W., 2005. Truth and beauty in metamorphic phase equilibria; conjugate variables and phase diagrams. *The Canadian Mineralogist*, **43**, 21-33.

Powell, R. & Holland, T. J. B., 2008. On thermobarometry. *Journal of Metamorphic Geology*, **26**, 155-179.

Powell, R., Holland, T. J. B. & Worley, B., 1998. Calculating phase diagrams involving solid solutions via non-linear equations, with examples using THERMOCALC. *Journal of Metamorphic Geology*, **16**, 577-588.

Rosenberg, C. L. & Handy, M. R., 2005. Experimental deformation of partially melted granite revisited: implications for the continental crust. *Journal of Metamorphic Geology*, **23**, 19-28.

Sawyer, E. W., 1996. Melt segregation and magma flow in migmatites; implications for the generation of granite magmas. *Special Paper - Geological Society of America*, **315**, 85-94.

Schmitz, S., Möller, A., Wilke, M., Malzer, W., Kanngiesser, B., Bousquet, R., Berger, A. & Schefer, S., 2009. Chemical U-Th-Pb dating of monazite by 3D-Micro X-ray fluorescence analysis with synchrotron radiation. *European Journal of Mineralogy*, **21**, 927-945.

Schoene, B., de Wit, M. J. & Bowring, S. A., 2008. Mesoarchean assembly and stabilization of the eastern Kaapvaal craton: A structural-thermochronological perspective. *Tectonics*, **27**.

Solar, G. S. & Brown, M., 2001. Petrogenesis of migmatites in Maine, USA; possible source of peraluminous leucogranite in plutons? *Journal of Petrology*, **42**, 789-823.

Spear, F. S., Kohn, M. J., Florence, F. P. & Menard, T., 1991. A model for garnet and plagioclase growth in pelitic schists: Implications for thermobarometry and *P–T* path determinations. *Journal of Metamorphic Geology*, **8**, 683-696.

Spear, F. S. & Pyle, J. M., 2010. Theoretical modeling of monazite growth in a low-Ca metapelite. *Chemical Geology*, **273**, 111-119.

Stern, R. J., 2007. When and how did plate tectonics begin? Theoretical and empirical considerations. *Chinese Science Bulletin*, **52**, 578-591.

Stern, R. J., 2008. Modern-style plate tectonics began in Neoproterozoic time; an alternative interpretation of Earth's tectonic history. *Special Paper - Geological Society of America*, **440**, 265-280.

Štipska, P. & Powell, R., 2005. Constraining the *P–T* path of a MORB-type eclogite using pseudosections, garnet zoning and garnet-clinopyroxene thermometry: an example from the Bohemian Massif. *Journal of Metamorphic Geology*, **23**, 725-743.

Stipska, P., Powell, R., White, R. W. & Baldwin, J. A., 2010. Using calculated chemical potential relationships to account for coronas around kyanite: an example from the Bohemian Massif. *Journal of Metamorphic Geology*, **28**, 97-116.

Stüwe, K., 1997. Effective bulk composition changes due to cooling: a model predicting complexities in retrograde reaction textures. *Contributions to Mineralogy and Petrology*, **129**, 43-52.

Tajcmanova, L., Connolly, J. A. D. & Cesare, B., 2009. A thermodynamic model for titanium and ferric iron solution in biotite. *Journal of Metamorphic Geology*, **27**, 153-165.

Taylor, R. J. M., Kirkland, C. L. & Clark, C., 2016. Accessories after the facts: Constraining the timing, duration and conditions of high-temperature metamorphic processes. *Lithos*, **264**, 239-257.

Taylor-Jones, K. & Powell, R., 2010. The stability of sapphirine plus quartz: calculated phase equilibria in FeO-MgO-Al2O3-SiO2-TiO2-O. *Journal of Metamorphic Geology*, **28**, 615-633.

Thompson, A. B. & England, P. C., 1984. Pressure-temperature-time paths of regional metamorphism II. Their inference and interpretation using mineral assemblages in metamorphic rocks. *Journal of Petrology*, **25**, 929-955.

Thompson, J. B., 1959. Local equilibrium in metasomatic processes. In: *Researches in Geochemistry* (ed Abelson, P. H.), pp. 427-457, Wiley, New York.

van der Molen, I. & Paterson, M. S., 1979. Experimental deformation of partially-melted granite. *Contributions to Mineralogy and Petrology*, **70**, 299-318.

van Hunen, J. & Moyen, J. F., 2012. Archean Subduction: Fact or Fiction? *Annual Review of Earth and Planetary Sciences, Vol 40*, **40**, 195-219.

van Hunen, J. & van den Berg, A. P., 2008. Plate tectonics on the early Earth: Limitations imposed by strength and buoyancy of subducted lithosphere. *Lithos*, **103**, 217-235.

Vorhies, S. H. & Ague, J. J., 2011. Pressure–temperature evolution and thermal regimes in the Barrovian zones, Scotland. *Journal of the Geological Society*, **168**, 1147-1166.

Walsh, A., Kelsey, D., Kirkland, C., Hand, M., Smithies, R., Clark, C. & Howard, H., 2014. *P–T*–t evolution of a large, long-lived, ultrahigh-temperature Grenvillian belt in central Australia. *Gondwana Research*.

Walther, J. & Orville, P., 1982. Volatile production and transport in regional metamorphism. *Contributions to Mineralogy and Petrology*, **79**, 252-257.

Waters, D. J. & Lovegrove, D. P., 2002. Assessing the extent of disequilibrium and overstepping of prograde metamorphic reactions in metapelites from the Bushveld Complex aureole, South Africa. *Journal of Metamorphic Geology*, **20**, 135-149.

White, R., Powell, R. & Halpin, J., 2004. Spatially‐focussed melt formation in aluminous metapelites from Broken Hill, Australia. *Journal of Metamorphic Geology*, **22**, 825-845.

White, R., Powell, R. & Holland, T., 2001. Calculation of partial melting equilibria in the system Na2O–CaO–K2O–FeO–MgO–Al2O3–SiO2–H2O (NCKFMASH). *Journal of metamorphic Geology*, **19**, 139-153.

White, R. W. & Powell, R., 2002. Melt loss and the preservation of granulite facies mineral assemblages. *Journal of Metamorphic Geology*, **20**, 621-632.

White, R. W. & Powell, R., 2011. On the interpretation of retrograde reaction textures in granulite facies rocks. *Journal of Metamorphic Geology*, **29**, 131-149.

White, R. W., Powell, R. & Baldwin, J. A., 2008. Calculated phase equilibria involving chemical potentials to investigate the textural evolution of metamorphic rocks. *Journal of Metamorphic Geology*, **26**, 181-198.

White, R. W., Powell, R. & Clarke, G. L., 2002. The interpretation of reaction textures in Fe-rich metapelitic granulites of the Musgrave Block, central Australia: constraints from mineral equilibria calculations in the system K2O–FeO–MgO–Al2O3–SiO2–H2O–TiO2–Fe2O3. *Journal of Metamorphic Geology*, **20**, 41-55.

White, R. W., Powell, R. & Holland, T. J. B., 2007. Progress relating to calculation of partial melting equilibria for metapelites. *Journal of Metamorphic Geology*, **25**, 511-527.

White, R. W., Powell, R., Holland, T. J. B., Johnson, T. E. & Green, E. C. R., 2014a. New mineral activity–composition relations for thermodynamic calculations in metapelitic systems. *Journal of Metamorphic Geology*, **32**, 261-286.

White, R. W., Powell, R., Holland, T. J. B. & Worley, B., 2000. The effect of TiO_2 and Fe_2O_3 on metapelitic assemblages at greenschist and amphibolite facies conditions: mineral equilibria calculations in the system K_2O-FeO-MgO-Al_2O_3-SiO_2-H_2O-TiO_2-Fe_2O_3. *Journal of Metamorphic Geology*, **18**, 497-511.

White, R. W., Powell, R. & Johnson, T. E., 2014b. The effect of Mn on mineral stability in metapelites revisited: new a–x relations for manganese-bearing minerals. *Journal of Metamorphic Geology*, **32**, 809-828.

Whitney, D. L. & Evans, B. W., 2010. Abbreviations for names of rock-forming minerals. *American Mineralogist*, **95**, 185-187.

Williams, M. L., Dumond, G., Mahan, K., Regan, S. & Holland, M., 2014. Garnet-forming reactions in felsic orthogneiss: Implications for densification and strengthening of the lower continental crust. *Earth and Planetary Science Letters*, **405**, 207-219.

Yakymchuk, C. & Brown, M., 2014. Consequences of open-system melting in tectonics. *Journal of the Geological Society*, **171**, 21-40.

Yakymchuk, C., Brown, M., Clark, C., Korhonen, F. J., Piccoli, P. M., Siddoway, C. S., Taylor, R. J. M. & Vervoort, J. D., 2015. Decoding polyphase migmatites using geochronology and phase equilibria modelling. *Journal of Metamorphic Geology*, **33**, 203-230.

Zeh, A., Klemd, R., Buhlmann, S. & Barton, J. M., 2004. Pro- and retrograde *P–T* evolution of granulites of the Beit Bridge Complex (Limpopo Belt, South Africa): constraints from quantitative phase diagrams and geotectonic implications. *Journal of Metamorphic Geology*, **22**, 79-95.

2.11 FIGURES

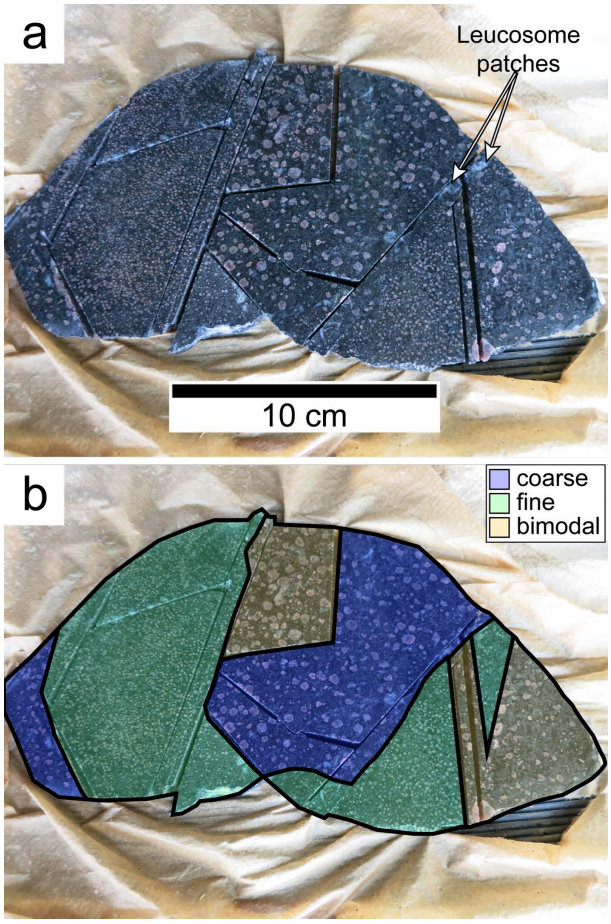

Figure 2.1: a) Photograph of hand sample studied here. Leucocratic patches (highlighted by white arrows) are interpreted to be leucosome. b) Photograph of hand sample with overlain map of macrodomains, showing coarse-grained, fine-grained, and bimodal domains (referred to as C, F, and CF, respectively in the text).

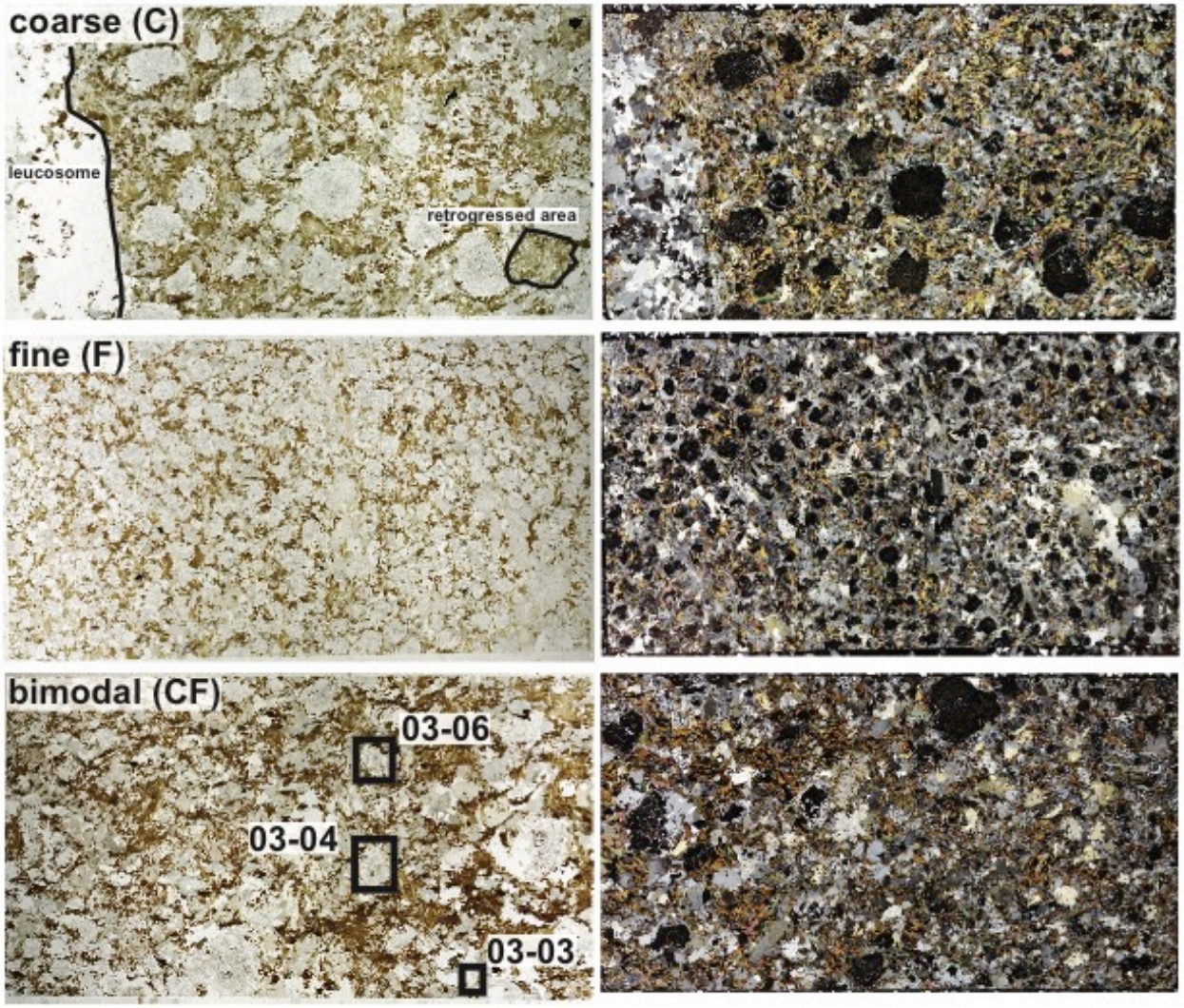

Figure 2.2: Photographs of standard size (24 x 46 mm) thin sections cut from various macrodomains, highlighting heterogeneity at the thin section scale. Left column in plane polarized light and right column in cross polarized light for each thin section. The microdomains studied here are also labeled. Examples of a more thoroughly retrogressed area, as well as a leucosome vein (discussed in text) are shown in the thin section of macrodomain C.

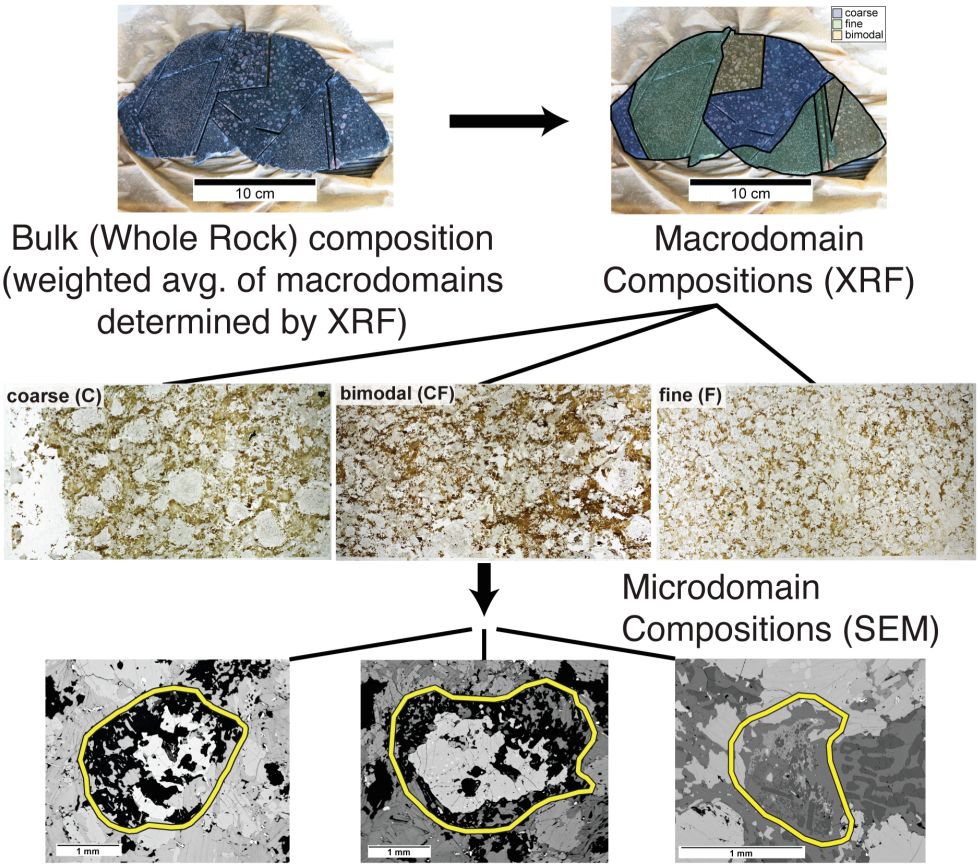

Figure 2.3: Flowchart illustrating the multi-scalar approach to thermodynamic modeling in this study, with the hypothesis that domains developed at different length scales will record successive metamorphic stages as equilibrium length scales decreased upon melt channelization, loss or consumption throughout the metamorphic evolution.

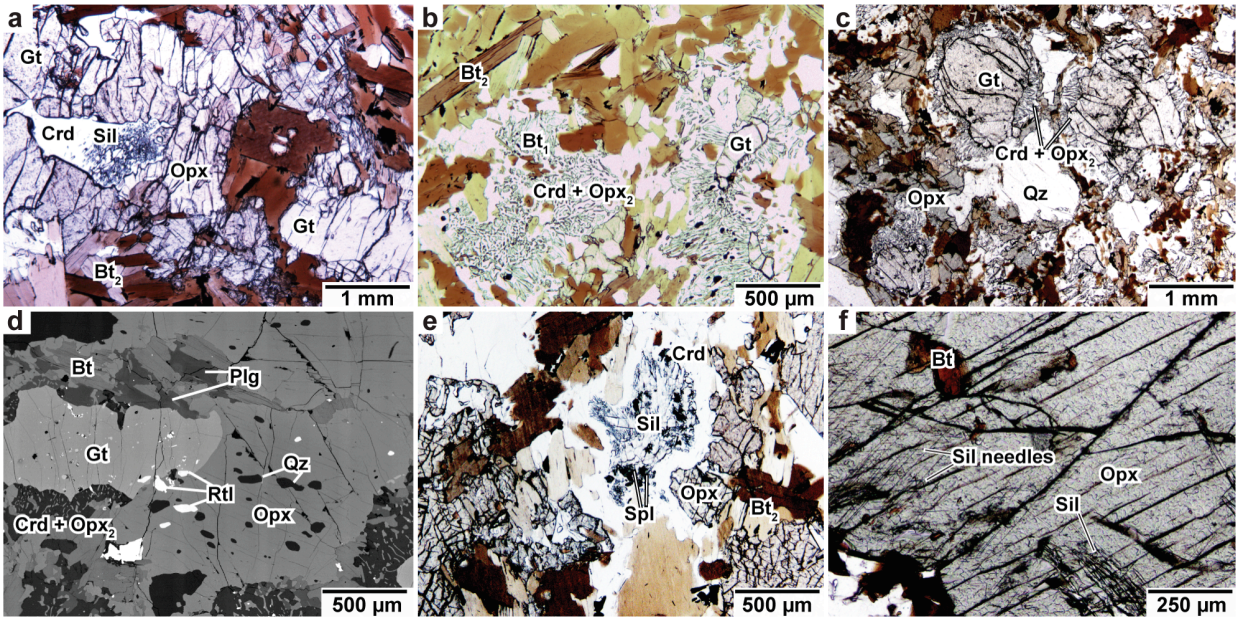

Figure 2.4: Thin section photomicrographs of representative textures from various macrodomains. Mineral abbreviations are after Whitney and Evans (2010). a) Sillimanite cluster in embayment in orthopyroxene, surrounded by cordierite from macrodomain CF. Retrograde biotite surrounds orthopyroxene and garnet. b) Symplectitic pseudomorph of cordierite and orthopyroxene after garnet, surrounded by retrograde biotite from macrodomain CF. c) Garnet with symplectitic coronae of cordierite and orthopyroxene, separated from coarse-grained, rounded quartz by a orthopyroxene necklace in macrodomain F. d) BSE image of orthopyroxene porphyroblast with abundant rutile and quartz inclusions in macrodomain F. Garnet is also included in orthopyroxene, but exhibits symplectitic orthopyroxene–cordierite and orthopyroxene–plagioclase coronae. e) Prismatic sillimanite surrounded by fine-grained spinel and cordierite from macrodomain CF. f) Sillimanite inclusion in orthopyroxene. Sillimanite also forms fine-grained, oriented exsolution needles.

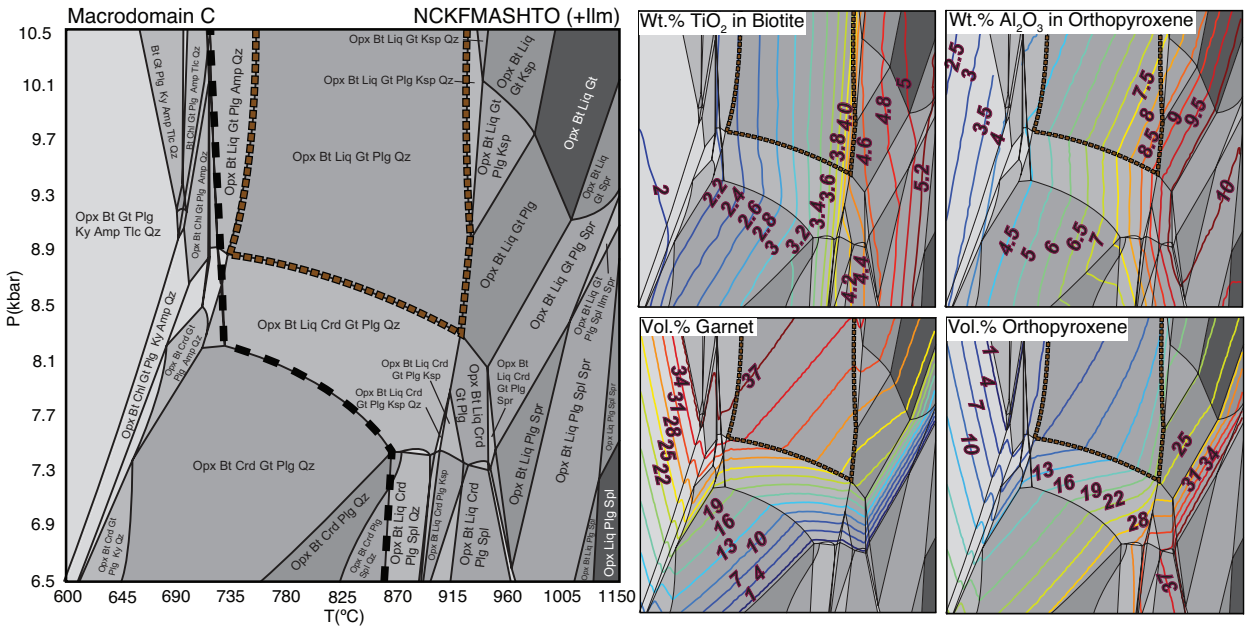

Figure 2.5: *P–T* pseudosection for Macrodomain C. Dashed black line represents the solidus. Dashed brown line outlines the stability of the inferred macrodomain assemblage of orthopyroxene + biotite + melt + garnet + plagioclase feldspar + quartz + ilmenite. Contours for wt.% TiO_2 in biotite, Al_2O_3 in orthopyroxene, vol.% garnet, and vol.% orthopyroxene are shown on the right. Warm colors indicate high concentration or abundance, cold colors indicate low concentration or abundance.

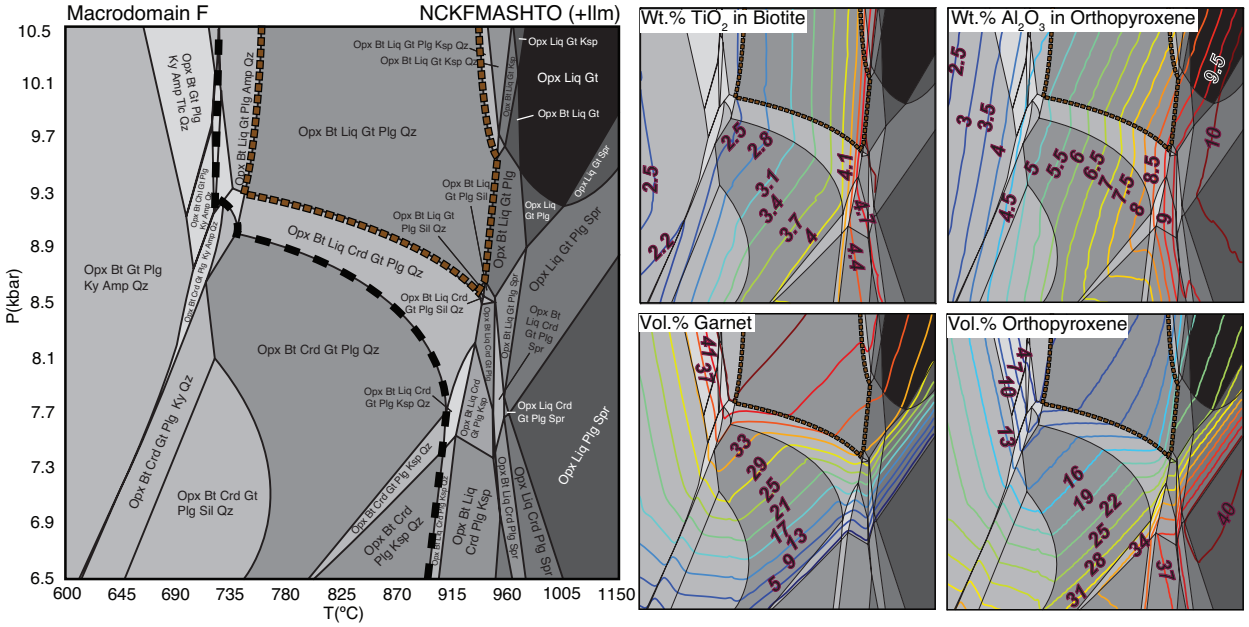

Figure 2.6: *P–T* pseudosection for Macrodomain F. Dashed black line represents the solidus. Dashed brown line outlines the stability of the inferred macrodomain assemblage of orthopyroxene + biotite + melt + garnet + plagioclase feldspar + quartz + ilmenite. Contours for wt.% TiO_2 in biotite, Al_2O_3 in orthopyroxene, vol.% garnet, and vol.% orthopyroxene are shown on the right.

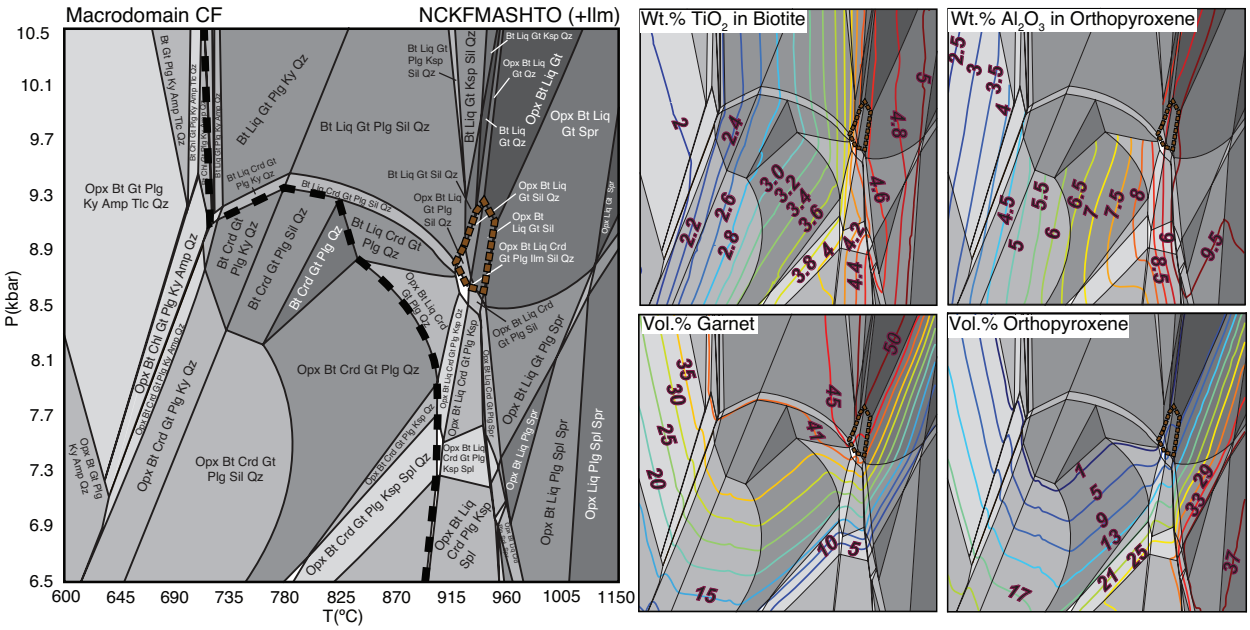

Figure 2.7: *P–T* pseudosection for Macrodomain CF. Dashed black line represents the solidus. Dashed brown line outlines the stability of the inferred macrodomain assemblage of orthopyroxene + biotite + melt + garnet + plagioclase feldspar + sillimanite + ilmenite ± quartz. Contours for wt.% TiO_2 in biotite, Al_2O_3 in orthopyroxene, vol.% garnet, and vol.% orthopyroxene are shown on the right.

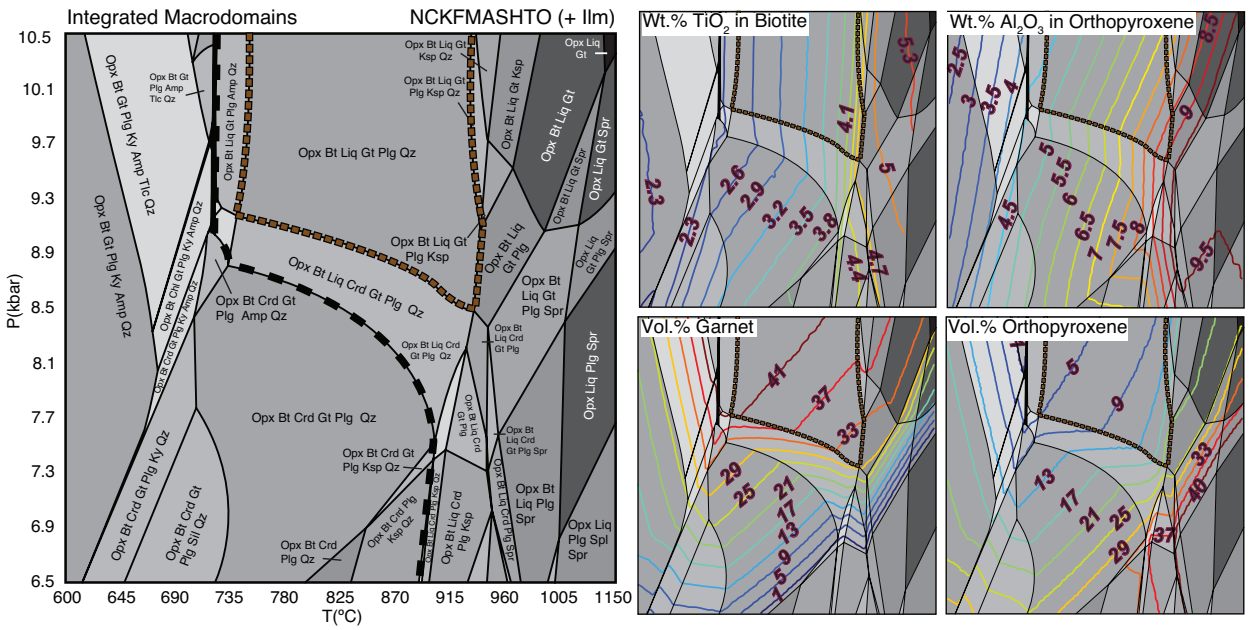

Figure 2.8: *P–T* pseudosection for integrated bulk composition, comprised of ~34% Macrodomain C, ~48% Macrodomain F, and ~18% Macrodomain CF. Dashed black line represents solidus. Dashed brown line outlines the stability of the inferred equilibrium assemblage of orthopyroxene + biotite + melt + garnet + plagioclase feldspar + quartz + ilmenite. Contours for wt.% TiO_2 in biotite, Al_2O_3 in orthopyroxene, vol.% garnet, and vol.% orthopyroxene are shown on the right.

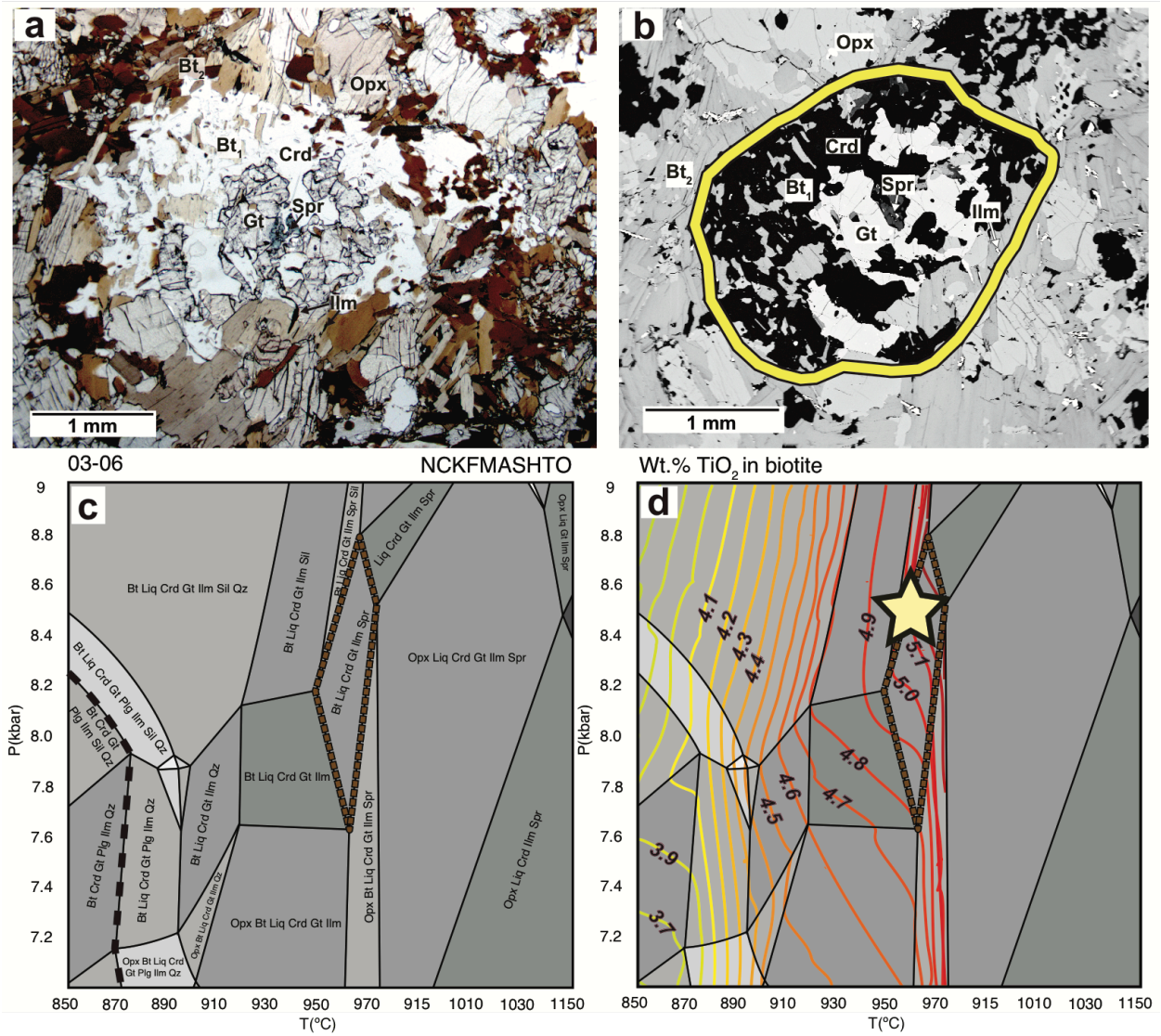

Figure 2.9: a) Photomicrograph of microdomain 03-06. b) Backscattered electron (BSE) image of microdomain 03-06 displaying the compositional domain (denoted by the yellow line) chosen for pseudosection modeling (note that section in b is rotated lightly counterclockwise, relative to in a). c) *P–T* pseudosection for the compositional domain in B. The field with the inferred equilibirium assemblage is outlined by the brown dashed line. d) *P–T* pseudosection countoured for TiO_2 content of biotite in weight percent. The yellow star corresponds to apparent peak *P–T* conditions recorded by the texture and analyzed mineral compositions.

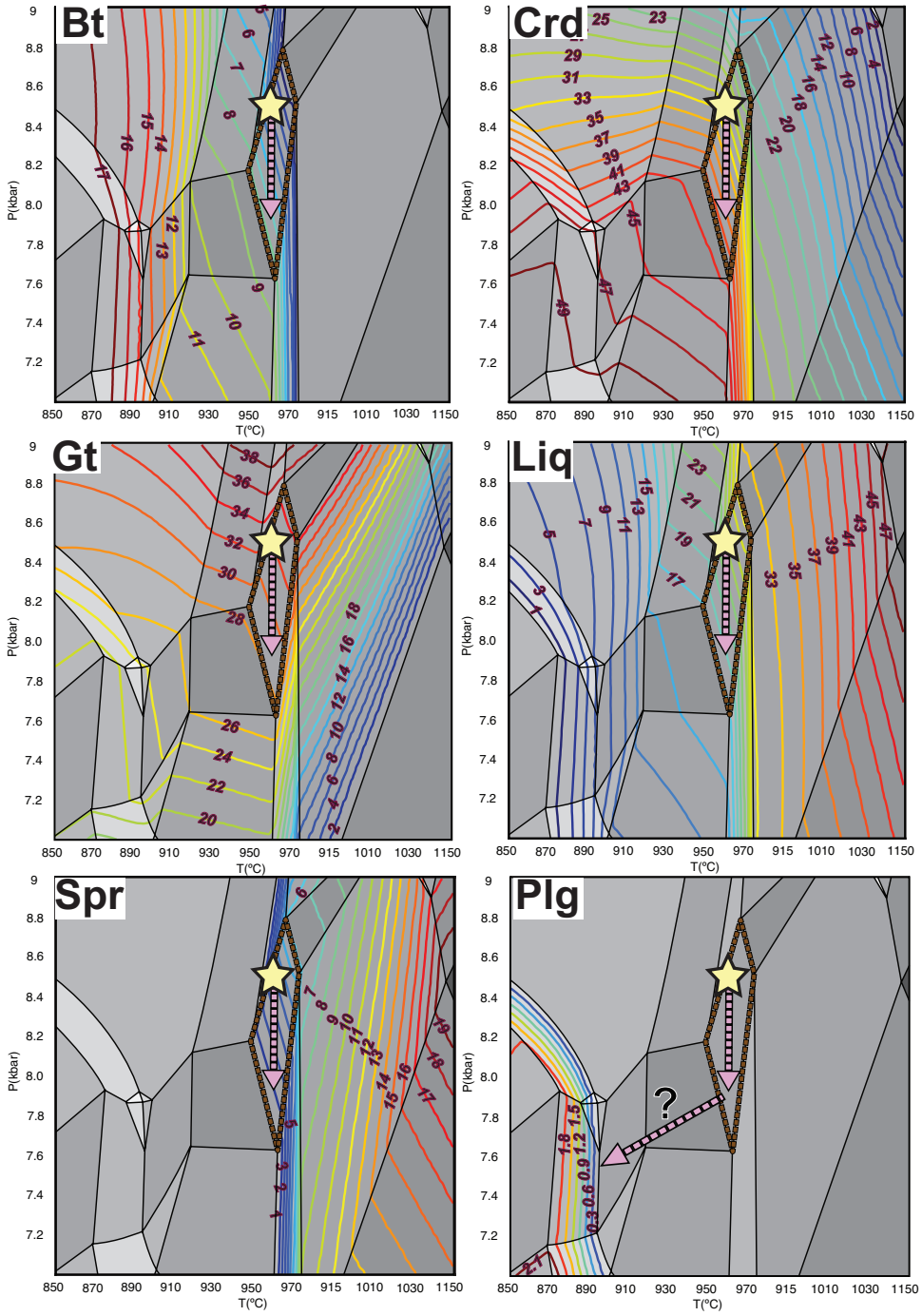

Figure 2.10: *P–T* pseudosection diagrams for microdomain 03-06 (from Figure 9c) contoured for modal abundance of: biotite (Bt), cordierite (Crd), garnet (Gt), melt (Liq), orthopyroxene (Opx), and sapphirine (Spr). Warm colors (red) indicate high abundance, cold (blue) colors indicate low abundance. Pink arrows indicate a *P–T* path consistent with development of the observed texture.

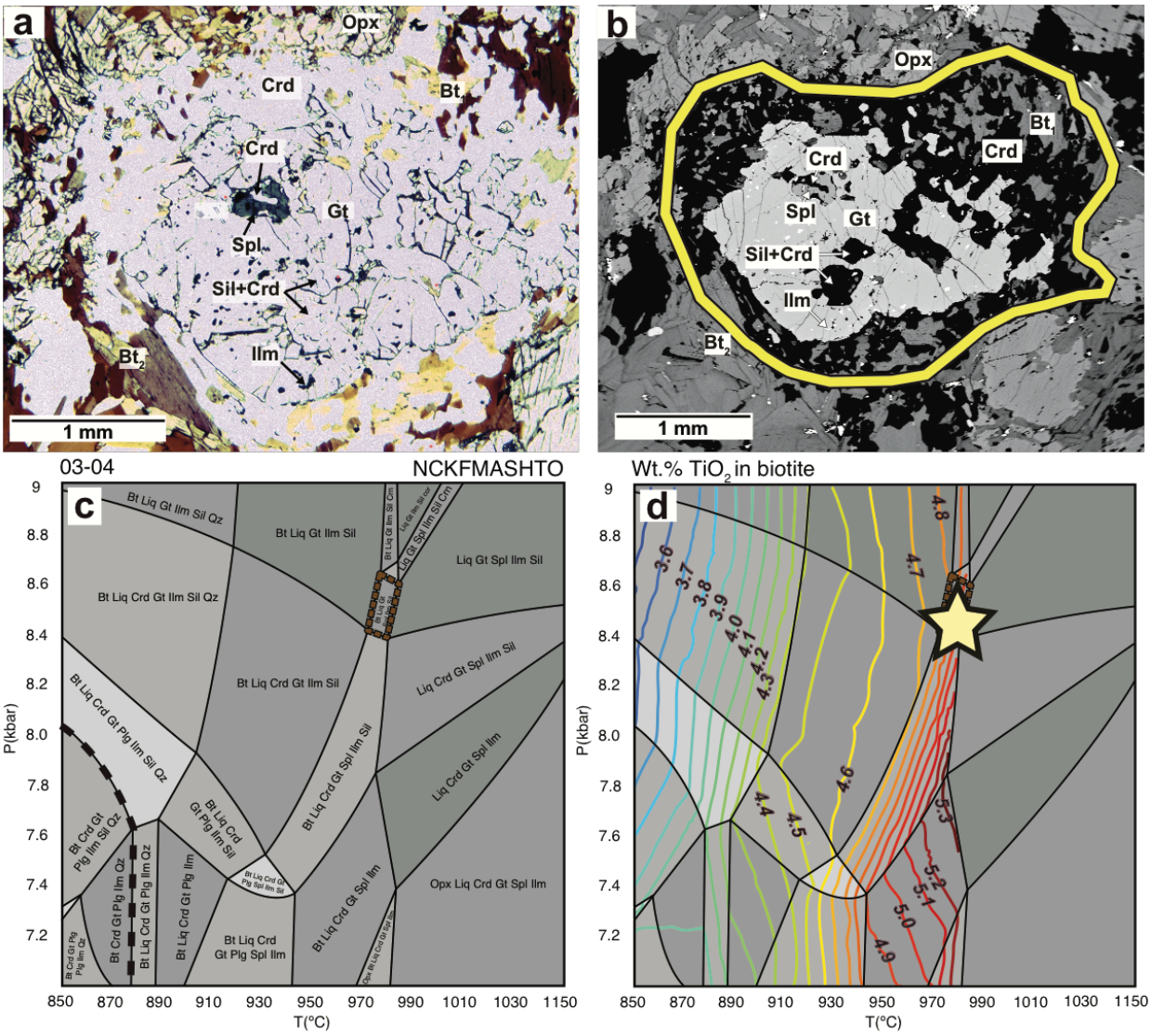

Figure 2.11: a) Photomicrograph, and b) BSE image of microdomain 03-04. c) *P–T* pseudosection, and d) TiO_2 content of biotite in weight percent, calculated for the composition of the domain highlighted by the yellow line in b). Pink dashed arrows represent the inferred *P–T* path based on changing mineral modes in. S4. Symbols are the same as in Fig. 10.

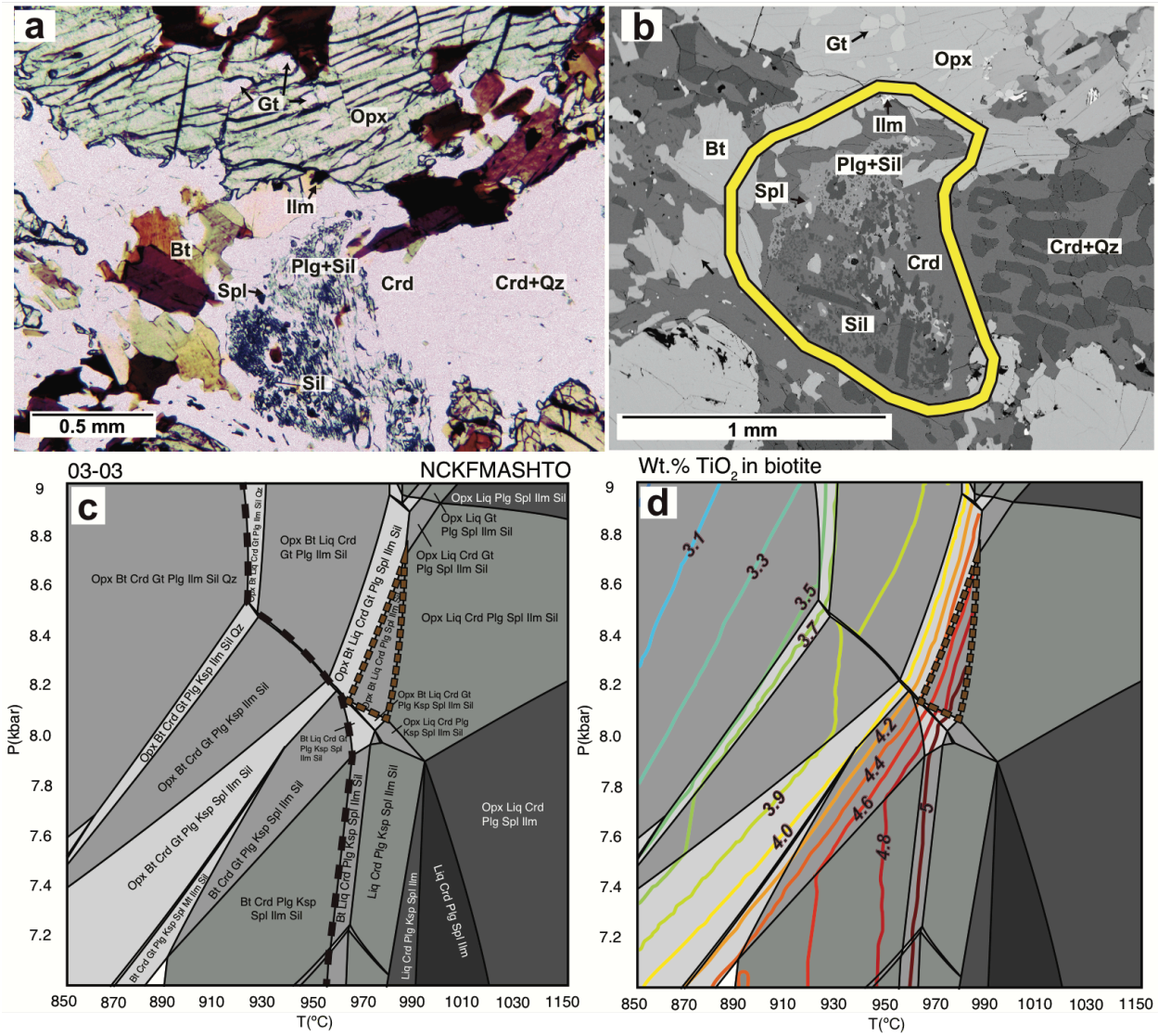

Figure 2.12: a) Photomicrograph, and b) BSE image of microdomain 03-03. c) *P–T* pseudosection, and d) TiO_2 content of biotite in weight percent, calculated for the composition of the domain highlighted by the yellow line in b). Pink dashed arrow represents the inferred *P–T* path based on changing mineral modes in Fig. S5. Symbols are the same as in Fig. 10.

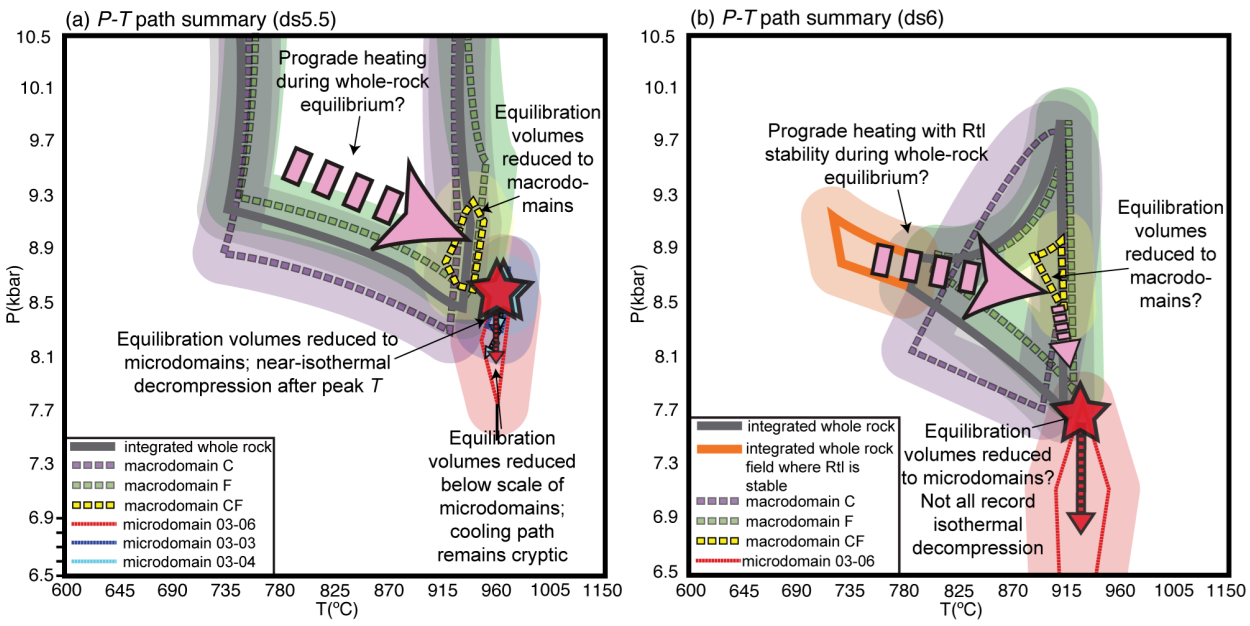

Figure 2.13: *P–T* path summaries for a) ds5.5 and b) ds6, showing differing interpretations of the *P–T* history inferred using two different thermodynamic datasets. Lightly shaded areas represent ± ~40 ˚C and ± ~0.25 kbar uncertainty on the bounds of each field, with ds5.5 fields coming from Figs 5-9, S4, & S5, and ds6 fields coming from Figs 14 & 15.

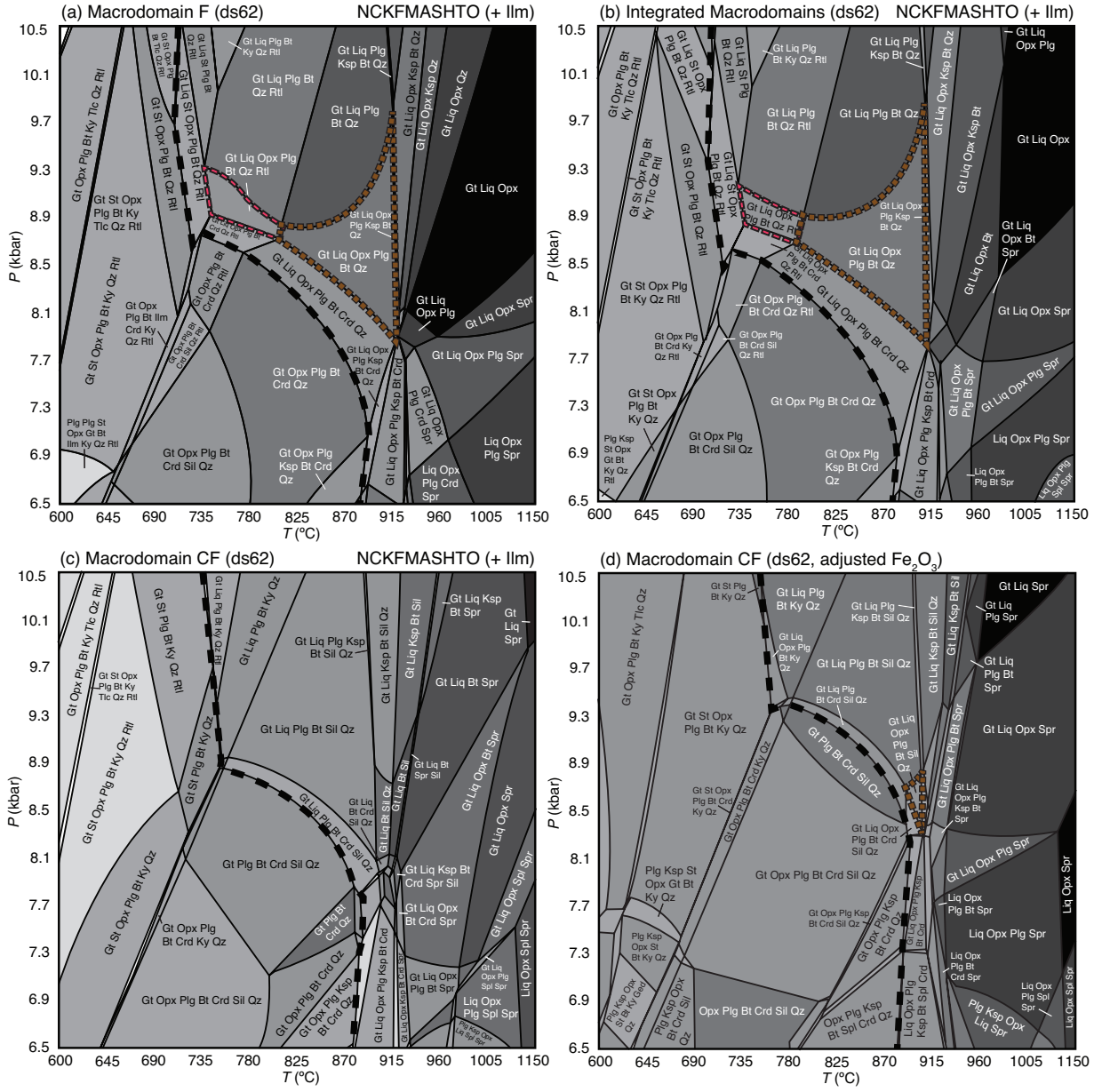

Figure 2.14: *P–T* pseudosections for a) macrodomain F, b) the integrated bulk composition, c) macrodomain CF, and d) macrodomain CF with adjusted Fe_2O_3 content, calculated using ds6. Macrodomain assemblage fields are outlined by the brown dashed line. Solidi are demarcated by the black dashed line. Fields in which rutile is predicted to be stable with the assemblage for macrodomain F and the integrated bulk composition are outlined by the red dashed line.

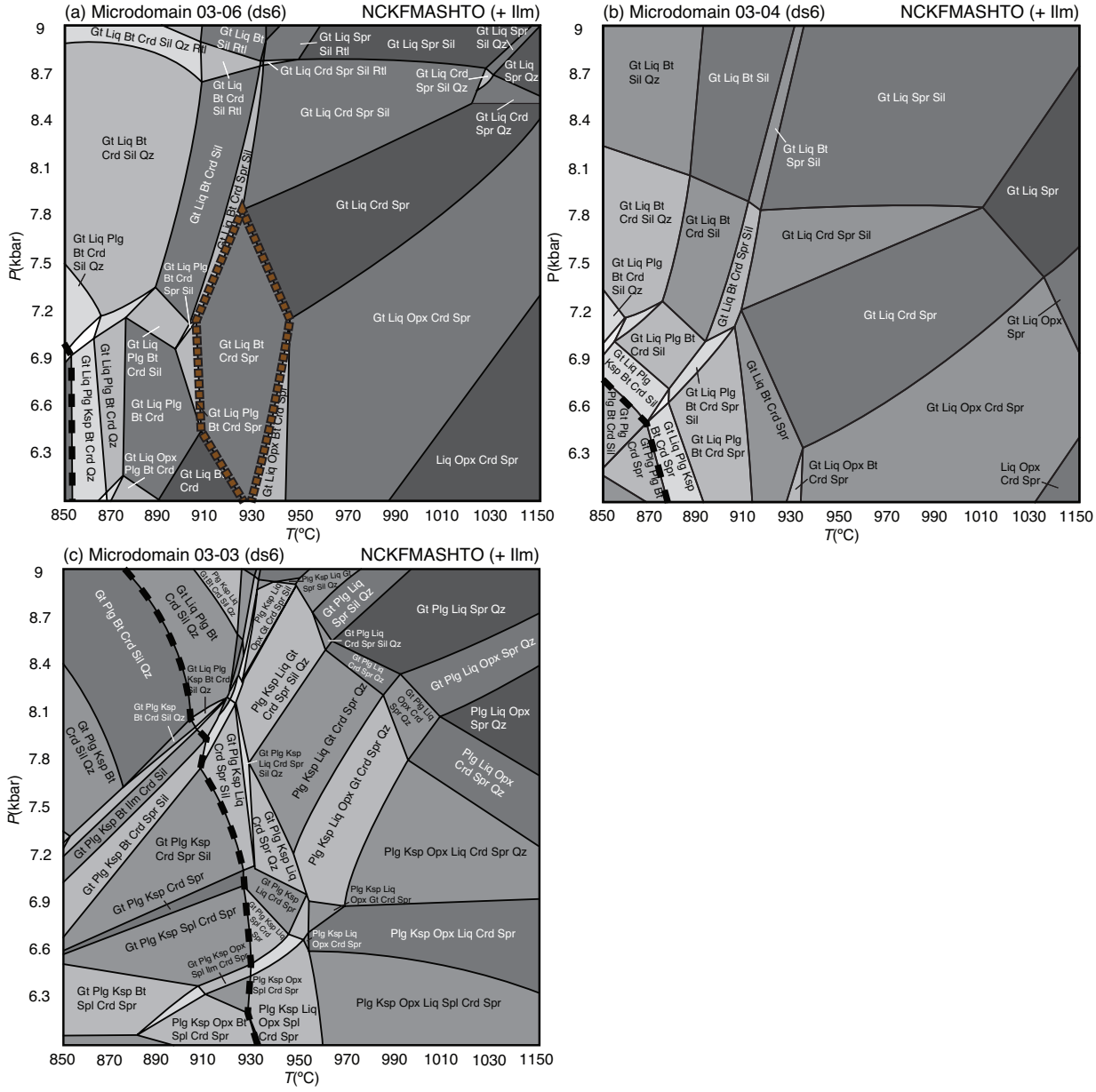

Figure 2.15: *P–T* pseudosections for microdomains a) 03-06, b) 03-04, and c) 03-03 constructed using ds6. The inferred equilibrium assemblage field is outlined by the brown dashed line in the diagram for 03-06 (a). The inferred equilibrium assemblages for the other two microdomains (03-04 and 03-03, b and c, respectively) were not predicted by the pseudosection. Solidi are indicated by the black dashed line.

2.12 TABLES

Table 2.1: a) representative garnet microprobe compositional analyses (wt.%) from macrodomains. b) representative orthopyroxene microprobe compositional analyses (wt.%) from macrodomains. b) representative biotite microprobe compositional analyses (wt.%) from macrodomains and microdomains.

Sample	SiO_2 (wt.%)	TiO_2	Al_2O_3	MgO	CaO	MnO	FeO_t	Na_2O	K_2O	Total	X_{pyr}	X_{grs}	X_{spss}	X_{alm}
Macrodomain C (core)	39.78	0.06	22.38	10.21	2.21	0.44	25.13	0.01	0.03	100.25	0.39	0.06	0.010	0.54
Macrodomain C (rim)	41.09	0.07	23.31	11.21	1.96	0.42	25.24	0.02	0	103.32	0.41	0.05	0.009	0.52
Macrodomain F (core)	38.61	0.04	22.30	10.55	4.48	0.36	23.92	0.02	0	100.28	0.39	0.12	0.007	0.49
Macrodomain F (rim)	39.25	0.07	22.89	10.09	2.10	0.43	26.78	0.02	0.01	101.64	0.38	0.06	0.009	0.56
Macrodomain CF (core)	39.46	0.02	23.15	10.89	3.63	0.36	24.65	0	0	102.16	0.40	0.09	0.007	0.50
Macrodomain CF (rim)	38.83	0.08	22.99	8.85	1.53	0.44	29.90	0.01	0	102.63	0.33	0.04	0.009	0.62

Table 2.1a

Table 2.1b

Sample	SiO_2 (wt.%)	TiO_2	Al_2O_3	MgO	CaO	MnO	FeO_t	Na_2O	K_2O	Total
Macrodomain C (core)	52.16	0.05	6.28	23.24	0.09	0.08	19.04	0.025	0	100.97
Macrodomain C (annulus)	50.18	0.21	9.89	22.3	0.10	0.06	19.71	0.03	0	102.48
Macrodomain C (rim)	52.16	0.05	6.27	23.24	0.09	0.08	19.03	0.02	0	100.94
Macrodomain F (core)	50.47	0.07	6.52	23.08	0.09	0.08	20.09	0	0	100.40
Macrodomain F (annulus)	52.45	0.14	9.99	22.80	0.28	0.08	15.84	0.02	0.12	101.73
Macrodomain F (rim)	51.52	0.10	5.19	23.12	0.10	0.09	20.64	0.01	0.01	100.78
Macrodomain F (symplectite)	52.66	0.04	5.36	22.66	0.09	0.13	20.51	0.03	0	101.48
Macrodomain CF (core)	50.65	0.13	4.87	23.22	0.09	0.13	21.43	0	0.01	100.53
Macrodomain CF (annulus)	51.33	0.13	9.34	23.59	0.15	0.12	17.52	0.02	0.01	102.21
Macrodomain CF (rim)	48.99	0.12	5.95	21.57	0.07	0.13	22.72	0	0.02	99.57

Table 2.1c

Sample		SiO_2 (wt.%)	TiO_2	Al_2O_3	MgO	CaO	MnO	FeO_t	Na_2O	K_2O	Total
Macrodomain (primary)	C	38.39	4.91	16.43	15.68	0.00	0.01	12.13	0.35	9.59	97.49
Macrodomain (retrograde)	C	39.10	3.41	16.34	16.74	0.03	0.01	10.79	0.36	9.05	95.82
Macrodomain (primary)	F	39.415	4.99	16.68	16.50	0.02	0.00	11.23	0.27	8.56	97.66
Macrodomain (primary)	CF	37.07	5.30	15.87	16.24	0.00	0.03	11.13	0.26	9.73	95.63
Macrodomain (retrograde)	CF	38.46	3.78	16.37	16.40	0.00	0.00	11.23	0.27	9.44	95.96
Microdomain (primary)	03-06	36.89	5.14	16.22	15.61	0.00	0.00	12.08	0.31	9.80	96.04
Microdomain (primary)	03-04	38.45	5.14	17.04	15.81	0.00	0.06	11.90	0.32	9.53	98.25
Microdomain (primary)	03-03	36.68	5.02	16.35	15.33	0.00	0.02	12.47	0.27	9.70	95.84

Table 2.2: a) XRF bulk compositions for each macrodomain (wt.%). B) Normalized compositions for each macrodomain used for thermodynamic modeling in NCKFMASHTO (wt.%), with H_2O and Fe_2O_3 content adjusted with constraints from calculated T–M_{H2O} and T–M_{Fe2O3} diagrams.

Table 2.2a

Sample	SiO_2 (wt.%)	TiO_2	Al_2O_3	Fe_2O_3	FeO	MnO	MgO	CaO	Na_2O	K_2O	LOI	Total
C	46.09	2.05	16.21	4.78	10.05	0.16	13.92	1.45	0.48	2.83	1.92	99.94
F	46.50	2.15	16.44	5.07	10.00	0.14	14.77	1.52	0.27	2.04	1.21	100.11
CF	43.42	2.14	19.31	5.71	9.88	0.14	13.58	1.21	0.26	2.75	1.43	99.83

Table 2.2b

Sample	SiO_2 (wt.%)	TiO_2	Al_2O_3	Fe_2O_3	FeO	MgO	CaO	Na_2O	K_2O	H_2O	Total
C	46.55	2.07	16.38	4.83	10.15	14.06	1.46	0.48	2.85	1.16	100
F	46.92	2.17	16.59	5.12	10.09	14.44	1.53	0.27	2.06	0.80	100
CF	43.72	2.15	19.44	5.75	9.95	13.67	1.22	0.26	2.76	1.07	100
"Whole Rock"	46.36	2.13	16.75	5.05	10.08	14.40	1.47	0.36	2.46	0.95	100

Table 2.3: a) Normalized SEM semi-quantitative bulk compositions for each microdomain (wt.%) b): Normalized compositions for each microdomain for thermodynamic modeling in NCKFMASHTO (wt.%), with H_2O and Fe_2O_3 content adjusted with constraints from calculated T–M_{H2O} and T–M_{Fe2O3} diagrams.

Table 2.3a

Sample	**SiO_2 (wt.%)**	**TiO_2**	**Al_2O_3**	**FeO**	**MnO**	**MgO**	**CaO**	**Na_2O**	**K_2O**	**Total**
03-06	46.14	1.51	25.72	12.08	0.16	11.63	0.62	0.18	1.96	100
03-04	43.64	1.46	25.37	15.59	0.16	11.08	0.78	0.30	1.62	100
03-03	44.26	1.11	34.62	6.26	0	9.76	2.24	0.22	1.54	100

Table 2.3b

Sample	**SiO_2 (wt.%)**	**TiO_2**	**Al_2O_3**	**Fe_2O_3**	**FeO**	**MgO**	**CaO**	**Na_2O**	**K_2O**	**H_2O**	**Total**
03-06	45.14	1.43	25.16	2.33	10.75	11.27	0.62	0.12	1.88	1.31	100
03-04	42.63	1.46	24.80	2.76	14.01	10.83	1.74	0.20	1.63	0.95	100
03-03	43.11	1.09	33.30	4.49	4.06	9.35	2.13	0.16	1.47	0.83	100

Chapter 3. A pulse of cryptic granulite-facies metamorphism in the Archean Wyoming Craton revealed by Sm-Nd garnet and U-Pb monazite geochronology

B. Dragovic[1], V.E. Guevara[1], M.J. Caddick[1], E.F. Baxter[2,3], and A.R.C. Kylander-Clark[3]

[1]Department of Geosciences, Virginia Polytechnic Institute and State University, Blacksburg, VA 24061, USA
[2]Department of Earth and Environmental Science, Boston College, 140 Commonwealth Ave., Chestnut Hill, MA 02467, USA
[3]Department of Earth Science and Environment, Boston University, 685 Commonwealth Ave., Boston, MA 02215, USA
[4]Department of Earth Science, University of California Santa Barbara, 1006 Webb Hall, Santa Barbara, CA 93106, USA

Published September 2016 in *Precambrian Research,* 283, 24-49

3.1 ABSTRACT

Granulite-facies metamorphism of large tracts of continental crust is a characteristic feature of Archean cratons, where metamorphism ultimately led to crustal stabilization and chemical differentiation. Constraining the timing and duration of this metamorphism can provide insight into the processes behind Archean cratonic evolution, and here we present new Sm-Nd garnet ages from granulite-facies metasediments from the eastern Beartooth Mountains of the Wyoming Craton. The eastern Beartooth Mountains are dominantly comprised of a ~2.8 Ga calc-alkaline batholith known as the Long Lake Magmatic Complex (LLMC). Within this batholith, numerous cm- to km-scale granulite-facies metasedimentary xenoliths and roof pendants have previously been interpreted to represent metamorphism due to contact heating with the LLMC or prior to LLMC emplacement. Garnet ages from five granulite-facies metasediments range from 2669 ± 48 Ma to 2681 ± 58 Ma: significantly younger than the LLMC and consistent with newly described field relations. Preserved major and trace element garnet zoning suggest that these dates are biased towards late stage garnet growth during granulite-facies metamorphism, and that this metamorphism post-dates LLMC emplacement. U-Pb monazite petrochronology of a metasediment and an tonalite reveals distinct periods of monazite (re)crystallization at 2.79-2.78 Ga (consistent with LLMC emplacement) and at 2.69-2.67 Ga (coincident with the garnet ages). The Sm-Nd bulk garnet ages exhibit larger errors and high MSWDs, which may result from sampling a polymetamorphic population, as suggested by REE zoning in garnet and supported by the U-Pb monazite data. Diffusion modeling of preserved major element garnet zoning suggests that the timescale at near-peak temperatures during the 2.69-2.67 Ga event was <1 Ma. Phase equilibria modeling suggests that the LLMC would have experienced minimal partial melting during this cryptic granulite-facies metamorphism, implying that large volumes of crust may have experienced a significant thermal event, but that only some parts of the crust record strong evidence for it. The ages presented here are similar to known granulite-facies metamorphic and mafic magmatic events in other parts of the Wyoming Craton, though no clear evidence of mafic magmas is present locally.

3.2 INTRODUCTION

High temperature (HT*)* metamorphic terranes are a common feature of Archean cratons (e.g., Brown, 2007), where metamorphism and associated partial melting/melt removal led to crustal differentiation and strengthening (e.g., Williams et al., 2014; Brown et al., 2011; Menegon et al., 2011), thus playing an important role in cratonic stabilization. Characterizing the age and duration of Archean HT metamorphism can therefore lead to better understanding of the geodynamic processes that led to cratonization. This study uses Sm-Nd garnet and U-Pb geochronology to place constraints on the timing of Archean HT metamorphism recorded in metasedimentary xenoliths in the eastern Beartooth Mountains of Montana and Wyoming, USA, with the goal of understanding the processes behind this metamorphism.

Garnet is almost ubiquitous in regional metamorphic settings and has been used successfully to establish the age of metamorphism in a variety of tectonic contexts (e.g., Lapen et

al., 2003; Pollington and Baxter, 2010; Baxter and Scherer, 2013; Smit et al., 2013; Kellett et al., 2014; Dragovic et al., 2015). However, the use of garnet as a HT (>750°C) geochronometer has proven challenging, particularly in terms of interpreting bulk ages of crystals that may contain inherent age complexity (Anczkiewicz et al., 2012; Smit et al., 2013). Significant scatter in isotopic data can exist between garnet fractions used for multi-point isochrons, with several factors contributing to scatter in resultant ages including sampling of garnet that records multiple growth events (polymetamorphism) or a long garnet growth duration, and protracted high temperatures resulting in diffusionally-controlled differential age resetting. Additionally, the removal of melt during HT metamorphism would result in rotation of the garnet-whole rock isochron, though the effect on the calculation of garnet growth ages is insignificant if the melting event happens soon after garnet growth, before significant radiogenic ingrowth accumulates.

Here, we couple bulk garnet Sm-Nd geochronology (i.e. dating based upon entire garnet crystals rather than portions thereof) with models of major element and REE diffusion to elucidate 1) the relative timing of HT metamorphism of the eastern Beartooth metasediments, and 2) what influence the aforementioned complicating factors can have on resultant bulk garnet ages. We use this chronology, along with U-Pb laser ablation split-stream (LASS) petrochronology of monazite, as well as field and petrologic relationships to suggest that HT metamorphism of metasedimentary xenoliths post-dates emplacement of the arc magmas in which they are hosted by ~100 Ma. Whole-rock major and trace element compositions help to distinguish between magmatic rocks of the arc and granitoids formed during HT anatexis of the metasedimentary xenoliths (i.e. leucosomes), and phase equilibria modeling allows us to determine what petrologic effect granulite-facies conditions might have on pre-existing LLMC granitoids, helping to clarify why this younger event has previously been undocumented. Geospeedometry modeling of major element diffusion in garnet places constraints on the duration of HT metamorphism.

3.3 GEOLOGIC SETTING

The Beartooth Mountains form an extensive exposure of Archean rocks in the northwestern part of the Wyoming Craton, uplifted as a result of thick-skinned thrusting during the Cretaceous Laramide Orogeny (e.g. Erslev et al., 1993; Mogk and Henry, 1988; Mueller and Frost, 2006). In the central and eastern parts of the range, they are dominated by Meso- to Neoarchean tonalite-trondjhemite-granodiorite gneisses (Figure 3.1), collectively known as the

Long Lake Magmatic Complex (LLMC). These granitoids, which represent part of a regional-scale protracted magmatic evolution dating back to at least 3.0 Ga (Mueller and Frost, 2006), were emplaced between 2.83 and 2.79 Ga and have been interpreted to be derived from subduction-related arc magmatism, based on major element, trace element and isotopic data (e.g. Henry et al., 2014; Montgomery and Lytwyn, 1984; Mueller et al., 2014; Mueller et al., 2010; Mueller et al., 1982; Mueller et al., 1983; Wooden et al., 1988). The western part of the range, known by previous workers as the North Snowy Block and the South Snowy Block, is dominantly comprised of greenschist to upper-amphibolite facies metasediments and tonalite-trondjhemite-granodiorite suites (e.g. Casella and Goldich, 1982; Jablinski and Holst, 1992; Mogk et al., 1988). The Stillwater complex, a layered mafic intrusion, comprises the northern margin of the range and records U-Pb zircon and baddeleyite ages ranging from 2704-2710 Ma (Premo et al., 1990; Wall et al., 2012; Wall and Scoates, 2016; Wall et al., 2016). Smaller mafic intrusions of varying composition have been described in the eastern Beartooth Mountains (e.g. Casella. 1969; Eckelmann and Poldervaart, 1957; Lopez, 2001; Mersmann, 1977), of which some have been temporally related to the Stillwater complex (Chamberlain et al., 2014) and display evidence of metamorphism (Eckelmann and Poldervaart, 1957; Lopez, 2001; Mersmann, 1981; Prinz, 1964), while others have younger emplacement ages of ~2550 Ma, ~1300 Ma, and ~750 Ma (Baadsgaard and Mueller, 1973; Harlan et al., 1997) and are effectively unmetamorphosed.

Several studies in the eastern Beartooth Mountains have described granulite-facies metapelites, ironstones, quartzites and amphibolites intercalated with felsic and mafic gneisses (Figure 3.1; Casella, 1969; Eckelmann and Poldervaart, 1957; Henry et al., 1982; Mogk et al., 2014). These exist as cm-to km-scale xenoliths and pendants within the LLMC, and are interpreted to represent relict supracrustal (metamorphosed basement and sedimentary) packages into which the LLMC intruded (Mueller et al., 1992; Mueller et al., 1998). Detrital zircon ages imply a maximum depositional age of ~3.3 Ga and reveal incorporation of the products of 3.3–3.9 Ga crustal production (Mueller et al., 1992). Previous studies have estimated peak *P–T* conditions of the granulites to be ~750-810°C, 5.6-8 kbar (Henry et al., 2014; Henry et al., 1982; Maas, 2004; Mogk et al., 2014, Will, 2013), with a counterclockwise *P–T* path based on inferred metamorphic reactions in aluminous migmatites (Maas, 2004). Quartzofeldspathic gneisses yielded Rb-Sr whole-rock model ages of ~3390 Ma and ~2800 Ma (Henry et al., 1982), initially

interpreted to reflect ~3.4 Ga granulite-facies metamorphism overprinted by a ~2.8 Ga amphibolite-facies event associated with contact heating during entrainment into the LLMC (Henry et al., 1982). Later studies yielded similar interpretations (Maier et al., 2012; Mogk et al., 2014; Will, 2013), though Maas (2004) interpreted the granulite-facies metamorphism to be solely due to heating followed by magmatic loading during LLMC emplacement. Recent work on intrusive igneous rocks supplemented the 3390 Ma model age with U-Pb zircon crystallization ages spanning 3.1-3.5 Ga, interpreted to reflect multiple emplacement episodes during the first major pulse of subduction-driven crustal growth (Mueller et al., 2014), and culminating in emplacement of the broadly tonalitic LLMC at ~ 2.8 Ga.

Despite the rich archive of zircon crystallization and whole-rock ages, no published work has directly dated granulite-facies metamorphism of metasedimentary roof pendants in the eastern Beartooth Mountains using modern geochronological methods. Linking the geochronologic and metamorphic history of these rocks is likely to yield important constraints on the tectonic history of the region and evolution of the Wyoming Craton, so here we focus explicitly on granulite formation by presenting and interpreting Sm-Nd garnet ages from metasediments and U-Pb monazite ages from a metasedimentary migmatite and a tonalite.

3.4 FIELD RELATIONS

Where exposed, the contact between granulite-facies metasediments and granitoids attributed to the LLMC always appears to be intrusive. Further indirect evidence for an intrusive contact includes a gradual increase in the abundance of biotite + garnet bearing schlieren (Figure 3.2a-b) and skeletal xenoliths (comprised of biotite + garnet ± sillimanite; Figure 3.2c-e) towards contacts with metasediments, suggesting partial assimilation of aluminous metasedimentary material by the granitoids. Finer-grained margins are also observed in more mafic lithologies of the LLMC at the contact with the metasediments, again supporting conventional interpretations of previous workers that the LLMC is intrusive to metasedimentary units (e.g. Henry et al., 1982; Mueller et al., 2010; Wooden et al., 1988).

Various field relationships tentatively suggest that HT metamorphism may post-date LLMC emplacement, with several examples shown in Figure 3.3 and summarized as: 1) leucosomes from pelitic migmatites cross-cut a granodiorite sill (Figure 3.3a-c); whole-rock major and trace element compositions confirm the arc affinity of the granodiorite sill (described below), suggesting that it is consistent with, though not uniquely identified as, the LLMC, 2)

veins of garnet-bearing peraluminous leucogranite, tentatively interpreted as derived from partial melting of metasediments, inject into granite interpreted here as LLMC without co-mingling of melts (Figure 3.3d), and 3) foliated amphibolites interlayered with granulite-facies metasediments are injected by folded veins of felsic (LLMC?) melt, with fold hinges axial-planar to a strong foliation defined by granulite-facies phases such as sillimanite (Figure 3e). We *provisionally* interpret this as suggesting that peak HT metamorphism was coeval with deformation, as seen in samples from other localities (e.g., see sample descriptions of BHP13-03D, BLP14-05), and that emplacement of the deformed granite likely predated HT metamorphism.

3.5 WHOLE ROCK GEOCHEMISTRY

In order to contextualize the field relationships described above (i.e. associate different granitoids with the LLMC vs. anatexis of metasediments), major and trace element concentrations were determined for representative specimens of rocks that we interpreted in the field to be: 1) LLMC tonalite (sample BQC13-01O, dated at ~2.78 Ga, below), 2) LLMC(?) granodiorite sill (sample BHP13-01G), and 3) a leucogranite derived from partial melting of metasediments (sample BHP14-11L). Sample locations are shown in Figure 3.1. Methods for whole-rock geochemistry are detailed in Appendix B.

3.5.1 Sample descriptions for granitoid whole-rock geochemistry

BQC13-01O – LLMC tonalite

Sample BQC13-01O is a tonalite collected ~10 m from a package of metasediments (Figure 2a) and contains quartz, plagioclase, biotite (~5 vol.%), minor potassium feldspar, apatite, muscovite, and zircon (Figure 3.3f-g). Quartz and plagioclase are dynamically recrystallized and define a weak foliation. Quartz grains show undulatory extinction.

BHP13-01G – LLMC(?) granodiorite sill

Sample BHP13-01G is a granodiorite sill intruded into pelitic migmatite (Figure 3.3a-c). It contains quartz, plagioclase, potassium feldspar, chlorite (after biotite), hornblende, epidote, and accessory garnet, apatite, ilmenite, and zircon. Epidote is always associated with clusters of chlorite. Abundant hornblende always occurs in association with plagioclase. Garnet occurs as a patch of 5-6 subhedral, partly resorbed 200-300 μm grains in association with one

plagioclase/hornblende-rich region (Figure 3h). Ilmenite occurs as needles with small alteration rinds.

BHP14-11L – leucogranite (leucosome of migmatitic pelite)

Sample BHP14-11L is a coarse-grained leucogranite, interpreted to be derived by partial melting of metasediments and occurring as leucosome next to a garnetitic residuum (Figure 3.3i). It is dominantly comprised of plagioclase and quartz, though minor garnet occurs as tiny (1-2 mm) subhedral porphyroblasts, and minor cordierite occurs as anhedral, grey-green blobs in hand sample.

3.5.2 Results of whole-rock geochemistry

Major element compositions are shown in Table B1 and Figure 3.4a, with trace element compositions shown in Figure 3.4b-c and in the supplementary material (Table B1). SiO_2 contents range from 68 to 75 wt.% (Table 3.1), with Al_2O_3 contents ranging from 14.5 to 15.7 wt.% and associated with the abundance of feldspar relative to quartz and the presence or absence of an aluminosilicate phase in each sample. The major element composition of the LLMC tonalite (BQC13-01O) falls in the range of LLMC granites analyzed by Mueller et al. (2010), albeit as a high sodium end-member (Figure 3.4a). The granodiorite sill (BHP13-01G) that intrudes pelites in Figure 3a also overlaps compositionally with LLMC granites and granodiorites analyzed by Mueller et al. (2010). The migmatitic leucogranite (BHP14-11L) is markedly less mafic, less TiO_2-rich and less CaO-rich than the tonalite, the granodiorite or previous LLMC analyses (Mueller et al., 2010).

Trace element concentrations and relative abundances in the tonalitic and the granodioritic samples are comparable to those observed in the range of LLMC lithologies from Mueller et al. (2010) (Figure 3.4b-c and Table 3.1). The leucogranite can be distinguished from the tonalite by elevated K_2O, Rb, and Ba concentrations, as well as relatively depleted levels of Nb and Th (Figure 4b). All three lithologies show broadly similar concave-downward chondrite-normalized REE patterns with variable Eu anomalies (Figure 3.4c; Table 3.1). The leucogranite has relatively depleted REE concentrations, and a slightly shallower LREE/MREE slope with a La_N/Gd_N (subscript N denotes normalization to chondrite) of >15. Furthermore, the leucosome has a strong positive Eu anomaly (Eu/Eu^* >1.8) compared to the granodiorite (~0.6) and the prominent negative anomaly in the tonalite (~0.1). While all three granitic lithologies display

depleted HREE concentrations, the leucogranite has a slightly positive HREE slope due to a slightly elevated Lu concentration, interpreted as resulting from either entrained garnet from the residuum or the presence of peritectic garnet (Figure 3.3a).

3.6 SM-ND GARNET GEOCHRONOLOGY AND GARNET MINERAL CHEMISTRY

Five samples of garnet-bearing metasedimentary granulites (BHP13-03D, BQC13-01A, BLP13-04, BLP14-05, and BPYR14-11B) were collected for Sm-Nd garnet geochronology and garnet major and trace element characterization. Sample locations are shown in Figure 3.1. Methods for garnet major and trace element characterization are detailed in the Appendix, with raw data presented in Tables B2 and B3. Methods for Sm-Nd garnet geochronology are also detailed in the Appendix.

3.6.1 Sample descriptions for Sm-Nd geochronology: metasedimentary granulites

BHP13-03D – restitic metapelite

BHP13-03D contains two garnet populations; small (< 2-mm-sized), stretched, highly fractured grains found solely along the dominant deformational fabric (Figure 3.5a), and large, subhedral porphyroblasts, ranging from ~3-8 mm in size, around which the foliation is defined (Figure 3.6a, c). Porphyroblastic garnet cores are inclusion-rich, containing quartz, ilmenite, biotite, and accessory zircon and monazite. Ilmenite inclusions in crystal cores are oriented subparallel to host garnet growth faces (Figure 3.5b). Garnet rims contain inclusions of only sillimanite. Potassium feldspar is the dominant matrix phase and displays undulatory extinction and recrystallized grain boundaries. Aggregates of biotite, sillimanite, quartz, partly sericitized plagioclase, and ilmenite define a strong foliation and are cross-cut by garnet crystal faces, suggesting that they represent prograde relicts of the reaction biotite + sillimanite + plagioclase + quartz = garnet + potassium feldspar + melt (Figure 6a). Thin brown films in plane polarized light and films of quartz + plagioclase around rounded potassium feldspar grains are interpreted to represent pseudomorphs after grain boundary melt (Holness et al., 2011). Larger biotite and ilmenite grains cut the foliation and across garnet rims, implying genesis from later-stage garnet breakdown, and minor chlorite and muscovite partially replace garnet, biotite, and sillimanite/potassium feldspar. However, the general retention of the granulite-facies peak assemblage (garnet, biotite, quartz, sillimanite, potassium feldspar, ilmenite, plagioclase, and melt), and the abundance of inferred peritectic phases (garnet and potassium feldspar) are

consistent with the removal of melt (White and Powell, 2002). The sample is thus inferred to represent a residuum after partial melting.

BQC13-01A – banded metaironstone

BQC13-01A consists of alternating Si-rich and Fe-rich layers, both of which contain garnet. In the Si-rich layer, garnet porphyroblasts range from 0.5-5 mm in diameter, are subhedral (some are atoll-shaped), and contain inclusions of quartz, plagioclase, and accessory apatite and monazite in the cores of larger crystals. The rims of the larger garnets and all of the smaller crystals are inclusion-poor, possibly representing a different generation of garnet growth. The matrix of the Si-rich layer consists of quartz, plagioclase and minor biotite.

In the Fe-rich layer (Figure 3.6b, d), 1-2 mm-sized, anhedral garnet porphyroblasts contain inclusions of ilmenite, quartz, and accessory monazite (Figure 3.5c). The matrix consists of orthopyroxene, quartz, ilmenite and magnetite, with minor hematite and apatite. Orthopyroxene is often adjacent to garnet crystals, sub-mm-sized, and contains inclusions of quartz and accessory zircon and monazite. Large biotite porphyroblasts near the interface between the Fe-rich and Si-rich layers, as well as late-stage alteration of garnet by biotite and chlorite along fractures in crystals from both layers possibly indicate later-stage fluid infiltration.

BLP13-04 – banded metaironstone

Sample BLP13-04 also consists of alternating Si-rich and Fe-rich layers, with both layers containing garnet (Figure 6e). The Si-rich layer contains quartz, garnet, magnetite, and grunerite. Garnet crystals are anhedral, ranging from 0.5-1.5 mm diameter and containing sparse inclusions of quartz and magnetite. Some garnets are atoll-shaped.

The Fe-rich layer contains abundant garnet, orthopyroxene and magnetite, with subsidiary quartz and clinopyroxene, and minor hematite and apatite. Garnet crystals are smaller than in the Si-rich layer, with all porphyroblasts ~0.5 mm in diameter and containing inclusions of quartz, magnetite, and accessory monazite. Orthopyroxene contains inclusions of quartz, magnetite, and accessory monazite, with many grains being rimmed by anthophyllite-gedrite, likely a result of later-stage retrogression (Figure 3.5d).

BLP14-05 – migmatitic heterogeneous metapelite

BLP14-05 is a layered pelite consisting of alternating quartzofeldpathic and micaceous bands (Figure 3.6f). Sparse garnet grains are located at the interface between these layers, are

relatively large (up to 4mm in diameter) and are euhedral to subhedral. Garnet cores are inclusion-rich, containing randomly oriented sillimanite needles (Figure 3.6h) and rare, rounded quartz. Crystal rims are inclusion-poor but contain polymineralic inclusions of quartz, plagioclase and biotite.

The foliation in the micaceous layers is defined by sillimanite and biotite (Figure 3.6f, h) and wraps around garnet porphyroblasts. Asymmetric sillimanite and biotite growth around garnet (e.g. Figure 3.6f, h) indicates growth in a pressure shadow during non-coaxial deformation (dextral shear), implying that HT metamorphism was coeval with deformation. Biotite also occurs as late porphyroblasts that cut across the foliation and contain inclusions of foliated sillimanite. Quartz, plagioclase and resorbed, pinnitized cordierite grains are wrapped by foliated biotite and sillimanite.

Quartzofeldspathic layers are dominated by large, rounded quartz, plagioclase, and potassium feldspar grains. Quartz and plagioclase grains contain rare clusters of randomly oriented sillimanite needles and are occasionally separated by coarse interstitial biotite crystals. Late stage grains of granophyre next to biotite and coarse quartz grains (Figure 3.5e) are interpreted to represent altered crystallized melt (e.g. Holness et al., 2011), as are thin, polycrystalline bands of fine-grained quartz on the boundaries of coarse plagioclase and potassium feldspar grains (Figure 3.5f).

BPYR14-11B – melanosome of metapelitic diatexite

BPYR14-11B represents the melanosome of a pelitic diatexite and contains garnet, biotite, quartz, plagioclase, cordierite, sillimanite, ilmenite, and accessory monazite. Garnet porphyroblasts up to ~4 mm in diameter are highly resorbed and contain inclusions of quartz, biotite, ilmenite, and sillimanite. Biotite forms weakly foliated aggregates with sillimanite in the matrix and also rims and cross-cuts garnet and cordierite porphyroblasts. Plagioclase and quartz occur as rounded, coarse grains in the matrix. Plagioclase is also present as thin grain boundary films infilling triple junctions between quartz and garnet grains: we interpret this to represent crystallized grain boundary melt (Figure 3.5g). Cordierite occurs as abundant, anhedral, pinnitized porphyroblasts in the matrix and rims garnet in embayments (Figure 3.5h). Rare, randomly oriented sillimanite needles cross-cut foliated biotite, and garnet and cordierite porphyroblasts.

3.6.2 Garnet major element zoning

Major element zoning in garnet from sample BHP13-03D is shown in Figure 7a. The crystal is relatively unzoned in Fe, Mg, and Mn, though with slight Fe and Mn decrease and Mg increase near the rim. Ca concentrations initially decrease smoothly away from the crystal core before increasing smoothly in the garnet 'mantle', and then abruptly decreasing from a sharp maximum near the garnet rim (X_{grs} = 0.04 at maxima, decreasing to ~0.03 at rim). Given the petrographic evidence described above, the high Ca rims are interpreted to represent peritectic garnet growth due to the partial melting reaction biotite + plagioclase + sillimanite + quartz = garnet + potassium feldspar + melt, with garnet incorporating more Ca due to plagioclase breakdown. Note that the locations at which Ca and Mn concentrations change near the garnet rim coincide. Likewise, the locations at which Fe and Mg concentrations change coincide, however this is rimward of the inflections in Ca and Mn.

Representative analyses of garnet from the Si-rich layer of the banded ironstone (sample BQC13-01A) are shown in Table B2. Crystal cores are not strongly zoned in Fe, Mg, and Mn, but display low-amplitude Ca zonation in smaller crystals (Figure 3.7b); X_{grs} increases slightly outwards from crystal cores (from ~0.11 to 0.13), before decreasing sharply near rims (to ~0.06). Near-rim changes in Fe, Mg, and Ca concentrations are observed at roughly the same radial position in all smaller garnet rims. Larger garnet crystals (>3 mm) contain inclusion-rich areas with relatively homogeneous low Ca content, similar to that of the smaller crystal rims (Figure 6d). Multiple distinct high-Ca spots separated by low-Ca zones surround these inclusion-rich areas, and may be polycrystalline aggregates of garnet, with the high-Ca spots possibly representing once distinct garnet crystals (Figure 3.6d). The presence of two chemically distinct populations of garnet (smaller crystals and polycrystalline aggregates with high Ca cores/low Ca rims, larger crystals with low Ca) may be evidence for diachronous garnet nucleation.

Garnet in samples BLP13-04 (Fe- and Si-rich layers), BPYR14-11B, and BLP14-05 displays little major element zoning and is not discussed further here.

3.6.3 Garnet REE compositions

Garnet crystals were analyzed for trace and REE compositions to aid in interpretation of geochronology results presented below, with concentrations and zoning of Lu, Sm, and Y highly variable between the studied lithologies (Figure 3.8; Table B3). Lu and Y are enriched in garnet crystal cores of all samples, although in BLP14-05 this local enrichment is far smaller than a

secondary enrichment in garnet crystal rims.

Sm is reversely zoned in sample BHP13-0D (restitic metapelite) compared to Lu and Y, with very low concentrations in cores (<0.2 ppm) and a relatively sharp increase (~1 ppm) towards crystal rims, coincident with a step in Ca content (Figure 3.7a). Garnet cores and mantles display a relatively flat HREE slope and a lack of a Eu anomaly (Figure 3.8a), while crystal rims display negative HREE slopes and negative Eu anomalies, though with generally higher Eu concentrations than in cores and mantles.

Lu and Y are enriched in annuli near the garnet rim in BQC13-01A. Sm concentrations are relatively low (<5 ppm) and are effectively unzoned. Chondrite-normalized REE patterns of crystal cores and rims have slightly positive HREE slopes (Figure 3.8b), with mantles having negative HREE slopes. Crystal cores and mantles have only slight Eu anomalies, compared to highly negative anomalies in rims.

Garnet mantles in the Si-rich layer of sample BLP13-04 are depleted and crystal rims are enriched in Lu and Y (Figure 8c). Sm is locally enriched in the garnet mantles, with decreased concentrations in both cores and rims. All analyses in this sample reveal depleted chondrite-normalized REE patterns and strong negative Eu anomalies (Figure 3.8b). Crystal cores and rims show flat HREE patterns, while mantles have negative HREE slopes. Garnet in the Fe-rich layer of BLP13-04 has a relative lack of Y+REE zoning. Lu, Sm, and Y concentrations are low, with Sm concentrations <1 ppm (Figure 3.8d; Table B3). To the extent that there is REE zoning, crystal cores are slightly enriched in HREE. The chondrite-normalized REE patterns for all garnet zones are relatively flat and display negative Eu anomalies.

Yttrium is oscillatory-zoned in garnet mantles in BLP14-05 (Figure 3.8e). Sm concentrations are low (1-2 ppm) throughout the crystal cores and mantles, with a slight enrichment (3-6 ppm) towards crystal rims. Both Lu and Y are highly enriched near crystal rims (up to 18 and 800 ppm, respectively). Chondrite-normalized REE patterns for all analyses display a positive LREE slope. Crystal cores have flat HREE patterns, with mantles and rims displaying slightly negative and positive HREE patterns, respectively. All analyses have a negative Eu anomaly, with crystal rims the most highly negative.

Sm concentrations in BPYR14-11B are generally low (< 0.5 ppm). Lu, Y, and Sm increase to maximum concentrations at crystal rims. Chondrite-normalized REE patterns have a

positive LREE slope, regardless of radial position. Crystal cores and rims have a slightly positive HREE slope that is absent in mantles. Crystal rims have a high negative Eu anomaly.

3.6.4 Sm-Nd garnet geochronology

Sm-Nd data

Sm-Nd data for all analyzed samples are shown in Table 3.2 (sample ID 'xxxx-60HF' implies 60 minutes in concentrated HF/1.5N HCl solution; see Appendix). Acid-cleansed garnet separates from all samples display a large range in $^{147}Sm/^{144}Nd$, from 0.56-4.98, but with far more restricted intrasample variation (0.56-0.79 for sample BHP13-03D, 1.30-1.35 for BLP13-04, 4.05-4.98 for BQC13-01A, 2.79-2.97 for BLP14-05, and 1.22-1.44 for BPYR14-11B). Uncleansed 'garnet' powders range in $^{147}Sm/^{144}Nd$ from 0.13-1.77 (with the magnetite separate from sample BLP13-04 also having a $^{147}Sm/^{144}Nd$ of 0.13). Nd concentrations in acid-cleansed garnet range from 0.71-1.1 μg/g (sample BHP13-03D), 1.9-2.1 μg/g (BLP13-04), 0.17-0.56 μg/g (BQC13-01A), 0.25-0.27 μg/g (BLP14-05) and 0.09-0.13 μg/g (BPYR14-11B). While the $^{147}Sm/^{144}Nd$ of sample BHP13-03D and the [Nd] for samples BHP13-03D and BLP13-04 appear outside the typical range for garnet (low and high, respectively), such cases are not entirely uncommon, especially for garnet grown at granulite-facies conditions (Baxter and Scherer, 2013).

Nd concentrations in uncleansed garnet powders are higher than the acid-cleansed garnet separates, with concentrations of 2.5 μg/g (BHP13-03D), 3.5 μg/g (BLP13-04), 0.82 μg/g (BQC13-01A), 0.75 μg/g (BLP14-05), and 18 μg/g (BPYR14-11B). Comparison of the acid cleansed garnet separates to the uncleansed 'garnet' powders highlights the value of the partial dissolution procedure employed here. The relatively high $^{147}Sm/^{144}Nd$ and low [Nd] in the cleansed garnet separates relative to the uncleansed 'garnet' powders indicates that the acid cleansing process was successful in removing adverse (i.e. REE-rich) inclusions, thus mitigating the contaminating effect these inclusion phases have on age determination (Baxter and Scherer, 2013).

The uncleansed garnet powders from two of the samples (BHP13-03D and BQC13-01A) fall considerably off the multi-point garnet-whole rock (WR) isochron, and are thus not included in either age interpretation. The uncleansed powders from samples BLP13-04, BLP14-05, and

BPYR14-11B fall on the multi-point garnet-WR isochrons calculated, and are thus included in the age interpretation for those samples.

Sm-Nd garnet ages

Sm-Nd isotopic data from acid cleansed garnet separates, uncleansed garnet powders (including a magnetite separate for sample BLP13-04), and whole rocks were used to calculate multiple 2- to 4-point isochron ages (using individual garnet separates) and 5 multi-point ages (one age for each sample, ranging from 5 to 6 points). All of the resulting multi-point ages (those including multiple garnet data) yield very high MSWD due to significant scatter between the different garnet fractions analyzed; thus these are not true isochrons and are rather termed 'errorchrons' (Wendt & Carl 1991), whose age significance is discussed further in Section 7. Isochrons and calculated ages are shown in Table 3.2 and Fig. 3.9, respectively. All age uncertainties are reported at 2**σ.**

BHP13-03D (restitic metapelite)

Four garnet fractions and a representative whole rock were used to calculate ages for sample BHP13-03D. Two-point garnet-WR ages were calculated for each garnet fraction and range from 2660.8 ± 4.2 Ma to 2689.9 ± 5.6 Ma (Table 2). Assembling all garnet fractions into a 5-point garnet-WR errorchron provides an age of 2669 ± 48 Ma (MWSD = 61; Table 2 and Fig. 3.9a). The high MSWD, as well as the large range of individual two-point garnet-WR ages (~ 30 Ma), highlights significant geological scatter between individual garnet fractions that were analyzed. Note that the uncleansed garnet powder and the acid leachate fall significantly below the isochron, and their inclusion on the isochron would result in a falsely younger age. The uncleansed garnet powder represents a sample including garnet with all its inclusion phases, while the acid leachate represents the partial dissolution of 'clean', handpicked garnet (i.e. a somewhat cleaner garnet fraction). While the acid leachate is positioned considerably closer to the 'true' isochron compared to the uncleansed garnet powder, both samples likely represent mixing between garnet and low $^{147}Sm/^{144}Nd$, inherited inclusion phases, likely monazite (Baxter and Scherer, 2013). This can be represented by the younger ages from two-point isochron ages of these samples (powder-WR age of 902 ± 26 Ma; leachate-WR age of 2587 ± 21 Ma; not shown in table or figure). This further indicates the effectiveness of acid cleansing, and the appropriate use of the more representative 5-point age of 2669 ± 48 Ma.

BQC13-01A (banded metaironstone)

Four garnet fractions and a representative 'whole rock' were used to calculate an age for BQC13-01A. Individual, 2-point garnet-WR ages were calculated for each garnet fraction, yielding ages ranging from 2651.5 ± 0.8 Ma to 2703.8 ± 0.9 Ma (Table 2). Assembling all garnet fractions (along with the WR analysis) onto a 5-point errorchron yields an age of 2677 ± 50 Ma (MSWD = 3300; Table 3.2 and Fig. 3.9b). As with sample BHP13-03D, note the significant scatter in the individual 2-point garnet-WR isochron ages and the very high MSWD. Also, the uncleansed garnet powder is not used in age calculations because the analysis falls sufficiently below the multi-point isochron. While the $^{147}Sm/^{144}Nd$ of the uncleansed garnet powder is high (compared to garnet in the other lithologies), it is relatively low compared to the acid cleansed garnet separates (and has a relatively high [Nd], see earlier discussion), and is thus interpreted to be comprised of a mixture of 'clean' garnet and low $^{147}Sm/^{144}Nd$, inherited phases (likely monazite as above). Indeed, a 2-point powder-WR isochron yields an age of 2562.3 ± 2.1 Ma (not shown). As a result, it is not included in the multi-point isochron calculation, with the 2677 ± 50 Ma age used in further discussion.

BLP13-04 (banded metaironstone)

A combination of three garnet fractions, one garnet powder, one magnetite separate, and a representative whole rock were used to calculate ages for sample BLP13-04. Individual 4-point (garnet-powder-magnetite-WR) ages were determined for each garnet fraction, providing ages of 2668.3 ± 6.7 Ma (MSWD = 2.6), 2686.4 ± 6.2 Ma (MSWD = 2.2), and 2698 ± 13 Ma (MSWD = 9.4; Table 2). Assembling all garnet fractions (with the uncleansed garnet powder, magnetite separate, and WR) to create a 6-point errorchron yields an age of 2684 ± 24 Ma (MSWD = 160; Table 2 and Fig. 3.9c). The individual garnet fraction isochron ages are relatively close to each other in time, so the 6-point age will be used in discussion below.

BLP14-05 (migmatitic pelite)

Four garnet fractions, one uncleansed garnet powder, and a representative whole rock were used to calculate ages for sample BLP14-05. Two-point garnet-WR ages were calculated for each garnet fraction, yielding ages ranging from 2654.5 ± 1.2 Ma to 2711.0 ± 1.3 Ma (Table

2). Compiling all garnet fractions, the uncleansed garnet powder, and whole rock onto a 6-point errorchron yields an age of 2681 ± 58 Ma (MSWD = 2400; Table 3.2 and Figure 3.9d). While the [Nd] of the uncleansed garnet powder is higher than the garnet separates, demonstrating the potential for the presence of adverse, REE-rich inclusions, a 2-point powder-WR age of 2707 ± 2.8 Ma falls within the range of 2-point garnet-WR ages shown above. Thus, the 6-point age of 2681 ± 58 Ma will be used in further discussion.

BPYR14-11B (melanosome of pelitic diatexite)

Age calculation of BPYR14-11B used a combination of four garnet fractions, an uncleansed garnet powder, and a whole rock. Two-point garnet-WR ages, calculated for each garnet fraction, yielded ages ranging from 2630.3 ± 2.8 Ma to 2722.2 ± 2.7 Ma (Table 3.2). This range of ages is the highest among the samples studied here (~ 90 Ma). Assembling the four garnet separates, uncleansed garnet powder, and the whole rock onto an errorchron provides a 6-point age of 2670 ± 64 Ma (MSWD = 950; Table 3.2 and Figure 3.9e).

3.6.5 Integration of results from Sm-Nd bulk garnet geochronology and trace element zoning

Trace element zoning of garnet, combined with major element zoning and petrographic observations, can enhance the interpretation of bulk Sm-Nd garnet geochronology, particularly for samples in which garnet is chemically and/or texturally complex. We discuss here our interpretations derived from the aforementioned datasets.

In sample BHP13-03D, Sm is preferentially concentrated in garnet rims (Fig. 3.8a), with the position of this increase coincident with the high-Ca rims interpreted to result from garnet growth during plagioclase breakdown and partial melting. We infer, therefore, that the bulk Sm-Nd age of this sample (2669 ± 48 Ma) may be biased toward the late stages of garnet growth (or a secondary event in the case of a polymetamorphic history) during partial melting. While diffusion during cooling from this HT event would have partially reset the bulk garnet ages (see discussion below), the observed retention of growth zoning recorded in Ca and REE profiles, and the results from age zonation calculations (see below), suggest that garnet growth histories can survive some degree of HT reworking to record processes such as partial melting. The Lu and Y profiles contain a secondary peak or ‘shoulder’ near the crystal rim (Figure 3.8a), which is

possibly indicative of a secondary growth stage, though such profiles have previously been attributed to diffusion-limited REE uptake during garnet growth (Skora et al., 2006). Taken together, the Sm, Lu, and Y zonation in garnet from this sample may be indicative of two distinct phases of garnet growth, of which the Sm-Nd chronology is more sensitive to the later phase.

Sm is relatively evenly distributed across garnet grains from samples BQC13-01A and BLP13-04 (Fig. 3.9b-d). Bulk Sm-Nd garnet ages from these samples (2677 ± 50 Ma and 2684 ± 24 Ma, respectively) thus likely represent time integration of the entire garnet growth history. Lu and Y spikes at the crystal rims of these samples may be suggestive of: 1) the redistribution of Lu (and Y) during partial garnet resorption and intracrystalline diffusion (e.g., Kelly et al., 2011), or 2) breakdown of a Y+HREE-rich phase (e.g., monazite or zircon) during garnet growth (Bea and Montero, 1999; Kohn et al., 2015). Garnet from the Si-rich layer of sample BLP13-04 is rounded and thus the Lu and Y enrichment at crystal rims may be at least partly due to the former scenario. In contrast, the garnet crystal analyzed in Figure 3.9 from sample BQC13-01A, preserves fairly euhedral crystal growth faces.

Garnet from sample BLP14-05 has a relatively even Sm distribution throughout crystal cores, but with higher-Sm annuli near rims (Fig. 3.8e). We therefore interpret the Sm-Nd bulk garnet age (2681 ± 58 Ma) as being biased toward the later stages of garnet growth. Garnet in this sample is not significantly resorbed, so the sharp increase in Lu and Y at the rims may tentatively imply syn-garnet growth breakdown of an Y+HREE-rich phase (e.g., zircon or monazite), in this case possibly during partial melting (e.g., Kohn et al., 2015; Yakymchuk and Brown, 2014a).

The highest Sm, Lu and Y concentrations in garnet from sample BPYR 14-11B occur in the rim (see left side of profile in Fig. 3.8f). This local Lu and Y spike is similar to those described for samples BQC13-01A, BLP13-04 (Si-rich layer), and BLP14-05. However, given the extent of crystal resorption in this sample (Figures 3.6g and 3.8f) and the location of monazite in garnet embayments, these features may represent retention of these elements during garnet breakdown, and thus the bulk Sm-Nd garnet age (2670 ± 64 Ma) for this sample may be biased towards the age of garnet resorption.

3.7 U-PB MONAZITE LASS PETROCHRONOLOGY

In-situ U-Pb LASS petrochronology on monazite was performed on samples BPYR14-11B (melanosome of migmatitic pelite) and BQC13-01O (tonalite from Figure 2a with presumed

LLMC affinity). The purpose of this was two-fold: 1) to identify whether metasediments experienced monazite growth post-dating LLMC intrusion, which would substantiate our interpretations of the Sm-Nd bulk garnet ages, and 2) to determine whether crystallization in sample BQC13-01O is consistent with it belonging to the LLMC (thus confirming our interpretations of field observations and whole-rock geochemistry). If BQC13-01O is of similar age to previously published LLMC samples, we also aim to understand the extent of monazite (re)crystallization and/or age resetting in the LLMC due to subsequent metamorphism suggested by the garnet data.

The methodology for U-Pb monazite LASS petrochronology is detailed in Appendix B, and data are located in Table B4 and B5. U-Pb dates in this paper are presented in the format A ± B [C], in which A is the mean calculated date or concordia intercept date of a group of analyses, B is the 2σ standard error of that mean (or concordia intercept), and C is the long-term reproducibility of laser ablation monazite dates at the UCSB LASS facility (~2% or ~33 Ma for ~2700-2800 Ma samples; e.g. Holder et al., 2015; Hacker et al., 2015).

3.7.1 Monazite sample descriptions and LASS results

BPYR14-11B (melanosome of migmatitic pelite)

Monazite in sample BPYR14-11B occurs as anhedral grains included in garnet, biotite, and matrix quartz and/or plagioclase (Figure 3.10a-j). Some matrix grains occur within resorbed embayments in garnet. Chemical zoning is variable; many grains exhibit resorbed, low-Y cores surrounded by high-Y overgrowths (Figure 3.10a-d), while others exhibit more patchy Y distribution (Figure 3.10e-j). Twelve monazite grains in this sample were analyzed, with 72 individual $^{207}Pb/^{206}Pb$ spot ages ranging from 2822 ± 33 to 2640 ± 33 Ma (Table B4). A linearized probability plot of all $^{207}Pb/^{206}Pb$ spot ages (Figure 3.11a) shows that results do not form a single, normal age distribution but instead reveal two apparent periods of monazite growth: a group of 'old' spot ages ranging from ~2822-2782 Ma (n=39), and a group of 'young' spot ages ranging from ~2705-2640 Ma (n=10), hereafter referred to as populations 1 and 2, respectively (Figure 3.11a). The grouping of these analyses is also consistent with variations in their REE profiles (Figure 3.11b-e). Population 1 analyses exhibit a range of HREE slopes from shallow to steep and variably pronounced negative Eu anomalies, with a general younging trend towards shallower HREE slopes and less pronounced negative Eu anomalies (Figure 3.11b). By

contrast, REE profiles of population 2 analyses show little variation (Figure 11c), and are distinguishable from population 1 by their less pronounced Eu anomalies, higher Eu concentrations, and narrower range of HREE slope. Age vs. Gd/Yb and age vs. Eu* relationships further illuminate this (Fig. 3.11d-e), with population 1 analyses exhibiting a wide range of Gd/Yb (31-1034) and Eu* (0.08-0.41) and population 2 exhibiting relatively narrow ranges of both (77-334 and 0.34-0.44, respectively). REE profiles and trace element concentrations also suggest that population 1 can tentatively be further subdivided into two chemically distinct populations, of which one has higher Gd/Yb values (Fig. 3.11d) and a steeper, more HREE depleted slope (highlighted in Figure 3.11c).

Analyses interpreted to represent mixed ages between populations 1 and 2 also exhibit intermediate REE profiles and span the entire range of Gd/Yb and Eu* values of populations 1 and 2 (Figure 3.11d-e). We interpret these as representing laser spots that sampled from both populations in varying ratios. Population 1 ages generally occur in resorbed, low-Y cores in matrix grains (Figure 3.10a-d) or in grains with patchy Y zoning (both in the matrix and as inclusions in in garnet, Figure 3.10d-j). Population 2 ages generally occur in high-Y overgrowths in matrix grains (Figure 3.10a-d). One matrix grain with patchy Y distribution yields population 2 spot ages in its rim (Figure 3.10e-f).

Many spot ages within both populations are 1-3% discordant (Figure 3.11f), so the wide age ranges of individual spot analyses within each population are more likely the result of Pb loss than prolonged periods of monazite (re)crystallization. However, each population describes well defined but seemingly separate discordia arrays, with upper intercepts at 2792 ± 3.9 [33] (MSWD = 2.1) for population 1 and 2692 ± 30 [33] Ma (MSWD = 5.4) for population 2 (Figure 3.11f). Weighted averages of $^{207}Pb/^{206}Pb$ spot ages from the HREE depleted segment of population 1, the HREE enriched segment of population 1, and population 2 are 2792 ± 12 (MSWD = 0.01; n=7), 2792 ± 6.5 (MSWD = 0.35; n=25), and 2667 ± 16 (MSWD = 1.8), respectively (Figure 11g-i). Thus both sub-groups of population 1 are indistinguishable in $^{207}Pb/^{206}Pb$ age but are clearly separated from population 2.

BQC13-01O (tonalite of tentative LLMC affinity)

Monazite in sample BQC13-01O (the 'LLMC tonalite' in Figure 3.2a) occurs as subhedral inclusions in plagioclase, quartz, and biotite (Figure 3.10k-p). Nine monazite grains were analyzed, with individual spot ages ranging from 2992 ± 36 to 2661 ± 33 Ma (n = 32;

Figure 3.12a, Table B5). Two other analyses are reversely discordant with 2σ error ellipses that do not overlap concordia and are thus not considered here. All monazite grains exhibit oscillatory zoning, with two grains featuring BSE-dark overgrowths that cross-cut oscillatory zoning (Figure 3.10k-n), and one grain with an oscillatory zoned overgrowth on a patchy core (Figure 3.10o-p). A probability plot of $^{207}Pb/^{206}Pb$ spot ages (Figure 3.12a) reveals a dominant period of monazite growth from 2771± 33 to 2796 ± 33 Ma, preserved in the oscillatory zoned domains (Figs. 3.10k-p, 3.12a). The oldest spot age of 2992 ± 36 Ma is from a patchy zoned core overgrown by an oscillatory-zoned rim (Figure 3.10p), and is interpreted as an inherited/xenocrystic core. Two spot ages (2661 and 2674 Ma) are significantly younger than all other analyses, overlapping within uncertainty with population 2 in the pelitic migmatite. These young analyses in the tonalite are unlikely to simply be the result of Pb loss because: 1) they are concordant and 1% reversely discordant but overlapping the concordia within uncertainty (Figure 3.12c), and 2) they have nearly identical REE profiles and Th contents that are distinguishable from the dominant population by their far less pronounced Eu anomalies and lower Th concentrations (Figure 3.12b, d, e). Therefore, we interpret that these young analyses record a separate period of limited monazite (re-)crystallization. Spot ages in the range of 2767–2738 Ma are interpreted to reflect mixing of the dominant older population and the younger age, consistent with their REE profiles, Eu* values, and Th concentrations (Figure 3.12b, d-f). The dominant population and the young analyses have upper concordia intercepts of 2775 ± 9 [33] Ma (MSWD = 0.28) and 2667 ± 16 [33] Ma, respectively. A weighted average of $^{207}Pb/^{206}Pb$ spot ages of the dominant population yields an age of 2781 ± 7 [33] Ma (MSWD = 0.18; n = 20; Figure 12f).

3.7.2 Discussion of U-Pb monazite LASS petrochronology

U-Pb monazite petrochronology from samples of both metasedimentary granulites (BPYR14-11B) and tonalite (BQC13-01O) suggests that there were distinct monazite (re)crystallization events at ~2.79-2.78 Ga and ~2.69-2.67 Ga, with the younger event coinciding with the Sm-Nd bulk garnet ages presented in this study. Population 2 in sample BPYR14-11B contains two concordant analyses (2705 ± 33 and 2690 ± 33 Ma), and eight discordant analyses, indicating Pb loss. Thus, we take the concordia intercept age of 2692 ± 30 [33] Ma as the best estimate for the age of this population, despite having a higher MSWD than the weighted average of the $^{207}Pb/^{206}Pb$ ages (2667 ± 17 [33] Ma), both of which overlap within uncertainty.

Regardless, neither the concordia age nor the weighted average age overlap within uncertainty with the age of population 1, implying that population 2 post-dates population 1 by ~100 Ma. The distinctly less pronounced negative Eu anomalies (i.e. higher Eu* values) of population 2 are likely to be due to Eu liberation into the reactive bulk composition upon partial plagioclase breakdown following growth of population 1. We tentatively ascribe this to plagioclase breakdown associated with partial melting during this younger, migmatite-forming event.

Population 1 in sample BPYR14-11B can be subdivided into two chemically distinct sub-groups: one with high Gd/Yb and a steeper HREE slope, and one with lower Gd/Yb and a shallower HREE slope (referred to as HREE-depleted and old HREE-enriched, respectively, in Figure 3.11c). The HREE depleted (high Gd/Yb) group is interpreted to have grown in the presence of garnet, possibly during garnet growth and prograde metamorphism since garnet strongly fractionates HREE from the reactive bulk composition. The HREE enriched (low Gd/Yb) group is tentatively interpreted to have grown during retrograde metamorphism and garnet breakdown, which would liberate HREE back to the reactive bulk composition. We note, however, that ages of both groups overlap, implying rapid metamorphism if this interpretation is appropriate. Weighted average $^{207}Pb/^{206}Pb$ and concordia intercept ages (~2792 Ma) of population 1 overlap with the published range of ages for LLMC crystallization (Mueller et al., 2010), and is therefore interpreted to record metamorphism due to heating from intrusion of the LLMC. Monazite grains included in garnet contain only population 1 spot ages (i.e. Figure 3.10i-j), with no population 2 or mixed spot ages, thus providing a maximum age of garnet growth and suggesting that some garnet grew at ~2.79 Ga due to heating from LLMC intrusion.

The dominant population in tonalitic sample BQC13-01O comes from oscillatory zoned domains with high Th concentrations (most >100,000 ppm Th; Figure 3.12e; Table B5) and REE profiles consistent with crystallization from a granitoid melt (e.g. Williams, 2014; Lederer et al., 2013; Parrish, 1990). This population has a weighted average $^{207}Pb/^{206}Pb$ age of 2781 ± 7.2 [33] Ma, and a concordia intercept age of 2775 ± 9 [33] Ma, both of which overlap within uncertainty with U-Pb SHRIMP zircon crystallization ages for granodioritic rocks of the LLMC (samples BTR-64 and HRR-70 from Mueller et al., 2010). The age of the dominant population, combined with monazite zoning and trace element chemical data, and with whole rock geochemical data (Figure 3.4a) suggest that BQC13-01O is indeed a part of the LLMC that crystallized at 2.78 Ga.

The two young monazite spot ages from the tonalite (2661 ± 33 and 2674 ± 33 Ma) have lower Th concentrations (~64,000-80,000 ppm) and, as in population 2 of sample BPYR14-11B, a far less pronounced Eu anomaly than the dominant population (Figure 3.12b, d, e). The less pronounced Eu anomaly could be due to localized, limited plagioclase breakdown during production of a trace amount of partial melt, though any petrographic evidence for this is cryptic. Regardless, these young spot ages overlap within uncertainty of both population 2 in sample BPYR14-11B and the Sm-Nd bulk garnet ages presented in this study, suggesting that a metamorphic event at ~2.69 Ga had a limited effect on isotopic resetting and recrystallization within LLMC granitoids. The preservation of LLMC-aged monazite domains in both BPYR14-11B and BQC13-01O suggests that Pb diffusion during this younger metamorphic event was sluggish, even if granulite-facies conditions were attained. This is consistent with closure temperature estimates for U-Pb in monazite that are probably ~100˚C greater than peak temperature estimates for the metasedimentary granulites (e.g., Spear and Parrish, 1996; Williams et al., 2014; Cherniak et al., 2004; Gardes et al., 2007).

3.8 TIMING OF HT METAMORPHISM IN THE EASTERN BEARTOOTH MOUNTAINS

This work is, to our knowledge, the first attempt to directly date both garnet and monazite growth (and, hence, HT metamorphism) in the eastern Beartooth Mountains. These ages represent a significant addition to the dataset from the Wyoming Province, as few *sensu stricto* metamorphic ages exist. Multi-point garnet ages were calculated for the five granulite-facies metasedimentary samples at 2669 ± 48 Ma, 2677 ± 50 Ma, 2684 ± 24 Ma, 2681 ± 58 Ma, and 2670 ± 64 Ma. These overlap with each other, within uncertainty, and are significantly younger than well-constrained ages representing the timing of arc-magmatic emplacement of the LLMC (~2790-2830 Ma; Mueller et al., 2010). Primary growth zoning of trace elements appears to be preserved in some samples and can be linked to HT garnet growth upon anatexis (e.g., in sample BHP13-03D). Combined with observed field relationships between intrusive rocks and metasedimentary roof pendants, supplemented by whole-rock geochemistry presented above, this suggests that garnet growth during HT metamorphism of the metasediments *post-dated* LLMC emplacement. This is substantiated by U-Pb LASS results, which reveal two distinct periods of monazite (re)crystallization: one at 2.79-2.78 Ga, and another at 2.69-2.67 Ga. The latter is only weakly preserved in the tonalite, is coincident with the Sm-Nd garnet ages, and exhibits less

pronounced negative Eu anomalies that may reflect monazite growth during plagioclase breakdown (potentially during partial melting).

The major question is thus "what do these garnet and monazite ages represent?" Have they somehow been modified after prograde metamorphism and are thus geologically meaningless, or are they a robust record of prograde metamorphism that must be reconciled with existing data in a suitable geodynamic context?

Considerable scatter between the ages calculated by the individual garnet fractions for each lithology results in garnet-WR (± powder ± magnetite) multi-point 'errorchron' ages which have high errors and MSWDs. This intra-sample garnet age scatter is important and simply means that the crystals in each sample variably sample more than one single age event. Scenarios that could lead to this include: a) a single phase of HT growth followed by slow cooling (during which each crystal partially resets its Sm-Nd age until reaching an effective closure temperature range that depends on crystal size and textural setting), b) a single, long duration, HT metamorphic event with protracted garnet growth that allows different sampled garnet fractions to record different times, c) multiple discrete garnet growth events (i.e. polymetamorphism), and d) combinations of the previous three factors. In any of these scenarios, the sampling of different garnet fractions from a bulk collection of crushed porphyroblasts would result in a range of two-point garnet-WR isochron ages (e.g. Kohn 2009; Baxter & Scherer 2013). Each of these scenarios assume that contact metamorphism associated with emplacement of the LLMC occurred at approximately 2810 Ma (e.g. Mueller et al., 2010), and the discussion below addresses whether any or all of these could result in the Sm-Nd dataset presented in this paper. This could help to elucidate the relative influence of contact heating from the LLMC on garnet ages, and any alternative (or additional) mechanisms/events contributing to garnet growth.

3.8.1 Scenario a): Garnet ages result from slow cooling from a single, HT event at 2810 Ma.

The range of ages presented above may result from slow cooling from a HT metamorphic event at 2810 Ma, essentially a consequence of contact heating associated with emplacement of the LLMC. In this scenario, garnet porphyroblasts of various sizes would have undergone differential resetting of their Sm-Nd ages during cooling from magmatic temperatures and this may alter the interpretation of any age from recording prograde growth to that of a cooling age (or hybrid age thereof). Determination of the 'cooling age' of minerals has been the basis of many low temperature thermochronologic studies, beginning with the introduction of the concept

of the closure temperature, T_C (Dodson 1973, 1986). Calculation of T_C, for any given geochronological system and mineral, is dependent on factors such as the cooling rate, grain size, and the elemental diffusivities in the mineral of interest, and extensive studies have led to a range of T_C estimates, including for Sm-Nd in garnet (Mezger et al 1992; Zhou and Hensen, 1995). Ganguly and Tirone (1999, 2001) formulated an expansion of the T_C calculation, including the addition of a 'memory function', incorporating a dependency of T_C on the peak temperature, T_0. Additionally, for slowly diffusing systems (such as Sm-Nd in garnet), the initial concentration of the daughter product may be retained in crystal cores. As temperature decreases, elemental concentrations are 'locked-in', with the effective diffusive lengthscale decreasing from the core to the rim of a mineral. This implies that a given garnet crystal would possess a T_C profile rather than a unique T_C (Dodson, 1986; Ganguly and Tirone, 1999).

The approach of Ganguly and Tirone (1999, 2001) allows us to model the expected extent of age resetting within a garnet crystal, based on peak temperature, grain size, elemental diffusivity, and inferred initial cooling rate from peak temperature. We use the diffusion data of Tirone et al. (2005), a peak temperature of 800°C, grain sizes of 3 and 7.5 mm (the range of grain sizes in sample BHP13-03D), and a range of initial cooling rates. In these calculations, the cooling rate decays with decreasing temperature, with the *T-t* path having a linear relation of $1/T$ vs t (Ganguly and Tirone, 1999). Figure 13 shows the extent of age resetting for the end-member garnet crystal sizes, demonstrating how an apparent age profile develops within each. Results indicate that even for grain sizes of just a few mm, the growth age is retained in garnet core for initial cooling rates > 5°C/My. In order for 2790-2830 Ma garnet growth to reset to the analyzed *bulk* Sm-Nd age of 2718 Ma (2σ *maximum* age for sample BHP13-03D), the initial cooling rate would need to be < 2°C/My (Figure 3.13a), with a lower cooling rate required for the 7.5 mm crystal (< 1.5°C/My; Figure 3.13b). The use of alternate, slower values for elemental diffusivity (i.e. Carlson, 2012) would mandate higher temperatures or even slower initial cooling rates to explain the data presented here by simple cooling from a 2790-2830 Ma growth event.

Several assumptions limit the applicability of the above calculations, including: a) that the initial garnet growth event was instantaneous, b) that no diffusion of REE (or radiogenic ingrowth of daughter product) occurred during prograde growth, and c) that there was an initially homogeneous distribution of REE within garnet (i.e. no REE zonation). As entrainment by the LLMC would have resulted in rapid heating of the sedimentary rocks, assumptions a) and b) are

deemed to be reasonable for the purposes of this discussion. The potential of continuous diffusion of REEs (and production of daughter isotopes) during a longer-lived prograde metamorphic history is discussed below in section 3.8.2.

Both theoretical models (Kohn, 2009) and field-based approaches (Lapen et al., 2003; Skora et al., 2006) have shown how the distribution of REEs in garnet (notably Lu and Sm) will affect the age interpretation of the related geochronometer. Lu-Hf ages from crystals showing strong Lu enrichment in cores are biased towards the timing of early garnet growth (Lapen et al., 2003), but, if Sm (and Nd) is more evenly distributed throughout garnet, Sm-Nd will yield a volumetrically averaged garnet growth age. In some cases, Sm concentrations (and thus $^{147}Sm/^{144}Nd$) are elevated in garnet rims, either as a result of diffusion-limited growth (Skora et al., 2006) or reactions involving accessory minerals in the evolving matrix. Bea and Montero (1999) documented the preferential uptake of mid- to heavy REE into garnet due to xenotime breakdown during the growth of garnet rims.

In any case, where Sm is homogeneously distributed throughout garnet crystals (e.g. in BQC13-01A and BLP13-04; Figure 3.8b-d), the age resetting calculations shown above are generally appropriate and require unrealistically low initial cooling rates (~1-1.5 °C/Myr) to produce the obtained Sm-Nd results by diffusional resetting from an 'LLMC emplacement age' alone. These age resetting calculations are probably less reliable for BHP13-03D, in which Sm is enriched in garnet rims (Figure 3.8a), but the preservation of complex REE zoning there suggests that substantial diffusion is unlikely to have occurred anyway. Therefore, we contest that reported bulk garnet Sm-Nd ages cannot *solely* represent the effect of slow cooling from ~800°C following contact heating associated with emplacement of the LLMC.

3.8.2 Scenario b): Garnet ages result from a single, long duration HT event

A consequence of maintaining elevated temperatures (>750°C) for long durations (>10^6-10^7 yr) could be the continuous growth of garnet, establishing a complex age zonation within crystals (and between garnet mineral separates). For systems in which even modest temperatures are attained (500-700°C), long durations of garnet growth could also lead to a scatter of Sm-Nd ages. In this scenario, the U-Pb monazite ages presented here could alternatively be interpreted as reflecting monazite growth at distinct times over a single, prolonged (>100 Ma) metamorphic cycle. The unbiased sampling of crushed fractions from portions of garnets that grew over substantial durations will result in a scatter in ages, and when assembled onto a multi-point

isochron may yield high MSWDs because the weighted age differences may greatly exceed the analytical resolution.

We infer that the sharp peak in Ca observed near garnet crystal rims in sample BHP13-03D (Figure 3.6a) was established at near-peak temperature after the initiation of melting. Given that this feature was not subsequently diffusively relaxed, the duration over which near-peak temperature was maintained could be approximated with a multicomponent garnet diffusion model. We thus performed a series of calculations for various peak temperatures, utilizing an inferred initial garnet zoning profile (Fig. 3.14a) and modeling diffusive relaxation of Fe, Mg, Mn and Ca with the multicomponent formulation of Lasaga (1979) and a finite difference approach. The region of interest is the outer ~1.6 mm of garnet from sample BHP13-03D, with the inferred initial zoning broadly defined as a series of steps that may result from evolving garnet producing reactions (Figure 3.14). We emphasize that we have little independent constraint on initial zoning without incorporation of equilibrium thermodynamic constraints and consideration of a *P–T* path (e.g. Caddick et al., 2010, Florence and Spear, 1991, Gaidies et al., 2008, Galli et al., 2011), but note that resultant metamorphic timescales are relatively insensitive to uncertainties on initial zoning, given the complexity of the preserved profile (e.g. Fig. 3.7a). Element exchange with the matrix at peak to post-peak conditions is not considered here since it cannot have substantially contributed to internal zoning patterns that were presumably established during prograde growth.

Figure 14 shows select results of multi-component garnet diffusion modeling from the initial profile (Fig. 3.14a) at a peak temperature of 800°C, calculated using a characteristic temperature of 768 ˚C (following Chakraborty and Ganguly, 1990; 1992) and with diffusivities from Chakraborty and Ganguly (1992). The best-fit diffusion durations for different characteristic temperatures are shown in Table 3. Given the retention of *sharp* zoning in Ca (Figs. 3.7a and 3.14), the best-fit timescale is brief, with relatively short (<1 Ma) implied durations for most temperatures examined. Results were relatively similar in calculations that used diffusivity data from Carlson (2006) rather than Chakraborty and Ganguly (1992), implying that the time spent near the 800 ˚C peak temperature determined by previous studies (‘near peak *T*’ using the concept of a characteristic temperature as defined by Chakraborty and Ganguly) was brief, likely <1 Ma. Although this does not preclude a single, long duration metamorphic event, it does imply that the time at high temperature after growth of the Ca-rich garnet portion, which

is interpreted to record the melt-forming event and is coincident with the majority of analyzed Sm in the crystal (Fig. 3.8a), was short.

3.8.3 Scenario c): Garnet ages result from a polymetamorphic history

Similar to the effects of long growth durations, multiple episodes of metamorphism could result in significant scatter in garnet ages and high MSWDs for multipoint isochrons. Field evidence suggests that emplacement of the LLMC entrained the metasediments as xenoliths/roof pendants (e.g. Henry et al., 1982; Mogk et al., 2014). Associated contact heating would likely result in some metamorphic garnet growth at 2790-2830 Ma, and was probably responsible for the 2792 Ma ($^{207}Pb/^{206}Pb$ age) monazite population 1 in sample BPYR14-11B. The HREE-depleted group of population 1 is interpreted to record monazite growth in the presence of garnet, presumably due to this contact heating with the LLMC. As shown earlier, it is unlikely that the Sm-Nd garnet ages solely represent slow cooling from this event. They may, however, reflect a mixed signal of early garnet cores overgrown during a second HT event that was considerably closer to the calculated ages. However, it is unlikely that this was responsible for the dominant episode of granulite-facies metamorphism preserved in the examined rocks of the eastern Beartooth Mountains, with the bulk of garnet growth being demonstrably younger than LLMC crystallization ages.

Garnet ages may also represent the combined effects of both polymetamorphism and protracted cooling from the granulite-facies event, in which case the absolute timing of this later HT event cannot be accurately constrained. Several studies have coupled the Lu-Hf and Sm-Nd garnet chronometers (Lapen et al., 2003; Kylander-Clark et al., 2007; Cheng et al., 2008; Smit et al., 2013) or microsampled distinct growth zones of garnet for isotopic dating for determinations of garnet growth durations (Ducea et al., 2003; Pollington and Baxter, 2010; Dragovic et al., 2012, 2015; Gatewood et al., 2015), and this would be a useful future step.

3.8.4 Effect of melt removal on bulk garnet ages

Samples BHP13-03D, BLP14-05, and BPYR14-11B show evidence for the production of melt, shown by petrographic observations and REE and major element zonation patterns in garnet. The high-Ca rims in sample BHP13-03D are interpreted to result from the breakdown of plagioclase via the reaction: plagioclase + biotite + sillimanite + quartz = garnet + k-feldspar + melt. This breakdown reaction did not go to completion, however, as plagioclase remains as a

stranded prograde relict in the matrix (Fig. 3.6a, c). Comparison of figures 7a and 8a shows that the 'spike' in Ca is coincident with an increase in Sm near the garnet rims. Therefore, this partial melting and subsequent melt removal (provided a critical melt loss threshold is surpassed; Rosenberg and Handy, 2005; Yakymchuk and Brown, 2014b) can be recorded in the REE zonation patterns of garnet grown during such melting. Given short timescales, the timing of such processes may be retained in isotopic data.

A possible limitation of the use of isochron ages to assess the timing of partial melting is the effect of melt removal on the residual bulk rock isotopic composition. An isochron typically relies on the sampling and measurement of a 'whole rock' or 'matrix', however these reservoirs are fractionated during melt removal. Fractionation of a low Sm/Nd melt will increase the Sm/Nd of the residuum, thereby rotating the two-point isochron such that the apparent age will increase. Differences in isotopic composition between the fractionated melt and the initial bulk rock can have profound effects on the apparent garnet growth age, depending on the timing of the melt removal event relative to the timing of garnet growth. As an example, garnet fraction 'BHP13-03D 90HF gt' from Table 3.2a (with a two-point isochron age of 2669.4 ± 5.2 Ma) was used as the stable 'lever point' of a two-point garnet-'WR' isochron, wherein the 'WR' composition is the residual WR composition 'BHP13-03D WR' (also shown in Table 2a) with melt of varying $^{147}Sm/^{144}Nd$ reintegrated back into it at varying timescales after garnet growth, with subsequent radiogenic ingrowth of the system. Ages were calculated using a range of leucogranitic $^{147}Sm/^{144}Nd$ values obtained from the literature (e.g. Harris et al., 2004; Korhonen et al., 2010). A few key assumptions are made in these calculations: 1) the melt is in Nd isotopic equilibrium with the residuum at the time of removal, 2) melt removal is instantaneous, and 3) occurred sometime after the termination of garnet growth. The last assumption is clearly not the case, as we suggest above that garnet rims show evidence of growth during partial melting, however for simplicity we use the bulk garnet isotopic composition for calculation of the isochron ages. These calculations show that for a modest amount of melt removal (e.g. 20 vol.%; $^{147}Sm/^{144}Nd$ of melt = 0.09) occurring 1 Ma after the termination of garnet growth, the 'true' garnet age is calculated to be ~0.04 Ma younger than the apparent age, with a similarly relative age difference of 0.4 Ma if melt is removed 10 Ma after the garnet growth event. As shown here, the effect of melt removal on a garnet-WR isochron age in this study is insignificant given the short timespan between initial garnet growth and subsequent melting. Because so little

radiogenic ingrowth had occurred during the short span between garnet growth and melting, the isochron at that point was still close to horizontal rendering any Sm/Nd fractionation (or even incongruent melting effects) negligible within our age resolution. Regardless, the resultant 'true' age is *younger* than the apparent garnet age, and is thus still significantly younger than LLMC emplacement (absent other discussed limitations such as polymetamorphism and slow cooling).

3.9 PHASE EQUILIBRIA MODELLING OF LLMC

Field relationships and garnet geochronology both suggest that HT metamorphism postdated emplacement of the LLMC, but there is little petrologic or geochronologic evidence of this event within the arc intrusives. In order to examine this further, phase equilibria modeling was undertaken for the whole rock composition of LLMC tonalite sample BQC13-01O (Table 1). Details of methodology are presented in the Appendix.

A *P–T* pseudosection for sample BQC13-01O is shown in Figure 15. The calculated assemblage of the LLMC tonalite at the granulite-facies peak *P–T* conditions established by previous estimates (~750-810°C, 5.6-8 kbar; Henry et al., 2014; Henry et al., 1982; Maas, 2004; Mogk et al., 2014) is biotite + plagioclase + quartz + magnetite + sillimanite + garnet ± melt ± cordierite ± ilmenite (Figure 3.15a). This is broadly consistent with the observed assemblage in LLMC sample BQC13-01O. Garnet, sillimanite, cordierite, and magnetite stabilities are calculated but are not observed texturally, but the calculated abundance of each is negligible at the *P–T* of interest (<0.5 vol.% garnet, Fig. 15b; ~0.4 vol.% sillimanite, Fig. 15c; ~0.2 vol.% cordierite; ~0.2 vol.% magnetite) and is considered to be well within the uncertainty associated with the modeling. The calculated solidus temperature (Fig. 3.15a) and melt fraction isopleths (Fig. 15d) demonstrate that partial re-melting of the LLMC during granulite-facies metamorphism at approximately 800˚C was probably extremely limited (<1 vol. %). This is consistent with dehydration melting experiments (e.g. Patiño Douce and Beard, 1995), which find sub-solidus biotite stability up to ~ 875˚C at 7 kbar. Although the absolute temperature of dehydration melting varies with rock composition and pressure (e.g. Patiño Douce and Johnston, 1991; Stevens et al., 1997; Thompson, 1982; Vielzeuf and Holloway, 1988; Vielzeuf and Schmidt, 2001), the vapor absent solidus for tonalitic compositions at 7-8 kbar is almost 900°C (e.g. see compilation presented in Fig. 3.11 of Patiño Douce, 2005). Thus we think it extremely unlikely that wholesale melt/fluid-enhanced recrystallization was likely to have occurred in

relatively dry tonalitic and granodioritic rocks that experienced the putative 2.68 Ga HT metamorphism.

3.10 DISCUSSION

3.10.1 Potentially widespread but weakly recorded metamorphism: a common phenomenon?

The general absence of evidence for granulite-facies conditions in the granitoid lithologies of the LLMC is consistent with field and petrographic observations, the scant record of younger monazite in tonalite presented here, the lack of a strong signal for this younger metamorphism in the extensive published zircon dataset (e.g. Maier et al., 2012; Mueller et al., 2010; Mueller et al., 2014) and the retention of Rb-Sr ages at ~ 2.8 Ga (Henry et al., 1982). This implies that large volumes of continental crust may have experienced a tectono-thermal event that only small regions of that crust preserve good evidence for (and perhaps then only as cryptic evidence). Such behavior may not be uncommon, with well-known and diverse Phanerozoic analogues including (i) the limited imprint of Barrovian-style metamorphism that closely followed emplacement of the Mount Stuart batholith (Evans and Berti, 1986), attributed partly to lack of fluid availability (Evans and Davidson, 1999), (ii) suppressed equilibration at UHP depths due to fluid-absent conditions following dehydration of subducting continental crust of the Western Gneiss Region, Norway (e.g. Hacker et al., 2015; Young and Kylander-Clark, 2015), (iii) a patchy record of Cambrian 800–870˚C overprinting on Proterozoic assemblages of the Rayner Orogeny, due to the inert nature of segments of the crust preconditioned by the earlier event (Morrissey et al., 2015), and (iv) the formation of high pressure granulitic assemblages only in restricted textural settings of the Eger Complex, NW Bohemian Massif, due to the brief duration of heating up to ~850˚C (Konopásek et al., 2014). In each of these cases, rapid metamorphism and/or anhydrous lithologies either completely inhibited recrystallization or substantially reduced effective equilibration length-scales, consistent with the models of Guiraud et al. (2001) and Carlson (2010), and with numerous publications demonstrating evolution of equilibration domains upon rock dehydration (e.g. Baldwin et al., 2005; Guevara & Caddick, 2016; White & Powell, 2002, 2011) and the role of fluids in catalyzing metamorphic reactions (e.g. Austrheim, 1987; Baxter 2003; Jamtveit and Austrheim, 2010; Putnis and John, 2010).

3.10.2 Implications for the tectono-metamorphic evolution of the Wyoming craton

Granulite-facies metamorphism of the supracrustal rocks appears to have postdated emplacement of the Long Lake Magmatic Complex and thus requires an alternative heating mechanism. The ~2670-2690 Ma bulk garnet Sm-Nd ages reported here do, however, correlate with the inferred timing of magmatic and metamorphic events recorded elsewhere in the northwestern Wyoming craton (Figure 3.16). High-pressure granulites in the Teton Range, ~200 km to the south of eastern Beartooth Mountains, contain 2700-2675 Ma metamorphic zircon, coincident with leucogranitic plutonism (Frost et al., 2007). These rocks have been interpreted to record regional metamorphism associated with E- to NE-directed terrane accretion/subduction (Frost et al., 2006; 2007). The garnet diffusion modeling presented here suggests that residence at peak temperatures of ~800˚C occurred for substantially shorter timescales ($<10^6$ yr) than expected for metamorphism in a collisional environment (e.g. England and Thompson, 1984), although recent studies suggest that metamorphism in collisional environments may occur on far shorter timescales (10^5-10^6 yr, Ague and Baxter, 2007; Spear et al., 2012; Viete et al., 2011; Chu and Ague, 2015), possibly resulting from punctuated thermal inputs superimposed on a broader regional thermal regime. Cases of brief ~800°C metamorphic pulses have been associated with heating via mafic magmatism (e.g. Dorfler et al., 2015) or focused fluid flow (e.g. Chamberlain and Rumble, 1988, 1989; Ague and Baxter, 2007; Ague et al., 2013; Chu and Ague, 2015).

U-Pb zircon and baddelyite ages from mafic rocks in the northwestern Wyoming craton broadly coincide with the Sm-Nd garnet ages reported here (Figure 3.16). The Stillwater Complex, a layered mafic intrusion located ~60 km northwest of the study area, is recently dated to ~2709-2711 Ma (Wall et al., 2012; Wall and Scoates, 2016). Tholeiitic dikes from the Owl Creek Mountains and Wind River Range, ~200 km south of the study area, are dated to ~2.68 Ga, and have been interpreted to result from back arc spreading (Frost et al., 2006). Additionally, arc-related mafic plutonism, represented by the Rendezvous Gabbro of the Teton Range (~200 km south of the study area), has been dated to ~2.67 Ga (Frost et al., 2006). The coincidence between the Sm-Nd garnet ages reported here and ages of mafic magmatic events both northwest and south of the study area, as well as the requirement of sufficiently short metamorphic timescales to preserve major element zoning in garnet, points to the possibility that mafic magmatism and associated advective fluid flow could have been an important heat source for this cryptic metamorphism. We note that field evidence for this heat source is currently lacking in the

eastern Beartooths, but we cannot completely discount its presence at currently unexposed crustal levels, as commonly invoked for some Phanerozoic terranes (e.g. Chamberlain and Rumble, 1988; Ague et al., 2013).

3.11 CONCLUSIONS

Metasediments from the eastern Beartooth Mountains of Montana and Wyoming, entrained as xenoliths/roof pendants during emplacement of the Long Lake Magmatic Complex (LLMC) at 2.79-2.83 Ga (Mueller et al., 2010), experienced a later granulite-facies metamorphic event at least 50 Ma after arc magma emplacement. Evidence that this HT metamorphic event postdated LLMC emplacement include: a) field observations of partial melts from pelitic granulites cross-cutting intrusive lithologies, b) U-Pb monazite ages on an LLMC tonalite and a granulite-facies metasediment, and c) Sm-Nd bulk garnet multi-point ages on five granulite-facies metasediments ranging from 2669 ± 48 Ma to 2681 ± 58 Ma. Significant scatter between garnet fractions used for the multi-point isochrons resulted in the high MSWDs, and may have risen from a combination of factors including a polymetamorphic growth history and slow cooling from high temperatures. The polymetamorphic history is supported by the U-Pb monazite ages and can be further confirmed with coupling of Sm-Nd and Lu-Hf chronometers or microsampling of distinct garnet growth zones. Melt removal during HT metamorphism is shown to have an insignificant effect on isochron ages. Phase equilibria modeling of the LLMC lithologies has shown that while the secondary metamorphic event resulted in granulite-facies metamorphism of the metasediments, this may not be expected to have substantially modified the LLMC rocks, tentatively explaining the paucity of ~2.68 Ga ages in the extensive and well-constrained zircon archive. If garnet growth during HT metamorphism postdated LLMC emplacement, an alternative heating mechanism for this later event is required. Diffusion modeling of garnet major element zoning mandates that this 800°C event was brief (<1 Ma). No clear field evidence for a magmatic heat source is currently available, in common with a growing number of studies on Phanerozoic terranes that have invoked 'thermal pulses' during granulite-facies metamorphism in settings where a direct heat source is similarly cryptic (Chamberlain and Rumble, 1988; Ague and Baxter, 2007; Ague et al., 2013).

3.12 ACKNOWLEDGMENTS

We thank K. Dorfler, M. Fame, J. Guevara, A. Mulholland and T. Palin for field assistance, S. Mertzman for XRF analysis, D. Honn for assistance with aspects of mass spectrometry, and L. Fedele for help with electron microprobe analysis and laser ablation ICP-MS at the Virginia Tech LA-ICP-MS Facility. Finally, we thank Paul Mueller for an insightful and helpful review and Randall Parrish for careful and constructive editorial handling. All isotopic analyses for this study were conducted at Boston University TIMS Facility, which is funded by NSF-0521266 and NSF EAR-0949390 (to EFB). We gratefully acknowledge NSF Grant EAR-1447568 (to MJC and BD), a Geological Society of America student research grant (to VEG), two Tobacco Root Geological Society field scholarships (to VEG), a Colorado Scientific Society student research grant (to VEG) and a National Geographic Young Explorer's grant (to VEG).

3.13 REFERENCES

Ague, J.J., Baxter, E.F., 2007. Brief thermal pulses during mountain building recorded by Sr diffusion in apatite and multicomponent diffusion in garnet. *Earth and Planetary Science Letters*, **261**, 500-516.

Ague, J.J., Eckert, J.O., Chu, X., Baxter, E.F., Chamberlain, C.P., 2013. Discovery of ultrahigh-temperature metamorphism in the Acadian orogen, Connecticut, USA. *Geology*, **41**, 271-274.

Aleinikoff, J.N., Schenck, W.S., Plank, M.O., Srogi, L., Fanning, C.M., Kamo, S.L., Bosbyshell, H., 2006. Deciphering igneous and metamorphic events in high-grade rocks of the Wilmington Complex, Delaware; morphology, cathodoluminescence and backscattered electron zoning, and SHRIMP U–Pb geochronology of zircon and monazite. *Geological Society of America Bulletin*, **118**, 39–64.

Amato, J.A., Johnson, C.M., Baumgartner, L.P., Beard, B.L., Rapid exhumation of the Zermatt-Saas ophiolite deduced from high-precision Sm-Nd and Rb-Sr geochronology. *Earth and Planetary Science Letters*, **171**, 425-438.

Anczkiewicz, R., Thirlwall, M., Alard, O., Rogers, N.W., Clark, C., 2012. Diffusional homogenization of light REE in garnet from the Day Nui Con Voi Massif in N-Vietnam: Implications for Sm-Nd geochronology and timing of metamorphism in the Red River shear zone. *Chemical Geology*, **318-319**, 16-30.

Austrheim, H., 1987. Eclogitization of lower crustal granulites by fluid migration through shear zones. *Earth and Planetary Science Letters*, **81**, 221-232.

Baadsgaard, H., Mueller, P.A., 1973. K-Ar and Rb-Sr ages of intrusive Precambrian mafic rocks, southern Beartooth Mountains, Montana and Wyoming. *Geological Society of America*, **84**, 3635-3644.

Baldwin, J.A., Powell, R., Brown, M., Moraes, R., Fuck, R.A., 2005. Modelling of mineral equilibria in ultrahigh-temperature metamorphic rocks from the Anápolis-Itauçu Complex, central Brazil. *Journal of Metamorphic Geology*, **23**, 511-531.

Baxter, E.F., 2003. Natural constraints on metamorphic reaction rates. *From* Vance, D., Muller, W., Villa, I.M. (eds). *Geochronology: Linking the Isotopic Record with Petrology and Textures*. Geological Society, London, Special Publications, **220**, 183-202.

Baxter, E.F., Scherer, E.E., 2013. Garnet geochronology: timekeeper of tectonometamorphic processes. *Elements*, **9**, 433-438.

Bea, F., Montero, P., 1999. Behavior of accessory phases and redistribution of Zr, REE, Y, Th, and U during metamorphism and partial melting of metapelites in the lower crust: an example from the Kingzigite Formation of Ivrea-Verbano, NW Italy. *Geochimica et Cosmochimica Acta*, **63**, 1133-1153.

Boyd, F.R., Mertzman, S.A., 1987. Composition and structure of the Kaapvaal lithosphere, southern Africa. In: *Magmatic Processes: Physiochemical Principles* (ed. Mysen, B.O.), *Geochemical Society Special Publication*, **1**, 13–24.

Brown, M. 2007. Metamorphic conditions in orogenic belts: A record of secular change. *International Geology Review*, **49**, 193–234.

Brown, M., Korhonen, F.J., Siddoway, C.S., 2011. Organizing melt flow through the crust. *Elements*, **7**, 261-266.

Caddick, M.J., Konopásek, J., Thompson, A.B., 2010. Preservation of garnet growth zoning and the duration of prograde metamorphism. *Journal of Petrology*, **51**, 2327-2347.

Carlson, W.D., 2006. Rates of Fe, Mg, Mn, and Ca diffusion in garnet. *American Mineralogist*, **91**, 1-11.
Carlson, W.D., 2010. Dependence of reaction kinetics on H_2O activity as inferred from rates of intergranular diffusion of aluminum. *Journal of Metamorphic Geology*, **28**, 735-752.
Carlson, W.D, 2012. Rates and mechanisms of Y, REE, and Cr diffusion in garnet. *American Mineralogist*, **97**, 1598-1618.
Casella, C.J., 1969. A review of the Precambrian geology of the eastern Beartooth Mountains, Montana and Wyoming: Memoir – Geological Society of America, 53-71.
Casella, C.J., Goldich, S.S., 1982. The Archean metasedimentary rocks of the Southwest Beartooth Mountains, Montana and Wyoming, IGCP, Archean Geochem. Proj., U.S. Working Group, 9.
Chakraborty, S., Ganguly, J., 1990. Compositional zoning and cation diffusion in aluminosilicate garnets. In: Ganguly, J., (ed) Diffusion, atomic ordering and mass transfer, advances in physical geochemistry, Vol 8., Berlin Heidelberg New York Tokyo, 120-175.
Chakraborty, S., Ganguly, J., 1992. Cation diffusion in aluminosilicate garnets: experimental determination in spessartine-almandine diffusion couples, evaluation of effective binary diffusion coefficients, and applications. *Contributions to Mineralogy and Petrology*, **111**, 74-86.
Chamberlain, C.P., Rumble, III, D., 1988. Thermal anomalies in a regional metamorphic terrane: An isotopic study of the role of fluids. *Journal of Petrology*, **29**, 1215-1232.
Chamberlain, C.P., Rumble, III, D., 1989. The influence of fluids on the thermal history of a metamorphic terrain: New Hampshire, USA. In: Daly, J.S., Cliff, R.A., Yardley, B.W.D., (Eds.), Evolution of Metamorphic Belts. *Geological Society Special Publication*, **43**. Blackwell, Oxford, pp. 203-213.
Chamberlain, K.R., Lilian, T.M., Bleeker, W., Ernst, R.E., 2014. Wyoming-Kaapvaal link ca. 2.7 Ga and evidence for a late Archean Supercontinent. *Geological Society of America Abstracts with Programs*, **46**, no. 6, p. 709.
Cheng, H., King, R.L., Nakamura, E., Vervoort, J.D., Zhou, Z., 2008. Coupled Lu-Hf and Sm-Nd geochronology constrains garnet growth in ultra-high-pressure eclogites from the Dabie orogen. *Journal of Metamorphic Geology*, **26**, 741-758.
Cherniak, D.J., Watson, E.B., Grove, M., Harrison, T.M., 2004. Pb diffusion in monazite: a combined RBS/SIMS study. *Geochimica et Cosmochimica Acta*, **68**, 829-840.
Chu, X., Ague, J.J., 2015. Analysis of experimental data on divalent cation diffusion kinetics in aluminosilicate garnets with application to timescales of peak Barrovian metamorphism, Scotland. *Contributions to Mineralogy and Petrology*, **170**, DOI 10.1007/s00410-015-1175-y
Coggon, R., Holland, T.J.B., 2002. Mixing properties of phengitic micas and revised garnet-phengite thermobarometers. *Journal of Metamorphic Geology*, **20**, 683-696.
Connolly, J.A.D., 2009. The geodynamic equation of state: what and how. *Geochemistry, Geophysics, Geosystems,* **10**: Q10014 DOI:10.1029/2009GC002540.
Dale, J., Powell, R., White, R.W., Elmer, F.L., Holland, T.J.B., 2005. A thermodynamic model for Ca-Na clinoamphiboles in Na_2O-CaO-FeO-MgO-AL_2O_3-SiO_2-H_2O-O for petrological calculations. *Journal of Metamorphic Geology*, **23**, 771-791.
Dodson, M.H., 1973. Closure temperature in cooling geochronological and petrological systems. *Contributions to Mineralogy and Petrology*, **40**, 259-274.
Dodson, M.H., 1986. Closure profiles in cooling systems. *Materials Science Forum*, **7**, 145-154.

Dorfler, K.M., Caddick, M.J., Tracy, R.J., 2015. Thermodynamic modeling of crustal melting using xenolith analogs from the Cortlandt Complex, New York, USA. *Journal of Petrology*, **56**, 389-408.

Ducea, M. N., Ganguly, J., Rosenberg, E.J., Patchett, P.J., Cheng, W., Isachsen, C., 2003. Sm-Nd dating of spatially controlled domains of garnet single crystals: a new method of high-temperature thermochronology. *Earth and Planetary Science Letters*, **213**, 31-42.

Dragovic, B., Samanta, L.H., Baxter, E.F., Selverstone, J., 2012. Using garnet to constrain the duration and rate of water-releasing metamorphic reactions during subduction: an example from Sifnos, Greece. *Chemical Geology*, **314-317**, 9-22.

Dragovic, B., Baxter, E.F., Caddick, M.J., 2015. Pulsed dehydration and garnet growth during subduction revealed by zoned garnet geochronology and thermodynamic modeling, Sifnos, Greece. *Earth and Planetary Science Letters*, **413**, 111-122.

Eckelmann, F.D., Poldervaart, A., 1957. Archean history of the Quad Creek area, Part 1 of Geologic evolution of the Beartooth Mountains, Montana and Wyoming. *Geological Society of America Bulletin*, **68**, no. 10, 1225-1261.

England, P.C., Thompson, A.B., 1984. Pressure-temperature-time paths of regional metamorphism I. Heat transfer during the evolution of regions of thickened continental crust. *Journal of Petrology*, **25**, 894-928.

Erslev, E.A., Frost, C.D., Karlstrom, K.E., Page, N.J., Zentek, M.L., Reed, J.C., Snyder, G.L., Worl, R.G., Bryant, B., Reynolds, M.W., Peterman, Z.E., 1993. The Wyoming Province. Geological Society of America, Boulder, CO. Precambrian, conterminous U.S.

Evans, B.W., Berti, J.W., 1986. Revised metamorphic history for the Chiwaukum Schist, North Cascades, Washington. *Geology*, **14**, 695-698.

Evans, B.W., Davidson, G.F., 1999. Kinetic controls of metamorphic imprint during synplutonic loading of batholiths: an example from Mount Stuart, Washington. *Geology*, **27**, 415-418.

Florence, F.P., Spear, F.S., 1991. Effects of diffusional modification of garnet growth zoning on *P–T* path calculations. *Contributions to Mineralogy and Petrology*, **107**, 487-500.

Frost, B.R., Frost, C.D., Cornia, M., Chamberlain, K., Kirkwood, R., 2006. The Teton-Wind River domain: a 2.68-2.67 Ga active margin in the western Wyoming Province. *Canadian Journal of Earth Sciences*, **43**, 1489-1510.

Frost, B.R., McFarlane, C., Swapp, S.M., Frost, C.D., Chamberlain, K.R., 2007. Timing and duration of high-P granulite facies metamorphism in the northern Teton Range, Wyoming. *Geological Society of America Abstracts with Programs*, **39**, 202.

Gaidies, F., De Capitani, C., Abart, R., 2008. THERIAG: a software program to numerically model prograde garnet growth. *Contributions to Mineralogy and Petrology*, **155**, 657-671.

Galli, A., Le Bayon, B., Schmidt, M.W., Burg, J.-P., Caddick, M.J., Reusser, E., 2011. Granulites and charnockites of the Gruf Complex: evidence for Permian ultra-high temperature metamorphism in the Central Alps. *Lithos*, **124**, 17-45.

Ganguly, J., Tirone, M., 1999. Diffusion closure temperature and age of a mineral with arbitrary extent of diffusion: theoretical formulation and applications. *Earth and Planetary Science Letters*, **170**, 131-140.

Ganguly, J., Tirone, M., 2001. Relationship between cooling rate and cooling age of a mineral: theory and applications to meteorites. *Meteoritics and Planetary Science*, **36**, 167-175.

Gardés, E., Montel, J.M., Seydoux-Guillaume, A.M., Wirth, R., 2007. Pb diffusion in monazite:

new constraints from the experimental study of Pb^{2+} - Ca^{2+} interdiffusion. *Geochimica et Cosmochimica Acta*, **71**, 4036-4043.

Gatewood, M.P., Dragovic, B., Stowell, H.H., Baxter, E.F., Hirsch, D.M., Bloom, R., 2015. Evaluating chemical equilibrium in metamorphic rocks using major element and Sm-Nd isotopic age zoning in garnet, Townshend Dam, Vermont, USA. *Chemical Geology*, **401**, 151-168.

Guevara, V.E., Caddick, M.J., 2016. Shooting at a moving target: phase equilibria modeling of high temperature metamorphism. *Journal of Metamorphic Geology,* **34**, 209-235.

Guiraud, M., Powell, R., Rebay, G., 2001. H_2O in metamorphism and unexpected behaviour in the preservation of metamorphic mineral assemblages. *Journal of Metamorphic Geology*, **19**, 445-454.

Hacker, B.R., Kylander-Clark, A.R.C., Holder, R., Andersen, T.B., Peterman, E.M., Walsh, E.O., Munnikhuis, J.K., 2015. Monazite response to ultrahigh-pressure subduction from U-Pb dating by laser ablation split stream. *Chemical Geology*, **409**, 28-41.

Harlan, S.S., Geissman, J.W., Snee, L.W., 1997. Paleomagnetic and $^{40}Ar/^{39}Ar$ geochronologic data from Late Proterozoic mafic dikes and sills, Montana and Wyoming. United States Geological Survey, 1580.

Harris, N.B.W., Caddick, M., Kosler, J., Goswami, S., Vance, D., Tindle, A.G., 2004. The pressure-temperature-time path of migmatites from the Sikkim Himalaya. *Journal of Metamorphic Geology*, **22**, 249-264.

Harvey, J., Baxter, E.F., 2009. An improved method for TIMS high precision neodymium isotope analysis of very small aliquots (1-10 ng). *Chemical Geology*, **258**, 251-257.

Henry, D.J., Mogk, D.M., Mueller, P., Wooden, J., 2014. Upper-to-middle level exposure of a 2.8 Ga continent in the northern Wyoming Province, USA. *Geological Society of America Abstracts with Programs*, **46**, 19.

Henry, D.J., Mueller, P.A., Wooden, J.L., Warner, J.L., Lee-Berman, R., 1982. Granulite grade supracrustal assemblages of the Quad Creek area, eastern Beartooth Mountains, Montana. Special Publication – State of Montana Bureau of Mines and Geology, **84**, 147-156.

Holland, T., Powell, R., 1996. Thermodynamics of order-disorder in minerals. 2. Symmetric formulation applied to solid solutions. *American Mineralogist*, **81**, 1425-1437.

Holland, T., Powell, R., 1998. Mixing properties and activity-composition relationships of chlorites in the system MgO-FeO-Al_2O_3-SiO_2-H_2O. *European Journal of Mineralogy*, **10**, 395-406.

Holland, T., Powell, R., 2001. Calculation of phase relations involving haplogranitic melts using an internally consistent thermodynamic dataset. *Journal of Petrology*, **42**, 673-683.

Holland, T., Powell, R., 2003. Activity-composition relations for phases in petrological calculations: an asymmetric multicomponent formulation. *Contributions to Mineralogy and Petrology*, **145**, 492-501.

Holness, M.B., Cesare, B., Sawyer, E.W., 2011. Melted rocks under the microscope: microstructures and their interpretation. *Elements*, **7**, 247-252.

Horstwood, M.S.A., Foster, G.L., Parrish, R.R., Noble, S.R., Nowell, G.M., 2003. Common-Pb corrected in situ U-Pb accessory mineral geochronology. *Journal of Analytical and Atomic Spectrometry*, **18**, 837-846.

Jablinski, J.D., Holst, T.B., 1992. Deformational history of Archean metasedimentary rocks of

the Beartooth Mountains in the vicinity of the Mineral Hill mine, Jardine, Montana. *Journal of Geology*, **100**, no. 5, p. 561-578.
Jamtveit, B., Austrheim, H., 2010. Metamorphism: The role of fluids. *Elements*, **6**, 153-158.
Kellett, D.A., Cottle, J.M., Smit, M., 2014. Eocene deep crust at Ama Drime, Tibet: early evolution of the Himalaya orogen. *Lithosphere*, **6**, 220-229.
Kelly, E.D., Carlson, W.D., Connelly, J.N., 2011. Implications of garnet resorption for the Lu-Hf garnet geochronometer: an example from the contact aureole of the Makhavinekh Lake Pluton, Labrador. *Journal of Metamorphic Geology*, **29**, 901-916.
Kohn, M.J., 2009. Models of garnet differential geochronology. *Geochimica et Cosmochimica Acta*, **73**, 170-182.
Kohn, M.J., Corrie, S.L., Markley, C., 2015. The fall and rise of metamorphic zircon. *American Mineralogist*, **100**, 897-908.
Konopásek, J., Pilátová, E., Košler, J., Sláma, J. 2014b. Zircon (re)crystallization during short-lived, high-P granulite facies metamorphism (Eger Complex, NW Bohemian Massif). *Journal of Metamorphic Geology,* **32**, 885-902.
Korhonen, F.J., Saito, S., Brown, M., Siddoway, C.S., Say, J.M.D., 2010. Multiple generations of granite in the Fosdick Mountains, Marie Byrd Land, West Antarctica: Implications for polyphase intracrustal differentiation in a continental margin setting. *Journal of Petrology*, **51**, 627-670.
Kylander-Clark, A.R.C., Hacker, B.R., Cottle, J.M., 2013. Laser-ablation split stream ICP petrochronology. *Chemical Geology*, **345**, 99-112.
Kylander-Clark, A.R.C., Hacker, B.R., Johnson, C.M., Beard, B.L., Mahlen, N.J., Lapen, T.J., 2007. Coupled Lu-Hf and Sm-Nd geochronology constrains prograde and exhumation histories of high- and ultrahigh-pressure eclogites from western Norway. *Chemical Geology*, **242**, 137-154.
Lapen, T.J., Johnson, C.M., Baumgartner, L.P., Mahlen, N.J., Beard, B.L., Amato, J.M., 2003. Burial rates during prograde metamorphism of an ultra-high-pressure terrane: an example from Lago di Cignana, western Alps, Italy. *Earth and Planetary Sciences*, **215**, 57-72.
Lasaga, A.C., 1979. Multicomponent exchange and diffusion in silicates. *Geochimica et Cosmochimica Acta*, **43**, 455-469.
Lederer, G.W., Cottle, J.M., Jessup, M.J., Langille, J.M., Ahmad, T., 2013. Timescales of partial melting in the Himalayan middle crust: insight from the Leo Pargil dome, northwest India. *Contributions to Mineralogy and Petrology*, **166**, 1415-1441.
Lopez, D.A., 2001. Preliminary geologic map of the Red Lodge 30' x 60' Quadrangle of South-Central Montana. Montana Bureau of Mines and Geology, scale 1:100,000.
Ludwig, K.R., 2000. Isoplot/Ex version 2.4. A geochronological toolkit for Microsoft Excel. Berkeley Geochronology Centre, Special Publication, **56**.
Ludwig, K.R., 2008. Isoplot. A geochronological toolkit for Microsoft Excel. Berkeley Geochronology Centre, Special Publication, vol. 4, p. 77.
Maas, A.T., 2004. Migmatization of Archean aluminous metasediments from the eastern Beartooth Mountains, Montana, USA. M.S. thesis, Louisiana State University, p. 155.
Maier, A.C., Cates, N.L., Trail, D., Mojzsis, S.J., 2012. Geology, age, and field relations Hadean zircon-bearing supracrustal rocks from Quad Creek, eastern Beartooth Mountains (Montana and Wyoming, USA). *Chemical Geology*, **312-313**, 47-57.
Menegon, L., Nasipuri, P., Stünitz, H., Behrens, H., Ravna, E., 2011. Dry and strong quartz during deformation of the lower crust in the presence of melt. *Journal of Geophysical*

Research, **116**, 1-23.
Mersmann, M.A., 1981. Metamorphism of a gabbronorite dike: corona development and amphibolitization. Hellroaring Lakes area, Beartooth Mountains, Montana. M.S. thesis, University of Cincinnati.
Mezger, K., Essene, E.J., Halliday, A.N., 1992. Closure temperatures of the Sm-Nd system in metamorphic garnets. *Earth and Planetary Sciences*, **113**, 397-409.
Mogk, D.M., Henry, D.J., 1988. Metamorphic geology of the northern Archean Wyoming Province, southwester Montana; evidence for Archean collisional tectonics. Rubey Volume, **7**, 363-382.
Mogk, D.W., Henry, D.J., Mueller, P., Wooden, J.L., 2014. Mesoarchean rocks of the eastern Beartooth Mountains, MT and WY. *Geological Society of America Abstracts with Programs*, **46**, no. 5, 19.
Mogk, D.W., Mueller, P.A., Wooden, J.L., 1988. Archean tectonics of the north Snowy Block, Beartooth Mountains, Montana. *Journal of Geology*, **96**, no. 2, p. 125-141.
Montgomery, C.W., Lytwyn, J.N., 1984. Rb-Sr systematics and ages of principal Precambrian lithologies in the South Snowy Block, Beartooth Mountains. *Journal of Geology*, **92**, no. 1, p. 103-112.
Morrissey, L.J., Hand, M., Kelsey, D.E., 2015. Multi-stage metamorphism in the Rayner-Eastern Ghats Terrane: *P–T-t* constraints from the northern Prince Charles Mountains, east Antarctica. *Precambrian Research*, **267**, 137-163.
Mueller, P.A., Frost, C.D., 2006. The Wyoming Province: a distinctive Archean craton in Laurentian North America. *Canadian Journal of Earth Sciences*, **43**, no. 10, p. 1391-1397.
Mueller, P.A., Mogk, D.W., Henry, D.J., Wooden, J.L., Foster, D.A., 2014. The plume to plate transition: Hadean and Archean crustal evolution in the northern Wyoming Province, U.S.A. In: *Evolution of Archean Crust and Early Life*, Dilek, Y. and Furnes, H. (eds.), DOI 10.1007/978-94-007-7615-9_2.
Mueller, P.A., Wooden, J.L., Mogk, D.W., Henry, D.J., Bowes, D.R., 2010. Rapid growth of an Archean continent by arc magmatism. *Precambrian Research*, **183**, 70-88.
Mueller, P.A., Wooden, J.L., Nutman, A.P., 1992. 3.96 Ga zircons from an Archean quartzite, Beartooth Mountains, Montana. *Geology*, **20**, 327-330.
Mueller, P.A., Wooden, J.L., Nutman, A.P., Mogk, D.W., 1998. Early Archean crust in the northern Wyoming province: Evidence from U-Pb ages of detrital zircons. *Precambrian Research*, **91**, 295-307.
Mueller, P.A., Wooden. J.L., Odom, A.L., Bowes, D.R., 1982. Geochemistry of the Archean rocks of the Quad Creek and Hellroaring Plateau areas of the eastern Beartooth Mountains. Special Publication – State of Montana Bureau of Mines and Geology, **84**, p. 69-82.
Mueller, P.A., Wooden, J.L., Schulz, K., Bowes, D.R., 1983. Incompatible-element-rich andesitic amphibolites from the Archean of Montana and Wyoming: evidence for mantle metasomatism. *Geology*, **11**, no. 4, p. 203-2-6.
Palin, R.M., Searle, M.P., Waters, D.J., Parrish, R.R., Roberts, N.M.W., Horstwood, M.S.A., Yeh, M.-W., Chung, S.-L., Anh, T.T., 2013. A geochronological and petrological study of anatectic paragneiss and associated granite dykes from the Day Nui Con Voi metamorphic core complex, North Vietnam; constraints upon the timing of metamorphism within the Red River shear zone. *Journal of Metamorphic Geology*, **31**,

359–387.
Parrish, R.R., 1990. U-Pb dating of monazite and its application to geological problems. *Canadian Journal of Earth Sciences*, **27**, 1431-1450.
Patiño Douce, A. E., 2005. Vapor-absent melting of tonalite at 15–32 kbar. *Journal of Petrology,* **46**, 275-290.
Patiño Douce, A.E., Beard, J.S., 1995. Dehydration melting of biotite gneiss and quartz amphibolite from 3 to 15 kbar. *Journal of Petrology*, **36**, 707-738.
Patiño Douce, A.E., Johnston, A.D., 1991. Phase equilibria and melt productivity in the pelitic system: implications for the origin of peraluminous granitoids and aluminous granulites. *Contributions to Mineralogy and Petrology,* **107**, 202-218.
Paton, C., Woodhead, J.D., Hellstrom, J.C., Hergt, J.M., Greig, A., Maas, R., 2010. Improved laser ablation U–Pb zircon geochronology through robust downhole fractionation correction. *Geochemistry, Geophysics, Geosystems*, **11,** Q0AA06.
Prinz, M., 1964. Geological evolution of the Beartooth Mountains, Montana and Wyoming. Part 5. Mafic dike swarms of the southern Beartooth Mountains. *Geological Society of America Bulletin*, **75**, 1217-1248.
Pollington, A.D., Baxter, E.F., 2010. High resolution Sm-Nd garnet geochronology reveals the uneven pace of tectonometamorphic processes. *Earth and Planetary Sciences*, **293**, 63-71.
Premo, W.R., Helz, R.T., Zientek, M.L., Langston, R.B., 1990. U-Pb and Sm-Nd ages for the Stillwater Complex and its associated sills and dikes, Beartooth Mountains, Montana – identification of a parent magma. *Geology*, **18**, 1065-1068.
Putnis, A., John, T., 2010. Replacement processes in the Earth's crust. *Elements*, **6**, 159-164.
Rosenburg, C.L., Handy, M.R., 2005. Experimental deformation of partially melted granite revisited: Implications for the continental crust. *Journal of Metamorphic Geology*, **23**, 19-28.
Scherer, E.E., Cameron, K.L., Blichert-Toft, J., 2000. Lu-Hf garnet geochronology: closure temperature relative to the Sm-Nd system and the effects of trace mineral inclusions. *Geochimica et Cosmochimica Acta*, **64**, 3413-3432.
Skora, S., Baumgartner, L.P., Mahlen, N.J., Johnson, C.M., Piet, S., Hellebrand, E., 2006. Diffusion-limited REE uptake by eclogite garnets and its consequences for Lu-Hf and Sm-Nd geochronology. *Contributions to Mineralogy and Petrology*, **152**, 703-720.
Smit, M.A., Scherer, E.E., Mezger, K., 2013. Lu-Hf and Sm-Nd garnet geochronology: chronometric closure and implications for dating petrologic processes. *Earth and Planetary Sciences*, **381**, 222-233.
Spear, F.S., Ashley, K.T., Webb, L.E., Thomas, J.B., 2012. Ti diffusion in quartz inclusions: implications for metamorphic time scales. *Contributions to Mineralogy and Petrology*, **164**, 977-986.
Spear, F.S., Parrish, R.R., 1996. Petrology and cooling rates of the Valhalla Complex, British Columbia, Canada. *Journal of Petrology*, **37**, 733-765.
Stevens, G., Clemens, J. D., Droop, G. T. R., 1997. Melt production during granulite-facies anatexis: experimental data from "primitive" metasedimentary protoliths. *Contributions to Mineralogy and Petrology,* **128**, 352-370.
Tajcmanová, L., Connolly, J.A.D., Cesare, B., 2009. A thermodynamic model for titanium and ferric iron solution in biotite. *Journal of Metamorphic Geology*, **27**, 153-164.

Thompson, A. B., 1982. Dehydration melting of pelitic rocks and the generation of H_2O-undersaturated granitic liquids. *American Journal of Science,* **282**, 1567-1595.

Thöni, M., 2003. Sm-Nd isotope systematics in garnet from different lithologies (Eastern Alps): age results, and an evaluation of potential problems for garnet Sm-Nd chronometry. *Chemical Geology*, **185**, 255-281.

Tirone, M., Ganguly, J., Dohmen, R., Langenhorst, F., Hervig, R., Becker, H.-W., 2005. Rare earth diffusion kinetics in garnet: experimental studies and applications. *Geochimica et Cosmochmica Acta*, **69**, 2385-2398.

Tomascak, P.B., Krogstad, E.J., Walker, R.J., 1996. U–Pb monazite geochronology of granitic rocks from Maine; implications for late Paleozoic tectonics in the Northern Appalachians. *Journal of Geology*, **104**, 185–195.

Vielzeuf, D., Holloway, J. R., 1988. Experimental determination of the fluid-absent melting relations in the pelitic system Consequences for crustal differentiation. *Contributions to Mineralogy and Petrology,* **98**, 257-276.

Vielzeuf, D. & Schmidt, M. W., 2001. Melting relations in hydrous systems revisited: application to metapelites, metagreywackes and metabasalts. *Contributions to Mineralogy and Petrology,* **141**, 251-267.

Viete, D.R., Hermann, J., Lister, G.S., Stenhouse, I.R., 2011. The nature and origin of the Barrovian metamorphism, Scotland: diffusion length scales in garnet and inferred thermal time scales. *Journal of the Geological Society, London*, **168**, 115-132.

Wall, C.J., Scoates, J.S., Friedman, R.M., Meurer, W.P., 2012. Age of the Stillwater Complex. *Mineralogical Magazine*, **76.6**, 2506.

Wall, C.J., Scoates, J.S., Weis, D., 2016. Zircon from the Anorthosite zone II of the Stillwater Complex as a U-Pb geochronological reference material for Archean rocks. *Chemical Geology*, DOI: 10.1016/j.chemgeo.2016.04.027.

Wall, C.J., Scoates, J.S., 2016. High-precision U-Pb zircon-baddeleyite dating of the J-M Reef platinum group element deposit in the Stillwater Complex, Montana (USA). *Economic Geology*, **111**, 771-782.

Wendt, I, Carl, C., 1991. The statistical distribution of the mean squared weighted deviation. *Chemical Geology*, **86**, 275-285.

White, R.W., Powell, R., Holland, T.J.B., Worley, B.A., 2000. The effect of TiO_2 and Fe_2O_3 on metapelitic assemblages at greenschist and amphibolite facies conditions: mineral equilibria calculations in the system K_2O-FeO-MgO-Al_2O_3-SiO_2-H_2O-TiO_2-Fe_2O_3. *Journal of Metamorphic Petrology*, **18**, 497-511.

White, R.W., Powell, R., 2002. Melt loss and the preservation of granulite facies mineral assemblages. *Journal of Metamorphic Geology*, **20**, 621-632.

White, R.W., Powell, R., 2011. On the interpretation of retrograde reaction textures in granulite facies rocks. *Journal of Metamorphic Geology,* **29**, 131-149.

White, R., Pomroy, N.R., Powell, R., 2005. An *in-situ* metatexite-diatexite transition in upper amphibolites facies rocks from Broken Hill, Australia. *Journal of Metamorphic Geology,* **23**, 579-602.

White, R.W., Powell, R., Holland, T.J.B., 2001. Calculation of partial melting equilibria in the system Na_2O-CaO-K_2O-FeO-MgO-Al_2O_3-SiO_2-H_2O (NCKFMASH). *Journal of Metamorphic Geology*, **19**, 139-153.

White, R.W., Powell, R., Holland, T.J.B., 2007. Progress relating to calculation of partial melting equilibria for metapelites. *Journal of Metamorphic Geology*, **25**, 511-527.

Whitney, D. L., Evans, B.W., 2010. Abbreviations for names of rock-forming minerals. *American Mineralogist*, **95**, 185-187.
Will, C.N., 2013. Temperature and pressure conditions of Archean amphibolite-granulite facies metamorphic xenoliths from the eastern Beartooth Mountains, Montana and Wyoming, USA. M.S. Thesis. Louisiana State University.
Williams, M.J., Dumond, G., Mahan, K., Regan, S., Holland, M., 2014. Garnet-forming reactions in felsic orthogneiss: implications for densification and strengthening of the lower continental crust. *Earth and Planetary Science Letters*, **405**, 207-219
Wooden, J.L., Mueller, P.A., Mogk, D.W., Bowes, D.R., 1988. A review of the geochemistry and geochronology of Archean rocks of the Beartooth Mountains, Montana and Wyoming. Special Publication – State of Montana Bureau of Mines and Geology, 23-42.
Yakymchuk, C., Brown, M., 2014a. Behaviour of zircon and monazite during open system melting. *Journal of the Geological Society, London,* **171**, 465-479.
Yakymchuk, C. Brown, M., 2014b. Consequences of open-system melting in tectonics. *Journal of the Geological Society, London*, **171**, 21-40.
Young, D.J., Kylander-Clark, A.R.C., 2015. Does continental crust transform during eclogite facies metamorphism? *Journal of Metamorphic Geology*, **33**, 331-357.
Zeng, L., Gao, L.-E., Dong, C., Tang, S., 2012. High-pressure melting of metapelite and the formation of Ca-rich granitic melts in Namche Barwa Massif, southern Tibet. *Gondwana Research*, **21**, 138-151.
Zhou, B., Hensen, B.J., 1995. Inherited Sm/Nd isotope components preserved in monazite inclusions within garnets in leucogneiss from East Antarctica and implications for closure temperature studies. *Chemical Geology*, **121**, 317-326.

3.13 FIGURES

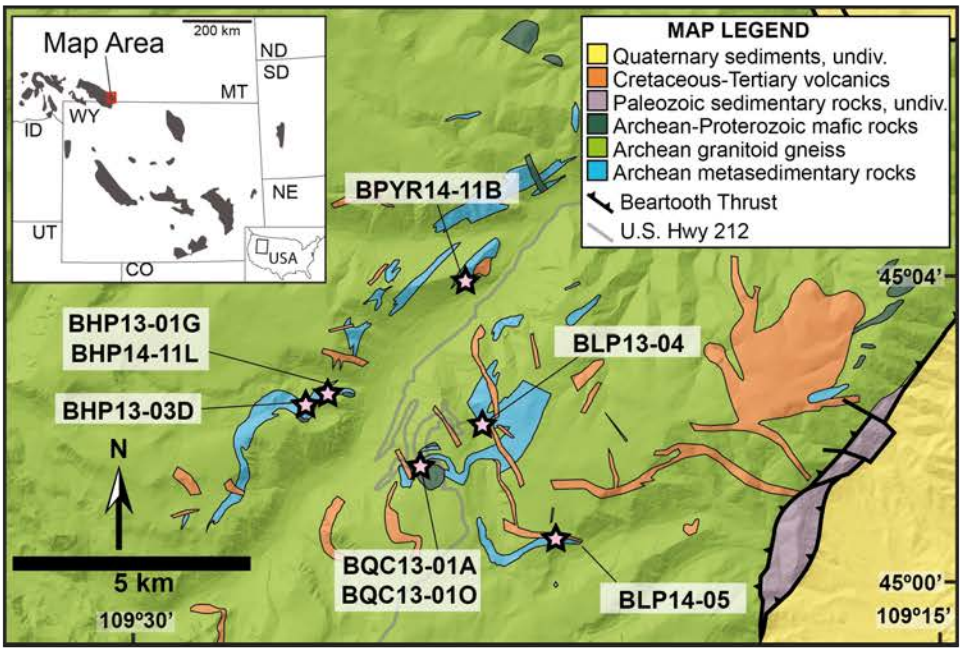

Figure 3.1: Geologic map (underlain by digital elevation model) of the eastern Beartooth Mountains modified after Lopez (2001). Inset map shows outcroppings of the Archean rocks (dark grey) in the western U.S. The map area of the eastern Beartooths is outlined in red in the inset. Inset modified after Foster et al. (2012) and Mueller and Frost (2006). Stars indicate sample locations.

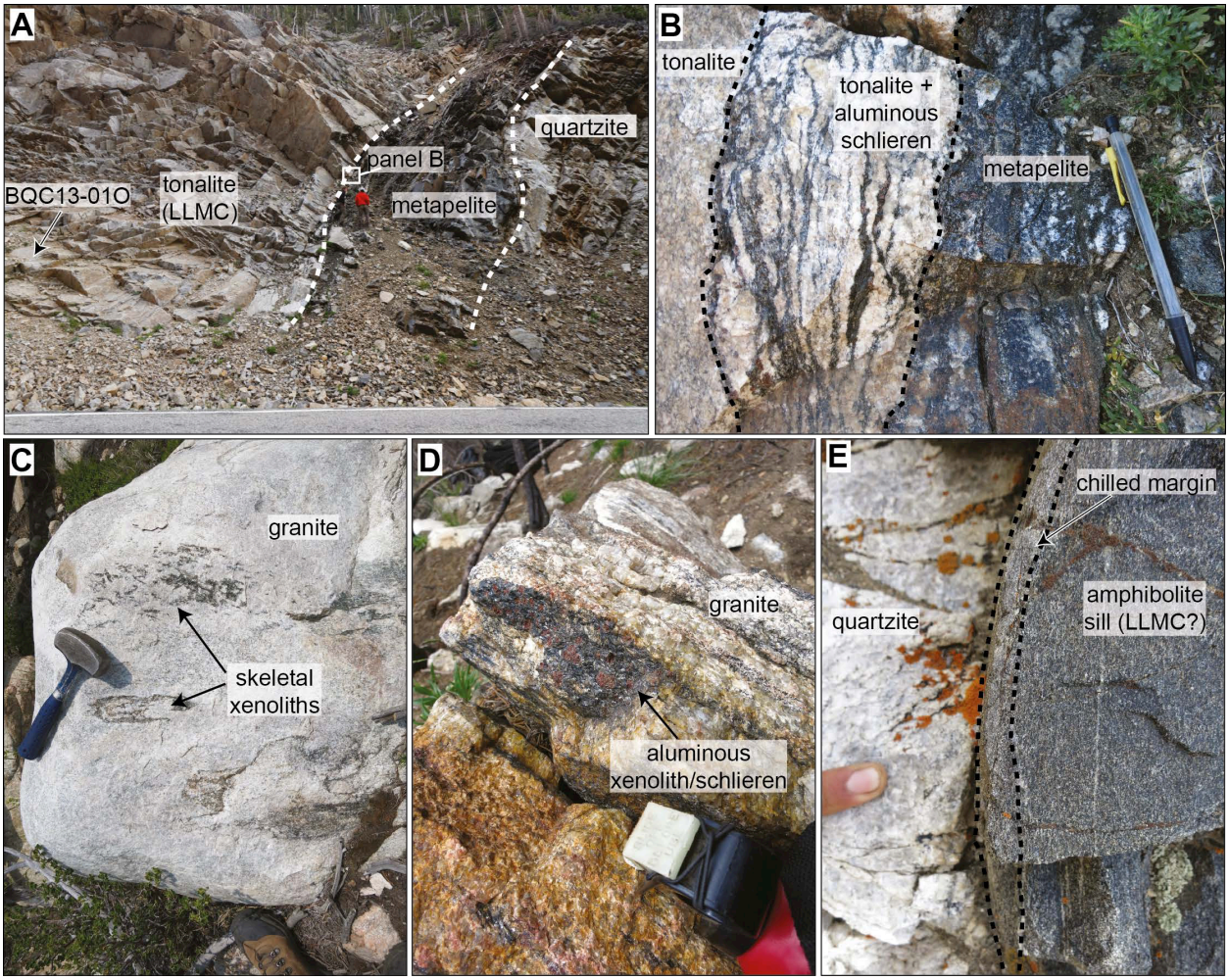

Figure 3.2: Field photographs displaying evidence for intrusive association between granitoids and metasediments (see discussion in section 3). a) Intrusive contact between LLMC tonalite (sample BQC13-01O) and Beartooth metapelites and quartzite. Location of sample BQC13-01O is indicated. b) Aluminous schlieren (biotite + garnet) at contact between LLMC tonalite and metapelite (area indicated in panel a). c) Skeletal aluminous xenoliths/schlieren (biotite + garnet ± sillimanite) in granitoid. d) Aluminous xenolith (biotite + garnet) entrained in granitoid. e) Fine-grained margin in amphibolite sill near contact with metasediments.

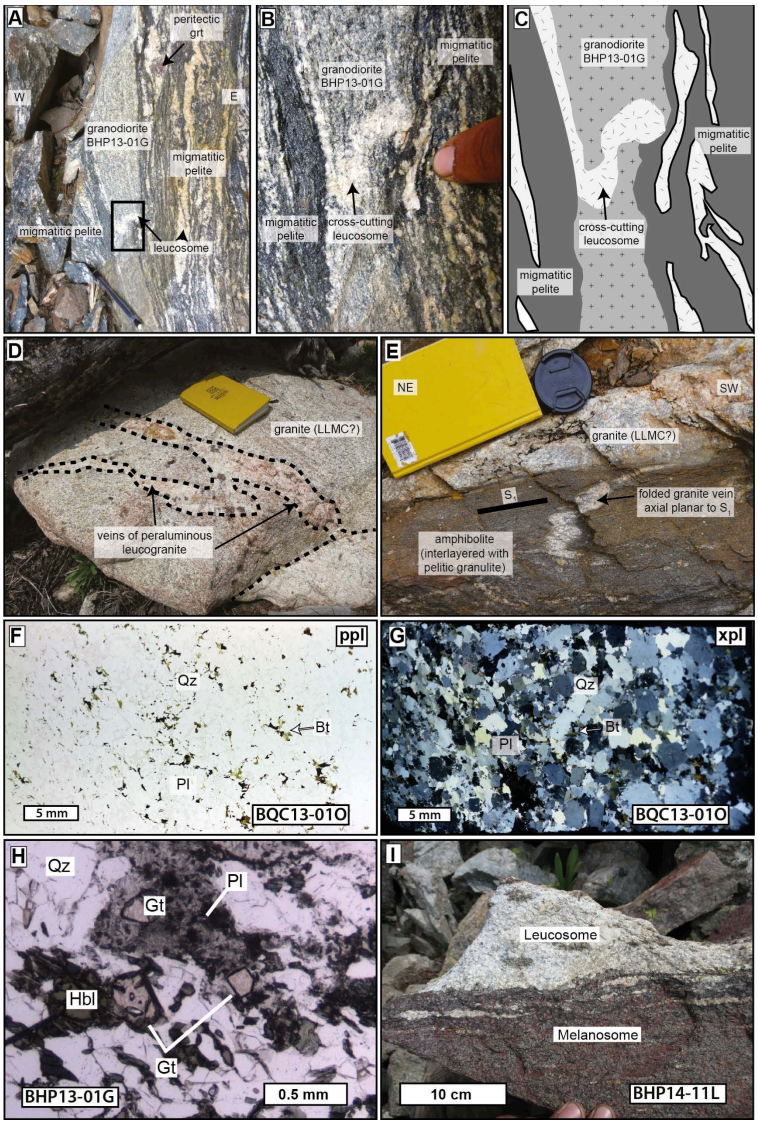

Figure 3.3: Field photographs displaying evidence for granulite-facies metamorphism (and associated partial melting) postdating granitoid (LLMC?) emplacement (see discussion in section 3) and sample photographs of granitoid lithologies. a-c) Granodiorite sill in migmatitic pelite cross-cut by leucosome. Black box in a) highlights field of view in b). c) Schematic diagram of relationship between granodiorite, migmatitic pelite, and leucosome. d) Boulder of granitoid injected with veins of peraluminous, garnet-bearing leucogranite, presumably derived from partial melting of adjacent pelitic rocks. e) Vein of granitoid intruding amphibolite that is interlayered with pelitic granulite. Vein is folded axial planar to dominant foliation in amphibolite, parallel to granulite-facies foliation in pelitic granulite. f) Full section photograph of sample BQC13-01O (LLMC tonalite) in plane polarized light. g) Full section photograph of sample BQC13-01O in cross-polarized light. h) Photomicrograph of granodiorite sill sample BHP13-01G, showing the presence of rare garnet crystals associated with hornblende/plagioclase-rich region. i) Field photograph of leucosome derived partial melting of metasediment and the residual garnet-rich melanosome (sample BHP14-11L). Mineral abbreviations after Whitney and Evans (2010).

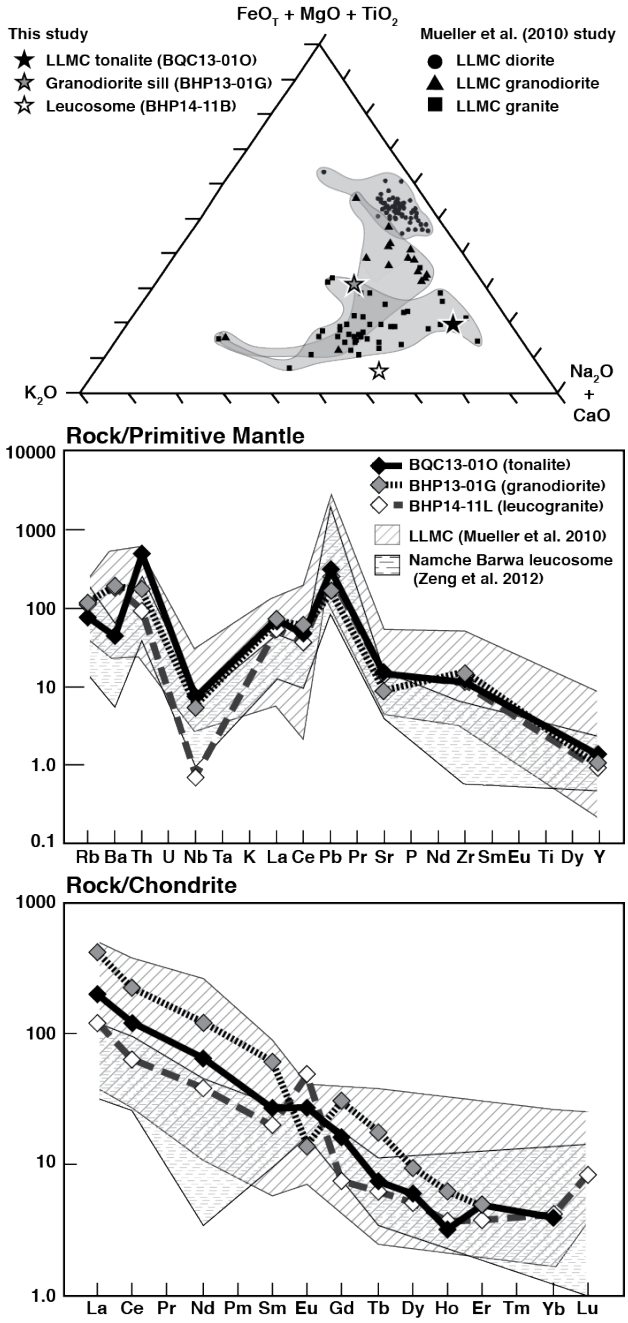

Figure 3.4: a) FeO_T + MgO + TiO_2) – (K_2O) – (Na_2O + CaO) ternary diagram displaying the compositional variability of LLMC granitoids and associated lithologies. Smaller, black symbols are data from Mueller et al. (2010). Larger, colored stars are data from this study. Normalized trace (b) and REE (c) distribution diagrams (after Sun and McDonough, 1989) of the LLMC granitoids used in this study and in Mueller et al. (2010). Example of leucosome elemental concentrations from Namche Barwa (Zeng et al. 2012) for reference.

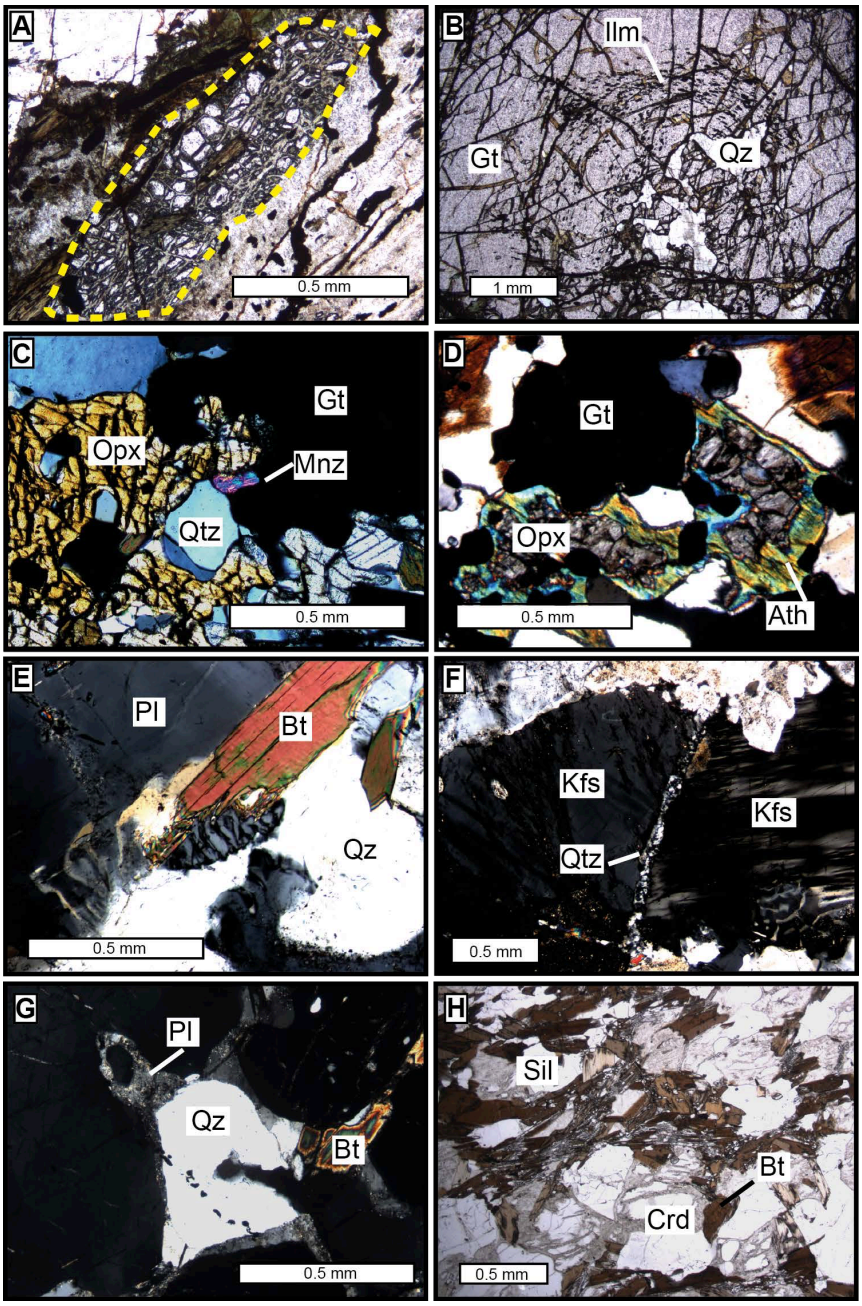

Figure 3.5: Photomicrographs displaying various petrographic observations in Beartooth metasediments. a) Highly fractured garnet crystal (outlined by yellow dashed line) along dominant deformational fabric in sample BHP13-03D, potentially recording early growth stage (see discussion in section 3.6.1). b) Ilmenite inclusions in garnet oriented subparallel to garnet growth faces in sample BHP13-03D. c) Monazite inclusion in garnet in sample BQC13-01A. d) Anthophyllite-gedrite rims around orthopyroxene in sample BLP13-04. e) Late-stage granophyre (center) adjacent to biotite grain in sample BLP14-05. f) Fine-grained polycrystalline quartz in between potassium feldspar grains in sample BLP14-05. g) Plagioclase infilling triple junction between quartz and garnet crystals in sample BPYR14-11B. h) Matrix assemblage in sample BPYR14-11B, including pinnitized cordierite porphyroblasts. All mineral abbreviations after Whitney and Evans (2010).

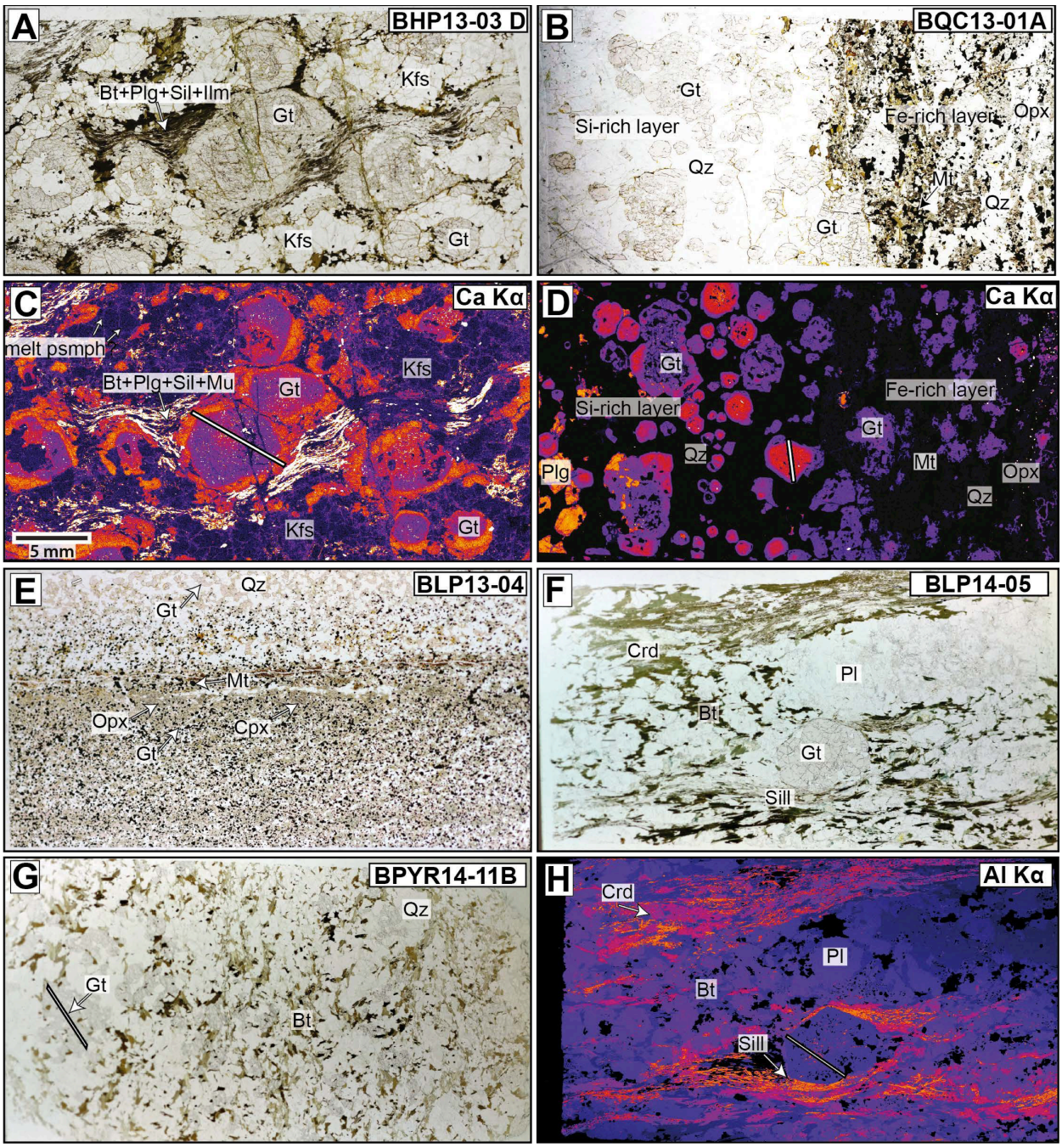

Figure 3.6: a), b), e), f), and g) Full thin section photographs of samples BHP13-03D, BQC13-01A, BLP13-04, BLP14-05, and BPYR14-11B, respectively. c), d), and h) False color X-ray maps for samples BHP13-03D (Ca), BQC13-01A (Ca), and BLP14-05 (Al) respectively. Warm colors represent high Ca (or Al) concentrations. Electron microprobe and LA-ICP-MS garnet traverse positions are shown by the white lines (with black outlines) in c), d), g), and h). Note the Si-rich and Fe-rich layers in banded ironstone samples BQC13-01A (left and right of b, respectively) and BLP13-04 (top and bottom, of e respectively). All mineral abbreviations after Whitney and Evans (2010).

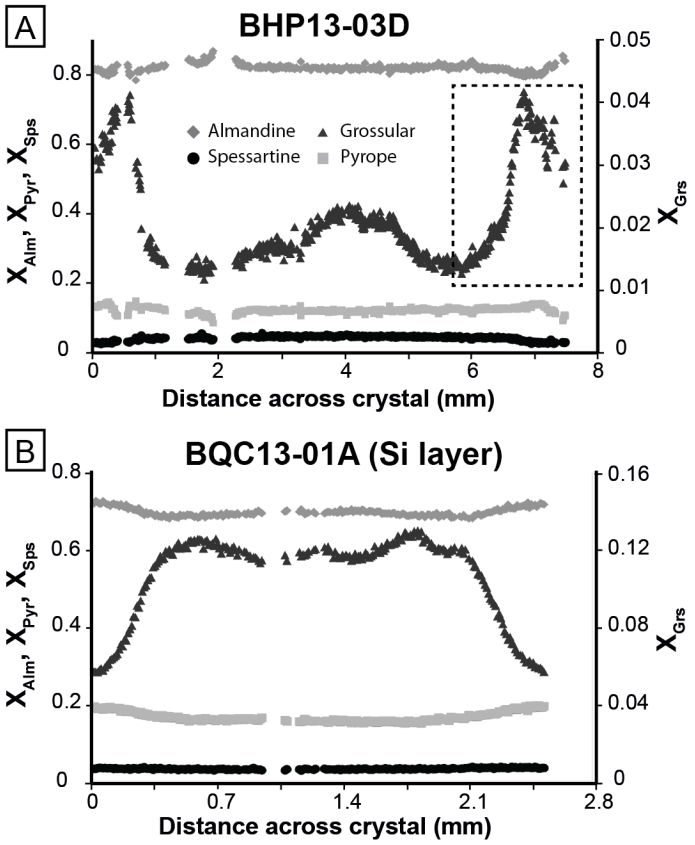

Figure 3.7: Representative rim to core to rim traverse of garnet major element composition for a) sample BHP13-03D and b) the Si-rich layer of sample BQC13-01A. The dashed rectangle highlights the portion of the crystal that is being referred to in Figure 3.12.

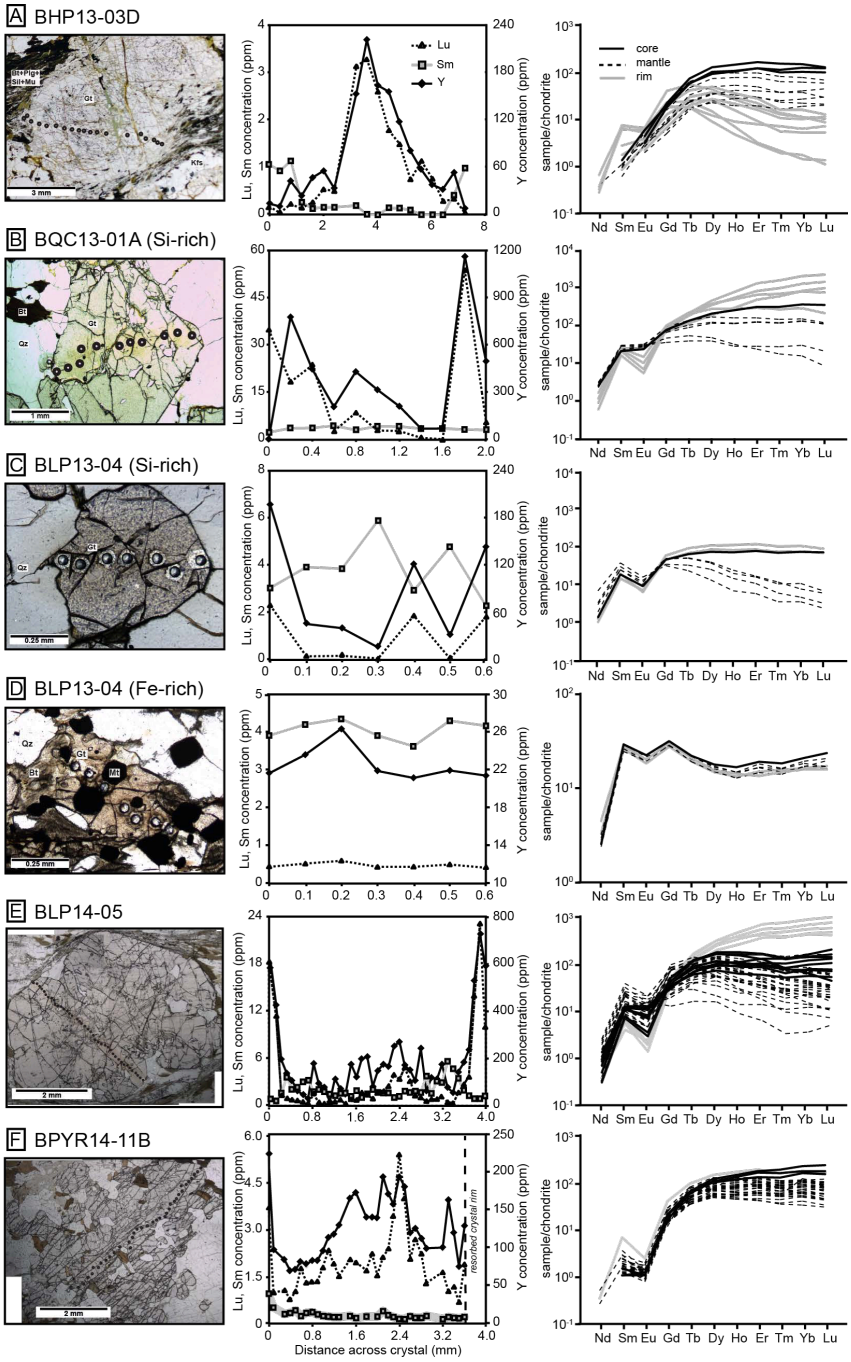

Figure 3.8: Representative rim to core to rim traverses for measurement of garnet trace element concentrations for samples a) BHP13-03D, b) the Si-rich layer of BQC13-01A, c) the Si-rich layer of BLP13-04, d) the Fe-rich layer of BLP13-04, e) BLP14-05, and f) BPYR14-11B. Photomicrographs of analyzed garnets (left column). Lu, Sm, and Y concentrations across garnet crystals (center column). Chondrite-normalized REE patterns (McDonough and Sun, 1995; right column).

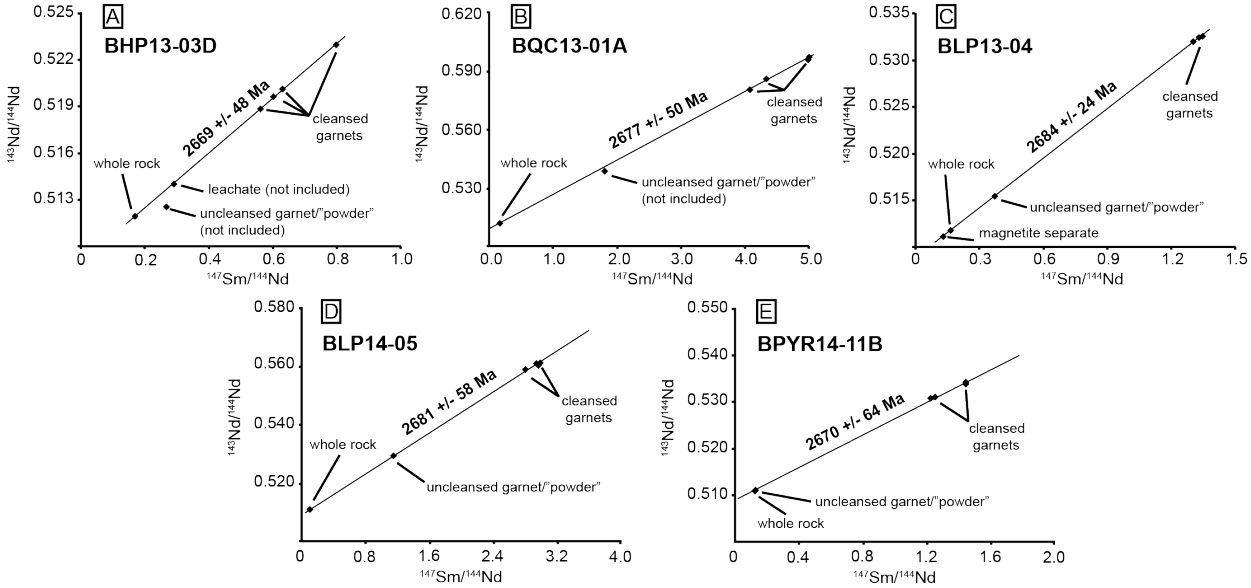

Figure 3.9: Multi-point garnet Sm-Nd isochron diagrams with age and error (2σ) shown. Note that the leachate point in sample BHP13-03D and the uncleansed garnet separate points in samples BHP13-03D and BQC13-01A do not fall on the line and are thus not used in any age calculations.

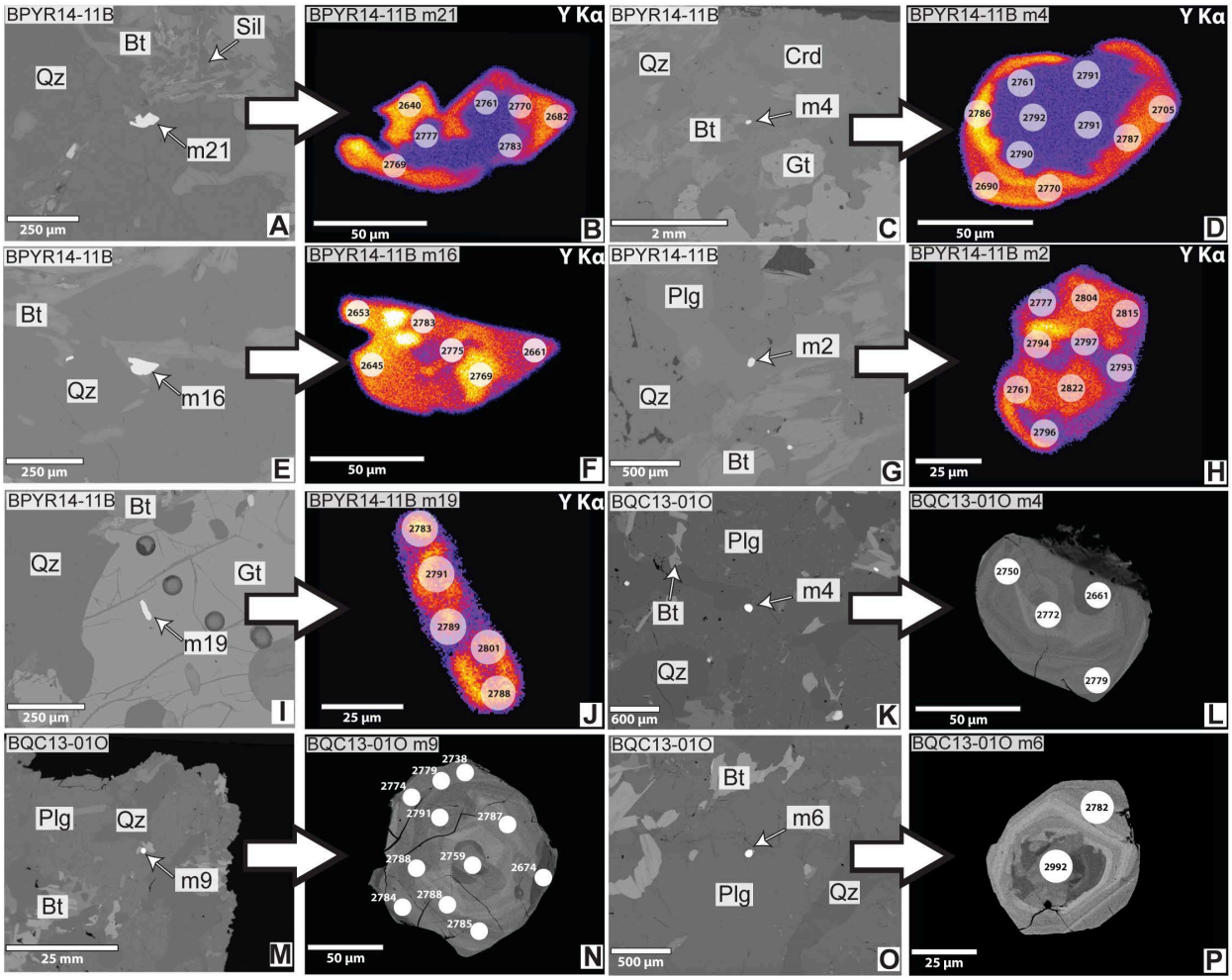

Figure 3.10: Backscatter electron (BSE) images of monazite grains showing textural locations and corresponding false color Y X-ray maps and/or BSE images of individual grains from samples BPYR14-11B (melanosome of pelitic diatexite; a-j) and BQC13-01O (LLMC tonalite; k-p).

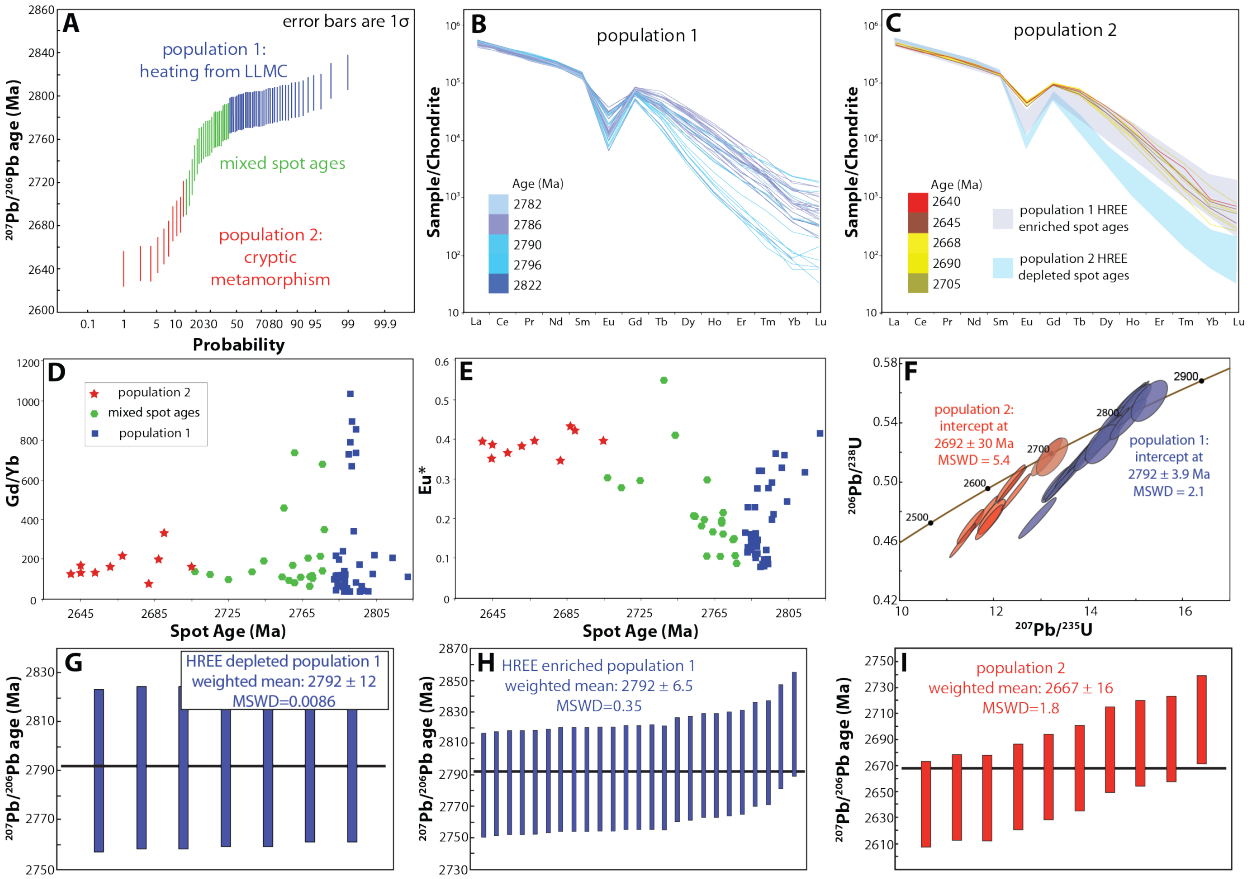

Figure 3.11: U-Pb and trace element monazite data from sample BPYR14-11B. a) Linearized probability plot of U-Pb monazite spot ages. b) REE plot of monazite population 1. Mixed ages (as shown in panel A) are excluded. c) REE plot of monazite population 2, overlain on the REE profiles of population 1 (represented by shaded areas). d) Age vs. Gd/Yb for all spot analyses. e) Age vs. Eu* for all spot analyses. Symbols are the same as in panel D. f) Concordia diagram of population 1 and 2 spot analyses. Mixed ages are excluded. g) Weighted average plot of $^{207}Pb/^{206}Pb$ spot ages from HREE depleted subgroup of population 1. h) Weighted average plot of $^{207}Pb/^{206}Pb$ spot ages from HREE enriched subgroup of population 1. i) Weighted average plot of $^{207}Pb/^{206}Pb$ spot ages from population 2.

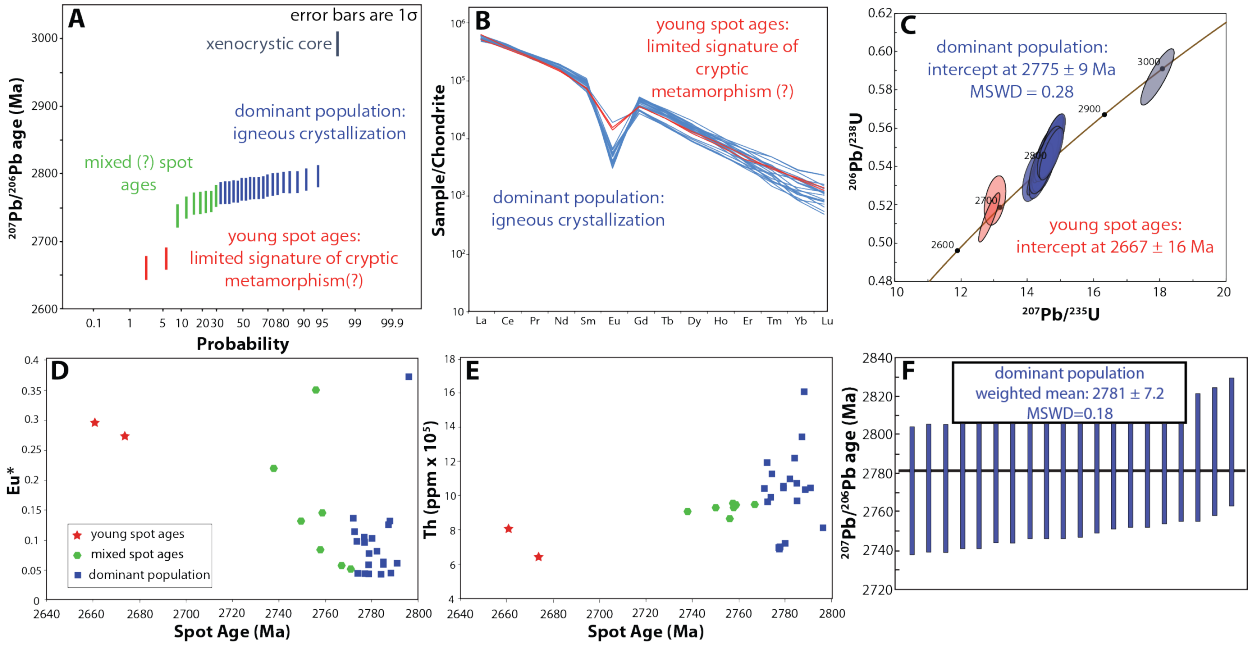

Figure 3.12: U-Pb and trace element monazite data from sample BQC13-01O. a) Linearized probability plot of U-Pb monazite spot ages. b) REE plot with mixed ages (as shown in panel A) excluded. c) Concordia plot with mixed ages excluded. d) Age vs. Eu* plot for all spot analyses. e) Age vs. Th (ppm) plot for all spot analyses. f) Weighted average plot of $^{207}Pb/^{206}Pb$ spot ages for the dominant population.

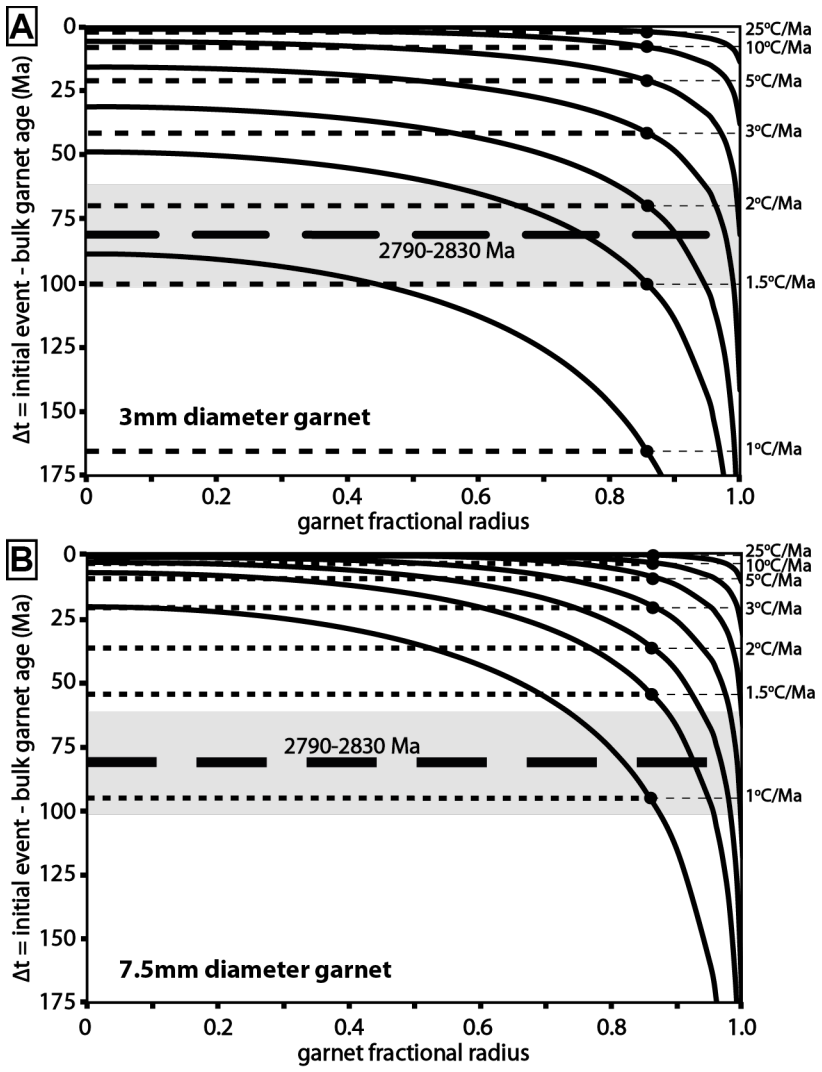

Figure 3.13: Age resetting profiles (solid lines) and weighted mean age resetting for the entire crystal (thin dashed lines) as a function of initial cooling rate (following the approach of Ganguly and Tirone (1999, 2001)) from a peak temperature of 800°C and E = 254 kJ/mol for a crystal of diameter a) 3 mm and b) 7.5 mm. The mean degree of age resetting (in Ma) in a garnet crystal, for a given initial cooling rate, corresponds to the age resetting profile to which it is connected by a large dot. Note that to reset the age from 2790-2830 Ma (LLMC emplacement) to the 2σ *maximum* age of 2718 Ma for sample BHP13-03D, would require initial cooling rates of ≤ 2°C/Ma and < 1.5°C/Ma for crystal sizes of 3 and 7.5 mm, respectively.

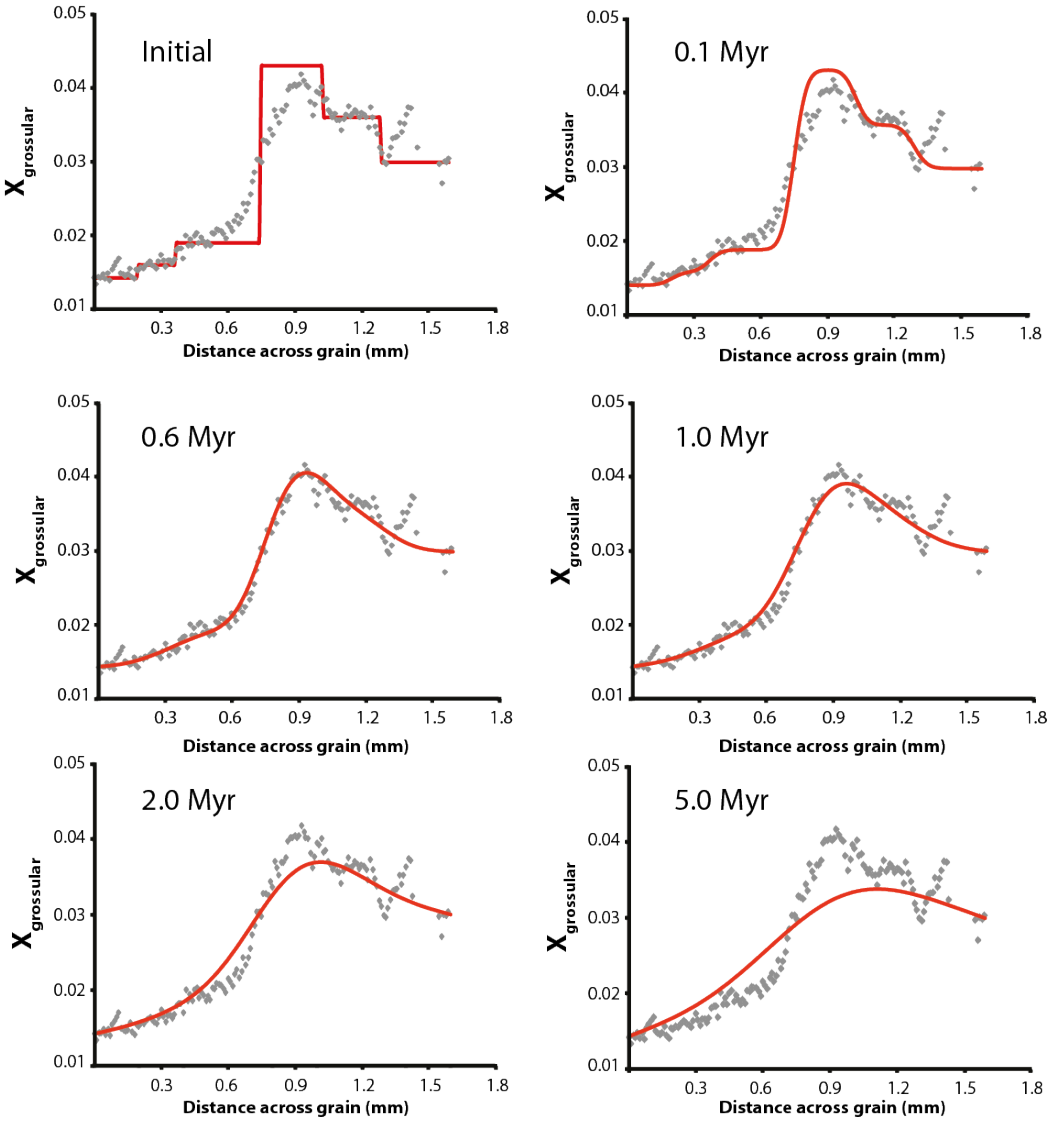

Figure 3.14: Results of garnet major element diffusion modeling for sample BHP13-03D. Gray symbols represent microprobe analyses sampled in a traverse from the crystal core towards the rim (rim on the right of diagrams). Red line in panel 'a' represents the assumed initial zoning. Red lines in other panels represent zoning profiles after diffusive modification at 768°C for increasing durations, calculated using diffusivity data from Chakraborty and Ganguly (1992). Characteristic temperature 768 ˚C was derived from the expression $T_{char} = 0.97\ T_{peak}$ (Chakraborty and Ganguly, 1990, 1992)), where T_{peak} for this figure is 800°C.

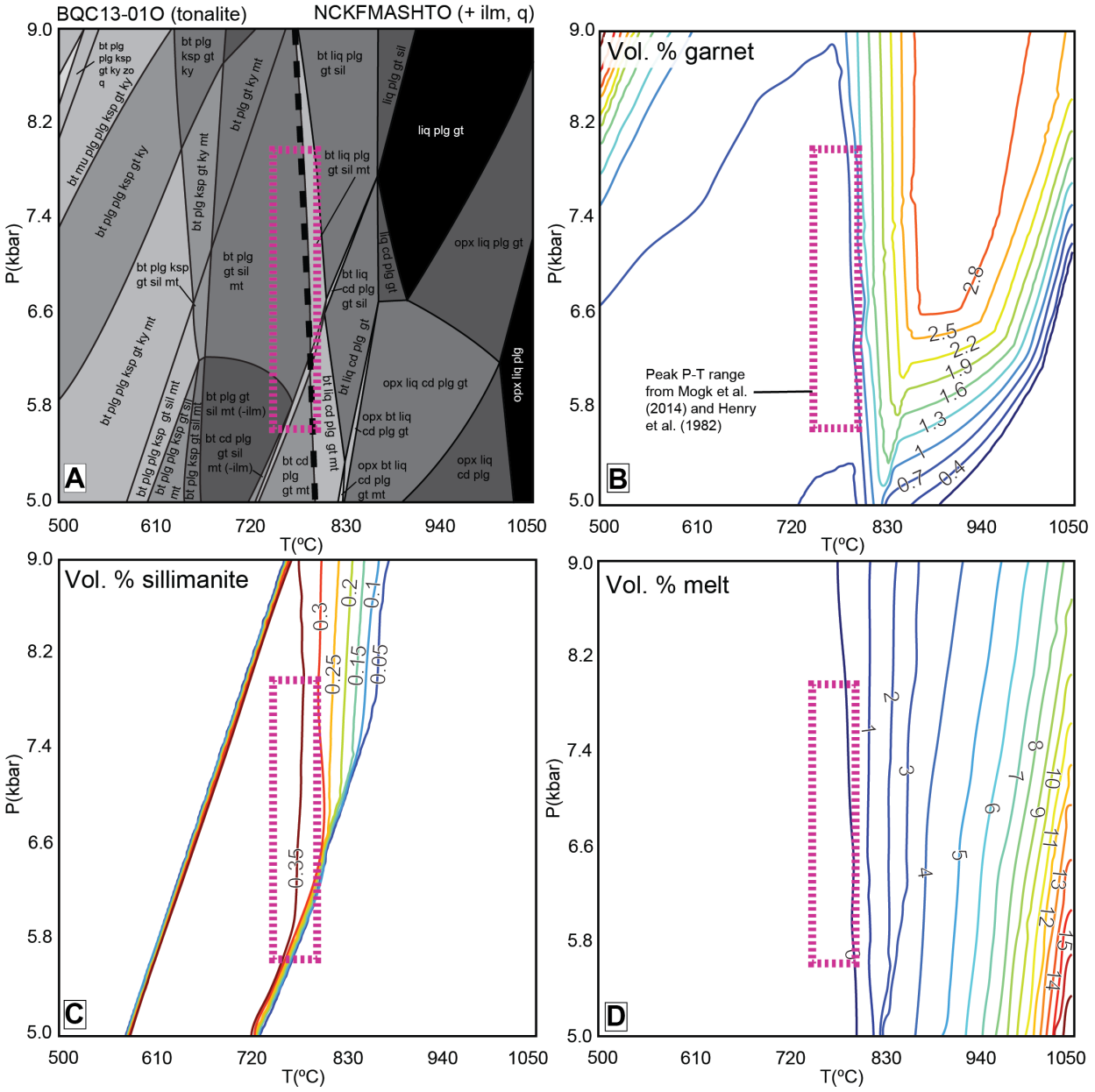

Figure 3.15: Phase equilibria modeling results for LLMC tonalite sample BQC13-01O. a) *P–T* pseudosection for BQC13-01O. Pink, dash-outlined box shows peak *P–T* range estimated from Mogk et al. (2014) and Henry et al. (1982). [bt – biotite, ky – kyanite, plg – plagioclase, gt – garnet, ksp – potassium feldspar, zo – zoisite, q – quartz, mt – magnetite, sil – sillimanite, cd, cordierite, opx – orthopyroxene, liq – melt, ilm – ilmenite] b) Diagram contoured for predicted volume % garnet. c) Diagram contoured for predicted volume % sillimanite. d) Diagram contoured for predicted volume % melt. Note the predicted minor occurrences of garnet + sillimanite + melt at the peak *P–T* conditions (see discussion in section 3.9 of text).

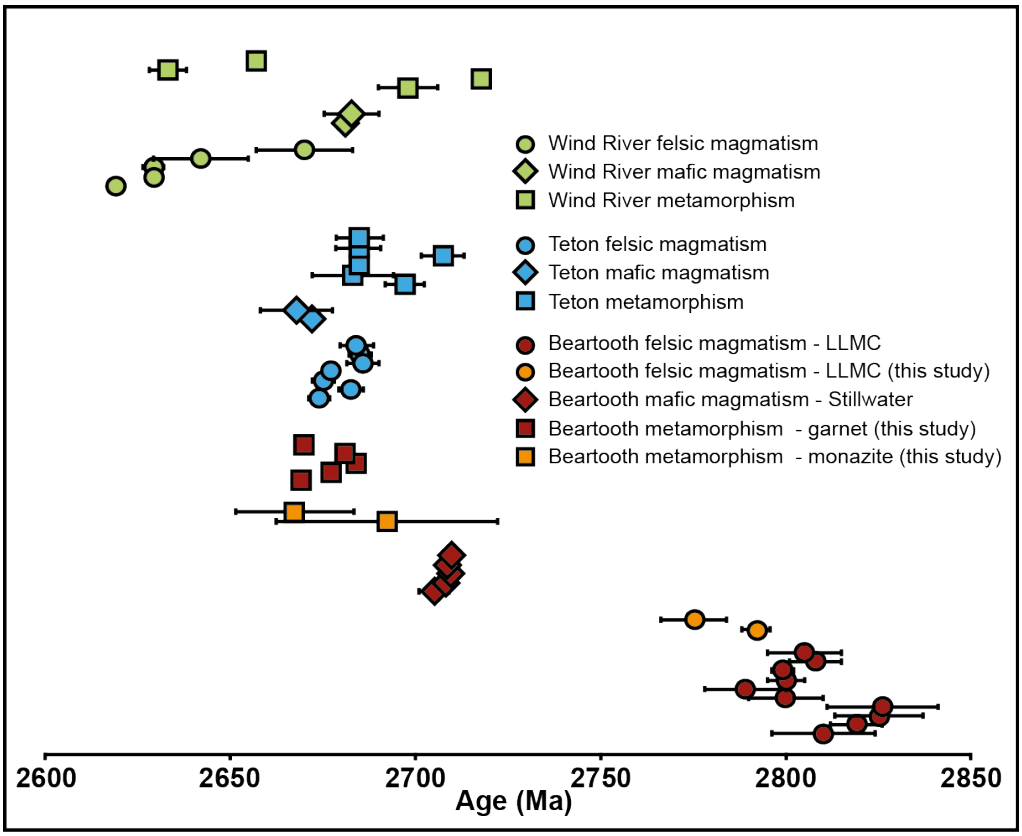

Figure 3.16: Compilation of published magmatic and metamorphic ages in the Teton, Wind River, and Beartooth ranges. References for ages in the compilation are provided in the supplement (Table B6).

Table 3.1: Sm-Nd isotopic data for samples BHP13-03D, BQC13-01A, and BLP13-04. a) Isotopic data for garnet. Ages shown are 2-point gt-WR ages for BHP13-03D and BQC13-01A, and 4-point gt-magnetite-uncleansed gt/"powder"-WR age for BLP13-04. b) Multi-point garnet ages (all garnet fractions and WR, uncleansed garnet and magnetite where applicable). Associated multi-point isochron diagrams shown in Figure 3.8.

	LLMC Tonalite	Granodiorite sill	Leucosome
Sample	**BQC13-01O**	**BHP13-01G**	**BHP14-11L**
SiO_2	71.98	67.89	75.31
TiO_2	0.17	0.38	0.03
Al_2O_3	15.71	15.12	14.48
Fe_2O_3*	0.29	1.08	0.04
FeO	1.17	2.35	0.51
MnO	0.02	0.06	0.02
MgO	0.59	1.01	0.17
CaO	2.70	2.92	1.47
Na_2O	5.12	3.41	4.01
K_2O	1.33	3.90	3.12
P_2O_5	0.04	0.10	0.06
LOI	0.68	1.43	0.57
Total	**99.80**	**99.65**	**99.79**
Fe_2O_3T	1.59	3.69	0.61
FeOT	1.43	3.32	0.55
Rb	46.7	74.9	68.9
Sr	307	192	294
Y	5.6	4.3	3.8
Zr	121	162	124
V	19	41	6
Ni	16	10	18
Cr	29	11	13
Nb	5.0	4.0	<0.5
Ga	26.4	19.3	16.0
Cu	13	11	7
Zn	32	32	17
Co	1	5	<1
Ba	303	1277	1285
La	48	47	36
Ce	79	100	59
U	0.9	<0.5	0.5
Th	39.5	13.9	7.9
Sc	1	3	<1
Pb	21	11	25

* Fe_2O_3 analyzed by titration

Table 3.2a. Isotopic data

Sample ID	Mass (mg)	Sm (µg/g)	Nd (µg/g)	ng Nd loaded	$^{147}Sm/^{144}Nd$	$^{143}Nd/^{144}Nd$	± 2 S.E. (abs)	Age (Ma)	± 2σ	MSWD
BHP13-03D WR	2.14	4.27	15.2	16	0.1699	0.5119456	0.0000094			
BHP13-03D uncleansed gt	10.7	1.10	2.49	13	0.2682	0.5125274	0.0000067			
BHP13-03D 60HF b gt	51.7	0.935	0.71	29	0.7978	0.5229668	0.0000056	2660.8	4.2	N/A
BHP13-03D 90HF gt	60.6	0.990	1.07	52	0.5621	0.5188518	0.0000058	2669.3	6.6	N/A
BHP13-03D 90HF b gt	54.1	1.07	1.07	46	0.6019	0.5196065	0.0000037	2687.6	6.0	N/A
BHP13-03D 120HF b gt	39.7	1.04	0.99	32	0.6315	0.5201370	0.0000046	2689.9	5.6	N/A
BHP13-03D 120HF b leachate	2.26	0.815	1.69	3.1	0.2915	0.5140208	0.0000092			
BQC13-01A WR	2.14	4.91	19.2	29	0.155	0.5116249	0.0000048			
BQC13-01A uncleansed gt	10.8	2.41	0.823	7.1	1.77	0.538893	0.000018			
BQC13-01A 15HF gt	56.2	1.40	0.170	7.8	4.98	0.5970414	0.0000089	2680.6	0.83	N/A
BQC13-01A 60HF gt	75.7	2.01	0.282	17	4.31	0.5857972	0.0000071	2703.8	0.90	N/A
BQC13-01A 60HF b gt	42.8	2.67	0.398	14	4.05	0.5804752	0.0000069	2676.1	0.92	N/A
BQC13-01A 90HF gt	31.1	4.61	0.561	14	4.97	0.595924	0.000011	2651.5	0.83	N/A
BLP13-04 WR	2.30	1.36	4.98	9.4	0.1646	0.5117433	0.0000064			
BLP13-04 magnetite	2.17	0.515	2.38	4.2	0.1311	0.511142	0.000011			
BLP13-04 uncleansed gt	6.70	2.13	3.46	19	0.3727	0.5154146	0.0000063			
BLP13-04 30HF gt	33.8	4.60	2.09	58	1.330	0.5323897	0.0000068	2686.4	6.2	2.2
BLP13-04 60HF gt	41.8	4.29	1.93	64	1.346	0.5325284	0.0000060	2668.4	6.7	2.6
BLP13-04 90HF gt	34.5	4.11	1.91	53	1.302	0.5319932	0.0000051	2698	13	9.4
BLP14-05 WR	1.96	0.609	3.45	5.4	0.1068	0.5106767	0.0000155			
BLP14-05 uncleansed gt	10.4	1.42	0.750	6.3	1.147	0.5292651	0.0000091			
BLP14-05 30HF gt	30.3	1.28	0.263	6.4	2.949	0.5604419	0.0000117	2654.5	1.2	N/A
BLP14-05 45HF gt	29.7	1.30	0.265	6.3	2.968	0.5612311	0.0000119	2678.3	1.2	N/A
BLP14-05 60HF gt	33.9	1.22	0.265	7.2	2.792	0.5587144	0.0000111	2711.0	1.3	N/A
BLP14-05 90HF gt	29.2	1.22	0.252	5.9	2.926	0.5609263	0.0000144	2701.9	1.3	N/A
BPYR14-11B WR	2.14	5.09	25.3	43	0.1218	0.510921	0.0000064			
BPYR14-11B uncleansed gt	10.7	3.79	18.2	160	0.1261	0.511018	0.0000028			
BPYR14-11B 30HF gt	25.7	0.197	0.083	1.7	1.441	0.533807	0.0000198	2630.3	2.8	N/A
BPYR14-11B 45HF gt	32.7	0.215	0.090	2.4	1.441	0.53404	0.000015	2657.3	2.3	N/A
BPYR14-11B 60HF gt	24.3	0.220	0.109	2.1	1.220	0.530653	0.0000146	2722.2	2.7	N/A
BPYR14-11B 90HF gt	19.7	0.273	0.132	2.1	1.251	0.530904	0.0000174	2682.8	2.9	N/A

Table 3.2b. Multi-point ages

Sample ID	Age (Ma)	± 2σ	MSWD	*n*
BHP13-0D	2669	48	61	5
BQC13-01A	2677	50	3285	5
BLP13-04	2684	24	160	6
BLP14-05	2681	58	2373	6
BPYR14-11B	2670	64	952	6

Table 3.2: Major and trace element whole rock analyses for Beartooth metasediments, LLMC granitoids, and leucosome.

Peak temperature	Characteristic Temperature	Best fit timescale (Ma)
750	719	2.8
775	744	1.1
800	**768**	**0.6**
825	792	0.3
850	816	0.2

Table 3.3: Best-fit durations (in Ma) for garnet major element diffusion modeling for various peak temperatures in model runs.

Chapter 4. Rapid high-temperature decompression recorded by Archean granulites in the northern Wyoming Province: insights from petrologic modelling

V.E. Guevara[1], M.J. Caddick[1], and B. Dragovic[1,2]

[1]*Department of Geosciences, Virginia Polytechnic Institute and State University, Blacksburg, VA 24061, USA*
[2]*Department of Geosciences, Boise State University, 1910 University Dr. Boise, ID 83725*

Revised manuscript resubmitted April 2017 to *Journal of Metamorphic Geology*

4.1 ABSTRACT

This study places new constraints on the pressure-temperature (*P–T*) path and duration of high-temperature (HT*)* metamorphism recorded by Archean granulite-facies metasedimentary rocks from the northern Wyoming Province in the eastern Beartooth Mountains, MT and WY, USA. These rocks exist as m- to km-scale xenoliths within a c. 2.8 Ga calc-alkaline granitoid batholith. Different interpretations of the timing of HT metamorphism relative to batholith intrusion in previous works has led to ambiguity over the mechanism by which these rocks were heated (i.e. batholith intrusion vs. a later, cryptic event). The *P–T* path recorded by these rocks and the duration of this path may be indicative of the heating mechanism but are not currently well-constrained. Here we combine phase equilibria thermobarometry and diffusion modelling of major element zonation in garnet in order to constrain the *P–T* path of HT metamorphism and the durations of different parts of this path. We show that these rocks record a tight, clockwise *P–T* path characterized by near-isobaric heating at ~6.5-7 kbar to ~770-800 °C, HT decompression to ~6 kbar, 780-800 °C, followed by limited decompression while cooling. Diffusion modelling of major element zonation in garnet suggests that HT decompression was brief (likely <1 Ma), and that cooling rates following this decompression were on the order of 10-100 °C/Ma. Substantial changes in apparent thermal gradient along this *P–T* path indicate that the rocks record a significant but short-lived thermal anomaly that occurred in the Wyoming mid-crust in the Late Archean.

4.2 INTRODUCTION

Granulite terranes are common features of Earth's stable Archean cratons, suggesting that crustal heating and high-temperature (>750 °C, HT) metamorphism involved in granulite genesis may be required to stabilize continental crust. HT metamorphism is a result of plate tectonic processes on modern Earth, with the depths, temperatures, paths, and durations recorded by exhumed HT metamorphic rocks providing insight into geodynamic processes at modern plate margins (e.g. Kohn, 2014; Mottram *et al.*, 2014; Pownall *et al.*, 2014; Stevens *et al.*, 2015). Likewise, the granulites found in Archean terranes may preserve a record of the processes responsible for heating of Earth's early continental crust, and whether such processes resemble those associated with modern plate tectonics.

Whether or not a modern, 'horizontal' style of plate tectonics involving lateral accretion of distinct lithospheric blocks operated on the Archean Earth remains a subject of vigorous debate (e.g. de Wit, 1998; van Hunen & Moyen, 2012; Brown, 2015), and studying the petrogenesis of preserved Archean crustal fragments can provide valuable insight into Archean tectonic processes. In contrast to a vast and still-growing wealth of literature on Archean igneous complexes (e.g. the origin of tonalite-trondjhemite-granodiorite suites; Moyen & Martin, 2012; Palin *et al.*, 2016b), the Archean metamorphic record remains relatively underexplored, particularly with respect to Archean granulite terranes. Recent advances in petrologic techniques

such as phase equilibria modelling and diffusion modelling (i.e. "geospeedometry") have been used extensively to understand metamorphic processes on modern Earth (e.g. Chambers *et al.*, 2009; Brown, 2014; Chakraborty *et al.*, 2016; Spear *et al.*, 2016), with fewer examples of their application to Archean settings (e.g. Cutts *et al.*, 2013; Bhowmik *et al.*, 2014; François *et al.*, 2014; Dumond *et al.*, 2015; Nicoli *et al.*, 2015; Bhadra & Nasipuri, 2017; White *et al.*, 2017) to reveal the pressure-temperature-time (*P*−*T*–*t*) paths that Archean HT rocks took through the crust. Several key questions can be answered from the metamorphic archive and would shed light on heating mechanisms in the Archean crust and Archean tectonic processes. For example, are there rocks from Archean terranes that followed a broad clockwise *P*–*T*–*t* path as might be expected to occur during collisional orogenesis (e.g. England & Thompson, 1984; Jamieson *et al.*, 2004)? Or did they follow a tight, clockwise path (e.g. Harrison *et al.*, 1998; Kohn *et al.*, 2001), or anti-clockwise path (e.g. Mezger *et al.*, 1990), with each path indicative of a different mode of heating? At what depths were they heated? What were the durations of different segments of these *P*–*T* paths, and what do these durations reveal about exhumation and cooling rates of tectonically active Archean middle and lower continental crust? This information is necessary to assess the tectonic processes that led to heating and stabilization of Archean crust, and it is thus paramount to apply modern petrologic techniques to Archean rocks in order to deduce quantitative *P*–*T*-*t* constraints on Archean metamorphic terranes.

In the present study, we combine phase equilibria modelling and *P*–*T* path-dependent diffusion modelling of major element zonation in garnet to place quantitative constraints on the *P*−*T* path and duration of HT metamorphism recorded by Archean granulites of the northern Wyoming Province, exposed in the eastern Beartooth Mountains of Montana and Wyoming, USA. Recent Sm-Nd garnet and U-Pb monazite petrochronology (Dragovic *et al.*, 2016) suggest that these rocks record a polyphase metamorphic history consisting of an early metamorphic event at ~2.8 Ga coeval with emplacement of a calc-alkaline batholith, followed by a cryptic granulite-facies event at ~2.7 Ga. Simple diffusion modelling of major element zonation in garnet using previously published thermobarometric constraints suggests that the duration of HT metamorphism was brief (<1 Ma; Dragovic *et al.*, 2016). However, Dragovic *et al.* (2016) did not provide any constraints on the *P*–*T* path of these rocks, and their diffusion model did not, therefore, account for the effects of *P*–*T* path dependence or post-peak cooling, which can drastically affect the inferred metamorphic timescales as determined by the model. Establishing

this *P–T*–t path is important for understanding the evolution of these rocks, and for evaluating the possible mechanisms for the crustal heating event they record.

Here we place new constraints on: 1) the *P–T* path of the Beartooth granulites through phase equilibria modelling, and 2) the duration of this path through a combination of two different *P–T* path-dependent diffusion models, using the new *P–T* path constraints derived here. One of these diffusion models uses the same sample modelled by Dragovic *et al.* (2016), but is re-calculated using these new constraints on the *P–T* path. We use the new constraints on the *P–T* path and metamorphic duration presented here to evaluate possible crustal heating mechanisms for the HT metamorphism recorded by the Beartooth granulites.

4.3 GEOLOGIC SETTING

The Beartooth granulites exist as m- to km-scale xenoliths and/or roof pendants of metasedimentary packages (interbedded pelites, quartzites, meta-ironstones, and metavolcanics) within a Meso- to Neoarchean granitoid batholith that comprises much of the eastern and central Beartooth Mountains, known as the Long Lake Magmatic Complex (LLMC, Fig. 4.1; Henry *et al.*, 1982; Mueller *et al.*, 2010). These granitoids were emplaced between 2.83 and 2.78 Ga and have been interpreted to be derived from subduction-related arc magmatism, based on bulk rock major and trace element, and isotopic data (e.g. Mueller *et al.*, 1982; Wooden *et al.*, 1982; Mueller *et al.*, 1983; Montgomery & Lytwyn, 1984; Wooden *et al.*, 1988; Mueller *et al.*, 2010; Dragovic *et al.*, 2016).

Previous studies have estimated peak *P–T* conditions of the granulite xenoliths contained within the LLMC to be ~750-810 °C, 5.6-8 kbar (Henry *et al.*, 1982; Maas, 2004; Will, 2013; Mogk *et al.*, 2014). Metamorphism to granulite facies was interpreted to be either the result of a Mesoarchean regional metamorphic event (Henry *et al.*, 1982) or contact heating with the LLMC, undergoing a counter-clockwise *P–T* path (Maas, 2004). However, recently presented field relations and Sm–Nd garnet and U–Pb monazite geochronology suggests a polymetamorphic history, with early metamorphism coincident with LLMC intrusion and a later, cryptic granulite-facies event at c. 2.69-2.67 Ga (Dragovic *et al.*, 2016). This later metamorphism has been interpreted as the main phase of granulite-facies metamorphism in the eastern Beartooth Mountains (Dragovic *et al.*, 2016), with limited obvious evidence for it recorded in the LLMC due to the relatively unreactive nature of the granitoids during HT metamorphism. Multicomponent diffusion modelling of major elements in garnet suggests that

the duration of peak *T* associated with this event was brief, likely < 1 Myr (Dragovic *et al.*, 2016). This cryptic 'pulse' of granulite facies metamorphism is intriguing since there is no obvious field evidence for a heat source, though Dragovic *et al.* (2016) note the coincidence between the Sm-Nd garnet and U-Pb monazite ages from the Beartooth granulites and metamorphic and magmatic zircon ages reported from the Teton and Wind River ranges ~200 km to the southwest, which hints at the possibility of a regional-scale phenomenon that led to localized thermal anomalies in the northern Wyoming Province at c. 2.7 to 2.67 Ga.

4.4 SAMPLE DESCRIPTIONS: PETROGRAPHY AND MINERAL CHEMISTRY

Two metasedimentary samples were selected for detailed study here based upon preserved textural and mineral compositional features (residual pelite BHP13-03D and pelitic diatexite BPYR14-11B), and were previously described and analyzed for Sm-Nd bulk garnet geochronology and U-Pb monazite geochronology Dragovic *et al.* (2016). These samples were collected from m- to km-scale metasedimentary packages that exist as xenoliths and roof pendants in the LLMC. These xenoliths exhibit strong compositional layering of different metasedimentary lithologies (meta-ironstones, quartzites, pelites), and contacts between the metasediments and the surrounding LLMC (e.g. chilled margins of the LLMC, LLMC granitoid veins in the metasediments) suggest that the LLMC intruded into the metasediments (see Dragovic *et al.* 2016 for further details). The petrographic characteristics and mineral chemistries of each sample are discussed below. Major element mineral compositions were determined through wavelength dispersive spectrometry (WDS) on a Cameca SX-50 electron probe microanalyzer at Virginia Tech, using a set of natural and synthetic standards and a ZAF matrix correction. Operating conditions for spot analyses were 15 kv accelerating voltage, 20 nA beam current, 40 s count time, and a beam diameter of < 5 μm. Representative analyses of garnet (from BHP13-03D and BPYR14-11B) and cordierite (BPYR14-11B) are shown in Table 4.1.

4.4.1 Sample BHP13-03D (garnet + sillimanite + K-feldspar residual pelite)

The mineral assemblage in sample BHP13-03D is dominated by porphyroblastic garnet (~30 vol.%), matrix K-feldspar (~30 vol.%), and quartz (~20 vol.%) (Fig. 4.2a-c). At the hand sample scale, the rock is heterogeneous, with domains consisting of variable proportions of matrix quartz and K-feldspar (Fig. 4.2c). Prominent aggregates of biotite, sillimanite, quartz, plagioclase, and ilmenite define a strong foliation and are cross-cut by or bend around garnet

crystal faces (Figs. 4.2a-b, 4.3a-b), and are interpreted to represent relict reactants of the prograde biotite breakdown melting reaction:

biotite + sillimanite + plagioclase ± quartz è garnet + K-feldspar + melt.

The strong foliation of these aggregates suggests that peak metamorphism and partial melting were coeval with deformation. Garnet porphyroblasts are subhedral, ranging from ~3-8 mm in diameter (Fig. 4.2a-c, 4.3a-c), around which the foliation is defined. Some parts of these crystals are euhedral (Fig. 4.2a-b, 4.3a). Garnet cores are inclusion-rich, containing ilmenite, quartz, biotite, plagioclase, zircon, and monazite. Garnet rims are relatively inclusion-free (compared to garnet cores) but contain sparse, tiny (<50 μm length) inclusions of sillimanite, oriented sub-parallel to crystal faces (Fig. 4.3b-c). Garnet porphyroblasts in both K-feldspar-rich domains and quartz-rich domains exhibit the same petrographic and chemical characteristics from core to rim, implying that garnet in both domains experienced a shared growth history. Thin films of fine-grained quartz ± plagioclase surrounding rounded K-feldspar grains are interpreted to represent pseudomorphs after grain boundary melt (Fig. 4.3d; e.g. Holness *et al.*, 2011). Large biotite and ilmenite grains cut across the foliation and across garnet rims (Fig. 3a-b). Minor chlorite and fine-grained sericite occur in the matrix, replacing biotite and sillimanite/K-feldspar, respectively, or filling in fractures in garnet, indicating minor, post-peak low temperature fluid alteration (Fig. 4.3e). Elongate and highly-fractured garnet porphyroblasts are found within strongly sericitized/chloritized zones. The preservation of the granulite-facies peak assemblage (garnet, biotite, quartz, sillimanite, K-feldspar, ilmenite, and plagioclase), as well as the abundance of inferred peritectic phases (garnet and K-feldspar) is consistent with the removal of melt, implying that the rock represents a residuum after partial melting (e.g. Brown, 2002; White & Powell, 2002, 2010).

Major element zoning in garnet from sample BHP13-03D is shown in Fig. 4.4a. This traverse was taken across the largest garnet in the thin section, and thus is the most likely garnet to have been sectioned through its true core. Representative garnet core, mantle, and rim compositions are shown in Table 1. Garnet is almandine-rich, and relatively unzoned in X_{alm}, X_{pyr}, and X_{sps} until the near the crystal rim, where X_{alm} and X_{sps} decrease and X_{pyr} increases. At the rim, X_{alm} increases and X_{pyr} decreases. X_{grs} zonation is better preserved, decreasing smoothly away from the crystal core, increasing smoothly in the garnet 'mantle', and decreasing from a sharp maximum near the garnet rim ($X_{grs} \approx 0.04$ at maxima, decreasing to ~0.03 at the rim).

Based on the petrographic observations described above, the high X_{grs} rims are interpreted to have grown during partial melting, with increased X_{grs} due to Ca liberation to the effective bulk composition during plagioclase breakdown. X_{grs} and X_{sps} change at the same position near the garnet rim. Likewise, X_{alm} and X_{pyr} change at the same position, however this change occurs towards the rim compared to the changes in X_{grs} and X_{sps}.

4.4.2 Sample BPYR14-11B (garnet + cordierite + sillimanite melanosome of diatexite migmatite)

BPYR14-11B is the melanosome of a pelitic diatexite (Fig. 4.2d) and contains garnet, biotite, quartz, plagioclase, cordierite, sillimanite, and ilmenite. Garnet porphyroblasts, 0.5-7 mm in diameter, are anhedral, fractured, and highly resorbed, containing inclusions of quartz, plagioclase, biotite, ilmenite, and sillimanite (Fig. 4.3f). Garnet porphyroblasts are common in small leucocratic pods, suggestive of peritectic garnet growth (Fig. 4.2d, e.g. Sawyer, 1999). Aggregates of biotite and sillimanite define a weak matrix foliation (Fig. 4.3g). Randomly oriented biotite flakes surround and crosscut garnet and cordierite porphyroblasts (Fig. 4.3f-h). Plagioclase and quartz occur in the matrix as rounded, coarse grains that display undulatory extinction with occasional lobate grain boundaries. Some plagioclase occurs as thin, grain boundary films filling in triple junctions between quartz and garnet grains, interpreted to represent crystallized grain boundary melt (Fig. 4.3g; Holness *et al.*, 2011; Vernon, 2011). Cordierite occurs as abundant, anhedral, partially pinitized porphyroblasts in the matrix, and occasionally rims garnet in embayments (Fig. 4.6h). Small, randomly oriented sillimanite needles crosscut foliated biotite and surround garnet and cordierite (Fig. 4.3h-i). Ilmenite is rare and occurs as small grains in the matrix. Major element zonation in garnet is shown in Fig 4.4b. Representative garnet core and rim compositions are shown in Table 4.1. Garnet is relatively unzoned, with gradually increased X_{alm} and decreased X_{pyr}, at the rim (core and rim X_{alm} and X_{pyr} are 0.71-0.72 and 0.23-0.25, and 0.75-0.76 and 0.18-0.19, respectively). There is no X_{grs} and X_{sps} zonation, as garnet cores and rims have similar compositions (0.02 and 0.03, respectively), though there is a slight apparent increase in X_{grs} at the crystal edge (Fig. 7b). Cordierite cores exhibit average Mg# ($Mg/(Mg+Fe^{2+}$) of 0.76.

4.5 PHASE EQUILIBRIA MODELLING

Phase equilibria modelling was employed here to reconstruct segments of the *P–T* path. Most previous thermobarometry on the Beartooth granulites utilized inverse exchange and net-transfer thermobarometery (e.g. Henry *et al.*, 1982), or compared microstructural observations to discontinuous metamorphic reactions on a petrogenetic grid (Maas, 2004; Will, 2013). The limitations and pitfalls of inverse thermobarometry on granulite-facies rocks has been discussed extensively in the literature (e.g. Frost & Chacko, 1989; Florence & Spear, 1995; Kelsey & Hand, 2014), with exchange thermometers (e.g. garnet-biotite) particularly prone to post-peak diffusional modification (thus underestimating peak *T*). Petrogenetic grids provide quantitative constraints on the *P–T* conditions of discontinuous univariant and invariant reactions, but strong evidence for the occurrence of such reactions is needed to effectively construct a *P–T* path, and natural rocks generally evolve via *continuous* reactions. Phase equilibria modelling for a known bulk-rock composition reveals a more holistic view of a rock's evolution, subject to an understanding of the evolution of the effective bulk composition of the system (e.g. White *et al.*, 2001a; Marmo *et al.*, 2002; White *et al.*, 2004), uncertainties associated with both bulk composition and thermodynamic properties of minerals (e.g. Palin *et al.*, 2016a), and potential inabilities for rock-wide equilibration under some conditions (e.g. White & Powell, 2011; Carlson *et al.*, 2015; Spear *et al.*, 2016). The predictions from modeled phase equilibria can be matched to observed mineral microstructures, compositions, compositional zoning, and modal abundances to infer a *P–T* path for a given rock, in what has become a well-established tool for reconstructing the *P–T* paths of granulite-facies rocks (e.g. White *et al.*, 2002; Powell & Holland, 2008; Korhonen *et al.*, 2014). Will (2013) applied such techniques to an orthopyroxene-cordierite gneiss from the eastern Beartooth Mountains, but large predicted *P–T* stability ranges of observed equilibrium assemblages and a lack of mineral composition information inhibited precise *P–T* path determination. Here we seek to build upon this work by integrating microstructural observations and mineral compositions with phase equilibria modelling to reconstruct the *P–T* paths of samples BHP13-03D and BPYR14-11B.

P–T pseudosections were constructed using Perple_X (version 6.7; Connolly, 2005) and dataset version 6.2 of Holland and Powell (2011) in the model system MnNCKFMASHTO, considering the solution phase descriptions of biotite, silicate melt, cordierite, garnet, orthopyroxene, staurolite, feldspar, ilmenite, and white mica from White *et al.* (2014), spinel

from White *et al.* (2002), and sapphirine from Wheller and Powell (2014). Bulk rock major element compositions were determined by X-ray fluorescence spectroscopy (XRF, Table 4.2a) using a Phillips 2404 XRF vacuum spectrometer at Franklin and Marshall College, together with loss on ignition (LOI) and Fe^{2+} titration (Table 4.2a).

Both samples exhibit strong evidence for partial melting, but have well-preserved granulite facies mineral assemblages and <5% leucosome patches/bands or grain boundary melt pseudomorphs. Thus, the bulk-rock compositions measured by XRF are interpreted to represent a residuum of a protolith that has been modified by melt loss. Equilibration length-scales may shrink during HT metamorphism as melt and/or fluid is lost or consumed (e.g. Carlson, 2010), with several studies highlighting the utility of domainal compositions of individual mm-scale microstructures in phase equilibria modelling of residual HT metamorphic rocks (e.g. White *et al.*, 2001b; Johnson *et al.*, 2004; Baldwin *et al.*, 2005; Nasipuri *et al.*, 2009; Anderson *et al.*, 2013; Guevara & Caddick, 2016). We did not use domainal compositions for phase equilibria modelling here, instead choosing to use bulk-rock compositions determined by XRF because: 1) garnet porphyroblasts up to 3 cm apart in sample BHP13-03D have similar chemical zonation, interpreted to record similar growth histories and suggesting that equilibrium length-scales during garnet growth were likely at the cm-scale, 2) petrographic observations in both samples suggest that melt was present on grain boundaries before and during cooling, which probably helped to facilitate equilibration over such length-scales, and 3) the rocks do not display any microstructures suggestive of diminished equilibrium length-scales at HT conditions (e.g. coronal structures or symplectites of HT minerals).

Bulk rock H_2O content was estimated with T–M_{H2O} pseudosections, and was set so that the inferred equilibrium assemblage was stable as close as possible to the solidus, so as to represent equilibration in the presence of grain boundary melt prior to melt consumption. We note that the bulk-rock loss-on-ignition (LOI) values are higher than the H_2O contents chosen from the T–M_{H2O} pseudosections (Table 4.2a, b). This is likely due to the addition of H_2O during post-peak, low-temperature, localized metasomatism (as suggested by the observation of sericitized feldspars, chlorite filling in garnet fractures, and pinitized cordierite, Fig. 4.3d,f,h) and/or the presence of other volatile components (e.g. CO_2) in the rock. Thus, the bulk-rock LOI values would overestimate the bulk-rock H_2O content during HT metamorphism. Bulk-rock Fe_2O_3 was estimated using T–M_{Fe2O3} pseudosections, with the titration values providing a

maximum constraint on bulk-rock Fe_2O_3 content. T–M_{Fe2O3} pseudosections for sample BHP13-03D suggested that the most appropriate bulk-rock Fe_2O_3 content for modelling was substantially lower than that determined by titration, but for sample BPYR14-11B, both Fe_2O_3 contents were similar (Table 2). The bulk compositions used for constructing P–T pseudosections are shown in Table 4.2b.

Effective bulk compositions used for modelling the conditions of peritectic garnet growth in sample BHP13-03D were estimated by two-stage volumetric fractionation of: 1) the compositions of garnet cores and mantles, and 2) the composition of all garnet, to estimate the P–T conditions at the beginning and end of garnet *rim* growth, respectively. The details of this are discussed below. Additionally, constraints on the prograde P–T path are explored via stepwise reintegration of melt into the measured bulk composition of sample BHP-13-03D following a similar approach to that used in other studies (e.g. White *et al.*, 2004; Korhonen *et al.*, 2013), in which 6 vol.% of the melt composition predicted to be in equilibrium (at P–T conditions where 1 vol.% melt is predicted) with the residual rock is added back to the composition in each integration stage.

4.5.1 Sample BHP13-03D

Chemical zoning in garnet in sample BHP13-03D is well-preserved, rendering the bulk rock composition determined by XRF inappropriate for phase equilibria modelling, as the fractionation of components in zoned porphyroblasts can have a significant effect on the effective bulk composition (EBC) from which subsequent phases grow (e.g. Marmo *et al.*, 2002; Zuluaga *et al.*, 2005; Caddick *et al.*, 2007; Konrad-Schmolke *et al.*, 2008). As discussed above and in Dragovic *et al.* (2016), the high grossular garnet rims in sample BHP13-03D are interpreted to have grown during partial melting. Thus, to constrain the P–T conditions of partial melting, an effective bulk composition was estimated by volumetrically fractionating garnet cores and mantles (using average core and mantle chemistries and assuming spherical geometry) from the bulk composition determined by XRF (Table 1; e.g. Marmo *et al.*, 2002; Mottram *et al.*, 2014). Image analysis was used to estimate the fraction of the rock comprised of garnet cores and mantles: assuming spherical geometry, the garnet cores and mantles were estimated to comprise 43.7 vol. % of all garnet in the rock, and 14.9 vol.% of the entire rock.

The P–T pseudosection for this EBC is shown in Fig. 4.5a. The peak assemblage of garnet, melt, K-feldspar, plagioclase, biotite, and sillimanite is stable directly above the solidus at

5.3-9.0 kbar, 750-800 °C. The isopleth of the highest measured X_{grs} value intersects the field of the peak assemblage at 6.0-6.5 kbar, 760-800 °C, interpreted to represent the *P–T* conditions at which the highest X_{grs} garnet rims grew (Fig. 4.5b). We note that the predicted $X_{alm,}$ $X_{pyr,}$ and X_{sps} values within the field of the peak assemblage are far from the measured garnet rim compositions. This is likely due to more advanced diffusional modification at near-peak *T* of the initial growth zonation of Fe, Mg, and Mn, which are thought to diffuse at least an order of magnitude faster than Ca in garnet (e.g. Chakraborty & Ganguly, 1992; Carlson, 2006), as modelled below. Additionally, initial X_{alm} and X_{pyr} zoning profiles were likely further modified throughout cooling via retrograde Fe and Mg exchange with biotite (e.g. Frost & Chacko, 1989; Florence & Spear, 1995). Figures 5c-f show isopleths for predicted modal abundances of garnet, melt, K-feldspar, and biotite. In each case, isopleths are sub-vertical and sub-parallel with the solidus in the field of the peak assemblage, with modal abundances of garnet, K-feldspar, and melt predicted to increase with increasing *T*, and plagioclase (not shown), quartz (not shown), and biotite modal abundances predicted to decrease with increasing *T*. This is consistent with garnet growth at these conditions occurring due to the aforementioned biotite breakdown melting reaction during heating.

Starting from the high-grossular peaks in garnet in BHP13-03D (Fig. 4.4), X_{grs} generally decreases towards the rim, but with small-length-scale fluctuations rather than a smoothly-curved profile that would be expected following significant diffusional modification (e.g. Florence & Spear, 1991; Carlson, 2006; Chakraborty, 2006; Caddick *et al.*, 2010). Garnet crystal faces are well-preserved in some places, suggesting minimal resorption during cooling. Therefore, the rimward decrease in X_{grs} is interpreted to approximate original garnet growth compositions as the garnet rims grew. To determine the *P–T* conditions at which the high-grossular garnet rims stopped growing, a different EBC was calculated by fractionating all garnet, essentially estimating a matrix composition. The *P–T* pseudosection for this EBC is shown in Fig. 4.6a. The peak assemblage is again stable directly above the solidus at 5.5-9.0 kbar, 780-840 °C. Isopleths for the measured rim X_{grs} values (~0.030-0.032) intersect the field of the peak assemblage at ~5.5 kbar, 800 °C (Fig. 4.6b), interpreted to represent the conditions at which peritectic garnet growth ceased. Again, we note that the predicted $X_{alm,}$ $X_{pyr,}$ and X_{sps} values within the field of the peak assemblage are far from the measured garnet rim compositions, likely due to more advanced diffusional modification of the initial growth zonation of these faster-diffusing elements, or

retrograde Fe-Mg exchange with adjacent biotite at or during cooling from near-peak *T*. Isopleths for garnet and melt modal abundances are sub-vertical in the field of the peak assemblage, and sub-parallel with the solidus (Fig. 4.6c-d). The low predicted melt abundance (<3 vol.%), where isopleths for the measured rim X_{grs} values (~0.31) intersect the field of the peak assemblage, is consistent with conditions representing the final stages of melt production (Fig. 4.6d).

4.5.2 Sample BPYR14-11B

A bulk rock composition determined by XRF was used for phase equilibria modelling of sample BPYR14-11B, with the *P–T* pseudosection shown in Fig. 4.7a. The peak assemblage of garnet, melt, plagioclase, biotite, cordierite, sillimanite, ilmenite, and quartz is predicted to be stable at ~6.0-6.8 kbar, 680-820 °C. We interpret the lack of zoning in garnet crystal cores in this sample to represent either near-complete compositional homogenization of garnet at HT conditions, or that substantial zoning was not formed during crystal growth. This contrasts with the strong chemical zoning preserved in garnet in sample BHP13-03D, and the difference between the two samples probably reflects the different garnet growth reaction histories that each sample experienced, owing primarily to their contrasting bulk-rock compositions (e.g. Tinkham *et al.*, 2003; Caddick & Thompson, 2008). Isopleths for the measured X_{alm} and X_{pyr} values of garnet crystal cores, as well as the average Mg# of cordierite, intersect the field of the peak assemblage at ~6.5-7 kbar, 750-810 °C (Fig. 4.7b). Isopleths for the measured X_{grs} and X_{sps} values of crystal cores do not intersect with those for X_{alm} and X_{pyr}, but the isopleth for the measured core X_{grs} suggests similar peak *P–T* conditions (Fig. 4.7b). Isopleths for the measured X_{alm} and X_{pyr}, and X_{sps} values of the garnet rims intersect the sub-solidus assemblage at ~5.0-5.5 kbar, 620-700 °C, part of the cooling path recorded by this sample (Fig. 4.7b). We note that that there is no apparent zoning between core and rim for X_{sps}, likely due to the slightly faster diffusivity of Mn (Chakraborty & Ganguly, 1992), and thus it is not surprising that these compositions appear to record equilibrium at sub-peak *P–T* conditions. Although isopleths for the measured X_{grs} in garnet rims (not shown) suggest higher pressures and/or lower temperatures, the increase in X_{grs} at the rim may be due to local retrograde diffusional re-equilibration with thin plagioclase films in contact with the crystal (interpreted as pseudomorphs after melt; Fig. 4.3h), and thus would be a less reliable indicator of peak *P–T* conditions.

Isopleths for predicted modal abundances of garnet, melt, cordierite, and sillimanite are shown in Fig. 4.7c-f. A two-stage *P–T* path is most consistent with the observed textures and

mineral compositions. The first stage (*I*) involves high-temperature decompression, similar to that recorded in sample BHP13-03D from >6.5 to 6 kbar at 760-800 °C. This results in breakdown of garnet, consumption of melt, and production of cordierite. The second stage (*II*) is dominated by cooling from ~6 kbar, 800 °C to ~5.5 kbar, 650 °C and is predicted to result in the complete consumption of melt upon crossing the solidus, breakdown of cordierite and garnet, and late growth of biotite (not shown) and sillimanite (Fig. 4.7c-f). Observed biotite surrounding garnet and fine-grained sillimanite rimming garnet and cordierite are consistent with this two-stage path, but would not form along a simple, linear decompression and cooling path from the inferred peak *P–T* conditions (~6.5 kbar, 780 °C) to ~5.5 kbar, 650 °C (where the garnet rim isopleths intersect the appropriate assemblage field below the solidus). The simple path would not produce late-stage sillimanite at the expense of cordierite, as interpreted from the observed microstructures.

4.5.3 Melt reintegration: constraints on the prograde path

Microstructural analysis and phase equilibria modelling reveals that both studied samples experienced a *P–T* path characterized by HT decompression at similar *P–T* conditions (identical within likely geologic and thermodynamic uncertainties). To place constraints on the prograde evolution, we reintegrated melt to the effective bulk composition (with garnet cores and mantles fractionated) of sample BHP13-03D. This EBC was chosen because textural observations suggest that the garnet cores and mantles likely formed prior to biotite breakdown melting, and thus would not have been part of the reactive bulk composition upon initiation of biotite breakdown melting (e.g. Marmo *et al.*, 2002; Zuluaga *et al.*, 2005). Moreover, if these rocks are indeed polymetamorphic, it is possible that the garnet cores and mantles grew during earlier contact heating via LLMC emplacement – as suggested by high MSWDs of Sm-Nd bulk garnet ages, possibly indicative of a mixed signal from multiple of garnet that grew during metamorphic events widely separated in time (Dragovic *et al.*, 2016). Whether mono- or polymetamorphic, the chemical zonation in garnet in sample BHP13-03D reflects multi-stage growth, likely due to distinct metamorphic reactions. We therefore assume that low-grossular garnet mantles represent approximate compositions of (former) garnet rims after the first garnet growth episode, prior to biotite breakdown melting and the growth of high-grossular rims during the second growth episode.

We followed the same stepwise down-temperature melt reintegration approach as other studies (e.g. White *et al.*, 2004; Korhonen *et al.*, 2013). This approach assumes that melt was lost instantaneously upon reaching a critical threshold of ~7 vol.% melt, (the melt connectivity transition of Rosenberg and Handy (2005) at which partial melts are most likely to mobilize), but that a small melt fraction of ~1 vol.% was retained on grain boundaries after each melt loss event (Yakymchuk & Brown, 2014). Thus, we chose a point in the field of the inferred peak assemblage in the pseudosection for sample BHP13-03D (garnet cores and mantles fractionated from the XRF bulk composition; Fig. 5a) at 765 °C, 6.5 kbar, wherein ~1 vol.% melt is predicted, and reintegrated 6 vol.% of the predicted melt composition to the effective bulk composition. This process was continued down-temperature, incrementally, until a H_2O-saturated solidus was reached, to approximate a plausible primary bulk composition with subsolidus grain boundary fluid present. The FeO/Fe_2O_3 ratio was kept constant through each melt reintegration step.

The results of the down-temperature stepwise melt reintegration are shown in Fig. 4.8. Melt compositions and bulk system compositions for each melt reintegration step are shown in Tables C1 and C2, respectively. Three melt reintegration steps were needed to achieve an H_2O-saturated solidus, suggesting that a maximum of ~18 vol.% melt was removed, consistent with the preservation of the observed, refractory granulite-facies assemblage. We consider the amount of reintegrated melt to be a maximum estimate of melt lost because H_2O saturation at the conditions of the predicted wet solidus (~660 °C) will not simulate natural processes in rocks if substantial H2O was lost during sub-solidus prograde reactions. Moreover, if the rock's history is polymetamorphic, as suggested by Dragovic *et al.* (2016), it likely experienced significant dehydration prior to the main granulite-facies event. Regardless, we propose that this melt reintegration provides a useful end-member constraint on the prograde heating path.

Predicted X_{grs} in garnet at the *P–T* point of each melt loss event decreases progressively towards the H_2O-saturated solidus, where predicted X_{grs} is ~0.021 at 6.5 kbar, ~660 °C. This is broadly consistent with the decreasing X_{grs} inward of the crystal rim from the X_{grs} peaks of ~0.042 near garnet rims to X_{grs} minima in garnet mantles of ~0.014. These results suggest that pressures during prograde heating were not significantly higher than 6.5 kbar because garnet mantles would be expected to have higher X_{grs} than observed (Fig. 8). Moreover, the melt-

reintegrated pseudosections predict that biotite would not be stable at $P > 6.5$-7 kbar during early partial melting (Fig. 4.8).

4.5.4 Summary of phase equilibria modelling

Both samples analyzed here appear to record maximum pressures of ~6.5 kbar, with thermodynamic modelling of melt reintegration of sample BHP13-03D suggesting that prograde heating and partial melting occurred effectively isobarically at ~6.5 kbar. The high-grossular garnet rims in BHP13-03D may have started growing during heating at ~6.5 kbar, with the highest grossular garnet growing at ~760-800 °C. The end of garnet growth in sample BHP13-03D is constrained to have occurred at ~780-800 °C, though at lower pressures, thus yielding a portion of the *P–T* path involving high-temperature decompression. While the *P–T* conditions of the inferred beginning and end of high-grossular garnet growth likely overlap within the uncertainties of the thermodynamic data and solution models, as well as any geological uncertainty induced by an incorrect EBC (e.g. Green, 2013; Palin *et al.*, 2016a), the sub-vertical isopleths of garnet modal abundance in both pseudosections (Figs. 4.5 & 4.6) suggest that some degree of heating is required for garnet growth to occur.

Sample BPYR14-11B yields similar peak *P–T* conditions of ~6.5-7 kbar, 750-800 °C, but with isopleths for predicted mineral modal abundances (Fig. 4.7c-f) suggesting that the observed microstructures (shown in Fig. 4.3f-i) were likely produced via a two-stage *P–T* path characterized by: 1) HT decompression to ~6 kbar, 800 °C (similar to that recorded by sample BHP13-03D), and 2) subsequent cooling and decompression to 5.0-5.5 kbar, 620-700 °C.

The peak *P–T* conditions determined here are similar to those estimated by previous studies (Henry *et al.*, 1982; Maas, 2004; Will, 2013; Mogk *et al.*, 2014). A clockwise *P–T* path characterized by limited (0.5-1 kbar) HT decompression followed by cooling and decompression (approximating a "hairpin" shape) is consistent with the microstructures and mineral chemistry in *both* samples, each with a different bulk composition and from different localities

The tight clockwise *P–T* path determined here contrasts with that deduced by Maas (2004), wherein a counterclockwise evolution was inferred based on a series of univariant reactions and on the assumption that the studied rocks experienced a single phase of metamorphism. In particular, Maas (2004) suggested a near-peak temperature pressure increase based on: 1) the observation of sillimanite replacing K-feldspar, used as evidence for crossing the low dP/dT reaction: cordierite + K-feldspar è garnet + sillimanite + melt, and 2) the

observation of ilmenite inclusions in garnet cores and rutile inclusions in garnet rims, which may suggest that garnet rims grew at higher pressure than garnet cores. We note that the observation of sillimanite replacing K-feldspar is also consistent with a cooling history, for example, by down-temperature crossing of the high dP/dT reaction: garnet + K-feldspar + melt = biotite + sillimanite + plagioclase + quartz. We also note that observations of cordierite rims on garnet (e.g. Fig. 4.3i) are difficult to reconcile with a counterclockwise *P–T* path and with reactions producing garnet, sillimanite and melt at the expense of cordierite and k-feldspar. While we did not observe the presence of ilmenite inclusions in garnet cores and rutile inclusions in garnet rims in our own samples, the observation by Maas (2004) is compelling. However, given the evidence for polymetamorphism provided by Dragovic *et al.* (2016), garnet cores and rims in some samples (such as BHP13-03D) may have grown during two distinct metamorphic events separated by ~100 Ma, and from different effective bulk compositions. We also note that the cooling path derived here (Figs. 4.7, 4.11) is similar to the cooling path presented by Maas (2004). In summary, the observations of Maas (2004) can be consistent with our interpretation of the *P–T-t* path of these rocks.

4.6 DIFFUSION MODELLING OF MAJOR ELEMENT ZONING IN GARNET

Diffusion modelling of major element zoning in garnet was employed to constrain the duration of the two distinct segments of the *P–T* path determined here: 1) HT decompression, and 2) cooling from HT conditions. Dragovic *et al.* (2016) showed that the sharp peak in X_{grs} near the garnet rims was likely established during biotite breakdown melting near peak *T*, and that the preserved zoning profile is sufficiently sharp such that an initial, step-like zoning profile could be inferred. Their modelling explored the effect of diffusion on the initial profile at a static characteristic temperature of 768 °C for various timescales (T_{char} = 0.97 of peak *T,* with peak *T* = 800 °C, following Chakraborty and Ganguly (1992)). Based on this modelling, Dragovic *et al.* (2016) suggested that this sample's residence at near peak-*T* was likely < 1 Myr. In light of the *P–T* path constraints from the phase equilibria modelling presented above, here we instead applied a *P–T* path-dependent diffusion model in which diffusion was allowed to proceed at each point along a specified *P–T* path. We also explicitly considered retrograde exchange between garnet and its neighboring assemblage, as described below.

Garnet crystals from samples BHP13-03D and BPYR14-11B contain preserved major element zoning (high-grossular overgrowths in BHP 13-03D, increased X_{alm} and decreased X_{pyr}

at the rim in BPYR14-11B; Figs. 4.4, 4.8-4.9). The samples were collected in the field ~5 km from each other, with no major tectonic boundary between them. The *P–T* paths inferred from phase equilibria modelling of both samples presented here, along with the Sm-Nd garnet geochronology from Dragovic *et al.* (2016), suggests that both samples share a common *P–T*-t history. Therefore, modelling of diffusion in garnet from each sample should be able to identify a range of metamorphic timescales that are mutually consistent with the preserved chemical zoning in both samples.

The *P–T* path used here for diffusion modelling, based on the results of phase equilibria modelling presented above, involved: 1) high-*T* decompression-heating from 6.7 kbar, 770 °C to 6.0 kbar, 795 °C (stage *I*; path connecting points a to b in Fig. 4.9b) and 2) a cooling-dominated path from 6.0 kbar, 795 °C to 5.2kbar, 600 °C (stage *II*; path connecting points b to c in Fig. 9b). Various timescales for each stage, with varying combinations of these timescales, were iteratively modelled for both samples to find a combination of stage *I* and *II* timescales that predicted zoning consistent with those observed in both samples. We used diffusivities of Fe, Mg, and Mn in garnet from Chakraborty and Ganguly (1991) and Ca in garnet from Vielzeuf *et al.* (2007).

For sample BHP13-03D, we assumed initial sharply-stepped zoning profiles for X_{grs}, X_{alm}, X_{pyr}, and X_{sps} from the low-grossular garnet mantles to the high-grossular garnet overgrowths (Fig. 9a). We then allowed the stepped profiles to diffuse along the prescribed *P–T* path with a 1D finite diffusion code, assuming a plane sheet geometry, element coupling as in Lasaga (1979) and fixed model space boundaries. The results of selected model runs are shown in Fig. 9. We find that a < 2 Ma duration for stage *I* and <10 Ma for stage *II* are required to produce a reasonably good fit to the observed compositional zonation. However, much of the preserved μm-scale X_{grs} zoning near the crystal rim is lost for stage *I* durations > 1 Ma, even for geologically extreme cooling rates during stage *II* (>200 °C/Myr). For stage *II*, the preserved μm-scale X_{grs} zoning near the crystal rim is lost for durations > 5 Ma, even for extremely short stage I durations (0.1 Ma, which would correspond to a ~20 km/Ma exhumation rate). This confirms that residence at HT conditions was rapid (Dragovic *et al.*, 2016), likely < 1 Ma, and shows that time-averaged cooling rates > 40 °C/Ma are required to preserve the observed chemical zonation in garnet.

Garnet in sample BPYR14-11B is unzoned except near the crystal rim, where Fe increases and Mg decreases, both with a smooth, curved profile. To model this profile, we assumed an initially unzoned garnet crystal at the starting point of the prescribed *P–T* path (point a in Fig. 9a), with a major element composition as predicted by the pseudosection at that *P–T* (Fig. 7). The edge of the garnet crystal was then allowed to re-equilibrate to the calculated thermodynamic equilibrium composition at each successive point along the decompression and then cooling path (e.g. in Fig. 7). Diffusive penetration of this evolving rim composition towards the crystal core was calculated at each *P–T* point by utilizing a spherical geometry finite difference model and a variety of cooling/decompression rates. The results of this model for X_{alm} and X_{pyr} profiles are shown in Fig. 10. Though model results depend on the input durations for both stages of the *P–T* path, we find that the timescale input for stage II has a far greater effect, as it is during this cooling stage that equilibrium rim compositions change most substantially (as in Storm and Spear, 2005). For a range of stage *I* durations of 0.1 to 1 Ma (as constrained by the diffusion modelling results for sample BHP13-03D), stage *II* durations of 3 to 10 Ma produce a good match to the observed curved diffusion profiles of Fe and Mg with durations of 4 to 6 Ma producing the best fit. These stage *II* durations are consistent with those inferred from diffusion modelling of sample BHP13-03D (Fig. 9). Modelled zoning profiles for X_{grs} and X_{spss} (not shown) broadly match the observed profiles, though the values do not match exactly (Fig. S1).

The results of any diffusion modelling exercise are dependent on: 1) The input *T* estimate(s), 2) the diffusion coefficients used, and 3) the initial profile. The *P–T* estimates here are subject to uncertainties that are difficult to quantify, though conservative estimates of *P–T* uncertainties in phase equilibria modelling suggest ±1 kbar and ±50 °C (Powell & Holland, 2008; Green, 2013; Palin *et al.*, 2016a). Hotter and cooler *P–T* paths would respectively require shorter and longer durations to produce the observed chemical zoning, though the results of modelling along 10-15 °C cooler and hotter *P–T* paths yield resultant 'best fit' durations of the same orders of magnitude. We note that the diffusivity of Ca in garnet from Vielzeuf *et al.* (2007) is substantially slower than other estimates (e.g. Chakraborty & Ganguly, 1992; Carlson, 2006; Chu & Ague, 2015). The use of faster Ca diffusivities for the diffusion modelling of sample BHP13-03D required significantly shorter durations for both stages in order to preserve the observed chemical zonation profile (about an order of magnitude shorter). Such durations are not sufficient to produce the X_{alm} and X_{pyr} diffusion profiles at garnet rims in sample BPYR14-

11B. This discrepancy in timescales derived from modelling with different diffusivities could be possible if the samples each experienced subtly different *P–T* histories (i.e. ±50 °C difference between samples). Thus, one sample may have been just cool enough to yield different thermal timescales from diffusion modelling. However, the samples were collected ~5 km apart with no apparent tectonic boundary (i.e. fault or shear zone) separating them, so it is likely that they shared the same heat source. In this case, we conclude that only a diffusivity dataset in which Ca diffuses substantially slower than Fe, Mg, and Mn is consistent with observations in these samples.

In summary, diffusion modelling of major element zonation in garnet from both samples suggests that the duration of stage *I* (HT decompression + heating) of the *P–T* path and residence at near-peak *T* was < 1 Ma, followed by stage *II* (cooling) durations between 3 and 10 Ma. These durations for stages *I* and *II* correspond respectively to exhumation rates of 1-10 mm/yr and heating rates on the order of 10s to 100s of °C/Ma for stage *I*, and cooling rates between 20 and 100 °C/Ma for stage *II*.

4.7 POTENTIAL MECHANISMS FOR HT METAMORPHISM

The *P–T* path and duration inferred here provide additional constraints on the possible mechanisms for HT metamorphism in the eastern Beartooth Mountains. Based on phase equilibria modelling of both samples, the *P–T* path of the Beartooth granulites appears to have been characterized by near-isobaric heating, HT decompression, and cooling with limited decompression, forming a tight, clockwise path (Fig. 4.11), with melt production largely occurring during heating at ~6-7 kbar (Fig. 4.8). Clockwise metamorphic *P–T* paths are both predicted from geodynamic models and inferred from the petrology of metamorphic rocks in modern orogenic settings (e.g. England & Thompson, 1984; Beaumont *et al.*, 2004; Kohn, 2014), but the tight path inferred here with ~0.5-1 kbar of decompression contrasts with more "open" *P–T* paths inferred from many Phanerozoic orogenic belts, which generally record heating at, and burial to, greater depths, and thus greater amounts of decompression (e.g. Vorhies & Ague, 2011; Cubley *et al.*, 2013; Kohn, 2014; Stevens *et al.*, 2015; Yakymchuk *et al.*, 2015). However, tight clockwise *P–T* paths characterized by limited HT decompression (~1 kbar or less) have been inferred from various settings interpreted to result from orogenic processes (e.g. Armstrong *et al.*, 1992; Williams & Karlstrom, 1996; Attoh, 1998; Buick *et al.*, 1998; Couëslan & Pattison, 2012; Diener *et al.*, 2013; Johnson *et al.*, 2015; Guevara & Caddick, 2016), including low-*P*

migmatites from the Himalaya (Groppo *et al.*, 2013). HT decompression appears to have occurred over a *P* range of ~0.5 to 1 kbar in the Beartooth samples, corresponding to ~1.8–3.8 km of exhumation, assuming an overburden with an average density of felsic continental crust (2.7 g/cm^3). The decompression range could be expanded within thermodynamic uncertainty, but textures such as cordierite growth on garnet preclude substantial reduction in the amount of decompression experienced. Based on our diffusion modelling, this exhumation appears to have been rapid, occurring over timescales <1 Myr. If decompression was purely driven by surface denudation, such rates (of the order 1 – 10s of mm/yr) are comparable to rapid erosion on modern Earth, generally observed in orogenic belts characterized by high elevation and extreme topographic relief (e.g. Galy & France-Lanord, 2001; Reiners *et al.*, 2003; Enkelmann *et al.*, 2011). These exhumation rates, as well as the inferred cooling rates, are also consistent with tectonically-driven exhumation, such as in a gneiss dome/core complex, thrust sheet, or mid-crustal channel (e.g. Spear & Parrish, 1996; Gordon *et al.*, 2008; Langille *et al.*, 2012; Stevens *et al.*, 2015). However, the apparent absence of major shear zones in the eastern Beartooth Mountains may suggest that rapid HT decompression/exhumation was not driven by tectonic extrusion such as in a core complex/gneiss dome or mid-crustal channel, although we cannot rule out this possibility. Regardless of exhumation mechanism, the unroofing rates estimated here for the Beartooth granulites appear to be similar to those estimated in modern convergent margin settings characterized by a thick crust and high topography.

Apparent thermal gradients along the inferred *P–T* path range from ~100 °C/kbar during prograde heating to >125 °C/kbar at the end of HT decompression (Fig. 4.11). These are warmer than a 'normal' conductive geotherm in modern continental crust (50 °C/kbar, Stüwe, 2007), though similar to apparent thermal gradients inferred from other Archean HT metamorphic settings (Brown, 2008). The > 25 °C/kbar difference in apparent thermal gradient along the *P–T* path suggests that the Beartooth granulites record a significant thermal anomaly in the middle crust, which was short-lived and accompanied by rapid but limited exhumation. The short duration of metamorphism (<1 Ma at near-peak conditions) discounts internal radiogenic heat production in thickened crust as the dominant heat source (Thompson & England, 1984), and requires thermal length-scales to be short (Carslaw & Jaeger, 1959). This suggests small-scale advective or conductive heating.

What mechanism could cause such a thermal anomaly with these characteristics? A simple explanation would be heating due to emplacement of the LLMC, the ~2.83-2.79 Ga calc-alkaline batholith (Mueller *et al.*, 2010) that hosts the Beartooth granulites as metasedimentary xenoliths/roof pendants. Indeed, this is the favoured interpretation by previous workers (e.g. Maas, 2004; Mueller *et al.*, 2010) based on field relationships and *P–T* data. Heating and the duration at HT conditions due to LLMC emplacement would be rapid, nearly isobaric, and the similarities between the LLMC and active continental arcs (Mueller *et al.*, 2010) may indicate that this region was characterized by high topography where rapid unroofing could occur. The *P–T* path and duration presented here are not inconsistent with this scenario.

However, Dragovic *et al.* (2016) suggest that the main HT metamorphic event occurred ~100 Ma *after* LLMC emplacement, based on Sm-Nd garnet and U-Pb monazite geochronology, with the rocks recording a polyphase metamorphic history. We note here that heating to HT conditions were probably not due to underplating of mafic magmas at the base of the crust, which would establish a far longer thermal timescale than suggested by our diffusion modelling (for example, in the Ivrea Zone, Central Alps, e.g. Peressini *et al.*, 2007). Further, crustal thicknesses in active continental arcs (50-70 km in the Andes, e.g. McGlashan *et al.*, 2008) are far greater than those suggested by the pressures determined by our phase equilibria modelling (6-7 kbar, or ~20-25 km assuming average density of overlying felsic continental crust of ~2.7 g/cm^3), and it is thus unlikely that the Beartooth granulites were at the base of their crustal section. However, emplacement of smaller bodies of mafic melt (that could be related to mafic underplating at the base of the crust but emplaced at structurally higher depths) may have transiently contributed to the crustal heat budget at this time, with successive emplacement of multiple melt bodies possibly maintaining a somewhat elevated geotherm over a longer timescale. Mafic intrusions with emplacement ages that coincide with the ~2.68-2.7 Ga Sm-Nd garnet and U-Pb monazite ages from (Dragovic *et al.*, 2016) have not been identified in the eastern Beartooth Mountains, but are common throughout other sections of the Wyoming Province, including the c. 2705-2710 Ma Stillwater complex (Wall & Scoates, 2016), a large (~180 km^2), layered mafic intrusion ~60 km northwest of the Beartooth granulites and smaller ~2.68 Ga mafic bodies of tholeiitic affinity in the Teton and Wind River Ranges, ~200 km southwest of the eastern Beartooth Mountains (Frost *et al.*, 2006). The Stillwater complex is thought to be the manifestation of a mafic underplate (Czamanske & Bohlen, 1990) with input

from both tholeiitic and boninitic magmas (e.g. McCallum, 1996), which may suggest that the Stillwater magmas were derived from both decompression melting and melting of metasomatized mantle. The origin of the Stillwater complex is outside the scope of this study, but we note that the generation of mantle-derived melts with these affinities could occur through upwelling of metasomatized mantle asthenosphere during slab break-off or lithospheric delamination after the termination of subduction (e.g. Elkins-Tanton, 2005), or during the transition from an arc to a back-arc magmatism (e.g. Kelley *et al.*, 2006). Both of these scenarios could be consistent with short duration HT metamorphism occurring ~100 Ma after LLMC emplacement in a continental arc setting. Additionally, there is evidence for HT metamorphism and arc magmatism at c. 2.69-2.68 Ga in the Teton and Wind River Ranges (e.g. Frost *et al.*, 2006; Frost *et al.*, 2016). The northern Wyoming Province appears to have been a dynamic and tectonically active area long after LLMC emplacement (e.g. Erslev *et al.*, 1993; Frost *et al.*, 2006; Mueller & Frost, 2006), and it is thus possible that HT metamorphism in the eastern Beartooth Mountains could be explained by heating mechanisms that operated ~100 Ma after LLMC emplacement.

4.8 CONCLUSIONS

The phase equilibria and diffusion modelling presented here place new constraints on the *P–T* path and duration of HT metamorphism recorded by granulite facies metasedimentary xenoliths and roof pendants in the eastern Beartooth Mountains. These rocks record a tight, clockwise *P–T* evolution characterized by near-isobaric heating at ~6.5-7 kbar, ~770-800 °C, HT decompression to ~6 bar, 780-800 °C, followed by limited decompression while cooling. Diffusion modelling of major element zonation in garnet suggests that HT decompression was brief (likely <1 Ma), and that cooling rates following this decompression were on the order of 10-100 °C/Ma. We note that the apparent exhumation and cooling rates found here are similar to those from HT metamorphic rocks in Phanerozoic orogenic settings. Apparent thermal gradients along this *P–T* path vary between ~100 and >125 °C/kbar, indicating that the rocks record a significant thermal anomaly in the Archean continental crust of the Wyoming Province. The mechanism to produce this thermal anomaly is poorly constrained due to conflicting interpretations of the timing of HT metamorphism (Mueller *et al.*, 2010; Henry *et al.*, 2014; Dragovic *et al.*, 2016), but is likely conductive or advective in nature, given the brief metamorphic timescales and radical changes in apparent thermal gradient involved.

4.9 ACKNOWLEDGMENTS

K. Dorfler, M. Fame, J. Guevara, A. Mulholland, and T. Palin are thanked for field assistance. S. Mertzmann is thanked for XRF analyses. M. Jercinovic is thanked for the full thin section X-ray map. L. Fedele and R.J. Tracy are thanked for electron microprobe assistance. J. Trela is thanked for a stimulating discussion. This manuscript was improved by constructive and critical comments by C. Yakymchuk and an anonymous reviewer. R. White is thanked for careful and considerate editorial handling. This research was funded by grants from the National Geographic Young Explorer's Program, Geological Society of America Foundation, Tobacco Root Geological Society, David R. Wones Scholarship, and Colorado Scientific Society to V.E. Guevara, and NSF Grant EAR-1447568 to M.J. Caddick and B. Dragovic.

4.10 REFERENCES

Anderson, J. R., Kelsey, D. E., Hand, M. & Collins, W. J., 2013. Conductively driven, high-thermal gradient metamorphism in the Anmatjira Range, Arunta region, central Australia. *Journal of Metamorphic Geology*, 31, 1003-1026.

Armstrong, T. R., Tracy, R. J. & Hames, W. E., 1992. Contrasting styles of Taconian, Eastern Acadian and Western Acadian metamorphism, central and western New England. *Journal of Metamorphic Geology*, 10, 415-426.

Attoh, K., 1998. High–Pressure Granulite Facies Metamorphism in the Pan–African Dahomeyide Orogen, West Africa. *The Journal of Geology*, 106, 236-246.

Baldwin, J. A., Powell, R., Brown, M., Moraes, R. & Fuck, R. A., 2005. Modelling of mineral equilibria in ultrahigh-temperature metamorphic rocks from the Anapolis-Itaucu Complex, central Brazil. *Journal of Metamorphic Geology*, 23, 511-531.

Beaumont, C., Jamieson, R. A., Nguyen, M. H. & Medvedev, S., 2004. Crustal channel flows: 1. Numerical models with applications to the tectonics of the Himalayan-Tibetan orogen. *Journal of Geophysical Research*, 109, B06406.

Bhadra, S. & Nasipuri, P., 2017. Tectonothermal evolution of a garnet-bearing quartzofeldspathic gneiss from the Moyar shear zone, south India and its bearing on the Neoarchean accretionary tectonics. *Lithos*, 274–275, 1-18.

Bhowmik, S. K., Wilde, S. A., Bhandari, A. & Basu Sarbadhikari, A., 2014. Zoned Monazite and Zircon as Monitors for the Thermal History of Granulite Terranes: an Example from the Central Indian Tectonic Zone. *Journal of Petrology*, 55, 585-621.

Brown, M., 2002. Retrograde processes in migmatites and granulites revisited. *Journal of Metamorphic Geology*, 20, 25-40.

Brown, M., 2008. Characteristic thermal regimes of plate tectonics and their metamorphic imprint throughout Earth history: When did Earth first adopt a plate tectonics mode of behavior. *Geological Society of America Special Papers*, 440, 97-128.

Brown, M., 2014. The contribution of metamorphic petrology to understanding lithosphere evolution and geodynamics. *Geoscience Frontiers*, 5, 553-569.

Brown, M., 2015. Paleo- to Mesoarchean polymetamorphism in the Barberton Granite-Greenstone Belt, South Africa: Constraints from U-Pb monazite and Lu-Hf garnet

geochronology on the tectonic processes that shaped the belt: Discussion. *Geological Society of America Bulletin*, 127, 1550-1557.

Buick, I. S., Cartwright, I. & Harley, S. L., 1998. The retrograde *P–T*–t path for low-pressure granulites from the Reynolds Range, central Australia: petrological constraints and implications for low-P/high-T metamorphism. *Journal of Metamorphic Geology*, 16, 511-529.

Caddick, M. J., Bickle, M. J., Harris, N. B. W., Holland, T. J. B., Horstwood, M. S. A. & Ahmad, T., 2007. Burial and exhumation history of a Lesser Himalayan schist: Recording the formation of an inverted metamorphic sequence in NW India. *Earth and Planetary Science Letters*, 264, 375-390.

Caddick, M. J., Konopásek, J. & Thompson, A. B., 2010. Preservation of garnet growth zoning and the duration of prograde metamorphism. *Journal of Petrology*, 51, 2327-2347.

Caddick, M. J. & Thompson, A. B., 2008. Quantifying the tectono-metamorphic evolution of pelitic rocks from a wide range of tectonic settings: Mineral compositions in equilibrium. *Contributions to Mineralogy and Petrology*, 156, 177-195.

Carlson, W. D., 2006. Rates of Fe, Mg, Mn, and Ca diffusion in garnet. *American Mineralogist*, 91, 1-11.

Carlson, W. D., 2010. Dependence of reaction kinetics on H_2O activity as inferred from rates of intergranular diffusion of aluminium. *Journal of Metamorphic Geology*, 28, 735-752.

Carlson, W. D., Pattison, D. R. & Caddick, M. J., 2015. Beyond the equilibrium paradigm: How consideration of kinetics enhances metamorphic interpretation. *American Mineralogist*, 100, 1659-1667.

Carslaw, H. S. & Jaeger, C. J., 1959. *Conduction of Heat in Solids*. Clarendon, Oxford.

Chakraborty, S., 2006. Diffusion modeling as a tool for constraining timescales of evolution of metamorphic rocks. *Mineralogy and Petrology*, 88, 7-27.

Chakraborty, S., Anczkiewicz, R., Gaidies, F., Rubatto, D., Sorcar, N., Faak, K., Mukhopadhyay, D. K. & Dasgupta, S., 2016. A review of thermal history and timescales of tectonometamorphic processes in Sikkim Himalaya (NE India) and implications for rates of metamorphic processes. *Journal of Metamorphic Geology*, 34, 785-803.

Chakraborty, S. & Ganguly, J., 1991. Compositional Zoning and Cation Diffusion in Garnets. In: *Diffusion, Atomic Ordering, and Mass Transport: Selected Topics in Geochemistry* (ed Ganguly, J.), pp. 120-175, Springer US, New York, NY.

Chakraborty, S. & Ganguly, J., 1992. Cation diffusion in aluminosilicate garnets: experimental determination in spessartine-almandine diffusion couples, evaluation of effective binary diffusion coefficients, and applications. *Contributions to Mineralogy and Petrology*, 111, 74-86.

Chambers, J., Caddick, M. J., Argles, T. W., Horstwood, M. S. A., Harris, N. B. W., Parrish, R. R. & Ahmad, T., 2009. Empirical constraints on extrusion mechanisms from the upper margin of an exhumed high-grade orogenic core, Sutlej Valley, NW India. *Tectonophysics*, 477, 77-92.

Chu, X. & Ague, J. J., 2015. Analysis of experimental data on divalent cation diffusion kinetics in aluminosilicate garnets with application to timescales of peak Barrovian metamorphism, Scotland. *Contributions to Mineralogy and Petrology*, 170, 1-27.

Connolly, J. A. D., 2005. Computation of phase equilibria by linear programming: A tool for geodynamic modeling and its application to subduction zone decarbonation. *Earth and Planetary Science Letters*, 236, 524-541.

Couëslan, C. G. & Pattison, D. R. M., 2012. Low-pressure regional amphibolite-facies to granulite-facies metamorphism of the Paleoproterozoic Thompson Nickel Belt, Manitoba. *Canadian Journal of Earth Sciences*, 49, 1117-1153.

Cubley, J., Pattison, D. R., Tinkham, D. & Fanning, C., 2013. U–Pb geochronological constraints on the timing of episodic regional metamorphism and rapid high-T exhumation of the Grand Forks complex, British Columbia. *Lithos*, 156, 241-267.

Cutts, K. A., Stevens, G., Hoffmann, J. E., Buick, I. S., Frei, D. & Münker, C., 2013. Paleo- to Mesoarchean polymetamorphism in the Barberton Granite-Greenstone Belt, South Africa: Constraints from U-Pb monazite and Lu-Hf garnet geochronology on the tectonic processes that shaped the belt. *Geological Society of America Bulletin*.

Czamanske, G. K. & Bohlen, S. R., 1990. The Stillwater Complex and its anorthosites: an accident of magmatic underplating? *American Mineralogist*, 75, 37-45.

de Wit, M. J., 1998. On Archean granites, greenstones, cratons and tectonics; does the evidence demand a verdict? *Precambrian Research*, 91, 181-227.

Diener, J. F. A., White, R. W., Link, K., Dreyer, T. S. & Moodley, A., 2013. Clockwise, low-P metamorphism of the Aus granulite terrain, southern Namibia, during the Mesoproterozoic Namaqua Orogeny. *Precambrian Research*, 224, 629-652.

Dragovic, B., Guevara, V. E., Caddick, M. J., Baxter, E. F. & Kylander-Clark, A. R. C., 2016. A pulse of cryptic granulite-facies metamorphism in the Archean Wyoming Craton revealed by Sm–Nd garnet and U–Pb monazite geochronology. *Precambrian Research*, 283, 24-49.

Dumond, G., Goncalves, P., Williams, M. L. & Jercinovic, M. J., 2015. Monazite as a monitor of melting, garnet growth and feldspar recrystallization in continental lower crust. *Journal of Metamorphic Geology*, 33, 735-762.

Elkins-Tanton, L. T., 2005. Continental magmatism caused by lithospheric delamination. *Geological Society of America Special Papers*, 388, 449-461.

England, P. C. & Thompson, A. B., 1984. Pressure-temperature-time paths of regional metamorphism I. Heat transfer during the evolution of regions of thickened continental crust. *Journal of Petrology*, 25, 894-928.

Enkelmann, E., Ehlers, T. A., Zeitler, P. K. & Hallet, B., 2011. Denudation of the Namche Barwa antiform, eastern Himalaya. *Earth and Planetary Science Letters*, 307, 323-333.

Erslev, E. A., Frost, C. D., Karlstrom, K. E., Page, N. J., Zientek, M. L., Reed, J. C., Jr., Snyder, G. L., Worl, R. G., Bryant, B., Reynolds, M. W. & Peterman, Z. E., 1993. *The Wyoming Province*. Geological Society of America, Boulder, CO.

Florence, F. P. & Spear, F. S., 1991. Effects of diffusional modification of garnet growth zoning on *P–T* path calculations. *Contributions to Mineralogy and Petrology*, 107, 487-500.

Florence, F. P. & Spear, F. S., 1995. Intergranular diffusion kinetics of Fe and Mg during retrograde metamorphism of a pelitic gneiss from the Adirondack Mountains. *Earth and Planetary Science Letters*, 134, 329-340.

Foster, D. A., Mueller, P. A., Mogk, D. W., Wooden, J. L. & Vogl, J. J., 2006. Proterozoic evolution of the western margin of the Wyoming craton: implications for the tectonic and magmatic evolution of the northern Rocky Mountains. *Canadian Journal of Earth Sciences*, 43, 1601-1619.

François, C., Philippot, P., Rey, P. & Rubatto, D., 2014. Burial and exhumation during Archean sagduction in the East Pilbara Granite-Greenstone Terrane. *Earth and Planetary Science Letters*, 396, 235-251.

Frost, B. R. & Chacko, T., 1989. The granulite uncertainty principle; limitations on thermobarometry in granulites. *Journal of Geology*, 97, 435-450.

Frost, B. R., Frost, C. D., Cornia, M., Chamberlain, K. R. & Kirkwood, R., 2006. The Teton – Wind River domain: a 2.68–2.67 Ga active margin in the western Wyoming Province. *Canadian Journal of Earth Sciences*, 43, 1489-1510.

Frost, C. D., Swapp, S. M., Frost, B. R., Finley-Blasi, L. & Fitz-Gerald, D. B., 2016. Leucogranites of the Teton Range, Wyoming: A record of Archean collisional orogeny. *Geochimica et Cosmochimica Acta*, 185, 528-549.

Galy, A. & France-Lanord, C., 2001. Higher erosion rates in the Himalaya: Geochemical constraints on riverine fluxes. *Geology*, 29, 23-26.

Gordon, S. M., Whitney, D. L., Teyssier, C., Grove, M. & Dunlap, W. J., 2008. Timescales of migmatization, melt crystallization, and cooling in a Cordilleran gneiss dome: Valhalla complex, southeastern British Columbia. *Tectonics*, 27, TC4010-TC4010.

Green, E. C. R., White, R.W., Powell, R., 2013. Exploring Uncertainties in Phase Diagram Calculations via a Monte Carlo Method. In: *pre-Goldschmidt 2013 workshop "Applying phase equilibria modelling to rocks"*, Florence, Italy.

Groppo, C., Rolfo, F. & Mosca, P., 2013. The cordierite-bearing anatectic rocks of the higher Himalayan crystallines (eastern Nepal): low-pressure anatexis, melt productivity, melt loss and the preservation of cordierite. *Journal of Metamorphic Geology*, 31, 187-204.

Guevara, V. E. & Caddick, M. J., 2016. Shooting at a moving target: phase equilibria modelling of high-temperature metamorphism. *Journal of Metamorphic Geology*, 34, 209-245.

Harrison, T. M., Grove, M., Lovera, O. M. & Catlos, E., 1998. A model for the origin of Himalayan anatexis and inverted metamorphism. *Journal of Geophysical Research: Solid Earth*, 103, 27017-27032.

Henry, D. J., Mogk, D. M., Mueller, P., Foster, D. A. & Wooden, J., 2014. Upper to middle level exposure of a 2.8 Ga continent in the northern Wyoming Province, USA. *Geological Society of America Abstracts with Programs*, 46, 19.

Henry, D. J., Mueller, P. A., Wooden, J. L., Warner, J. L. & Lee-Berman, R., 1982. Granulite grade supracrustal assemblages of the Quad Creek area, eastern Beartooth Mountains, Montana. *Special Publication - State of Montana Bureau of Mines and Geology*, 147-156.

Holland, T. J. B. & Powell, R., 2011. An improved and extended internally consistent thermodynamic dataset for phases of petrological interest, involving a new equation of state for solids. *Journal of Metamorphic Geology*, 29, 333-383.

Holness, M. B., Cesare, B. & Sawyer, E. W., 2011. Melted Rocks under the Microscope: Microstructures and Their Interpretation. *Elements*, 7, 247-252.

Jamieson, R. A., Beaumont, C., Medvedev, S. & Nguyen, M. H., 2004. Crustal channel flows: 2. Numerical models with implications for metamorphism in the Himalayan-Tibetan orogen. *Journal of Geophysical Research: Solid Earth*, 109, n/a-n/a.

Johnson, T., Brown, M., Gibson, R. & Wing, B., 2004. Spinel–cordierite symplectites replacing andalusite: evidence for melt-assisted diapirism in the Bushveld Complex, South Africa. *Journal of Metamorphic Geology*, 22, 529-545.

Johnson, T. E., Clark, C., Taylor, R. J., Santosh, M. & Collins, A. S., 2015. Prograde and retrograde growth of monazite in migmatites: An example from the Nagercoil Block, southern India. *Geoscience Frontiers*, 6, 373–387.

Kelley, K. A., Plank, T., Grove, T. L., Stolper, E. M., Newman, S. & Hauri, E., 2006. Mantle melting as a function of water content beneath back-arc basins. *Journal of Geophysical Research: Solid Earth*, 111, n/a-n/a.

Kelly, E. D., Hoisch, T. D., Wells, M. L., Vervoort, J. D. & Beyene, M. A., 2015. An Early Cretaceous garnet pressure–temperature path recording synconvergent burial and exhumation from the hinterland of the Sevier orogenic belt, Albion Mountains, Idaho. *Contributions to Mineralogy and Petrology*, 170, 20.

Kelsey, D. E. & Hand, M., 2014. On ultrahigh temperature crustal metamorphism: Phase equilibria, trace element thermometry, bulk composition, heat sources, timescales and tectonic settings. *Geoscience Frontiers*, 6, 311-356.

Kohn, M. J., 2014. Himalayan metamorphism and its tectonic implications. *Annual Review of Earth and Planetary Sciences*, 42, 381-419.

Kohn, M. J., Catlos, E. J., Ryerson, F. J. & Harrison, T. M., 2001. Pressure-temperature-time path discontinuity in the Main Central thrust zone, central Nepal. *Geology*, 29, 571-574.

Konrad-Schmolke, M., O'Brien, P. J., De Capitani, C. & Carswell, D. A., 2008. Garnet growth at high- and ultra-high pressure conditions and the effect of element fractionation on mineral modes and composition. *Lithos*, 103, 309-332.

Korhonen, F. J., Brown, M., Clark, C. & Bhattacharya, S., 2013. Osumilite-melt interactions in ultrahigh temperature granulites: phase equilibria modelling and implications for the *P–T*-t evolution of the Eastern Ghats Province, India. *Journal of Metamorphic Geology*, 31, 881-907.

Korhonen, F. J., Clark, C., Brown, M. & Taylor, R. J. M., 2014. Taking the temperature of Earth's hottest crust. *Earth and Planetary Science Letters*, 408, 341-354.

Langille, J. M., Jessup, M. J., Cottle, J. M., Lederer, G. & Ahmad, T., 2012. Timing of metamorphism, melting and exhumation of the Leo Pargil dome, northwest India. *Journal of Metamorphic Geology*, 30, 769-791.

Lasaga, A. C., 1979. Multicomponent exchange and diffusion in silicates. *Geochimica et Cosmochimica Acta*, 43, 455-469.

Lopez, D. A., 2001. Preliminary Geologic Map of the Red Lodge 30' x 60' Quadrangle of South-Central Montana, Montana Bureau of Mines and Geology, Butte, MT.

Maas, A. T., 2004. *Migmatization of Archean Aluminous Metasediments from the Eastern Beartooth Mountains, Montana, USA*, Louisiana State University.

Marmo, B. A., Clarke, G. L. & Powell, R., 2002. Fractionation of bulk rock composition due to porphyroblast growth: effects on eclogite facies mineral equilibria, Pam Peninsula, New Caledonia. *Journal of Metamorphic Geology*, 20, 151-165.

McCallum, I. S., 1996. The Stillwater Complex. *Developments in Petrology*, 15, 441-483.

McGlashan, N., Brown, L. & Kay, S., 2008. Crustal thickness in the central Andes from teleseismically recorded depth phase precursors. *Geophysical Journal International*, 175, 1013-1022.

Mezger, K., Bohlen, S. R. & Hanson, G. N., 1990. Metamorphic History of the Achean Pikwitonei Granulite Domain and the Cross Lake Subprovince, Superior Province, Manitoba, Canada. *Journal of Petrology*, 31, 483-517.

Mogk, D. W., Henry, D. J., Mueller, P. & Wooden, J. L., 2014. Mesoarchean rocks of the eastern Beartooth Mountains, MT and WY. *Geological Society of America Abstracts with Programs*, 46, 19.

Montgomery, C. W. & Lytwyn, J. N., 1984. Rb-Sr systematics and ages of principal Precambrian lithologies in the South Snowy Block, Beartooth Mountains. *Journal of Geology*, 92, 103-112.

Mottram, C. M., Warren, C. J., Regis, D., Roberts, N. M. W., Harris, N. B. W., Argles, T. W. & Parrish, R. R., 2014. Developing an inverted Barrovian sequence; insights from monazite petrochronology. *Earth and Planetary Science Letters*, 403, 418-431.

Moyen, J.-F. & Martin, H., 2012. Forty years of TTG research. *Lithos*, 148, 312-336.

Mueller, P. A. & Frost, C. D., 2006. The Wyoming Province: a distinctive Archean craton in Laurentian North America. *Canadian Journal of Earth Sciences*, 43, 1391-1397.

Mueller, P. A., Wooden, J. L., Mogk, D. W., Henry, D. J. & Bowes, D. R., 2010. Rapid growth of an Archean continent by arc magmatism. *Precambrian Research*, 183, 70-88.

Mueller, P. A., Wooden, J. L., Odom, A. L. & Bowes, D. R., 1982. Geochemistry of the Archean rocks of the Quad Creek and Hellroaring Plateau areas of the eastern Beartooth Mountains. *Special Publication - State of Montana Bureau of Mines and Geology*, 69-82.

Mueller, P. A., Wooden, J. L., Schulz, K. & Bowes, D. R., 1983. Incompatible-element–rich andesitic amphibolites from the Archean of Montana and Wyoming: Evidence for mantle metasomatism. *Geology*, 11, 203-206.

Nasipuri, P., Bhattacharya, A. & Das, S., 2009. Metamorphic reactions in dry and aluminous granulites: a Perple_X *P–T* pseudosection analysis of the influence of effective reaction volume. *Contributions to Mineralogy and Petrology*, 157, 301-311.

Nicoli, G., Stevens, G., Moyen, J. F. & Frei, D., 2015. Rapid evolution from sediment to anatectic granulite in an Archean continental collision zone: the example of the Bandelierkop Formation metapelites, South Marginal Zone, Limpopo Belt, South Africa. *Journal of Metamorphic Geology*, 33, 177-202.

Palin, R. M., Weller, O. M., Waters, D. J. & Dyck, B., 2016a. Quantifying geological uncertainty in metamorphic phase equilibria modelling; a Monte Carlo assessment and implications for tectonic interpretations. *Geoscience Frontiers*, 7, 591–607.

Palin, R. M., White, R. W. & Green, E. C., 2016b. Partial melting of metabasic rocks and the generation of tonalitic–trondhjemitic–granodioritic (TTG) crust in the Archaean: Constraints from phase equilibrium modelling. *Precambrian Research*, 287, 73-90.

Peressini, G., Quick, J. E., Sinigoi, S., Hofmann, A. W. & Fanning, M., 2007. Duration of a Large Mafic Intrusion and Heat Transfer in the Lower Crust: a SHRIMP U–Pb Zircon Study in the Ivrea–Verbano Zone (Western Alps, Italy). *Journal of Petrology*, 48, 1185-1218.

Powell, R. & Holland, T. J. B., 2008. On thermobarometry. *Journal of Metamorphic Geology*, 26, 155-179.

Pownall, J. M., Hall, R., Armstrong, R. A. & Forster, M. A., 2014. Earth's youngest known ultrahigh-temperature granulites discovered on Seram, eastern Indonesia. *Geology*, 42, 279-282.

Reiners, P. W., Ehlers, T. A., Mitchell, S. G. & Montgomery, D. R., 2003. Coupled spatial variations in precipitation and long-term erosion rates across the Washington Cascades. *Nature*, 426, 645-647.

Rosenberg, C. L. & Handy, M. R., 2005. Experimental deformation of partially melted granite revisited: implications for the continental crust. *Journal of Metamorphic Geology*, 23, 19-28.

Sawyer, E. W., 1999. Criteria for the recognition of partial melting. *Physics and Chemistry of the Earth. Part A: Solid Earth and Geodesy*, 24, 269-279.

Spear, F. S. & Parrish, R. R., 1996. Petrology and cooling rates of the Valhalla Complex, British Columbia, Canada. *Journal of Petrology*, 37, 733-765.

Spear, F. S., Pattison, D. R. M. & Cheney, J. T., 2016. The metamorphosis of metamorphic petrology. *Geological Society of America Special Papers*, 523.

Spikings, R. A., Winkler, W., Seward, D. & Handler, R., 2001. Along-strike variations in the thermal and tectonic response of the continental Ecuadorian Andes to the collision with heterogeneous oceanic crust. *Earth and Planetary Science Letters*, 186, 57-73.

Stevens, L. M., Baldwin, J. A., Cottle, J. M. & Kylander-Clark, A. R. C., 2015. Phase equilibria modelling and LASS monazite petrochronology: *P–T*–t constraints on the evolution of the Priest River core complex, northern Idaho. *Journal of Metamorphic Geology*, 33, 385-411.

Stüwe, K., 2007. *Geodynamics of the Lithosphere*. Springer-Verlag Berlin Heidelberg.

Thompson, A. B. & England, P. C., 1984. Pressure-temperature-time paths of regional metamorphism II. Their inference and interpretation using mineral assemblages in metamorphic rocks. *Journal of Petrology*, 25, 929-955.

Tinkham, D. K., Zuluaga, C. A. & Stowell, H. H., 2003. Metapelite phase equilibria modeling in MnNCKFMASH: the effect of variable Al2O3 and MgO/(MgO+ FeO) on mineral stability. *American Mineralogist*, 88, 1174-1174.

van Hunen, J. & Moyen, J. F., 2012. Archean Subduction: Fact or Fiction? *Annual Review of Earth and Planetary Sciences, Vol 40*, 40, 195-219.

Vernon, R. H., 2011. Microstructures of melt-bearing regional metamorphic rocks. *Geological Society of America Memoirs*, 207, 1-11.

Vielzeuf, D., Baronnet, A., Perchuk, A., Laporte, D. & Baker, M., 2007. Calcium diffusivity in alumino-silicate garnets: an experimental and ATEM study. *Contributions to Mineralogy and Petrology*, 154, 153-170.

Vorhies, S. H. & Ague, J. J., 2011. Pressure-temperature evolution and thermal regimes in the Barrovian zones, Scotland. *Journal of the Geological Society*, 168, 1147-1166.

Wall, C. J. & Scoates, J. S., 2016. HIGH-PRECISION U-Pb ZIRCON-BADDELEYITE DATING OF THE JM REEF PLATINUM GROUP ELEMENT DEPOSIT IN THE STILLWATER COMPLEX, MONTANA (USA). *Economic Geology*, 111, 771-782.

Wheller, C. J. & Powell, R., 2014. A new thermodynamic model for sapphirine: calculated phase equilibria in K2O–FeO–MgO–Al2O3–SiO2–H2O–TiO2–Fe2O3. *Journal of Metamorphic Geology*, 32, 287-299.

White, R., Palin, R. & Green, E., 2017. High‐grade metamorphism and partial melting in Archean composite grey gneiss complexes. *Journal of Metamorphic Geology*, 35, 181-195.

White, R., Powell, R. & Halpin, J., 2004. Spatially‐focussed melt formation in aluminous metapelites from Broken Hill, Australia. *Journal of Metamorphic Geology*, 22, 825-845.

White, R., Powell, R. & Holland, T., 2001a. Calculation of partial melting equilibria in the system Na2O–CaO–K2O–FeO–MgO–Al2O3–SiO2–H2O (NCKFMASH). *Journal of metamorphic Geology*, 19, 139-153.

White, R. W. & Powell, R., 2002. Melt loss and the preservation of granulite facies mineral assemblages. *Journal of Metamorphic Geology*, 20, 621-632.

White, R. W. & Powell, R., 2010. Retrograde melt–residue interaction and the formation of near-anhydrous leucosomes in migmatites. *Journal of Metamorphic Geology*, 28, 579-597.

White, R. W. & Powell, R., 2011. On the interpretation of retrograde reaction textures in granulite facies rocks. *Journal of Metamorphic Geology*, 29, 131-149.

White, R. W., Powell, R. & Clarke, G. L., 2002. The interpretation of reaction textures in Fe-rich metapelitic granulites of the Musgrave Block, central Australia: constraints from mineral equilibria calculations in the system K2O–FeO–MgO–Al2O3–SiO2–H2O–TiO2–Fe2O3. *Journal of Metamorphic Geology*, 20, 41-55.

White, R. W., Powell, R. & Holland, T. J. B., 2001b. Calculation of partial melting equilibria in the system Na_2O-CaO-K_2O-FeO-MgO-Al_2O_3-SiO_2-H_2O (NCKFMASH). *Journal of Metamorphic Geology*, 19, 139-153.

White, R. W., Powell, R., Holland, T. J. B., Johnson, T. E. & Green, E. C. R., 2014. New mineral activity–composition relations for thermodynamic calculations in metapelitic systems. *Journal of Metamorphic Geology*, 32, 261-286.

Whitney, D. L. & Evans, B. W., 2010. Abbreviations for names of rock-forming minerals. *American Mineralogist*, 95, 185-187.

Will, C. N., 2013. *Temperature and pressure conditions of Archean amphibolite-granulite facies metamorphic xenoliths from the eastern Beartooth Mountains, Montana and Wyoming, USA*, Louisiana State University.

Williams, M. L. & Karlstrom, K. E., 1996. Looping *P–T* paths and high-T low-P middle crustal metamorphism: Proterozoic evolution of the southwestern United States. *Geology*, 24, 1119-1122.

Wooden, J. L., Mueller, P. A., Hunt, D. K. & Bowes, D. R., 1982. Geochemistry and Rb-Sr geochronology of Archean rocks from the interior of the southeastern Beartooth Mountains, Montana and Wyoming. *Special Publication - State of Montana Bureau of Mines and Geology*, 45-55.

Wooden, J. L., Mueller, P. A., Mogk, D. W. & Bowes, D. R., 1988. A review of the geochemistry and geochronology of Archean rocks of the Beartooth Mountains, Montana and Wyoming. *Special Publication - State of Montana Bureau of Mines and Geology*, 23-42.

Yakymchuk, C. & Brown, M., 2014. Consequences of open-system melting in tectonics. *Journal of the Geological Society*, 171, 21-40.

Yakymchuk, C., Brown, M., Clark, C., Korhonen, F. J., Piccoli, P. M., Siddoway, C. S., Taylor, R. J. M. & Vervoort, J. D., 2015. Decoding polyphase migmatites using geochronology and phase equilibria modelling. *Journal of Metamorphic Geology*, 33, 203-230.

Zuluaga, C. A., Stowell, H. H. & Tinkham, D. K., 2005. The effect of zoned garnet on metapelite pseudosection topology and calculated metamorphic PT paths. *American Mineralogist*, 90, 1619-1628.

4.11 FIGURES

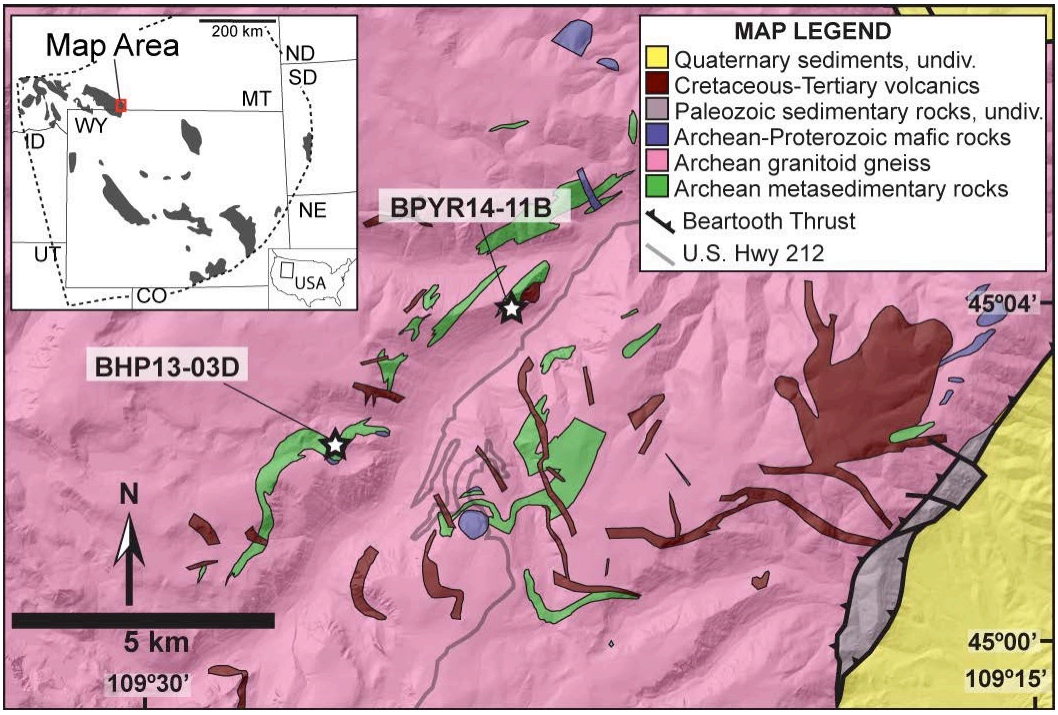

Figure 4.1: Geologic map (underlain by a digital elevation model) of the eastern Beartooth Mountains, modified after Lopez (2001) and Dragovic *et al.* (2016). Inset map shows outcroppings of Archean rocks of the Wyoming Province in the western U.S (dark fill) and outline of Wyoming Province (black dashed line). The map area is outlined in red in the inset. Inset modified after Foster (2006) and Mueller and Frost (2006). Stars indicate the sample locations in this study.

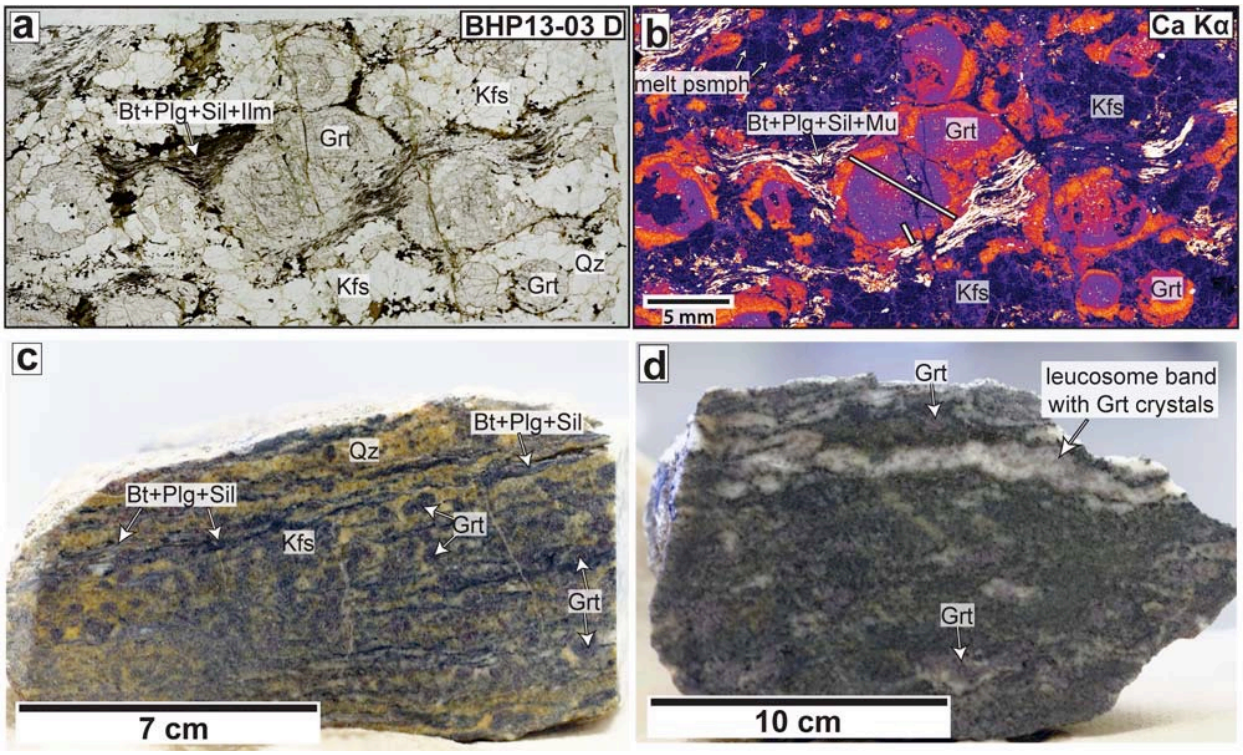

Figure 4.2: (a) Full-section photograph of sample BHP13-03D. (b) False color X-ray map for sample BHP13-03D (for element Ca). Warm colors represent high Ca concentrations. Electron microprobe garnet traverse position for sample BHP13-03D is shown by the white arrow. Scale bar for (a) and (b) shown in (b). All mineral abbreviations after Whitney and Evans (2010). (c, d) Hand samples of BHP13-03D and BPYR14-11B, respectively, showing macro-scale features and heterogeneity. Sample widths in (c) and (d) are 7 and 10 cm, respectively.

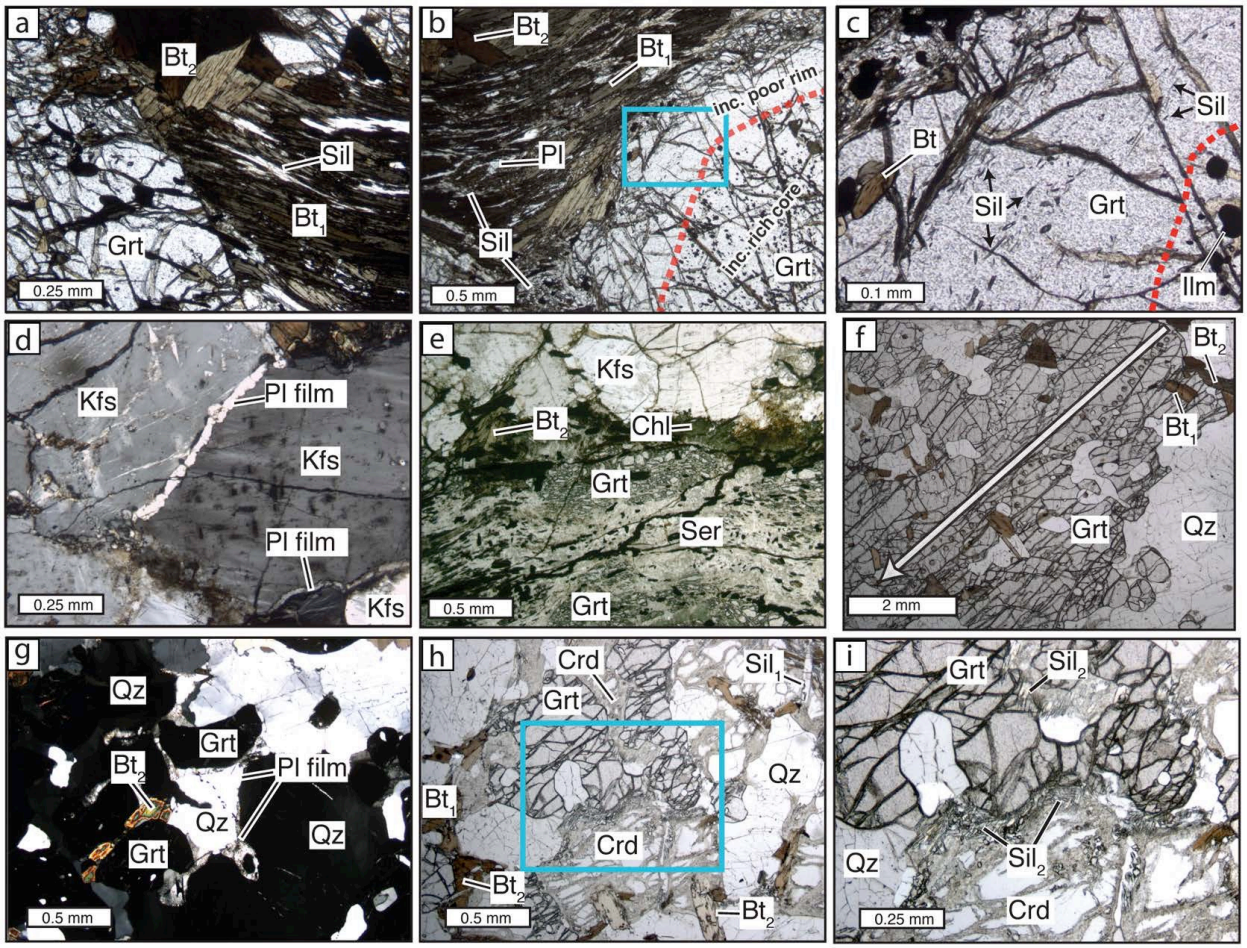

Figure 4.3: Photomicrographs of samples BHP13-03D and BPYR14-11B showing various petrographic observations described in the text. (a) Foliation dominated by biotite (Bt_1) and sillimanite crosscut by garnet porphyroblast. Bt_2 refers to later-stage biotite that crosscuts the foliation and/or embays garnet. (b) Biotite + sillimanite aggregates crosscut by and wrapping around garnet porphyroblast. Teal-outlined box denotes image shown in panel c. Red, dashed line delineates inclusion-rich garnet core from inclusion poor garnet rim. (c) Relatively inclusion-poor garnet rim. Note the abundant oriented sillimanite inclusions in the garnet rim. Red, dashed line as in panel (b). (d) Grain boundary plagioclase ± quartz pseudomorphs after melt, surrounding rounded K-feldspar grains. (e) Replacement of chlorite and sericite after biotite, garnet, and K-feldspar. An elongate, highly-fractured garnet is also shown. (f) Highly resorbed garnet porphyroblast from BYPR14-11B. Arrow indicates position of microprobe traverse shown in Fig. 4b. Round pits are laser ablation spots from Dragovic *et al.* (2016). (g) Thin films of plagioclase between quartz and garnet along grain boundaries and filling in triple junctions, interpreted as representing melt. (h) Garnet porphyroblast resorbed by quartz and cordierite. Late biotite is seen surrounding garnet and replacing cordierite. Prismatic sillimanite is shown at top right of image. Teal-outlined box denotes area of image shown in panel i. (i) Garnet porphyroblast resorbed by quartz and cordierite. Late-stage sillimanite needles rim both garnet and cordierite. Cordierite is partially pinitized.

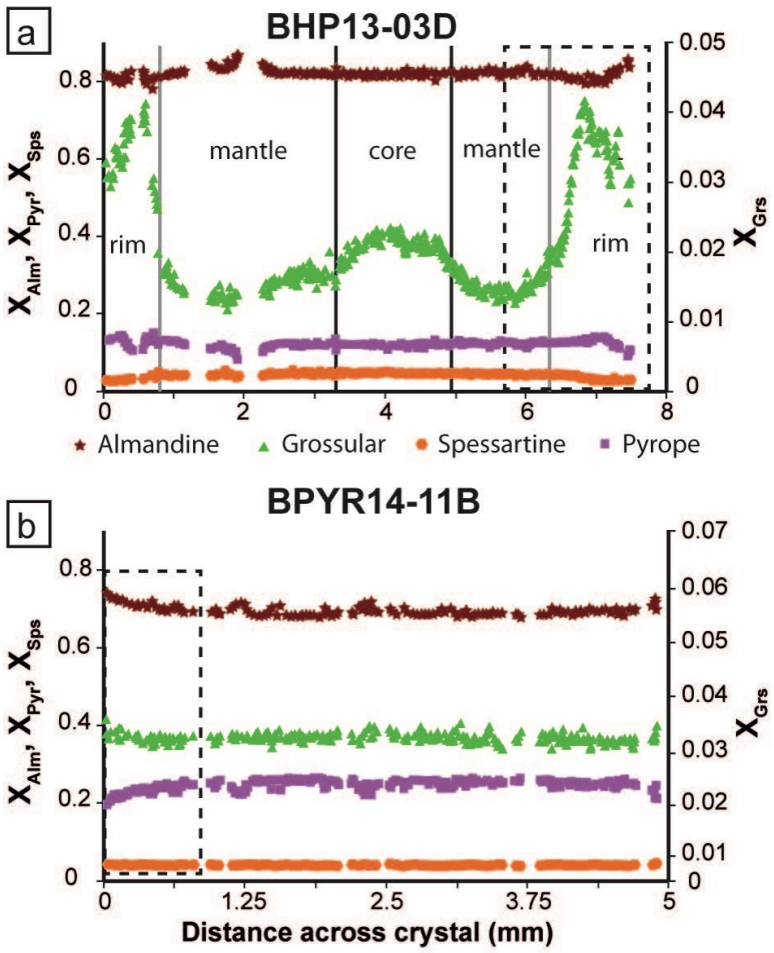

Figure 4.4: Representative garnet major element analyses for (a) sample BHP13-03D (modified from Dragovic *et al*. (2016) and (b) sample BPYR14-11B. Dashed rectangles in both panels highlight the garnet rim in each sample that is displayed in Figs. 4.9 and 4.10.

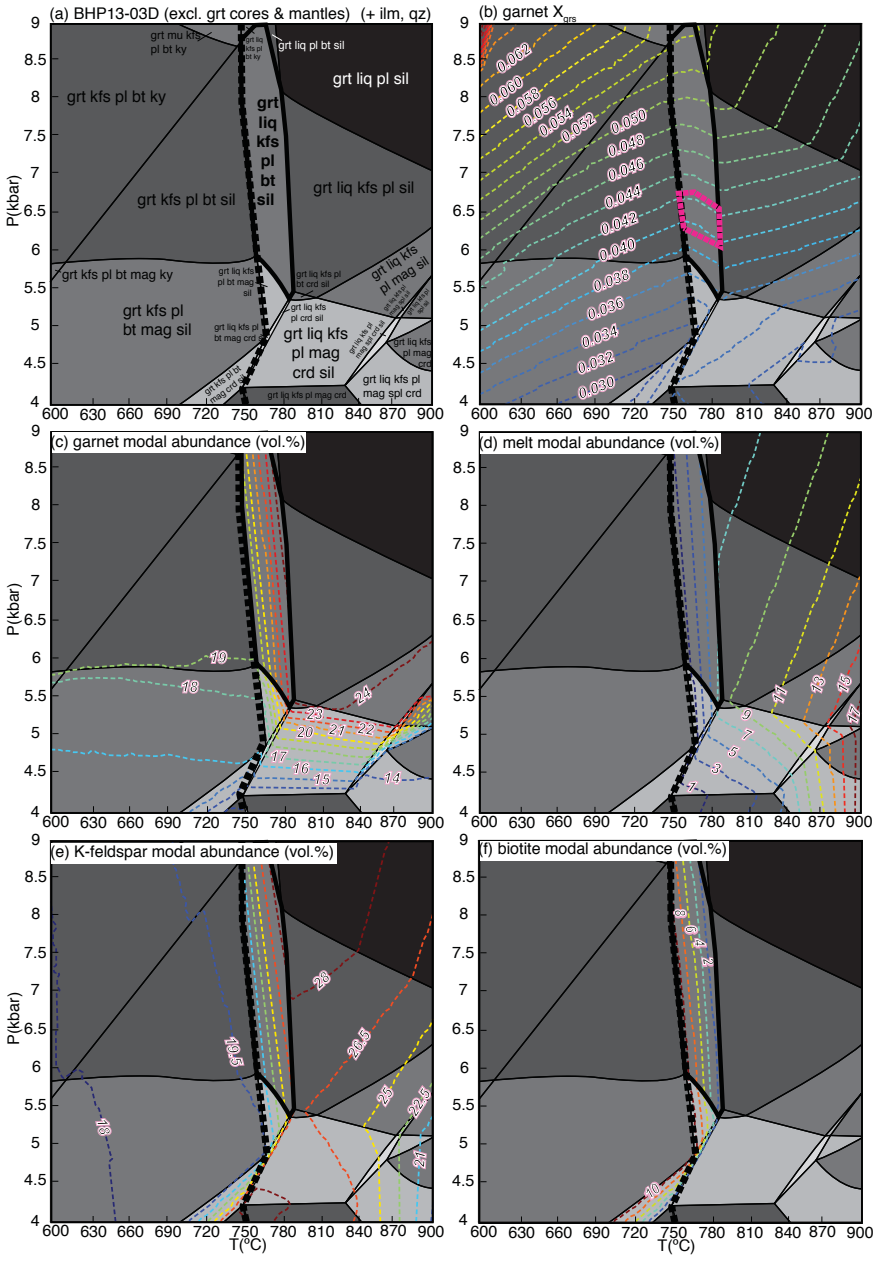

Figure 4.5: Phase equilibria modelling of the effective bulk composition (from an XRF composition) for the growth conditions of the highest-Ca rims in sample BHP13-03D *(volumetrically-weighted average garnet core and mantle chemistries removed)*. (a) *P–T* pseudosection with predicted mineral equilibria labeled. Black, dashed line denotes the solidus. Phase assemblage field outlined in bold denotes inferred assemblage in which biotite and melt coexist. Mineral abbreviations after Whitney and Evans (2010). (b-f) Diagrams contoured for (b) mole fraction grossular, (c) garnet abundance, (d) melt abundance, (e) potassium feldspar abundance, and (f) biotite abundance. Pink, dashed-outline oval in (b) denotes inferred *P–T* conditions based on garnet chemistry and phase abundances.

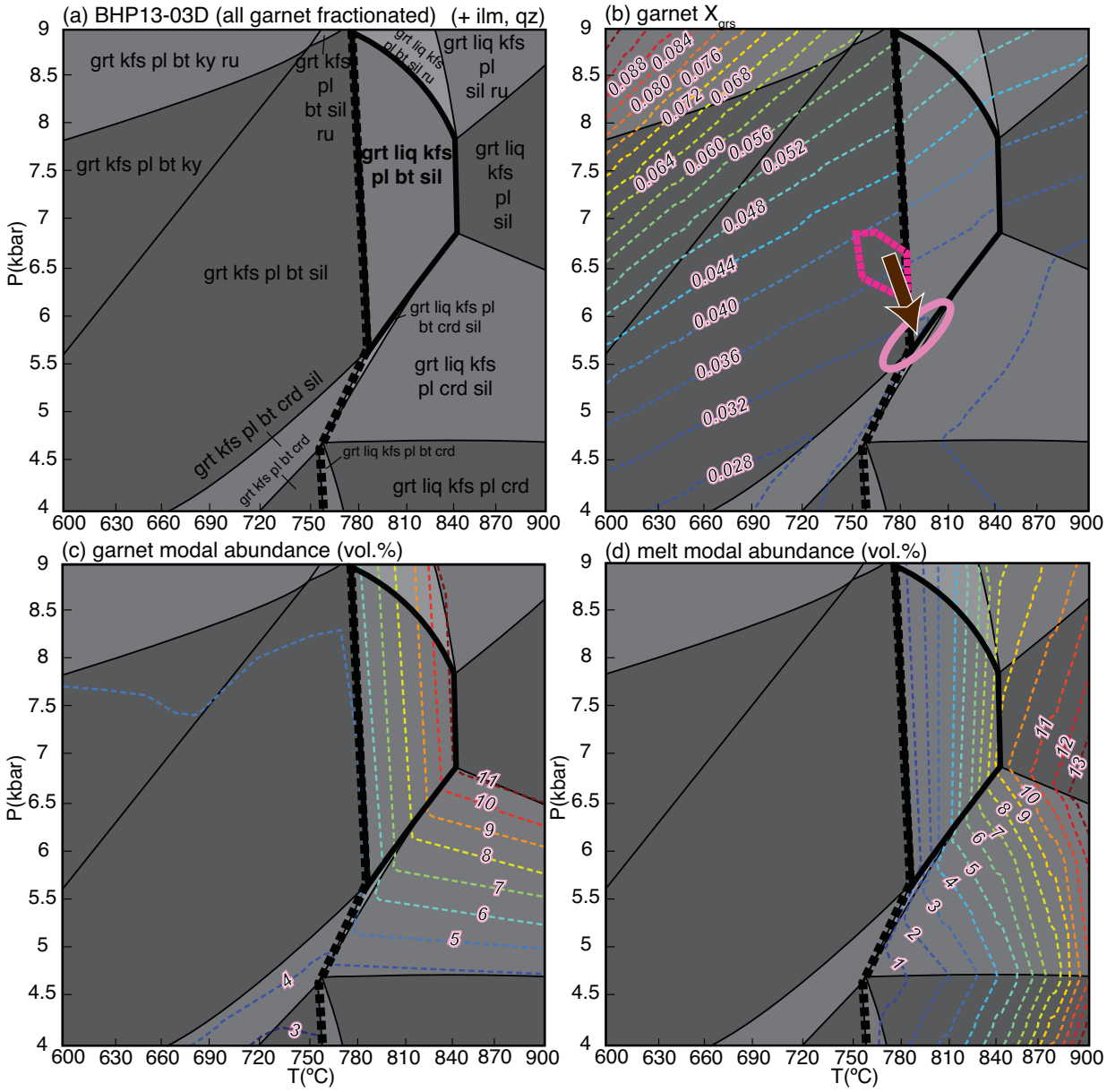

Figure 4.6: Phase equilibria modelling of effective bulk composition (from an XRF composition) for the end of high-Ca garnet rim growth in sample BHP13-03D *(volumetrically-weighted average of all garnet removed)*. Black, dashed line denotes the solidus. Phase assemblage field outlined in bold denotes inferred peak assemblage. (a) *P–T* pseudosection with mineral assemblage labeled. [most mineral abbreviations as in Fig. 4.5; ru = rutile] (b) Mole fraction grossular. Light pink, solid-lined oval denotes inferred *P–T* conditions for the end of garnet growth based on garnet chemistry and phase abundances. Deep pink, dashed oval denotes inferred *P–T* conditions for the start of high-Ca garnet growth from Fig. 4.5. Arrow denotes inferred *P–T* path between the two ovals. Calculated (c) garnet abundance, and (d) melt abundance.

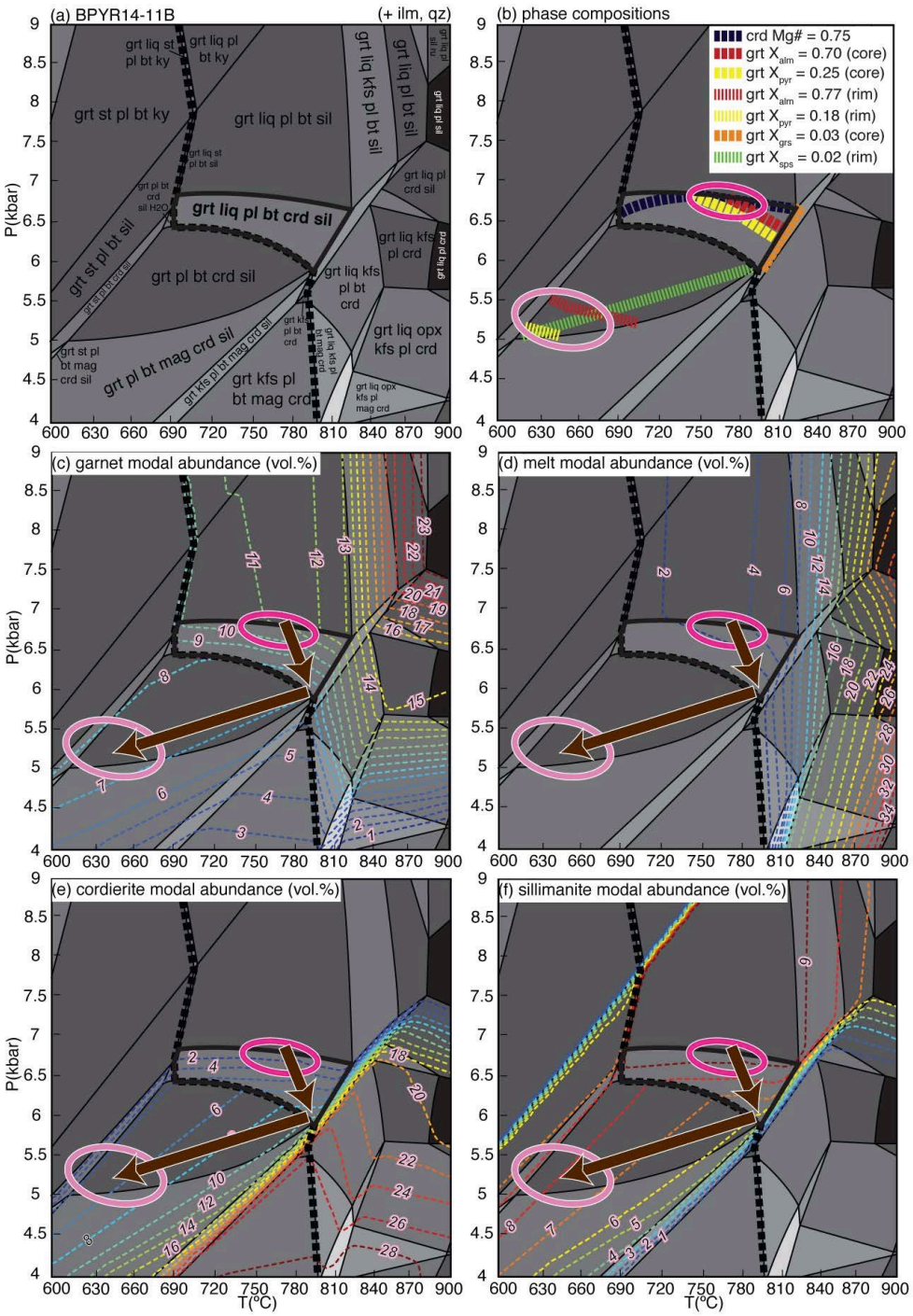

Figure 4.7: Phase equilibria modelling for sample BPYR14-11B. (a) *P–T* pseudosection. Black, dashed line and bold outlined mineral stability field denote the solidus and inferred peak assemblage, respectively. [mineral abbreviations as in Figs. 4.5 and 4.6; st = staurolite; opx = orthopyroxene] (b-f) Diagrams contoured for (b) garnet (core and rim) and cordierite compositional isopleths, (c) garnet abundance, (d) melt abundance, (e) cordierite abundance, and (f) sillimanite abundance. Dark pink outlined oval denotes *P–T* condition at intersecting garnet core and cordierite compositional isopleths. Light pink outlined oval denotes *P–T* condition at intersecting garnet rim isopleths. Arrow denotes inferred *P–T* path.

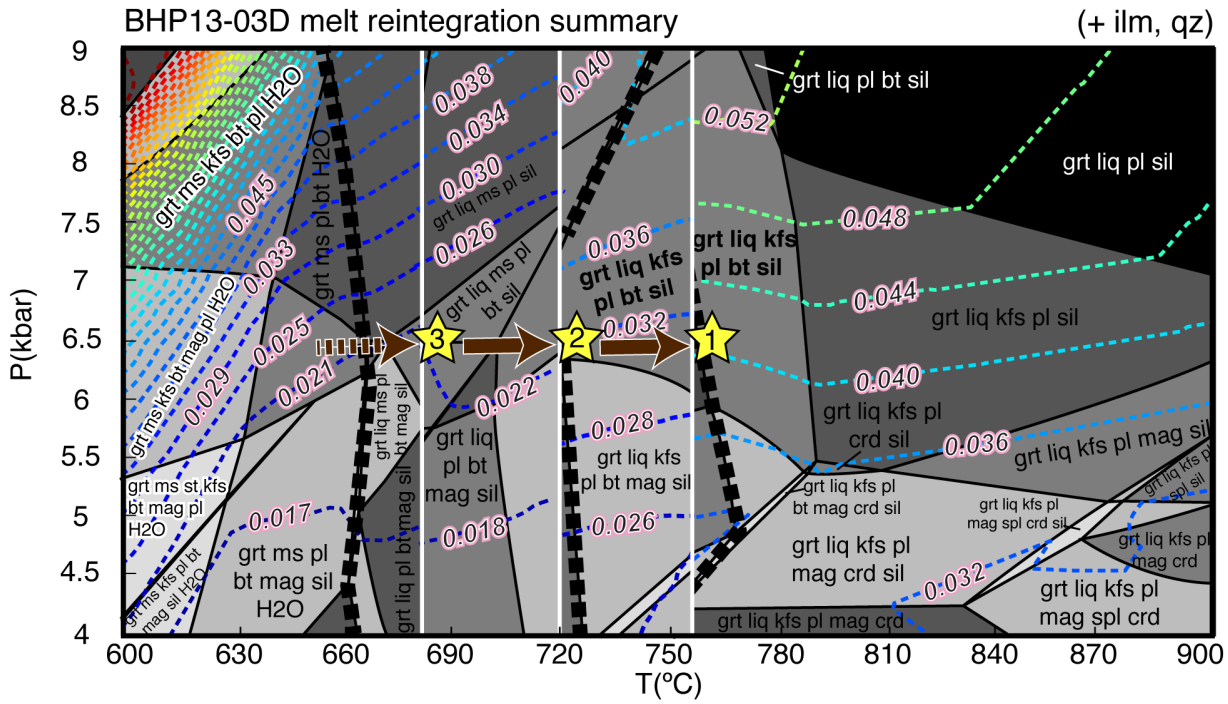

Figure 4.8: Composite *P–T* pseudosection for sample BHP13-03D showing all down-temperature melt reintegration steps until an H_2O-saturated solidus is reached. Each melt reintegration step is represented by a white vertical line, with the *P–T* point at which ~6 vol.% of the predicted melt composition was reintegrated into the bulk composition represented by yellow stars. The number in each star indicates the melt reintegration step. Isopleths shown are for mole fraction of grossular. Solidi are represented by dashed black lines. The far right panel is a segment of the pseudosection shown in Fig. 4.6.

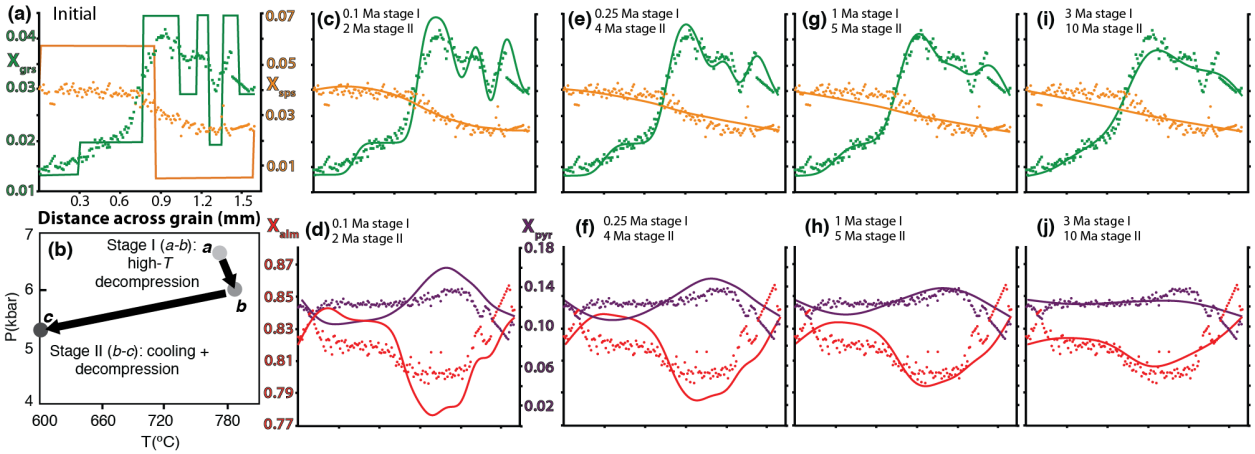

Figure 4.9: Garnet diffusion modelling for sample BHP13-03D. Symbols represent microprobe analyses from near the garnet core (left) towards the garnet rim (right) and lines represent model conditions after a specified duration. (a) Assumed initial chemical zoning of Ca and Mn in garnet. (b) Assumed two-stage *P–T* path taken by sample, consisting of decompressional heating (stage *I*) and cooling and decompression (stage *II*). (c-j) Garnet zoning profiles after diffusive modification for various timescales of stages I and II. Panels c, e, g, and i show profiles of mole fraction of grossular and spessartine. Panels d, f, h, and j show profiles for mole fraction of almandine and pyrope.

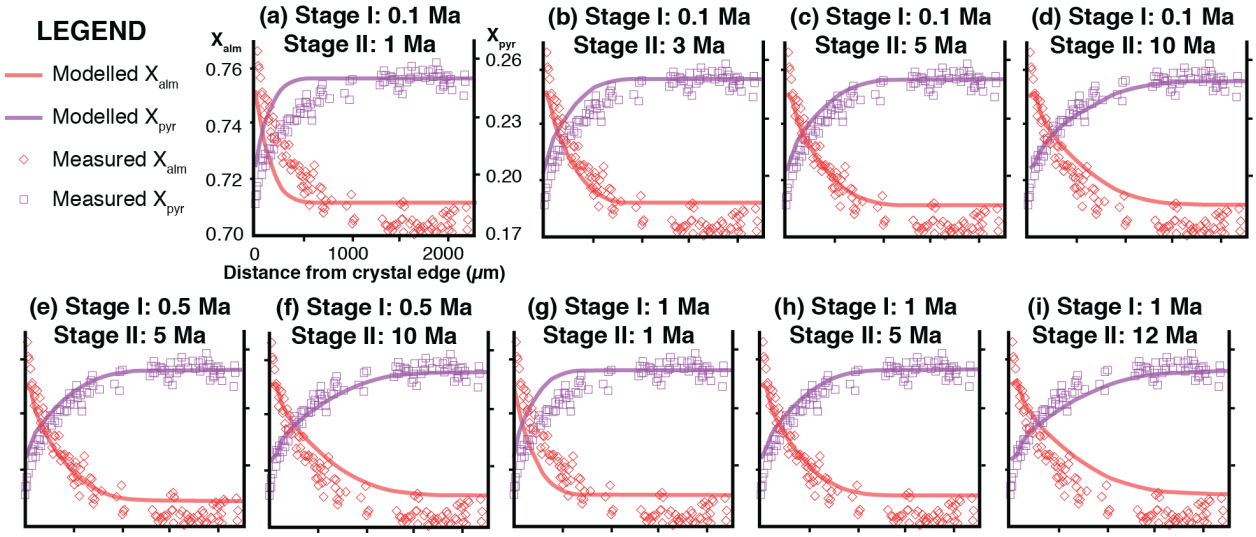

Figure 4.10: Garnet major element diffusion modelling for sample BPYR14-11B as a function of various combinations of stage *I* and stage *II* durations, with the *P–T* evolution of these stages as in Fig. 4.9b.

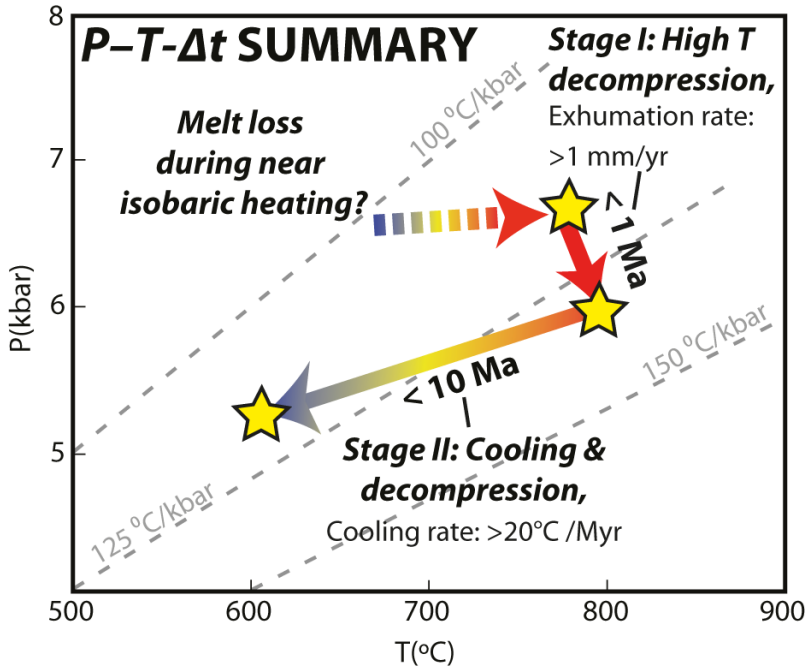

Figure 4.11: Summary of *P–T-Δt* for the eastern Beartooth metasediments from phase equilibria modelling and diffusion modelling from this study. Minimum exhumation and cooling rates are shown. Gray, dashed lines show geothermal gradients of 100, 125, and 150 °C/kbar.

4.12 TABLES

Table 1a: Representative microprobe analyses (wt.%) of garnet cores, mantle (BHP13-03D only), and rims from samples BHP13-03D and BPYR14-11B. Calculated mole fractions of pyrope (X_{pyr}), grossular (X_{grs}), spessartine (X_{spss}), and almandine (X_{alm}) are also shown.

Sample	SiO_2 (wt.%)	TiO_2	Al_2O_3	MgO	CaO	MnO	FeO_t	Na_2O	K_2O	Total	X_{pyr}	X_{grs}	X_{spss}	X_{alm}
BHP13-03D (core)	38.48	0.01	21.43	2.96	0.81	1.85	37.02	0.01	0	102.58	0.12	0.02	0.04	0.82
BHP13-03D (mantle)	38.38	0.03	21.64	3.08	0.51	1.83	37.32	0.02	0	102.81	0.12	0.01	0.04	0.82
BHP13-03D (rim)	38.86	0.02	21.67	3.31	1.19	1.11	37.74	0	0.04	103.94	0.13	0.03	0.02	0.82
BPYR14-11B (core)	39.53	0.02	22.48	6.66	1.07	0.88	32.88	0.06	0	103.59	0.25	0.03	0.02	0.70
BPYR14-11B (rim)	39.25	0.00	22.46	4.82	1.18	0.80	35.63	0.01	0.01	104.16	0.18	0.03	0.02	0.77

Table 1b: Representative microprobe analysis (wt.%) of cordierite from sample BPYR14-11B. Magnesium number (Mg/(Mg+Fe)) and Iron number (Fe/(Mg+Fe)) are also shown.

Sample	SiO_2 (wt.%)	TiO_2	Al_2O_3	MgO	CaO	MnO	FeO_t	Na_2O	K_2O	Total	Mg#	Fe#
BPYR14-11B	49.01	0.00	34.09	9.84	0.02	0.02	5.64	0.32	0.01	98.94	0.76	0.24

Table 2a: Bulk rock compositions (mol.%) determined by XRF, loss on ignition, and titration for samples BHP13-03D and BPYR14-11B.

Sample	SiO_2 (mol.%)	TiO_2	Al_2O_3	Fe_2O_3	FeO	MnO	MgO	CaO	Na_2O	K_2O	LOI	Total
BHP 13-03D	59.05	1.51	10.60	3.09	11.98	0.67	3.92	0.77	1.26	1.83	5.31	100
BPYR 14-11B	63.74	0.53	9.15	0.36	5.55	0.08	7.30	0.49	1.05	1.46	10.29	100

Table 2b: Bulk rock compositions used for phase equilibria modelling after adjustment of H_2O and Fe_2O_3 content based on T–M_{H2O} and T–M_{Fe2O3} psedosection anlaysis (see text for explanation), and, in the case of BHP13-03D, after volumetrically fractionating different amounts of garnet from the whole-rock composition.

Sample	SiO_2 (mol.%)	TiO_2	Al_2O_3	Fe_2O_3	FeO	MgO	CaO	Na_2O	K_2O	H_2O	Total
BHP13-03D (garnet cores + mantles fractionated)	65.18	1.85	10.88	1.53	10.74	3.94	0.83	0.97	2.26	1.31	100
BHP13-03D (all garnet fractionated)	71.74	2.38	9.90	0.74	5.20	3.51	0.65	1.25	2.91	1.39	100
BPYR14-11B	69.16	0.58	9.93	0.39	6.02	7.72	0.53	0.72	1.58	3.29	100

Chapter 5. Timescales of Archean ultrahigh-temperature metamorphic processes: integration of high-spatial resolution and high-precision U-Pb petrochronology

V.E. Guevara[1], S.A. Maclennan[2], B. Schoene[2], M.J. Caddick[1], B. Dragovic[1,3], A.R.C. Kylander-Clark[4], and C.G. Couëslan[5]

[1]*Department of Geosciences, Virginia Polytechnic Institute and State University, Blacksburg, VA 24061, USA*
[2]*Department of Geosciences, Princeton University, Guyot Hall, Princeton, NJ 08544*
[3]*Department of Geosciences, Boise State University, 1910 University Dr. Boise, ID 83725*
[4]*Department of Earth Science, University of California Santa Barbara, 1006 Webb Hall, Santa Barbara, CA 93106, USA*
[5]*Manitoba Geological Survey, 360-1395 Ellice Ave., Winnipeg, MB R3G 3P2*

Manuscript in preparation for submission to *Journal of Petrology*

5.1 ABSTRACT

Quantifying the timescales of metamorphism is crucial to understanding the mechanisms for crustal heat transfer on Earth. The timescales of metamorphism in Archean terranes remain enigmatic due to a lack of high-precision petrochronology studies, in which isotopic dates are coupled with trace element geochemistry, which can be closely linked to the petrologic evolution of a rock. This study combines quantitative thermobarometry and U-Pb monazite (mnz) and zircon (zrn) petrochronology using high-spatial resolution laser ablation split-stream inductively coupled mass spectrometry (LASS) and high-precision isotope dilution thermal ionization mass spectrometry + solution ICP-MS trace element analyses (ID-TIMS-TEA) on a combination of *in-situ* grains and separated grain fragments to place constraints on the timescales of ultrahigh temperature (UHT) metamorphic processes recorded by a single hand sample.

We show that the rock, which is from the Archean Pikwitonei granulite domain on the northwest edge of the Superior Province, records peak *P–T* conditions of ~920-970 °C, 8.5-9 kbar and followed a *P–T* path characterized by UHT decompression followed by near-isobaric cooling at ~7.5-8 kbar. *In-situ* LASS monazite analyses provide important information on the prograde metamorphic history of the sample, showing multiple generations of monazite growth concurrent with or after garnet growth and feldspar breakdown from >2700 Ma to ~2675 Ma. Younger monazite populations suggest melt crystallization at ~2655-2650 Ma. *In-situ* LASS zircon data could be interpreted to record a single episode of zircon growth at ~2665 Ma due to identical weighted mean ages between texturally different zircon populations, apparent homogeneity of REE content among the zircon spot analyses, and the high age uncertainties of LASS spot dates. By contrast, the TIMS-TEA zircon data reveal a more complex zircon crystallization history, with at least five apparently distinct episodes of zircon growth over a ~23 Ma period from ~2673 to 2650 Ma, with REE chemistry of grain fragments within each group suggesting variable feldspar growth and dissolution during this period. TIMS analyses of monazite show a similar apparent episodicity. This could record zircon/monazite growth in response to dynamic petrologic processes within localized equilibrium domains such as zircon/monazite melt saturation in isolated melt pockets, fluxing of externally-derived melt, or different local effective bulk compositions during melt crystallization.

This study highlights how *in-situ* LASS and ID-TIMS-TEA can be used as complementary techniques to constrain the metamorphic histories of Archean rocks: the high-spatial resolution *in-situ* LASS technique allowed for sampling of a volumetrically small prograde monazite population, while high-precision ID-TIMS-TEA reveals a complex accessory phase crystallization history that is not apparent in the LASS data. Collectively, the data suggest a long duration (>50 Ma) of high temperature conditions in the Pikwitonei granulite domain, and could reflect either multiple heating and cooling episodes or a single, long-lived metamorphic cycle, characterized by decompression at UHT conditions followed by near-isobaric cooling in the middle to lower crust.

5.2 INTRODUCTION

Crustal metamorphism is a consequence of heat and mass transfer driven by plate tectonic processes. Ultrahigh-temperature (UHT) metamorphic terranes record temperatures in excess of 900 °C, and their ubiquity in Archean cratons (e.g. Brown, 2008) implies that Earth's early continental crust sustained extreme geothermal gradients, but the geodynamic mechanisms for generating extreme crustal heat flux on the Archean Earth and their implications for Archean tectonic style remain elusive (e.g. England & Bickle, 1984; Brown, 2008; van Hunen & Moyen, 2012). Geodynamic drivers for crustal heating may occur over different timescales (and thus different length-scales, e.g. Carslaw & Jaeger, 1959; England & Thompson, 1984), and therefore quantifying metamorphic timescales recorded by rocks is crucial to understanding: 1) the mechanisms that drive crustal mass and heat transfer, and 2) how these mechanisms have evolved through Earth history.

Recent breakthroughs in the development and application of various petrochronologic techniques such as *in-situ* U-Pb accessory phase geochronology combined with trace element analyses, Lu-Hf and Sm-Nd garnet geochronology, and diffusion geospeedometry (e.g. Caddick *et al.*, 2010; Baxter & Scherer, 2013; Kohn, 2016) have led to robust constraints on durations of regional metamorphism at modern (Phanerozoic) tectonic plate margins (e.g. Ague & Baxter, 2007; Kylander-Clark *et al.*, 2012; Dragovic *et al.*, 2015; Chakraborty *et al.*, 2016), but the timescales of Archean UHT metamorphism remain particularly enigmatic. The extreme thermal conditions attained during UHT metamorphism result in rapid intracrystalline diffusion, which imposes limits on the utility of isotopic and geospeedometric tools through isotopic resetting, mineral dissolution into partial melts, and flattening of compositional zoning in minerals through diffusion (e.g. Kelly & Harley, 2005; Kooijman *et al.*, 2010; Kelsey & Powell, 2011; Baxter & Scherer, 2013; Yakymchuk & Brown, 2014b; Harley, 2016).

Many studies of UHT terranes have thus utilized isotopic systems with estimated closure temperatures above UHT, such as U-Pb in zircon and/or monazite (Cherniak & Watson, 2001; Cherniak *et al.*, 2004), with recent studies coupling *in-situ* isotopic measurements (e.g. SIMS, LA-ICPMS, EPMA) with trace element analyses to preserve the textural context of the dated crystals and geochemically link dates of accessory phase growth with the growth and breakdown of major phases (e.g. Baldwin & Brown, 2008; Korhonen *et al.*, 2013; Dumond *et al.*, 2015; Johnson *et al.*, 2015). However, these high-spatial resolution *in-situ* techniques are prone to large

age uncertainties when applied to Precambrian settings (typically on the order of ~10^1 Ma), which in some cases may be greater than the metamorphic duration. On the other hand, isotopic analysis of separated grains or grain fragments via isotope-dilution thermal ionization mass spectrometry (ID-TIMS) can result in age uncertainties < 1 Ma for Archean rocks (e.g. Baldwin *et al.*, 2003; Schoene & Bowring, 2010; Heaman *et al.*, 2011), but lack spatial, textural, and/or geochemical context, potentially leading to ambiguity over the petrologic significance of isotopic dates.

The recently developed TIMS-TEA method integrates high precision U-Pb ID-TIMS accessory phase geochronology on whole crystals of microsampled crystal fragments with trace element analyses (TEA) via solution ICP-MS of the dated crystal volumes. This approach has been successful in revealing the timescales of rapid petrologic processes of igneous systems (e.g. Barboni *et al.*, 2013; Samperton *et al.*, 2015) and ultrahigh pressure metamorphism (DesOrmeau *et al.*, 2014; DesOrmeau *et al.*, 2015), but otherwise remains underexplored for deciphering metamorphic timescales.

Here we apply two different approaches to U-Pb zircon and monazite petrochronology on a single hand sample of UHT granulite: 1) high-spatial resolution *in-situ* laser ablation split stream (LASS) ICP-MS on grains in thin section, and 2) high-precision TIMS-TEA on microsampled fragments of separated monazite and zircon grains. We use the results to infer the timing and timescales of metamorphic processes recorded by the sample, which is from the Archean Pikwitonei Granulite Domain (PGD) in Manitoba, Canada, and compare this information with previous studies to evaluate previous interpretations of the crustal heating mechanism in the PGD.

5.3 GEOLOGIC BACKGROUND

The PGD in Manitoba, Canada is a large (>15,000 km^2) HT/UHT (HT > 750 °C) metamorphic terrane situated along the northwestern margin of the Superior Province, Earth's largest Archean craton (Fig. 5.1a). It forms part of the Hudson Bay Terrane, distinguished from crust of the North Caribou Terrane to the south by its ancient (3.5-4.2) Nd model ages (e.g. Percival, 2012). Collision between the Hudson Bay and North Caribou Terranes is believed to have occurred at ~2720 Ma via subduction-accretion-style processes (Percival, 2012). The PGD is bounded on the west and north by Paleoproterozoic metasediments and retrogressed Archean granulites (presumed to be reworked PGD) that were metamorphosed during the

Paleoproterozoic Trans-Hudson orogen, and on the south by a prominent high-strain zone separating it from the lower-grade granite-greenstone belts of the North Caribou Terrane (Fig. 1a). The adjacent Split Lake Block north of the PGD records a similar Archean HT metamorphic history to the PGD and here are considered part of the PGD to simplify discussion (Fig. 1; Böhm *et al.*, 1999; Bowerman, 2008; Downey *et al.*, 2009).

The PGD consists primarily of orthopyroxene-bearing metagranitoids, along with less prominent meta-anorthosites, enderbites, and metagabbros. Metasedimentary packages consisting of interbedded metamorphosed banded iron formations, metavolcanics, quartzites, metawackes, and aluminous pelites occur as m- to km-scale bands/rafts within the metagranitoids (e.g. Hubregtse, 1980; Weber, 1987; Couëslan, 2013; Couëslan & Guevara, 2015). A range of peak pressure-temperature (*P–T*) conditions has been reported for the PGD from different locations using a variety of thermobarometric techniques (e.g. Arima & Barnett, 1984; Mezger *et al.*, 1990; Bowerman, 2008; Kooijman *et al.*, 2012; Couëslan, 2014), suggesting attainment of HT/UHT conditions over several thousand contiguous km^2. The spatial distribution of metamorphic conditions revealed in these studies suggests the presence of a metamorphic gradient in the PGD, with peak *P–T* conditions ranging from ~750 °C, 7 kbar in the southeast PGD in the Cauchon Lake area, to >900 °C, 7.5-9 kbar in the Split Lake, Natawwahunan Lake, and Sipiwesk Lake areas in the northernmost, central and southwestern PGD, respectively (Fig. 5.1a).

Early studies proposed two distinct deformational and metamorphic events in the PGD (e.g. Hubregtse, 1980). The first event (D_1/M_1) is thought to have resulted in widespread amphibolite facies metamorphism with localized granulite conditions. The second event (D_2/M_2) is thought to have involved widespread granulite facies metamorphism throughout the entire PGD (e.g. Heaman *et al.*, 2011). Through high-precision ID-TIMS U-Pb zircon geochronology, Heaman *et al.* (2011) documented four distinct stages of metamorphic zircon growth at 2716, 2695, 2680, and 2642 Ma in samples from the Natawahunan, Sipiwesk, and Cauchon Lake areas (Fig. 5.1a), attributing the first two stages to either the M_1 aphibolite facies or M_2 granulite facies events, though without textural context or trace element compositions of the dated grains, it is difficult to determine the petrologic significance of U-Pb zircon dates (Fig. 5.1b). Three distinct groups of U-Pb garnet ages from the Cauchon Lake area (Mezger *et al.*, 1989) have been interpreted to represent garnet growth during: 1) prograde metamorphism (2700-2687 Ma), 2)

peak metamorphism (2660–2637 Ma), and 3) crystallization of peraluminous granite dykes, marking the end of HT conditions in the PGD (2605–2591 Ma). Lu-Hf (2724-2680 Ma) and Sm-Nd (2628-2610 Ma) bulk garnet dates have been interpreted to record prograde garnet growth (Lu-Hf) and early cooling (Sm-Nd) stages, with the range of ages from both chronometers interpreted as a function of grain size and differential diffusive resetting (Smit *et al.*, 2013). The results from these studies have thus been variably interpreted as reflecting either a single, long-lived (>100 Ma) HT/UHT metamorphic cycle in which the Lu-Hf ages record the timing of prograde garnet growth, a wide spread of U-Pb zircon ages records prolonged HT conditions, and the Sm-Nd garnet ages record cooling (e.g. Smit et al. 2013), or multiple, heating–cooling cycles over a ~80 Ma timespan (Fig. 1b; e.g. Heaman *et al.*, 2011). Late-stage cooling in the PGD through ~500-600 °C is constrained by ~2.45-2.28 Ga U-Pb rutile ages, implying slow cooling of < 2 ºC/Ma (Kooijman *et al.*, 2010).

Recent Sm-Nd whole-rock isotope geochemistry suggests that rocks of the southern PGD have affinity to the North Caribou Terrane, while rocks from the northern PGD have isotopic signatures characteristic of the Hudson Bay Terrane (Couëslan, 2016). Additionally, low-*P*, high-*T* conditions (~575 °C, 3 kbar) have been inferred for rocks south of Cauchon Lake in the Hudson Bay Terrane, with existing geochronology suggesting that this metamorphism was concurrent with peak metamorphism of hotter and deeper rocks of the PGD (Mezger *et al.*, 1990). These observations suggest that metamorphism of the PGD overprints the boundary between the Hudson Bay and North Caribou terranes, and that the heating mechanism responsible for UHT conditions post-dates the ~2720 Ma collision between the terranes.

5.4 METHODS

5.4.1 U-Pb monazite and zircon petrochronology

Our approach to accessory phase petrochronology involves: 1) high-spatial resolution, *in-situ* laser-ablation split stream inductively coupled mass spectrometry (LASS) analysis of zircon and monazite in thin section, in which both isotopic and trace element (REE + Y + P ± Ca ± Sr) analyses were performed the same volume of ablated material, 2) LASS analysis of separated grains of zircon and monazite, and 3) high-precision TIMS-TEA analysis of fragments of the separated grains analyzed by LASS. The details of grain imaging, grain separation, sample preparation, and LASS and TIMS-TEA analyses are presented in Appendix

D. LASS analyses were performed at the University of California, Santa Barbara and TIMS-TEA analyses were performed at Princeton University. LASS U-Pb dates in this paper are presented in the format A ± B [C], in which A is the mean calculated date or concordia intercept date of a group of analyses, B is the 2σ standard error of that mean (or concordia intercept), and C is the long-term reproducibility of laser ablation monazite dates at the UCSB LASS facility (~2% or ~33 Ma for ~2700-2800 Ma samples; e.g. Holder et al., 2015).

5.4.2 Putting 'petro' in petrochronology: Quantitative Thermobarometry

Quantitative phase equilibria modelling combined with microstructural observations and major element chemistry of orthopyroxene, as well as Zr in rutile thermometry were used to estimate peak *P–T* conditions and reconstruct the *P–T* path of the rock in order to provide a petrologic framework upon which isotopic dates can be linked to metamorphic process. The details of these methods are presented in Appendix D.

5.5 SAMPLE DESCRIPTION

The studied sample is an aluminous metapelite collected from the western edge of the PGD in the Partridge Crop Lake area (Fig. 5.1), where Archean granulites are variably retrogressed by Paleoproterozoic amphibolite-facies metamorphism from the Trans-Hudson orogen (Couëslan, 2013). The outcrop consists of coarse- and fine-grained layers (5-30 cm thick, Fig. 5.2a), with the sample studied here coming from a coarse-grained layer. Coarse-grained layers primarily consist of garnet and orthopyroxene porphyroblasts ~0.1-2 cm in diameter, as well as quartz, plagioclase, rutile, ilmenite, minor sillimanite and biotite, and accessory zircon and monazite (Fig. 5.2). Fine-grained layers exhibit the same assemblage but contain less garnet, smaller orthopyroxene porphyroblasts (up to 1 cm in diameter), prismatic sillimanite, cordierite, and ternary feldspar (Fig. 5.2a-b). The assemblage orthopyroxene + sillimanite ± garnet indicates that this rock reached UHT conditions (e.g. Kelsey & Hand, 2015). Within ~10-30 m of well-preserved granulite facies mineral assemblages, the same lithology is retrogressed to amphibolite facies assemblages, with kyanite blades up to 1 cm long and garnet porphyroblasts replaced by fine-grained biotite (Fig 5.2c). The retrogression is interpreted as recording fluid flow and recrystallization during Paleoproterozoic Trans-Hudsonian metamorphism (Couëslan, 2013).

In thin section, garnet porphyroblasts are subhedral with inclusion-free mantles and rims, and cores with inclusions of rounded quartz and plagioclase blebs, subhedral to euhedral rutile,

ilmenite, apatite, zircon, and monazite (Fig. 5.2d). Polymineralic inclusions are comprised of rounded plagioclase + quartz ± rutile ± K-feldspar ± biotite ± monazite ± apatite. Relatively inclusion-free garnet mantles contain sparse small (< 50 μm wide) stubby sillimanite inclusions, as well as oriented exsolution needles of apatite and rutile, which have been observed in other UHT rocks (Axler & Ague, 2015). Rare sapphirine occurs as small (~50 μm) anhedral inclusions in orthopyroxene (Fig. 5.2e). Orthopyroxene porphyroblasts are subhedral and contain thin (1-5 μm), oriented exsolution needles of sillimanite, indicating high Al content. Indeed, orthopryoxene cores contain up to 10-11.2 wt.% Al_2O_3 (y(Al) = 0.21-0.24, Fig. 5.2f; Table D1). Orthopyroxene is zoned, with the highest Al content in the core, and a sharp decrease near the rim to 7.4 wt.% Al_2O_3 (y(Al) = 0.16 (Fig. 5.2f). Orthopyroxene compositions across the traverse indicated in Fig. 5.2f, with representative compositions shown in Table D1. Othopyroxene contains garnet inclusions and in some cases partially surrounds garnet (Fig. 5.2g). Quartz, plagioclase, and minor K-feldspar dominantly occur as coarse (1-2 mm diameter), rounded grains in the matrix, with this type of quartz containing thin (1-5 μm thick) oriented rutile needles (interpreted to result from Ti exsolution, Fig. 5.2h). Quartz and plagioclase also occur as fine-grained intergrowths with each other, interpreted to represent pseudomorphs after grain boundary melt (e.g. Holness *et al.*, 2011). These intergrowths form distinct rims and bands that follow grain boundaries, surround coarse-grained quartz, feldspar, and garnet porphyroblasts, and fill in triple junctions between them (Fig. 5.2i).

. Rutile occurs as subhedral to euhedral grains in the matrix and on the edge of resorbed garnet. Some rutile grains contain thin (1-5 μm thick), oriented zircon needles interpreted to result from Zr exsolution. Rare, fine-grained sillimanite occurs in the matrix. Minor biotite occurs in the matrix as large flakes surrounding orthopyroxene, garnet, rutile, and ilmenite porphyroblasts, and filling in embayments in garnet and orthopyroxene. Minor, localized metasomatic alteration of the rock is evident in thin section: feldspars are partly sericitized (Fig. 5.2i), some grain boundaries are lined by fine-grained biotite ± chlorite, and some garnet fractures are filled in with biotite and/or chlorite. The inferred equilibrium assemblage at peak *P–T* conditions is interpreted to be garnet + orthopyroxene + quartz + plagioclase + rutile + ilmenite ± sillimanite ± K-feldspar ± sapphirine.

5.5.1 Zircon and monazite petrography

Monazite and zircon both occur as sub- to euhedral grains as inclusions in garnet, on the edges of resorbed garnet, and in matrix quartz. Zircon is also found as inclusions in rutile (included in garnet). Monazite also occurs as grains in polymineralic inclusions in garnet typically with quartz, feldspar, rutile and biotite. Monazite and zircon grains are ~50-500 μm across and exhibit a wide range of shapes and internal zonation textures (described and shown in Figs. 5.3 & 5.4). There is no obvious correlation between internal zonation/grain morphology of zircon/monazite and textural setting.

5.6 RESULTS

5.6.1 *In-situ* LASS: Zircon

Eleven zircon grains were analyzed by LASS in thin section (sixty one spot analyses), with individual $^{207}Pb/^{206}Pb$ spot dates ranging from 3178 ± 35 to 2502 ± 37 Ma (Table D2). After filtering out analyses of detrital cores (identified based on BSE images, spot date, and chemistry), analyses that mix domains, and analyses that plot off concordia, a 'metamorphic' zircon population of forty-three spot analyses yield $^{207}Pb/^{206}Pb$ spot dates from 2743 ± 42 to 2634 ± 41 Ma. Most analyses cluster between 2687 to 2634 Ma, approximating a normal bell-curve shaped distribution with a single peak at ~2662 Ma (Fig. 5.5a). These analyses exhibit similar REE chemistry to each other (Fig. 5.5b, Table 5.1), with negative Eu anomalies (Eu/Eu* = 0.04-0.11) and flat HREE profiles (Lu_n/Dy_n = 0.7-2.5, with one outlier; Fig. 5.5b). Th/U varies from 0.02 to 0.6, showing no correlation with spot date (Fig. 5.5c, Table 5.1). Inclusions in garnet and rutile generally give lower Th/U than matrix grains, though their ranges overlap. The weighted mean age of all analyses that overlap concordia is 2664 ± 6 [42] Ma (with two outliers filtered out, Fig. 5.5d). Weighted mean ages derived by grouping the analyses by textural setting (e.g. inclusions in garnet, matrix grains) give nearly identical weighted mean ages within uncertainty (Fig. 5e-f). Ti concentrations range from 12 to 46 ppm (Table 5.1, D2), yielding calculated Ti in zircon temperatures using the calibration of Ferry and Watson (2007) from 767 ± 35 to 913 ± 77 °C, with a weighted mean of 833 ± 6 °C (MSWD = 1.9). The two oldest analyses that give spot dates of 2743 ± 42 and 2735 ± 39 give Ti in zircon temperatures of 852 ± 40 and 845 ± 38 Ma, respectively (Table D2).

5.6.2 *In-situ* LASS: Monazite

Nine monazite grains were analyzed by LASS in thin section (eighty-four spot analyses), with individual $^{207}Pb/^{206}Pb$ spot dates ranging from 2747 ± 33 to 2219 ± 41 Ma (Table D3). Eighty analyses overlap concordia within 2σ uncertainty, with most clustered from ~2747 to 2616 Ma, and younger ages < 2600 Ma spread along concordia (Fig. 5.5g). REE, Sr, and Th/U content are variable, and we categorized analyses into five chemically distinct groups based on age and chemical signature (Fig. 5.5h-l, Table 5.2).

Group 1 (three analyses from the low-Y core of a grain included in garnet, Fig. 4a) is characterized by a weak positive Eu anomaly (Eu/Eu* = 0.90-1.26), steep HREE profile (Gd_n/Yb_n = 491-1251), high Sr (38-54 ppm), low Y (847-2000 ppm) and Th/U = 12-17, with $^{207}Pb/^{206}Pb$ spot dates of 2747 ± 33 to 2711 ± 33 Ma. These analyses give a concordia age of 2705 ± 25 [33] Ma (MSWD = 7.4) and a weighted mean age of 2726 ± 47 [33] Ma (MSWD = 1.3, Fig. 5.5m). Group 2 (three analyses from a high-Y core of a grain included in garnet, Fig. 4b) also lacks a negative Eu anomaly (Eu/Eu* >1), exhibits shallow HREE profiles (Gd_n/Yb_n = 24-27), lower Sr than Group 1 (11-14 ppm), high Y (12700-12800 ppm), and low Th/U (~3), with $^{207}Pb/^{206}Pb$ spot dates of 2688 ± 33 to 2679 ± 33 Ma, and give a concordia age of 2685 ± 11 [33] Ma (MSWD = 0.43, Fig. 5.5m) and a weighted mean age of 2685 ± 19 [33] Ma (MSWD = 0.099). Group 3 (nine analyses) exhibits a steeper HREE slope than Group 2 (Gd_n/Yb_n = 86-327), a weak negative Eu anomaly (Eu/Eu* = 0.44-0.90), similar Sr (10-18 ppm), and low Th/U (6-8). $^{207}Pb/^{206}Pb$ spot dates range from 2688 ± 33 to 2649 ± 33 Ma and give a concordia age of 2674 ± 7 [33] Ma (MSWD = 1.04, Fig. 5.5m) and a weighted mean age of 2675 ± 11 [33] Ma (MSWD = 0.76, Table 2). Group 3 analyses come from patchy overgrowths (Fig. 5.4a) or resorbed cores (Fig. 5.4e) of grains included in garnet. Group 4 (nineteen analyses) is characterized by strong negative Eu anomalies (Eu/Eu* = 0.18-0.34) and similar HREE slopes to Group 3 (Gd_n/Yb_n = 145-293; average of 184), low Sr (4-10 ppm) and low Th/U (< 33), with $^{207}Pb/^{206}Pb$ spot dates ranging from 2670 ± 34 to 2628 ± 35 Ma and give a weighted mean age of 2652 ± 8 [35] Ma (MSWD = 0.45, Fig. 5.5n). These analyses come from high-Y, low-Th domains as rims (Fig. 5.4a, g) or euhedral cores (Fig. 5.4c), and from one grain intergrown with biotite in a garnet fracture. Group 5 (thirty-five analyses) gives a nearly identical REE profile to group 4, but with stronger negative Eu anomalies (Eu/Eu* = 0.13-0.20), higher total REE content, and higher Th/U (46-120) than the other groups. The higher Th/U is due to both Th

enrichment and U depletion compared to group 4. $^{207}Pb/^{206}Pb$ spot dates range from 2682 ± 40 to 2616 ± 36 Ma and a weighted mean age of 2656 ± 6 [40] Ma (MSWD = 0.82, Fig. 5.5o). These analyses come from cores, mantles, and rims of grains included in garnet (Fig. 5.4c, e, g). In some cases, group 5 monazite is overgrown on group 4 monazite (Fig. 5.4c), but in other cases the opposite occurs (Fig. 5.4e, g).

Fifteen analyses with anomalously young $^{207}Pb/^{206}Pb$ spot dates (2603-2217 Ma) come exclusively from grains in the matrix outside resorbed garnet, or as inclusions in late-stage biotite filling in voids between partially resorbed garnet porphyroblasts (Fig. 5.5g). These young spot dates come from grains that contain group 4 and 5 analyses (e.g. Fig. 5.4g). These analyses range from 2 to -3% discordance, with eleven analyses overlapping concordia within 2σ uncertainty. These dates form two weakly defined age clusters: one group (Group 6) consists of three analyses with a weighted mean $^{207}Pb/^{206}Pb$ age of 2592 ± 19 [34] Ma (MSWD = 0.71) and REE profiles similar to that of Groups 4 and 5 (Fig. 5.5h). Another group (Group 7) consists of five analyses that give a concordia age of 2504 ± 16 [36] Ma (MSWD = 0.1) and a weighted mean $^{207}Pb/^{206}Pb$ age of 2504 ± 16 Ma (MSWD = 0.69). Most of these analyses have similar REE chemistry to groups 4 and 5 but two analyses have elevated MREE, HREE, and Y (Fig. 5.5h). Three other analyses are significantly younger and do not fall into either of these age groups (Fig. 5.5g).

5.6.3 TIMS-TEA + LASS on separated grain fragments: Zircon

Thirty fragments were broken off from twelve separated zircon grains for TIMS-TEA petrochronology (Table D4). These fragments comprised pieces of apparently unzoned grains (Fig. 3g, h, l), rims overgrown on detrital cores (Fig. 5.3i-k), or core + rim mixtures (Fig. 5.3j, k). Twenty-seven of these fragments were analyzed by LASS prior to dissolution and TIMS-TEA analysis. Through BSE imaging and LASS analysis, ten fragments were identified as consisting of multiple age and/or chemical domains and are not considered here for petrochronologic interpretation, as isotopic dates and chemical analyses from these fragments would be spuriously mixed and thus difficult to interpret. TIMS analysis of the fragments that appear homogeneous in BSE images (twenty-two analyses) exhibit variable amounts of discordance, ranging from -8.15 to 0.60 % (Fig. 5.6a, Table D4). Isotopic analyses of fifteen fragments from nine grains overlap concordia within 2σ uncertainty (Fig. 5.6a-b, Tables 5.3, 5.4), with $^{207}Pb/^{206}Pb$ dates ranging from 2673.4 ± 1.0 to 2649.6 ± 2.20 Ma. These dates do not form a single, bell-curve shaped

distribution (as with the LASS zircon data), but rather multiple distinct peaks on a probability density plot (Fig. 5.6b). However, we note that such peaks may simply be the result of the extremely low age uncertainties and/or having a small dataset (n = 15). From this data, at least five temporally distinct generations of zircon over a 23.8 ± 2.4 Ma span are observed (Fig. 5.6c): a 3.6 ± 1.4 Ma period of apparently continuous zircon crystallization from ~2673-2670 Ma (n = 8, generation 1), followed by apparent episodes (based on weighted mean ages of distinct date groupings) at 2666.2 ± 1.2 (n = 1 (generation 2), 2661.4 ± 1.4 (n = 2, generation 3), 2657.1 ± 0.7 (n = 3, MSWD = 0.31, generation 4), and 2649.6 ± 2.2 Ma (n = 1, generation 5).

Trace element chemistry is variable both within and among each zircon generation (Fig. 5.6d-i, Table 5.3), but some trends are apparent in the dataset. In general, Th/U varies widely within each generation, but this variation is narrower in the younger generations (Fig. 5.6d). Eu/Eu* shows a similar trend, with a wide spread from positive to negative Eu anomalies in generation 1, and less variation (weak negative Eu anomalies) in subsequent generations (Fig 5.6e, g-i). In contrast, variations in HREE (Lu_n/Dy_n) are small in generation 1, which exhibits the lowest Lu_n/Dy_n, while Lu_n/Dy_n values as well as the spread in Lu_n/Dy_n appear to increase in subsequent generations (Fig. 5.6f, g-i). The apparent trends discussed above may be due to the relative lack of data points in younger generations compared to generation 1. Trace element data from fragments that appear homogeneous in BSE and are < 1% discordant but do not overlap concordia (within 2σ uncertainty) are also plotted in Figs. 5.6d-f, and agree with the apparent trends discussed above.

LASS spot analyses on these grain fragments yield $^{207}Pb/^{206}Pb$ spot dates from 2756 ± 33 to 2649 ± 33 Ma (Table D5). With the exception of one fragment, the LASS $^{207}Pb/^{206}Pb$ spot dates are older than the $^{207}Pb/^{206}Pb$ TIMS date of the same fragment, often not overlapping within their uncertainties (Fig. 5.6j). Trace element ratios are generally similar, but absolute concentrations of trace elements determined by LASS spot analyses (both for the separated fragments and *in-situ* analyses) are generally lower than those determined for the grain fragments by solution ICP-MS (Fig. 5.6g-i). Eu concentrations determined by LASS are notably lower (<1-5 ppm vs. 9-44 ppm), thus giving apparently stronger negative Eu anomalies (Fig. 5.6g-i).

5.6.4 TIMS + LASS on separated grain fragments: Monazite

Fourteen fragments were broken off from four separated monazite grains for TIMS-TEA petrochronology. $^{207}Pb/^{206}Pb$ TIMS dates of these fragments range from 2674.7 ± 1.2 to 2616 ±

1.1, with varying levels of concordance, from -2.02 % to 1.34 % (Table D6). Three of these fragments gave $^{207}Pb/^{206}Pb$ TIMS dates that overlap with concordia of 2674.1 ± 1.2 (m2f), 2666.5 ± 1.2 (m1a), and 2665.5 ± 2.4 (m3b) Ma and are used here for petrochronologic interpretation (Fig. 5.6k, Table 5.5). These analyses give Th/U of 28, 122, and 102, respectively. At the time of this writing, solution ICP-MS analyses to determine the trace element contents of these monazite fragments is still in progress.

Two of the fragments that overlap with concordia, m1a and m3b, were analyzed by LASS prior to TIMS analysis (Fig. 5.4h, i). All spot analyses from fragment m1a exhibit similar REE profiles characterized by strong negative Eu anomalies (Eu/Eu* = 0.10-0.14), a range of Th/U (39-192), steep HREE profiles (Gd_n/Yb_n = 315-680), and notable Nd enrichment and Sm depletion (Fig. 5.6l). Seven of ten spot analyses of fragment m1a were reversely discordant (from -2% to -12%), with most coming from both a 20-30 μm wide BSE-bright zone with high-Th/U (131-192) and a ~40 μm wide BSE dark zone with low Th/U (38-52; Fig. 5.4e Table D7). Three spot analyses from fragment 1a that overlap concordia within 2σ uncertainty give $^{207}Pb/^{206}Pb$ dates of 2649 ± 39, 2630 ± 41, and 2621 ± 38 Ma with Th/U ranging from 134 to 162.

Ten spot analyses from fragment m3b are concordant or 1% discordant and give $^{207}Pb/^{206}Pb$ dates of 2660 ± 42 to 2572 ± 34 Ma. These analyses exhibit similar REE profiles to each other, characterized by strong negative Eu anomalies (Eu/Eu* = 0.11-0.2) and steep HREE profiles (Gd_n/Yb_n = 205-311). Th/U varies from 7 to 121. REE profiles of LASS analyses from m3b are enriched in M-HREE compared to fragment m1a, but with similar Gd_n/Yb_n (Fig. 5.6l).

5.6.5 Quantitative Thermobarometry

Thermodynamic Modelling

The results of thermodynamic modelling are shown in Fig. 5.7a-d. The bulk compositions determined by XRF and used for phase equilibria modelling after fixing H_2O and Fe_2O_3 contents are shown in Table 5.6. The inferred peak assemblage is predicted to be stable at 900 to >1000 °C, 7.5-8.5 kbar (Fig. 5.7a). Isopleths for predicted y(Al) in orthopyroxene that match the highest measured compositions intersect the field(s) of the peak assemblage at ~920-990 °C (Fig. 5.7b). The sillimanite exsolution needles in orthopyroxene indicate that measured Al contents are minima, and thus these temperatures are taken to be minimum estimates of peak *T*. Isopleths for

the predicted volumetric modal abundances of garnet and orthopyroxene (Figs. 5.7c-d) are sub-horizontal, and agree well with estimates from hand sample and thin section (5-10 vol.% orthopyroxene and 20-25 vol.% garnet). The observed microstructure of orthopyroxene replacing garnet is consistent with decompression at UHT conditions from at least ~8-8.5 kbar. Cordierite is predicted to form below 7.5-8 kbar, and the lack of cordierite in the modelled sample (cordierite-absent coarse-grained layer in the sample description) suggests that cooling below the solidus occurred at >7.5-8 kbar (Fig. 5.7e-f).

Zr in rutile thermometry

Zr in rutile thermometry via LA-ICPMS was performed on rutile grains that contain exsolved zircon needles, as such exsolution is indicative of formerly high Zr concentrations, and thus equilibration/growth at high temperatures (e.g. Tomkins *et al.*, 2007). Large laser spot diameters (40-100 μm) were used so that the exsolved zircon would be reintegrated to the measured Zr concentration, thus approximating an original, pre-exsolution composition (e.g. Pape *et al.*, 2016; Mitchell & Harley, 2017). Three large (100-1000 μm across) rutile grains were analyzed. One grain (r12) occurs with perthitic K-feldspar and monazite as part of a polyphase inclusion in garnet, another grain (r13) occurs as an inclusion in the rim of garnet, and the third grain (r19) occurs as an inclusion in orthopyroxene (Fig. 5.7e). Temperatures were calculated using the calibration of Tomkins *et al.* (2007) at P = 8 kbar (as constrained by the pseudosection) with uncertainties on temperature incorporating a ± 1 kbar P uncertainty in the pseudosection (e.g. Palin *et al.*, 2016).

The results of Zr in rutile analyses and calculated apparent temperatures are shown in Table 5.7. The calculated apparent temperatures indicate rutile growth/equilibration at UHT conditions, ranging from 889 ± 33 °C to 970 ± 36. Weighted mean apparent temperatures of analyses from grains r12, r13, and r19 are 943 ± 20 °C (MSWD = 0.96), 903 ± 9.2 °C (MSWD = 0.29), and 962 ± 20 °C (MSWD = 0.13), respectively, and overlap with the field(s) of the peak assemblage in the pseudosection (Fig. 5.7f, Table 5.7). Taken together, the thermodynamic modelling and Zr in rutile thermometry suggest that the rock reached peak UHT conditions of 8-8.5 kbar, 920-970 °C. Microstructural observations combined with pseudosection constraints suggest decompression at UHT conditions, followed by near-isobaric cooling at ~7.5-8 kbar (Fig. 5.7f).

5.7 DISCUSSION

5.7.1 *In-situ* LASS zircon and monazite petrochronology

In-situ LASS petrochronology of zircon suggests either: 1) metamorphic zircon crystallized over a 109 ± 59 Ma timespan (determined by the difference between the oldest and youngest spot dates), with most zircon crystallizing between 2687 to 2634 Ma, based on the distribution of zircon spot dates, or 2) in a single episode based on identical weighted mean ages (within 2σ uncertainty) of all analyses, of inclusions in garnet, and of matrix grains. Similar REE profiles among the zircon analyses, characterized by negative Eu anomalies and flat HREE profiles, suggest zircon crystallization in the presence of abundant feldspar and garnet (e.g. Rubatto, 2002). Th/U varies widely, with inclusions in garnet and rutile generally giving lower Th/U than matrix grains (but occupying the same range), suggesting dependence of Th/U on either local effective bulk composition or (re)crystallization mechanism. However, any temporal distinction between zircon with different Th/U or in different microstructural settings is unresolvable with this dataset. Calculated Ti in zircon temperatures exhibit a wide range, though there is no correlation between microstructural setting and temperature. One analysis gave a calculated Ti in zircon temperature at UHT (913 °C), but with large uncertainty (± 77 °C). Thus, most of the metamorphic zircon crystallized below peak UHT conditions. The low MSWD (1.9) of the weighted mean apparent temperature of all analyses (833 ± 6 °C) suggests minimal geologic scatter in the dataset and therefore zircon growth may have occurred at similar temperatures, regardless of whether growth was continuous or episodic. Alternatively, local variations in a_{TiO2} combined with varying temperature during zircon growth could result in low scatter among the calculated Ti in zircon temperatures.

Zircon in HT/UHT rocks is expected to dissolve during partial melting, and grow during cooling as partial melt crystallizes (e.g. Baldwin *et al.*, 2007; Kelsey & Powell, 2011; Yakymchuk & Brown, 2014a), often with variations in trace element chemistry (e.g. Möller *et al.*, 2003), consistent with our data. Zircon in our sample therefore may have crystallized from partial melts during cooling, though some zircon grown on the prograde path may have survived: the presence of zircon inclusions in garnet and rutile suggests some zircon growth during prograde garnet and rutile growth prior to peak UHT conditions. Indeed, zircon may grow during prograde metamorphism through subsolidus dissolution/reprecitpitation (e.g. Harley *et al.*, 2007) or even during partial melting via Ostwald Ripening (Nemchin *et al.*, 2001; Gervais & Crowley,

2017). However, our data lacks sufficient resolution to decipher whether garnet/rutile inclusions are older than matrix grains. If so, then some inclusions in garnet/rutile (re)crystallized during cooling, as the weighted mean ages of inclusions in garnet and in rutile are identical to that of matrix grains within uncertainty. Several studies suggest that accessory phase inclusions and their hosts may not be completely isolated from later re-equilibration due to dissolution/reprecipitation, fracturing/healing of the host mineral, or granular exsoultion of zircon from rutile (e.g. see discussion in Kohn, 2016; Mitchell & Harley, 2017). The two anomalously older spot dates >2700 Ma may be interpreted as crystallizing along the prograde path or during an early metamorphic event unrelated to the UHT event. Regardless, the Ti in zircon temperatures from these two analyses indicate HT conditions > 800 °C were attained prior to 2700 Ma.

In-situ LASS petrochronology of monazite reveals several chemically and/or temporally distinct groups. Most of the analyses belong to groups 1-5 (sixty-nine analyses), and the weighted mean ages of these groups are consistent with the range of existing temporal constraints on metamorphism in the PGD (see discussion below, Fig. 1b, 8; e.g. Heaman *et al.*, 2011; Smit *et al.*, 2013). However, fifteen analyses give are distributed along concordia and are younger than metamorphic ages from previous studies in the PGD. These analyses are exclusively from matrix grains and exhibit similar REE chemistries and Th/U to groups 4 and 5, and their apparent spread along concordia could represent previously unidentified metamorphic episodes and monazite growth from 2600-2200 Ma. Some of these young dates overlap with U-Pb rutile ages (2450-2280 Ma) from Kooijman *et al.* (2010) from the southern PGD, as well as a concordant $^{207}Pb/^{206}Pb$ TIMS monazite date of 2444 ± 4 Ma from the Assean Lake Complex north of the PGD (Böhm *et al.*, 2003), which hints at the possibility of a early Paleoproterozoic metamorphic event in the northwest Superior Province. Alternatively, the young dates could be produced by mixing between pre-2600 Ma monazite with thin, younger rims (unidentifiable through X-ray mapping/BSE imaging), or variable amounts of Pb loss during Paleoproterozoic overprinting, causing apparently younger $^{207}Pb/^{206}Pb$ dates. In the mixing scenario, analyses would either be distributed along concordia with no major age clusters, while in the case of Pb loss, analyses would lie along a cord between >2600 Ma and ~1800-1700 Ma. Though most of the analyses appear concordant, the relatively large uncertainties in isotope ratios of each analysis hide any deviations from concordia, and it is possible that these domains experienced Pb

loss. Moreover, variable Pb loss within matrix moanzite could account for the similarity in REE chemistry between the young ages and groups 4 and 5. Monazite could retain original trace element growth compositions but yield younger ages due to Pb loss, and thus more data is needed to discern among the scenarios discussed above.

Monazite groups 1-5 each have distinct trace element chemistries that may be used to link isotopic dates to metamorphic evolution. Groups 1-3 are characterized by weak positive to negative Eu anomalies, while groups 4 and 5 exhibit strong negative Eu anomalies. Variations in Eu anomaly between different monazite groups may be due to: 1) changing oxidation state during monazite crystallization, as monazite only incorporates divalent Eu, and thus would be depleted in Eu in an oxidized system where Eu becomes trivalent (e.g. Holder *et al.*, 2015; Kohn, 2016), 2) monazite crystallization in the presence of modally abundant garnet, which would reduce MREE and HREE in monazite, thus making the Eu anomaly appear weakly negative to positive (e.g. Dumond *et al.*, 2015), or 3) monazite crystallization in the absence or during dissolution of Eu-rich minerals such as plagioclase, K-feldspar, or apatite (e.g. Dumond *et al.*, 2015; Holder *et al.*, 2015). There is no obvious petrologic evidence for changes in oxidation state during metamorphism, and the bulk Fe_2O_3 content derived from titration is low (FeO/Fe_2O_3 = 5.07), suggesting minimal oxidation. Monazite growth in the presence of modally abundant garnet may contribute to the weak Eu anomalies in group 1, as the strong HREE depletion suggests growth in the presence of stable or growing garnet. However, this explanation alone does not account for the HREE and Y enrichment of group 2, which also has a weak negative to positive Eu anomaly, or the strong Eu depletion of groups 4 and 5 (which likely grew in the presence of modally abundant garnet based on their younger weighted mean ages and relative HREE depletion). Eu/Eu* values correlate with both Sr and La + Ce content (Figs. 5.5j-k): analyses with higher Eu/Eu* (representing weak negative to positive Eu anomalies) also generally have higher Sr and La + Ce. Breakdown of apatite and/or feldspar would result in monazite enriched in Eu and La + Ce (e.g. Villaseca *et al.*, 2003), with feldspar breakdown also releasing Sr for monazite to incorporate, while apatite/feldspar growth would have the opposite effect. Likewise, HREE+Y enrichment/depletion also varies among the monazite groups, which may be attributed to the growth or dissolution of HREE-rich phases such as garnet or xenotime during metamorphism.

Groups 1-3 give the oldest weighted mean/concordia ages, with trace element characteristics that we interpret to indicate monazite crystallization during prograde heating from >2705-2675 Ma, prior to peak UHT metamorphism. The weighted mean ages of these monazite groups agree with previous U-Pb zircon and U-Pb and Lu-Hf garnet dates interpreted to date prograde metamorphism in the PGD (Mezger *et al.*, 1989; Heaman *et al.*, 2011; Smit *et al.*, 2013), as well as the two oldest *in-situ* LASS zircon dates presented above, which suggest the rock was at HT conditions (>800 °C) prior to 2700 Ma. Groups 1 and 3 are HREE+Y-depleted with elevated Sr and Eu/Eu*, suggesting monazite growth during or after garnet growth and feldspar dissolution. Group 2 also has a weak positive Eu anomaly but is the most HREE and Y-enriched group, and has less Sr than either groups 1 or 3. The low Sr content suggests either: 1) monazite growth after growth of high-Sr group 1 monazite and complete dissolution of feldspar, or 2) monazite growth during or after apatite breakdown during prograde heating, potentially coincident with partial melting (e.g. Johnson *et al.*, 2015; Yakymchuk, 2017). The HREE + Y enrichment of group 2 monazite indicates growth during or after breakdown of a HREE-rich phase, such as garnet or xenotime. Xenotime is expected to dissolve during suprasolidus heating and partial melting (e.g. Spear & Pyle, 2002), while garnet is typically expected to grow (e.g. Caddick & Kohn, 2013), though some partial melting reactions at ~8-10 kbar with high dP/dT involve garnet as a reactant (White *et al.*, 2014), particularly orthopyrexene-forming reactions that may occur during heating to or at UHT conditions. Evidence for the former presence of xenotime or an early phase of garnet breakdown in our sample is cryptic at best, however, either scenario would produce the HREE enrichment observed in group 2 monazite.

Monazite is expected to dissolve during partial melting (e.g. Yakymchuk & Brown, 2014a), and several mechanisms have been proposed for prograde suprasolidus monazite growth, including: 1) apatite breakdown and LREE saturation of the melt to crystallize monazite (e.g. Johnson *et al.*, 2015; Yakymchuk, 2017), and 2) Ostwald ripening, in which small monazite grains dissolve and re-precipitate on larger grains (e.g. Nemchin *et al.*, 2001). The large grain size of monazite (100-300 μm diameter) in our sample may suggest Ostwald ripening during prograde monazite growth. Inclusion of prograde monazite in growing garnet and/or significant melt loss after monazite growth would mitigate monazite dissolution into melt during further heating (Yakymchuk, 2017). The low Th content of groups 2 and 3 may suggest monazite

growth after Th partitioning into partial melt and subsequent removal of that melt (Dumond *et al.*, 2015).

Although the location of group 4 and 5 monazite as inclusions in garnet may be interpreted as crystallization during prograde garnet growth, their trace element characteristics suggest they crystallized during cooling. Indeed, textural location may not always be indicative of the relative timing of formation between an inclusion and its host (e.g. Kohn, 2016). Moreover, textural evidence suggests that groups 4 and 5 monazite postdate groups 1-3 (Figs. 5.4a, b, e). Groups 4 and 5 exhibit strong negative Eu anomalies and low Sr contents, suggesting crystallization in the presence of abundant feldspar. HREE and Y contents are similar to group 3, indicating crystallization in the presence of modally abundant garnet. Most of the feldspar in the rock occurs in fine-grained plagioclase + quartz intergrowths interpreted to be melt pseudomorphs. We therefore interpret group 4 and 5 monazite to have grown during cooling and melt crystallization at ~2655 Ma. The high Th and low U content of group 5 may suggest direct crystallization from a high-Th melt and/or crystallization in equilibrium with a U-rich mineral, such as zircon. Indeed, the weighted mean age of both groups 4 and 5 overlap with the weighted mean ages of zircon analyzed *in-situ* by LASS and the younger ID-TIMS dates of zircon and monazite presented here. Despite their differences in trace element chemistry, the relative timing of crystallization of groups 4 and 5 appears to be variable in different parts of the rock: textures of some grains suggest that group 5 postdated group 4 (Fig. 5.4c), while other textures suggest the opposite relationship (Fig. 5.4e, g).

In summary, *in-situ* LASS petrochronology constrains the timing of prograde and retrograde metamorphism in our sample. The zircon data suggest zircon crystallization in the presence of modally abundant garnet and feldspar, likely from partial melts during cooling from UHT conditions at ~2665 Ma, though some zircon may have crystallized at HT conditions during prograde heating or an early unrelated metamorphic event prior to ~2700 Ma. This data could alternatively be interpreted to suggest continuous zircon crystallization from ~2690 to ~2635 Ma, but the large age uncertainties limit interpretation. The *in-situ* LASS monazite data suggest at least five chemically distinct groups of monazite, some of which likely grew during heating to UHT prior to ~2675 Ma (groups 1-3), and a larger population (groups 4 and 5) that likely grew during cooling and melt crystallization at ~2660-2650 Ma, in some cases in equilibrium with crystallizing zircon. This is supported by textures that suggest matrix group 4

and 5 monazite and zircon growth due to garnet breakdown (Fig. 5.4f). These relationships are displayed in Fig. 5.4d-e, which show a monazite grain within a polymineralic inclusion in garnet with rutile (that gives UHT Zr in rutile temperatures), K-feldspar, sillimanite, and late biotite. The monazite contains a resorbed group 3 core surrounded by a 'moat' of group 5 monazite, all of which is overgrown by a rim of sub- to euhedral group 4 monazite. The resorbed group 3 core suggests that a period of partial monazite dissolution occurred prior to group 4 and 5 'moat' and rim growth, and prior to continued heating to UHT (recorded by adjacent rutile). The group 4 rim appears to have grown interstitially and is euhedral in some parts, consistent with crystallization from melt. Anomalously young spot dates occur solely in matrix monazite and are distributed along concordia. Monazite grains armoured from the matrix as inclusions in garnet do not exhibit these young dates, which may represent previously unrecognized metamorphic events and tectonism in the PGD, or, more likely, variable Pb loss during Paleoproterozoic metamorphic overprinting. The ability to obtain a large dataset with *in-situ* LASS allowed us to capture the volumetrically minor early prograde and 'young' populations, while the ability to analyze grain domains with preserved microstructural and textural context allowed for thorough assessment of the significance of the data.

5.7.2 TIMS-TEA of grain fragments: The Devil is in the Detail

The TIMS-TEA zircon data reveal complexity in the zircon crystallization history that is not apparent in the *in-situ* LASS data: at least five episodes of metamorphic zircon (re)crystallization are recognized over a 23.8 ± 2.4 Ma period from ~2673 to 2650 Ma. We note that this duration represents a minimum duration, and that both older and younger zircon could be detected with a larger dataset. Additionally, more data could reveal that zircon (re)crystallization was continuous rather than episodic. Zircon trace element chemistry appears to vary both within each generation and among the generations, with no direct correlation between $^{207}Pb/^{206}Pb$ date and trace element chemistry. This chemical variability and the apparent episodic nature of zircon growth could be explained by multiple mechanisms.

One possibility is that the rock underwent a polyphase thermal evolution, with different generations of zircon recording multiple heating/cooling and partial melting/melt crystallization cycles over ~24 Ma. The variability in Eu anomaly among the different zircon generations could result from this, with positive Eu anomalies indicating crystallization in the absence of feldspar and negative Eu anomalies indicating crystallization in the presence of feldspar. Since most

feldspar in the rock occurs as pseudomorphs after melt, strong negative Eu anomalies are interpreted to represent zircon crystallization during cooling and melt crystallization. Both positive and negative Eu anomalies are found in the first zircon generation, which records apparently continuous zircon crystallization over 3.6 ± 2.4 Ma. The second generation (2666 Ma) exhibits a strong negative Eu anomaly. The third generation (2661 Ma) has a weaker negative Eu anomaly, while the fourth and fifth generations (2657 and 2650 Ma) again have strong negative Eu anomalies. Therefore, the multiple generations of zircon may reflect zircon growth in response to multiple cycles of feldspar dissolution and (re)crystallization, which in this case could be related to partial melting and melt crystallization, recording multiple heating/cooling cycles (Fig. 5.8b). Preservation of the 2673-2670 Ma generation 1 zircon through subsequent heating events could be due to local melt loss and variably reduced fertility of different rock domains (e.g. Morrissey *et al.*, 2015; Dragovic *et al.*, 2016), with zircon preservation occurring in more residual domains and zircon dissolution/(re-)crystallization in more fertile domains.

Metamorphic timescales are correlated to their thermal length-scales (e.g. Carslaw & Jaeger, 1959): short-duration metamorphism requires crustal heating over short length-scales to allow for efficient and rapid conductive cooling, and vice-versa. Moreover, hot lower crust is especially difficult to cool quickly, as thermal diffusivities of continental crust are believed to be lowest in the deep crust (e.g. Clauser, 2009). Given the extreme thermal conditions, near-isobaric cooling in the lower crust, and large length-scales over which HT/UHT conditions in the PGD appear to have been attained (e.g. Fig. 5.1a), it is unlikely that the rock experienced multiple, punctuated heating and cooling cycles with such brief recurrence intervals (< 5 Ma) over the ~24 Ma zircon crystallization duration.

Episodic zircon growth could also occur in partially melted rocks through local zircon saturation of melt in isolated pockets. As partial melt is lost and/or channelized, local grain boundary melts can become isolated from each other, creating domainal equilibrium volumes and potentially disconnected pockets of grain boundary melt on the cm-scale within a larger hand sample of rock (e.g. Johnson *et al.*, 2004; Guevara & Caddick, 2016). This isolation of melt pockets would create localized closed-system conditions, with each melt pocket having variable melt chemistry, zircon saturation temperature, and solidus temperature, as well as different melt-residue reactions (e.g. White & Powell, 2002; White & Powell, 2010; Harley & Nandakumar, 2014). Other possible local scale processes could achieve similar results, such as: 1) the

generation of chemical potential gradients in H_2O to drive local isothermal melt crystallization (White & Powell, 2010), 2) localized fractional crystallization of partial melts, 3) fluxing of externally-derived melt(s) to locally saturate a domain with zircon, or 4) differences in (re-) crystallization mechanism due to different local zircon-forming reactions. Thus, the TIMS-TEA zircon data may suggest that zircon crystallization was dominantly controlled by dynamic, local petrologic processes during ~23 Ma of cooling from UHT conditions.

It is also possible that zircon growth in this case may not be episodic, with the apparent episodicity being an artifact of the relatively small dataset and/or biased sampling. Over half of the TIMS zircon dates crystallized from 2673-2670 Ma, with the other half spread from 2666-2650 Ma (showing a "kink" in Fig. 6c), which may suggest that most of the zircon was grown early. Thus, even if zircon growth was continuous (i.e. not episodic), it appears to be non-linear, with high initial growth rates at saturation conditions, consistent with predictions of zircon growth in melt-bearing rocks from other studies (e.g. Yakymchuk & Brown, 2014a).

TIMS dates of monazite fragments overlap with zircon generations 1 and 2 (Figs. 5.6c, 5.8a). This coincidence suggests that monazite may have been crystallizing simultaneously with zircon at ~2673 and ~2666 Ma. Multiple LASS spot analyses on each of the two ~2666 Ma monazite fragments (m1a and m3b, Fig 5.4i) show that they combine low and high Th domains and potentially different age domains, and that the age and chemistry of the whole fragment may reflect domain mixing. However, the LASS analyses indicate that each fragment is relatively homogeneous in REE content. Both fragments have strong negative Eu anomalies (Fig. 5.6i), indicative of crystallization in the presence of abundant plagioclase, and high Th/U (>100) similar to group 5 monazite from the *in-situ* LASS data. Analyses from fragment m3b exhibit REE profiles nearly identical to group 5 monazite from the *in-situ* LASS data (Figs. 5.4i & 5.6i), while analyses from the fragment m1a are significantly more depleted in HREE (Figs. 5.4i & 5.6i). This difference in chemistry between two fragments of the same age from different grains provides further evidence that local reactions may have controlled accessory phase crystallization and chemical signature in this rock.

5.7.3 Disparities between LASS on grain fragments and TIMS-TEA

LASS spot analyses of the grain fragments analyzed by TIMS give some $^{207}Pb/^{206}Pb$ dates that do not overlap the TIMS $^{207}Pb/^{206}Pb$ date of the fragment within 2σ uncertainty, even for some fragments that appear homogeneous in BSE images. For the zircon fragments, the

$^{207}Pb/^{206}Pb$ TIMS dates are generally younger than $^{207}Pb/^{206}Pb$ LASS spot dates on the fragment, with eight $^{207}Pb/^{206}Pb$ TIMS dates that do not overlap the LASS spot dates within 2σ uncertainties (Fig. 5.5j). One possibility is the presence of thin rims of zircon that are not observed through grain imaging or detected in the LASS analyses, and that the TIMS dates may be biased toward such rims. Previous studies have shown that in many cases, thin zircon rims can only be detected through depth profiling or single-shot laser ablation techniques (e.g. Gordon *et al.*, 2009; Viete *et al.*, 2015; Skipton *et al.*, 2016). However, our polishing of the grain mounts in this study limits the possibility of sampling thin rims via LASS. The disparity between TIMS and LASS dates could also be due to spatially heterogeneous distribution of radiogenic Pb due to Pb mobilization at HT/UHT conditions (e.g. Kusiak *et al.*, 2013; Peterman *et al.*, 2016). This would result in local domains enriched in radiogenic Pb with spuriously old spot dates, while other domains would be Pb-depleted with apparently younger spot dates, though this alone would not account for the observed differences in trace element chemistry between the two techniques. Another related possibility is that we sampled zircon that was enriched in radiogenic Pb on the LASS, but was dissolved during chemical abrasion prior to TIMS analysis, thus biasing the TIMS date to younger domains.

REE concentration also differs between LASS and TIMS-TEA analyses of the zircon grain fragments (Fig. 5.5g-i), with LASS generally giving lower REE concentrations, but having similar element ratios (e.g. Lu_n/Dy_n). Previous studies that combined these techniques (e.g. DesOrmeau *et al.*, 2015; Samperton *et al.*, 2015) using the same laboratories and analytical instruments found good agreement between REE chemistries determined by LASS vs. solution ICP-MS. Perhaps the zircon fragments in our study are chemically zoned on a scale larger than the LASS spot size (but not observed in grain images), or that REEs were mobilized and heterogeneously redistributed at or during HT/UHT. Constraints on REE diffusion in zircon (Cherniak *et al.*, 1997) suggest closure temperatures > 950-1000 °C for effective diffusion length scales > 25 μm (LASS spot size). These temperatures are similar to the peak conditions for our sample, but the zircon fragments analyzed here likely crystallized below peak conditions (based on the Ti in zircon temperatures among all analyses from the *in-situ* LASS data). However, the slow cooling rates inferred for the PGD of 1-2 °C/Ma (e.g. Kooijman *et al.*, 2010) would lower REE closure temperature in zircon, and it may be possible that REE were still mobile in newly crystallized zircon as the terrane cooled slowly. Another possibility is the presence of REE-rich

inclusions in the dissolved grain fragments that were not apparent in grain images. REE-rich minerals seem to favour intake of LREE over HREE, or vice-versa (e.g. monazite is enriched in LREE, garnet in HREE). If there were inclusions of e.g. monazite in the zircon fragments, this would be expected to produce a shift to higher LREE, while HREE content would likely be unaffected. This is not the case here, as it appears that all REE are shifted to higher concentrations as measured by solution-ICP-MS. At the time of this writing, we are currently investigating the reasons behind these disparities.

The monazite data show a different relationship: some $^{207}Pb/^{206}Pb$ LASS spot dates do not overlap with the TIMS date of the fragment, but in this case the non-overlapping LASS dates are younger than the TIMS date. In fragment m1a, all non-overlapping LASS analyses are reversely discordant by up to 9%, despite a TIMS analysis that overlaps concordia. The presence of reversely discordant domains in the fragment suggests that the TIMS date is either heavily biased toward a more concordant domain, or mixes domains with both reverse and normal discordance. Fragment 3b also has non-overlapping, concordant to 1% discordant LASS dates that are younger than the TIMS date. In this case, intragrain Pb mobilization, Pb loss obscured by the high uncertainty of isotope ratios in the LASS spot analyses, or bias of the TIMS date to an older domain could explain the younger LASS dates.

5.7.4 Implications for the Archean tectonometamorphic evolution of the PGD

Combining petrochronology with quantitative constraints on *P–T* evolution can be a useful tool for reconstructing the tectonic evolution of metamorphic terranes. We interpret the combined data from *in-situ* LASS and grain fragment TIMS-TEA petrochronology from a single rock hand sample to record prograde metamorphism and partial melting from >2700 to ~2680-2675 Ma followed by apparently episodic zircon and monazite crystallization from partial melts from 2674 to 2650 Ma. This episodic crystallization likely reflects localized metamorphic and melt-residue interactions during slow cooling over a minimum ~23 Ma duration (Fig. 5.8a), though we acknowledge that the apparent episodicity could simply be due to the small dataset and high precision of the TIMS analyses, and thus could be consistent with continuous, but non-linear zircon crystallization (Fig. 8). Regardless, our data constrain the timing of peak UHT conditions and subsequent decompression to be older than 2674 Ma, and the total duration of Archean metamorphism in the western PGD to be at least 50 Ma, and potentially longer than 100 Ma. These constraints are broadly similar to those of previous studies of the PGD, and could be

consistent with either a polymetamorphic evolution over a > 50 Ma timespan (e.g. Heaman *et al.*, 2011) or a single, long-lived thermal event (e.g. Mezger *et al.*, 1989; Smit *et al.*, 2013).

The results of quantitative thermobarometry give similar *P* to previous studies, but the peak *T* determined for our sample is higher than existing quantitative constraints on peak *T* from other parts of the PGD (Fig. 5.7f). UHT conditions of ~900-910 °C have been determined in the Natawahunan lake area, ~25 km northwest of our sample location (Kooijman *et al.*, 2012) and 920 °C in the Split Lake Block, ~120 km northeast (Bowerman, 2008). UHT conditions have also been proposed for rocks in the Sipiwesk Lake area (~55 km southwest), where diagnostic UHT assemblages have been observed, but exact *P–T* conditions are poorly constrained (Arima & Barnett, 1984; Couëslan *et al.*, 2012). Lower temperatures of 750-850 °C are recorded in the Cauchon Lake area (55-60 km southeast), where the transition from upper-amphibolite to granulite facies mineral assemblages is observed (Hubregtse, 1980; Couëslan & Guevara, 2015), and suggests that UHT conditions may have been restricted to the northern, central, and western PGD, with increasing *T* towards the west.

Previous studies in the PGD have suggested a counterclockwise *P–T* path (Mezger *et al.*, 1990; Vry & Brown, 1991) characterized by syn-burial heating and near-isobaric cooling after peak *P–T* conditions (Fig. 7f). This was interpreted to suggest crustal heating by underplating of mantle-derived melts at the base of a continental arc or by upwelling asthenosphere due to lithospheric delamination (Mezger *et al.*, 1990; Heaman *et al.*, 2011), both of which could occur after the proposed collision between the North Caribou and Hudson Bay Terranes, as suggested by field evidence and isotope geochemistry (Couëslan, 2016). However, the thermodynamic modelling and microstructural observations presented here suggest a clockwise *P–T* path marked by UHT decompression to ~8 kbar (corresponding to lower crustal depths), followed by near-isobaric cooling (Fig. 5.7f), thus requiring a geodynamic setting that accounts for limited tectonic or erosional exhumation while the rock was at UHT, such as, for example, the 'ultrahot orogen' model proposed by Chardon *et al.* (2009). In this model, deformation is accommodated by dominantly lateral flow of weak lower crust instead of, for example, mid- to lower-crustal exhumation via nappe stacking or detachment faulting. However, we note that our findings do not preclude counterclockwise paths in other localities throughout the PGD. If different parts of the PGD experienced different *P–T* paths, and/or peak metamorphism in different parts of the PGD occurred at different times over varying durations, or if the entire PGD simultaneously

experienced a single long-lived, clockwise path, then the tectonic mechanisms for crustal heating may need to be re-evaluated through a campaign-style thermobarometric and pterochronologic study across the PGD.

5.8 CONCLUDING REMARKS: COMBINING HIGH-SPATIAL RESOLUTION LASS AND HIGH-PRECISION TIMS-TEA TO ELUCIDATE ARCHEAN HT/UHT METAMORPHIC PROCESSES

The extreme temperatures recorded by UHT metamorphic terranes present multiple challenges to quantifying the timescales of UHT metamorphic processes. The seemingly common occurrence of UHT metamorphism in Archean terranes makes this even more problematic, as their antiquity results in age uncertainties for most petrochronologic techniques that are too large to accurately quantify metamorphic durations in many settings. Several recent studies have recognized transient (e.g. <1 Myr) metamorphic processes superimposed upon a longer thermal timescale in Phanerozoic metamorphic terranes (e.g. Ague & Baxter, 2007; DesOrmeau *et al.*, 2015; Dragovic *et al.*, 2015; Viete *et al.*, 2015), highlighting the level of complexity that metamorphic rocks are capable of recording. By combining high-spatial resolution LASS and high-precision TIMS-TEA U-Pb petrochronology, we show here that similarly transient processes can be revealed in Archean UHT rocks.

TIMS-TEA analyses of separated grain fragments reveal a far more complex and detailed zircon and monazite crystallization history than the *in-situ* LASS analyses, raising further questions about the metamorphic evolution of the rock and highlighting the potential importance of localized processes in controlling zircon/monazite crystallization. This complexity suggests that care must be taken when interpreting *in-situ* geochronologic data for Archean HT/UHT rocks from which melt has been extracted, resulting in reduced equilibration length-scales. In our case, the *in-situ* LASS data was limited to the scale of the analyzed thin section ($< 4*10^{-5}$ cm^3), and this data could be spuriously interpreted as recording a single phase of zircon growth due to low geologic scatter in the weighted mean age resulting from large individual spot date uncertainties. In contrast, TIMS-TEA data of grain fragments separated from a rock volume several orders of magnitude larger than that of a thin section ($>10^4$ cm^3) suggest that zircon and monazite may have been crystallizing at the same time with variable trace element concentrations, likely due to different local petrologic processes operating in different parts of the rock because of reduced chemical equilibration volumes resulting from melt loss. This

complexity is not surprising for a residual rock that likely experienced open-system processes, as local zircon and monazite saturation and reactivity should be dynamic and transient as partial melt is removed, externally-derived melt is fluxed through, and/or different domains within the rock become chemically isolated from each other due to melt loss.

While the TIMS-TEA results reveal a highly complex retrograde history, *in-situ* LASS analysis of monazite places important constraints on the timing of prograde heating. This is not recorded in the TIMS-TEA data, perhaps due to the limited number of TIMS-TEA analyses and the low volumetric abundance of prograde monazite that was not sampled for TIMS-TEA. Moreover, using LASS as a reconnaissance tool prior to TIMS-TEA analyses can improve the chances of obtaining meaningful TIMS-TEA results by identifying distinct age and chemical domains to separate for TIMS-TEA analysis, particularly for rocks that experienced a complex metamorphic evolution. The two techniques are thus complementary to each other, and further advances in quantifying timescales of Archean metamorphic processes could be made by combining and applying these techniques to other terranes.

By combining the results of these two petrochronologic techniques with quantitative thermobarometry, we show that the western PGD experienced a clockwise *P–T* path marked by UHT decompression followed by near isobaric cooling at pressures corresponding to middle to lower crustal depths. This *P–T* evolution is consistent with the geochronologic data, which suggests that HT conditions were sustained in this part of the PGD over a long duration (>50 Ma), thus requiring any HT/UHT exhumation to be limited and the rocks to remain at depth. However, the *P–T* evolution determined here contrasts with the counterclockwise paths previously proposed for the PGD. Though our geochronologic data are broadly consistent with previous grochronology in the PGD, more data is needed to determine if other parts of the PGD experienced a similar *P–T-t* history to that shown here in order to elucidate the mechanism(s) for UHT metamorphism in the PGD.

5.9 ACKNOWLEDGMENTS

This research was funded by a grant from the NSF-Earthscope Awards for Geochronology Student Research Program awarded to V. Guevara, and NSF Grant EAR-1447568 to M.J. Caddick and B. Dragovic. We thank N. Brandsson and the Manitoba Geological Survey for field support and field equipment, as well as assistance with sample shipment. Wings Over Kississing is thanked for field transportation. M. Fame and J.A. Spotila helped with grain

separation and picking. J. Trela provided assistance for grain mounting in epoxy, and H. Lamadrid and R.J. Bodnar provided assistance during grain annealing. C.A. Mako is thanked for assistance with LASS analyses. K. Samperton is thanked for assistance with TIMS analyses. L. Fedele and A. Conde assisted with LA-ICPMS analyses of rutile. R.J. Tracy provided excellent assistance with electron microprobe mapping and analyses. L. Fedele also provided assistance with grain imaging and mapping.

5.10 REFERENCES

Ague, J. J. & Baxter, E. F., 2007. Brief thermal pulses during mountain building recorded by Sr diffusion in apatite and multicomponent diffusion in garnet *Earth and Planetary Science Letters*, **261**, 500-516.

Arima, M. & Barnett, R. L., 1984. Sapphirine bearing granulites from the Sipiwesk Lake area of the late Archean Pikwitonei Granulite Terrain, Manitoba, Canada. *Contributions to Mineralogy and Petrology*, **88**, 102-112.

Axler, J. A. & Ague, J. J., 2015. Exsolution of rutile or apatite precipitates surrounding ruptured inclusions in garnet from UHT and UHP rocks. *Journal of Metamorphic Geology*, **33**, 829-848.

Baldwin, J. A., Bowring, S. A. & Williams, M. L., 2003. Petrological and geochronological constraints on high pressure, high temperature metamorphism in the Snowbird tectonic zone, Canada. *Journal of Metamorphic Geology*, **21**, 81-98.

Baldwin, J. A. & Brown, M., 2008. Age and duration of ultrahigh-temperature metamorphism in the Anapolis-Itaucu Complex, Southern Brasilia Belt, central Brazil - constraints from U-Pb geochronology, mineral rare earth element chemistry and trace-element thermometry. *Journal of Metamorphic Geology*, **26**, 213-233.

Baldwin, J. A., Brown, M. & Schmitz, M. D., 2007. First application of titanium-in-zircon thermometry to ultrahigh-temperature metamorphism. *Geology*, **35**, 295-298.

Barboni, M., Schoene, B., Ovtcharova, M., Bussy, F., Schaltegger, U. & Gerdes, A., 2013. Timing of incremental pluton construction and magmatic activity in a back-arc setting revealed by ID-TIMS U/Pb and Hf isotopes on complex zircon grains. *Chemical Geology*, **342**, 76-93.

Baxter, E. F. & Scherer, E. E., 2013. Garnet Geochronology: Timekeeper of Tectonometamorphic Processes. *Elements*, **9**, 433-438.

Böhm, C. O., Heaman, L. M. & Corkery, M. T., 1999. Archean crustal evolution of the northwestern Superior craton margin: U-Pb zircon results from the Split Lake Block. *Canadian Journal of Earth Sciences*, **36**, 1973-1987.

Böhm, C. O., Heaman, L. M., Stern, R. A., Corkery, M. T. & Creaser, R. A., 2003. Nature of assean lake ancient crust, Manitoba: a combined SHRIMP–ID-TIMS U–Pb geochronology and Sm–Nd isotope study. *Precambrian Research*, **126**, 55-94.

Bowerman, M. S., 2008. *The Tectnothermal History of the Split Lake Block, Superior Province, Manitoba*. University of Alberta (Canada).

Brown, M., 2008. Characteristic thermal regimes of plate tectonics and their metamorphic imprint throughout Earth history: When did Earth first adopt a plate tectonics mode of behavior. *Geological Society of America Special Papers*, **440**, 97-128.

Caddick, M. J. & Kohn, M. J., 2013. Garnet: Witness to the evolution of destructive plate boundaries. *Elements*, **9**, 427-432.

Caddick, M. J., Konopásek, J. & Thompson, A. B., 2010. Preservation of garnet growth zoning and the duration of prograde metamorphism. *Journal of Petrology*, **51**, 2327-2347.

Carslaw, H. S. & Jaeger, C. J., 1959. *Conduction of Heat in Solids*. Clarendon, Oxford.

Chakraborty, S., Anczkiewicz, R., Gaidies, F., Rubatto, D., Sorcar, N., Faak, K., Mukhopadhyay, D. K. & Dasgupta, S., 2016. A review of thermal history and timescales of tectonometamorphic processes in Sikkim Himalaya (NE India) and implications for rates of metamorphic processes. *Journal of Metamorphic Geology*, **34**, 785-803.

Chardon, D., Gapais, D. & Cagnard, F., 2009. Flow of ultra-hot orogens: A view from the Precambrian, clues for the Phanerozoic. *Tectonophysics*, **477**, 105-118.

Cherniak, D. J., Hanchar, J. M. & Watson, E. B., 1997. Rare-earth diffusion in zircon. *Chemical Geology*, **134**, 289-301.

Cherniak, D. J. & Watson, E. B., 2001. Pb diffusion in zircon. *Chemical Geology*, **172**, 5-24.

Cherniak, D. J., Watson, E. B., Grove, M. & Harrison, T. M., 2004. Pb diffusion in monazite: A combined RBS/SIMS study. *Geochimica Et Cosmochimica Acta*, **68**, 829-840.

Clauser, C., 2009. Heat Transport Processes in the Earth's Crust. *Surveys in Geophysics*, **30**, 163-191.

Couëslan, C. G., 2013. Preliminary results from bedrock mapping in the Partridge Crop Lake area, eastern margin of the Thompson nickel belt, central Manitoba (parts of NTS 63P11, 12). In: *Report of Activities 2013, Manitoba Mineral Resources*, pp. 34-45, Manitoba Geological Survey.

Couëslan, C. G., 2014. Preliminary results from bedrock mapping in the Armstrong Lake area, Pikwitonei granulite domain, central Manitoba (parts of NTS 63P10, 11). In: *Report of Activities 2014, Manitoba Mineral Resources*, pp. 7-17, Manitoba Geological Survey.

Couëslan, C. G., 2016. The Pikwitonei Granulite Domain, Manitoba: A collisional orogenic zone along the northwestern margin of the Superior Craton. In: *GAC-MAC Annual Conference* (ed Canada, G. A. o.), Whitehorse, Yukon, Canada.

Couëslan, C. G., Böhm, C. O. & Martins, T., 2012. Preliminary results from geological mapping in the central Sipiwesk Lake area, Pikwitonei Granulite Domain, central Manitoba (part of NTS 63P4). In: *Report of Activities 2012, Manioba Innovation, Energy and Mines*, pp. 79-89, Manitoba Geological Survey

Couëslan, C. G. & Guevara, V. E., 2015. Preliminary results from bedrock mapping in the southern and central Cauchon Lake area, eastern margin of the Pikwitonei granulite domain, central Manitoba (parts of NTS 63P7, 8). *Manitoba Geological Survey Report of Activities 2015*, 24-37.

DesOrmeau, J. W., Gordon, S. M., Kylander-Clark, A. R. C., Hacker, B. R., Bowring, S. A., Schoene, B. & Samperton, K. M., 2015. Insights into (U)HP metamorphism of the Western Gneiss Region, Norway: A high-spatial resolution and high-precision zircon study. *Chemical Geology*, **414**, 138-155.

DesOrmeau, J. W., Gordon, S. M., Little, T. A. & Bowring, S. A., 2014. Tracking the exhumation of a Pliocene (U)HP terrane: U-Pb and trace-element constraints from zircon, D'Entrecasteaux Islands, Papua New Guinea. *Geochemistry Geophysics Geosystems*, **15**, 3945-3964.

Downey, M. W., Lin, S., Bohm, C. O. & Rayner, N. M., 2009. Timing and kinematics of crustal movement in the northern Superior Superterrane; insights from the Gull Rapids area of the Split Lake Block, Manitoba. *Precambrian Research*, **168**, 134-148.

Dragovic, B., Baxter, E. & Caddick, M., 2015. Pulsed dehydration and garnet growth during subduction revealed by zoned garnet geochronology and thermodynamic modelling, Sifnos, Greece. Earth and Planetary Science Letters. *Earth and Planetary Science Letters*, **413**, 111-122.

Dragovic, B., Guevara, V. E., Caddick, M. J., Baxter, E. F. & Kylander-Clark, A. R. C., 2016. A pulse of cryptic granulite-facies metamorphism in the Archean Wyoming Craton revealed by Sm–Nd garnet and U–Pb monazite geochronology. *Precambrian Research*, **283**, 24-49.

Dumond, G., Goncalves, P., Williams, M. L. & Jercinovic, M. J., 2015. Monazite as a monitor of melting, garnet growth and feldspar recrystallization in continental lower crust. *Journal of Metamorphic Geology*, **33**, 735-762.

England, P. & Bickle, M., 1984. Continental Thermal and Tectonic Regimes during the Archaean. *The Journal of Geology*, **92**, 353-367.

England, P. C. & Thompson, A. B., 1984. Pressure-temperature-time paths of regional metamorphism I. Heat transfer during the evolution of regions of thickened continental crust. *Journal of Petrology*, **25**, 894-928.

Ferry, J. M. & Watson, E. B., 2007. New thermodynamic models and revised calibrations for the Ti-in-zircon and Zr-in-rutile thermometers. *Contributions to Mineralogy and Petrology*, **154**, 429-437.

Gervais, F. & Crowley, J. L., 2017. Prograde and near-peak zircon growth in a migmatitic pelitic schist of the southeastern Canadian Cordillera. *Lithos*.

Gordon, S. M., Grove, M., Whitney, D. L., Schmitt, A. K. & Teyssier, C., 2009. Fluid-rock interaction in orogenic crust tracked by zircon depth profiling. *Geology*, **37**, 735-738.

Guevara, V. E. & Caddick, M. J., 2016. Shooting at a moving target: phase equilibria modelling of high-temperature metamorphism. *Journal of Metamorphic Geology*, **34**, 209-245.

Harley, S. L., 2016. A matter of time: The importance of the duration of UHT metamorphism. *Journal of Mineralogical and Petrological Sciences*, **111**, 50-72.

Harley, S. L., Kelly, N. M. & Möller, A., 2007. Zircon Behaviour and the Thermal Histories of Mountain Chains. *Elements*, **3**, 25-30.

Harley, S. L. & Nandakumar, V., 2014. Accessory Mineral Behaviour in Granulite Migmatites: a Case Study from the Kerala Khondalite Belt, India. *Journal of Petrology*, **55**, 1965-2002.

Heaman, L. M., Böhm, C., Machado, N., Krogh, T. E., Weber, W. & Corkery, M. T., 2011. The Pikwitonei Granulite Domain, Manitoba: a giant Neoarchean high-grade terrane in the northwest Superior Province. *Canadian Journal of Earth Sciences*, **48**, 205-245.

Holder, R. M., Hacker, B. R., Kylander-Clark, A. R. C. & Cottle, J. M., 2015. Monazite trace-element and isotopic signatures of (ultra)high-pressure metamorphism: Examples from the Western Gneiss Region, Norway. *Chemical Geology*, **409**, 99-111.

Holness, M. B., Cesare, B. & Sawyer, E. W., 2011. Melted Rocks under the Microscope: Microstructures and Their Interpretation. *Elements*, **7**, 247-252.

Hubregtse, J. J. M. W., 1980. The Archean Pikwitonei granulite domain and its position at the margin of the northwestern Superior Province (central Manitoba). *Geological Paper (Winnipeg)*, 16.

Johnson, T., Brown, M., Gibson, R. & Wing, B., 2004. Spinel–cordierite symplectites replacing andalusite: evidence for melt-assisted diapirism in the Bushveld Complex, South Africa. *Journal of Metamorphic Geology*, **22**, 529-545.

Johnson, T. E., Clark, C., Taylor, R. J., Santosh, M. & Collins, A. S., 2015. Prograde and retrograde growth of monazite in migmatites: An example from the Nagercoil Block, southern India. *Geoscience Frontiers*, **6**, 373–387.

Kelly, N. M. & Harley, S. L., 2005. An integrated microtextural and chemical approach to zircon geochronology: refining the Archaean history of the Napier Complex, east Antarctica. *Contributions to Mineralogy and Petrology*, **149**, 57-84.

Kelsey, D. E. & Hand, M., 2015. On ultrahigh temperature crustal metamorphism: Phase equilibria, trace element thermometry, bulk composition, heat sources, timescales and tectonic settings. *Geoscience Frontiers*, **6**, 311-356.

Kelsey, D. E. & Powell, R., 2011. Progress in linking accessory mineral growth and breakdown to major mineral evolution in metamorphic rocks: a thermodynamic approach in the Na2O-CaO-K2O-FeO-MgO-Al2O3-SiO2-H2O-TiO2-ZrO2 system. *Journal of Metamorphic Geology*, **29**, 151-166.

Kohn, M. J., 2016. Metamorphic chronology—a tool for all ages: Past achievements and future prospects. *American Mineralogist*, **101**, 25-42.

Kooijman, E., Mezger, K. & Berndt, J., 2010. Constraints on the U-Pb systematics of metamorphic rutile from in situ LA-ICP-MS analysis. *Earth and Planetary Science Letters*, **293**, 321-330.

Kooijman, E., Smit, M. A., Mezger, K. & Berndt, J., 2012. Trace element systematics in granulite facies rutile: implications for Zr geothermometry and provenance studies. *Journal of Metamorphic Geology*, **30**, 397-412.

Korhonen, F. J., Clark, C., Brown, M., Bhattacharya, S. & Taylor, R., 2013. How long-lived is ultrahigh temperature (UHT) metamorphism? Constraints from zircon and monazite geochronology in the Eastern Ghats orogenic belt, India. *Precambrian Research*.

Kusiak, M. A., Whitehouse, M. J., Wilde, S. A., Nemchin, A. A. & Clark, C., 2013. Mobilization of radiogenic Pb in zircon revealed by ion imaging: Implications for early Earth geochronology. *Geology*.

Kylander-Clark, A. R. C., Hacker, B. R. & Mattinson, C. G., 2012. Size and exhumation rate of ultrahigh-pressure terranes linked to orogenic stage. *Earth and Planetary Science Letters*, **321**, 115-120.

Mezger, K., Bohlen, S. R. & Hanson, G. N., 1990. Metamorphic History of the Achean Pikwitonei Granulite Domain and the Cross Lake Subprovince, Superior Province, Manitoba, Canada. *Journal of Petrology*, **31**, 483-517.

Mezger, K., Hanson, G. N. & Bohlen, S. R., 1989. U-Pb Systematics of Garnet - Dating the Growth of Garnet in the Late Archean Pikwitonei Granulite Domain at Cauchon and Natawahunan Lakes, Manitoba, Canada. *Contributions to Mineralogy and Petrology*, **101**, 136-148.

Mitchell, R. J. & Harley, S. L., 2017. Zr-in-rutile resetting in aluminosilicate bearing ultra-high temperature granulites: Refining the record of cooling and hydration in the Napier Complex, Antarctica. *Lithos*, **272–273**, 128-146.

Möller, A., O'Brien, P. J., Kennedy, A. & Kröner, A., 2003. Linking growth episodes of zircon and metamorphic textures to zircon chemistry: an example from the ultrahigh-

temperature granulites of Rogaland (SW Norway). *Geological Society, London, Special Publications*, **220**, 65-81.

Morrissey, L. J., Hand, M. & Kelsey, D. E., 2015. Multi-stage metamorphism in the Rayner–Eastern Ghats Terrane: P–T–t constraints from the northern Prince Charles Mountains, east Antarctica. *Precambrian Research*, **267**, 137-163.

Nemchin, A. A., Giannini, L. M., Bodorkos, S. & Oliver, N. H. S., 2001. Ostwald ripening as a possible mechanism for zircon overgrowth formation during anatexis: theoretical constraints, a numerical model, and its application to pelitic migmatites of the Tickalara Metamorphics, northwestern Australia. *Geochimica et Cosmochimica Acta*, **65**, 2771-2788.

Palin, R. M., Weller, O. M., Waters, D. J. & Dyck, B., 2016. Quantifying geological uncertainty in metamorphic phase equilibria modelling; a Monte Carlo assessment and implications for tectonic interpretations. *Geoscience Frontiers*, **7**, 591–607.

Pape, J., Mezger, K. & Robyr, M., 2016. A systematic evaluation of the Zr-in-rutile thermometer in ultra-high temperature (UHT) rocks. *Contributions to Mineralogy and Petrology*, **171**, 44.

Percival, J. A., Skulski, T., Stott, G., 2012. Geology and Tectonic Evolution of the Superior Province, Canada. In: *Tectonic Styles in Canada: The LITHOPROBE Perspective* (ed Percival, J. A., Cook, F.A., Clowes, R.M.), pp. 321-378, Geological Association of Canada, Special Paper.

Peterman, E. M., Reddy, S. M., Saxey, D. W., Snoeyenbos, D. R., Rickard, W. D. A., Fougerouse, D. & Kylander-Clark, A. R. C., 2016. Nanogeochronology of discordant zircon measured by atom probe microscopy of Pb-enriched dislocation loops. *Science Advances*, **2**.

Rubatto, D., 2002. Zircon trace element geochemistry: partitioning with garnet and the link between U-Pb ages and metamorphism. *Chemical Geology*, **184**, 123-138.

Samperton, K. M., Schoene, B., Cottle, J. M., Keller, C. B., Crowley, J. L. & Schmitz, M. D., 2015. Magma emplacement, differentiation and cooling in the middle crust: Integrated zircon geochronological–geochemical constraints from the Bergell Intrusion, Central Alps. *Chemical Geology*, **417**, 322-340.

Schoene, B. & Bowring, S. A., 2010. Rates and mechanisms of Mesoarchean magmatic arc construction, eastern Kaapvaal craton, Swaziland. *Geological Society of America Bulletin*, **122**, 408-429.

Skipton, D. R., Schneider, D. A., McFarlane, C. R. M., St-Onge, M. R. & Jackson, S. E., 2016. Multi-stage zircon and monazite growth revealed by depth profiling and in situ U–Pb geochronology: Resolving the Paleoproterozoic tectonics of the Trans-Hudson Orogen on southeastern Baffin Island, Canada. *Precambrian Research*, **285**, 272-298.

Smit, M. A., Scherer, E. E. & Mezger, K., 2013. Lu–Hf and Sm–Nd garnet geochronology: Chronometric closure and implications for dating petrological processes. *Earth and Planetary Science Letters*, **381**, 222-233.

Spear, F. S. & Pyle, J. M., 2002. Apatite, Monazite, and Xenotime in Metamorphic Rocks. *Reviews in Mineralogy and Geochemistry*, **48**, 293-335.

Tomkins, H. S., Powell, R. & Ellis, D. J., 2007. The pressure dependence of the zirconium-in-rutile thermometer. *Journal of Metamorphic Geology*, **25**, 703-713.

van Hunen, J. & Moyen, J. F., 2012. Archean Subduction: Fact or Fiction? *Annual Review of Earth and Planetary Sciences, Vol 40*, **40**, 195-219.

Viete, D. R., Kylander-Clark, A. R. & Hacker, B. R., 2015. Single-shot laser ablation split stream (SS-LASS) petrochronology deciphers multiple, short-duration metamorphic events. *Chemical Geology*, **415**, 70-86.

Villaseca, C., Martín Romera, C., De la Rosa, J. & Barbero, L., 2003. Residence and redistribution of REE, Y, Zr, Th and U during granulite-facies metamorphism: behaviour of accessory and major phases in peraluminous granulites of central Spain. *Chemical Geology*, **200**, 293-323.

Vry, J. K. & Brown, P. E., 1991. Texturally early fluid inclusions in garnets – evidence of the prograde metamorphic path. *Contributions to Mineralogy and Petrology*, **108**, 271-282.

Weber, W., 1987. Geology of the Pikwitonei granulite domain at Cauchon Lake. In: *Unpublished field trip guidebook* (ed Survey, M. G.), pp. 1-18.

White, R. W. & Powell, R., 2002. Melt loss and the preservation of granulite facies mineral assemblages. *Journal of Metamorphic Geology*, **20**, 621-632.

White, R. W. & Powell, R., 2010. Retrograde melt–residue interaction and the formation of near-anhydrous leucosomes in migmatites. *Journal of Metamorphic Geology*, **28**, 579-597.

White, R. W., Powell, R., Holland, T. J. B., Johnson, T. E. & Green, E. C. R., 2014. New mineral activity–composition relations for thermodynamic calculations in metapelitic systems. *Journal of Metamorphic Geology*, **32**, 261-286.

Yakymchuk, C., 2017. Behaviour of apatite during partial melting of metapelites and consequences for prograde suprasolidus monazite growth. *Lithos*, **274–275**, 412-426.

Yakymchuk, C. & Brown, M., 2014a. Behaviour of zircon and monazite during crustal melting. *Journal of the Geological Society*.

Yakymchuk, C. & Brown, M., 2014b. Consequences of open-system melting in tectonics. *Journal of the Geological Society*, **171**, 21-40.

5.11 FIGURES

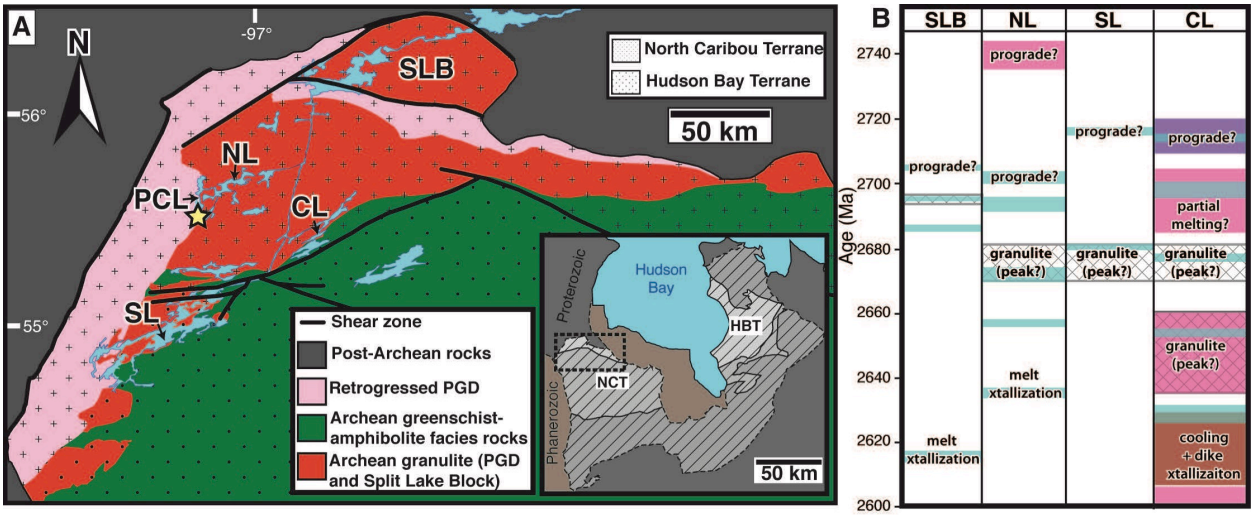

Figure 5.1: a) Simplified geologic map of the northwest Superior Province showing outline of PGD using map data from Manitoba Mineral Resources (2013). Sample location is indicated by the yellow star. Region with dotted pattern represents the North Caribou Terrane (NCT), region with crosses represents the Hudson Bay Terrane (HBT). Inset shows outline of Superior Province (diagonal line pattern) with the NCT and HBT labeled and indicated by different shades of grey. CL = Cauchon Lake, NL = Natawahunan Lake, PCL = Partridge Crop Lake, SL = Sipiwesk Lake, SLB = Split Lake Block. b) Graphical summary of previous geochronological studies in various locations throughout the PGD modified after Fig. 11 from Heaman *et al.* (2011). Data for SLB are from Downey *et al.* (2009) and Böhm *et al.* (1999). Ranges of U-Pb zircon (blue bands), U-Pb garnet (pink bands), Lu-Hf garnet (purple band), and Sm-Nd garnet (dark red band) dates are shown, with previous workers' interpretations on the significance of each date (or range of dates). Patterned bands (diagonal crisscrossing lines) indicate previous workers' interpretations of the timing of peak metamorphism in each locality.

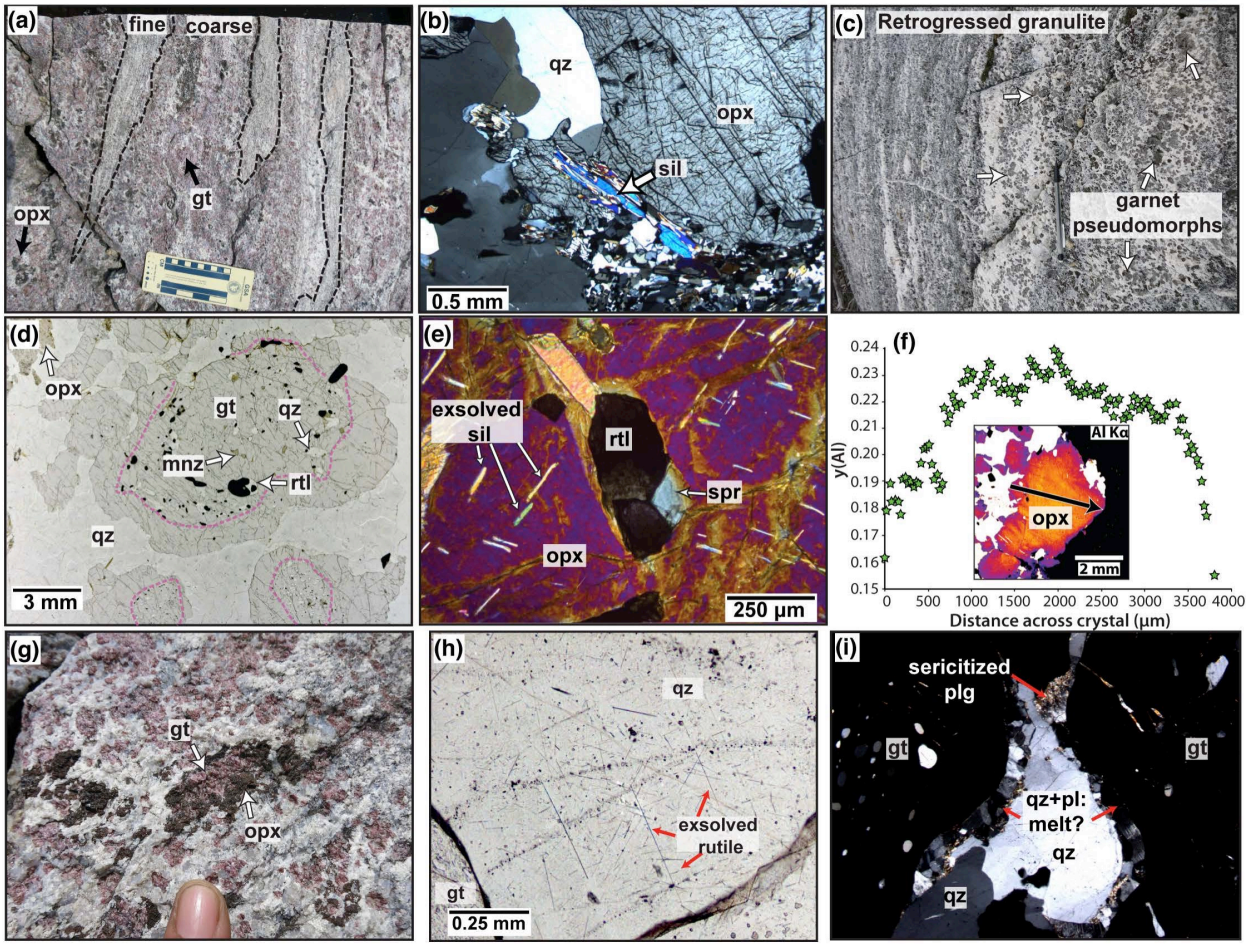

Figure 5.2: Photographs of the rock in outcrop and thin section. a) Outcrop photo of pristine granulite showing fine-grained bands and coarse-grained bands with abundant orthopyroxene (opx) and garnet (gt) porphyroblasts. b) Photomicrograph of a sample from the fine-grained band showing prismatic sillimanite (sil) in contact with porphyroblastic orthopyroxene (opx) in a quartz (qz) matrix. c) Outcrop photo taken ~15 m away from panel A showing extreme retrogression, with garnet porphyroblasts nearly completely pseudomorphed to fine-grained biotite-rich polyphase aggregates. d) Photomicrograph of our sample, taken from a coarse-grained band showing garnet porphyroblasts with inclusion-rich cores and relatively inclusion-free rims. Mnz = monazite, rtl = rutile. e) Photomicrograph of porphyroblastic orthopyroxene with exsolved needles of sillimanite and a polymineralic inclusion consisting of rutile and sapphirine (spr). f) electron microprobe traverse of y(Al) across orthopyroxene porphyroblast. Inset shows WDS X-ray map showing Al in opx and location of the analytical traverse. g) Outcrop photograph showing garnet porphyroblast rimmed by orthopyroxene. h) Coarse-grained matrix quartz with exsolved rutile needles. i) Garnet porphyroblasts and coarse-grained matrix quartz lined by fine-grained quartz + plagioclase (pl) aggregates interpreted to be pseudomorphs after partial melt. Some plagioclase is sericitized.

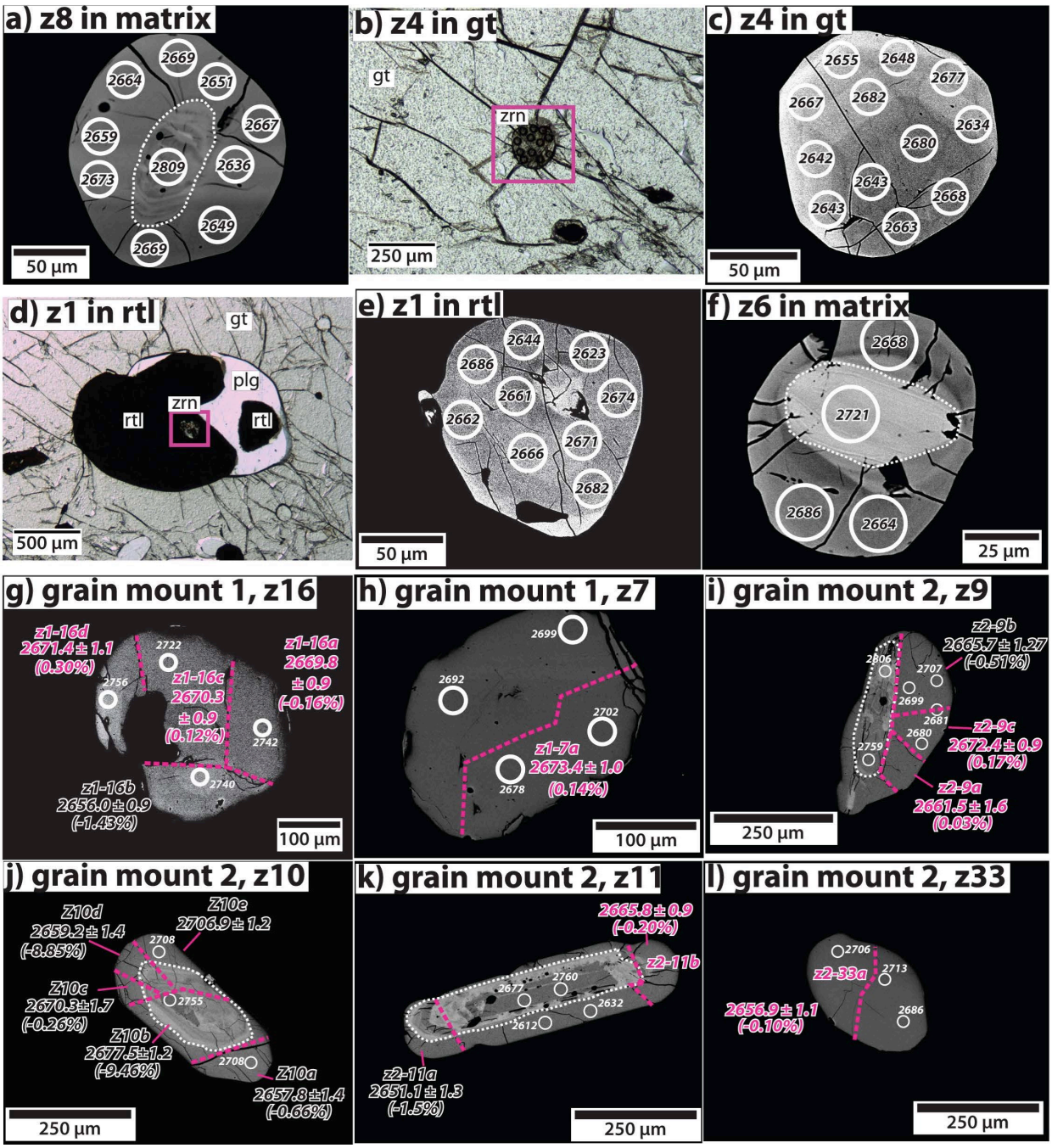

Figure 5.3: a-f) BSE images and photomicrographs of representative zircon grains analyzed *in-situ*. White circles indicate LASS spot locations, with associated $^{207}Pb/^{206}Pb$ spot dates. Uncertainties for each spot date are not shown, but range from 34-52 Ma. White dashed lines dermarcate domain boundaries between inherited cores and metamorphic rims. a) grain z8 in the matrix, showing an inherited ~2.8 Ga core with oscillatory zoning surrounded by a lower-BSE response rim with cracks radiating outward from the core. b) photomicrograph of grain z4 (zrn) included in garnet. c) BSE image of grain z4 showing sector zoning. d) photomicrograph of grain z1 included in rutile. e) BSE image of grain z1, showing low-BSE response overgrowth on BSE bright core. f) BSE image of grain z6 outside of resorbed garnet (see Fig. 4f for photomicrograph

of location), showing BSE-bright core and metamorphic overgrowth with fractures radiating ourward from the core. g-l) BSE images of representative separated zircon grains analyzed by LASS and TIMS-TEA. Dashed pink lines indicate boundaries of the analyzed grain fragments. $^{207}Pb/^{206}Pb$ TIMS dates for each fragment are shown, with pink font indicating dates from fragments that do not exhibit apparent chemical or age domain mixing and overlap concordia within 2σ uncertainty. Concordance (%) is indicated in parentheses for each fragment. Mineral abbreviations in panels b and d are the same as in Figure 5.2.

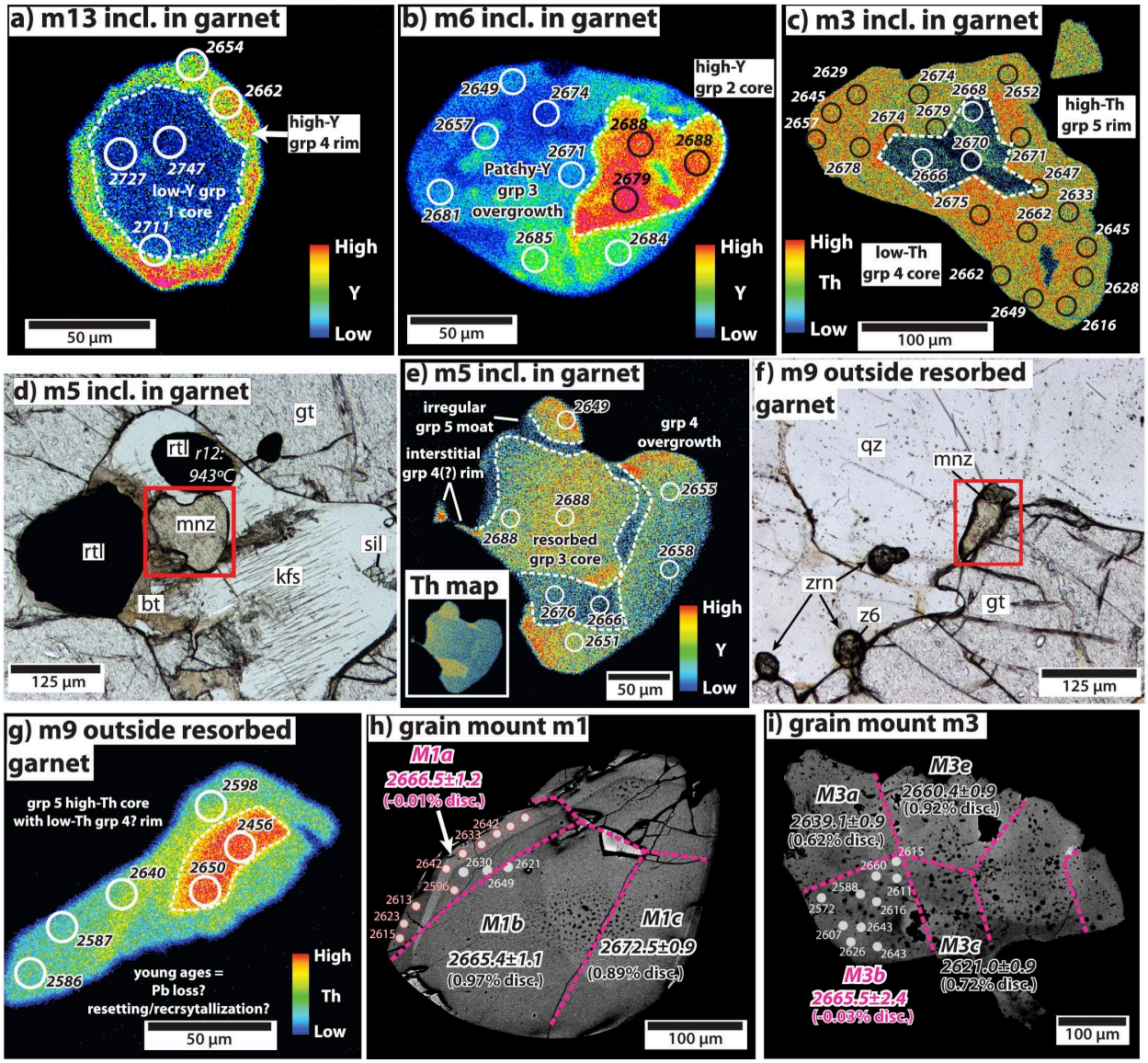

Figure 5.4: a-g) X-ray maps, BSE images, and photomicrographs of representative monazite grains. LASS spot analyses are represented by white and black circles. $^{207}Pb/^{206}Pb$ dates are shown for each spot analysis, each with uncertainties of 33-51 Ma. Red boxes in panels d and f indicate locations of monazite grains in panes e and g. a) Y X-ray map of inclusion in garnet showing partially resorbed low-Y group 1 core and high-Y group 4 rim. b) Y X-ray map of inclusion in garnet showing high-Y group 2 core with patchy-zoned group 3 overgrowth. c) Th X-ray map of inclusion in garnet showing euhedral low-Th group 4 core and euhedral high-Th group 5 rim. d) photomicrograph of polymineralic inclusion in garnet consisting of rutile, monazite, biotite (bt), sillimanite, and K-feldspar (kfs). Rutile grain r12 (labeled) gives Zr in rutile temperatures indicating growth at UHT conditions (Table 5.7). e) Y X-ray map of monazite in panel d showing resorbed group 3 core overgrown by irregular group 5 moat and sub- to euhedral group 4 rim. f) photomicrograph of monazite and zircon (zrn) outside resorbed garnet in the matrix. Location of z6 from Fig. 3f is indicated. g) Y x-ray map of grain outside resorbed garnet showing one group 5 analysis in high-Th core and one group 4 analysis in the

lower-Th rim. Other analyses are significantly younger. h-i) BSE images of separated monazite grains m1 and m3 analyzed by both LASS and TIMS-TEA. Dashed pink lines indicate boundaries of the analyzed grain fragments. $^{207}Pb/^{206}Pb$ TIMS dates for each fragment are shown, with pink font indicating fragments that overlap concordia within 2σ uncertainty (concordance indicated in parentheses for each fragment). LASS spot analyses for the fragments M1a and M3b are shown as white circles with $^{207}Pb/^{206}Pb$ dates determined by LASS. LASS spot analyses that do not overlap concordia within 2σ uncertainty are indicated with red outline. Mineral abbreviations in panels d and f are the same as in Figure 5.2.

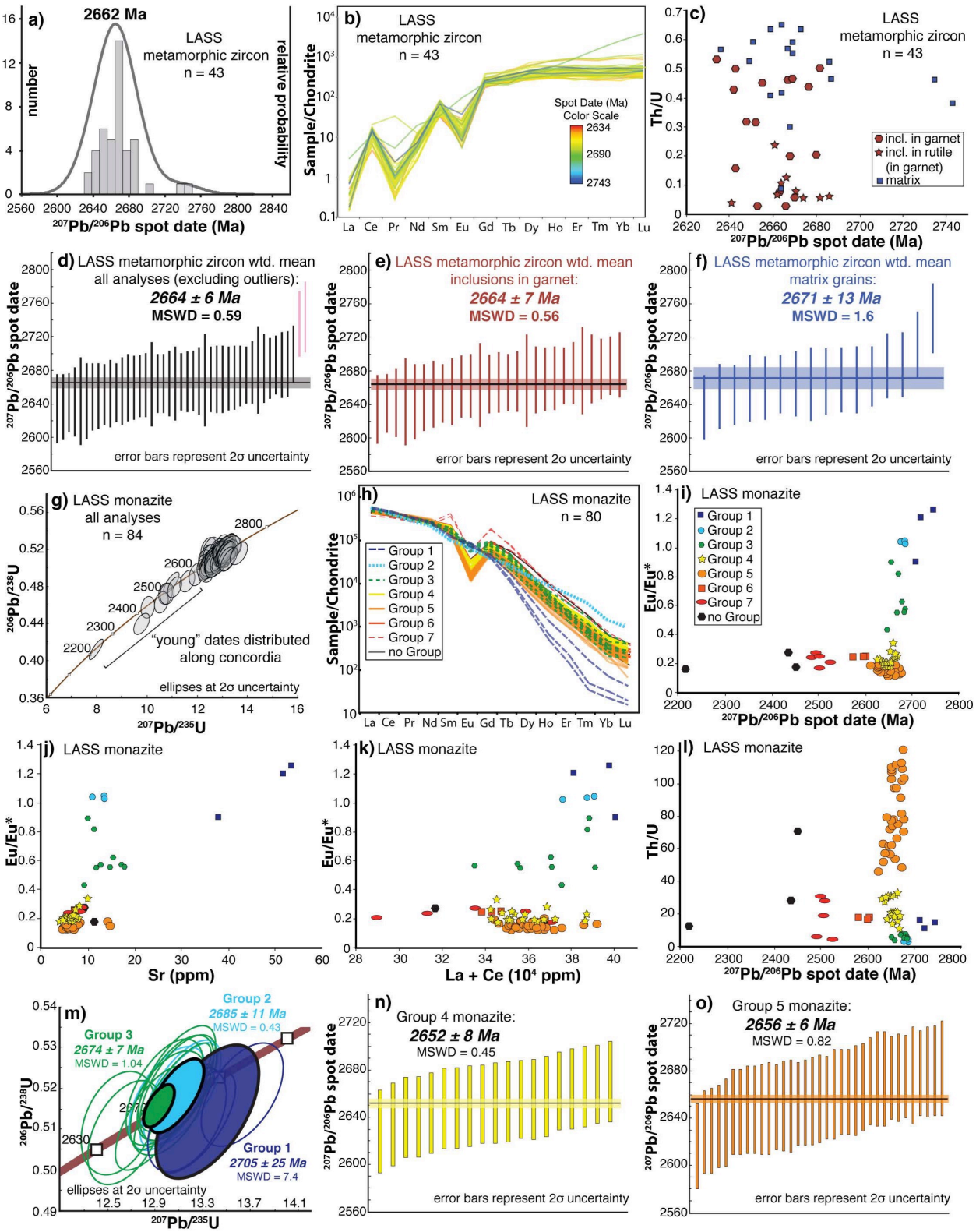

Figure 5.5: Results of *in-situ* LASS petrochronology. a) Probability density plot of zircon dates of metamorphic zircon. b) REE plot of metamorphic zircon analyses that overlap concordia within 2σ uncertainty. c) Plot of Th/U vs. $^{207}Pb/^{206}Pb$ date of zircon d-f) Weighted mean age plots of: all metamorphic zircon (d), analyses of grains included in garnet (e) and analyses of

grains included in rutile (f). Pink bars represent outliers excluded from the weighted mean calculation. g) Concordia diagram of all monazite analyses. h) REE plot of monazite analyses that overlap concordia within 2σ uncertainty. i) Plot of Eu/Eu* vs. $^{207}Pb/^{206}Pb$ date of monazite. j) Plot of Eu/Eu* vs. Sr of monazite. Symbols are the same as panel i. k) Plot of Eu/Eu* vs. La + Ce of monazite. Symbols are the same as panel i. l) Plot of Th/U vs. $^{207}Pb/^{206}Pb$ date of monazite Symbols are the same as panel i. m) Concordia diagram showing monazite concordia ages (filled ovals) of groups 1 (dark blue), 2 (light blue), and 3 (green). n-o) weighted mean age plots of group 4 and 5 monazite analyses.

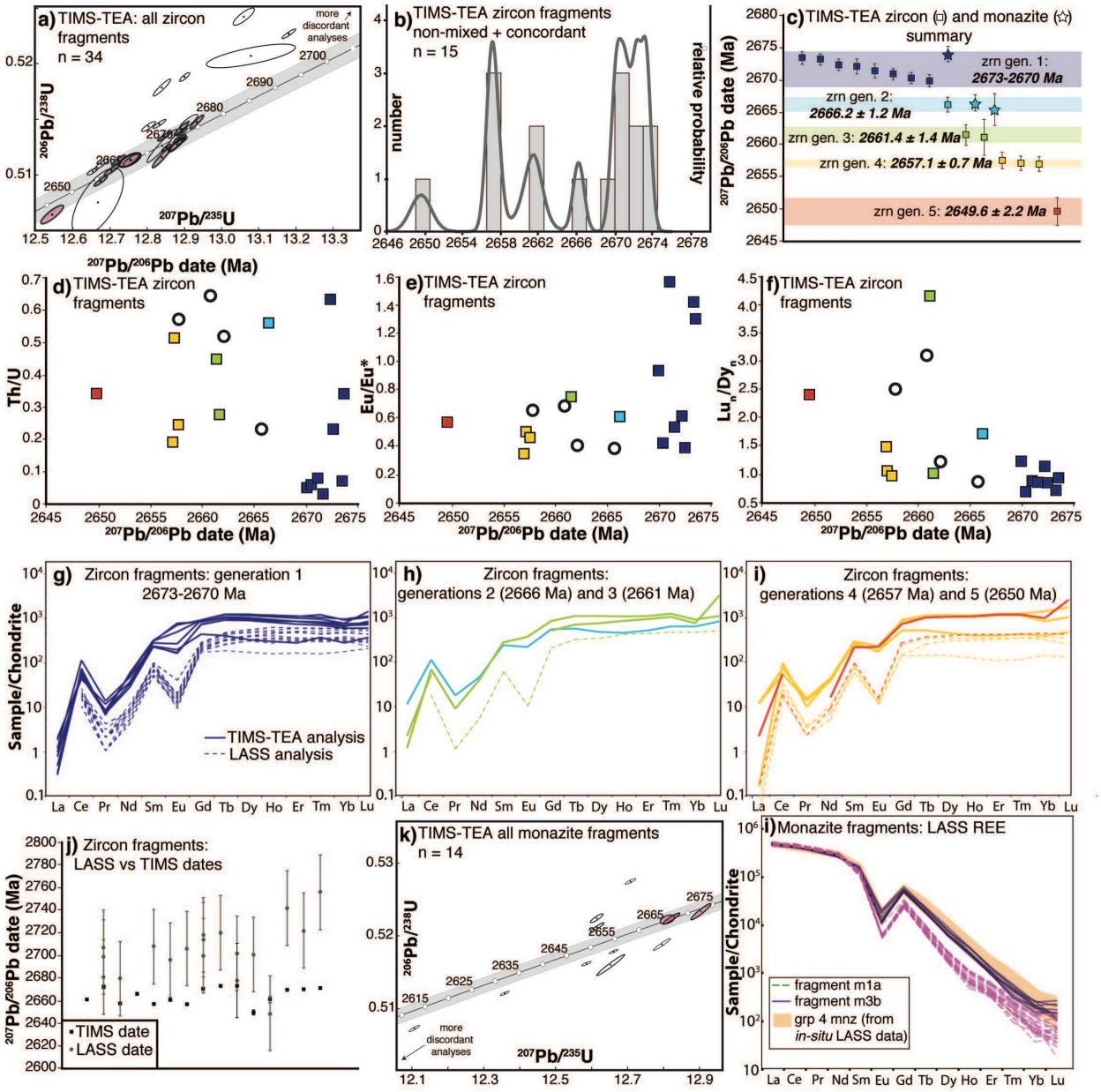

Figure 5.6: Results of TIMS-TEA petrochronology of zircon and monazite grain fragments. a) Concordia diagram of all zircon analyses. Five analyses plot outside of the area shown. Error ellipses represent 2σ analytical uncertainty. Pink ellipses with thick black outlines represent apparently homogeneous, concordant fragments that are used for further interpretation. Unfilled ellipses represent discordant fragments and/or fragments with multiple age/chemical domains identified in BSE images and/or through LASS analyses. Grey shaded area around concordia line represents 2σ uncertainty of decay constants on the location of concordia. b) Probability density plot of $^{207}Pb/^{206}Pb$ dates of homogeneous fragments that overlap with concordia within 2σ uncertainty. c) Plot of zircon and monazite fragment $^{207}Pb/^{206}Pb$ dates, grouped into temporally distinct generations. Weighted mean ages of each generation are indicated. Error bars are at the 2σ level. d-f) Plots of: d) Th/U, e) vs. Eu/Eu*, and f) Lu_n/Dy_n vs. $^{207}Pb/^{206}Pb$ date for zircon. Colors for each generation are the same as in panel c. Open circles represent fragments that are apparently homogeneous in BSE and are <1% discordant but do not overlap concordia within 2σ

uncertainty. g-i) REE plot for zircon fragments (solid lines). Results of LASS spot analyses of the same fragments are indicated by dashed lines. j) Comparison plot of $^{207}Pb/^{206}Pb$ dates for zircon fragments determined by TIMS (black squares) and LASS (grey circles). Error bars are at the 2σ level. k) Concordia diagram of all monazite analyses. Two analyses plot outside of the area shown. Symbols are the same as in panel a).

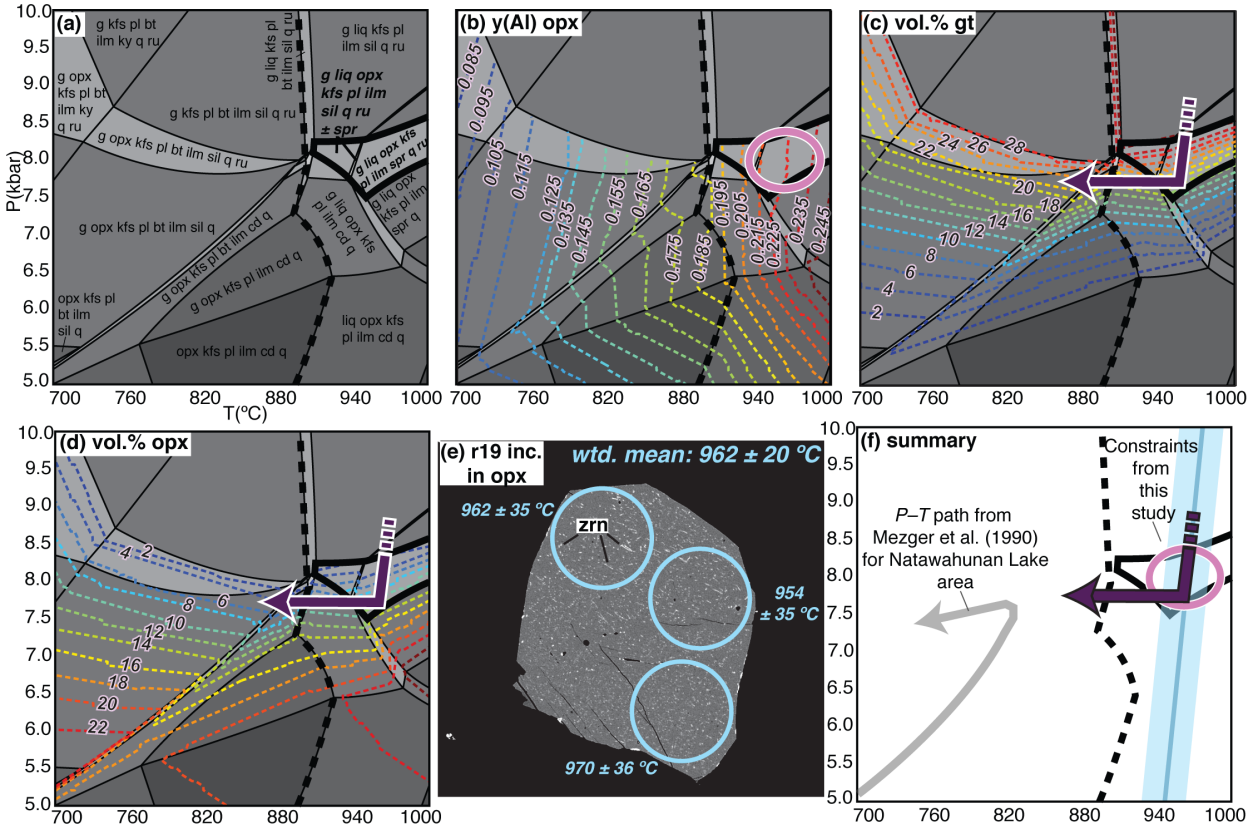

Figure 5.7: Results of phase equilibria modelling and Zr in rutile thermometry. a) *P–T* pseudosection for our sample. Predicted stability field of the inferred peak assemblage is outlined by thick solid line and indicated by bold font. Solidus is indicated by the thick black dashed line. b-d) *P–T* pseudosection from panel a contoured for: b) predicted y(Al) in orthopyroxene (colored dashed lines) with range of observed values intersecting with the predicted stability field of the peak assemblage indicated by pink oval, c) predicted volumetric modal abundance of garnet, d) predicted volumetric modal abundance of orthopyroxene (colored dashed lines). Warm (red) and cold (blue) colors represent high values and low values, respectively. A *P–T* path consistent with microstructural observations is indicated by purple arrow in panels c and d. e) BSE image of rutile grain r19 with exsolved zircon needles. LA-ICP-MS spot analyses and calculated Zr in rutile temperatures are shown in light blue. f) Summary *P–T* diagram of quantitative thermobarometry. Blue line represents weighted mean Zr in rutile temperature from grain r19, with blue shaded area representing 2σ uncertainty. Grey arrow shows counterclockwise *P–T* path for the Natawahunan Lake area determined by Mezger *et al.* (1990). [bt = biotite, cd = cordierite, g = garnet, ilm = ilmenite, kfs = K-feldspar, pl = plagioclase, q = quartz, ru = rutile, sil = sillimanite, spr = sapphirine]

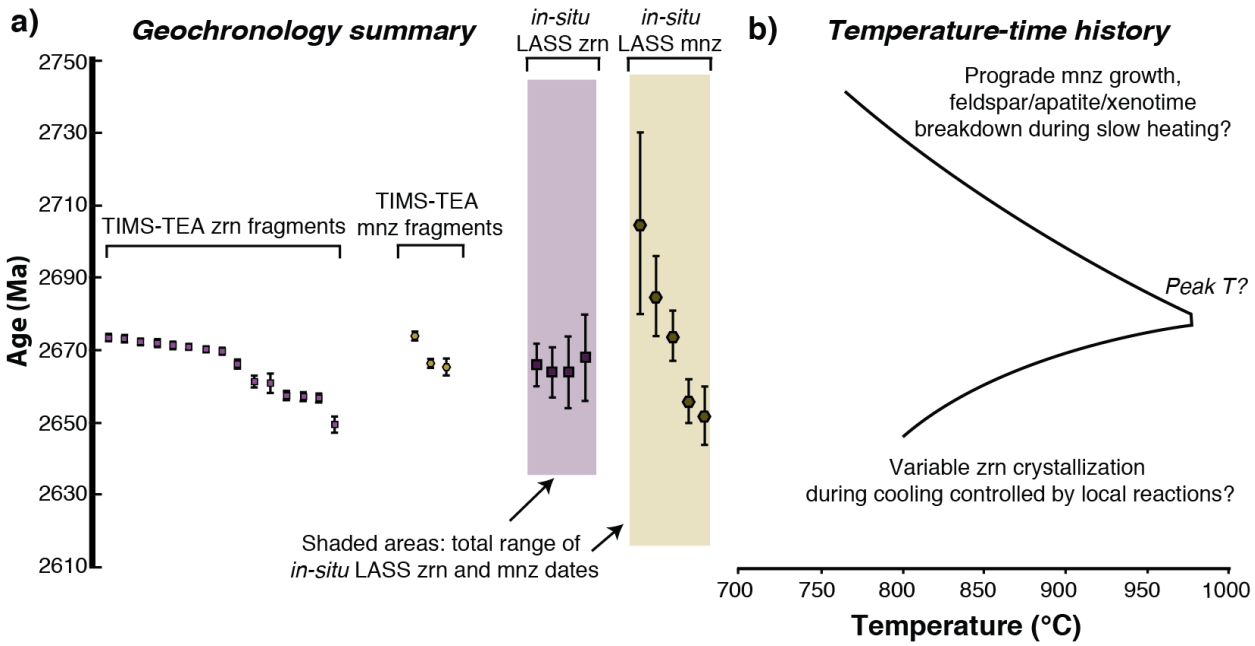

Figure 5.8: a) summary of geochronology, showing $^{207}Pb/^{206}Pb$ dates of TIMS zircon (purple squares) and monazite (gold circles) analyses, weighted mean ages of $^{207}Pb/^{206}Pb$ dates determined by *in-situ* LASS for different zircon (inclusions in garnet, inclusions in rutile, matrix grains, and all analyses) and monazite (groups 1-5). Purple and gold shaded areas represent the range of *in-situ* LASS spot $^{207}Pb/^{206}Pb$ dates for zircon and monazite, respectively. b) Temperature (horizontal axis) vs. age (vertical axis from panel a) plot showing two schematic temperature-time paths for our sample that could be interpreted from our data.

5.12 TABLES

Table 5.1: Summary of *in-situ* LASS zircon data

Textural setting	Number of analyses	Weighted mean age (Ma)	MSWD	Th/U	Eu/Eu*	Lu_n/Dy_n	Ti (ppm)	Weighted mean Ti in zircon Temp. (°C)	MSWD
All analyses	43	2664 ± 6	0.59	0.02-0.59	0.04 - 1.09	0.77-9.22	12-46	833 ± 6	1.9
Inclusions in garnet	27	2664 ± 7	0.56	0.04-0.47	0.04-0.26	0.97-2.54	14-46	831 ± 9	1.6
Inclusions in rutile	8	2668 ± 12	0.64	0.07-0.22	0.04-0.26	1.04-2.54	16-46	837 ± 19	1.6
Matrix grains	16	2671 ± 13	1.6	0.02-0.59	0.04 - 1.09	0.78-9.22	16-34	829 ± 16	2.3

Table 5.2: Summary of *in-situ* LASS monazite data

Group	Number of analyses	Concordia age (Ma)	MSWD	Weighted mean age (Ma)	MSWD	Th/U	Eu/Eu*	Gd_n/Yb_n	Sr (ppm)	Y (ppm)
1	3	2705 ± 25	7.4	2726 ± 47	1.3	12-17	0.90-1.26	491-1251	38-54	800-2000
2	3	2685 ± 11	0.43	2685 ± 19	0.43	3	1.03-1.04	24-27	11-14	12700-12800
3	9	2674 ± 7	1.04	2675 ± 11	0.76	6-8	0.44-0.90	86-327	10-18	4000-7800
4	19	-	-	2652 ± 8	0.45	11-31	0.18-0.34	145-293	4-10	4800-6800
5	35	-	-	2656 ± 6	0.82	46-120	0.13-0.20	136-293	5-15	3600-6800
"young" ages (incl. groups 6 and 7)	15	2504 ± 16 (group 7)	0.1 (group 7)	2592 ± 19 (group 6), 2504 ± 16 (group 7)	0.71 (group 6), 0.69 (group 7)	5-71	0.17-0.28	139-363	6-12	4400-12200

***Table 5.3*:** ID-TIMS isotopic analyses of zircon grain fragments (overlapping with concordia)

Fragment	Grain Mount	$^{207}Pb/^{206}Pb$ date	2s	%disc	Th/U	Pb* (pg)	Pbc (pg)	$^{206}Pb/^{204}Pb$	$^{206}Pb/^{238}U$	2s (%)	$^{207}Pb/^{235}U$	2s (%)	$^{207}Pb/^{206}Pb$	2s (%)
PPC15-01-01z7a	1	2673.4	1	0.14	0.34	141	1.32	6129	0.51308	0.066	12.893	0.11	0.182327	0.053
PPC15-01-01z5b	1	2673.2	0.88	-0.14	0.07	537	0.56	58520	0.51475	0.12	12.933	0.14	0.182304	0.042
PPC15-01-02z9b 37 dt	1	2672.36	0.90	0.17	0.23	401.44	0.55	42945.16	0.51	0.12	12.87	0.14	0.18	0.04
PPC15-01-02z18a	1	2672.10	1.16	0.06	0.63	182.02	0.31	32082.33	0.51	0.07	12.89	0.13	0.18	0.06
PPC15-01-01z16d	1	2671.4	1.1	0.3	0.03	171	0.73	14449	0.51157	0.18	12.839	0.19	0.1821	0.055
PPC15-01-01z5a	1	2670.91	0.89	-0.09	0.08	248	0.91	16599	0.51388	0.069	12.893	0.1	0.182052	0.043
PPC15-01-01z16c	1	2670.28	0.86	0.12	0.06	683	0.35	118320	0.51243	0.062	12.852	0.099	0.181982	0.04
PPC15-01-01z16a	1	2669.83	0.97	-0.16	0.05	147	0.71	12691	0.51411	0.11	12.891	0.14	0.181934	0.049
PPC15-01-02z11b	2	2666.16	1.16	-0.20	0.56	182.63	0.45	22217.11	0.51	0.08	12.85	0.13	0.18	0.06
PPC15-01-02z9a	2	2661.46	1.64	-0.03	0.28	82.50	0.94	5101.67	0.51	0.11	12.76	0.16	0.18	0.09
PPC15-01-01z15c	2	2661.1	2.8	-0.05	0.45	26	1.16	1272	0.51134	0.12	12.754	0.22	0.18098	0.16
PPC15-01-02z9c	2	2657.49	1.27	-0.04	0.25	89.72	0.74	7149.67	0.51	0.10	12.70	0.15	0.18	0.07
PPC15-01-02z25b	2	2657.08	1.14	-0.20	0.51	433.37	0.39	61914.85	0.51	0.09	12.72	0.14	0.18	0.06
PPC15-01-02z33a	2	2656.91	1.13	0.10	0.19	936.78	0.35	157288.94	0.51	0.09	12.67	0.14	0.18	0.06
PPC15-01-01z15a	2	2649.6	2.2	0.31	0.34	32.4	1.01	1853	0.50643	0.16	12.544	0.24	0.17972	0.13

***Table 5.4*:** Solution ICP-MS analyses of zircon grain fragments from Table 3

Fragment	Grain Mount	Hf (ppm)	Y (ppm)	La	Ce	Pr	Nd	Sm	Eu	Gd	Tb	Dy	Ho	Er	Tm	Yb	Lu	Eu/Eu*	Lun/Dyn
PPC15-01-01z7a	1	13784	2880	0.3	75.0	6.8	57.9	311.1	693.2	905.3	1185.8	1200.0	1168.4	1107.1	1046.6	938.3	1121.6	1.31	0.93
PPC15-01-01z5b	1	15771	2389	0.8	53.7	8.6	51.7	303.6	724.1	851.5	1059.7	1012.7	924.4	841.9	768.3	685.7	719.8	1.42	0.71
PPC15-01-02z9b 37dt	1	14328	2268	0.3	64.7	7.9	32.9	237.0	162.0	736.8	902.5	918.8	870.8	844.3	828.5	744.7	774.1	0.39	0.84
PPC15-01-02z18a	1	13891	783	1.2	114.8	14.0	46.1	234.9	196.9	438.7	407.7	328.5	299.5	277.1	370.1	276.4	368.5	0.61	1.12
PPC15-01-01z16d	1	14614	2938	2.1	43.6	11.8	35.7	275.8	266.4	899.7	1233.8	1220.1	1155.7	1091.9	1195.8	900.5	1038.7	0.53	0.85
PPC15-01-01z5a	1	15632	2318	0.5	56.4	8.0	53.7	300.1	775.6	820.0	1005.4	964.0	888.2	841.1	762.3	657.3	835.6	1.56	0.87
PPC15-01-01z16c	1	15321	2084	1.0	49.3	7.3	27.9	225.4	170.4	714.7	895.3	884.2	796.6	737.7	697.8	596.6	594.4	0.42	0.67
PPC15-01-01z16a	1	15162	2720	1.8	51.0	0.0	51.7	306.6	493.1	904.6	1194.3	1155.7	1062.1	986.4	945.7	758.1	1401.9	0.94	1.21
PPC15-01-02z11b	2	13811	1175	11.4	114.7	18.1	46.8	239.4	221.1	555.4	568.5	482.9	461.1	508.2	637.4	641.3	827.7	0.61	1.71
PPC15-01-02z9a	2	13393	2869	1.2	70.0	9.1	40.7	276.9	365.3	838.9	1095.1	1090.0	1076.3	1084.3	1226.8	907.5	1101.5	0.76	1.01
PPC15-01-01z15c	2	11901	2235	2.2	53.2	0.0	0.0	131.6	0.0	518.9	699.5	757.8	838.0	935.3	1050.8	750.2	3164.0	0.00	4.18
PPC15-01-02z9c	2	13464	2563	11.9	71.0	15.0	43.4	284.1	223.8	819.4	1018.8	1024.9	994.6	1103.2	1085.5	810.5	985.5	0.46	0.96
PPC15-01-02z25b	2	14124	1009	0.2	95.0	9.9	41.6	239.5	175.7	503.6	501.6	434.1	388.8	390.0	419.8	389.0	454.9	0.51	1.05
PPC15-01-02z33a	2	14208	2888	11.5	52.6	13.6	37.8	272.2	167.7	855.3	1080.7	1125.0	1097.2	1159.3	1205.0	1346.8	1651.0	0.35	1.47
PPC15-01-01z15a	2	12523	2715	2.2	54.0	0.0	16.2	207.6	217.2	702.3	964.8	1017.0	1040.8	1156.8	1155.5	958.0	2448.7	0.57	2.41

***Table 5.5*:** ID-TIMS isotopic analyses of monazite grain fragments (overlapping with concordia)

Fragment	$^{207}Pb/^{206}Pb$ date	2s	% disc	Th/U	Pb* (pg)	Pbc (pg)	$^{206}Pb/^{204}Pb$	$^{206}Pb/^{238}U$	2s (%)	$^{207}Pb/^{235}U$	2s (%)	$^{207}Pb/^{206}Pb$	2s (%)
PPC15-01-m2f	2674.1	1.2	0.12	27.5	2500	2.7	7666	0.5133	0.22	12.904	0.22	0.1824	0.066
PPC15-01-m1a	2666.5	1.2	-0.01	122.35	33700	11.64	6018	0.51238	0.15	12.822	0.18	0.18157	0.063
PPC15-01-m3b	2665.5	2.4	-0.03	101.47	9650	6.72	3582	0.51226	0.12	12.811	0.15	0.18146	0.14

***Table 5.6*:** Bulk composition (mol.%) determined by XRF and bulk composition used for phase equilibria modelling after adjustment of H_2O and Fe_2O_3.

	SiO_2 (mol.%)	**TiO_2**	**Al_2O_3**	**Fe_2O_3**	**FeO**	**MnO**	**MgO**	**CaO**	**Na_2O**	**K_2O**	**LOI**	**H2O**	**Total**
XRF	68.03	0.58	7.84	0.89	4.52	0.08	12.47	0.97	0.58	1.09	2.96	-	100
Adjusted	69.57	0.59	8.02	0.55	4.97	0.08	12.75	0.99	0.59	1.11	-	0.78	100

***Table 5.7*:** Results of Zr in rutile thermometry

Grain	Textural notes	ppm Zr	2 σ (ppm)	P (kbar)	T (C)	2 σ Error (C)
r19	inclusion in opx	6401	0.011	8	962	35
r19	inclusion in opx	6054	0.012	8	955	35
r19	inclusion in opx	6750	0.012	8	970	36
r12	inclusion in Kfs in garnet	5137	0.047	8	932	34
r12	inclusion in Kfs in garnet	5124	0.086	8	932	34
r12	inclusion in Kfs in garnet	6679	0.086	8	968	36
r13	inclusion at garnet edge	4504	0.086	8	915	34
r13	inclusion at garnet edge	4070	0.086	8	901	33
r13	inclusion at garnet edge	3891	0.086	8	896	33
r13	inclusion at garnet edge	4616	0.086	8	918	34
r13	inclusion at garnet edge	3700	0.086	8	889	33
r13	inclusion at garnet edge	4312	0.086	8	909	34
r13	inclusion at garnet edge	3881	0.086	8	895	33
r13	inclusion at garnet edge	4405	0.086	8	912	34
r13	inclusion at garnet edge	4537	0.086	8	915	34
r13	inclusion at garnet edge	4477	0.086	8	914	34
r13	inclusion at garnet edge	3215	0.086	8	872	32
r13	inclusion at garnet edge	4287	0.086	8	908	33
r13	inclusion at garnet edge	3977	0.086	8	898	33
wtd. mean r19	-	-	-	-	962	20
wtd. mean r12	-	-	-	-	943	20
wtd. mean r13	-	-	-	-	903	9

Chapter 6. Concluding Remarks

6.1 SUMMARY

The research in this dissertation explores two broad themes: 1) novel approaches to applying petrologic and geochronologic techniques for 'reading' HT/UHT metamorphic rocks and reconstructing their *P–T–*t histories, and 2) reconstruction and quantification of the *P–T–t* paths of granulites, with particular emphasis on rocks from two Neoarchean terranes. The study in Chapter 2 presented a novel approach to phase equilibria modelling of a texturally heterogeneous residual granulite, showing that models calculated for 'bulk' compositions representing successively decreasing length-scales provide snapshots of a *P–T* path that would be difficult to reconstruct through conventional methods. I showed that the sample, from the Central Alpine Gruf complex, records near-isothermal decompression at UHT conditions. This is compatible with previously proposed tectonic mechanisms for generating UHT conditions in the Gruf complex, though the absolute timing of UHT metamorphism remains elusive.

The studies in Chapters 3 and 4 focused on reconstructing the *P–T–t* history of Neoarchean granulites exposed in the eastern Beartooth Mountains of the northern Wyoming Province. In Chapter 3, I showed that these rocks record a HT metamorphic event at ~2.7 Ga, ~100 Ma later than previously proposed, in which partial melting and HT metamorphism is obvious in metasedimentary lithologies but cryptic in surrounding (meta-) granitoids. This conclusion is based on bulk Sm-Nd garnet and U-Pb monazite dates, which suggest a polyphase metamorphic history. A novel approach to interpreting bulk Sm-Nd garnet dates is presented in Chapter 3. In Chapter 4, phase equilibria and diffusion modelling of major element zonation in garnet suggests that these rocks record evidence of brief (< 1 Ma) residence at HT conditions in the middle crust, followed by limited (~0.5-1 kbar) decompression and rapid cooling (10^1–10^2 °C/Ma). The significant variation in apparent thermal gradient (from < 100 to 125 °C/kbar) along the *P–T* path and the brevity of this thermal anomaly suggest a convective/advective heat source, and I note the coincidence between the geochronologic constraints on HT metamorphism presented in Chapter 3 and crystallization ages of mafic magmas elsewhere in the Wyoming Craton. Though there are no exposed mafic intrusions of this age in the vicinity of the eastern Beartooth mountains, I postulate that mafic rocks may exist at currently unexposed crustal levels

and provided the heat for HT metamorphism, similar to that proposed for some Phanerozoic terranes in which a heat source may be similarly cryptic (e.g. Chu & Ague, 2015).

Finally, the study presented in Chapter 5 follows a novel approach to constraining timescales of UHT metamorphic processes by combining two different U-Pb monazite and zircon petrochronologic techniques on the same hand-sample from the PGD of the northern Superior Province: high-spatial resolution laser-ablation split-stream ICP-MS on grains in thin section and high-precision TIMS-TEA on separated grain fragments. Quantitative thermobarometry suggests that the rock records peak *P–T* conditions of ~960 °C, 8.5-9 kbar and followed a *P–T* path characterized by UHT decompression followed by near-isobaric cooling at ~7.5-8 kbar. *In-situ* LASS monazite ages provide information on the prograde metamorphic history of the sample, showing multiple generations of monazite with trace element signatures consistent with growth after/during garnet growth and feldspar breakdown from >2700-2675 Ma. *In-situ* LASS zircon data could be interpreted to record a single episode of zircon growth due to the high age uncertainties of LASS spot dates, and similar REE chemistries. In contrast, the TIMS-TEA zircon data reveal a complex zircon crystallization history, with at least five apparently distinct episodes of zircon growth over a ~24 Ma period from 2674-2650 Ma. The REE chemistry of grain fragments within each growth episode suggests variable feldspar growth and dissolution during this period. TIMS analyses of monazite show a similar apparent episodicity. The TIMS-TEA data could record zircon/monazite growth in response to dynamic petrologic processes within localized equilibrium domains such as zircon/monazite melt saturation in isolated melt pockets, fluxing of externally-derived melt, or different local effective bulk compositions leading to different reaction histories among chemically isolated domains during melt crystallization and slow cooling. The high-spatial resolution *in-situ* LASS technique allowed for sampling of a volumetrically small prograde monazite population, and preservation of textural context, while high-precision ID-TIMS-TEA reveals a complex accessory phase crystallization history that is not apparent in the LASS data but yields important insight into the petrologic evolution of the rock. Collectively, the data suggest that HT conditions in the Pikwitonei granulite domain may have been sustained over a long duration (>50 Ma), and could reflect either multiple heating and cooling episodes over this period or a single, long-lived metamorphic cycle characterized by decompression at UHT conditions followed by near-isobaric cooling in the mid- to lower crust. Notably, this path is significantly hotter than previous constraints in the PGD and is different from previously proposed anti-clockwise paths.

The Beartooth granulites and the western PGD record similar apparent thermal gradients (100 to ~125 °C/kbar) and clockwise *P–T* paths (limited HT/UHT decompression followed by near isobaric cooling). However, the peak *P–T* conditions and recorded metamorphic durations differ greatly. The Beartooth granulites record brief, mid-crustal heating to ~800 °C and rapid cooling, while the western PGD records long-duration HT conditions, peak UHT metamorphism at ~960 °C, and slow cooling at greater crustal depths. In the case of the Beartooth granulites, it is possible that UHT conditions were attained deeper in the crustal column: if mafic magmas are indeed the heat source for the HT metamorphism documented in Chapters 3 and 4, the mechanism for mantle melting could involve upwelling of mantle asthenosphere, producing UHT metamorphism over long timescales and length-scales in the lowermost crust. Thus, the brevity of HT metamorphism of the Beartooth granulites may simply reflect their proximity to mafic intrusions in the middle crust where conduction can be efficient (allowing for rapid heating and cooling), but distal from upwelling mantle asthenosphere at the lithosphere-asthenosphere boundary.

Could crustal heating in each terrane (Beartooth granulites and PGD) be driven by the same mechanism (or combination of mechanisms)? Rocks from the southern PGD in the Cauchon Lake area (Figure 5.1) record similar *P–T* conditions to the Beartooth granulites (6.5 kbar, 750 °C; Mezger *et al.*, 1990; Kooijman *et al.*, 2012), and suggest the geothermal gradient was not substantially different from the deeper UHT rocks in the western PGD (Chapter 5). Available geochronological constraints from this part of the PGD suggest a long duration (10^1-10^2 Ma) of HT conditions (Heaman *et al.*, 2011; Smit *et al.*, 2013a). The Beartooth granulites and the PGD therefore record maintenance of HT conditions over substantially different timescales (one to two orders of magnitude difference) at similar depths and temperatures, which suggests that crustal heating was ultimately driven by different mechanisms in each terrane in the Neoarchean, when Earth may have been transitioning from a stagnant lid tectonic regime to one defined by subduction and horizontal terrane accretion (Brown, 2007b, a; Brown, 2008; Sizova *et al.*, 2010).

6.2 OUTSTANDING QUESTIONS AND FUTURE RESEARCH DIRECTIONS

The research presented in this dissertation has raised new questions about HT/UHT metamorphic processes, analytical approaches to reading HT/UHT rocks, and the crustal heating

mechanisms and tectonic settings of the Beartooth and Pikwitonei granulites, several of which are discussed below.

Is there a more effective way to couple in-situ LASS and TIMS–TEA petrochronology to *quantify metamorphic timescales?* The study presented in Chapter 5 combined *in–situ* LASS on grains in thin section with TIMS-TEA petrochronology on separated grain fragments. The problem with this approach is that the spatial/microstructural context of the grains analyzed by high-precision TIMS-TEA is unknown. Moreover, sampling for TIMS-TEA may be biased to the largest grains due to spatial limitations imposed by the size of the picking tools used to break fragments. Microdrilling grains out of thin section (previously characterized *in-situ* by LASS) for TIMS-TEA analysis (Paquette *et al.*, 2004), followed by microsampling of chemically/temporally distinct grain domains using a more precise method for breaking fragments from grains (e.g. using a focused ion beam or laser ablation to break grain fragments) may be a more effective approach than that taken in Chapter 5, especially for complexly zoned monazite grains.

What is the precise timing of the 'cryptic' HT metamorphism in the Beartooth granulites? Both Sm-Nd bulk garnet ages and U-Pb monazite ages appear to record a HT metamorphic event at ~2.7 Ga in the eastern Beartooth mountains, but suffer from large age uncertainties (± 16–64 Ma). Knowledge of the precise timing of this event is crucial for determining the mechanism that drove heating in a local and regional context (e.g. Fig. 3.16). In the case of the garnet ages, this uncertainty is likely due to mixing of temporally distinct garnet populations. Textural evidence suggests that high-Ca and high-Sm garnet rims observed in one sample grew during partial melting. Therefore, microsampling and Sm-Nd geochronology of these rims may provide more precise constraints on the timing of HT metamorphism.

How widespread is the cryptic HT metamorphic event in the Beartooth Mountains? The Beartooth granulites investigated here are from a 150 km^2 area in the eastern Beartooth Mountains in which the HT metamorphism is obvious in metasedimentary xenoliths contained within the LLMC, but is cryptic in the LLMC itself. The LLMC dominates much of the Beartooth Mountains, which cover an expanse > 1500 km^2. The inferred brief timescales of metamorphism from Chapter 4 suggest that heating occurred over short-length-scales and imply a conductive/advective heat source, but this does not preclude similar short length-scale heat sources existing as isolated occurrences throughout the terrane. Is there any textural or

geochronologic evidence for this cryptic HT metamorphism in the LLMC distal to the area studied here?

If mafic magmas are indeed the heat source for cryptic HT metamorphism in the Beartooth granulites, what tectonic setting were they generated in? The answer to this relates directly to those of the two previous questions. With precise constraints on the timing of HT metamorphism, bulk-rock major element, trace element, and isotope geochemistry of similarly aged mafic rocks (e.g. Stillwater) in the northern Wyoming Province may be indicative of tectonic setting.

What was the mechanism for crustal heating in the Pikwitonei granulite domain? The results of the study in Chapter 5 suggest that HT conditions in the PGD were maintained for at least 24 Ma, and likely > 50 Ma, and that the westernmost part of the PGD reached at least ~960 °C, 8.5-9 kbar, with UHT decompression to ~7.5-8 kbar followed by near-isobaric cooling in the middle to lower crust. The *P–T–t* data from Chapter 5 are compatible with a scenario in which the western PGD was heated in the lower crust near upwelling hot asthenosphere after delamination/foundering of lithospheric mantle (such as in a stagnant lid tectonic regime), slab break-off/opening of a slab window, or during lithospheric extension. Evidence from modern settings suggests that such mechanisms could generate UHT conditions in the lower crust (e.g. Sandiford & Powell, 1986; Pownall *et al.*, 2014; Kelsey & Hand, 2015). However, these data could also be compatible with radiogenic heating in the lower portions of a thickened crust experiencing high radiogenic heat production (e.g. Clark *et al.*, 2011; Horton *et al.*, 2016), for example, beneath a high orogenic plateau. Indeed, lower crustal xenoliths from the Tibetan Plateau record similar *P–T* conditions to the western PGD (Hacker *et al.*, 2000), and seismic tomography is consistent with the presence of hot, partially melted middle and lower crust beneath the Tibetan Plateau (e.g. Nelson *et al.*, 1996; Hacker *et al.*, 2014). The Neoarchean Napier Complex in Antarctica records UHT metamorphism over similar timescales and length-scales to the PGD, as well as a path of UHT decompression followed by near-isobaric cooling in the middle to lower crust, and has been interpreted to represent the trapped lower crust of a large hot orogen (e.g. Harley, 2016). Though closure and burial of a hot, highly radioactive back-arc basin has been proposed as a mechanism for UHT metamorphism in other terranes, the clockwise *P–T* path determined here may be incompatible with this mechanism (e.g. Clark *et al.*, 2011; Sizova *et al.*, 2014). Distinguishing between crustal heating mechanisms consistent with the study presented in Chapter 5 (upwelling asthenosphere vs. burial of highly radioactive crust

and subsequent radiogenic heating) requires more data from rocks throughout the terrane. Questions that bear on the crustal heating mechanism in the PGD are discussed below.

How do peak P–T conditions, P–T paths, and timing and duration of metamorphism vary spatially throughout the PGD? At the time of this writing, UHT metamorphism in the PGD has been recorded and quantified in the Natawahunan Lake (Kooijman *et al.*, 2012) and Partridge Crop Lake areas (Chapter 5), with UHT conditions suggested in the Sipiwesk Lake area in the southwestern part of the terrane (Arima & Barnett, 1984; Couëslan *et al.*, 2012; Couëslan, 2016; Guevara *et al.*, 2016). Lower-*P/T* granulites (~6.5 kbar, 750 °C) occur in the Cauchon Lake area in the southern margin of the PGD, and even lower-*P* amphibolite-facies rocks (~3 kbar, 575 °C) that record a similarly high apparent thermal gradient occur in the adjacent North Caribou terrane (Mezger *et al.*, 1990) south of Cauchon Lake. This suggests that heating to UHT in the deeper parts of the PGD and the generation of high geothermal gradients likely post-dates the proposed collision between the North Caribou and Hudson Bay Terranes at ~2720 Ma, consistent with existing geochronology and whole-rock isotope geochemistry (Couëslan, 2016). Additionally, this raises the question of whether the PGD represents a single, tilted crustal column (Mezger *et al.*, 1990) with shallow levels exposed in the southeast, and deeper/hotter crustal levels in the northwest, or whether any spatial variability in *P–T* conditions/apparent thermal gradients is due to exhumation along shear zones that have not been mapped or observed.

Did all of the Pikwitonei Granulite Domain experience a decompressional P–T path? The clockwise *P–T* path presented in Chapter 6 is different from the anti-clockwise paths previously proposed for the PGD (Mezger *et al.*, 1990; Vry & Brown, 1991). Preliminary evidence from thermodynamic modelling combined with microstructural observations suggest that rocks from several localities in the PGD record HT decompression followed by near-isobaric cooling (Couëslan *et al.*, 2012; Couëslan, 2014; Couëslan & Guevara, 2015; Guevara *et al.*, 2016). If the entire terrane experienced HT/UHT decompression, how much decompression is recorded in different localities throughout the terrane, and how can these paths (and differences between them) inform us about crustal heat and mass transfer during this event? The path derived in Chapter 5 for the western PGD indicates that exhumation was limited, especially compared to rocks exposed in modern orogenic settings (e.g. Himalaya) – thus, the heating mechanism needs to account for the trapping/stalling of rocks at middle to lower crustal depths.

Did rocks throughout the PGD reach peak P–T conditions at the same time and were high thermal gradients maintained over the same durations at different depths throughout the

terrane? Different parts of the PGD appear to record different peak *P–T* conditions, but available geochronologic constraints suggest they record a similar temporal history (e.g. Figure 5.1b; Heaman *et al.*, 2011; Smit *et al.*, 2013b). Zoned Sm-Nd and Lu-Hf garnet geochronology, as well as garnet major element diffusion modelling (in rocks that preserve major element zonation in garnet) can aid in further constraining the timing and duration of metamorphism in different localities throughout the PGD.

Was the PGD crust 'preconditioned' prior to UHT metamorphism? Geologic evidence suggests that the UHT event that generated high thermal gradients in the PGD post-dates the proposed ~2720 Ma collision between the North Caribou and Hudson Bay Terranes. Was metamorphism associated with terrane accretion a distinct thermal cycle from the UHT event? If so, was this early metamorphism hot enough to partially melt some of the PGD and 'precondition' the PGD crust prior to the UHT event? Several workers have recognized that the latent heat of melting poses a significant energetic barrier to attaining UHT at crustal depths, and that UHT conditions are significantly easier to attain in residual crust that has already experienced partial melting and melt loss (Clark *et al.*, 2011; Caddick, 2013; Kelsey & Hand, 2015). If the PGD crust was indeed preconditioned, then this must be taken into account when considering possible crustal heating mechanisms.

Were juvenile magmas emplaced in the crust coeval with UHT metamorphism in the PGD? If heating in the PGD was indeed due to upwelling asthenosphere after lithospheric foundering/delamination, slab breakoff, or lithospheric thinning/extension, then voluminous juvenile magmatism coeval with UHT conditions might be expected. The PGD is dominantly comprised of felsic intrusive rocks, as well as more minor mafic intrusive rocks, many of which show evidence for metamorphism to granulite-facies conditions and partial melting (Weber, 1987; Couëslan *et al.*, 2012; Couëslan, 2014; Couëslan & Guevara, 2015). The protolith ages of the meta-granitoids may range from > 3300 Ma to ~2708 Ma (Böhm *et al.*, 1999; Heaman *et al.*, 2011). The younger end of this range is coincident with early heating (potentially to UHT) in the PGD, but the volumetric extent of syn-HT/UHT juvenile magmatism is unknown.

What was the radiogenic heat production of the PGD crust in the Neoarchean? If the PGD represents lower crust that was radiogenically heated at the base of an orogenic plateau, there should be little to no juvenile magmatism coeval with UHT metamorphism. Moreover, rocks from the PGD (particularly the voluminous meta-igneous rocks) should have sufficient K,

Th, and U to produce UHT conditions in the lower crust from self-heating (e.g. Horton *et al.*, 2016).

What do structures and rock fabrics tell us about HT/UHT metamorphism in the PGD? Field observations suggest the PGD is characterized by steep-dipping (60-80°) planar fabrics, with small, localized transpressional shear zones (Couëslan *et al.*, 2012; Couëslan, 2013, 2014; Couëslan & Guevara, 2015; Guevara *et al.*, 2016), and that development of planar rock fabrics preceded, was coeval with, and outlasted HT/UHT conditions (Couëslan & Guevara, 2015). The steep planar fabrics of the PGD contrast with subhorizontal linear fabrics predicted to form in extensional settings on modern Earth where weak, partially melted lower crust flows laterally (e.g. Sandiford & Powell, 1986), and thus may eliminate lithospheric extenstion as a tectonic setting for generating UHT in the PGD. Moreover, the dome and keel geometry observed in Archean greenstone terranes that has led several workers to infer a stagnant-lid tectonic processes is absent in the PGD, where linear, steep-dipping planar fabrics seem to dominate the terrane. Moreover, bounding shear zones to the north and south of the PGD may represent terrane boundaries/sutures suggestive of horizontal terrane accretion as proposed by Percival (2012).

Answers to the questions posed above will help to further elucidate the crustal heating mechanisms of the Beartooth granulites and the PGD, as well as inform our understanding of Archean geodynamics and HT/UHT metamorphic processes in general. At the time of this writing, work that addresses many of these questions is underway by myself, my advisor and other collaborators.

6.3 REFERENCES

Arima, M. & Barnett, R. L., 1984. Sapphirine bearing granulites from the Sipiwesk Lake area of the late Archean Pikwitonei Granulite Terrain, Manitoba, Canada. *Contributions to Mineralogy and Petrology*, **88**, 102-112.

Böhm, C. O., Heaman, L. M. & Corkery, M. T., 1999. Archean crustal evolution of the northwestern Superior craton margin: U-Pb zircon results from the Split Lake Block. *Canadian Journal of Earth Sciences*, **36**, 1973-1987.

Brown, M., 2007a. Crustal melting and melt extraction, ascent and emplacement in orogens: mechanisms and consequences. *Journal of the Geological Society*, **164**, 709-730.

Brown, M., 2007b. Metamorphic conditions in orogenic belts: A record of secular change. *International Geology Review*, **49**, 193-234.

Brown, M., 2008. Characteristic thermal regimes of plate tectonics and their metamorphic imprint throughout Earth history: When did Earth first adopt a plate tectonics mode of behavior. *Geological Society of America Special Papers*, **440**, 97-128.

Caddick, M. J., 2013. Petrologic preconditioning: a predisposition to polymetamorphism? In: *Goldschmidt*, Florence.

Chu, X. & Ague, J. J., 2015. Analysis of experimental data on divalent cation diffusion kinetics in aluminosilicate garnets with application to timescales of peak Barrovian metamorphism, Scotland. *Contributions to Mineralogy and Petrology*, **170**, 1-27.

Clark, C., Fitzsimons, I. C. W., Healy, D. & Harley, S. L., 2011. How Does the Continental Crust Get Really Hot? *Elements*, **7**, 235-240.

Couëslan, C. G., 2013. Preliminary results from bedrock mapping in the Partridge Crop Lake area, eastern margin of the Thompson nickel belt, central Manitoba (parts of NTS 63P11, 12). In: *Report of Activities 2013, Manitoba Mineral Resources*, pp. 34-45, Manitoba Geological Survey.

Couëslan, C. G., 2014. Preliminary results from bedrock mapping in the Armstrong Lake area, Pikwitonei granulite domain, central Manitoba (parts of NTS 63P10, 11). In: *Report of Activities 2014, Manitoba Mineral Resources*, pp. 7-17, Manitoba Geological Survey.

Couëslan, C. G., 2016. The Pikwitonei Granulite Domain, Manitoba: A collisional orogenic zone along the northwestern margin of the Superior Craton. In: *GAC-MAC Annual Conference* (ed Canada, G. A. o.), Whitehorse, Yukon, Canada.

Couëslan, C. G., Böhm, C. O. & Martins, T., 2012. Preliminary results from geological mapping in the central Sipiwesk Lake area, Pikwitonei Granulite Domain, central Manitoba (part of NTS 63P4). In: *Report of Activities 2012, Manioba Innovation, Energy and Mines*, pp. 79-89, Manitoba Geological Survey

Couëslan, C. G. & Guevara, V. E., 2015. Preliminary results from bedrock mapping in the southern and central Cauchon Lake area, eastern margin of the Pikwitonei granulite domain, central Manitoba (parts of NTS 63P7, 8). *Manitoba Geological Survey Report of Activities 2015*, 24-37.

Guevara, V. E., Dragovic, B., Caddick, M. J., Kylander-Clark, A. R. C. & Couëslan, C. G., 2016. Ultrahigh temperature metamorphism of the Pikwitonei Granulite Domain. In: *Geological Society of America*, Denver, CO.

Hacker, B. R., Gnos, E., Ratschbacher, L., Grove, M., McWilliams, M., Sobolev, S. V., Wan, J. & Zhenhan, W., 2000. Hot and dry deep crustal xenoliths from Tibet. *Science*, **287**, 2463-2466.

Hacker, B. R., Ritzwoller, M. H. & Xie, J., 2014. Partially melted, mica-bearing crust in Central Tibet. *Tectonics*, **33**, 1408-1424.

Harley, S. L., 2016. A matter of time: The importance of the duration of UHT metamorphism. *Journal of Mineralogical and Petrological Sciences*, **111**, 50-72.

Heaman, L. M., Böhm, C., Machado, N., Krogh, T. E., Weber, W. & Corkery, M. T., 2011. The Pikwitonei Granulite Domain, Manitoba: a giant Neoarchean high-grade terrane in the northwest Superior Province. *Canadian Journal of Earth Sciences*, **48**, 205-245.

Horton, F., Hacker, B., Kylander-Clark, A., Holder, R. & Jöns, N., 2016. Focused radiogenic heating of middle crust caused ultrahigh temperatures in southern Madagascar. *Tectonics*.

Kelsey, D. E. & Hand, M., 2015. On ultrahigh temperature crustal metamorphism: Phase equilibria, trace element thermometry, bulk composition, heat sources, timescales and tectonic settings. *Geoscience Frontiers*, **6**, 311-356.

Kooijman, E., Smit, M. A., Mezger, K. & Berndt, J., 2012. Trace element systematics in granulite facies rutile: implications for Zr geothermometry and provenance studies. *Journal of Metamorphic Geology*, **30**, 397-412.

Mezger, K., Bohlen, S. R. & Hanson, G. N., 1990. Metamorphic History of the Achean Pikwitonei Granulite Domain and the Cross Lake Subprovince, Superior Province, Manitoba, Canada. *Journal of Petrology*, **31**, 483-517.

Nelson, K. D., Zhao, W., Brown, L. D., Kuo, J., Che, J., Liu, X., Klemperer, S. L., Makovsky, Y., Meissner, R., Mechie, J., Kind, R., Wenzel, F., Ni, J., Nabelek, J., Leshou, C., Tan, H., Wei, W., Jones, A. G., Booker, J., Unsworth, M., Kidd, W. S. F., Hauck, M., Alsdorf, D., Ross, A., Cogan, M., Wu, C., Sandvol, E. & Edwards, M., 1996. Partially Molten Middle Crust Beneath Southern Tibet: Synthesis of Project INDEPTH Results. *Science*, **274**, 1684-1688.

Paquette, J.-L., Goncalves, P., Devouard, B. & Nicollet, C., 2004. Micro-drilling ID-TIMS U-Pb dating of single monazites: A new method to unravel complex poly-metamorphic evolutions. Application to the UHT granulites of Andriamena (North-Central Madagascar). *Contributions to Mineralogy and Petrology*, **147**, 110-122.

Percival, J. A., Skulski, T., Stott, G., 2012. Geology and Tectonic Evolution of the Superior Province, Canada. In: *Tectonic Styles in Canada: The LITHOPROBE Perspective* (ed Percival, J. A., Cook, F.A., Clowes, R.M.), pp. 321-378, Geological Association of Canada, Special Paper.

Pownall, J. M., Hall, R., Armstrong, R. A. & Forster, M. A., 2014. Earth's youngest known ultrahigh-temperature granulites discovered on Seram, eastern Indonesia. *Geology*, **42**, 279-282.

Sandiford, M. & Powell, R., 1986. Deep crustal metamorphism during continental extension: modern and ancient examples. *Earth and Planetary Science Letters*, **79**, 151-158.

Sizova, E., Gerya, T. & Brown, M., 2014. Contrasting styles of Phanerozoic and Precambrian continental collision. *Gondwana Research*, **25**, 522-545.

Sizova, E., Gerya, T., Brown, M. & Perchuk, L. L., 2010. Subduction styles in the Precambrian; insight from numerical experiments. *Lithos (Oslo)*, **116**, 209-229.

Smit, M. A., Scherer, E. E. & Mezger, K., 2013a. Lu–Hf and Sm–Nd garnet geochronology: Chronometric closure and implications for dating petrological processes. *Earth and Planetary Science Letters*, **381**, 222-233.

Smit, M. A., Scherer, E. E. & Mezger, K., 2013b. Peak metamorphic temperatures from cation diffusion zoning in garnet. *Journal of Metamorphic Geology*, **31**, 339-358.

Vry, J. K. & Brown, P. E., 1991. Texturally early fluid inclusions in garnets – evidence of the prograde metamorphic path. *Contributions to Mineralogy and Petrology*, **108**, 271-282.

Weber, W., 1987. Geology of the Pikwitonei granulite domain at Cauchon Lake. In: *Unpublished field trip guidebook* (ed Survey, M. G.), pp. 1-18.

B.2. Tables

Table B1 Trace element concentrations (ppm) of granitic lithologies

Element	Na	Mg	Al	Si	P	K	Ca	Ti	Mn	Fe	Y	Zr	Cs	La	Ce	Pr	Nd	Sm	Eu	Gd	Tb	Dy	Ho	Er	Tm	Yb	Lu	Hf	Ta
Mass	23	25	27	28	31	39	40	49	55	56	89	90	133	139	140	141	143	147	153	157	159	163	165	166	169	172	175	178	181
BQC13-01O-1	33680	3944	121446	320179	294.5	10258	21190	1240	104.0	10717	8.816	151.3	0.5906	99.49	135.3	14.08	56.35	11.09	0.9104	6.667	0.7077	2.658	0.3284	0.5760	b.d.	b.d.	b.d.	4.009	0.4026
BQC13-01O-2	35438	3903	115892	324180	293.6	10390	21032	1266	108.2	11328	8.115	145.7	0.5903	95.69	134.7	13.55	52.86	7.996	0.7122	7.017	0.4564	2.122	0.3250	0.3123	0.1025	b.d.	b.d.	3.179	0.4589
BQC13-01O-3	34061	3823	119777	316184	285.1	10161	21519	1280	112.1	11004	8.696	139.8	0.5939	97.20	142.3	14.57	50.22	10.56	0.6816	6.487	0.7851	2.533	0.4333	1.307	0.000	b.d.	b.d.	3.330	0.5561
BQC13-01O-4	34108	3900	125952	319126	276.6	9958	21542	1289	110.7	10725	9.746	151.5	0.6243	104.6	140.5	14.91	56.42	8.659	0.7605	6.402	0.8898	2.843	0.5052	0.6209	0.0000	b.d.	b.d.	5.436	0.4682
BQC13-01O-5	33850	3964	125494	325820	284.7	10200	21880	1284	107.8	10884	9.708	156.3	0.7156	101.2	139.3	15.09	55.20	8.725	0.7837	6.291	0.5987	2.364	0.2600	0.6895	0.000	b.d.	b.d.	4.123	0.3149
BQC13-01O-6	34350	3996	123365	328238	281.7	10603	22617	1362	115.7	11778	9.281	158.1	0.6680	100.9	143.0	15.21	59.41	9.040	0.8902	6.324	0.6799	2.526	0.3201	0.8472	0.000	b.d.	b.d.	3.660	0.4515
BQC13-01O	**34248**	**3922**	**121988**	**322288**	**286.0**	**10262**	**21630**	**1287**	**109.8**	**11073**	**9.060**	**150.5**	**0.6305**	**99.85**	**139.2**	**14.57**	**55.08**	**9.345**	**0.7897**	**6.531**	**0.6863**	**2.507**	**0.3620**	**0.7254**	**0.1025**	**b.d.**	**b.d.**	**3.956**	**0.4420**
BHP13-01G-1	22339	6785	117923	308779	326.4	29220	24833	2851	384.9	25558	6.844	185.3	0.3220	52.86	76.91	7.780	30.01	3.943	1.746	2.584	0.2824	1.567	0.1907	0.7351	b.d.	0.8175	b.d.	4.775	0.3476
BHP13-01G-2	22338	6845	118277	306568	310.0	29199	24747	2862	382.5	25572	7.058	187.7	0.2424	52.67	76.72	7.676	30.71	4.177	1.646	3.356	0.2219	0.9683	0.1396	0.7073	b.d.	0.6804	b.d.	3.869	0.5348
BHP13-01G-3	22344	6830	118587	307325	313.8	29330	24851	2828	386.5	25642	6.851	191.3	0.2989	54.12	76.88	8.094	30.16	3.748	1.497	2.808	0.3429	1.826	0.1949	0.8736	b.d.	0.7572	b.d.	5.410	0.4633
BHP13-01G-4	22289	6845	118214	307374	306.8	29569	24892	2863	384.4	25584	6.899	196.6	0.2523	54.55	78.06	8.039	29.58	4.542	1.565	3.787	0.2710	1.500	0.2225	0.8597	b.d.	0.4824	b.d.	4.345	0.4691
BHP13-01G-5	22353	6928	122308	307376	305.3	29648	25437	2920	386.3	25440	7.313	198.5	0.2664	56.46	77.66	8.043	31.59	4.239	1.410	3.741	0.3588	1.455	0.2255	0.5938	b.d.	0.5762	b.d.	5.502	0.3990
BHP13-01G-6	22392	6984	121720	309432	303.2	29249	26172	2839	389.6	26118	7.406	196.2	0.2614	56.45	79.28	8.257	31.67	4.025	1.588	3.721	0.2455	1.575	0.1513	0.8531	b.d.	0.6401	b.d.	4.745	0.4565
BHP13-01G	**22342**	**6869**	**119505**	**307809**	**310.9**	**29369**	**25155**	**2860**	**385.7**	**25652**	**7.062**	**192.6**	**0.2739**	**54.52**	**77.58**	**7.982**	**30.62**	**4.112**	**1.575**	**3.333**	**0.2871**	**1.482**	**0.1874**	**0.7704**	**b.d.**	**0.6590**	**b.d.**	**4.774**	**0.4451**
BHP14-11L-1	27262	1080	94233	295534	287.6	25318	10083	306.6	76.09	4595	5.009	111.6	b.d.	27.97	37.81	4.248	19.85	2.832	2.781	2.091	0.2352	1.255	0.1902	0.6123	0.1085	0.3424	0.000	3.393	0.2071
BHP14-11L-2	24787	1137	96753	296185	289.1	24068	10098	312.6	77.11	4625	4.868	119.0	b.d.	28.08	37.61	4.593	15.88	2.850	2.765	1.718	0.2327	1.876	0.2178	0.4714	0.0343	1.015	0.2291	3.364	0.2366
BHP14-11L-3	27186	1178	100645	304589	300.7	24675	10672	338.7	78.35	4881	5.366	121.2	b.d.	28.83	40.56	4.559	19.06	3.481	2.942	1.262	0.2546	0.9736	0.1922	0.6298	0.1927	0.8605	b.d.	4.388	0.1704
BHP14-11L-4	24553	1124	95353	288344	284.4	24754	10077	305.8	75.02	4671	3.814	117.5	b.d.	28.56	37.98	4.570	16.67	2.715	2.751	1.371	0.2231	1.379	0.2188	0.6374	0.1530	0.6269	b.d.	4.156	0.2026
BHP14-11L-5	26145	1107	94568	284988	278.6	23601	10041	294.2	78.35	4821	4.412	111.7	b.d.	28.58	39.14	4.127	17.88	2.413	2.881	1.276	0.1789	1.131	0.2186	0.6641	0.1992	0.8103	b.d.	3.653	0.1804
BHP14-11L-6	26816	1097	102040	300146	279.6	25929	10766	307.0	77.68	4526	5.213	120.8	b.d.	31.25	39.51	4.696	19.25	3.318	2.696	1.576	0.2962	1.425	0.2373	0.6361	0.0912	0.5667	0.2070	3.932	0.1823
BHP14-11L	**26125**	**1120**	**97265**	**294964**	**286.7**	**24724**	**10289**	**310.8**	**77.10**	**4687**	**4.780**	**117.0**	**b.d.**	**28.88**	**38.77**	**4.465**	**18.10**	**2.935**	**2.803**	**1.549**	**0.2368**	**1.340**	**0.2125**	**0.6085**	**0.1298**	**0.7036**	**0.2180**	**3.814**	**0.1966**

Table B2. Major element concentrations (wt.%) of garnets

Analysis	SiO_2	TiO_2	Al_2O_3	MgO	CaO	MnO	FeO	Na_2O	K_2O	Total	X_{Mg}	X_{Ca}	X_{Mn}	X_{Fe}
BHP13-03D														
garnet core	38.437	0.023	21.609	2.924	0.788	1.959	36.760	0.014	0.025	102.539	0.113	0.022	0.043	0.821
low Ca garnet "mantle"	38.480	0.072	21.634	2.975	0.460	1.791	37.841	0.033	0	103.286	0.115	0.013	0.039	0.833
high Ca garnet inner rim	38.564	0.008	21.786	3.406	1.504	1.371	36.768	0.023	0	103.430	0.132	0.042	0.030	0.796
garnet rim	38.258	0.045	21.677	2.630	1.085	1.154	38.614	0	0.009	103.472	0.102	0.030	0.026	0.842
BQC13-01A-L														
garnet core	38.921	0.005	21.669	3.946	4.418	1.346	32.370	0.012	0.012	102.699	0.151	0.122	0.029	0.698
low Ca garnet "mantle"	39.958	0.014	21.965	4.198	4.264	1.337	32.099	0.018	0	103.853	0.157	0.114	0.028	0.701
high Ca garnet inner rim	39.017	0.026	21.354	3.990	4.726	1.427	32.308	0	0.011	102.859	0.152	0.130	0.031	0.687
garnet rim	39.697	0.002	22.089	5.062	2.143	1.560	32.533	0.007	0.002	103.095	0.190	0.058	0.033	0.719
BLP13-04 - Si-rich layer														
garnet core	38.002	0.032	22.070	2.367	2.903	2.824	34.571	0.004	0.012	102.785	0.093	0.082	0.063	0.762
garnet rim	37.798	0.011	21.888	2.017	3.833	2.994	33.610	0	0	102.151	0.080	0.109	0.067	0.744
BLP13-04 -Fe-rich layer														
garnet core	38.288	0	21.692	1.715	4.441	3.601	33.049	0	0.006	102.792	0.067	0.125	0.080	0.727
garnet rim	38.077	0.021	21.387	1.511	4.452	3.788	33.205	0.010	0.004	102.455	0.059	0.126	0.084	0.731

Table B3 Trace element concentrations (ppm) of garnets

Element	Na	Mg	Al	Si	P	K	Ca	Ti	Mn	Fe	Y	Zr	La	Ce	Pr	Nd	Sm	Eu	Gd	Tb	Dy	Ho	Er	Tm	Yb	Lu	Hf
Mass	23	25	27	28	31	39	40	49	55	56	89	90	139	140	141	143	147	153	157	159	163	165	166	169	172	175	178
BHP13-03D grt2-1	20.13	18820	133500	183200	206.4	3.442	6982	49.54	7340	236700	13.83	7.002	b.d.	b.d.	0.0152	0.2972	1.064	0.3730	3.913	0.6724	3.064	0.4914	1.295	0.1796	1.013	0.1756	0.1025
BHP13-03D grt2-2	26.05	19600	134200	181400	202.2	b.d.	7565	68.04	7765	236600	10.69	10.22	b.d.	b.d.	b.d.	0.1445	0.9259	0.3370	4.727	0.8824	3.745	0.3829	0.5088	0.0526	0.2282	0.0328	0.1682
BHP13-03D grt2-3	22.76	18420	136600	180900	195.1	b.d.	8239	71.24	8780	233700	42.42	11.42	b.d.	0.0132	0.0154	0.1241	1.137	0.3647	8.302	2.023	11.13	1.482	2.939	0.3223	1.835	0.2173	0.2087
BHP13-03D grt2-4	57.95	17430	133700	182200	218.2	b.d.	3722	32.25	11380	239400	24.03	5.332	b.d.	b.d.	b.d.	b.d.	0.2557	0.1891	2.558	0.9407	6.512	0.8707	1.477	0.1385	0.8688	0.1308	0.0808
BHP13-03D grt2-5	62.58	16880	133100	181700	214.7	5.827	2992	1820	12010	239500	46.30	4.127	b.d.	b.d.	b.d.	b.d.	0.1248	0.1495	1.676	1.105	9.497	1.637	3.640	0.3478	1.862	0.2593	0.0954
BHP13-03D grt2-6	59.15	17010	136500	179300	215.9	b.d.	2943	47.31	12530	240300	55.46	3.460	b.d.	b.d.	b.d.	b.d.	0.1547	0.1981	1.660	0.8957	9.078	1.850	4.906	0.5886	3.658	0.5333	0.0369
BHP13-03D grt2-7	135.8	16920	136200	178900	266.6	b.d.	3200	30.26	12790	240900	33.29	3.943	0.0755	0.2271	0.0297	0.1767	0.162	0.1885	1.172	0.6565	5.676	1.105	3.171	0.4120	3.141	0.4977	0.0810
BHP13-03D grt2-8	61.67	16220	134600	182000	216.6	b.d.	3658	46.41	13200	238000	152.7	3.492	b.d.	b.d.	b.d.	b.d.	0.1968	0.3345	4.049	2.233	24.03	6.042	20.55	2.906	21.00	3.110	0.0687
BHP13-03D grt2-9	52.04	16390	134200	179500	199.7	b.d.	3805	43.41	13630	241900	220.8	3.472	b.d.	b.d.	b.d.	b.d.	b.d.	0.2455	4.474	2.798	32.84	8.259	27.50	3.958	25.15	3.629	0.0389
BHP13-03D grt2-10	63.99	16710	133300	177800	210.3	b.d.	3675	56.47	13690	245800	163.6	3.320	b.d.	b.d.	b.d.	b.d.	b.d.	0.1782	3.654	2.177	26.39	6.212	20.49	2.578	17.27	2.583	0.0724
BHP13-03D grt2-11	63.68	16170	129900	185400	220.1	b.d.	3519	60.03	13140	239500	155.4	2.739	b.d.	b.d.	b.d.	b.d.	0.1394	0.2967	4.576	2.393	24.52	5.583	16.39	2.125	13.09	1.766	0.0487
BHP13-03D grt2-12	74.81	16090	129600	185900	224.5	b.d.	3332	48.70	12940	239700	117.4	3.124	b.d.	b.d.	b.d.	b.d.	0.137	0.2367	3.230	1.761	18.82	4.406	12.92	1.636	10.47	1.496	0.0940
BHP13-03D grt2-13	76.56	16240	129100	186400	233.6	b.d.	2936	45.81	12890	239900	80.06	3.005	b.d.	b.d.	0.0076	b.d.	0.0878	0.1662	2.018	1.244	12.67	3.027	8.177	0.9641	6.225	0.7386	0.0797
BHP13-03D grt2-14	80.70	16820	131600	181100	226.0	b.d.	2737	36.83	12890	244600	56.76	3.033	b.d.	b.d.	b.d.	b.d.	b.d.	0.1451	1.859	0.8688	8.509	2.314	6.707	0.9660	6.721	1.128	0.0269
BHP13-03D grt2-15	95.63	16630	128800	186700	242.4	b.d.	2613	34.27	12420	240200	37.62	3.496	b.d.	b.d.	b.d.	b.d.	b.d.	0.1097	1.005	0.5892	6.182	1.555	4.838	0.6337	4.442	0.7568	0.0693
BHP13-03D grt2-16	60.09	17020	129200	186600	222.5	b.d.	2868	32.28	11650	239800	31.31	4.160	b.d.	b.d.	b.d.	b.d.	b.d.	0.1237	1.360	0.7485	6.902	1.208	2.640	0.2679	1.666	0.2882	0.0717
BHP13-03D grt2-17	35.73	17580	130200	184300	210.3	b.d.	5863	57.04	10680	239100	53.90	4.067	b.d.	b.d.	b.d.	b.d.	0.4121	0.2179	4.198	1.542	12.61	2.030	4.608	0.4027	2.634	0.3231	0.0595
BHP13-03D grt2-18	20.95	18540	129600	186100	203.1	3.990	7867	70.73	7617	236800	7.057	8.424	b.d.	0.0199	0.0111	0.1648	0.9731	0.2968	3.693	0.6632	2.224	0.2663	0.4772	0.0476	0.2844	0.0268	0.1558
BQC13-01A-L grt1-1	57.79	28070	135700	175800	180.6	1.405	14700	28.08	10460	221100	845.5	5.447	b.d.	0.0102	0.0115	0.2753	2.390	0.3104	15.72	6.632	85.62	29.35	131.2	23.55	199.6	34.92	0.1162
BQC13-01A-L grt1-2	40.97	25710	136100	173700	172.8	b.d.	26300	39.72	10150	215100	776.6	6.363	b.d.	0.0108	0.0176	0.7492	3.612	0.8414	19.52	7.811	92.96	26.83	103.1	16.82	128.5	18.26	0.1216
BQC13-01A-L grt1-3	29.24	23950	135700	173100	172.7	b.d.	30730	64.25	9715	214800	446.0	7.402	b.d.	0.0217	0.0294	1.165	3.625	1.428	13.49	4.137	46.79	16.02	76.52	14.39	129.3	23.55	0.1235
BQC13-01A-L grt1-4	22.15	23910	135100	174600	175.5	b.d.	30050	72.72	9641	214600	209.9	13.76	b.d.	0.0189	0.0380	1.352	4.428	1.782	14.21	3.622	29.58	6.207	20.16	2.913	21.37	2.688	0.2076
BQC13-01A-L grt1-5	27.85	23340	135400	175400	173.2	b.d.	28520	55.03	9419	215000	433.2	8.698	b.d.	0.0361	0.0553	1.141	3.090	1.320	15.16	4.827	50.38	13.69	49.31	7.591	56.93	8.560	0.1371
BQC13-01A-L grt1-6	26.25	23110	134800	175300	174.1	b.d.	28960	80.72	9330	216300	313.3	12.46	b.d.	0.0227	0.0388	1.041	4.112	1.671	18.12	4.981	41.08	8.496	24.95	3.610	24.14	2.922	0.2157
BQC13-01A-L grt1-7	20.32	23100	136900	173600	169.3	b.d.	28960	70.49	9299	216100	211.0	6.446	b.d.	0.0331	0.0393	1.225	4.161	1.590	13.23	3.185	27.80	6.138	19.59	2.820	20.46	2.760	0.0860
BQC13-01A-L grt1-8	13.13	23260	136500	174200	173.0	b.d.	29010	49.49	9428	215600	71.24	6.316	b.d.	0.0699	0.0602	1.406	3.425	1.693	7.107	1.399	9.453	1.547	4.516	0.6828	4.828	0.5106	0.1100
BQC13-01A-L grt1-9	13.19	24620	135100	174600	172.5	b.d.	28840	59.70	10270	214500	73.42	6.578	b.d.	0.0620	0.0685	1.454	3.304	1.544	9.261	1.911	11.63	1.710	3.829	0.4317	2.561	0.2064	0.1053
BQC13-01A-L grt1-10	54.27	25850	137800	173100	170.9	b.d.	23730	33.42	10480	215100	1155	4.958	b.d.	0.0139	0.0099	0.5353	3.388	0.574	16.68	7.517	109.9	41.91	204.7	38.47	319.7	53.74	0.0698
BQC13-01A-L grt1-11	34.97	26960	137500	174800	173.4	1.409	15860	28.96	10650	220800	495.8	5.115	b.d.	0.0106	0.0124	0.4145	3.105	0.3922	19.86	7.161	67.60	14.97	46.00	6.611	45.13	5.160	0.1269
BLP13-04 grt3-1	30.77	12340	118700	192700	174.8	b.d.	19600	23.86	19410	225200	196.8	4.930	0.0147	0.0195	0.0264	0.5864	3.033	0.3785	12.33	3.569	28.54	6.621	20.07	2.709	18.20	2.325	0.0593
BLP13-04 grt3-2	21.33	12710	120700	190500	170.9	b.d.	17650	41.00	19380	227700	45.36	16.43	0.0186	0.0409	0.0536	1.4186	3.923	0.6089	9.876	1.945	10.57	1.412	2.817	0.3042	1.326	0.1541	0.4092
BLP13-04 grt3-3	20.17	12890	120800	190000	173.8	b.d.	17650	36.02	19000	228600	40.44	20.92	b.d.	0.0238	0.0313	0.9042	3.853	0.6887	10.62	1.925	9.922	1.151	2.689	0.2725	1.840	0.1804	0.4119
BLP13-04 grt3-4	18.02	12950	120100	190100	167.7	b.d.	16560	94.98	18980	230600	15.71	19.91	b.d.	0.0955	0.1232	3.3465	5.902	0.9528	6.752	0.8965	3.468	0.3988	0.9831	0.0927	0.5998	0.0620	0.4172
BLP13-04 grt3-5	25.18	12820	120300	189200	166.7	b.d.	18570	23.39	19100	229500	121.6	12.92	b.d.	0.0209	0.0226	0.647	2.942	0.5437	9.584	2.454	19.59	4.159	13.42	1.834	12.52	1.880	0.3427
BLP13-04 grt3-6	19.63	12830	119800	191000	166.0	b.d.	17610	47.32	19400	228100	31.05	20.11	b.d.	0.0342	0.0582	1.611	4.780	0.7892	7.336	1.271	6.587	0.8490	1.800	0.1567	0.7989	0.0832	0.3313
BLP13-04 grt3-7	23.31	12180	119600	191500	164.6	b.d.	20380	18.51	19340	225400	143.5	10.36	b.d.	0.0179	0.0150	0.4848	2.284	0.4190	9.652	2.588	22.30	4.804	14.50	1.938	13.17	1.833	0.1942
BLP13-04 grt5-1	10.85	8865	124500	184700	170.5	42.06	27160	5.607	25960	220000	21.61	1.372	0.2156	0.5181	0.0846	1.526	3.907	1.029	5.502	0.7041	3.669	0.7335	2.396	0.3872	2.626	0.4247	0.0631
BLP13-04 grt5-2	6.279	9500	128100	179800	165.6	4.316	27800	5.190	25690	221200	23.58	1.346	0.0357	0.1535	0.0582	1.365	4.200	1.135	5.663	0.7830	4.240	0.8083	2.897	0.4037	3.107	0.5068	0.0570
BLP13-04 grt5-3	8.677	8883	124400	184100	164.3	8.004	27560	6.375	25560	221100	26.36	2.072	0.0262	0.1155	0.0770	1.179	4.340	1.260	6.266	0.7997	4.386	0.9109	3.070	0.4540	3.398	0.5786	0.0693
BLP13-04 grt5-4	6.318	9971	128600	177400	162.0	b.d.	29090	6.555	25660	222900	21.84	1.088	0.0902	0.2035	0.0661	1.480	3.895	1.103	6.237	0.7382	3.973	0.7837	2.676	0.4003	2.969	0.4176	0.0945
BLP13-04 grt5-5	4.864	9862	128200	178700	158.2	b.d.	28970	5.225	25480	221800	21.09	0.6806	0.0996	0.1951	0.0681	1.109	3.622	1.085	5.723	0.6949	3.705	0.7023	2.335	0.3488	2.766	0.4199	0.0475
BLP13-04 grt5-6	4.506	9740	128100	177600	154.1	b.d.	28960	5.311	25760	223600	21.91	1.071	0.0619	0.1449	0.0473	1.293	4.298	1.210	5.587	0.7835	4.143	0.8069	2.641	0.3687	2.718	0.4822	0.0854
BLP13-04 grt5-7	15.58	9855	127600	179200	166.7	113.4	26620	17.15	25620	224100	21.36	1.679	0.2801	0.8822	0.1163	2.072	4.163	1.139	5.958	0.7541	3.823	0.7755	2.164	0.367	2.565	0.3913	0.0995

Element	Na	Mg	Al	Si	P	K	Ca	Ti	Mn	Fe	Y	Zr	La	Ce	Pr	Nd	Sm	Eu	Gd	Tb	Dy	Ho	Er	Tm	Yb	Lu	Hf
Mass	23	25	27	28	31	39	40	49	55	56	89	90	139	140	141	143	147	153	157	159	163	165	166	169	172	175	178
BLP14-05 grt1-1	46.24	18940	129600	174100	165.1	b.d.	5803	9.486	95090	169800	605.5	2.073	0.0143	b.d.	0.0093	b.d.	0.791	0.0766	7.137	4.593	64.77	21.12	85.86	13.81	105.2	17.79	b.d.
BLP14-05 grt1-2	46.17	21720	131500	173100	165.4	b.d.	5956	7.891	88130	172200	425.8	4.071	0.0070	b.d.	0.0091	0.2167	0.5795	0.1280	6.902	3.560	46.79	14.09	55.69	8.952	68.74	11.22	0.1156
BLP14-05 grt1-3	43.42	22910	131100	173800	169.5	b.d.	5791	25.61	84230	174500	193.5	12.30	0.0129	b.d.	0.0131	0.3373	1.571	0.3509	14.29	4.806	33.66	5.917	14.69	1.789	12.18	1.358	0.3371
BLP14-05 grt1-4	41.97	23420	131000	173800	165.6	b.d.	5821	38.86	83050	175200	135.1	13.27	0.0000	b.d.	0.0104	0.4775	3.5619	0.6300	18.58	4.930	26.46	3.834	8.888	1.080	5.906	0.8321	0.3093
BLP14-05 grt1-5	37.69	23600	130600	174900	168.6	b.d.	5542	33.84	82130	175200	105.4	15.42	0.0034	b.d.	0.0137	0.4178	2.086	0.4382	14.24	3.568	22.80	3.427	7.331	0.8492	5.618	0.7375	0.3382
BLP14-05 grt1-6	36.70	23550	130300	174400	170.1	b.d.	5341	35.63	82980	175700	62.92	18.44	0.0097	b.d.	0.0172	0.4325	2.3149	0.5729	10.43	2.280	13.26	2.271	5.386	0.6234	4.467	0.6090	0.2956
BLP14-05 grt1-7	35.8	23460	129900	174700	172.3	b.d.	5505	57.31	83080	175700	45.67	22.17	0.0062	b.d.	0.0202	0.6966	2.9957	0.7988	7.085	1.433	8.323	1.269	3.987	0.4571	3.454	0.4463	0.4235
BLP14-05 grt1-8	34.45	23400	129400	175500	174.4	b.d.	5554	62.19	82750	175600	27.79	21.96	0.0119	0.0219	0.0247	0.6686	3.1882	0.9926	5.436	1.010	5.065	0.7357	2.118	0.2590	1.899	0.2709	0.5675
BLP14-05 grt1-9	33.83	23000	129100	176200	173.2	11.61	5610	16.99	82810	175100	177.0	17.96	0.0073	b.d.	0.0095	0.2264	1.776	0.6835	5.615	1.760	19.03	4.191	13.35	2.022	13.22	1.421	0.3957
BLP14-05 grt1-10	26.96	23290	129200	175600	175.5	b.d.	5682	39.43	82710	175600	92.36	14.21	0.0059	b.d.	0.0162	0.3874	2.055	0.7150	3.788	1.354	12.85	2.384	6.380	0.6720	3.917	0.3741	0.3860
BLP14-05 grt1-11	24.66	23660	129000	175400	174.0	b.d.	5731	59.30	83020	175500	76.87	11.05	0.0060	b.d.	0.0213	0.3551	1.7369	0.6328	4.499	1.628	13.39	2.252	5.181	0.5478	2.329	0.2506	0.4175
BLP14-05 grt1-12	24.63	23560	128900	175300	171.8	b.d.	5431	97.53	82950	176300	15.46	14.13	0.0059	0.0265	0.0192	0.6747	1.4008	0.8631	2.480	0.5687	3.766	0.4731	0.9837	0.0799	0.5633	0.1226	0.3101
BLP14-05 grt1-13	28.67	23640	129100	175300	173.2	232.0	5885	31.31	82980	175100	113.2	12.02	b.d.	b.d.	0.0133	0.2857	1.267	0.2660	7.384	2.809	23.28	3.659	6.855	0.6535	3.093	0.4794	0.3036
BLP14-05 grt1-14	26.21	23630	129600	175000	173.3	21.41	5881	46.43	83470	174800	69.70	12.47	b.d.	b.d.	b.d.	0.1816	1.569	0.3525	6.228	2.425	17.94	2.577	5.340	0.5694	3.448	0.7383	0.5279
BLP14-05 grt1-15	23.78	23500	128900	174900	171.8	4.291	5926	80.68	83900	175700	48.04	9.903	b.d.	b.d.	0.0135	0.5875	1.586	0.6458	4.226	1.435	10.49	1.502	2.748	0.2262	1.353	0.1713	0.3539
BLP14-05 grt1-16	29.05	23380	129200	175000	175.4	4.483	5937	19.41	83900	175000	175.2	10.81	b.d.	b.d.	b.d.	0.132	1.105	0.2530	7.277	3.370	30.84	5.309	12.35	1.216	6.930	0.8550	0.4138
BLP14-05 grt1-17	26.68	23440	129900	173900	176.0	3.877	5828	35.04	85070	175600	121.0	14.48	b.d.	b.d.	b.d.	0.3091	1.8591	0.5092	6.632	2.438	20.90	3.523	7.915	0.8650	5.004	0.6766	0.4215
BLP14-05 grt1-18	33.13	23220	129900	173800	169.6	b.d.	5925	15.04	84620	175600	195.6	16.20	b.d.	b.d.	b.d.	0.2153	1.0253	0.2581	7.345	3.460	31.42	5.650	14.69	1.688	10.50	1.499	0.4903
BLP14-05 grt1-19	26.01	23320	129900	174700	166.6	b.d.	5709	15.83	84300	175400	207.5	11.33	b.d.	b.d.	b.d.	0.3809	1.441	0.2501	8.693	3.608	34.75	6.910	17.24	1.969	10.71	1.375	0.3245
BLP14-05 grt1-20	28.25	24080	129400	171000	177.8	b.d.	5739	40.89	86690	177800	79.95	13.58	b.d.	b.d.	b.d.	0.4767	2.045	0.8061	5.899	1.878	13.25	2.132	5.573	0.6640	5.018	0.8436	0.6309
BLP14-05 grt1-21	31.97	23810	131000	172700	169.2	31.92	5813	29.08	85070	174600	146.6	20.54	b.d.	b.d.	b.d.	0.4149	1.610	0.652	7.626	2.830	23.02	4.606	13.21	1.517	12.18	1.819	0.4812
BLP14-05 grt1-22	32.13	23410	132700	174000	173.9	12.86	5834	17.33	83140	172400	175.1	19.52	b.d.	b.d.	b.d.	0.2218	1.581	0.402	7.786	3.026	27.78	5.262	14.34	1.804	11.64	1.673	0.4551
BLP14-05 grt1-23	29.12	23860	132100	173800	172.9	17.07	5723	17.94	83570	172600	163.7	22.72	0.0790	0.0335	0.0177	0.4771	1.579	0.440	8.004	3.090	27.08	5.515	14.94	1.954	14.99	2.481	0.5800
BLP14-05 grt1-24	26.30	24000	133100	173100	172.3	4.619	5861	12.42	83240	172200	251.0	14.11	b.d.	b.d.	b.d.	0.1364	1.014	0.161	8.356	4.088	39.47	8.473	24.43	3.010	22.27	3.839	0.3919
BLP14-05 grt1-25	38.64	23370	141600	170800	168.7	121.4	5636	9.346	80750	167100	268.1	13.03	0.0191	b.d.	b.d.	0.1463	1.102	0.192	8.194	4.144	41.69	9.383	25.36	3.146	21.60	3.325	0.2996
BLP14-05 grt1-26	27.40	24480	137700	166900	157.0	5.551	5552	16.53	85060	173900	169.0	14.04	0.0197	b.d.	0.0314	0.5859	1.788	0.589	6.538	2.434	24.21	5.842	20.09	3.087	25.10	4.771	0.3703
BLP14-05 grt1-27	25.41	24290	137800	168500	160.0	b.d.	5515	15.27	83560	172800	148.4	17.69	0.0238	0.0152	b.d.	0.4135	1.703	0.574	5.970	2.395	21.98	4.899	16.30	2.471	18.42	3.114	0.4324
BLP14-05 grt1-28	26.13	24350	137900	169000	159.1	27.86	5486	19.41	83610	171700	103.7	16.94	0.0283	0.0125	b.d.	0.3811	1.808	0.6901	6.920	2.104	17.43	3.279	9.171	1.229	8.622	1.252	0.4270
BLP14-05 grt1-29	19.92	24540	142800	163800	153.7	17.46	6026	13.03	83830	172000	241.3	9.758	0.0163	0.0166	b.d.	0.3098	1.707	0.384	9.955	4.244	39.24	7.914	19.31	1.910	9.815	1.036	0.3632
BLP14-05 grt1-30	37.54	24470	138700	167200	162.6	270.5	5850	62.06	83630	172700	60.10	21.78	0.0182	0.0199	0.0386	0.9269	3.690	1.134	8.736	2.032	12.67	2.192	5.421	0.7009	3.800	0.5344	0.5613
BLP14-05 grt1-31	33.24	20220	122900	209800	196.1	658.6	4600	17.96	69940	145300	115.7	18.34	0.0764	0.0300	b.d.	0.2984	1.550	0.3263	6.850	2.356	19.31	3.498	9.105	1.194	6.198	0.7674	0.5960
BLP14-05 grt1-32	23.21	24560	139600	167200	158.7	4.570	5748	25.37	83160	172300	111.5	15.14	0.0036	b.d.	b.d.	0.4175	3.082	0.5968	10.96	2.898	20.53	3.667	9.080	1.124	6.427	0.8076	0.4203
BLP14-05 grt1-33	24.90	24370	138400	165700	161.2	4.880	5988	24.27	82390	171500	172.6	14.81	0.0247	0.0332	b.d.	0.4821	2.944	0.5507	13.85	3.997	31.25	5.652	14.05	1.698	9.431	1.080	0.3339
BLP14-05 grt1-34	33.99	24810	140300	165700	156.8	11.46	6368	86.50	82940	172800	75.43	19.61	0.0085	0.0310	0.0190	1.138	5.597	1.153	16.09	3.055	16.14	2.182	4.725	0.7285	3.792	0.4788	0.3489
BLP14-05 grt1-35	31.32	24830	140500	166100	154.7	4.640	6265	73.53	82450	172500	55.31	12.57	0.0117	0.0242	0.0263	1.047	4.631	0.8189	14.67	2.836	13.60	1.547	3.265	0.3639	2.157	0.2464	0.3392
BLP14-05 grt1-36	34.21	24900	140700	165700	157.3	b.d.	6128	53.47	82350	172800	141.7	20.33	0.0039	0.0139	0.0182	0.8594	3.444	0.6573	16.37	4.145	27.35	4.530	11.64	1.501	11.05	1.645	0.4280
BLP14-05 grt1-37	33.09	25700	144500	157800	150.0	b.d.	6094	29.03	85110	176700	181.2	15.14	0.0077	b.d.	b.d.	0.3491	1.918	0.3537	12.84	3.727	29.75	6.524	18.96	2.647	18.47	2.668	0.4267
BLP14-05 grt1-38	35.23	24520	141200	165400	159.5	b.d.	6175	13.29	82660	172700	235.3	13.27	0.0160	b.d.	b.d.	b.d.	1.213	0.1927	9.804	3.599	34.36	7.950	25.12	3.454	25.30	3.689	0.3176
BLP14-05 grt1-39	41.68	23420	141500	166000	154.1	b.d.	6429	8.987	83420	171300	525.8	3.877	b.d.	b.d.	0.0250	b.d.	0.905	0.1158	7.834	4.385	59.39	17.96	69.28	11.38	85.45	13.79	0.1456
BLP14-05 grt1-40	42.52	22060	141500	163800	154.3	b.d.	6347	8.011	89410	170300	725.8	2.884	b.d.	b.d.	b.d.	0.1685	0.837	0.1040	8.747	5.226	75.41	25.43	108.0	17.96	138.8	23.06	0.0404
BLP14-05 grt1-41	40.26	17960	141500	163200	154.0	b.d.	6519	9.188	98140	167900	588.3	2.994	b.d.	b.d.	b.d.	b.d.	1.198	0.1121	9.987	5.896	76.10	19.83	64.11	9.132	64.99	9.923	0.0730

Element	Na	Mg	Al	Si	P	K	Ca	Ti	Mn	Fe	Y	Zr	La	Ce	Pr	Nd	Sm	Eu	Gd	Tb	Dy	Ho	Er	Tm	Yb	Lu	Hf
Mass	23	25	27	28	31	39	40	49	55	56	89	90	139	140	141	143	147	153	157	159	163	165	166	169	172	175	178
BPYR14-11B grt1-1	64.35	29790	129900	175000	176.9	606.8	5627	33.22	6503	242800	226.1	6.491	b.d.	0.019	b.d.	0.151	0.9455	0.1312	7.522	3.215	33.14	8.453	27.62	3.665	26.00	3.696	0.1290
BPYR14-11B grt1-2	56.48	29400	130100	175500	190.9	b.d.	6134	28.68	6548	242500	97.62	6.732	b.d.	b.d.	b.d.	b.d.	0.5039	0.0738	5.306	2.051	16.28	3.181	9.148	1.181	7.359	0.9819	0.1425
BPYR14-11B grt1-3	68.88	31740	129900	176200	199.9	b.d.	5947	29.69	6472	239000	83.88	11.08	b.d.	b.d.	b.d.	b.d.	0.2944	0.0932	3.981	1.450	13.67	2.825	8.118	1.168	7.906	1.060	0.2017
BPYR14-11B grt1-4	85.11	32820	130800	175300	204.0	90.85	5888	31.99	6448	237600	69.52	15.90	b.d.	b.d.	b.d.	b.d.	0.3355	0.0750	2.987	1.271	11.77	2.272	6.133	0.8380	6.087	0.7575	0.3342
BPYR14-11B grt1-5	67.77	33180	131000	175400	200.8	b.d.	5754	30.81	6447	237000	71.56	12.33	b.d.	b.d.	b.d.	b.d.	0.4213	0.0482	2.682	1.166	11.09	2.252	6.809	1.006	7.554	1.016	0.2669
BPYR14-11B grt1-6	78.81	33570	131000	175600	206.1	3.221	5878	31.56	6446	236000	81.93	14.76	b.d.	b.d.	b.d.	b.d.	0.2476	0.0482	2.965	1.188	12.56	2.919	9.943	1.532	12.64	1.744	0.3233
BPYR14-11B grt1-7	75.39	34800	133700	171400	197.9	b.d.	5840	31.19	6508	237500	77.75	15.37	b.d.	b.d.	b.d.	b.d.	0.3424	0.0783	2.573	1.160	11.63	2.617	8.049	1.214	8.835	1.302	0.2983
BPYR14-11B grt1-8	69.28	34400	131000	176000	201.2	b.d.	5825	32.77	6459	234300	83.28	14.01	b.d.	b.d.	b.d.	b.d.	0.3485	0.0676	2.971	1.296	12.76	2.735	8.903	1.360	9.721	1.322	0.3208
BPYR14-11B grt1-9	63.38	34640	130900	175700	197.6	b.d.	5921	27.67	6478	234700	83.72	12.14	b.d.	b.d.	b.d.	b.d.	0.2769	0.0657	3.169	1.314	13.06	2.884	8.749	1.279	9.242	1.325	0.2215
BPYR14-11B grt1-10	64.78	34690	131600	173900	201.9	94.12	6048	29.57	6547	236100	96.01	13.48	b.d.	0.0237	b.d.	b.d.	0.2434	0.0542	3.151	1.395	15.20	3.342	11.29	1.739	12.60	1.795	0.2855
BPYR14-11B grt1-11	71.46	35270	132400	173500	206.3	b.d.	6050	32.39	6544	235000	113.6	17.25	b.d.	b.d.	b.d.	b.d.	0.2211	0.0639	3.362	1.594	17.12	4.036	13.91	2.133	15.91	2.325	0.3193
BPYR14-11B grt1-12	68.29	35000	130000	176100	202.9	b.d.	5917	30.55	6489	234600	118.0	13.13	b.d.	b.d.	b.d.	b.d.	0.2125	0.0497	3.574	1.897	18.77	4.012	12.56	1.837	12.94	1.879	0.2774
BPYR14-11B grt1-13	67.32	35100	130700	175800	200.4	b.d.	5842	28.87	6496	234000	130.2	12.59	b.d.	b.d.	b.d.	b.d.	0.1944	0.0729	3.485	1.918	20.00	4.312	12.72	1.704	11.77	1.516	0.3444
BPYR14-11B grt1-14	62.36	35000	129800	177600	201.2	10.21	5828	28.54	6495	232400	165.2	12.37	b.d.	0.0074	0.0065	b.d.	0.2375	0.0693	3.933	2.203	24.15	5.501	16.34	2.255	15.66	2.026	0.2388
BPYR14-11B grt1-15	62.04	35000	130500	175900	196.1	4.741	5831	24.36	6540	234300	173.6	9.726	b.d.	b.d.	b.d.	b.d.	0.1659	0.0636	4.042	2.322	25.91	5.774	17.74	2.520	16.94	1.934	0.2634
BPYR14-11B grt1-16	107.6	37690	129300	175300	237.7	935.5	5544	26.29	6179	233200	140.3	10.82	0.0806	0.1844	0.0164	0.1166	0.2310	0.0770	2.859	1.891	21.26	5.069	15.16	2.036	13.92	1.686	0.2681
BPYR14-11B grt1-17	249.6	35320	132800	165700	230.1	363.7	5272	22.45	7178	246900	140.8	10.47	b.d.	0.1977	b.d.	b.d.	b.d.	b.d.	2.169	2.687	16.58	6.811	11.90	1.249	18.13	2.219	1.1335
BPYR14-11B grt1-18	65.61	35090	133100	171700	190.1	b.d.	6119	29.95	6658	236900	139.7	10.21	b.d.	0.0088	0.0108	b.d.	0.2240	0.0492	4.783	2.139	21.77	4.662	13.42	1.770	12.83	1.529	0.2192
BPYR14-11B grt1-19	61.38	34460	131300	174600	193.7	61.20	6057	29.48	6628	235500	194.4	8.1588	0.2814	1.543	0.0862	0.2231	0.3975	0.1044	5.359	2.660	28.75	6.528	19.13	2.524	16.88	2.093	0.1769
BPYR14-11B grt1-20	58.37	34430	130400	175800	184.7	b.d.	5987	21.64	6536	235100	172.2	6.9735	b.d.	b.d.	b.d.	b.d.	0.2675	0.0694	4.554	2.481	26.86	6.114	18.15	2.394	16.18	2.365	0.2034
BPYR14-11B grt1-21	68.69	34010	130700	175000	202.3	11.92	5970	22.60	6586	236400	157.3	13.20	b.d.	b.d.	b.d.	b.d.	0.2090	0.0578	3.684	2.084	22.59	5.886	19.26	2.941	23.48	3.425	0.3455
BPYR14-11B grt1-22	59.52	32890	129900	176100	192.4	2.6	5830	28.13	6694	237200	194.2	11.38	b.d.	b.d.	b.d.	b.d.	0.1519	0.0574	3.879	2.174	26.92	7.342	26.20	4.321	32.85	5.356	0.2424
BPYR14-11B grt1-23	72.88	33200	129500	177600	204.1	57.88	5845	24.74	6547	235000	180.6	9.721	b.d.	b.d.	b.d.	b.d.	0.1487	0.0668	2.953	1.980	23.94	6.638	23.94	3.605	26.00	3.979	0.3119
BPYR14-11B grt1-24	69.69	32650	129900	176100	202.6	70.63	5744	26.22	6628	237900	119.5	12.86	b.d.	b.d.	b.d.	b.d.	0.2202	0.0450	3.038	1.605	17.52	3.968	12.92	1.990	15.01	2.050	0.2994
BPYR14-11B grt1-25	69.72	33290	130200	175500	204.5	35.59	5697	26.69	6544	237600	126.4	11.06	b.d.	b.d.	b.d.	b.d.	0.1757	0.0549	2.783	1.549	17.98	4.393	14.99	2.270	16.67	2.684	0.3170
BPYR14-11B grt1-26	70.44	33420	130200	176200	206.4	b.d.	5814	24.05	6505	236300	113.4	11.572	b.d.	b.d.	b.d.	b.d.	0.1799	0.0686	3.041	1.640	16.35	3.901	12.82	1.960	14.89	2.213	0.3243
BPYR14-11B grt1-27	64.51	32860	128900	179500	196.6	211.7	5809	20.00	6435	233400	99.52	8.848	b.d.	b.d.	0.0070	b.d.	0.2491	0.0954	3.685	1.751	15.50	3.143	9.408	1.330	10.50	1.284	0.1869
BPYR14-11B grt1-28	92.90	32510	130200	174100	227.0	4.470	5792	28.28	6601	240800	100.3	27.46	b.d.	b.d.	b.d.	b.d.	0.1506	0.0601	3.110	1.640	16.62	3.673	11.34	1.533	10.65	1.631	0.6944
BPYR14-11B grt1-29	36.05	32850	130900	174200	170.5	64.41	5626	19.42	6533	239600	162.9	2.611	b.d.	b.d.	b.d.	b.d.	0.2107	0.0763	3.636	2.166	24.88	5.853	16.04	1.696	8.691	1.016	0.0928
BPYR14-11B grt1-30	65.34	32810	130000	175900	200.2	17.45	5590	28.55	6530	238200	121.5	10.01	b.d.	b.d.	b.d.	b.d.	0.1763	0.0421	2.493	1.724	18.96	4.286	12.16	1.520	9.338	1.151	0.2358
BPYR14-11B grt1-31	63.85	29030	117700	202400	229.8	10.91	5173	27.57	5883	218100	74.91	8.399	b.d.	b.d.	b.d.	b.d.	0.1661	0.0929	2.797	1.445	12.24	2.468	6.288	0.8155	5.016	0.6878	0.1738
BPYR14-11B grt1-32	80.86	32580	130500	175600	212.8	2.367	5812	27.66	6481	237900	128.9	12.42	b.d.	b.d.	b.d.	b.d.	0.2030	0.0729	3.228	1.609	18.96	4.385	13.34	1.945	13.82	1.902	0.3124

Table B4a: Monazite U-Pb isotopic data from sample BPYR14-11B.

Spot Name	Grain, Grain Location	$^{207}Pb/^{235}U$	2s	$^{206}Pb/^{238}U$	2s	rho	$^{238}U/^{206}Pb$	2s	$^{207}Pb/^{206}Pb$	2s	rho	$^{208}Pb/^{232}Th$	2s	$^{207}Pb/^{206}Pb$ Age (Ma)	2s	Concordance	$^{206}Pb/^{204}Pb$
BPYR14-11B-71	m21, matrix quartz	11.503	0.231	0.47	0.01	0.93	2.13	0.04	0.179	0.004	0.16	0.128	0.003	2640	33	0.97	321940
BPYR14-11B-56	m16, inclusion in biotite	11.789	0.239	0.48	0.01	0.97	2.09	0.04	0.179	0.004	0.04	0.133	0.003	2645	33	0.97	306563
BPYR14-11B-63	m20, matrix quartz	11.336	0.229	0.46	0.01	0.98	2.17	0.04	0.179	0.004	-0.26	0.127	0.003	2645	33	0.96	220513
BPYR14-11B-55	m16, inclusion in biotite	12.350	0.253	0.50	0.01	0.96	2.00	0.04	0.180	0.004	-0.64	0.140	0.003	2653	33	0.99	575676
BPYR14-11B-51	m16, inclusion in biotite	12.382	0.251	0.50	0.01	0.99	2.01	0.04	0.181	0.004	-0.40	0.139	0.003	2661	33	0.99	441923
BPYR14-11B-6	m1, garnet embayment	11.945	0.240	0.48	0.01	0.86	2.10	0.04	0.182	0.004	0.18	0.135	0.003	2668	33	0.97	261915
BPYR14-11B-66	m21, matrix quartz	11.895	0.241	0.47	0.01	0.93	2.11	0.04	0.183	0.004	-0.45	0.127	0.003	2682	33	0.96	308182
BPYR14-11B-47	m14, inclusion in biotite	12.465	0.253	0.49	0.01	0.98	2.03	0.04	0.184	0.004	-0.29	0.140	0.003	2687	33	0.98	381702
BPYR14-11B-29	m4, matrix quartz	13.112	0.264	0.52	0.01	0.90	1.93	0.04	0.184	0.004	0.02	0.138	0.003	2690	33	1.00	375957
BPYR14-11B-25	m4, matrix quartz	13.230	0.273	0.52	0.01	0.66	1.93	0.04	0.186	0.004	-0.18	0.139	0.003	2705	34	1.00	602941
BPYR14-11B-4	m1, garnet embayment	11.935	0.240	0.47	0.01	0.93	2.15	0.04	0.186	0.004	0.03	0.132	0.003	2707	33	0.95	265769
BPYR14-11B-46	m14, inclusion in biotite	13.056	0.269	0.51	0.01	0.98	1.97	0.04	0.187	0.004	-0.15	0.144	0.003	2715	33	0.99	384286
BPYR14-11B-42	m14, inclusion in biotite	12.943	0.262	0.50	0.01	0.96	2.00	0.04	0.188	0.004	0.55	0.139	0.003	2725	33	0.98	468537
BPYR14-11B-35	m10, inclusion in biotite	13.731	0.283	0.53	0.01	0.98	1.90	0.04	0.189	0.004	0.73	0.139	0.003	2738	33	1.00	781111
BPYR14-11B-34	m10, inclusion in biotite	14.090	0.287	0.54	0.01	0.98	1.86	0.04	0.190	0.004	0.66	0.139	0.003	2744	33	1.01	512727
BPYR14-11B-2	m1, garnet embayment	12.727	0.261	0.48	0.01	0.91	2.08	0.04	0.191	0.004	-0.04	0.145	0.003	2754	33	0.95	428889
BPYR14-11B-1	m1, garnet embayment	13.599	0.276	0.51	0.01	0.82	1.94	0.04	0.192	0.004	-0.18	0.137	0.003	2755	33	0.98	244474
BPYR14-11B-62	m20, matrix quartz	12.925	0.261	0.49	0.01	0.98	2.04	0.04	0.192	0.004	-0.29	0.136	0.003	2758	33	0.96	344894
BPYR14-11B-68	m21, matrix quartz	12.704	0.264	0.48	0.01	1.00	2.07	0.04	0.192	0.004	0.67	0.136	0.003	2760	33	0.95	430000
BPYR14-11B-18	m2, matrix plagioclase	13.110	0.288	0.49	0.01	0.99	2.02	0.04	0.192	0.004	-0.09	0.138	0.003	2761	33	0.96	398400
BPYR14-11B-21	m4, matrix quartz	14.850	0.324	0.56	0.01	0.96	1.79	0.04	0.192	0.004	-0.61	0.148	0.003	2761	33	1.02	214194
BPYR14-11B-40	m13, matrix quartz	13.815	0.278	0.52	0.01	0.84	1.92	0.04	0.193	0.004	0.30	0.143	0.003	2764	33	0.99	287640
BPYR14-11B-72	m21, matrix quartz	12.915	0.265	0.49	0.01	0.98	2.05	0.04	0.193	0.004	-0.65	0.133	0.003	2768	33	0.96	269623
BPYR14-11B-31	m10, inclusion in biotite	13.581	0.285	0.51	0.01	0.99	1.96	0.04	0.193	0.004	-0.89	0.139	0.003	2769	33	0.98	668889
BPYR14-11B-52	m16, inclusion in biotite	13.351	0.270	0.50	0.01	0.96	1.99	0.04	0.193	0.004	-0.12	0.137	0.003	2769	33	0.97	461538
BPYR14-11B-27	m4, matrix quartz	13.682	0.277	0.51	0.01	0.92	1.95	0.04	0.193	0.004	0.80	0.144	0.003	2770	33	0.98	561190
BPYR14-11B-67	m21, matrix quartz	13.124	0.264	0.50	0.01	0.93	2.02	0.04	0.193	0.004	-0.15	0.137	0.003	2770	33	0.96	713784
BPYR14-11B-53	m16, inclusion in biotite	13.913	0.280	0.52	0.01	0.97	1.91	0.04	0.194	0.004	0.34	0.143	0.003	2775	33	0.99	408043
BPYR14-11B-13	m2, matrix plagioclase	14.171	0.287	0.53	0.01	0.86	1.89	0.04	0.194	0.004	0.08	0.140	0.003	2776	33	0.99	374200

Spot Name	Grain, Grain Location	$^{207}Pb/^{235}U$	2s	$^{206}Pb/^{238}U$	2s	rho	$^{238}U/^{206}Pb$	2s	$^{207}Pb/^{206}Pb$	2s	rho	$^{208}Pb/^{232}Th$	2s	$^{207}Pb/^{206}Pb$ Age (Ma)	2s	Concordance	$^{206}Pb/^{204}Pb$
BPYR14-11B-48	m14, inclusion in biotite	14.819	0.301	0.56	0.01	0.88	1.80	0.04	0.194	0.004	-0.17	0.150	0.003	2776	33	1.02	607400
BPYR14-11B-70	m21, matrix quartz	13.860	0.306	0.52	0.01	0.99	1.92	0.04	0.194	0.004	0.63	0.136	0.003	2777	33	0.99	240270
BPYR14-11B-8	m1, garnet embayment	13.587	0.284	0.51	0.01	0.98	1.98	0.04	0.195	0.004	-0.75	0.138	0.003	2782	33	0.97	502857
BPYR14-11B-54	m16, inclusion in biotite	13.896	0.280	0.52	0.01	0.99	1.93	0.04	0.195	0.004	0.05	0.146	0.003	2783	33	0.98	608269
BPYR14-11B-61	m19, inclusion in garnet	13.339	0.269	0.50	0.01	0.91	2.01	0.04	0.195	0.004	0.19	0.141	0.003	2783	33	0.96	159538
BPYR14-11B-69	m21, matrix quartz	13.373	0.270	0.50	0.01	0.98	2.00	0.04	0.195	0.004	0.18	0.138	0.003	2783	33	0.97	331833
BPYR14-11B-43	m14, inclusion in biotite	13.628	0.275	0.51	0.01	0.96	1.97	0.04	0.195	0.004	0.04	0.147	0.003	2784	33	0.97	490571
BPYR14-11B-10	m1, garnet embayment	14.220	0.313	0.53	0.01	0.99	1.89	0.04	0.195	0.004	-0.30	0.143	0.003	2785	33	0.99	316857
BPYR14-11B-36	m10, inclusion in biotite	13.865	0.280	0.52	0.01	0.99	1.94	0.04	0.195	0.004	-0.23	0.142	0.003	2785	33	0.98	590000
BPYR14-11B-44	m14, inclusion in biotite	13.965	0.284	0.52	0.01	0.99	1.92	0.04	0.195	0.004	-0.30	0.148	0.003	2785	33	0.98	714444
BPYR14-11B-22	m4, matrix quartz	14.388	0.292	0.54	0.01	0.97	1.87	0.04	0.195	0.004	-0.06	0.149	0.003	2786	33	1.00	394615
BPYR14-11B-26	m4, matrix quartz	14.913	0.306	0.55	0.01	0.99	1.81	0.04	0.195	0.004	-0.14	0.148	0.003	2787	33	1.01	368704
BPYR14-11B-32	m10, inclusion in biotite	14.470	0.292	0.54	0.01	0.98	1.86	0.04	0.195	0.004	-0.23	0.144	0.003	2787	33	1.00	943158
BPYR14-11B-37	m13, matrix quartz	14.049	0.283	0.52	0.01	0.99	1.91	0.04	0.195	0.004	0.20	0.141	0.003	2787	33	0.99	946000
BPYR14-11B-41	m13, matrix quartz	14.367	0.290	0.53	0.01	0.97	1.87	0.04	0.195	0.004	-0.06	0.146	0.003	2787	33	0.99	672821
BPYR14-11B-45	m14, inclusion in biotite	14.849	0.305	0.55	0.01	0.98	1.81	0.04	0.195	0.004	-0.06	0.151	0.003	2787	33	1.01	260263
BPYR14-11B-33	m10, inclusion in biotite	14.143	0.285	0.53	0.01	0.99	1.90	0.04	0.195	0.004	-0.10	0.142	0.003	2788	33	0.99	2373333
BPYR14-11B-38	m13, matrix quartz	14.441	0.290	0.54	0.01	0.98	1.86	0.04	0.195	0.004	0.14	0.145	0.003	2788	33	1.00	874483
BPYR14-11B-39	m13, matrix quartz	14.472	0.295	0.54	0.01	0.99	1.86	0.04	0.195	0.004	-0.08	0.147	0.003	2788	33	1.00	707105
BPYR14-11B-57	m19, inclusion in garnet	13.905	0.281	0.52	0.01	0.95	1.93	0.04	0.195	0.004	-0.02	0.142	0.003	2788	33	0.98	266604
BPYR14-11B-9	m1, garnet embayment	13.692	0.280	0.51	0.01	0.98	1.97	0.04	0.195	0.004	-0.03	0.143	0.003	2788	33	0.97	856667
BPYR14-11B-59	m19, inclusion in garnet	13.429	0.283	0.50	0.01	0.99	2.00	0.04	0.196	0.004	-0.48	0.139	0.003	2789	33	0.96	274146
BPYR14-11B-28	m4, matrix quartz	14.828	0.300	0.55	0.01	0.90	1.82	0.04	0.196	0.004	-0.18	0.150	0.003	2790	33	1.01	147921
BPYR14-11B-20	m4, matrix quartz	14.846	0.302	0.55	0.01	0.93	1.81	0.04	0.196	0.004	0.01	0.150	0.003	2791	33	1.01	321053
BPYR14-11B-24	m4, matrix quartz	14.789	0.299	0.55	0.01	0.83	1.82	0.04	0.196	0.004	0.15	0.149	0.003	2791	33	1.01	136949
BPYR14-11B-60	m19, inclusion in garnet	14.062	0.287	0.52	0.01	0.98	1.91	0.04	0.196	0.004	-0.32	0.146	0.003	2791	33	0.99	321905
BPYR14-11B-23	m4, matrix quartz	14.880	0.302	0.55	0.01	0.82	1.82	0.04	0.196	0.004	-0.11	0.149	0.003	2792	33	1.01	384286
BPYR14-11B-5	m1, garnet embayment	14.535	0.306	0.54	0.01	0.97	1.86	0.04	0.196	0.004	0.00	0.144	0.003	2792	33	1.00	232963
BPYR14-11B-16	m2, matrix plagioclase	14.417	0.294	0.53	0.01	0.88	1.88	0.04	0.196	0.004	0.01	0.147	0.003	2793	33	0.99	245385
BPYR14-11B-14	m2, matrix plagioclase	14.043	0.286	0.52	0.01	0.90	1.92	0.04	0.196	0.004	-0.15	0.145	0.003	2794	33	0.98	184324

Spot Name	Grain, Grain Location	$^{207}Pb/^{235}U$	2s	$^{206}Pb/^{238}U$	2s	rho	$^{238}U/^{206}Pb$	2s	$^{207}Pb/^{206}Pb$	2s	rho	$^{208}Pb/^{232}Th$	2s	$^{207}Pb/^{206}Pb$ Age (Ma)	2s	Concordance	$^{206}Pb/^{204}Pb$
BPYR14-11B-3	m1, garnet embayment	14.511	0.294	0.54	0.01	0.80	1.86	0.04	0.196	0.004	-0.05	0.145	0.003	2794	33	1.00	243333
BPYR14-11B-7	m1, garnet embayment	14.772	0.303	0.55	0.01	0.94	1.83	0.04	0.196	0.004	0.05	0.143	0.003	2794	33	1.00	206875
BPYR14-11B-19	m2, matrix plagioclase	14.960	0.303	0.55	0.01	0.88	1.81	0.04	0.196	0.004	-0.33	0.147	0.003	2796	33	1.01	226667
BPYR14-11B-49	m15, inclusion in garnet	14.359	0.296	0.53	0.01	0.99	1.88	0.04	0.196	0.004	-0.15	0.145	0.003	2796	33	0.99	360571
BPYR14-11B-15	m2, matrix plagioclase	14.278	0.289	0.53	0.01	0.93	1.90	0.04	0.196	0.004	0.17	0.147	0.004	2797	33	0.99	237857
BPYR14-11B-50	m15, inclusion in garnet	14.460	0.326	0.54	0.01	0.99	1.87	0.04	0.197	0.004	-0.19	0.147	0.003	2798	33	0.99	195000
BPYR14-11B-58	m19, inclusion in garnet	14.364	0.292	0.53	0.01	0.92	1.88	0.04	0.197	0.004	0.01	0.147	0.004	2801	33	0.99	191714
BPYR14-11B-30	m7, inclusion in garnet	12.920	0.327	0.48	0.01	0.97	2.10	0.05	0.197	0.004	-0.50	0.147	0.003	2803	33	0.94	40953
BPYR14-11B-12	m2, matrix plagioclase	14.291	0.291	0.53	0.01	0.62	1.90	0.04	0.197	0.004	0.34	0.139	0.004	2804	33	0.98	65714
BPYR14-11B-11	m2, matrix plagioclase	14.839	0.310	0.54	0.01	0.90	1.84	0.04	0.199	0.004	-0.46	0.145	0.003	2814	33	1.00	180455
BPYR14-11B-17	m2, matrix plagioclase	15.287	0.314	0.55	0.01	0.63	1.80	0.04	0.199	0.004	-0.02	0.137	0.003	2822	33	1.00	74900
Standards																	
fc1-1		0.055	0.007	0.009	0.000	0.476	114.850	2.405	0.046	0.006	-0.429	0.003	0.000	56	1	1.02	11707
fc1-10		0.051	0.008	0.009	0.000	0.113	113.340	2.478	0.042	0.006	-0.016	0.003	0.000	57	1	1.12	6695
fc1-11		0.058	0.006	0.009	0.000	-0.146	113.921	2.388	0.048	0.005	0.224	0.003	0.000	56	1	0.98	7176
fc1-12		0.058	0.004	0.009	0.000	0.068	115.181	2.412	0.049	0.004	0.020	0.003	0.000	56	1	0.97	14910
fc1-13		0.059	0.006	0.009	0.000	0.211	113.225	2.426	0.049	0.005	-0.119	0.003	0.000	57	1	0.97	5672
fc1-14		0.061	0.005	0.009	0.000	0.141	114.811	2.389	0.051	0.004	-0.048	0.003	0.000	56	1	0.93	6591
fc1-15		0.057	0.006	0.009	0.000	0.004	114.600	2.361	0.047	0.005	0.082	0.003	0.000	56	1	1	6958
fc1-16		0.059	0.004	0.009	0.000	-0.122	114.312	2.397	0.049	0.004	0.204	0.003	0.000	56	1	0.96	8127
FC1-17		0.060	0.006	0.009	0.000	0.208	113.675	2.390	0.049	0.005	-0.150	0.003	0.000	56	1	0.96	11573
fc1-2		0.061	0.007	0.009	0.000	0.004	114.168	2.393	0.050	0.005	0.076	0.003	0.000	56	1	0.94	14080
fc1-3		0.063	0.007	0.009	0.000	0.369	114.325	2.430	0.052	0.005	-0.277	0.003	0.000	56	1	0.91	3115
fc1-4		0.060	0.008	0.009	0.000	0.423	113.986	2.397	0.049	0.006	-0.398	0.003	0.000	56	1	0.96	5009
fc1-5		0.057	0.006	0.009	0.000	0.152	113.882	2.447	0.048	0.004	-0.046	0.003	0.000	56	1	1	10297
fc1-6		0.055	0.005	0.009	0.000	0.271	114.692	2.372	0.045	0.004	-0.211	0.003	0.000	56	1	1.03	5646
fc1-7		0.055	0.004	0.009	0.000	0.212	114.824	2.412	0.046	0.004	-0.132	0.003	0.000	56	1	1.02	8955
fc1-8		0.052	0.006	0.009	0.000	-0.364	112.994	2.464	0.042	0.005	0.449	0.003	0.000	57	1	1.11	10082
fc1-9		0.048	0.005	0.009	0.000	0.195	114.666	2.486	0.040	0.004	-0.129	0.003	0.000	56	1	1.17	5539

Spot Name	Grain, Grain Location	$^{207}Pb/^{235}U$	2s	$^{206}Pb/^{238}U$	2s	rho	$^{238}U/^{206}Pb$	2s	$^{207}Pb/^{206}Pb$	2s	rho	$^{208}Pb/^{232}Th$	2s	$^{207}Pb/^{206}Pb$ Age (Ma)	2s	Concordance	$^{206}Pb/^{204}Pb$
sTERN-1		0.652	0.026	0.082	0.002	-0.021	12.130	0.246	0.058	0.002	0.103	0.025	0.001	510	10	1	22167
sTERN-10		0.637	0.028	0.082	0.002	0.132	12.243	0.248	0.056	0.002	-0.030	0.026	0.001	507	10	1.01	31889
sTERN-11		0.665	0.032	0.084	0.002	0.155	11.965	0.244	0.057	0.003	-0.071	0.025	0.001	518	10	1	21571
sTERN-12		0.651	0.022	0.082	0.002	0.168	12.154	0.248	0.057	0.002	-0.039	0.025	0.001	510	10	1	20523
sTERN-13		0.643	0.024	0.082	0.002	0.134	12.137	0.244	0.057	0.002	-0.043	0.026	0.001	511	10	1.01	68400
sTERN-14		0.635	0.020	0.082	0.002	-0.388	12.188	0.250	0.057	0.002	0.515	0.026	0.001	509	10	1.02	19578
sTERN-15		0.679	0.024	0.083	0.002	0.020	12.025	0.245	0.059	0.002	0.160	0.026	0.001	514	10	0.98	27545
sTERN-16		0.648	0.021	0.083	0.002	0.183	12.057	0.246	0.057	0.002	-0.026	0.026	0.001	514	10	1.01	19094
sTERN-17		0.645	0.026	0.083	0.002	0.203	12.025	0.245	0.057	0.002	-0.080	0.026	0.001	516	10	1.02	30967
sTERN-2		0.688	0.028	0.086	0.002	0.128	11.604	0.238	0.058	0.002	0.001	0.025	0.001	533	11	1	25735
sTERN-3		0.697	0.026	0.087	0.002	-0.065	11.510	0.241	0.058	0.002	0.263	0.026	0.001	537	11	1	13118
sTERN-4		0.646	0.027	0.082	0.002	-0.003	12.197	0.247	0.057	0.002	0.111	0.026	0.001	508	10	1	28879
sTERN-5		0.647	0.028	0.082	0.002	0.136	12.191	0.246	0.057	0.002	-0.060	0.026	0.001	508	10	1	27273
sTERN-6		0.622	0.021	0.082	0.002	-0.093	12.162	0.249	0.055	0.002	0.212	0.026	0.001	511	10	1.04	74750
sTERN-7		0.635	0.024	0.082	0.002	0.056	12.188	0.248	0.056	0.002	0.074	0.026	0.001	509	10	1.02	20204
sTERN-8		0.623	0.024	0.082	0.002	0.082	12.186	0.248	0.055	0.002	0.036	0.025	0.001	510	10	1.03	52100
sTERN-9		0.630	0.023	0.082	0.002	0.380	12.192	0.248	0.056	0.002	-0.257	0.026	0.001	509	10	1.02	29143
44069-1		0.527	0.018	0.069	0.001	0.050	14.558	0.299	0.056	0.002	0.102	0.021	0.000	428	9	1	13820
44069-10		0.526	0.020	0.069	0.001	0.222	14.592	0.296	0.056	0.002	-0.095	0.021	0.000	427	9	1	24933
44069-11		0.520	0.013	0.068	0.001	0.079	14.622	0.296	0.055	0.001	0.129	0.021	0.000	427	9	1	30300
44069-12		0.526	0.015	0.068	0.001	-0.095	14.758	0.297	0.056	0.002	0.213	0.021	0.000	422	8	0.98	40488
44069-13		0.510	0.018	0.068	0.001	0.052	14.706	0.297	0.054	0.002	0.050	0.021	0.000	425	8	1.01	74133
44069-14		0.517	0.018	0.068	0.001	0.204	14.663	0.296	0.055	0.002	-0.127	0.021	0.000	425	8	1.01	23200
44069-15		0.549	0.029	0.068	0.001	0.161	14.669	0.301	0.059	0.003	-0.081	0.021	0.000	423	9	0.96	19207
44069-16		0.516	0.019	0.068	0.001	0.081	14.741	0.298	0.055	0.002	0.036	0.021	0.000	423	8	1	28194
44069-17		0.531	0.023	0.071	0.001	0.396	14.170	0.289	0.055	0.002	-0.287	0.020	0.000	440	9	1.02	22435
44069-2		0.520	0.015	0.068	0.001	0.081	14.691	0.298	0.055	0.002	0.063	0.021	0.000	425	8	1	63259
44069-3		0.520	0.014	0.067	0.001	-0.062	14.843	0.300	0.056	0.001	0.238	0.021	0.000	420	8	0.99	35522
44069-4		0.519	0.017	0.068	0.001	0.152	14.654	0.297	0.055	0.002	-0.013	0.021	0.000	426	9	1	24721
44069-5		0.519	0.025	0.068	0.001	-0.077	14.680	0.296	0.055	0.003	0.141	0.021	0.000	425	9	1	24833

Spot Name	Grain, Grain Location	$^{207}Pb/^{235}U$	2s	$^{206}Pb/^{238}U$	2s	rho	$^{238}U/^{206}Pb$	2s	$^{207}Pb/^{206}Pb$	2s	rho	$^{208}Pb/^{232}Th$	2s	$^{207}Pb/^{206}Pb$ Age (Ma)	2s	Concordance	$^{206}Pb/^{204}Pb$
44069-6		0.503	0.016	0.068	0.001	0.458	14.693	0.297	0.054	0.002	-0.372	0.021	0.000	425	8	1.03	40353
44069-7		0.517	0.017	0.068	0.001	0.270	14.717	0.296	0.055	0.002	-0.191	0.021	0.000	424	8	1	30212
44069-8		0.526	0.014	0.068	0.001	0.219	14.704	0.300	0.056	0.001	-0.033	0.021	0.000	424	9	0.99	127231
44069-9		0.505	0.013	0.068	0.001	0.365	14.797	0.298	0.054	0.001	-0.229	0.021	0.000	422	8	1.02	30964

Table B4b: Monazite trace element data from sample BPYR14-11B. REE concentrations are presented as chondrite-normalized values.

Spot Name	Grain	Si ppm	Ca ppm	Sr ppm	Y ppm	Th ppm	U ppm	La	Ce	Pr	Nd	Sm	Eu	Gd	Tb	Dy	Ho	Er	Tm	Yb	Lu	Eu/ Eu*	Th/ U	Gd/ Yb
BPYR14-11B-71	m21, matrix quartz	1960	11800	29	20850	41800	17400	430380	328059	279095	201969	137162	44405	91960	73130	39146	17821	6575	3211	925	699	0.40	2.40	123
BPYR14-11B-56	m16, inclusion in biotite	350	12600	26	18500	36300	15990	440084	331158	243534	179650	126622	37478	89698	68144	34837	13883	5894	2097	839	622	0.35	2.27	132
BPYR14-11B-63	m20, matrix quartz	3680	12900	33	15200	41800	17400	480591	357259	279095	192560	135811	42451	87940	61496	30122	12326	4288	1445	646	354	0.39	2.40	168
BPYR14-11B-55	m16, inclusion in biotite	680	12520	30	20500	39800	16800	440506	339315	245690	207221	135811	41563	93970	74238	34675	14835	5925	2227	876	545	0.37	2.37	133
BPYR14-11B-51	m16, inclusion in biotite	1230	12210	33	19200	38000	18770	432489	344209	255388	201313	136081	44760	98995	73961	34797	15220	5588	1883	764	553	0.39	2.02	160
BPYR14-11B-6	m1, garnet embayment	8460	11380	28	14000	36600	11630	497046	357259	265086	198031	128378	42274	87487	59003	24919	10842	3700	1356	503	280	0.40	3.15	215
BPYR14-11B-66	m21, matrix quartz	4510	12000	24	24400	38900	15380	467511	371941	280172	206565	135135	39432	94975	78116	38171	19212	7975	3781	1522	772	0.35	2.53	77
BPYR14-11B-47	m14, inclusion in biotite	900	13200	30	14280	40600	17840	465823	357423	247845	189059	134865	47425	87940	64266	27276	11300	4225	1320	553	301	0.44	2.28	197
BPYR14-11B-29	m4, matrix quartz	1810	11900	30	11750	41300	15800	472574	368679	266164	191904	132432	46892	92060	63435	25447	8755	3013	1004	340	260	0.42	2.61	334
BPYR14-11B-25	m4, matrix quartz	3900	11810	30	18000	36500	16600	476793	349266	243534	194967	131757	43517	89799	69806	30325	13059	4981	2300	696	520	0.40	2.20	160
BPYR14-11B-4	m1, garnet embayment	22100	12300	29	20400	34200	16700	497046	358891	261853	199781	128378	33393	94472	68144	31951	14908	6475	2243	857	606	0.30	2.05	136
BPYR14-11B-46	m14, inclusion in biotite	1540	12500	32	11120	47000	11210	435021	336052	247845	201751	129054	27886	77387	44875	20488	8352	3781	1595	801	614	0.28	4.19	119
BPYR14-11B-42	m14, inclusion in biotite	2730	12700	29	19300	39500	17100	451055	345840	255388	178775	120946	30195	84422	62881	32520	15348	6288	2826	1118	699	0.30	2.31	93
BPYR14-11B-35	m10, inclusion in biotite	4000	13100	28	18370	36400	17300	486498	362153	246767	192123	132230	58437	85427	66482	32764	13352	5375	2470	789	427	0.55	2.10	134
BPYR14-11B-34	m10, inclusion in biotite	2400	13520	35	15000	41500	21900	489451	376835	256466	194092	142568	44938	83417	60942	28984	10806	4369	1534	540	402	0.41	1.89	191
BPYR14-11B-2	m1, garnet embayment	41200	10770	27	12890	35600	11560	451899	357259	265086	202188	129054	20639	75980	45069	20569	9286	4175	1927	863	557	0.21	3.08	109
BPYR14-11B-1	m1, garnet embayment	6900	10400	27	6010	43700	7620	458650	360522	284483	216630	142568	21421	74070	36150	11911	3828	1263	478	202	167	0.21	5.73	454
BPYR14-11B-62	m20, matrix quartz	3280	11930	26	15300	43000	13700	494515	373573	278017	214661	129054	17620	71106	48199	22398	11667	4888	2061	975	549	0.18	3.14	90
BPYR14-11B-68	m21, matrix quartz	3160	13910	30	13100	39900	22200	480591	361501	275862	211816	135135	20071	75176	51524	24675	11136	4475	1773	553	264	0.20	1.80	168
BPYR14-11B-18	m2, matrix plagioclase	3060	9860	26	10570	38700	9100	506751	396411	296336	233698	135135	30462	76884	42548	17724	8370	4019	2874	1199	805	0.30	4.25	79
BPYR14-11B-21	m4, matrix quartz	5300	11160	28	2370	52500	5070	501266	391517	302802	232166	131757	8757	50603	18892	5772	1703	669	263	85	49	0.11	10.36	735
BPYR14-11B-40	m13, matrix quartz	2860	12710	31	19340	43100	21100	482278	358891	269397	216411	131081	17229	80201	58172	30976	14469	5956	2506	938	736	0.17	2.04	106
BPYR14-11B-72	m21, matrix quartz	2370	11400	23	7210	43500	11200	491983	393148	289871	210941	129054	9201	57940	30582	13089	5824	2406	895	354	268	0.11	3.88	202
BPYR14-11B-31	m10, inclusion in biotite	3800	12730	30	17550	37000	23600	452321	352365	254310	194967	131757	20480	83920	60111	31545	14560	5706	2551	957	679	0.19	1.57	108

Spot Name	Grain	Si ppm	Ca ppm	Sr ppm	Y ppm	Th ppm	U ppm	La	Ce	Pr	Nd	Sm	Eu	Gd	Tb	Dy	Ho	Er	Tm	Yb	Lu	Eu/ Eu*	Th/ U	Gd/ Yb
BPYR14-11B-52	m16, inclusion in biotite	1560	12200	24	27800	39000	14480	421941	326264	247845	184464	131081	19947	81407	67867	40081	21575	9625	3935	1665	1012	0.19	2.69	60
BPYR14-11B-27	m4, matrix quartz	2700	13700	27	15830	37500	19670	468354	336052	264009	190810	126351	21314	77085	54571	27683	12491	5100	2381	901	724	0.22	1.91	106
BPYR14-11B-67	m21, matrix quartz	2430	13710	27	17530	39200	20400	468354	357749	279095	198468	140068	17584	83417	59003	28537	13590	5681	2393	907	650	0.16	1.92	114
BPYR14-11B-13	m2, matrix plagioclase	1900	10400	23	5450	43400	7520	481435	375204	276940	218184	133108	13819	62613	28006	10203	4286	2044	1170	552	325	0.15	5.77	140
BPYR14-11B-48	m14, inclusion in biotite	1650	10410	23	3200	45100	5210	480591	393148	267241	216411	130473	9840	63317	27119	8130	2344	962	296	116	85	0.11	8.66	677
BPYR14-11B-70	m21, matrix quartz	2850	10880	27	4900	49400	6300	489030	393148	312500	223851	138514	8242	63317	25762	8902	3919	1588	709	228	126	0.09	7.84	343
BPYR14-11B-8	m1, garnet embayment	2280	10500	20	11440	39800	7990	499156	391517	286638	214661	129730	15737	69497	39058	17683	8388	4000	1810	894	516	0.17	4.98	96
BPYR14-11B-54	m16, inclusion in biotite	2100	15050	32	15200	43700	25800	416878	318597	235991	183151	124324	12291	72010	54294	26179	12344	5050	1733	801	545	0.13	1.69	111
BPYR14-11B-61	m19, inclusion in garnet	27100	14800	31	8220	48500	13200	507173	381729	273707	200875	112162	16448	45779	23213	11748	6319	3538	2219	1472	1037	0.23	3.67	38
BPYR14-11B-69	m21, matrix quartz	1780	11650	29	9560	42600	14310	469198	371941	289871	197374	128378	11297	74372	44321	18333	7527	2975	1328	422	427	0.12	2.98	218
BPYR14-11B-43	m14, inclusion in biotite	2650	12240	23	20500	42000	14340	422363	310277	242457	187527	125676	12931	74372	53740	30813	16062	7500	2733	1311	1024	0.13	2.93	70
BPYR14-11B-10	m1, garnet embayment	2060	10810	24	7770	42600	9200	528270	387765	287716	231729	147838	12504	70854	34072	13089	6044	2363	1073	441	309	0.12	4.63	199
BPYR14-11B-36	m10, inclusion in biotite	10670	14220	30	16100	37800	26200	442616	344209	231681	177462	126351	14369	70553	54294	27520	11374	5025	2089	789	431	0.15	1.44	111
BPYR14-11B-44	m14, inclusion in biotite	2720	12100	24	22800	42000	16200	440084	344209	251078	187746	138514	16519	75879	56787	34146	17894	8625	3413	1453	1049	0.16	2.59	65
BPYR14-11B-22	m4, matrix quartz	4000	10080	25	12440	38000	13100	451477	360522	258621	207002	129054	13410	67136	40166	21829	9396	4363	2097	720	407	0.14	2.90	115
BPYR14-11B-26	m4, matrix quartz	2660	11620	23	24600	33300	15200	431646	349103	251078	189716	124324	23091	80905	68144	36016	18919	8750	4696	1752	1496	0.23	2.19	57
BPYR14-11B-32	m10, inclusion in biotite	2680	14000	29	15800	37800	26400	438397	349103	253233	198468	132432	16270	74874	53740	29024	12271	4419	2154	783	467	0.16	1.43	118
BPYR14-11B-37	m13, matrix quartz	3540	12900	26	16240	47400	22500	454852	341599	253017	189497	122162	10835	76884	55125	27114	13938	5794	2219	870	724	0.11	2.11	109
BPYR14-11B-41	m13, matrix quartz	2430	12500	27	16890	42800	20370	488608	360522	270797	195405	124324	9876	74523	48144	26463	12711	5313	2231	789	512	0.10	2.10	117
BPYR14-11B-45	m14, inclusion in biotite	2330	11600	25	6730	46000	8170	466667	375204	293103	213348	135135	11048	72864	37839	13984	5495	2431	907	379	195	0.11	5.63	238
BPYR14-11B-33	m10, inclusion in biotite	3270	15500	31	17480	42000	30800	471308	366884	265086	197155	139865	15737	82412	59834	30935	12949	5506	2522	981	593	0.15	1.36	104
BPYR14-11B-38	m13, matrix quartz	2110	12200	23	20770	39000	19780	460338	362153	264009	193217	133514	13659	79648	55402	33577	16447	6856	2955	1391	809	0.13	1.97	71
BPYR14-11B-39	m13, matrix quartz	3840	13400	27	17040	45800	22800	493671	380098	282328	218140	140135	11616	74874	56233	29675	14066	5713	2291	795	691	0.11	2.01	116
BPYR14-11B-57	m19, inclusion in garnet	2710	12570	36	14800	54300	11140	491139	355628	267241	201532	112838	22913	60302	37950	20407	11465	6469	4291	2404	2016	0.28	4.87	31
BPYR14-11B-9	m1, garnet embayment	2640	10520	22	9230	43100	10080	490717	360522	272629	218315	134459	12362	62563	32604	14593	7033	2925	1336	559	341	0.13	4.28	138
BPYR14-11B-59	m19, inclusion in garnet	2000	12500	33	10070	53300	8940	540928	404568	285560	208753	121622	26465	55377	35208	16220	7674	4238	2377	1342	1159	0.32	5.96	51

Spot Name	Grain	Si ppm	Ca ppm	Sr ppm	Y ppm	Th ppm	U ppm	La	Ce	Pr	Nd	Sm	Eu	Gd	Tb	Dy	Ho	Er	Tm	Yb	Lu	Eu/ Eu*	Th/ U	Gd/ Yb
BPYR14-11B-28	m4, matrix quartz	3480	9300	28	1580	49300	4520	469620	392985	292026	220569	128581	6359	48995	17729	4195	1229	488	223	83	0	0.08	10.91	728
BPYR14-11B-20	m4, matrix quartz	4380	10000	26	1710	52500	5070	518143	384992	294181	226696	141892	7318	51357	17008	4244	1271	475	178	81	33	0.09	10.36	786
BPYR14-11B-24	m4, matrix quartz	3750	10160	27	1492	56600	4570	496624	389886	295259	229103	133108	6465	46784	14958	4138	1214	425	198	56	57	0.08	12.39	1034
BPYR14-11B-60	m19, inclusion in garnet	1820	10580	34	13500	40500	10910	498734	388254	284483	196718	123041	28064	61608	40776	21057	10659	6063	4154	2335	1902	0.32	3.71	33
BPYR14-11B-23	m4, matrix quartz	4500	11420	24	1520	54000	4520	518565	401305	302802	223195	131081	6536	50804	14571	3671	1086	430	138	70	61	0.08	11.95	895
BPYR14-11B-5	m1, garnet embayment	2340	9190	23	3280	47500	4550	509283	395269	321121	231729	140338	9307	62714	24986	6504	1941	731	239	117	61	0.10	10.44	664
BPYR14-11B-16	m2, matrix plagioclase	2800	10660	25	3590	43600	5350	500844	386623	302802	221225	136351	11812	67940	25706	7439	2711	1150	587	248	195	0.12	8.15	338
BPYR14-11B-3	m1, garnet embayment	2490	9980	22	2261	48600	3800	531646	399674	307112	228884	136824	8064	61206	22244	5268	1584	535	202	88	138	0.09	12.79	858
BPYR14-11B-7	m1, garnet embayment	3420	10550	28	2590	44800	4730	505907	381729	290948	226039	145946	9556	63819	22438	5386	1700	644	296	107	81	0.10	9.47	734
BPYR14-11B-19	m2, matrix plagioclase	2880	9090	23	5110	41700	4740	476371	365416	270474	214004	132432	18028	62462	29169	10244	4158	2056	1142	447	337	0.20	8.80	173
BPYR14-11B-49	m15, inclusion in garnet	1900	15500	43	15400	59000	10310	486498	352365	253341	188840	115541	25222	65427	39834	20813	11447	6881	3781	2286	1805	0.29	5.72	35
BPYR14-11B-15	m2, matrix plagioclase	2580	11200	28	9600	47300	7880	468776	357259	281250	199562	128378	19183	64020	34349	14024	7399	4188	2713	1323	1256	0.21	6.00	60
BPYR14-11B-50	m15, inclusion in garnet	3220	11500	38	14400	54200	6000	483122	357259	259375	189934	112905	30302	60854	39834	22033	11429	5831	3036	1925	1516	0.37	9.03	39
BPYR14-11B-58	m19, inclusion in garnet	2960	12720	39	12800	58200	5260	478903	350734	273707	207221	116014	28597	64673	40997	20000	10275	5563	3360	2193	1512	0.33	11.06	36
BPYR14-11B-30	m7, inclusion in garnet	139000	8600	21	9600	27300	7300	394093	324633	261853	185996	120270	31439	63317	38227	19106	7949	3681	1579	634	581	0.36	3.74	124
BPYR14-11B-12	m2, matrix plagioclase	12030	12200	47	6100	55100	4460	487764	376835	278017	220350	129392	22735	66533	31302	11423	4634	2063	935	373	211	0.25	12.35	221
BPYR14-11B-11	m2, matrix plagioclase	3910	11400	30	8100	64700	3320	529114	373573	286638	216193	126014	29840	69548	36842	15976	6941	2731	1506	416	325	0.32	19.49	207
BPYR14-11B-17	m2, matrix plagioclase	5880	14700	42	10980	104800	1836	469620	332790	245690	187527	110811	36430	69246	43269	19593	9432	4119	2372	795	630	0.42	57.08	108
Standards																								
fc1-1		1560	10260	19	32500	50900	15200	432911	329527	274784	202626	152027	12398	87437	67313	38537	24908	12250	6721	4547	3740	0.11	3.35	
fc1-10		2110	10980	22	27800	47900	11300	440928	382219	282328	214223	143919	11083	80905	65928	35854	20513	11813	8178	4093	3012	0.10	4.24	
fc1-11		2310	9890	24.8	33000	46400	15000	422363	355628	266164	207877	154730	11474	84925	62327	41138	24908	13750	9393	4317	3049	0.10	3.09	
fc1-12		1950	10030	23.5	35000	45100	18690	428692	350734	259698	211816	166216	13108	91457	72022	41341	26099	14500	8543	4391	3711	0.11	2.41	
fc1-13		2310	10640	24.2	28300	56800	12310	405907	353997	264009	212035	148649	10675	85427	71745	42358	21612	12563	6842	4130	2980	0.09	4.61	
fc1-14		510	10590	22.9	31700	51800	14900	435021	331158	255388	201532	161486	11314	90452	67313	38374	23443	14750	7571	4168	3411	0.09	3.48	
fc1-15		1390	10300	25.3	35500	51100	16210	443038	331158	275862	205252	163514	11581	88442	75069	43130	26740	14750	8219	4627	3976	0.10	3.15	
fc1-16		2310	11200	25.9	36200	47100	18900	438819	337684	275862	204814	167568	12433	91960	73130	43089	27839	15813	9028	5031	4106	0.10	2.49	
FC1-17		1750	12610	24.8	31400	56500	14450	430380	357259	301940	209190	153378	10924	86432	68144	40650	23810	13125	10526	4466	3459	0.09	3.91	

Spot Name	Grain	Si ppm	Ca ppm	Sr ppm	Y ppm	Th ppm	U ppm	La	Ce	Pr	Nd	Sm	Eu	Gd	Tb	Dy	Ho	Er	Tm	Yb	Lu	Eu/ Eu*	Th/ U	Gd/ Yb
fc1-2		2340	9450	23.4	29500	43500	12900	410970	347471	281250	202845	137838	13037	85427	66759	38089	22711	13750	7126	4093	2870	0.12	3.37	
fc1-3		5400	9610	25.7	29500	39300	12570	476371	349103	275862	198906	143243	11528	76482	57064	36789	20256	12438	6437	3845	3012	0.11	3.13	
fc1-4		1210	8530	23.2	28900	40100	11990	457806	362153	285560	213786	138514	11758	78945	61496	38293	20275	11688	7004	3981	3033	0.11	3.34	
fc1-5		1660	9410	23.6	27600	38800	10770	427426	340946	285560	207002	133784	11350	76030	56704	35000	20879	11063	6595	3714	2886	0.11	3.60	
fc1-6		2570	10900	23.4	35200	49700	17400	461181	340946	299569	221225	160135	13375	92462	70083	44309	27015	13688	8219	4901	3695	0.11	2.86	
fc1-7		1690	10400	24.2	32900	49500	15700	373418	349103	268319	200656	143919	12789	85930	73961	41707	23077	13375	8664	4981	3500	0.11	3.15	
fc1-8		1700	10000	22.2	31200	46800	12700	393249	344209	261853	181400	136486	10391	88945	60665	32764	21429	12481	7733	3944	3114	0.09	3.69	
fc1-9		2840	9440	24	32500	53300	13230	418565	334421	272629	213129	156081	10622	81910	64266	38415	24158	13244	8502	4410	3130	0.09	4.03	
sTERN-10		3670	5970	0.69	14770	51800	3510	405485	373409	311422	217505	288514	2751	105025	61219	21545	\	1975	1065	621	390	0.02	14.76	
sTERN-11		3690	7190	3.57	14060	53600	3580	410970	370310	316810	223851	275000	2629	107035	57895	18699	5330	1963	1089	534	333	0.02	14.97	
sTERN-12		4150	6300	0.36	13600	52800	3750	401266	381729	320043	222538	276351	2789	111508	66205	20488	5403	1981	1170	534	402	0.02	14.08	
sTERN-13		4050	7180	0.95	13430	56200	4120	387764	373573	325323	219912	260135	2789	113065	64820	20447	5275	1975	1057	640	370	0.02	13.64	
sTERN-14		3210	6400	0.57	14680	53100	3710	394093	381729	324353	239387	314189	2824	110553	67313	20528	5879	1944	1150	584	337	0.02	14.31	
sTERN-15		3970	6170	0.59	14300	52100	3600	395359	352365	295259	210941	277027	2487	103015	58172	20000	5403	2038	1016	590	382	0.01	14.47	
sTERN-16		4050	6850	0.43	15600	57300	4320	416034	380098	322198	224289	293919	2693	114573	66759	21138	5513	1963	1255	671	435	0.01	13.26	
sTERN-17		3850	6450	0.63	14600	54300	3980	384388	370310	312500	229322	289865	2877	107889	59501	20122	5806	1975	1077	534	378	0.02	13.64	
sTERN-2		3000	7710	9.6	14830	58200	3700	391561	380098	351293	241794	273649	2824	113065	65928	21138	5751	2075	1016	671	423	0.02	15.73	
sTERN-3		3810	6490	3.1	13620	51500	3570	389873	371941	303879	210284	277703	2575	102010	60942	20528	5330	1969	1109	562	354	0.02	14.43	
sTERN-4		4230	6670	0.52	14550	54900	3870	396624	375204	328664	226039	284459	2664	113568	62105	20407	5440	1969	1053	609	415	0.01	14.19	
sTERN-5		3550	6030	0.53	14100	52700	3500	362447	358891	300647	200656	249324	2647	102513	60665	19390	5421	2013	1117	540	415	0.02	15.06	
sTERN-6		4000	6100	0.56	14600	53600	3920	416878	401305	326509	234573	280405	2966	110553	65928	20854	5458	1956	1186	534	350	0.02	13.67	
sTERN-7		3890	6450	0.54	14300	52800	4110	391139	365416	314655	220569	275000	2718	111055	63158	20366	5495	1969	988	696	301	0.02	12.85	
sTERN-8		3860	7430	0.32	15950	60000	4500	402532	398042	337284	243107	291892	3055	115578	66482	21220	6410	1976	1235	752	427	0.02	13.33	
sTERN-9		4130	6520	0.9	12690	53600	3550	376793	352365	294181	202845	255405	2451	98492	57341	18780	4982	1969	1097	528	337	0.02	15.10	
44069-1		210	4870	19.3	28700	17360	7680	475949	386623	295259	217068	163514	56483	81407	57618	32154	20879	10438	5583	3807	3045	0.49	2.26	
44069-10		1680	7230	29.1	23700	35400	5640	450633	367047	285560	223195	149324	49911	75075	54294	30935	18095	10563	7571	3534	2772	0.47	6.28	
44069-11		790	6890	35	26500	19500	9280	437975	373573	276940	194748	151351	46359	79899	61219	34634	19762	11625	8097	3981	3248	0.42	2.10	
44069-12		1330	7570	33	28100	26400	8490	416878	363785	279418	212910	157432	52398	82915	63712	36301	22161	12188	8040	4242	3598	0.46	3.11	
44069-13		550	9250	37.8	25100	42600	6260	476371	419250	315733	231729	167568	56661	79899	60111	36179	19414	12563	7247	4472	3171	0.49	6.81	
44069-14		700	10090	41.3	23190	48600	5150	457384	380098	296336	237637	152027	56483	78392	55402	31626	17875	12063	6559	4075	3211	0.52	9.44	

Spot Name	Grain	Si ppm	Ca ppm	Sr ppm	Y ppm	Th ppm	U ppm	La	Ce	Pr	Nd	Sm	Eu	Gd	Tb	Dy	Ho	Er	Tm	Yb	Lu	Eu/ Eu*	Th/ U	Gd/ Yb
44069-15		1180	6860	27.2	23400	36500	2810	446835	358891	301724	247921	151351	44760	78945	59003	32886	19304	11113	5385	2925	2081	0.41	12.99	
44069-16		360	10650	38.2	21700	50600	5390	437553	360522	266164	207440	140541	51155	74874	52355	29634	17601	11063	6964	3944	3386	0.50	9.39	
44069-17		1490	11300	44.3	23800	63600	5170	409705	346982	289871	221663	143243	51332	77387	53740	31179	18645	11063	9433	4441	3602	0.49	12.30	
44069-2		210	6980	23.9	30800	22600	9020	454430	358891	302802	211160	157432	57371	90452	62604	37073	24359	13813	7409	4398	3756	0.48	2.51	
44069-3		640	6880	29.7	30600	26500	8070	423207	357259	294181	205252	149324	52220	85427	64266	36016	22527	13313	7126	4242	2850	0.46	3.28	
44069-4		1060	7260	25	25700	32500	5470	443460	367047	298491	227133	148649	44050	84422	59557	34228	17015	9625	4696	2584	2098	0.39	5.94	
44069-5		1600	7570	24	17500	35000	3940	439241	384992	324353	250766	156892	36412	90452	58199	29309	12949	4906	2279	1099	764	0.31	8.88	
44069-6		2100	5770	22.5	25200	25700	6440	457384	381729	300647	213786	148041	52398	79196	59834	32886	19359	10875	6296	3789	2825	0.48	3.99	
44069-8		1100	6620	26.3	30500	22600	8840	451477	386623	309267	222319	167568	57549	84623	64820	35203	22344	12500	8745	4683	3333	0.48	2.56	
44069-9		1490	7260	33.7	29400	25400	8580	416034	342577	281250	208534	152703	49201	83266	62327	36463	21703	13500	8988	4540	3740	0.44	2.96	

Table B5a: Monazite U-Pb isotopic data from sample BQC13-01A

Spot Name	Grain	$^{207}Pb/^{235}U$	2s	$^{206}Pb/^{238}U$	2s	rho	$^{238}U/^{206}Pb$	2s	$^{207}Pb/^{206}Pb$	2s	rho	$^{208}Pb/^{232}Th$	2s	$^{207}Pb/^{206}Pb$ Age	2s	Concordance	$^{206}Pb/^{204}Pb$
BQC13-01Omnz-2	m2, oscillatory zoned mantle	12.130	0.275	0.52	0.01	0.55	1.94	0.04	0.172	0.004	-0.08	0.135	0.003	2572	36	1.03	31272
BQC13-01Omnz-12	m4, BSE dark rim	13.026	0.267	0.52	0.01	0.37	1.91	0.04	0.181	0.004	0.34	0.142	0.003	2661	34	1.01	88571
BQC13-01Omnz-25	m9, BSE dark rim	12.847	0.262	0.51	0.01	0.88	1.95	0.04	0.182	0.004	-0.28	0.143	0.003	2674	33	1.00	175792
BQC13-01Omnz-23	m9, oscillatory zoned rim	13.574	0.276	0.52	0.01	0.60	1.92	0.04	0.190	0.004	0.01	0.144	0.003	2738	33	1.00	48081
BQC13-01Omnz-10	m4, oscillatory zoned mantle	14.200	0.293	0.54	0.01	0.70	1.86	0.04	0.191	0.004	-0.05	0.143	0.003	2750	33	1.01	112414
BQC13-01Omnz-19	m8, patchy zoned core	14.630	0.313	0.56	0.01	0.76	1.80	0.04	0.192	0.004	-0.02	0.146	0.003	2756	34	1.02	93750
BQC13-01Omnz-6	m2, oscillatory zoned mantle	14.309	0.293	0.54	0.01	0.78	1.85	0.04	0.192	0.004	0.29	0.145	0.003	2757	33	1.01	75556
BQC13-01Omnz-7	m2, oscillatory zoned mantle	14.080	0.289	0.53	0.01	0.65	1.88	0.04	0.192	0.004	-0.23	0.142	0.003	2758	33	1.00	127346
BQC13-01Omnz-26	m9, patchy zoned core	14.222	0.287	0.54	0.01	0.58	1.85	0.04	0.192	0.004	0.20	0.145	0.003	2759	33	1.01	204762
BQC13-01Omnz-5	m2, oscillatory zoned mantle	14.541	0.296	0.55	0.01	0.74	1.83	0.04	0.193	0.004	0.11	0.143	0.003	2767	33	1.01	127742
BQC13-01Omnz-4	m2, oscillatory zoned mantle	14.559	0.297	0.55	0.01	0.70	1.83	0.04	0.193	0.004	0.12	0.146	0.003	2771	33	1.01	159739
BQC13-01Omnz-11	m4, patchy zoned core	14.560	0.301	0.54	0.01	0.61	1.84	0.04	0.193	0.004	0.24	0.146	0.003	2772	33	1.00	158882
BQC13-01Omnz-8	m3, oscillatory zoned core	14.748	0.303	0.55	0.01	0.83	1.81	0.04	0.193	0.004	-0.03	0.145	0.003	2772	33	1.01	133880
BQC13-01Omnz-1	m2, oscillatory zoned mantle	14.722	0.299	0.55	0.01	0.79	1.81	0.04	0.194	0.004	-0.05	0.148	0.003	2774	33	1.02	89720
BQC13-01Omnz-21	m9, oscillatory zoned rim	14.209	0.292	0.54	0.01	0.56	1.87	0.04	0.194	0.004	0.00	0.143	0.003	2774	33	1.00	102927
BQC13-01Omnz-15	m5, unzoned grain	14.462	0.294	0.54	0.01	0.77	1.85	0.04	0.194	0.004	-0.13	0.145	0.003	2777	33	1.00	148600
BQC13-01Omnz-16	m5, unzoned grain	14.507	0.296	0.54	0.01	0.61	1.85	0.04	0.194	0.004	0.39	0.145	0.003	2777	33	1.00	147450
BQC13-01Omnz-13	m4, oscillatory zoned mantle	14.666	0.301	0.55	0.01	0.74	1.83	0.04	0.194	0.004	0.06	0.146	0.003	2779	33	1.01	153409
BQC13-01Omnz-22	m9, oscillatory zoned rim	14.346	0.293	0.54	0.01	0.87	1.86	0.04	0.194	0.004	-0.13	0.146	0.003	2779	33	1.00	56763
BQC13-01Omnz-9	m3, oscillatory zoned rim	14.669	0.300	0.55	0.01	0.69	1.83	0.04	0.194	0.004	-0.02	0.146	0.003	2779	33	1.01	42127
BQC13-01Omnz-14	m5, unzoned grain	14.417	0.293	0.54	0.01	0.72	1.86	0.04	0.194	0.004	0.07	0.143	0.003	2780	33	1.00	43500
BQC13-01Omnz-18	m6, oscillatory zoned rim	14.493	0.295	0.54	0.01	0.59	1.85	0.04	0.195	0.004	0.13	0.145	0.003	2782	33	1.00	197333
BQC13-01Omnz-29	m9, oscillatory zoned rim	14.550	0.295	0.55	0.01	0.71	1.83	0.04	0.195	0.004	-0.04	0.145	0.003	2784	33	1.01	130818
BQC13-01Omnz-20	m8, oscillatory zoned rim	15.340	0.361	0.57	0.01	0.96	1.75	0.04	0.195	0.004	0.06	0.150	0.003	2785	33	1.03	150857
BQC13-01Omnz-27	m9, oscillatory zoned rim	14.531	0.300	0.55	0.01	0.88	1.83	0.04	0.195	0.004	0.03	0.146	0.003	2785	33	1.01	97469
BQC13-01Omnz-24	m9, oscillatory zoned rim	14.780	0.302	0.55	0.01	0.72	1.81	0.04	0.195	0.004	0.12	0.147	0.003	2787	33	1.01	169286
BQC13-01Omnz-28	m9, oscillatory zoned rim	14.585	0.296	0.55	0.01	0.73	1.83	0.04	0.195	0.004	0.07	0.143	0.003	2788	33	1.01	95658
BQC13-01Omnz-30	m9, oscillatory zoned rim	14.421	0.291	0.54	0.01	0.60	1.85	0.04	0.195	0.004	0.17	0.144	0.003	2788	33	1.00	42381
BQC13-01Omnz-31	m9, oscillatory zoned rim	14.668	0.299	0.55	0.01	0.66	1.83	0.04	0.196	0.004	0.21	0.147	0.003	2791	33	1.01	80615

Spot Name	Grain	$^{207}Pb/^{235}U$	2s	$^{206}Pb/^{238}U$	2s	rho	$^{238}U/^{206}Pb$	2s	$^{207}Pb/^{206}Pb$	2s	rho	$^{208}Pb/^{232}Th$	2s	$^{207}Pb/^{206}Pb$ Age	2s	Concordance	$^{206}Pb/^{204}Pb$
BQC13-01Omnz-3	m2, patchy zoned core	14.722	0.299	0.55	0.01	0.75	1.83	0.04	0.196	0.004	0.29	0.147	0.003	2796	33	1.00	91321
BQC13-01Omnz-17	m6, patchy zoned core	17.920	0.410	0.59	0.01	0.85	1.70	0.03	0.222	0.005	-0.67	0.158	0.003	2992	36	1.00	130541
Standards																	
44069-1		0.519	0.020	0.07	0.00	0.22	14.71	0.30	0.055	0.002	-0.14	0.021	0.000	424	8	1.00	18344
44069-2		0.519	0.014	0.07	0.00	0.05	14.70	0.30	0.055	0.002	0.10	0.021	0.000	424	8	1.00	21418
44069-3		0.516	0.016	0.07	0.00	0.07	14.71	0.30	0.055	0.002	0.04	0.021	0.000	424	8	1.00	24227
44069-4		0.525	0.018	0.07	0.00	0.16	14.70	0.30	0.056	0.002	-0.04	0.021	0.000	424	9	0.99	41240
44069-5		0.513	0.015	0.07	0.00	-0.04	14.71	0.30	0.055	0.002	0.16	0.021	0.000	424	8	1.01	27702
44069-6		0.526	0.020	0.07	0.00	0.15	14.69	0.30	0.055	0.002	-0.07	0.021	0.000	424	9	0.99	21491
FC1-1		0.055	0.006	0.01	0.00	-0.27	110.27	2.34	0.045	0.005	0.32	0.003	0.000	58	1	1.07	9139
FC1-2		0.059	0.007	0.01	0.00	0.00	112.17	2.41	0.048	0.005	0.10	0.003	0.000	57	1	0.99	10434
FC1-3		0.057	0.007	0.01	0.00	0.13	113.07	2.35	0.048	0.006	-0.07	0.003	0.000	57	1	1.01	16210
FC1-4		0.051	0.006	0.01	0.00	-0.07	111.16	2.35	0.043	0.005	0.12	0.003	0.000	58	1	1.14	8095
FC1-5		0.058	0.007	0.01	0.00	0.28	112.15	2.33	0.047	0.006	-0.24	0.003	0.000	57	1	1.00	7120
FC1-6		0.060	0.007	0.01	0.00	0.16	111.58	2.49	0.048	0.005	-0.06	0.003	0.000	57	1	0.97	6756
Stern-1		0.674	0.036	0.08	0.00	0.30	11.94	0.24	0.059	0.003	-0.20	0.026	0.001	518	10	0.99	25219
Stern-2		0.659	0.031	0.08	0.00	0.28	11.95	0.24	0.057	0.003	-0.19	0.025	0.001	518	10	1.01	20557
Stern-3		0.658	0.028	0.08	0.00	0.02	12.21	0.25	0.059	0.002	0.08	0.025	0.001	507	10	0.99	31440
Stern-4		0.636	0.027	0.08	0.00	0.09	12.03	0.24	0.056	0.002	-0.01	0.025	0.001	516	10	1.03	20486
Stern-5		0.630	0.024	0.08	0.00	0.00	12.03	0.25	0.055	0.002	0.11	0.025	0.001	516	10	1.04	23219
Stern-6		0.629	0.028	0.08	0.00	0.28	12.07	0.25	0.055	0.002	-0.20	0.025	0.001	515	10	1.04	18489

Table B5a: Monazite trace element data from sample BQC13-01A. REE concentrations are presented as chondrite-normalized values.

Spot Name	Grain	Si ppm	Y ppm	Th ppm	U ppm	La	Ce	Pr	Nd	Sm	Eu	Gd	Tb	Dy	Ho	Er	Tm	Yb	Lu	Eu/Eu*	Th/U	Gd/Yb
BQC13-01Omnz-2	m2, oscillatory zoned mantle	9700	10000	86100	943	587764	394780	253233	177681	89189	18330	38342	24875	13902	7454	3575	1332	553	276	0.313	91	47
BQC13-01Omnz-12	m4, BSE dark rim	6500	11000	80700	2550	513924	353997	233836	145295	74459	15169	35176	21607	12195	7454	4275	3109	1963	1236	0.296	32	27
BQC13-01Omnz-25	m9, BSE dark rim	4300	12580	64800	3810	628692	381729	248922	150109	71486	13766	35276	21634	13049	8333	4988	2931	2037	1374	0.274	17	32
BQC13-01Omnz-23	m9, oscillatory zoned rim	15500	11780	90700	3260	556962	394780	250000	168271	83514	13108	42764	25789	14553	8132	4275	2105	1385	1000	0.219	28	22
BQC13-01Omnz-10	m4, oscillatory zoned mantle	9700	12070	92700	2720	535865	363785	241379	166083	84932	7851	40503	25512	14309	8791	4969	3749	1845	1346	0.134	34	55
BQC13-01Omnz-19	m8, patchy zoned core	10100	11790	86800	1790	537553	404568	258621	173085	85608	21314	42613	28144	16220	8883	4550	2223	1236	736	0.353	48	15
BQC13-01Omnz-6	m2, oscillatory zoned mantle	9200	12560	95700	2760	560338	375204	250000	178556	98581	5506	44422	27590	15488	8663	5119	3725	1714	1285	0.083	35	17
BQC13-01Omnz-7	m2, oscillatory zoned mantle	7780	12210	92400	2730	554852	384502	252155	169584	96959	5400	42312	26898	13902	8974	4731	3182	1658	1341	0.084	34	17
BQC13-01Omnz-26	m9, patchy zoned core	10200	12300	94700	3600	590717	424144	267241	173742	92568	9094	42261	27008	16138	9231	4800	2555	1720	1211	0.145	26	22
BQC13-01Omnz-5	m2, oscillatory zoned mantle	7600	17200	95000	3260	561181	394780	257543	175711	109459	4458	51558	36233	20122	12363	6669	4093	1963	1463	0.059	29	23
BQC13-01Omnz-4	m2, oscillatory zoned mantle	11000	10690	104100	3140	581435	412724	276940	192998	108108	3641	47538	28781	15407	7894	3975	2190	857	715	0.051	33	43
BQC13-01Omnz-11	m4, patchy zoned core	14400	7330	96500	2290	596203	401305	258621	160832	64054	5684	27035	15928	8740	5238	3119	2470	1050	817	0.137	42	86
BQC13-01Omnz-8	m3, oscillatory zoned core	11700	9140	119300	2900	616034	414356	242134	160613	69662	5204	30402	18033	10285	6593	4113	3020	1727	1171	0.113	41	27
BQC13-01Omnz-1	m2, oscillatory zoned mantle	9300	13340	99200	3590	522785	360522	257543	187090	102027	3073	48844	29751	17480	9872	4831	2765	1292	854	0.044	28	57
BQC13-01Omnz-21	m9, oscillatory zoned rim	12000	11510	112800	3820	522363	415987	267241	189059	93919	6536	47789	29695	16504	8205	3888	1850	1043	780	0.098	30	56
BQC13-01Omnz-15	m5, unzoned grain	6300	15000	69600	3300	515190	419250	242457	154267	72838	5435	36985	25125	16098	10604	7194	4777	2739	2240	0.105	21	38
BQC13-01Omnz-16	m5, unzoned grain	5900	13360	68600	2590	505907	394780	248922	154923	75000	5009	36633	23767	13496	9542	6431	3996	2596	1476	0.096	26	30
BQC13-01Omnz-13	m4, oscillatory zoned mantle	9200	10770	106200	2950	510549	381729	269397	184902	99459	2984	50101	27673	14268	7674	4131	2291	1118	809	0.042	36	21
BQC13-01Omnz-22	m9, oscillatory zoned rim	12000	10260	106100	3450	490295	384992	251078	168928	88041	4725	42362	27202	13984	7234	3444	1478	932	533	0.077	31	30
BQC13-01Omnz-9	m3, oscillatory zoned rim	9900	12380	104900	2850	535443	378467	253233	173742	91216	3730	44573	27424	15000	8810	5250	3409	1677	1098	0.058	37	28
BQC13-01Omnz-14	m5, unzoned grain	6500	14530	72100	3070	521097	387765	237069	153611	74662	5222	34673	24543	14715	10256	6313	4704	2876	2280	0.103	23	27
BQC13-01Omnz-18	m6, oscillatory zoned rim	13100	11610	109800	2900	559072	401305	270474	167177	70135	4032	35678	21939	12642	8516	5419	3166	1932	1577	0.081	38	55
BQC13-01Omnz-29	m9, oscillatory zoned rim	12200	12790	122100	3810	507595	409462	265086	181619	103378	3108	51960	30388	18008	8425	4200	1749	1174	638	0.042	32	46
BQC13-01Omnz-20	m8, oscillatory zoned rim	12300	11800	97100	2620	477215	393148	266164	169803	86014	3446	40452	24931	13780	8425	4788	2478	1870	1122	0.058	37	32
BQC13-01Omnz-27	m9, oscillatory zoned rim	9000	13760	107100	2460	543460	380098	251509	166521	83176	3783	43920	25540	15691	9579	5506	3036	1950	1341	0.063	44	26
BQC13-01Omnz-24	m9, oscillatory zoned rim	16300	7940	134500	3050	610549	393148	250000	155580	64054	5506	29849	15568	8943	5421	3250	1810	1224	1020	0.126	44	69
BQC13-01Omnz-28	m9, oscillatory zoned rim	16700	9500	161000	3300	619831	425775	266164	161926	72297	6199	30503	16150	9699	6007	3538	2000	1379	1159	0.132	49	32
BQC13-01Omnz-30	m9, oscillatory zoned rim	11700	16230	103600	3470	517300	368679	241379	157987	96014	3126	49598	32050	20041	11319	6225	3101	1919	1069	0.045	30	32
BQC13-01Omnz-31	m9, oscillatory zoned rim	9600	14030	104600	2670	552321	389886	267241	167615	91892	3872	45276	25485	16626	9670	5569	3223	2137	1309	0.060	39	32

Spot Name	Grain	Si ppm	Y ppm	Th ppm	U ppm	La	Ce	Pr	Nd	Sm	Eu	Gd	Tb	Dy	Ho	Er	Tm	Yb	Lu	Eu/Eu*	Th/U	Gd/Yb
BQC13-01Omnz-3	m2, patchy zoned core	3100	6920	81200	4120	599156	383361	226293	163020	80405	18721	31206	17036	8943	5476	2969	1704	839	476	0.374	20	22
BQC13-01Omnz-17	m6, patchy zoned core	5200	18300	75000	3760	468776	355628	259159	169147	107432	20782	59899	43490	25203	14286	7125	5061	3404	2187	0.259	20	33
Standards																						
44069-1		1710	25200	68100	6670																	
44069-2		1500	27800	67300	7320																	
44069-3		1100	23800	57000	6460																	
44069-4		1690	23500	57600	6350																	
44069-5		1420	27100	62500	6890																	
44069-6		2120	26000	66600	7690																	
FC1-1		1490	23300	41800	13600																	
FC1-2		1900	26400	43300	15500																	
FC1-3		1000	24100	42800	16500																	
FC1-4		1490	23900	42000	13990																	
FC1-5		1200	29200	45400	13600																	
FC1-6		1700	25300	50300	10030																	
Stern-1		3890	14300	53600	3660																	
Stern-2		3910	14300	53300	3770																	
Stern-3		3600	14260	54900	3800																	
Stern-4		3800	14420	57500	4190																	
Stern-5		3700	14190	50000	3450																	
Stern-6		4000	14420	62200	4280																	

Table B6: Compilation of ages for Wyoming Craton from Figure 3.16

Sample type	Age	Error	Reference
Wind River felsic magmatism			
Union Peak granodiortie dike	2618.9	1.5	Frost et al., 1998a
Louis Lake batholith, Boulder Canyon	2629.5	1.5	Frost et al., 1998a
Louis Lake charnockite, Boulder Canyon	2629.2	2.8	Frost et al., 1998a
Louis Lake batholith	2642	13	Naylor et al., 1970
Bridger Batholith	2670	13	Aleinikoff et al., 1989
Wind River mafic magmatism			
Tholeiitic dike	2681.3	1.7	Frost BR et al., 2006
Owl Creek tholeiitic dike	2682.7	7.5	Frost BR et al., 2006
Wind River metamorphism			
Washakie Block granulite	2699	7	Aleinikoff et al., 1989
Paradise Basin (metapelitic granulite)	2718	1	Keane et al., 2006
Medina Mountain (metapelitic granulite)	2633	5	Keane et al., 2006
Crescent Lake (metapelitic granulite)	2657	2	Keane et al., 2006
Teton felsic magmatism			
Webb Canyon gneiss	2674	2.8	Frost, B.R. et al., 2007
Webb Canyon gneiss	2682.6	3.3	Finley-Blasi, 2009
Webb Canyon gneiss	2675	3	Finley-Blasi, 2009
Webb Canyon gneiss	2677.2	3.1	Finley-Blasi, 2009
Webb Canyon gneiss	2685.7	4.6	Finley-Blasi, 2009
Webb Canyon gneiss	2685.1	2.9	Fitz-gerald, 2008
Bitch Creek orthogneiss	2684.3	4.5	Fitz-gerald, 2008
Teton mafic magmatism			
Rendezvous Gabbro	2672	2	Frost, B.R. et al., 2005
Rendezvous Gabbro	2668	9.8	Frost, B.R. et al., 2006
Teton metamorphism			
Moose Basin mafic granulite	2697	5.3	Frost, B.R. et al., 2007
Moose Basin mafic granulite	2683	11	Frost, B.R. et al., 2007
Layered gneiss (leucosome-rich metagraywacke)	2684.8	2.4	Fitz-gerald, 2008
Moose Basin mafic granulite (leucosome)	2707.3	5.8	Fitz-gerald, 2008
Moose Basin mafic granulite (leucosome)	2684.6	6.1	Fitz-gerald, 2008
Moose Basin metapelite	2685.2	6.4	Fitz-gerald, 2008
Beartooth felsic magmatism			
LLMC granite BTR-62	2810	14	Mueller et al., 2010
LLMC granite QC-140	2819	7	Mueller et al., 2010
LLMC granite QC-141	2825	12	Mueller et al., 2010
LLMC granite BTR-201	2826	15	Mueller et al., 2010
LLMC granodiorite BTR-32	2800	10	Mueller et al., 2010
LLMC granodiorite BTR-64	2789	11	Mueller et al., 2010
LLMC diorite	2800	5	Mueller et al., 2010
Yellowstone (quartz diorite)	2799	3	Maloney et al., 2011
Yellowstone Crevice pluton (granite)	2808	7	Philbrick et al., 2011
Yellowstone Hellroaring pluton	2805	10	Philbrick et al., 2011
Beartooth mafic magmatism			
Stillwater Complex	2705	4	Premo et al., 1990
Stillwater Complex (Banded series)	2708	0.75	Wall et al., 2012
Stillwater Complex (trocolite)	2709.05	0.85	Wall et al., 2012
Stillwater Complex (olivine gabbro norite)	2708.7	0.82	Wall et al., 2012
Stillwater Complex (anorthosite)	2709.82	0.51	Wall et al., 2012
BQC13-01O – LLMC tonalite (monazite dominant population)	2775	9	This study
Beartooth metamorphism			
BHP13-03D - restitic metapelite (garnet)	2669	48	This study
BQC13-01A - banded ironstone (garnet)	2677	50	This study
BLP13-04 - banded ironstone (garnet)	2684	24	This study
BLP14-05 – migmatitic heterogeneous metapelite (garnet)	2681	58	This study
BPYR14-11B – melanosome of metapelitic diatexite (garnet)	2670	64	This study
BPYR14-11B – melanosome of metapelitic diatexite (monazite population 1)	2792	3.9	This study
BPYR14-11B – melanosome of metapelitic diatexite (monazite population 2)	2692	30	This study
BQC13-01O – LLMC tonalite (monazite younger population)	2667	16	This study

References cited in Table B6

Aleinikoff, J.N., Williams, I.S., Compston, W., Stuckless, J.S., Worl, R.G., 1989. Evidence for an early Archean component in the Middle to Late Archean gneisses of the Wind River Range, west-central Wyoming: conventional and ion microprobe U-Pb data. *Contributions to Mineralogy and Petrology*, **101**, 198-206.

Finley-Blasi, L., 2009. The significance of the Webb Canyon gneiss in the Archean rocks of the northern Teton Range, Wyoming. M.S. Thesis. University of Wyoming.

Fitz-gerald, D.B., 2008. Evidence for an Archean Himalayan-style orogenic event in the northern Teton Range, Wyoming. M.S. Thesis. University of Wyoming.

Frost, C.D., Frost, B.R., Chamberlain, K.R., Hulseboch, T.P., 1998. The Late Archean history of the Wyoming Province as recorded by granitic magmatism in the Wind River Range, Wyoming. *Precambrian Research*, **89**, 145-173.

Frost, B.R., Frost, C.D., Chamberlain, K.R., Hughes, P.J., 2005. The 2.68-2.67 Teton-Wind River domain; evidence for active-margin tectonics and continent-continent collision on the western margin of the Wyoming Province. *Geological Society of America Abstracts with Programs*, **37**, 505.

Frost, B.R., Frost, C.D., Cornia, M., Chamberlain, K., Kirkwood, R., 2006. The Teton-Wind River domain: a 2.68-2.67 Ga active margin in the western Wyoming Province. *Canadian Journal of Earth Sciences*, **43**, 1489-1510.

Frost, B.R., McFarlane, C., Swapp, S.M., Frost, C.D., Chamberlain, K.R., 2007. Timing and duration of high-P granulite facies metamorphism in the northern Teton Range, Wyoming. *Geological Society of America Abstracts with Programs*, **39**, 202.

Keane, S.D., Hall, C.M., Essene, E.J., Cosca, M.A., DeWolf, C.P., Halliday, A.N., 2006. Isotopic constraints on the thermal history of the Wind River Range, Wyoming: implications for Archean metamorphism. *Canadian Journal of Earth Sciences*, **43**, 1511-1532.

Mueller, P.A., Wooden, J.L., Mogk, D.W., Henry, D.J., Bowes, D.R., 2010. Rapid growth of an Archean continent by arc magmatism. *Precambrian Research*, **183**, 70-88.

Naylor, R.S., Steigher, R.H., Wasserburg, G.J., 1970. U-Th-Pb and Rb-Sr systematics in 2700 Ma old pluotns from the southern Wind River Range, Wyoming. *Geochimica et Cosmochimica Acta*, **34**, 1133-1159.

Philbrick, K., Ware, B., Henry, D., Mogk, D., Mueller, P., Foster, D.A., 2011. Evolution of the Precambrian rocks of Yellowstone National Park (YNP): Late Archean felsic plutons. *Geological Society of America Abstracts with Programs*, **43.4**, 62.

Premo, W.R., Helz, R.T., Zientek, M.L., Langston, R.B., 1990. U-Pb and Sm-Nd ages for the Stillwater Complex and its associated sills and dikes, Beartooth Mountains, Montana – identification of a parent magma. *Geology*, **18**, no. 11, p. 1065-1068.

Wall, C.J., Scoates, J.S., Friedman, R.M., Meurer, W.P., 2012. Age of the Stillwater Complex. *Mineralogical Magazine*, **76.6**, 2506.

Appendix C. Supplementary Information to Chapter 4

Table C1: Melt compositions (mol.%) at each melt reintegration step.

Melt reintegration step	SiO_2 (mol.%)	TiO_2	Al_2O_3	Fe_2O_3	FeO	MgO	CaO	Na_2O	K_2O	H_2O	Total
1	68.74	0	14.37	0	0.43	0.1	0.46	3.62	5.33	6.97	100
2	67.99	0	14.04	0	0.26	0.04	0.26	4.24	4.68	8.48	100
3	66.84	0	13.71	0	0.18	0.03	0.16	5.14	3.35	10.58	100

Table C2: Bulk system compositions used at each melt reintegration step for pseudosection calculations.

Melt reintegration step	SiO_2 (mol.%)	TiO_2	Al_2O_3	Fe_2O_3	FeO	MgO	CaO	Na_2O	K_2O	H_2O	Total
1	64.63	1.71	10.59	1.41	9.93	3.64	0.80	1.78	2.30	2.74	100
2	63.61	1.57	10.23	1.29	9.11	3.34	0.76	3.01	2.30	4.36	100
3	62.98	1.45	9.96	1.19	8.42	3.09	0.71	3.28	2.26	6.27	100

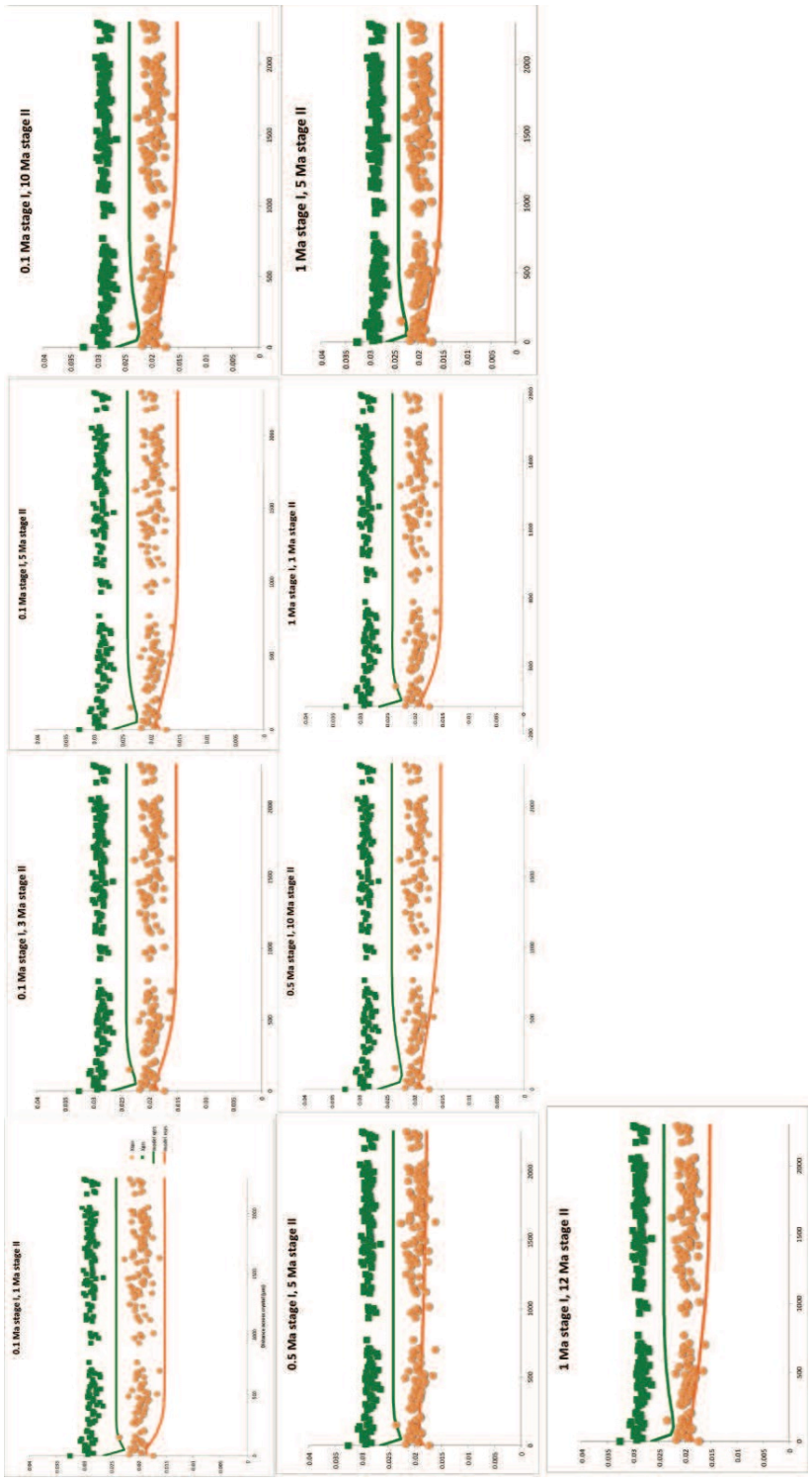

Fig. C1. Garnet major element diffusion modelling results (showing X_{grs} and X_{sps}) for sample BPYR14-11B as a function of various combinations of stage *I* and stage *II* durations (same as in Fig. 10), with the *P–T* evolution of these stages as in Fig. 9b.

Appendix D. Supplementary Information to Chapter 5

D1 METHOD DETAILS

D1.1 U-Pb MONAZITE AND ZIRCON PETROCHRONOLOGY

D1.1.1 Grain imaging

Monazite and zircon grains were located in thin section through back-scatter (BSE) electron imaging on a CAMSCAN series II scanning electron microscope at Virginia Tech. X-ray maps of Y, Th, and Ca were obtained for monazite grains on either: a CAMECA SX-50 electron microprobe (EMP), or a CAMSCAN series II scanning electron microscope (SEM) at Virginia Tech in order to determine chemical zonation. Operating conditions were 25 kV, 40 nA, and 80 ms on the electron microprobe and 15 kV, 50 nA, and 80 ms on the SEM. BSE images were obtained for zircon grains to determine the presence of possible chemical and/or age zonation.

Monazite and zircon grains were also separated from the rock using conventional rock crushing, magnetic separation, and heavy liquid separation techniques. Grains were picked in ethanol under a microscope and annealed in a platinum capsule at 900 °C for 48 hours. The annealed grains were then mounted in epoxy. BSE images were obtained on the SEM described above, but at 10 nA due to the risk of burning the epoxy mount at high beam current. We note that X-ray maps of monazite grains mounted in epoxy were not obtained for this reason.

D1.1.2 LASS

U–Pb zircon and monazite LASS petrochronology of grains in thin section (*in-situ*) and of separated grains mounted in epoxy was performed at the University of California, Santa Barbara following the methods outlined in Kylander-Clark *et al.* (2013). Laser ablation was performed using a Photon Machines *Excite 193* excimer ArF laser-ablation system equipped with a HeLex sample cell. The resulting aerosol stream was split, with part of it directed to a Nu *Plasma HR* multi-collector-ICPMS for isotopic analyses and the other part directed to a Nu AttoM single-collector-ICPMS for trace element and REE analyses. Spots were ablated during a 15 second analysis, run at 4 Hz and ~1 j/cm^2, yielding a pit depth of ~5 μm; zircon and monazite spots were 20-25 and 10 μm, respectively. Sample analyses were preceded by a 15 second baseline measurement and unknown analyses were corrected with the 91500 reference material

(1062 Ma; Wiedenbeck *et al.*, 1995) approximately every 10 analyses; for monazite analyses, the 44069 reference material was used (424 Ma; Aleinikoff *et al.*, 2006). For quality control, secondary RMs included GJ-1 (602 Ma; Jackson *et al.*, 2004; Kylander-Clark *et al.*, 2013), Plešovice (337 Ma; Sláma *et al.*, 2008), and SL1 (564 Ma; Gehrels, 2000) for zircon and Stern (512 Ma; Palin *et al.*, 2013) and FC1 (56 Ma; Horstwood *et al.*, 2003) for monazite, and returned ages within 2% of the accepted $^{206}Pb/^{238}U$ ages. All age errors reported are 2σ, unless explicitly stated otherwise; uncertainties on ages reflect analytical uncertainties only, as well as propagated uncertainties in brackets; 2% is propagated to reflect long-term reproducibility. Post-data processing was performed using *Iolite* (Paton *et al.*, 2011), and concordia and weighted mean plots were produced with *Isoplot* (Ludwig, 2003).

D1.1.3 TIMS-TEA

Grain separation, annealing, and imaging

Monazite and zircon grains were separated from the rock using conventional rock crushing, magnetic separation, and heavy liquid separation techniques. Grains were picked in ethanol under a microscope and annealed in a platinum capsule at 900 °C for 48 hours. The annealed grains were then mounted in epoxy. BSE images were obtained on the SEM described above, but at 10 nA due to the risk of burning the epoxy mount at high beam current. We note that X-ray maps of monazite grains mounted in epoxy were not obtained for this reason.

ID-TIMS isotopic analysis of monazite and zircon

Individual grain fragments were then selected (based on the imaging) for U-Pb isotope analysis and broken off using dental tools before transferring them to PFA hex beakers in distilled acetone. Zircon grains were then transferred to 200 µl Savillex "micro" capsules using distilled acetone. The "micro" caps were then dried down before adding 100 µl 29 M HF and 15 µl 3N HNO_3 to perform chemical abrasion, where the capsules were placed in a high pressure Parr bomb in an oven at 195°C for 12 hours. This process selectively dissolves portions of zircons that have undergone radiation damage and Pb loss. Following chemical abrasion, the zircons were rinsed with 6N HCl, MQ water and HNO_3. The zircons were then spiked with either the single or double EARTHTIME spike containing ^{202}Pb, ^{205}Pb, ^{233}U and ^{235}U, and 100 µl 29 M HF and 15 µl 3N HNO_3 were added prior to full dissolution in a Parr bomb at 210°C for 48 to 60

hours. After dissolution, the aliquots were dried down and converted to chlorides at 195°C for 12 hours. The 6N HCl solutions were dried down and redissolved in 50 µl of 3N HCl prior to ion separation via anion exchange chromatography using 50 µl columns with AG-1 X8 resin. Eichrom 200-400 mesh chloride form resin was used. During column chemistry, trace elements other than U and Pb were collected as a separate aliquot for further analysis.

The same procedure was followed for monazite with two exceptions. Chemical abrasion is not possible with monazite as it is very soluble in HF. As such, monazites were rinsed and fluxed in MQ water and 6N HCl on a hotplate before total dissolution. Column chemistry followed the zircon procedure except with the exception that more 3N HCl was used to strip off rare earth elements given their high concentration in monazite.

For both zircon and monazite, the U and Pb washes were dried down with a microdrop of 0.05M H_3PO_4. The dried down U and Pb aliquots were then redissolved in a silica gel emitter (Gersenberger and Haase 1997) and deposited on outgassed filaments of zone refined Re. U and Pb isotopic abundances were then measured using an IsotopX PhoeniX-62 TIMS at Princeton University. Pb analyses were either performed in peak-hopping mode on a Daly photonmultiplier ion counting detector, or in peak hopping mode using Faraday cups and Daly photonmultiplier depending on the signal intensity of the sample and spike.

U was measured in oxide form, and isotopic abundances were measured using either static measurements on faraday cups with 10^{12} ohm resistors, or through peak hopping on the Daly photonmultiplier if the sample beam intensity was weak. The Pb and U deadtime characteristics of the Daly photonmultiplier were monitored by running standards (NBS982 and CRM U500) on a weekly basis.

Zircon Trace element geochemistry

The trace element washes from zircon and monazite were collected during column chemistry. The procedure set forward by Schoene et al (2010) was followed to measure their REE abundances. The dried trace element washes were re-dissolved in 1 ml of 1.5 M HF + 0.1MHNO_3 + 1ppb Ir. Trace element abundance measurements were made on a Thermo Fisher ELEMENT2 sector field inductively coupled plasma- mass spectrometer (SF-ICP-MS). The Ir tracer was used to monitor drift during analysis. A gravimetric calibration solution was prepared for zircon and monazite with trace element abundances that were matrix matched, and was

diluted into a dilution series to convert raw counts of a particular element into a concentration in the solution. Nitric blanks were included in every set of 24 unknowns.

The concentration of REEs in the solution were converted into concentration within a particular zircon aliquot based on the assumption that all trace elements partition into the Zr^{4+} site in $ZrSiO_4$, such that Zr + Hf + trace elements = 497646 ppm.

D1.2. QUANTITATIVE THERMOBAROMETRY

D1.2.1. Phase Equilibria Modelling

Phase equilibria modelling was undertaken with the software Perple_X (version 6.7; Connolly, 2005) and dataset version 6 of Holland and Powell (2011) in the model system MnNCKFMASHTO, considering the solution phase descriptions of biotite, silicate melt, cordierite, garnet, orthopyroxene, staurolite, feldspar, ilmenite, and white mica from White *et al.* (2014), spinel from White *et al.* (2002), and sapphirine from Wheller and Powell (2014). The sample is from the coarse-grained layer in the outcrop (see main text for description, Fig. 2a), and we determined the bulk rock major element composition through X-ray fluorescence spectroscopy (XRF, Table 2a) of a ~200 cm^3 hand sample from the same rock piece from which the thin section was cut. This was done using a Phillips 2404 XRF vacuum spectrometer at Franklin and Marshall College, together with loss on ignition (LOI) and Fe^{2+} titration (Table S?).

The sample contains well-preserved granulite facies and UHT mineral assemblages, with volumetrically minor grain boundary melt pseudomorphs. Thus, the bulk-rock composition measured by XRF is interpreted to represent a residuum of a protolith that has been modified by melt loss. We did not use domainal compositions for phase equilibria modelling here, instead choosing to use bulk-rock composition determined by XRF because: 1) observed melt pseudomorphs suggest that partial melt was present on grain boundaries before and during cooling, which would facilitate equilibration at the mm- to cm-scale, and the sample does not display any microstructures in thin section suggestive of diminished equilibrium length-scales at HT conditions.

Bulk-rock H_2O content was estimated with T–M_{H2O} pseudosections, and was set so that the inferred equilibrium assemblage was stable as close as possible to the solidus, to represent equilibration in the presence of grain boundary melt prior to melt consumption. This resulted in a set H_2O content lower than that suggested by bulk-rock loss-on-ignition (LOI) (Table 5.6). This

is likely due to the addition of H_2O during post-peak, localized metasomatism at amphibolite-facies metamorphic conditions (as suggested by the observation of sericitized feldspars and biotite filling in garnet) and/or the presence of other volatile components (e.g. CO_2) in the rock. Thus, the bulk-rock LOI values are likely to overestimate bulk-rock H_2O content during peak HT/UHT metamorphism. Bulk-rock Fe_2O_3 was estimated using T–M_{Fe2O3} pseudosections, with the titration values providing a maximum constraint on bulk-rock Fe_2O_3 content. The bulk composition used for constructing P–T pseudosections is shown in Table 5.6.

D1.2.2. Orthopyroxene major element characterization

The major element composition of orthopyroxene was determined using a CAMECA SX50 electron microprobe at Virginia Tech, using a combination of natural and synthetic standards, and ZAF matrix correction. Operating conditions were a 20 nA beam current, 15kV accelerating voltage, and 40s count time. The spot size used for analyses was < 5μm. Othopyroxene porphyroblasts were mapped prior to analysis through Wavelength Dispersive Spectrometry (WDS) to determine the presence of compositional zoning. WDS mapping was done using a 100 nA beam current, 15 kV accelerating voltage, and 40 ms count time. Results of EMP analysis across the orthopyroxene traverse indicated in Fig. 2f are shown in Table D1.

D1.2.3. Zr in Rutile Thermometry

Trace element (REE, Hf, Y, Zr) contents of rutile were analyzed using a Agilent 7500ce ICP-MS coupled with a 193 nm Geolas laser ablation system at Virginia Tech. Analyses were performed with a beam diameter between 44 and 120 μm, depending on the size of the rutile grain. Count rates were normalized using NIST-610 as an external standard. Data were reduced using the AMS v.1.1.0 software. Zr in rutile temperatures were calculated using the calibration of Tomkins *et al.* (2007) at a pressure of 8 kbar. Reported uncertainties on temperature include a ± 1 kbar uncertainty on pressure. Raw data and calculated Zr in rutile temperatures are shown in Table 5.7.

D1.3. REFERENCES

Aleinikoff, J. N., Schenck, W. S., Plank, M. O., Srogi, L., Fanning, C. M., Kamo, S. L. & Bosbyshell, H., 2006. Deciphering igneous and metamorphic events in high-grade rocks of the Wilmington Complex, Delaware: Morphology, cathodoluminescence and

backscattered electron zoning, and SHRIMP U-Pb geochronology of zircon and monazite. *Geological Society of America Bulletin*, **118**, 39-64.

Connolly, J. A. D., 2005. Computation of phase equilibria by linear programming: A tool for geodynamic modeling and its application to subduction zone decarbonation. *Earth and Planetary Science Letters*, **236**, 524-541.

Holland, T. J. B. & Powell, R., 2011. An improved and extended internally consistent thermodynamic dataset for phases of petrological interest, involving a new equation of state for solids. *Journal of Metamorphic Geology*, **29**, 333-383.

Horstwood, M. S., Foster, G. L., Parrish, R. R., Noble, S. R. & Nowell, G. M., 2003. Common-Pb corrected in situ U–Pb accessory mineral geochronology by LA-MC-ICP-MS. *Journal of Analytical Atomic Spectrometry*, **18**, 837-846.

Jackson, S. E., Pearson, N. J., Griffin, W. L. & Belousova, E. A., 2004. The application of laser ablation-inductively coupled plasma-mass spectrometry to in situ U–Pb zircon geochronology. *Chemical Geology*, **211**, 47-69.

Kylander-Clark, A. R. C., Hacker, B. R. & Cottle, J. M., 2013. Laser-ablation split-stream ICP petrochronology. *Chemical Geology*, **345**, 99-112.

Ludwig, K. R., 2003. User's Manual for Isoplot 3.00 : A Geochronological Toolkit for Microsoft Excel, [Kenneth R. Ludwig?], Berkeley CA :.

Palin, R. M., Searle, M. P., Waters, D. J., Parrish, R. R., Roberts, N. M. W., Horstwood, M. S. A., Yeh, M. W., Chung, S. L. & Anh, T. T., 2013. A geochronological and petrological study of anatectic paragneiss and associated granite dykes from the Day Nui Con Voi metamorphic core complex, North Vietnam: constraints on the timing of metamorphism within the Red River shear zone. *Journal of Metamorphic Geology*, **31**, 359-387.

Paton, C., Hellstrom, J., Paul, B., Woodhead, J. & Hergt, J., 2011. Iolite: Freeware for the visualisation and processing of mass spectrometric data. *Journal of Analytical Atomic Spectrometry*, **26**, 2508-2518.

Sláma, J., Košler, J., Condon, D. J., Crowley, J. L., Gerdes, A., Hanchar, J. M., Horstwood, M. S. A., Morris, G. A., Nasdala, L., Norberg, N., Schaltegger, U., Schoene, B., Tubrett, M. N. & Whitehouse, M. J., 2008. Plešovice zircon — A new natural reference material for U–Pb and Hf isotopic microanalysis. *Chemical Geology*, **249**, 1-35.

Wheller, C. J. & Powell, R., 2014. A new thermodynamic model for sapphirine: calculated phase equilibria in K2O–FeO–MgO–Al2O3–SiO2–H2O–TiO2–Fe2O3. *Journal of Metamorphic Geology*, **32**, 287-299.

White, R. W., Powell, R. & Clarke, G. L., 2002. The interpretation of reaction textures in Fe-rich metapelitic granulites of the Musgrave Block, central Australia: constraints from mineral equilibria calculations in the system K2O–FeO–MgO–Al2O3–SiO2–H2O–TiO2–Fe2O3. *Journal of Metamorphic Geology*, **20**, 41-55.

White, R. W., Powell, R., Holland, T. J. B., Johnson, T. E. & Green, E. C. R., 2014. New mineral activity–composition relations for thermodynamic calculations in metapelitic systems. *Journal of Metamorphic Geology*, **32**, 261-286.

Wiedenbeck, M., Allé, P., Corfu, F., Griffin, W. L., Meier, M., Oberli, F., Quadt, A. V., Roddick, J. C. & Spiegel, W., 1995. Three natural zircon standards for U-Th-Pb, Lu-Hf, and trace element and REE analyses. *Geostandards Newsletter*, **19**, 1-23.

D2. TABLES

Table D1: Representative orthopyroxene major element compositions (oxides in wt.%)

Zone	SiO_2	TiO_2	Al_2O_3	Cr_2O_3	MgO	CaO	MnO	FeO	Na_2O	Total	X_{Mg}	X_{Fe}	y(Al)
Inner Core	48.85	0.11	11.01	0.11	24.37	0.11	0.04	15.54	0.02	100.16	0.74	0.26	0.23
Outer Core	49.10	0.10	10.45	0.12	24.42	0.11	0	15.63	0.03	99.96	0.74	0.26	0.22
Rim	51.26	0.07	7.35	0.07	25.94	0.07	0.04	15.43	0	100.23	0.75	0.25	0.16

Table D2a: All *in-situ* LASS zircon analyses: isotopic data

Analysis Name	Grain	Grain Texture	U ppm	Th ppm	$^{207}Pb/^{235}U$	2s	$^{206}Pb/^{238}U$	2s	$^{238}U/^{206}Pb$	2s	$^{207}Pb/^{206}Pb$	2s	$^{208}Pb/^{232}Th$	2s	Concordance
Inclusions in garnet															
PPC15-01A3zrc-26	z4 inclusion in garnet	homogeneous grain	153	83	12.55	0.32	0.52	0.01	1.94	0.04	0.18	0.00	0.14	0.00	1.01
PPC15-01A3zrc-13	z3 inclusion in rutile in garnet	metamorphic core	245	11	12.97	0.30	0.53	0.01	1.90	0.04	0.18	0.00	0.15	0.03	1.02
PPC15-01A3zrc-20	z4 inclusion in garnet	homogeneous grain	149	70	12.71	0.31	0.52	0.01	1.93	0.04	0.18	0.00	0.14	0.01	1.01
PPC15-01A3zrc-18	z4 inclusion in garnet	homogeneous grain	103	15	12.75	0.40	0.52	0.01	1.93	0.04	0.18	0.01	0.15	0.02	1.01
PPC15-01A3zrc-19	z4 inclusion in garnet	homogeneous grain	135	68	12.67	0.33	0.52	0.01	1.93	0.04	0.18	0.00	0.13	0.01	1.01
PPC15-01A3zrc-24	z4 inclusion in garnet	homogeneous grain	171	59	12.85	0.32	0.52	0.01	1.92	0.04	0.18	0.00	0.14	0.01	1.01
PPC15-01A3zrc-59	z14 inclusion in garnet	rim	137	48	13.02	0.32	0.52	0.01	1.92	0.04	0.18	0.00	0.15	0.01	1.01
PPC15-01A3zrc-10	z2 inclusion in garnet	metamorphic core	270	9	12.47	0.27	0.50	0.01	1.99	0.04	0.18	0.00	0.13	0.03	1
PPC15-01A3zrc-22	z4 inclusion in garnet	homogeneous grain	158	71	12.96	0.32	0.52	0.01	1.91	0.04	0.18	0.00	0.14	0.01	1.01
PPC15-01A3zrc-4	z1 inclusion in rutile in garnet	rim	185	44	13.03	0.30	0.53	0.01	1.90	0.04	0.18	0.00	0.13	0.01	1.02
PPC15-01A3zrc-1	z1 inclusion in rutile in garnet	rim	212	16	12.86	0.30	0.52	0.01	1.94	0.04	0.18	0.00	0.14	0.02	1.01
PPC15-01A3zrc-17	z4 inclusion in garnet	homogeneous grain	92	9	13.03	0.42	0.52	0.01	1.91	0.04	0.18	0.01	0.17	0.03	1.01
PPC15-01A3zrc-15	z3 inclusion in rutile in garnet	metamorphic core	243	27	13.10	0.30	0.53	0.01	1.90	0.04	0.18	0.00	0.16	0.01	1.01
PPC15-01A3zrc-5	z1 inclusion in rutile in garnet	rim	224	34	12.98	0.29	0.52	0.01	1.92	0.04	0.18	0.00	0.14	0.01	1.01
PPC15-01A3zrc-11	z2 inclusion in garnet	metamorphic core	301	9	12.95	0.28	0.52	0.01	1.93	0.04	0.18	0.00	0.15	0.04	1.01
PPC15-01A3zrc-21	z4 inclusion in garnet	homogeneous grain	157	74	12.99	0.30	0.52	0.01	1.92	0.04	0.18	0.00	0.14	0.01	1.01
PPC15-01A3zrc-16	z4 inclusion in garnet	homogeneous grain	83	18	12.85	0.46	0.52	0.01	1.94	0.04	0.18	0.01	0.14	0.01	1
PPC15-01A3zrc-60	z14 inclusion in garnet	rim	131	58	13.27	0.32	0.53	0.01	1.90	0.04	0.18	0.00	0.15	0.01	1.01
PPC15-01A3zrc-12	z2 inclusion in garnet	metamorphic core/rim	208	14	13.05	0.31	0.52	0.01	1.91	0.04	0.18	0.00	0.13	0.02	1.01
PPC15-01A3zrc-7	z1 inclusion in rutile in garnet	rim	212	16	13.09	0.30	0.52	0.01	1.91	0.04	0.18	0.00	0.13	0.02	1.01
PPC15-01A3zrc-8	z1 inclusion in rutile in garnet	rim	215	12	12.94	0.29	0.52	0.01	1.94	0.04	0.18	0.00	0.14	0.02	1
PPC15-01A3zrc-25	z4 inclusion in garnet	homogeneous grain	160	73	13.15	0.32	0.53	0.01	1.90	0.04	0.18	0.00	0.14	0.01	1.01
PPC15-01A3zrc-27	z4 inclusion in garnet	homogeneous grain	97	21	13.08	0.40	0.52	0.01	1.91	0.04	0.18	0.01	0.14	0.01	1.01
PPC15-01A3zrc-23	z4 inclusion in garnet	homogeneous grain	141	80	13.12	0.34	0.52	0.01	1.91	0.04	0.18	0.00	0.14	0.01	1.01
PPC15-01A3zrc-6	z1 inclusion in rutile in garnet	rim	198	11	13.09	0.29	0.52	0.01	1.92	0.04	0.18	0.00	0.13	0.02	1.01
PPC15-01A3zrc-2	z1 inclusion in rutile in garnet	rim	252	17	13.02	0.29	0.52	0.01	1.94	0.04	0.18	0.00	0.14	0.02	1

Analysis Name	Grain	Grain Texture	U ppm	Th ppm	$^{207}Pb/^{235}U$	2s	$^{206}Pb/^{238}U$	2s	$^{238}U/^{206}Pb$	2s	$^{207}Pb/^{206}Pb$	2s	$^{208}Pb/^{232}Th$	2s	Concordance
PPC15-01A3zrc-58	z14 inclusion in garnet	rim	121	59	13.32	0.32	0.52	0.01	1.92	0.04	0.18	0.00	0.16	0.01	1
Matrix															
PPC15-01A3zrc-45	z8 matrix	rim	144	85	12.92	0.33	0.53	0.01	1.90	0.04	0.18	0.00	0.14	0.00	1.02
PPC15-01A3zrc-46	z8 matrix	rim	147	84	13.02	0.31	0.53	0.01	1.90	0.04	0.18	0.00	0.14	0.01	1.02
PPC15-01A3zrc-43	z8 matrix	rim	146	89	13.01	0.28	0.53	0.01	1.90	0.04	0.18	0.00	0.14	0.01	1.02
PPC15-01A3zrc-57	z13 outside resorbed garnet	rim	147	59	13.04	0.32	0.52	0.01	1.93	0.04	0.18	0.00	0.15	0.01	1.01
PPC15-01A3zrc-40	z8 matrix	rim	135	87	13.11	0.30	0.53	0.01	1.90	0.04	0.18	0.00	0.14	0.01	1.02
PPC15-01A3zrc-28	z5 matrix outside resorbed garnet	rim	258	24	12.79	0.29	0.52	0.01	1.94	0.04	0.18	0.00	0.16	0.01	1.01
PPC15-01A3zrc-41	z8 matrix	rim	138	92	13.08	0.32	0.52	0.01	1.91	0.04	0.18	0.00	0.14	0.00	1.01
PPC15-01A3zrc-31	z6 matrix outside resorbed garnet	rim	134	61	13.21	0.36	0.53	0.01	1.88	0.04	0.18	0.00	0.15	0.01	1.02
PPC15-01A3zrc-44	z8 matrix	rim	135	79	13.10	0.31	0.52	0.01	1.91	0.04	0.18	0.00	0.14	0.01	1.01
PPC15-01A3zrc-42	z8 matrix	rim	145	88	13.09	0.30	0.52	0.01	1.91	0.04	0.18	0.00	0.14	0.01	1.01
PPC15-01A3zrc-38	z8 matrix	rim	152	98	13.28	0.33	0.53	0.01	1.88	0.04	0.18	0.00	0.14	0.00	1.02
PPC15-01A3zrc-39	z8 matrix	rim	152	102	13.08	0.31	0.52	0.01	1.92	0.04	0.18	0.00	0.14	0.00	1.01
PPC15-01A3zrc-32	z6 matrix outside resorbed garnet	rim	143	74	13.30	0.32	0.53	0.01	1.90	0.04	0.18	0.00	0.15	0.01	1.01
PPC15-01A3zrc-58	z14 inclusion in garnet	rim	121	59	13.32	0.32	0.52	0.01	1.92	0.04	0.18	0.00	0.16	0.01	1
PPC15-01A3zrc-50	z11 matrix next to ilm	rim	101	37	13.94	0.37	0.53	0.01	1.89	0.04	0.19	0.00	0.16	0.01	1
PPC15-01A3zrc-55	z13 outside resorbed garnet	rim:mixed?	135	62	13.80	0.33	0.53	0.01	1.90	0.04	0.19	0.00	0.18	0.01	1
PPC15-01A3zrc-34	z6 matrix outside resorbed garnet	rim	156	53	13.38	0.34	0.54	0.01	1.86	0.04	0.18	0.00	0.14	0.01	1.03
PPC15-01A3zrc-34	z6 matrix outside resorbed garnet	rim	156	53	13.38	0.34	0.54	0.01	1.86	0.04	0.18	0.00	0.14	0.01	1.03
Inclusions in rutile															
PPC15-01A3zrc-13	z3 inclusion in garnet	metamorphic core	245	11	12.97	0.30	0.53	0.01	1.90	0.04	0.18	0.00	0.15	0.03	1.02
PPC15-01A3zrc-4	z1 inclusion in garnet	rim	185	44	13.03	0.30	0.53	0.01	1.90	0.04	0.18	0.00	0.13	0.01	1.02

Analysis Name	Grain	Grain Texture	U ppm	Th ppm	$^{207}Pb/^{235}U$	2s	$^{206}Pb/^{238}U$	2s	$^{238}U/^{206}Pb$	2s	$^{207}Pb/^{206}Pb$	2s	$^{208}Pb/^{232}Th$	2s	Concordance
PPC15-01A3zrc-1	z1 inclusion in rutile in garnet	rim	212	16	12.86	0.30	0.52	0.01	1.94	0.04	0.18	0.00	0.14	0.02	1.01
PPC15-01A3zrc-15	z3 inclusion in garnet	metamorphic core	243	27	13.10	0.30	0.53	0.01	1.90	0.04	0.18	0.00	0.16	0.01	1.01
PPC15-01A3zrc-5	z1 inclusion in garnet	rim	224	34	12.98	0.29	0.52	0.01	1.92	0.04	0.18	0.00	0.14	0.01	1.01
PPC15-01A3zrc-7	z1 inclusion in garnet	rim	212	16	13.09	0.30	0.52	0.01	1.91	0.04	0.18	0.00	0.13	0.02	1.01
PPC15-01A3zrc-8	z1 inclusion in garnet	rim	215	12	12.94	0.29	0.52	0.01	1.94	0.04	0.18	0.00	0.14	0.02	1
PPC15-01A3zrc-6	z1 inclusion in garnet	rim	198	11	13.09	0.29	0.52	0.01	1.92	0.04	0.18	0.00	0.13	0.02	1.01
PPC15-01A3zrc-2	z1 inclusion in rutile in garnet	rim	252	17	13.02	0.29	0.52	0.01	1.94	0.04	0.18	0.00	0.14	0.02	1
Inherited Cores															
PPC15-01A3zrc-54	z13 outside resorbed garnet	igneous? core	649	4	14.16	0.30	0.55	0.01	1.83	0.04	0.19	0.00	0.53	0.33	1.02
PPC15-01A3zrc-53	z13 outside resorbed garnet	rim	167	45	14.29	0.43	0.53	0.01	1.88	0.04	0.19	0.00	0.23	0.01	0.99
PPC15-01A3zrc-47	z8 matrix	igneous core	166	94	15.27	0.38	0.56	0.01	1.79	0.04	0.20	0.00	0.15	0.01	1.01
PPC15-01A3zrc-51	z11 matrix next to ilm	rim	84	16	14.64	0.42	0.52	0.01	1.92	0.04	0.20	0.01	0.29	0.03	0.97
PPC15-01A3zrc-56	z13 outside resorbed garnet	rim	151	56	15.73	0.46	0.55	0.01	1.82	0.04	0.21	0.00	0.27	0.01	0.99
PPC15-01A3zrc-52	z13 outside resorbed garnet	mixed?	139	54	20.50	0.60	0.60	0.01	1.68	0.03	0.25	0.01	0.50	0.01	0.97
Discordant/Mixed Analyses															
PPC15-01A3zrc-35	z7 matrix	rim	304	37	14.94944731	0.385885366	0.5801	0.012673453	1.723841	0.037660778	0.186470588	0.004559021	0.305	0.014360014	1.05
PPC15-01A3zrc-33	z6 matrix outside resorbed garnet	etched zoned core	756	9	14.05367949	0.330941997	0.5465	0.011149211	1.829826	0.037330495	0.187563452	0.003795458	0.139	0.031124402	1.02
PPC15-01A3zrc-34	z6 matrix outside resorbed garnet	rim	156	53	13.38211639	0.336485506	0.539	0.011397298	1.855288	0.039230556	0.181670823	0.004283391	0.1448	0.006933745	1.03
PPC15-01A3zrc-48	z11 matrix next to ilm	mantle	259	22	13.39095919	0.296835948	0.5263	0.010796142	1.900057	0.038976413	0.184280443	0.004008052	0.159	0.013383288	1.01
PPC15-01A3zrc-49	z11 matrix next to ilm	mantle	251	21	13.50695874	0.311685568	0.5312	0.011067044	1.882532	0.039220698	0.185193622	0.004099581	0.177	0.014440623	1.01
PPC15-01A3zrc-61	z14 inclusion in garnet	core	256	1	14.54498163	0.351227307	0.5546	0.011348677	1.803101	0.036896521	0.188461538	0.004046595	-0.07	-0.310003161	1.02
PPC15-01A3zrc-37	z7 matrix	patchy zoned core	2560	26	12.69905021	0.359717481	0.513	0.016561027	1.949318	0.062929252	0.182437851	0.003738618	0.14	0.01329812	1
PPC15-01A3zrc-36	z7 matrix	rim	802	24	12.30197004	0.482171345	0.519	0.017428264	1.926782	0.064702254	0.172681704	0.003875359	0.238	0.020558638	1.03
PPC15-01A3zrc-29	z5 matrix outside resorbed	rim	193	41	12.92261269	0.306927128	0.5217	0.010777679	1.916811	0.039598931	0.180902413	0.004167929	0.1433	0.007379292	1.01

	garnet														
Analysis Name	**Grain**	**Grain Texture**	**U ppm**	**Th ppm**	**$^{207}Pb/^{235}U$**	**2s**	**$^{206}Pb/^{238}U$**	**2s**	**$^{238}U/^{206}Pb$**	**2s**	**$^{207}Pb/^{206}Pb$**	**2s**	**$^{208}Pb/^{232}Th$**	**2s**	**Concordance**
PPC15-01A3zrc-3	z1 inclusion in garnet	rim	211	12	13.22833225	0.328985862	0.5371	0.011052175	1.861851	0.038312237	0.179065239	0.004081638	0.197	0.022350025	1.03
PPC15-01A3zrc-14	z3 inclusion in garnet	metamorphic core	191	13	12.55875262	0.286127445	0.5554	0.011840509	1.800504	0.038384741	0.164446721	0.003641993	0.145	0.020209156	1.08
PPC15-01A3zrc-9	z1 inclusion in garnet	rim	236	13	12.87054392	0.311549697	0.5318	0.011024269	1.880406	0.038981017	0.176801406	0.003949907	0.237	0.027412909	1.03
Standards															
SL1-1	-	-	483.6	125.8	0.724398581	0.053872779	0.0882	0.001821858	11.32888	0.233822578	0.059905413	0.004578783	0.0236	0.001477425	0.99
SL1-2	-	-	440.7	114.6	0.773683051	0.066863615	0.0889	0.001879919	11.24733	0.237814291	0.063542266	0.005557207	0.025	0.002159167	0.94
SL1-3	-	-	444.4	119.8	0.723722762	0.051188329	0.0896	0.001863737	11.15698	0.231994575	0.058559821	0.004175873	0.0233	0.001956312	1
SL1-4	-	-	460	119.2	0.774004148	0.054179331	0.0886	0.001872151	11.27777	0.238115296	0.061942751	0.004186931	0.0283	0.002078547	0.94
SL1-5	-	-	463.3	118.9	0.721064169	0.049387899	0.0880	0.001854815	11.35203	0.239027319	0.058120459	0.004095483	0.0257	0.001968298	0.99
SL1-6	-	-	476.2	124.5	0.678300769	0.048801791	0.0887	0.001886103	11.27269	0.239673733	0.054595086	0.003634263	0.0258	0.001586271	1.04
91500-1	-	-	80.6	30.3	1.5423421	0.372223406	0.1788	0.004934347	5.592841	0.154345751	0.062888199	0.015531185	0.0509	0.008858686	1.12
91500-2	-	-	79	29.72	1.745314283	0.335197104	0.1792	0.004673869	5.580357	0.145546099	0.070643642	0.013808735	0.054	0.006490485	1.04
91500-3	-	-	81.8	30.2	2.244204228	0.373488356	0.1795	0.004876279	5.571031	0.151342101	0.090773816	0.014393976	0.0558	0.008176519	0.89
91500-4	-	-	80.3	29.97	1.684859901	0.434033638	0.1798	0.005018089	5.561735	0.155224001	0.067607727	0.018400417	0.0486	0.008356721	1.06
91500-5	-	-	79.21	30	1.743267102	0.394534409	0.1783	0.004596342	5.608525	0.144580463	0.071054603	0.015292162	0.0582	0.006701858	1.03
91500-6	-	-	78.37	29.8	2.095280908	0.332464316	0.1802	0.004954676	5.549394	0.152582874	0.083880379	0.013601844	0.0573	0.009469676	0.93
91500-7	-	-	83.8	30.15	1.616639228	0.253760597	0.1784	0.004597893	5.605381	0.144467177	0.065852003	0.011207577	0.053	0.005404961	1.08
91500-8	-	-	79.4	29.93	1.749860472	0.266255511	0.1795	0.004678472	5.571031	0.145202853	0.070138889	0.010807092	0.0478	0.008255054	1.04
91500-9	-	-	80.2	29.99	1.910551718	0.355511528	0.1792	0.004153921	5.580357	0.129354686	0.076610169	0.013835646	0.0553	0.005806031	0.98
GJ1-1	-	-	304.6	10.73	0.798529904	0.108303857	0.0981	0.002101023	10.19056	0.218186127	0.059306229	0.008101653	0.014	0.027001452	1.01
GJ1-2	-	-	302.1	10.5	0.866005178	0.109627499	0.0986	0.002115062	10.13274	0.217158486	0.063249727	0.008138313	0.036	0.029008937	0.96
GJ1-3	-	-	300.7	10.36	0.824532171	0.096704334	0.1001	0.002284295	9.990019	0.227973319	0.059367224	0.007095549	0.023	0.021005037	1.01
GJ1-4	-	-	285.7	10.49	0.848431655	0.108606741	0.0994	0.002203867	10.05733	0.222920817	0.062664165	0.007810677	0.02	0.0250032	0.98
GJ1-5	-	-	305.6	11.5	0.805736251	0.067210279	0.0995	0.002099762	10.05025	0.212091781	0.058943782	0.005122784	0.018	0.016004049	1.02
GJ1-6	-	-	299.6	10.86	0.801433746	0.078217701	0.0994	0.002129254	10.0553	0.215286935	0.058443765	0.005518511	0.028	0.021007465	1.02
GJ1-7	-	-	301.2	10.65	0.852441824	0.087027447	0.0979	0.002090593	10.20929	0.217901737	0.062354118	0.006310761	0.017	0.018003211	0.96
GJ1-8	-	-	299.3	11.35	0.760555322	0.082388039	0.0981	0.002080926	10.18745	0.215967118	0.055354201	0.005885413	0.031	0.02100915	1.05

Analysis Name	Grain	Grain Texture	U ppm	Th ppm	$^{207}Pb/^{235}U$	2s	$^{206}Pb/^{238}U$	2s	$^{238}U/^{206}Pb$	2s	$^{207}Pb/^{206}Pb$	2s	$^{208}Pb/^{232}Th$	2s	Concordance
Plesovice-1	-	-	1139	119.2	0.389002751	0.022715667	0.05332	0.001083194	18.75469	0.381000848	0.053406998	0.002793298	0.0146	0.002318462	1
Plesovice-2	-	-	813	90.7	0.397126127	0.037130896	0.05355	0.001139799	18.67414	0.397474494	0.054490414	0.005712845	0.0142	0.002182255	0.99
Plesovice-3	-	-	790	89.1	0.419909688	0.032641383	0.05373	0.001153761	18.61158	0.399652333	0.056352201	0.004186731	0.0139	0.002913294	0.95
Plesovice-4	-	-	765	89.4	0.394131449	0.031325789	0.05342	0.001140824	18.71958	0.399770493	0.053360698	0.004132496	0.0171	0.002820809	0.99
Plesovice-5	-	-	810	92.3	0.428384493	0.030375153	0.05365	0.001111499	18.63933	0.386161934	0.057915974	0.003788957	0.0155	0.001925123	0.93
Plesovice-6	-	-	722	76.4	0.367033937	0.038280814	0.05374	0.001103492	18.60811	0.382097218	0.049427684	0.005135724	0.0145	0.002516764	1.06
Plesovice-7	-	-	714	76.4	0.406916498	0.039832253	0.05314	0.001104334	18.81822	0.391071084	0.055179594	0.004760152	0.0142	0.002119117	0.96
Plesovice-8	-	-	703	78.7	0.392923734	0.038589756	0.0532	0.001102813	18.79699	0.389653395	0.052740434	0.005096714	0.0168	0.002621621	0.99

Table D2b: All *in-situ* LASS zircon analyses: trace element data. REE concentrations are reported as chondrite normalized values

Analysis Name	Grain	Grain Texture	Ti ppm	2s	Y ppm	Hf ppm	La	Ce	Pr	Nd	Sm	Eu	Gd	Tb	Dy	Ho	Er	Tm	Yb	Lu	Eu/Eu*	Lun/Dyn	Th/U	Ti in zircon Temp. (°C)	2s
Inclusions in garnet																									
PPC15-01A3zrc-26	z4 inclusion in garnet	homogeneous grain	26	5	562	11730	0.0	15.8	1.3	4.8	32.4	8.0	170.9	241.8	303.7	346.2	353.8	384.6	350.3	301.6	0.11	0.99	0.49	842	22
PPC15-01A3zrc-13	z3 inclusion in rutile in garnet	metamorphic core	46	22	475	10210	0.5	4.7	0.7	5.0	58.1	21.0	178.4	246.5	321.5	296.7	288.1	261.9	298.8	333.3	0.21	1.04	0.04	913	77
PPC15-01A3zrc-20	z4 inclusion in garnet	homogeneous grain	25	7	538	11170	0.7	13.7	0.3	7.4	35.8	10.3	226.1	223.3	279.7	309.5	327.5	328.7	331.1	341.5	0.11	1.22	0.40	839	38
PPC15-01A3zrc-18	z4 inclusion in garnet	homogeneous grain	14	5	1217	10830	0.8	8.0	1.3	4.6	50.0	28.8	256.3	470.9	646.3	804.0	881.3	830.0	956.5	874.0	0.25	1.35	0.15	781	38
PPC15-01A3zrc-19	z4 inclusion in garnet	homogeneous grain	27	9	540	11440	0.2	14.4	0.8	7.4	61.5	5.5	195.0	254.8	313.0	391.9	353.8	360.3	354.0	369.9	0.05	1.18	0.46	849	44
PPC15-01A3zrc-24	z4 inclusion in garnet	homogeneous grain	30	9	512	11800	0.0	15.5	0.7	12.7	41.2	6.0	227.1	241.0	272.8	316.8	331.9	310.1	354.0	317.1	0.06	1.16	0.30	862	39
PPC15-01A3zrc-59	z14 inclusion in garnet	rim	19	6	571	11200	0.4	17.6	2.5	5.9	54.7	11.0	243.7	241.0	345.9	370.0	382.5	372.5	372.0	369.9	0.10	1.07	0.30	810	36
PPC15-01A3zrc-10	z2 inclusion in garnet	metamorphic core	24	7	451	10360	0.2	6.2	0.4	2.6	39.2	25.9	199.5	254.8	261.8	298.5	283.1	268.4	254.0	321.1	0.29	1.23	0.03	835	37
PPC15-01A3zrc-22	z4 inclusion in garnet	homogeneous grain	28	8	590	12520	0.0	17.3	0.6	8.1	83.8	13.7	249.7	265.9	345.5	375.5	374.4	306.9	386.3	357.7	0.09	1.04	0.42	854	37
PPC15-01A3zrc-4	z1 inclusion in rutile in garnet	rim	33	10	606	12070	0.0	15.5	0.6	7.4	61.5	10.7	216.6	257.6	363.8	379.1	320.0	306.5	397.5	390.2	0.09	1.07	0.22	873	40
PPC15-01A3zrc-1	z1 inclusion in rutile in garnet	rim	16	6	706	12900	0.0	11.7	0.8	4.6	56.1	8.3	229.1	326.9	418.7	443.2	496.3	457.5	490.7	500.0	0.07	1.19	0.06	794	43
PPC15-01A3zrc-17	z4 inclusion in garnet	homogeneous grain	16	7	942	11040	0.3	6.4	0.0	4.2	32.4	23.4	243.7	382.3	548.8	580.6	564.4	465.6	503.7	536.6	0.26	0.98	0.07	791	52

Analysis Name	Grain	Grain Texture	Ti ppm	2s	Y ppm	Hf ppm	La	Ce	Pr	Nd	Sm	Eu	Gd	Tb	Dy	Ho	Er	Tm	Yb	Lu	Eu/Eu*	Lun/Dyn	Th/U	Ti in zircon Temp. (°C)	2s
PPC15-01A3zrc-15	z3 inclusion in rutile in garnet	metamorphic core	23	6	491	10480	0.0	9.5	0.3	4.2	47.3	25.4	197.5	224.4	284.6	304.0	336.3	372.5	484.5	723.6	0.26	2.54	0.10	831	31
PPC15-01A3zrc-5	z1 inclusion in rutile in garnet	rim	29	5	576	12820	0.0	17.0	1.0	7.0	59.0	18.0	219.0	313.0	354.0	370.0	366.0	356.0	409.0	350.0	0.20	0.99	0.12	858	19
PPC15-01A3zrc-11	z2 inclusion in garnet	metamorphic core	22	8	514	10530	0.0	6.5	0.3	3.0	39.9	20.8	226.1	290.9	317.5	320.5	268.1	308.1	385.1	459.3	0.22	1.45	0.03	826	48
PPC15-01A3zrc-21	z4 inclusion in garnet	homogeneous grain	23	10	578	12360	0.0	17.0	0.6	10.1	70.3	12.3	273.4	299.2	349.6	377.3	408.8	352.2	366.5	463.4	0.09	1.33	0.43	829	57
PPC15-01A3zrc-16	z4 inclusion in garnet	homogeneous grain	17	5	1259	11750	0.2	8.2	1.2	5.3	36.5	7.3	381.9	415.5	727.6	811.4	950.0	862.3	956.5	1016.3	0.06	1.40	0.19	799	35
PPC15-01A3zrc-60	z14 inclusion in garnet	rim	17	6	643	11630	0.3	15.2	0.5	9.8	62.8	9.6	260.3	274.2	402.4	424.9	425.0	429.1	454.7	451.2	0.07	1.12	0.43	799	42
PPC15-01A3zrc-12	z2 inclusion in garnet	metamorphic core/rim	20	6	558	10770	0.3	6.9	0.4	2.6	37.8	18.5	175.9	271.5	333.7	348.0	395.6	340.1	370.2	406.5	0.23	1.22	0.05	814	37
PPC15-01A3zrc-7	z1 inclusion in rutile in garnet	rim	26	9	745	12350	0.2	10.1	0.5	6.1	52.7	20.1	242.7	271.5	402.0	485.3	498.1	570.9	540.4	532.5	0.18	1.32	0.07	845	45
PPC15-01A3zrc-8	z1 inclusion in rutile in garnet	rim	25	9	746	12510	1.0	9.6	1.3	7.0	54.7	20.1	220.6	357.3	381.7	494.5	462.5	514.2	509.3	512.2	0.18	1.34	0.05	839	47
PPC15-01A3zrc-25	z4 inclusion in garnet	homogeneous grain	27	6	478	11770	0.0	17.5	0.9	4.2	52.7	11.4	188.9	198.3	298.4	331.5	277.5	287.4	309.9	296.7	0.11	0.99	0.41	850	27
PPC15-01A3zrc-27	z4 inclusion in garnet	homogeneous grain	22	8	1214	11190	0.0	6.5	0.5	5.0	45.3	25.9	306.5	412.7	605.7	831.5	925.0	910.9	1068.3	1158.5	0.22	1.91	0.19	826	48
PPC15-01A3zrc-23	z1 inclusion in garnet	homogeneous grain	25	8	741	11690	0.0	14.3	1.0	4.8	78.4	10.1	301.5	340.7	483.7	507.3	488.1	485.8	478.9	471.5	0.07	0.97	0.47	839	39
PPC15-01A3zrc-6	z1 inclusion in rutile in garnet	rim	24	5	803	12720	0.0	7.4	0.0	4.2	49.3	12.8	208.0	324.1	460.6	500.0	598.8	554.7	638.5	609.8	0.13	1.32	0.05	835	26
PPC15-01A3zrc-2	z14 inclusion in rutile in garnet	rim	24	5	674	12330	0.0	11.1	1.0	5.5	82.4	19.9	256.3	262.9	377.6	483.5	465.6	408.9	482.6	455.3	0.14	1.21	0.06	833	28
PPC15-01A3zrc-58	inclusion in garnet	rim	18	5	724	11800	0.4	16.6	1.3	10.7	67.6	9.9	251.3	357.3	435.0	516.5	543.8	510.1	544.1	577.2	0.08	1.33	0.43	802	31
																							0.22		
Matrix																									
PPC15-01A3zrc-45	z8 matrix	rim	19	6	708	11440	0.0	15.7	1.2	7.4	80.4	11.5	232.2	313.0	430.9	514.7	511.3	400.8	473.3	475.6	0.08	1.10	0.53	812	37
PPC15-01A3zrc-46	z8 matrix	rim	24	9	743	11930	0.1	15.5	0.3	5.9	52.0	15.6	277.4	362.9	471.5	511.0	463.1	514.2	503.1	548.8	0.13	1.16	0.49	835	49
PPC15-01A3zrc-43	z8 matrix	rim	24	9	543	11690	0.0	17.1	0.9	9.6	37.8	8.2	228.6	257.6	330.5	370.0	368.8	332.0	359.0	410.6	0.09	1.24	0.55	837	47
PPC15-01A3zrc-57	z13 outside resorbed garnet	rim	25	9	607	12040	0.2	16.6	1.2	6.3	51.4	8.5	246.2	265.9	383.7	417.6	397.5	368.4	410.6	378.0	0.08	0.99	0.38	838	51
PPC15-01A3zrc-40	z8 matrix	rim	12	4	710	12240	0.4	16.9	0.8	5.7	62.2	12.4	254.8	277.0	410.6	448.7	432.5	373.3	443.5	435.0	0.10	1.06	0.59	767	35

Analysis Name	Grain	Grain Texture	Ti ppm	2s	Y ppm	Hf ppm	La	Ce	Pr	Nd	Sm	Eu	Gd	Tb	Dy	Ho	Er	Tm	Yb	Lu	Eu/Eu*	Lun/Dyn	Th/U	Ti in zircon Temp. (°C)	2s
PPC15-01A3zrc-28	z5 matrix outside resorbed garnet	rim	16	6	565	11470	0.8	9.8	2.2	2.6	50.0	42.8	234.2	254.8	365.9	315.0	360.0	311.7	321.7	308.9	0.40	0.84	0.08	789	49
PPC15-01A3zrc-41	z8 matrix	rim	21	6	718	11750	0.0	17.3	0.6	7.4	53.4	9.2	276.4	338.0	391.9	454.2	468.1	392.7	424.2	398.4	0.08	1.02	0.60	823	35
PPC15-01A3zrc-31	z6 matrix outside resorbed garnet	rim	21	10	559	11990	0.4	16.0	0.7	4.8	41.2	11.5	214.6	249.3	324.4	353.5	418.8	348.2	382.0	418.7	0.12	1.29	0.39	821	66
PPC15-01A3zrc-44	z8 matrix	rim	19	7	666	11660	0.2	14.2	1.7	7.7	54.1	13.9	203.5	274.2	386.2	452.4	433.8	481.8	455.9	439.0	0.13	1.14	0.53	808	46
PPC15-01A3zrc-42	z8 matrix	rim	34	8	576	11850	0.2	15.9	0.7	10.7	51.4	11.7	196.0	254.8	313.0	384.6	388.1	319.8	370.2	390.2	0.12	1.25	0.52	874	31
PPC15-01A3zrc-38	z8 matrix	rim	29	11	592	11660	0.3	18.6	0.3	12.5	43.2	10.8	266.3	315.8	387.8	393.8	373.8	348.2	423.0	300.8	0.10	0.78	0.55	857	53
PPC15-01A3zrc-39	z8 matrix	rim	27	6	787	11900	0.0	19.4	31.3	12.3	65.5	13.9	301.0	357.3	475.6	457.9	486.3	473.7	424.8	430.9	0.10	0.91	0.59	849	26
PPC15-01A3zrc-32	z6 matrix outside resorbed garnet	rim	24	6	554	11800	0.7	15.7	0.9	7.2	71.6	5.3	229.1	263.2	301.6	353.5	354.4	348.2	345.3	451.2	0.04	1.50	0.49	835	32
PPC15-01A3zrc-58	z14 inclusion in garnet	rim	18	5	724	11800	0.4	16.6	1.3	10.7	67.6	9.9	251.3	357.3	435.0	516.5	543.8	510.1	544.1	577.2	0.08	1.33	0.43	802	31
PPC15-01A3zrc-50	z11 matrix next to ilm	rim	28	8	784	11600	0.7	13.4	2.4	7.2	66.9	37.3	258.3	349.0	459.3	589.7	531.3	506.1	537.3	512.2	0.28	1.12	0.35	852	40
PPC15-01A3zrc-55	z13 outside resorbed garnet	rim:mixed?	26	8	638	12230	0.2	15.7	1.1	5.9	74.3	8.0	236.7	288.1	390.2	377.3	410.0	396.8	395.0	455.3	0.06	1.17	0.43	845	38
PPC15-01A3zrc-34	z6 matrix outside resorbed garnet	rim	21	9	619	11990	0.4	15.0	1.2	7.0	52.7	15.3	246.2	277.0	391.5	408.4	431.3	404.9	422.4	398.4	0.13	1.02	0.28	818	60
PPC15-01A3zrc-34	z6 matrix outside resorbed garnet	rim	21	9	619	11990	0.4	15.0	1.2	7.0	52.7	15.3	246.2	277.0	391.5	408.4	431.3	404.9	422.4	398.4	0.13	1.02	0.28	818	60
																							0.45		
Inclusions in rutile																									
PPC15-01A3zrc-13	z3 inclusion in garnet	metamorphic core	46	22	475	10210	1.0	5.0	1.0	5.0	58.0	21.0	178.0	247.0	322.0	297.0	288.0	262.0	299.0	333.0	0.20	1.04	0.04	913	77
PPC15-01A3zrc-4	z1 inclusion in garnet	rim	33	10	606	12070	0.0	15.5	0.6	7.4	61.5	10.7	216.6	257.6	363.8	379.1	320.0	306.5	397.5	390.2	0.09	1.07	0.22	873	40
PPC15-01A3zrc-1	z1 inclusion in rutile in garnet	rim	16	6	706	12900	0.0	11.7	0.8	4.6	56.1	8.3	229.1	326.9	418.7	443.2	496.3	457.5	490.7	500.0	0.07	1.19	0.06	794	43
PPC15-01A3zrc-15	z3 inclusion in garnet	metamorphic core	23	6	491	10480	0.0	9.5	0.3	4.2	47.3	25.4	197.5	224.4	284.6	304.0	336.3	372.5	484.5	723.6	0.26	2.54	0.10	831	31
PPC15-01A3zrc-5	z1 inclusion in garnet	rim	29	5	576	12820	0.0	17.0	1.0	7.0	59.0	18.0	219.0	313.0	354.0	370.0	366.0	356.0	409.0	350.0	0.20	0.99	0.12	858	19
PPC15-01A3zrc-7	z1 inclusion in garnet	rim	26	9	745	12350	0.2	10.1	0.5	6.1	52.7	20.1	242.7	271.5	402.0	485.3	498.1	570.9	540.4	532.5	0.18	1.32	0.07	845	45
PPC15-01A3zrc-8	z1 inclusion in garnet	rim	25	9	746	12510	1.0	9.6	1.3	7.0	54.7	20.1	220.6	357.3	381.7	494.5	462.5	514.2	509.3	512.2	0.18	1.34	0.05	839	47

Analysis Name	Grain	Grain Texture	Ti ppm	2s	Y ppm	Hf ppm	La	Ce	Pr	Nd	Sm	Eu	Gd	Tb	Dy	Ho	Er	Tm	Yb	Lu	Eu/Eu*	Lun/Dyn	Th/U	Ti in zircon Temp. (°C)	2s
PPC15-01A3zrc-6	z1 inclusion in garnet	rim	24	5	803	12720	0.0	7.4	0.0	4.2	49.3	12.8	208.0	324.1	460.6	500.0	598.8	554.7	638.5	609.8	0.13	1.32	0.05	835	26
PPC15-01A3zrc-2	z1 inclusion in rutile in garnet	rim	24	5	674	12330	0.0	11.1	1.0	5.5	82.4	19.9	256.3	262.9	377.6	483.5	465.6	408.9	482.6	455.3	0.14	1.21	0.06	833	28
Inherited Cores																									
PPC15-01A3zrc-54	z13 outside resorbed garnet	igneous? core	18	4.8	1670	14450	1.8	3.4	2.2	3.7	16.9	17.9	64.3	113.3	321.1	983.5	2256.3	4024.3	6701.9	9634.1	0.54	3.00	0.01	804	32
PPC15-01A3zrc-53	z13 outside resorbed garnet	rim	40	17	694	12570	1.4	19.2	1.3	7.9	56.8	20.8	246.2	293.6	422.8	410.3	419.4	425.1	424.8	475.6	0.18	0.11	0.25	895	65
PPC15-01A3zrc-47	z8 matrix	igneous core	29.1	7.1	1350	11000	4.0	22.8	6.4	22.5	89.2	34.1	280.4	349.0	573.2	906.6	1356.3	1659.9	2528.0	3622.0	0.22	0.63	0.57	857	31
PPC15-01A3zrc-51	z11 matrix next to ilm	rim	36	12	1072	12190	9.8	24.1	11.5	29.5	117.6	52.0	385.4	462.6	674.8	701.5	650.0	599.2	708.1	743.9	0.24	0.11	0.32	882	47
PPC15-01A3zrc-56	z13 outside resorbed garnet	rim	18	7.1	695	12620	2.6	20.1	1.5	9.2	83.8	12.3	295.0	313.0	402.4	408.4	463.8	453.4	470.8	479.7	0.08	0.12	0.33	804	50
PPC15-01A3zrc-52	z13 outside resorbed garnet	mixed?	18.5	9	550	12080	0.8	19.1	1.1	6.6	82.4	22.2	216.1	263.4	321.5	359.0	393.8	404.9	414.9	483.7	0.17	0.15	0.37	807	66
Discordant/Mixed Analyses																									
PPC15-01A3zrc-35	z7 matrix	rim	18.8	6.3	1120	11610	10.1	24.5	8.3	27.4	263.5	90.6	673.4	617.7	695.1	800.4	800.0	874.5	1018.6	1341.5	0.22	0.19	0.08	809	42
PPC15-01A3zrc-33	z6 matrix outside resorbed garnet	etched zoned core	19	5.9	474	9380	0.4	2.6	2.4	0.0	6.8	11.7	49.7	85.0	183.7	258.2	373.8	550.6	906.8	1422.8	0.64	0.77	0.01	810	38
PPC15-01A3zrc-34	z6 matrix outside resorbed garnet	rim	20.5	9.1	619	11990	0.4	15.0	1.2	7.0	52.7	15.3	246.2	277.0	391.5	408.4	431.3	404.9	422.4	398.4	0.13	0.10	0.28	818	60
PPC15-01A3zrc-48	z11 matrix next to ilm	mantle	28.9	9.7	497	12480	0.0	8.3	0.5	4.6	43.2	34.5	256.8	290.9	365.9	318.7	233.8	230.8	244.7	288.6	0.33	0.08	0.08	856	45
PPC15-01A3zrc-49	z11 matrix next to ilm	mantle	26.7	8.1	448	11330	2.1	12.2	3.3	10.9	43.9	36.4	232.2	285.3	320.7	265.6	233.8	186.2	192.5	215.4	0.36	0.07	0.08	847	40
PPC15-01A3zrc-61	z14 inclusion in garnet	core	26.4	7.5	756	15000	4.4	5.7	3.4	6.1	16.2	24.2	48.7	108.0	219.5	428.6	818.8	1279.4	2000.0	2426.8	0.86	1.11	0.00	846	37
PPC15-01A3zrc-37	z7 matrix	patchy zoned core	6	12	1470	15120	3.4	8.5	2.2	7.4	35.8	40.5	120.6	199.4	556.9	1128.2	2131.3	3603.2	6335.4	10243.9	0.62	1.84	0.01	700	-
PPC15-01A3zrc-36	z7 matrix	rim	16.2	8.8	962	12440	3.8	14.8	5.5	9.2	70.9	79.9	247.2	279.8	475.6	653.8	843.8	1121.5	1770.2	2317.1	0.60	0.49	0.03	793	75
PPC15-01A3zrc-29	z5 matrix outside resorbed garnet	rim	370	140	528	11400	0.5	13.5	0.8	4.2	50.7	14.6	166.3	243.8	285.0	348.0	299.4	303.6	344.7	353.7	0.16	0.12	0.17	1254	94
PPC15-01A3zrc-3	z1 inclusion in garnet	rim	530	280	869	13190	0.9	9.1	1.6	6.1	60.8	14.4	271.4	335.2	463.4	589.7	618.8	611.3	654.0	658.5	0.11	0.14	0.05	1334	158
PPC15-01A3zrc-14	z3 inclusion in garnet	metamorphic core	4120	900	527	10310	0.2	6.2	9.7	4.4	41.2	28.8	221.1	252.1	337.4	353.5	367.5	311.7	365.8	365.9	0.30	0.11	0.07	2017	111
PPC15-01A3zrc-9	z1 inclusion in garnet	rim	193	76	904	12220	2.4	13.1	1.8	10.5	86.5	27.0	366.8	407.2	569.1	600.7	618.8	603.2	610.6	666.7	0.15	0.12	0.05	1128	84

Analysis Name	Grain	Grain Texture	Ti ppm	2s	Y ppm	Hf ppm	La	Ce	Pr	Nd	Sm	Eu	Gd	Tb	Dy	Ho	Er	Tm	Yb	Lu	Eu/Eu*	Lun/Dyn	Th/U	Ti in zircon Temp. (°C)	2s
Standards																									
SL1-1	-	-	6	7.3	233	8810	0.0	2.7	0.2	3.5	29.1	2.8	31.7	49.6	84.1	133.7	196.3	255.1	317.4	430.9	0.09	0.51	0.23		
SL1-2	-	-	1	5.1	217	8560	0.0	2.2	0.2	2.3	27.0	2.8	41.2	60.7	95.9	142.9	206.3	247.8	395.0	508.1	0.09	0.53	0.22		
SL1-3	-	-	6.5	5.2	237	8550	0.0	2.7	0.5	1.8	3.0	5.0	37.7	61.2	89.0	147.8	213.8	287.4	313.0	435.0	0.47	0.49	0.23		
SL1-4	-	-	3.7	6.2	224	8150	0.0	1.7	0.7	2.4	8.1	6.7	51.3	39.9	78.0	141.0	209.4	251.4	335.4	426.8	0.33	0.55	0.22		
SL1-5	-	-	-0.9	3.4	234	8490	0.0	2.0	0.4	2.1	7.6	3.9	29.1	41.8	74.0	130.0	199.4	222.7	347.8	471.5	0.26	0.64	0.22		
SL1-6	-	-	-3.8	5.2	232	8400	0.0	2.8	0.3	1.5	3.9	3.9	40.7	49.0	102.0	126.4	230.0	267.2	396.9	443.1	0.31	0.43	0.21		
91500-1	-	-	3.2	4.2	132.4	5550	0.0	4.2	0.0	1.5	5.4	5.2	14.1	27.1	35.4	95.2	174.4	267.2	349.7	650.4	0.59	1.84	0.37		
91500-2	-	-	8.1	5.5	144.5	5720	0.2	4.8	0.0	0.9	6.1	2.0	9.0	19.4	42.3	104.4	150.0	242.9	432.9	638.2	0.26	1.51	0.31		
91500-3	-	-	3.6	4.6	153	5850	0.0	3.6	0.2	0.9	6.0	0.9	15.1	16.6	45.1	76.9	183.1	287.4	409.9	646.3	0.09	1.43	0.32		
91500-4	-	-	3.7	4.6	140	5770	0.0	3.7	0.3	3.1	1.6	0.8	18.6	18.8	56.5	89.4	176.3	275.3	421.7	642.3	0.15	1.14	0.33		
91500-5	-	-	8	7.3	130.8	5440	0.0	4.6	0.2	0.4	4.7	3.6	11.6	19.9	47.6	75.8	148.8	279.4	336.6	585.4	0.48	1.23	0.33		
91500-6	-	-	-1.6	4	142.5	5460	0.0	3.6	0.3	0.0	0.0	5.5	11.6	15.2	45.1	106.2	131.9	249.8	398.8	495.9	-	1.10	0.34		
91500-7	-	-	3.5	4.1	141	5470	0.0	4.0	0.0	0.7	1.3	2.3	15.6	19.7	38.2	97.1	170.6	246.6	402.5	544.7	0.52	1.43	0.29		
91500-8	-	-	-2.9	4.5	152	5990	7.6	4.2	0.0	1.4	2.9	8.3	16.1	26.6	37.8	102.6	153.1	210.5	409.9	609.8	1.22	1.61	0.34		
91500-9	-	-	2.2	3.5	141.3	5060	0.0	3.5	0.0	0.4	10.8	1.8	11.6	19.1	50.8	74.0	140.0	214.6	408.7	516.3	0.16	1.02	0.31		
GJ1-1	-	-	1.9	6.5	258	6680	0.0	25.3	0.4	0.5	4.7	12.6	33.2	53.5	74.8	131.9	193.1	227.5	424.8	528.5	1.01	0.71	0.03		
GJ1-2	-	-	1.8	3.4	245	6790	0.0	28.5	0.5	1.8	8.8	19.2	27.1	54.6	72.8	146.5	183.1	267.2	360.9	528.5	1.24	0.73	0.03		
GJ1-3	-	-	8.9	4.7	248	6270	0.0	25.1	0.5	1.7	3.0	23.4	26.6	47.9	77.2	122.7	186.3	247.0	384.5	552.8	2.63	0.72	0.03		
GJ1-4	-	-	2.2	4	234	6460	0.0	25.4	0.5	2.5	21.6	14.7	35.2	46.5	88.6	111.7	203.1	238.9	377.0	516.3	0.53	0.58	0.03		
GJ1-5	-	-	3.2	5	247	6550	0.2	25.8	0.0	0.8	5.4	13.5	36.7	59.8	89.4	122.7	168.8	283.4	355.3	487.8	0.96	0.55	0.03		
GJ1-6	-	-	2.3	3.4	252	6890	0.0	26.6	0.3	1.5	14.2	25.6	40.7	49.3	91.5	106.2	203.8	271.3	386.3	565.0	1.06	0.62	0.04		
GJ1-7	-	-	3.3	4.2	250	6440	0.0	27.2	0.4	1.6	15.5	14.0	41.2	56.5	67.9	126.4	186.9	271.3	397.5	504.1	0.55	0.74	0.03		
GJ1-8	-	-	4.5	2.3	251	6540	0.0	24.6	0.2	240.7	263.5	17.6	41.2	66.5	82.9	131.9	170.0	259.1	419.3	597.6	0.17	0.72	0.04		
Plesovice-1	-	-	55	11	569	10530	0.2	4.2	0.3	7.7	29.7	15.8	68.8	127.7	204.1	289.4	399.4	449.4	409.9	337.4	0.35	0.17	0.09		
Plesovice-2	-	-	83	12	593	10790	0.8	5.1	0.6	7.7	40.5	6.2	82.9	144.0	216.7	355.3	398.1	449.4	515.5	540.7	0.11	0.25	0.10		
Plesovice-3	-	-	59	16	573	10800	1.9	5.6	1.2	6.6	48.0	18.7	90.5	121.9	268.7	311.4	368.8	473.7	520.5	520.3	0.28	0.19	0.09		
Plesovice-4	-	-	83	13	567	10800	0.0	4.9	1.4	3.3	36.5	15.5	71.9	129.4	229.3	318.7	424.4	433.2	514.3	504.1	0.30	0.22	0.10		
Plesovice-5	-	-	84	11	723	11190	0.0	4.3	1.9	10.3	50.7	28.2	88.9	185.6	286.2	370.0	484.4	522.3	583.9	617.9	0.42	0.22	0.10		

Analysis Name	Grain	Grain Texture	Ti ppm	2s	Y ppm	Hf ppm	La	Ce	Pr	Nd	Sm	Eu	Gd	Tb	Dy	Ho	Er	Tm	Yb	Lu	Eu/Eu*	Lun/Dyn	Th/U	Ti in zircon Temp. (°C)	2s
Plesovice-6	-	-	75	17	574	10400	0.0	3.9	1.3	3.5	35.1	9.8	78.9	149.6	215.9	305.9	384.4	421.1	496.9	475.6	0.19	0.22	0.11		
Plesovice-7	-	-	76	9.9	570	10680	0.0	5.1	0.9	8.8	19.6	8.3	83.9	124.7	244.3	346.2	399.4	392.7	528.0	532.5	0.21	0.22	0.10		
Plesovice-8	-	-	59	11	558	10660	0.8	3.4	1.4	5.3	19.6	21.3	80.4	126.3	239.0	320.5	388.8	421.1	451.6	487.8	0.54	0.20	0.09		

Table D3a: All *in-situ* LASS monazite analyses: isotopic data

Spot Analysis	Grain	Zone	U ppm	Th ppm	$^{207}Pb/^{235}U$	2s	$^{206}Pb/^{238}U$	2s	$^{238}U/^{206}Pb$	2s	$^{207}Pb/^{206}Pb$	2s	$^{208}Pb/^{232}Th$	2s	$^{207}Pb/^{206}Pb$ Age	2s	Concordance
Group 1																	
PPC15-01A3-76	m14 inclusion in garnet	high-Y rim	1471	15090	13.17	0.27	0.51	0.01	1.95	0.04	0.19	0.00	0.14	0.00	2711	33	0.99
PPC15-01A3-77	m14 inclusion in garnet	low-Y core	2142	14910	13.24	0.27	0.51	0.01	1.95	0.04	0.19	0.00	0.14	0.00	2721	33	0.99
PPC15-01A3-78	m14 inclusion in garnet	low-Y core	1568	15410	13.63	0.28	0.52	0.01	1.93	0.04	0.19	0.00	0.14	0.00	2747	33	0.99
Group 2																	
PPC15-01A3-59	m6 inclusion in garnet	high-Y patch	5730	11010	13.00	0.26	0.52	0.01	1.93	0.04	0.18	0.00	0.14	0.00	2679	33	1
PPC15-01A3-60	m6 inclusion in garnet	high-Y patch	5650	11010	13.10	0.26	0.52	0.01	1.93	0.04	0.18	0.00	0.14	0.00	2688	33	1
PPC15-01A3-61	m6 inclusion in garnet	high-Y patch	5740	10740	13.13	0.26	0.52	0.01	1.93	0.04	0.18	0.00	0.14	0.00	2688	33	1
Group 3																	
PPC15-01A3-54	m6 inclusion in garnet	low-Y patch	2171	10500	12.59	0.25	0.51	0.01	1.96	0.04	0.18	0.00	0.15	0.00	2649	33	1.01
PPC15-01A3-53	m6 inclusion in garnet	low-Y patch	2163	7640	12.64	0.26	0.51	0.01	1.96	0.04	0.18	0.00	0.14	0.00	2657	33	1
PPC15-01A3-52	m6 inclusion in garnet	low-Y patch	3393	12730	12.88	0.26	0.51	0.01	1.95	0.04	0.18	0.00	0.14	0.00	2681	33	1
PPC15-01A3-56	m6 inclusion in garnet	low-Y patch	2389	13140	12.98	0.26	0.52	0.01	1.93	0.04	0.18	0.00	0.14	0.00	2671	33	1.01
PPC15-01A3-58	m6 inclusion in garnet	medium-Y patch	3598	15820	13.01	0.26	0.52	0.01	1.94	0.04	0.18	0.00	0.14	0.00	2684	33	1
PPC15-01A3-57	m6 inclusion in garnet	medium-Y patch	3504	18330	13.04	0.26	0.52	0.01	1.93	0.04	0.18	0.00	0.14	0.00	2685	33	1
PPC15-01A3-47	m5 inclusion in garnet - in melt inclusion?	high-Y core	4450	16160	13.07	0.26	0.52	0.01	1.92	0.04	0.18	0.00	0.14	0.00	2688	33	1.01
PPC15-01A3-55	m6 inclusion in garnet	low-Y patch	2144	12340	13.08	0.26	0.52	0.01	1.91	0.04	0.18	0.00	0.14	0.00	2674	33	1.01
PPC15-01A3-48	m5 inclusion in garnet - in melt inclusion?	high-Y overgrowth	4294	17540	13.09	0.26	0.52	0.01	1.92	0.04	0.18	0.00	0.14	0.00	2688	33	1.01
Group 4																	
PPC15-01A3-68	m11 in grt fracture	low-Y	905	14120	12.33	0.25	0.50	0.01	1.98	0.04	0.18	0.00	0.14	0.00	2628	35	1
PPC15-01A3-69	m11 in grt fracture	low-Y	853	13170	12.29	0.26	0.50	0.01	2.00	0.04	0.18	0.00	0.14	0.00	2634	35	0.99
PPC15-01A3-41	m4 inclusion in garnet	high-Y overgrowth	872	19720	12.53	0.27	0.51	0.01	1.96	0.04	0.18	0.00	0.14	0.00	2640	34	1.01
PPC15-01A3-64	m9 outside resorbed garnet	High-Y band	1650	15520	12.54	0.26	0.51	0.01	1.96	0.04	0.18	0.00	0.14	0.00	2640	34	1
PPC15-01A3-39	m4 inclusion in garnet	low-Y	968	21480	12.50	0.26	0.51	0.01	1.96	0.04	0.18	0.00	0.14	0.00	2644	34	1
PPC15-01A3-36	m4 inclusion in garnet	high-Y	997	15610	12.36	0.25	0.50	0.01	1.99	0.04	0.18	0.00	0.14	0.00	2647	34	1

Spot Analysis	Grain	Zone	U ppm	Th ppm	$^{207}Pb/^{235}U$	2s	$^{206}Pb/^{238}U$	2s	$^{238}U/^{206}Pb$	2s	$^{207}Pb/^{206}Pb$	2s	$^{208}Pb/^{232}Th$	2s	$^{207}Pb/^{206}Pb$ Age	2s	Concordance
PPC15-01A3-42	m4 inclusion in garnet	low Y	901	19000	12.43	0.26	0.51	0.01	1.97	0.04	0.18	0.00	0.14	0.00	2648	34	1
PPC15-01A3-49	m5 inclusion in garnet - in melt inclusion?	high-Y core	1872	18700	12.66	0.26	0.52	0.01	1.94	0.04	0.18	0.00	0.14	0.00	2649	34	1.01
PPC15-01A3-44	m5 inclusion in garnet - in melt inclusion?	high-Y overgrowth	2105	20480	12.62	0.25	0.51	0.01	1.95	0.04	0.18	0.00	0.14	0.00	2651	33	1.01
PPC15-01A3-40	m4 inclusion in garnet	high-Y overgrowth	1307	18700	12.35	0.26	0.50	0.01	2.00	0.04	0.18	0.00	0.14	0.00	2652	34	1
PPC15-01A3-35	m4 inclusion in garnet	high-Y	1099	16530	12.64	0.26	0.51	0.01	1.95	0.04	0.18	0.00	0.14	0.00	2653	34	1.01
PPC15-01A3-50	m5 inclusion in garnet - in melt inclusion?	high-Y overgrowth	1993	20550	12.58	0.25	0.51	0.01	1.96	0.04	0.18	0.00	0.14	0.00	2655	33	1
PPC15-01A3-80	m13 inclusion in garnet	high-Y rim	1218	16280	12.57	0.26	0.51	0.01	1.98	0.04	0.18	0.00	0.14	0.00	2655	34	1
PPC15-01A3-43	m4 inclusion in garnet	low-Y	896	19040	12.57	0.26	0.51	0.01	1.97	0.04	0.18	0.00	0.14	0.00	2658	34	1
PPC15-01A3-79	m13 inclusion in garnet	high-Y rim	1341	17460	12.61	0.26	0.51	0.01	1.98	0.04	0.18	0.00	0.14	0.00	2662	33	0.99
PPC15-01A3-6	m2 inclusion in garnet	high-Y rim	918	20170	12.82	0.27	0.51	0.01	1.97	0.04	0.18	0.00	0.14	0.00	2664	34	0.99
PPC15-01A3-25	m3 inclusion in garnet	high-Y, low-Th core	1176	13060	13.20	0.27	0.53	0.01	1.90	0.04	0.18	0.00	0.14	0.00	2666	34	1.01
PPC15-01A3-33	m3 inclusion in garnet	high-Y, low-Th core	1369	12400	12.98	0.26	0.52	0.01	1.93	0.04	0.18	0.00	0.14	0.00	2668	33	1.01
PPC15-01A3-24	m3 inclusion in garnet	high-Y, low-Th core	1020.5	15640	13.15	0.27	0.53	0.01	1.90	0.04	0.18	0.00	0.14	0.00	2670	34	1.01
Group 5																	
PPC15-01A3-16	m3 inclusion in garnet	high-Y rim	650	24910	12.35	0.26	0.51	0.01	1.96	0.04	0.18	0.00	0.14	0.00	2616	36	1.01
PPC15-01A3-15	m3 inclusion in garnet	high-Y rim	635	25190	12.48	0.26	0.51	0.01	1.97	0.04	0.18	0.00	0.14	0.00	2628	35	1
PPC15-01A3-30	m3 inclusion in garnet	high-Y rim	527	26610	12.55	0.27	0.52	0.01	1.94	0.04	0.18	0.00	0.14	0.00	2629	36	1.01
PPC15-01A3-20	m3 inclusion in garnet	low-Y mantle	623	26160	12.39	0.26	0.50	0.01	1.98	0.04	0.18	0.00	0.14	0.00	2633	35	1
PPC15-01A3-19	m3 inclusion in garnet	low-Y mantle	468	27180	12.59	0.29	0.51	0.01	1.96	0.04	0.18	0.00	0.14	0.00	2636	37	1
PPC15-01A3-14	m2 inclusion in garnet	high-Y rim	581.1	25010	12.61	0.28	0.51	0.01	1.97	0.04	0.18	0.00	0.14	0.00	2645	36	1
PPC15-01A3-29	m3 inclusion in garnet	high-Y rim	563.9	26770	12.63	0.27	0.51	0.01	1.95	0.04	0.18	0.00	0.14	0.00	2645	36	1
PPC15-01A3-11	m2 inclusion in garnet	high-Y rim	359.6	28260	13.10	0.29	0.53	0.01	1.90	0.04	0.18	0.00	0.14	0.00	2647	37	1.01
PPC15-01A3-21	m3 inclusion in garnet	low-Y mantle	516	26300	12.61	0.28	0.51	0.01	1.96	0.04	0.18	0.00	0.14	0.00	2647	37	1
PPC15-01A3-37	m4 inclusion in garnet	low-Y	401	22070	12.85	0.30	0.52	0.01	1.92	0.04	0.18	0.00	0.14	0.00	2647	38	1.01
PPC15-01A3-4	m2 inclusion in garnet	lower-Y outer rim	349.3	27430	13.05	0.31	0.52	0.01	1.92	0.04	0.18	0.00	0.14	0.00	2648	39	1.01
PPC15-01A3-17	m3 inclusion in garnet	high-Y rim	456.6	26780	12.74	0.28	0.51	0.01	1.95	0.04	0.18	0.00	0.14	0.00	2649	36	1
PPC15-01A3-65	m9 outside resorbed garnet	low-Y core	430	25600	12.72	0.29	0.51	0.01	1.95	0.04	0.18	0.00	0.14	0.00	2650	38	1.01
PPC15-01A3-9	m2 inclusion in garnet	high-Y rim	368.9	26760	12.93	0.30	0.52	0.01	1.93	0.04	0.18	0.00	0.14	0.00	2650	39	1.01
PPC15-01A3-34	m4 inclusion in garnet	high-Y rim	566.7	28400	12.58	0.26	0.51	0.01	1.96	0.04	0.18	0.00	0.14	0.00	2652	35	1

Spot Analysis	Grain	Zone	U ppm	Th ppm	$^{207}Pb/^{235}U$	2s	$^{206}Pb/^{238}U$	2s	$^{238}U/^{206}Pb$	2s	$^{207}Pb/^{206}Pb$	2s	$^{208}Pb/^{232}Th$	2s	$^{207}Pb/^{206}Pb$ Age	2s	Concordance
PPC15-01A3-1	m2 inclusion in garnet	lower-Y outer rim	488	24420	12.69	0.28	0.51	0.01	1.98	0.04	0.18	0.00	0.14	0.00	2653	36	0.99
PPC15-01A3-38	m4 inclusion in garnet	medium Y	406.2	21870	12.64	0.28	0.51	0.01	1.95	0.04	0.18	0.00	0.14	0.00	2654	37	1.01
PPC15-01A3-3	m2 inclusion in garnet	lower-Y outer rim	386.1	26200	12.91	0.30	0.52	0.01	1.94	0.04	0.18	0.00	0.14	0.00	2656	37	1
PPC15-01A3-28	m3 inclusion in garnet	high-Y rim	670	27000	12.74	0.27	0.51	0.01	1.95	0.04	0.18	0.00	0.14	0.00	2657	35	1
PPC15-01A3-13	m2 inclusion in garnet	high-Y rim	339.9	27740	13.21	0.30	0.53	0.01	1.90	0.04	0.18	0.00	0.14	0.00	2660	38	1.01
PPC15-01A3-18	m3 inclusion in garnet	high-Y rim	517	25140	12.82	0.28	0.51	0.01	1.95	0.04	0.18	0.00	0.14	0.00	2662	36	1
PPC15-01A3-8	m2 inclusion in garnet	low-Y core	360.5	24870	13.15	0.29	0.52	0.01	1.91	0.04	0.18	0.00	0.14	0.00	2662	36	1.01
PPC15-01A3-7	m2 inclusion in garnet	low-Y core	372.5	30500	13.13	0.30	0.52	0.01	1.92	0.04	0.18	0.00	0.14	0.00	2663	38	1.01
PPC15-01A3-45	m5 inclusion in garnet - in melt inclusion?	low-Y mantle	474	25410	12.92	0.29	0.52	0.01	1.93	0.04	0.18	0.00	0.14	0.00	2666	37	1.01
PPC15-01A3-23	m3 inclusion in garnet	low-Y mantle	378.5	25650	12.95	0.29	0.52	0.01	1.94	0.04	0.18	0.00	0.14	0.00	2671	37	1
PPC15-01A3-10	m2 inclusion in garnet	high-Y rim	370.7	29150	13.02	0.30	0.52	0.01	1.94	0.04	0.18	0.00	0.14	0.00	2673	40	1
PPC15-01A3-5	m2 inclusion in garnet	high-Y rim	359.3	26320	13.31	0.32	0.53	0.01	1.90	0.04	0.18	0.00	0.14	0.00	2673	40	1.01
PPC15-01A3-26	m3 inclusion in garnet	low-Y mantle	655	23560	13.04	0.28	0.52	0.01	1.93	0.04	0.18	0.00	0.14	0.00	2674	35	1
PPC15-01A3-31	m3 inclusion in garnet	low-Y mantle	410	26260	12.96	0.29	0.52	0.01	1.94	0.04	0.18	0.00	0.14	0.00	2674	37	1
PPC15-01A3-22	m3 inclusion in garnet	low-Y mantle	374.7	31120	12.99	0.29	0.52	0.01	1.93	0.04	0.18	0.00	0.14	0.00	2675	35	1
PPC15-01A3-46	m5 inclusion in garnet - in melt inclusion?	low-Y mantle	367.7	29490	13.00	0.32	0.52	0.01	1.92	0.04	0.18	0.00	0.14	0.00	2676	41	1.01
PPC15-01A3-27	m3 inclusion in garnet	low-Y mantle	420.4	24510	13.19	0.28	0.52	0.01	1.91	0.04	0.18	0.00	0.14	0.00	2678	36	1.01
PPC15-01A3-32	m3 inclusion in garnet	low-Y mantle	406	25450	13.07	0.29	0.52	0.01	1.93	0.04	0.18	0.00	0.14	0.00	2679	38	1
PPC15-01A3-2	m2 inclusion in garnet	lower-Y outer rim	402	27620	13.27	0.30	0.52	0.01	1.92	0.04	0.18	0.00	0.14	0.00	2680	38	1
PPC15-01A3-12	m2 inclusion in garnet	high-Y rim	373.9	27670	13.33	0.33	0.52	0.01	1.91	0.04	0.18	0.00	0.14	0.00	2682	40	1.01
"Young" ages																	
PPC15-01A3-83	m15 outside resorbed garnet		806	7073	7.96	0.23	0.41	0.01	2.42	0.05	0.14	0.00	0.12	0.00	2217	41	1
PPC15-01A3-72	m11 in grt fracture	high-Y patch	841	13500	10.02	0.22	0.46	0.01	2.18	0.04	0.16	0.00	0.13	0.00	2437	37	1
PPC15-01A3-66	m9 outside resorbed garnet	low-Y core	623	23690	9.77	0.25	0.44	0.01	2.27	0.05	0.16	0.00	0.13	0.00	2454	42	0.98
PPC15-01A3-82	m15 outside resorbed garnet	low-Th patch	809	3849	10.95	0.25	0.49	0.01	2.06	0.04	0.16	0.00	0.14	0.00	2488	36	1.01
PPC15-01A3-71	m11 in grt fracture	high-Y patch	844	12980	10.72	0.23	0.47	0.01	2.11	0.04	0.16	0.00	0.13	0.00	2496	36	1
PPC15-01A3-75	m11 in grt fracture	low-Y patch	1139	13220	10.55	0.23	0.46	0.01	2.16	0.04	0.16	0.00	0.13	0.00	2504	36	0.99
PPC15-01A3-70	m11 in grt fracture	high-Y patch	816	12360	10.78	0.23	0.47	0.01	2.11	0.04	0.16	0.00	0.13	0.00	2505	36	1
PPC15-01A3-81	m15 outside resorbed garnet	low-Th patch	1060	3424	11.08	0.23	0.48	0.01	2.08	0.04	0.17	0.00	0.14	0.00	2527	35	1

Spot Analysis	Grain	Zone	U ppm	Th ppm	$^{207}Pb/^{235}U$	2s	$^{206}Pb/^{238}U$	2s	$^{238}U/^{206}Pb$	2s	$^{207}Pb/^{206}Pb$	2s	$^{208}Pb/^{232}Th$	2s	$^{207}Pb/^{206}Pb$ Age	2s	Concordance
PPC15-01A3-73	m11 in grt fracture	low-Y patch	1113	14500	11.58	0.24	0.49	0.01	2.05	0.04	0.17	0.00	0.13	0.00	2576	34	1
PPC15-01A3-67	m9 outside resorbed garnet	high-Y rim	1350	13440	12.36	0.25	0.52	0.01	1.94	0.04	0.17	0.00	0.14	0.00	2598	34	1.02
PPC15-01A3-74	m11 in grt fracture	low-Y patch	1594	15110	11.95	0.25	0.50	0.01	2.02	0.04	0.17	0.00	0.14	0.00	2603	34	1
PPC15-01A3-62	m9 outside resorbed garnet	medium-Y patch	1168	14080	12.44	0.26	0.01	0.28	1.91	0.04	0.17	0.00	0.14	0.00	2586	34	1
PPC15-01A3-63	m9 outside resorbed garnet	medium-Y patch	1201	14050	12.50	0.26	0.01	0.45	1.91	0.04	0.17	0.00	0.14	0.00	2587	34	1.03
PPC15-01A3-66	m9 outside resorbed garnet	low-Y core	623	23690	9.77	0.25	0.01	0.53	2.27	0.05	0.16	0.00	0.13	0.00	2456	42	0.98
PPC15-01A3-75	m11 in grt fracture	low-Y patch	1139	13220	10.55	0.23	0.01	0.28	2.16	0.04	0.16	0.00	0.13	0.00	2502	36	0.99
Standards																	
stern-1			3133	30940	0.65	0.03	0.08	0.00	11.95	0.24	0.06	0.00	0.03	0.00	519	10	1.02
stern-10			4393	36190	0.66	0.02	0.08	0.00	11.90	0.24	0.06	0.00	0.03	0.00	520	10	1.01
stern-11			3870	36280	0.67	0.02	0.08	0.00	11.91	0.24	0.06	0.00	0.03	0.00	520	10	1
stern-12			3234	32870	0.68	0.02	0.08	0.00	11.92	0.24	0.06	0.00	0.03	0.00	519	10	0.98
stern-13			3203	34160	0.65	0.02	0.08	0.00	11.84	0.24	0.06	0.00	0.03	0.00	524	10	1.03
stern-14			3032	33770	0.66	0.02	0.08	0.00	11.82	0.24	0.06	0.00	0.03	0.00	525	10	1.02
stern-15			3321	35520	0.67	0.02	0.08	0.00	11.81	0.24	0.06	0.00	0.03	0.00	524	10	1.01
stern-16			3350	33120	0.66	0.02	0.08	0.00	11.93	0.24	0.06	0.00	0.03	0.00	519	10	1.01
stern-17			4229	38660	0.64	0.02	0.08	0.00	12.10	0.24	0.06	0.00	0.03	0.00	513	10	1.02
stern-18			3654	36770	0.66	0.02	0.08	0.00	12.00	0.24	0.06	0.00	0.03	0.00	516	10	1
stern-19			3731	37760	0.66	0.02	0.08	0.00	11.97	0.24	0.06	0.00	0.03	0.00	518	10	1.01
stern-2			3163	33580	0.67	0.02	0.08	0.00	11.83	0.24	0.06	0.00	0.03	0.00	523	10	1
stern-20			3866	33900	0.65	0.02	0.08	0.00	12.04	0.24	0.06	0.00	0.03	0.00	515	10	1.02
stern-3			3680	39790	0.65	0.02	0.09	0.00	11.76	0.24	0.06	0.00	0.03	0.00	527	10	1.03
stern-4			3255	38040	0.67	0.02	0.08	0.00	11.84	0.24	0.06	0.00	0.03	0.00	523	10	1
stern-5			3730	41060	0.65	0.02	0.08	0.00	11.88	0.24	0.06	0.00	0.03	0.00	522	10	1.02
stern-6			3692	36140	0.65	0.02	0.08	0.00	11.86	0.24	0.06	0.00	0.03	0.00	523	10	1.03
stern-7			3620	35160	0.65	0.02	0.08	0.00	11.90	0.24	0.06	0.00	0.03	0.00	521	10	1.02
stern-8			4110	35530	0.65	0.02	0.08	0.00	11.95	0.24	0.06	0.00	0.03	0.00	519	10	1.03
stern-9			4290	32430	0.65	0.02	0.08	0.00	12.01	0.24	0.06	0.00	0.03	0.00	516	10	1.01

Spot Analysis	Grain	Zone	U ppm	Th ppm	$^{207}Pb/^{235}U$	2s	$^{206}Pb/^{238}U$	2s	$^{238}U/^{206}Pb$	2s	$^{207}Pb/^{206}Pb$	2s	$^{208}Pb/^{232}Th$	2s	$^{207}Pb/^{206}Pb$ Age	2s	Concordance
44069-1			3842	21910	0.52	0.02	0.07	0.00	14.70	0.30	0.06	0.00	0.02	0.00	424	8	0.99
44069-10			3640	19970	0.51	0.02	0.07	0.00	14.61	0.30	0.05	0.00	0.02	0.00	428	9	1.02
44069-11			3724	22050	0.54	0.02	0.07	0.00	13.87	0.28	0.05	0.00	0.02	0.00	450	9	1.02
44069-12			4004	22930	0.52	0.02	0.07	0.00	14.81	0.30	0.06	0.00	0.02	0.00	421	8	0.99
44069-13			3769	21950	0.52	0.02	0.07	0.00	14.70	0.30	0.06	0.00	0.02	0.00	424	8	1
44069-14			3982	22330	0.52	0.02	0.07	0.00	14.69	0.30	0.06	0.00	0.02	0.00	425	8	1
44069-15			3781	21060	0.51	0.01	0.07	0.00	14.73	0.30	0.05	0.00	0.02	0.00	424	8	1.02
44069-16			4192	22450	0.53	0.02	0.07	0.00	14.72	0.30	0.06	0.00	0.02	0.00	423	8	0.98
44069-17			3517	22860	0.52	0.02	0.07	0.00	14.67	0.30	0.06	0.00	0.02	0.00	425	9	1
44069-18			4403	20070	0.53	0.02	0.07	0.00	14.65	0.30	0.06	0.00	0.02	0.00	425	9	0.98
44069-19			4027	27110	0.52	0.02	0.07	0.00	14.71	0.30	0.06	0.00	0.02	0.00	424	8	1
44069-2			4020	22790	0.52	0.02	0.07	0.00	14.70	0.30	0.05	0.00	0.02	0.00	425	8	1
44069-20			3533	21850	0.51	0.02	0.07	0.00	14.74	0.30	0.05	0.00	0.02	0.00	424	9	1.01
44069-3			3811	22460	0.51	0.02	0.07	0.00	14.75	0.30	0.05	0.00	0.02	0.00	424	8	1.02
44069-4			3810	20920	0.53	0.02	0.07	0.00	14.65	0.30	0.06	0.00	0.02	0.00	425	9	0.99
44069-5			3885	22550	0.52	0.02	0.07	0.00	14.66	0.30	0.06	0.00	0.02	0.00	425	8	1
44069-6			3860	23670	0.51	0.02	0.07	0.00	14.78	0.30	0.06	0.00	0.02	0.00	422	8	1.01
44069-7			3970	21090	0.53	0.02	0.07	0.00	14.65	0.30	0.06	0.00	0.02	0.00	425	9	0.99
44069-8			4105	17590	0.53	0.02	0.07	0.00	14.69	0.30	0.06	0.00	0.02	0.00	424	8	0.99
44069-9			3816	24330	0.53	0.02	0.07	0.00	14.70	0.30	0.06	0.00	0.02	0.00	424	9	0.99
FC1-1			4550	31170	0.05	0.01	0.01	0.00	110.50	2.65	0.04	0.01	0.00	0.00	59	2	1.27
FC1-10			8610	27680	0.06	0.01	0.01	0.00	112.44	2.34	0.05	0.01	0.00	0.00	57	1	0.91
FC1-11			12990	35280	0.06	0.00	0.01	0.00	112.71	2.36	0.05	0.00	0.00	0.00	57	1	1.01
FC1-12			6640	34230	0.07	0.01	0.01	0.00	110.94	2.50	0.06	0.00	0.00	0.00	57	1	0.86
FC1-13			11170	31360	0.06	0.00	0.01	0.00	115.67	2.42	0.05	0.00	0.00	0.00	55	1	0.99
FC1-14			12340	35630	0.05	0.00	0.01	0.00	110.07	2.31	0.04	0.00	0.00	0.00	59	1	1.08
FC1-15			6980	30890	0.06	0.01	0.01	0.00	111.43	2.31	0.05	0.01	0.00	0.00	58	1	1.05
FC1-16			5260	31260	0.06	0.01	0.01	0.00	111.48	2.55	0.05	0.01	0.00	0.00	58	2	0.97
FC1-17			5380	29720	0.06	0.01	0.01	0.00	111.11	2.60	0.05	0.01	0.00	0.00	58	2	0.96
FC1-18			6190	29440	0.06	0.01	0.01	0.00	112.93	2.50	0.05	0.01	0.00	0.00	57	1	0.93

Spot Analysis	Grain	Zone	U ppm	Th ppm	$^{207}Pb/^{235}U$	2s	$^{206}Pb/^{238}U$	2s	$^{238}U/^{206}Pb$	2s	$^{207}Pb/^{206}Pb$	2s	$^{208}Pb/^{232}Th$	2s	$^{207}Pb/^{206}Pb$ Age	2s	Concordance
FC1-19			11690	29650	0.06	0.00	0.01	0.00	103.75	2.15	0.05	0.00	0.00	0.00	62	1	0.97
FC1-2			6320	34710	0.05	0.01	0.01	0.00	111.69	2.53	0.04	0.01	0.00	0.00	58	1	1.06
FC1-20			9180	30380	0.05	0.01	0.01	0.00	112.83	2.39	0.04	0.01	0.00	0.00	57	1	1.09
FC1-3			9820	34380	0.06	0.00	0.01	0.00	113.82	2.37	0.05	0.00	0.00	0.00	56	1	0.96
FC1-4			10750	34870	0.06	0.01	0.01	0.00	108.64	2.27	0.05	0.00	0.00	0.00	59	1	0.99
FC1-5			11660	39010	0.06	0.00	0.01	0.00	111.54	2.29	0.05	0.00	0.00	0.00	57	1	0.95
FC1-6			4866	30810	0.07	0.01	0.01	0.00	109.23	2.44	0.05	0.01	0.00	0.00	58	1	0.88
FC1-7			4680	31260	0.06	0.01	0.01	0.00	111.36	2.55	0.05	0.01	0.00	0.00	58	1	1.02
FC1-8			6740	32920	0.06	0.01	0.01	0.00	114.65	2.49	0.05	0.01	0.00	0.00	56	1	0.97
FC1-9			7208	25690	0.06	0.01	0.01	0.00	110.69	2.48	0.05	0.01	0.00	0.00	58	1	0.92

Table D3b: All *in-situ* LASS monazite analyses: trace element data. REE concentrations are reported as chondrite normalized values.

Spot Analysis	Grain	Zone	Ca ppm	Sr ppm	Y ppm	La	Ce	Pr	Nd	Sm	Eu	Gd	Tb	Dy	Ho	Er	Tm	Yb	Lu	Eu/Eu*	Th/U	Gdn/Ybn
Group 1																						
PPC15-01A3-76	m14 inclusion in garnet	high-Y rim	4230	38	2000	536709	445351	322198	229759	124324	71226	49799	18421	5447	1648	638	223	101	61	0.91	17	492
PPC15-01A3-77	m14 inclusion in garnet	low-Y core	4590	52	1149	513924	422512	337284	246608	119324	86856	43568	13740	3411	872	313	72	46	29	1.20	12	948
PPC15-01A3-78	m14 inclusion in garnet	low-Y core	4150	54	847	554008	433931	308190	244639	122973	91297	42764	12521	2711	652	206	52	34	23	1.26	16	1252
Group 2																						
PPC15-01A3-59	m6 inclusion in garnet	high-Y patch	5660	11	12790	563291	414356	286638	215098	106081	67851	40050	24571	14837	9597	5775	3644	1472	1134	1.04	3	27
PPC15-01A3-60	m6 inclusion in garnet	high-Y patch	5260	14	12730	543882	403100	276940	205470	96892	63055	38844	24127	14350	9011	5988	3777	1578	943	1.03	3	25
PPC15-01A3-61	m6 inclusion in garnet	high-Y patch	6070	14	12890	567932	417618	294181	220788	106757	68561	40352	27507	15691	9249	5919	3656	1497	955	1.04	3	27
Group 3																						
PPC15-01A3-54	m6 inclusion in garnet	low-Y patch	5560	10	6930	543038	402936	313578	238074	182432	50799	72312	34626	12805	5000	2275	1093	446	386	0.44	7	162
PPC15-01A3-53	m6 inclusion in garnet	low-Y patch	3400	10	7810	538397	425775	326509	270460	144865	79751	53769	28366	12561	6465	3275	1559	621	407	0.90	5	87
PPC15-01A3-52	m6 inclusion in garnet	low-Y patch	4850	16	6170	513080	406199	295259	224289	150878	66430	73216	35014	12764	4725	1713	818	316	268	0.63	6	232
PPC15-01A3-56	m6 inclusion in garnet	low-Y patch	5000	12	4660	552321	424144	311422	241794	158108	54352	59899	24349	9024	3626	1563	619	294	228	0.56	8	204
PPC15-01A3-58	m6 inclusion in garnet	medium-Y patch	6260	15	7140	481857	394780	309267	254048	189189	70337	82864	43213	15528	5293	2006	866	361	240	0.56	7	229

Spot Analysis	Grain	Zone	Ca ppm	Sr ppm	Y ppm	La	Ce	Pr	Nd	Sm	Eu	Gd	Tb	Dy	Ho	Er	Tm	Yb	Lu	Eu/Eu*	Th/U	Gdn/Ybn
PPC15-01A3-57	m6 inclusion in garnet	medium-Y patch	7450	18	7490	502110	411093	307112	244858	185811	73179	89950	46454	16667	5934	1963	874	371	248	0.57	8	242
PPC15-01A3-47	m5 inclusion in garnet - in melt inclusion?	high-Y core	6980	13	5390	449367	372594	286638	214880	159189	66075	81910	39806	12886	4304	1638	704	250	175	0.58	5	327
PPC15-01A3-55	m6 inclusion in garnet	low-Y patch	4710	12	4060	567511	412724	320043	243764	133108	65719	47688	20554	7602	3114	1256	534	198	183	0.82	8	241
PPC15-01A3-48	m5 inclusion in garnet - in melt inclusion?	high-Y overgrowth	8550	17	6170	472996	396248	298491	238512	185811	71758	80804	41828	15041	4341	1681	769	294	224	0.59	6	275
Group 4																						
PPC15-01A3-68	m11 in grt fracture	low-Y	4640	7	6030	463291	405383	323276	273523	193243	28810	80704	35069	13211	4597	1825	879	323	252	0.23	29	250
PPC15-01A3-69	m11 in grt fracture	low-Y	5090	7	6270	490295	442088	340517	271554	210811	30906	82915	35762	13293	4799	1956	874	349	154	0.23	27	238
PPC15-01A3-41	m4 inclusion in garnet	high-Y overgrowth	6060	8	4930	501266	389886	324353	257549	158784	18845	57588	24737	9593	3755	1600	692	348	211	0.20	31	166
PPC15-01A3-64	m9 outside resorbed garnet	High-Y band	5590	7	7210	435021	391517	316810	255580	181757	23801	79146	37839	14228	5549	2294	988	422	407	0.20	16	187
PPC15-01A3-39	m4 inclusion in garnet	low-Y	6190	6	5020	473840	446982	339440	286652	175676	18970	57739	25152	9878	3718	1488	773	314	171	0.19	31	184
PPC15-01A3-36	m4 inclusion in garnet	high-Y	5230	5	5820	484810	386623	326509	249234	157432	19059	59196	27091	10407	4103	1950	980	406	280	0.20	21	146
PPC15-01A3-42	m4 inclusion in garnet	low Y	5760	6	4820	462025	393148	316810	262144	158108	18046	55327	24875	9187	3462	1494	814	280	172	0.19	31	198
PPC15-01A3-49	m5 inclusion in garnet - in melt inclusion?	high-Y core	7170	4	8370	443882	393148	309267	253611	179054	20497	73216	35319	14878	6099	2625	1336	504	370	0.18	15	145
PPC15-01A3-44	m5 inclusion in garnet - in melt inclusion?	high-Y overgrowth	7760	7	7760	483966	404568	334052	270241	173649	21563	70151	35125	14959	5952	2400	1206	460	289	0.20	13	153
PPC15-01A3-40	m4 inclusion in garnet	high-Y overgrowth	5460	7	5960	492405	417618	339440	257987	175000	21261	65729	32632	12073	4927	2081	984	370	285	0.20	19	178
PPC15-01A3-35	m4 inclusion in garnet	high-Y	5020	6	5760	479747	414356	330819	251204	150270	18313	54472	24792	10285	4304	1925	903	416	248	0.20	20	131
PPC15-01A3-50	m5 inclusion in garnet - in melt inclusion?	high-Y overgrowth	7700	6	7360	475949	419250	337284	265646	166892	20142	66533	33712	13740	5788	2294	1138	466	317	0.19	15	143
PPC15-01A3-80	m13 inclusion in garnet	high-Y rim	5830	8	5440	458650	424144	294181	223414	163514	30906	69849	30997	11301	3993	1706	765	311	138	0.29	21	225
PPC15-01A3-43	m4 inclusion in garnet	low-Y	5570	7	5070	489873	404568	349138	270897	167568	17584	55528	24737	9593	3718	1631	765	329	248	0.18	31	169
PPC15-01A3-79	m13 inclusion in garnet	high-Y rim	6020	10	5300	463291	383687	310345	237856	146622	33748	67337	28947	10650	4121	1581	628	247	187	0.34	21	272
PPC15-01A3-6	m2 inclusion in garnet	high-Y rim	5560	7	6130	445570	404568	354526	269365	152770	23623	62060	28837	11626	5165	2331	1215	559	382	0.24	33	111
PPC15-01A3-25	m3 inclusion in garnet	high-Y, low-Th core	4930	6	6580	416034	406199	362069	273304	176351	28686	78894	36288	12927	4707	1875	939	273	183	0.24	15	289
PPC15-01A3-33	m3 inclusion in garnet	high-Y, low-Th core	4190	8	6350	416456	398042	336207	273085	191216	31634	72362	35789	12480	5458	1975	1040	441	203	0.27	11	164
PPC15-01A3-24	m3 inclusion in garnet	high-Y, low-Th core	5530	7	7340	424473	410767	335129	265864	175270	28419	71457	35042	13333	5678	2431	1121	444	329	0.25	19	161
Group 5																						
PPC15-01A3-16	m3 inclusion in garnet	high-Y rim	7790	15	6760	435021	392985	337284	275492	155405	17744	61307	32271	13374	5220	2006	1000	410	214	0.18	46	150

Spot Analysis	Grain	Zone	Ca ppm	Sr ppm	Y ppm	La	Ce	Pr	Nd	Sm	Eu	Gd	Tb	Dy	Ho	Er	Tm	Yb	Lu	Eu/Eu*	Th/U	Gdn/Ybn
PPC15-01A3-15	m3 inclusion in garnet	high-Y rim	7190	9	6510	422785	427406	346983	273742	139865	16021	58945	31053	11870	4762	2006	870	435	183	0.18	52	136
PPC15-01A3-30	m3 inclusion in garnet	high-Y rim	5960	7	4700	426582	430669	356681	274179	147027	14654	56131	26648	10000	3755	1488	696	302	268	0.16	63	186
PPC15-01A3-20	m3 inclusion in garnet	low-Y mantle	8300	8	5960	436709	412724	337284	279650	152703	17389	60352	30609	11911	4121	1763	826	398	244	0.18	57	152
PPC15-01A3-19	m3 inclusion in garnet	low-Y mantle	7180	7	4890	442616	406199	341595	282276	147973	13837	58492	26953	9837	3846	1644	684	304	207	0.15	79	192
PPC15-01A3-14	m2 inclusion in garnet	high-Y rim	6830	7	5900	441350	393148	329741	253829	141216	16217	57940	28532	11220	4524	1881	810	360	211	0.18	56	161
PPC15-01A3-29	m3 inclusion in garnet	high-Y rim	5940	6	4770	437553	425775	334052	266740	148649	15933	55377	24931	9959	3663	1538	834	272	159	0.18	61	204
PPC15-01A3-11	m2 inclusion in garnet	high-Y rim	5460	6	3660	443460	414356	346983	270022	130541	11741	52211	21911	7480	3168	1363	567	292	199	0.14	109	179
PPC15-01A3-21	m3 inclusion in garnet	low-Y mantle	7630	7	5130	432489	398042	324353	265427	147973	14956	55477	25734	9512	3736	1494	676	311	203	0.17	63	179
PPC15-01A3-37	m4 inclusion in garnet	low-Y	4410	6	2770	506329	443719	349677	271991	155405	13748	44121	17285	5874	2161	906	441	150	106	0.17	72	294
PPC15-01A3-4	m2 inclusion in garnet	lower-Y outer rim	4460	5	3610	439241	411093	334052	272648	135135	11137	52211	21884	8159	2985	1300	522	311	207	0.13	110	168
PPC15-01A3-17	m3 inclusion in garnet	high-Y rim	6150	7	5120	452321	422512	352371	275492	141892	15151	58794	24571	9390	3681	1694	652	330	159	0.17	78	178
PPC15-01A3-65	m9 outside resorbed garnet	low-Y core	5240	7	2992	458650	422512	339440	268709	149324	10675	46432	17950	6280	2416	1050	389	214	65	0.13	107	217
PPC15-01A3-9	m2 inclusion in garnet	high-Y rim	5360	7	4350	452743	415987	345905	286433	139865	12309	55226	24044	8963	3626	1506	692	346	159	0.14	103	160
PPC15-01A3-34	m4 inclusion in garnet	high-Y rim	7640	8	5250	451899	415987	341595	284902	149459	14583	55879	24737	10081	3919	1656	794	407	175	0.16	63	137
PPC15-01A3-1	m2 inclusion in garnet	lower-Y outer rim	5600	6	4020	461603	402936	343750	271772	132432	15240	56030	23850	8740	3040	1369	595	260	142	0.18	74	215
PPC15-01A3-38	m4 inclusion in garnet	medium Y	4570	6	2890	509283	432300	338362	265864	148649	13357	45327	17562	5711	2093	930	356	181	110	0.16	78	250
PPC15-01A3-3	m2 inclusion in garnet	lower-Y outer rim	4930	6	3530	440506	404568	331897	265427	127297	11847	50452	21053	7358	2875	1175	534	261	163	0.15	97	193
PPC15-01A3-28	m3 inclusion in garnet	high-Y rim	7220	7	5010	442616	422512	330819	264551	153378	15311	57085	25319	9309	3864	1681	830	305	236	0.16	53	187
PPC15-01A3-13	m2 inclusion in garnet	high-Y rim	4870	5	3620	438397	401305	343750	269365	137770	11385	49899	21634	7358	2766	1263	494	228	163	0.14	111	219
PPC15-01A3-18	m3 inclusion in garnet	high-Y rim	6280	7	4760	444304	402936	344828	268928	141892	13428	54020	23490	8699	3571	1619	688	305	203	0.15	66	177
PPC15-01A3-8	m2 inclusion in garnet	low-Y core	5490	6	4040	456962	414356	338362	271772	136486	13943	54322	22133	7520	3223	1356	591	245	240	0.16	97	221
PPC15-01A3-7	m2 inclusion in garnet	low-Y core	5220	6	3840	459494	415987	355603	285558	149324	12202	51558	21773	8020	3223	1300	494	237	113	0.14	111	217
PPC15-01A3-45	m5 inclusion in garnet - in melt inclusion?	low-Y mantle	5780	6	5870	491139	409462	336207	267177	172297	18668	62915	29030	10976	4377	1869	927	410	252	0.20	75	153
PPC15-01A3-23	m3 inclusion in garnet	low-Y mantle	5060	6	4100	446835	427406	352371	286652	154730	13055	54523	23241	8862	3608	1450	644	258	179	0.14	91	212
PPC15-01A3-10	m2 inclusion in garnet	high-Y rim	5070	5	4000	437553	401305	338362	264989	131757	11545	52261	21468	7720	3040	1431	555	254	191	0.14	113	206
PPC15-01A3-5	m2 inclusion in garnet	high-Y rim	5010	5	4170	444304	415987	343750	283807	142230	11652	52312	22964	8130	3370	1450	688	414	179	0.14	102	126
PPC15-01A3-26	m3 inclusion in garnet	low-Y mantle	5180	7	5630	457806	415987	351293	293654	160811	17069	61055	27729	10407	4084	1625	850	307	187	0.17	48	199
PPC15-01A3-31	m3 inclusion in garnet	low-Y mantle	4560	5	4290	448101	433931	342672	269365	166216	12380	58241	24598	8659	3443	1494	579	225	159	0.13	82	258
PPC15-01A3-22	m3 inclusion in garnet	low-Y mantle	5360	6	3930	438397	430669	345905	281838	148649	12469	53769	23186	8496	3095	1306	672	250	167	0.14	109	215

Spot Analysis	Grain	Zone	Ca ppm	Sr ppm	Y ppm	La	Ce	Pr	Nd	Sm	Eu	Gd	Tb	Dy	Ho	Er	Tm	Yb	Lu	Eu/Eu*	Th/U	Gdn/Ybn
PPC15-01A3-46	m5 inclusion in garnet - in melt inclusion?	low-Y mantle	4890	7	3680	465401	414356	340517	268490	149797	11634	52261	21302	7317	2842	1250	518	230	150	0.13	120	227
PPC15-01A3-27	m3 inclusion in garnet	low-Y mantle	5070	5	4030	466245	432300	363147	303501	166892	13623	59749	24349	9049	3278	1319	652	299	150	0.14	71	200
PPC15-01A3-32	m3 inclusion in garnet	low-Y mantle	4770	6	3970	447257	401305	322198	280744	161486	12149	56181	24183	8199	3311	1406	571	241	161	0.13	78	233
PPC15-01A3-2	m2 inclusion in garnet	lower-Y outer rim	5320	15	4020	461603	394780	325431	272648	136486	12700	53819	21551	7683	3223	1338	510	267	130	0.15	103	202
PPC15-01A3-12	m2 inclusion in garnet	high-Y rim	5100	6	3940	432068	396411	336207	278775	135135	12629	54472	23407	7967	3187	1369	563	255	175	0.15	106	214
"Young" ages																						
PPC15-01A3-83	m15 outside resorbed garnet		2730	6	5020	469620	437194	340517	279650	197297	20142	72864	29252	10163	3590	1506	794	224	228	0.17	13	325
PPC15-01A3-72	m11 in grt fracture	high-Y patch	4800	9	12090	420675	353670	285560	246608	175000	35346	94171	53740	23089	9066	3738	1672	578	394	0.28	29	163
PPC15-01A3-66	m9 outside resorbed garnet	low-Y core	4880	12	3590	436709	430669	349138	262582	150676	15648	51508	22105	7439	2733	1194	599	239	126	0.18	71	215
PPC15-01A3-82	m15 outside resorbed garnet	low-Th patch	3030	6	10980	406751	353997	267241	236980	350000	58970	170352	74792	25244	7729	3213	1413	553	285	0.24	7	308
PPC15-01A3-71	m11 in grt fracture	high-Y patch	4880	9	11910	423207	383361	299569	240263	183108	36412	95427	55956	23537	9725	3900	1579	590	362	0.28	32	162
PPC15-01A3-75	m11 in grt fracture	low-Y patch	4010	6	4360	480591	419250	342672	271772	172973	17922	60553	25152	8455	3137	1306	607	286	183	0.18	20	212
PPC15-01A3-70	m11 in grt fracture	high-Y patch	4670	9	12180	458650	407830	292026	239387	214189	35879	94824	56787	25447	9377	4006	1660	683	390	0.25	29	139
PPC15-01A3-81	m15 outside resorbed garnet	low-Th patch	2320	7	10760	367089	331158	269397	259081	404054	57194	182412	70914	23049	7894	3075	1462	503	402	0.21	5	363
PPC15-01A3-73	m11 in grt fracture	low-Y patch	3840	7	4460	435865	398042	320043	247702	152703	18561	60000	25512	8943	3297	1438	814	279	203	0.25	19	215
PPC15-01A3-67	m9 outside resorbed garnet	high-Y rim	5240	7	7490	435443	383361	298491	288840	231081	34813	96985	46260	16341	5824	2219	1126	460	252	0.25	19	211
PPC15-01A3-74	m11 in grt fracture	low-Y patch	5470	7	5720	429958	393148	337284	269147	170270	22291	73467	31025	11301	4249	1856	777	276	305	0.25	19	266
PPC15-01A3-62	m9 outside resorbed garnet	medium-Y patch	4850	23	6210	463713	383361	307112	247265	197297	26110	81910	32853	12358	4762	1925	883	382	163	0.21	21	265
PPC15-01A3-63	m9 outside resorbed garnet	medium-Y patch	4860	5	6190	452321	389886	322198	268928	187838	25897	82714	36288	12480	4524	1919	842	312	252	0.21	21	327
PPC15-01A3-66	m9 outside resorbed garnet	low-Y core	4880	12	3590	436709	430669	349138	262582	150676	15648	51508	22105	7439	2733	1194	599	239	126	0.18	71	266
PPC15-01A3-75	m11 in grt fracture	low-Y patch	4010	6	4360	480591	419250	342672	271772	172973	17922	60553	25152	8455	3137	1306	607	286	183	0.18	20	262
Standards																						
stern-1			7000	1	14600	392827	396411	352371	250328	279730	2718	106030	70637	22602	5733	2050	1174	702	480	0.02	14	151
stern-10			6490	1	15600	402954	389886	322198	233917	290541	2948	110553	62050	21382	5788	2044	1158	652	374	0.02	13	170
stern-11			6800	0	15650	418143	378467	327586	229322	302027	3144	116080	66482	21707	5641	2181	1101	621	394	0.02	15	187
stern-12			6420	0	12930	366245	384339	306034	216849	256757	2313	107035	60942	19593	4963	1800	1162	565	264	0.01	16	189

Spot Analysis	Grain	Zone	Ca ppm	Sr ppm	Y ppm	La	Ce	Pr	Nd	Sm	Eu	Gd	Tb	Dy	Ho	Er	Tm	Yb	Lu	Eu/Eu*	Th/U	Gdn/Ybn
stern-13			6720	1	15420	402532	373573	342672	249672	293919	2735	105025	65651	21992	5604	2000	1263	609	390	0.02	14	172
stern-14			6260	0	12700	378481	355628	296336	212473	255405	2558	105528	54017	18171	5165	2081	1016	547	386	0.02	15	193
stern-15			7130	0	15030	397468	359706	332974	244858	289865	2824	114724	67036	21911	5842	2006	1130	634	398	0.02	15	181
stern-16			6750	1	15820	405063	389886	344828	263676	293919	3002	120101	70083	23455	5934	2081	1101	602	467	0.02	15	199
stern-17			6990	1	13820	381857	367047	302802	200219	260135	2771	107538	60111	19634	5421	1900	1016	590	313	0.02	15	182
stern-18			6550	1	15500	426582	380098	313578	232604	302027	2771	109045	62327	21789	5714	2206	1142	571	431	0.02	13	191
stern-19			6520	0	12850	383544	375204	316810	212254	259459	2575	103568	63158	19715	5018	1688	1126	565	301	0.02	15	183
stern-2			6140	1	14770	397468	367374	306034	219256	272973	2948	106884	61662	20203	5513	1881	1008	568	362	0.02	14	188
stern-20			5970	1	14700	410970	371941	302802	218293	284459	2824	110050	58172	19512	5421	1975	1130	677	415	0.02	13	163
stern-3			6550	1	16900	411814	371941	321121	238950	296622	2984	108543	65374	22033	6154	2025	1162	671	350	0.02	13	162
stern-4			6270	1	13040	381857	371941	316810	201094	269595	2533	103015	57285	18780	4927	1900	1045	565	362	0.02	16	182
stern-5			7280	0	14170	400000	380098	339440	238731	305405	2629	111558	67590	21870	5531	1894	1126	646	370	0.01	15	173
stern-6			6630	1	13520	394093	370310	313039	207002	275608	2718	111859	60720	19309	5421	1975	1198	547	297	0.02	14	205
stern-7			6810	1	15040	397468	378467	339440	237199	299324	2718	109146	67590	21748	5440	1869	1178	658	407	0.02	15	166
stern-8			6090	1	13100	387764	386623	297414	208534	276351	2860	104523	59280	19146	5147	1975	1150	553	325	0.02	14	189
stern-9			6590	1	13570	393249	362153	298491	200875	270946	2860	106030	58726	19512	5385	2025	980	584	390	0.02	14	182
44069-1			6810	21	18200	404641	347471	261853	223851	128378	34281	85930	58172	28537	13132	4700	1660	418	220	0.33	8	206
44069-10			6210	24	23600	421013	370310	300647	226258	142568	46004	79397	57341	32439	17875	10188	6235	2621	1870	0.43	10	30
44069-11			7200	21	16390	439241	401305	310345	245952	175000	35613	89296	62050	31301	12381	4375	1599	391	224	0.28	9	228
44069-12			8120	25	20200	403797	364763	309698	246389	164189	35915	93467	66482	33293	15128	5081	1806	517	480	0.29	9	181
44069-13			6750	21	19380	419409	357259	285560	231729	153108	35346	86834	62050	33089	14158	5281	1899	509	220	0.31	8	170
44069-14			7540	27	23900	417300	372431	329310	261926	162162	38597	97487	70914	39715	17179	6150	2595	708	443	0.31	7	138
44069-15			6530	22	18300	413080	357259	303879	236105	137838	32700	87739	59834	30366	13333	4913	1818	484	244	0.30	8	181
44069-16			7120	23	19410	423629	376835	304957	241357	157432	38899	89196	61219	34472	15385	5931	2328	801	427	0.33	8	111
44069-17			7880	27	25000	429114	383361	306034	244858	155405	48490	79095	58726	37236	18553	10638	7004	3534	2760	0.44	10	22
44069-18			6060	26	18230	457384	383687	298491	222976	136486	74956	75980	51801	30122	15366	8250	4534	2037	1472	0.74	6	37
44069-19			8580	40	23000	449367	357259	303879	228228	150676	65719	74874	53740	31829	16465	9663	6883	3410	2439	0.62	10	22
44069-2			7160	22	20100	431224	370310	301724	245514	153378	37904	85528	60111	33699	14121	4831	1680	571	309	0.33	7	150
44069-20			6730	25	22180	453586	341925	276940	225821	145946	43872	78040	52632	30976	16538	9469	5709	2509	2004	0.41	10	31
44069-3			7100	24	19700	435865	375204	296336	231729	164189	37300	88392	63158	32114	14652	5513	2109	758	443	0.31	8	117

Spot Analysis	Grain	Zone	Ca ppm	Sr ppm	Y ppm	La	Ce	Pr	Nd	Sm	Eu	Gd	Tb	Dy	Ho	Er	Tm	Yb	Lu	Eu/Eu*	Th/U	Gdn/Ybn
44069-4			6090	23	27200	460759	391517	311422	251422	166216	41563	88442	61773	36098	19817	9250	3927	1565	874	0.34	7	57
44069-5			6630	20	20400	432489	352365	337284	256236	172297	35169	91960	66205	32764	15073	5125	1822	547	309	0.28	8	168
44069-6			6650	19	15120	415190	345677	284483	221225	159459	33304	80804	55319	26545	10989	3731	1206	400	215	0.29	9	202
44069-7			7060	25	27400	450211	362153	308190	250547	185135	39076	88643	67313	39106	19048	8563	3834	1304	659	0.31	8	68
44069-8			5960	26	19580	445148	376835	329741	264989	151351	67496	73266	54294	30528	15806	8625	4534	2031	1618	0.64	8	36
44069-9			7810	36	21700	413502	371941	294181	230197	140270	56838	73467	52078	28659	16465	10169	6939	3404	2894	0.56	12	22
FC1-1			5800	20	25100	509705	370310	280172	203720	119595	7123	66583	44044	27480	20147	11625	7045	3460	2244	0.08	9	19
FC1-10			7290	29	26100	397046	342577	273707	215974	115541	7655	63668	49778	30813	18956	11750	7409	3739	2732	0.09	5	17
FC1-11			8530	32	22600	381013	337684	244612	165208	125000	11314	69246	48476	29350	18040	10500	8219	3559	2606	0.12	4	19
FC1-12			8980	32	32200	464135	368679	299569	241794	148649	8721	76382	57341	37317	22711	13063	8623	4342	3589	0.08	7	18
FC1-13			8820	23	31000	389451	342577	284483	215536	137162	7194	76683	60388	39959	22601	13000	9879	4851	3862	0.07	4	16
FC1-14			10280	32	28500	444726	375204	270474	199781	145270	12291	72060	53186	33577	20714	12563	8462	3994	3618	0.12	4	18
FC1-15			7280	26	27600	475949	370310	281250	228228	120946	8899	64322	46814	30163	20110	11313	6883	3565	2874	0.10	6	18
FC1-16			6390	21	23600	406329	370310	261853	188403	107432	6838	63216	43823	28293	17088	10388	7032	2832	2451	0.08	9	22
FC1-17			5760	21	25200	497890	358891	273707	217899	118243	6394	63116	47091	29593	19231	11450	6640	3199	2760	0.07	8	20
FC1-18			7350	26	22500	446835	352365	274784	205033	113311	6501	61910	45042	26992	16465	10438	6721	3578	2549	0.08	7	17
FC1-19			10700	32	26300	476793	388254	280172	217068	140541	10089	68342	50416	34187	17637	9813	7733	4143	2980	0.10	4	16
FC1-2			8450	28	28800	406329	380098	308190	237637	138514	8401	77236	55679	35610	20293	11438	8097	4615	2598	0.08	8	17
FC1-20			8710	28	26500	487764	384992	284483	233698	132432	8188	66633	50416	33862	17894	11938	7611	3969	3362	0.09	6	17
FC1-3			7910	25	34400	422785	368679	264009	194967	143919	8739	75729	53712	38374	24267	14313	9879	5366	3467	0.08	4	14
FC1-4			8420	27	24100	455274	349103	254310	184245	133784	11155	70201	51330	28618	18205	11563	7611	4068	2850	0.12	4	17
FC1-5			9680	29	25000	433755	326264	259698	197155	152027	12202	71859	53186	31748	18223	11938	8219	3795	2919	0.12	4	19
FC1-6			6690	22	23000	489451	415987	289871	214661	120270	6696	62864	47368	27276	16905	10813	6806	3416	2195	0.08	10	18
FC1-7			5620	19	24300	475949	371941	252155	202188	123649	6803	62261	45152	27276	18114	10938	6640	2963	1980	0.08	10	21
FC1-8			7190	22	25900	417722	345840	264009	198031	119527	6856	72864	49584	28862	18425	11313	7935	3596	2443	0.07	9	20
FC1-9			7360	21	22100	412658	365416	287716	201313	118041	7531	65126	50166	27033	17692	10800	7692	3447	2618	0.09	7	19

Table D4a: All TIMS-TEA zircon analyses: isotopic data

Fragment	rim/core/mantle?	grain mount	$^{207}Pb/^{206}Pb$ date	2s	Discordance (%)	Th/U	Pb* (pg)	Pbc (pg)	$^{206}Pb/^{204}Pb$	$^{206}Pb/^{238}U$	2s (%)	$^{207}Pb/^{235}U$	2s (%)	$^{207}Pb/^{206}Pb$	2s (%)
PPC15-01-02z1a	rim	2	2672.73	12.93	-1.10	0.53	21.93	5.67	231.49	0.52	0.20	13.08	0.92	0.18	0.78
PPC15-01-02z9a	rim	2	2661.46	1.64	-0.03	0.28	82.50	0.94	5101.67	0.51	0.11	12.76	0.16	0.18	0.09
PPC15-01-02z9b	rim	2	2665.73	1.27	-0.51	0.23	403.19	0.55	43187.96	0.52	0.13	12.89	0.17	0.18	0.07
PPC15-01-02z9b 37 dt	rim	2	2672.36	0.90	0.17	0.23	401.44	0.55	42945.16	0.51	0.12	12.87	0.14	0.18	0.04
PPC15-01-02z9c	rim	2	2657.49	1.27	-0.04	0.25	89.72	0.74	7149.67	0.51	0.10	12.70	0.15	0.18	0.07
PPC15-01-02z10a	rim	2	2657.79	1.40	-0.66	0.57	102.78	0.64	8740.08	0.51	0.09	12.80	0.15	0.18	0.08
PPC15-01-02z10b	core +rim (mostly core)	2	2677.82	1.46	-9.46	0.23	81.82	0.82	5870.03	0.58	0.82	14.50	0.83	0.18	0.08
PPC15-01-02z10c	rim+core (mostly rim)	2	2670.28	1.72	-0.26	0.43	33.96	0.49	3914.30	0.51	0.13	12.91	0.19	0.18	0.10
PPC15-01-02z10d	rim+core (mostly core)	2	2659.22	1.45	-8.85	0.38	41.20	0.55	4274.33	0.57	0.35	14.12	0.38	0.18	0.08
PPC15-01-02z10e	rim+core (mostly core)	2	2706.90	1.20	-0.41	0.49	236.86	0.97	13500.97	0.52	0.10	13.45	0.15	0.19	0.07
PPC15-01-02z11b	rim	2	2666.16	1.16	-0.20	0.56	182.63	0.45	22217.11	0.51	0.08	12.85	0.13	0.18	0.06
PPC15-01-02z11c	rim+mantle (mostly mantle)	2	2651.08	1.33	-4.44	0.55	83.94	0.56	8179.41	0.54	0.10	13.30	0.15	0.18	0.07
PPC15-01-02z17a	rim +mantle (mostly rim)	2	2651.18	1.16	-1.47	0.62	584.04	0.99	32012.95	0.52	0.15	12.84	0.18	0.18	0.06
PPC15-01-02z18a	rim	2	2672.10	1.16	0.06	0.63	182.02	0.31	32082.33	0.51	0.07	12.89	0.13	0.18	0.06
PPC15-01-02z25a	homogeneous grain fragment	2	2662.12	8.24	0.60	0.52	1912.23	0.91	115791.21	0.51	0.61	12.67	0.55	0.18	0.50
PPC15-01-02z25b	homogeneous grain fragment	2	2657.08	1.14	-0.20	0.51	433.37	0.39	61914.85	0.51	0.09	12.72	0.14	0.18	0.06
PPC15-01-02z29a	rim	2	2660.80	1.20	-0.58	0.64	126.01	0.39	17504.69	0.51	0.08	12.83	0.14	0.18	0.06
PPC15-01-02z29b	rim	2	2659.10	2.10	-2.18	0.78	23.77	0.56	2241.29	0.52	0.15	13.06	0.22	0.18	0.12
PPC15-01-02z29c	core	2	2679.29	1.17	-1.17	0.65	456.12	2.02	12124.65	0.52	0.08	13.18	0.14	0.18	0.06
PPC15-01-02z33a	homogeneous grain fragment	2	2656.91	1.13	0.10	0.19	936.78	0.35	157288.94	0.51	0.09	12.67	0.14	0.18	0.06
PPC15-01-02z34a	rim + core (mostly rim)	2	2652.27	1.20	-0.32	0.68	269.52	0.72	20039.06	0.51	0.10	12.68	0.15	0.18	0.06
PPC15-01-01z5a	homogeneous grain fragment	1	2670.91	0.89	-0.09	0.08	248	0.91	16599	0.51388	0.069	12.893	0.1	0.182052	0.043
PPC15-01-01z5b	homogeneous grain fragment	1	2673.2	0.88	-0.14	0.07	537	0.56	58520	0.51475	0.12	12.933	0.14	0.182304	0.042
PPC15-01-01z7a	homogeneous grain fragment	1	2673.4	1	0.14	0.34	141	1.32	6129	0.51308	0.066	12.893	0.11	0.182327	0.053
PPC15-01-01z15a	rim	1	2649.6	2.2	0.31	0.34	32.4	1.01	1853	0.50643	0.16	12.544	0.24	0.17972	0.13
PPC15-01-01z15b	rim + mantle (mostly mantle)	1	2668.1	1.5	0.01	0.37	82.6	1.07	4397	0.5126	0.29	12.84	0.32	0.18175	0.087
PPC15-01-01z15c	rim	1	2661.1	2.8	-0.05	0.45	26	1.16	1272	0.51134	0.12	12.754	0.22	0.18098	0.16
PPC15-01-01z15d	rim + mantle (mostly rim)	1	2651.2	1.2	-0.26	0.36	193	1.48	7447	0.51032	0.065	12.653	0.11	0.1799	0.064
PPC15-01-01z16a	homogeneous grain fragment	1	2669.83	0.97	-0.16	0.05	147	0.71	12691	0.51411	0.11	12.891	0.14	0.181934	0.049

Fragment	rim/core/mantle?	grain mount	$^{207}Pb/^{206}Pb$ date	2s	Discordance (%)	Th/U c	Pb* (pg)	Pbc (pg)	$^{206}Pb/^{204}Pb$	$^{206}Pb/^{238}U$	2s (%)	$^{207}Pb/^{235}U$	2s (%)	$^{207}Pb/^{206}Pb$	2s (%)
PPC15-01-01z16b	homogeneous grain fragment	1	2656.04	0.94	-1.43	0.04	769	0.48	99074	0.5188	0.076	12.9	0.11	0.180425	0.046
PPC15-01-01z16c	homogeneous grain fragment	1	2670.28	0.86	0.12	0.06	683	0.35	118320	0.51243	0.062	12.852	0.099	0.181982	0.04
PPC15-01-01z16d	homogeneous grain fragment	1	2671.4	1.1	0.3	0.03	171	0.73	14449	0.51157	0.18	12.839	0.19	0.1821	0.055

Table D4b: All TIMS-TEA zircon analyses: trace element data. REE concentrations are reported as chondrite-normalized values.

Fragment	rim/core/mantle?	grain mount	Hf (ppm)	Y (ppm)	La	Ce	Pr	Nd	Sm	Eu	Gd	Tb	Dy	Ho	Er	Tm	Yb	Lu	Eu/Eu*	Lun/Dyn	Th/U
PPC15-01-02z1a	rim	2	11912	5364	37	96	52	85	362	476	742	1040	1305	2125	3226	5268	6392	9176	0.92	7.03	0.53
PPC15-01-02z9a	rim	2	13393	2869	1	70	9	41	277	365	839	1095	1090	1076	1084	1227	908	1101	0.8	1.01	0.28
PPC15-01-02z9b	rim	2	14328	2268	0	65	8	33	237	162	737	903	919	871	844	829	745	774	0.4	0.84	0.23
PPC15-01-02z9b 37 dt	rim	2	14328	2268	0	65	8	33	237	162	737	903	919	871	844	829	745	774	0.4	0.84	0.23
PPC15-01-02z9c	rim	2	13464	2563	12	71	15	43	284	224	819	1019	1025	995	1103	1085	811	985	0.5	0.96	0.25
PPC15-01-02z10a	rim	2	13439	2200	144	124	90	108	292	288	644	728	738	880	1142	1501	1487	1853	0.7	2.51	0.57
PPC15-01-02z10b	core +rim (mostly core)	2	13006	8103	31	98	51	85	375	366	990	1621	2253	3205	4490	5727	6328	7510	0.6	3.33	0.23
PPC15-01-02z10c	rim+core (mostly rim)	2	12686	1820	3	95	15	36	176	237	467	587	566	710	857	1448	1105	1651	0.8	2.92	0.43
PPC15-01-02z10d	rim+core (mostly core)	2	12909	6546	21	124	45	79	316	430	838	1302	1775	2596	3716	5092	5386	6762	0.8	3.81	0.38
PPC15-01-02z10e	rim+core (mostly core)	2	12201	3618	7	79	18	44	208	219	600	804	1045	1441	2013	2485	2941	3714	0.6	3.56	0.49
PPC15-01-02z11b	rim	2	13811	1175	11	115	18	47	239	221	555	568	483	461	508	637	641	828	0.6	1.71	0.56
PPC15-01-02z11c	rim+mantle (mostly mantle)	2	13331	2288	108	155	62	83	336	376	746	827	797	908	1132	1673	1713	2343	0.8	2.94	0.55
PPC15-01-02z17a	rim +mantle (mostly rim)	2	13199	1787	7	147	9	30	196	179	487	556	610	727	975	1206	1478	1903	0.6	3.12	0.62
PPC15-01-02z18a	rim	2	13891	783	1	115	14	46	235	197	439	408	328	300	277	370	276	368	0.6	1.12	0.63
PPC15-01-02z25a	homogeneous grain fragment	2	14282	875	1	65	7	30	197	119	421	418	376	354	367	383	395	454	0.4	1.21	0.52
PPC15-01-02z25b	homogeneous grain fragment	2	14124	1009	0	95	10	42	240	176	504	502	434	389	390	420	389	455	0.5	1.05	0.51
PPC15-01-02z29a	rim	2	13006	2612	44	121	50	80	291	285	581	686	805	1031	1408	1760	1931	2511	0.7	3.12	0.64
PPC15-01-02z29b	rim	2	12215	2580	1191	1089	1093	966	611	392	602	636	659	1005	1361	2215	1950	2924	0.6	4.44	0.78
PPC15-01-02z29c	core	2	12222	2520	52	86	39	52	162	164	385	513	699	975	1386	1732	2090	2648	0.7	3.79	0.65
PPC15-01-02z33a	homogeneous grain fragment	2	14208	2888	12	53	14	38	272	168	855	1081	1125	1097	1159	1205	1347	1651	0.3	1.47	0.19
PPC15-01-02z34a	rim + core (mostly rim)	2	13682	2331	5	70	2	37	46	41	109	22	176	50	199	39	304	63	0.6	0.36	0.68
PPC15-01-01z5a	homogeneous grain fragment	1	15632	2318	0	56	8	54	300	776	820	1005	964	888	841	762	657	836	1.6	0.87	0.08
PPC15-01-01z5b	homogeneous grain fragment	1	15771	2389	1	54	9	52	304	724	851	1060	1013	924	842	768	686	720	1.4	0.71	0.07
PPC15-01-01z7a	homogeneous grain fragment	1	13784	2880	0	75	7	58	311	693	905	1186	1200	1168	1107	1047	938	1122	1.3	0.93	0.34

Fragment	rim/core/mantle?	grain mount	Hf (ppm)	Y (ppm)	La	Ce	Pr	Nd	Sm	Eu	Gd	Tb	Dy	Ho	Er	Tm	Yb	Lu	Eu/Eu*	Lun/Dyn	Th/U
PPC15-01-01z15a	rim	1	12523	2715	2	54	0	16	208	217	702	965	1017	1041	1157	1155	958	2449	0.6	2.41	0.34
PPC15-01-01z15b	rim + mantle (mostly mantle)	1	13526	2681	26	74	8	40	232	452	774	1038	1058	1088	1077	1084	929	1585	1.1	1.50	0.37
PPC15-01-01z15c	rim	1	11901	2235	2	53	0	0	132	0	519	700	758	838	935	1051	750	3164	0.0	4.18	0.45
PPC15-01-01z15d	rim + mantle (mostly rim)	1	13715	3202	12	68	13	61	297	568	917	1259	1337	1380	1384	1332	1198	1558	1.1	1.17	0.36
PPC15-01-01z16a	homogeneous grain fragment	1	15162	2720	2	51	0	52	307	493	905	1194	1156	1062	986	946	758	1402	0.9	1.21	0.05
PPC15-01-01z16b	homogeneous grain fragment	1	15314	3143	22	64	30	50	304	203	983	1289	1315	1229	1171	1089	947	935	0.4	0.71	0.04
PPC15-01-01z16c	homogeneous grain fragment	1	15321	2084	1	49	7	28	225	170	715	895	884	797	738	698	597	594	0.4	0.67	0.06
PPC15-01-01z16d	homogeneous grain fragment	1	14614	2938	2	44	12	36	276	266	900	1234	1220	1156	1092	1196	900	1039	0.5	0.85	0.03

Table D5a: LASS zircon analyses of separated grain fragments: isotopic data

LASS spot number	Grain fragment	Grain texture	U ppm	Th ppm	$^{207}Pb/^{235}U$	2s	$^{206}Pb/^{238}U$	2s	$^{238}U/^{206}Pb$	2s	$^{207}Pb/^{206}Pb$	2s	$^{208}Pb/^{232}Th$	2s	$^{207}Pb/^{206}Pb$ date	2s	Concordance
24	PPC15-01-02z1a	rim	99	89	12.78	0.27	0.51	0.01	1.97	0.04	0.18	0.00	0.14	0.00	2670	34	1.00
26	PPC15-01-02z1a	rim	105	60	12.53	0.28	0.50	0.01	1.98	0.04	0.18	0.00	0.14	0.00	2649	33	0.99
45	PPC15-01-02z9b	rim	132	68	13.03	0.29	0.51	0.01	1.95	0.04	0.19	0.00	0.14	0.00	2699	33	1.00
44	PPC15-01-02z9b	rim	192	42	13.10	0.28	0.51	0.01	1.95	0.04	0.19	0.00	0.14	0.00	2707	33	0.99
46	PPC15-01-02z9b	rim	206	39	12.68	0.28	0.50	0.01	1.98	0.04	0.18	0.00	0.14	0.00	2681	33	0.99
47	PPC15-01-02z9c	rim	183	51	12.67	0.28	0.50	0.01	1.98	0.04	0.18	0.00	0.14	0.00	2680	33	0.99
53	PPC15-01-02z10a	rim	127	62	12.74	0.29	0.51	0.01	1.98	0.04	0.18	0.00	0.15	0.00	2679	33	0.99
52	PPC15-01-02z10b	outer core	155	26	14.16	0.36	0.54	0.01	1.86	0.04	0.19	0.00	0.14	0.01	2755	33	1.01
55	PPC15-01-02z10b	rim	131	77	13.51	0.29	0.52	0.01	1.93	0.04	0.19	0.00	0.14	0.00	2736	33	0.99
50	PPC15-01-02z10e	rim	143	65	13.01	0.29	0.51	0.01	1.96	0.04	0.19	0.00	0.14	0.00	2708	33	0.99
14	PPC15-01-02z17a	rim	129	70	12.33	0.27	0.50	0.01	2.01	0.04	0.18	0.00	0.14	0.00	2651	34	0.99
17	PPC15-01-02z18a	rim	183	92	12.64	0.28	0.51	0.01	1.98	0.04	0.18	0.00	0.14	0.00	2665	33	0.99
59	PPC15-01-02z25a	rim	108	75	13.36	0.31	0.52	0.01	1.92	0.04	0.19	0.00	0.14	0.00	2708	33	1.00
60	PPC15-01-02z25a	rim	152	74	12.98	0.29	0.51	0.01	1.97	0.04	0.19	0.00	0.14	0.00	2704	33	0.99
58	PPC15-01-02z25b	rim	117	97	13.07	0.28	0.51	0.01	1.96	0.04	0.19	0.00	0.14	0.00	2708	33	0.99
80	PPC15-01-02z29a	rim	165	54	13.10	0.29	0.51	0.01	1.94	0.04	0.18	0.00	0.15	0.00	2696	33	1.00
79	PPC15-01-02z29b	rim	162	102	12.88	0.28	0.51	0.01	1.96	0.04	0.18	0.00	0.14	0.00	2679	33	0.99
77	PPC15-01-02z29c	core	31	30	13.19	0.34	0.52	0.01	1.94	0.05	0.18	0.00	0.14	0.00	2696	35	1.00
113	PPC15-01-02z33a	whole grain	233	29	13.08	0.29	0.51	0.01	1.96	0.04	0.19	0.00	0.14	0.00	2706	33	0.99
93	PPC15-01-02z34a	rim	102	69	13.25	0.30	0.53	0.01	1.89	0.04	0.18	0.00	0.14	0.00	2671	33	1.01
94	PPC15-01-02z34a	rim	109	93	12.84	0.29	0.51	0.01	1.95	0.04	0.18	0.00	0.14	0.00	2668	33	1.00
95	PPC15-01-02z34a	rim	110	82	13.06	0.28	0.53	0.01	1.90	0.04	0.18	0.00	0.14	0.00	2647	33	1.02
171	PPC15-01-01z5a	whole grain	319	34	12.95	0.27	0.51	0.01	1.97	0.04	0.19	0.00	0.14	0.00	2700	33	0.99
172	PPC15-01-01z5a	whole grain	256	25	13.22	0.27	0.51	0.01	1.95	0.04	0.19	0.00	0.15	0.00	2718	33	0.99
174	PPC15-01-01z5a	whole grain	275	23	13.24	0.27	0.51	0.01	1.94	0.04	0.19	0.00	0.15	0.01	2714	33	0.99
173	PPC15-01-01z5b	whole grain	246	27	13.26	0.28	0.51	0.01	1.95	0.04	0.19	0.00	0.15	0.01	2720	33	0.99
166	PPC15-01-01z7a	whole grain	198	67	13.03	0.27	0.51	0.01	1.95	0.04	0.19	0.00	0.14	0.00	2702	33	0.99
164	PPC15-01-01z7a	whole grain	125	75	12.91	0.27	0.51	0.01	1.95	0.04	0.18	0.00	0.15	0.00	2678	33	1.00
126	PPC15-01-01z15a	rim	132	66	13.01	0.29	0.51	0.01	1.97	0.04	0.19	0.00	0.15	0.00	2701	34	0.99

LASS spot number	Grain fragment	Grain texture	U ppm	Th ppm	$^{207}Pb/^{235}U$	2s	$^{206}Pb/^{238}U$	2s	$^{238}U/^{206}Pb$	2s	$^{207}Pb/^{206}Pb$	2s	$^{208}Pb/^{232}Th$	2s	$^{207}Pb/^{206}Pb$ date	2s	Concordance
123	PPC15-01-01z15b	rim	123	61	12.66	0.40	0.51	0.02	1.98	0.06	0.18	0.00	0.14	0.00	2660	34	0.99
124	PPC15-01-01z15b	core	463	19	12.78	0.28	0.50	0.01	2.02	0.04	0.19	0.00	0.16	0.01	2717	33	0.97
122	PPC15-01-01z15c	rim	134	56	12.62	0.28	0.51	0.01	1.96	0.04	0.18	0.00	0.14	0.00	2649	34	1.00
125	PPC15-01-01z15d	core	374	11	13.24	0.32	0.51	0.01	1.95	0.04	0.19	0.00	0.16	0.01	2729	33	0.99
156	PPC15-01-01z16a	whole grain	273	21	13.48	0.30	0.51	0.01	1.96	0.04	0.19	0.00	0.14	0.01	2742	33	0.98
153	PPC15-01-01z16b	whole grain	395	32	13.43	0.32	0.51	0.01	1.96	0.05	0.19	0.00	0.14	0.00	2740	33	0.98
154	PPC15-01-01z16c	whole grain	277	23	13.27	0.29	0.51	0.01	1.97	0.04	0.19	0.00	0.14	0.01	2722	33	0.98
155	PPC15-01-01z16d	whole grain	481	13	13.60	0.30	0.51	0.01	1.96	0.04	0.19	0.00	0.13	0.01	2756	33	0.98
Standards																	
91500-1			80	30	1.84	0.04	0.18	0.00	5.59	0.12	0.07	0.00	0.05	0.00	1062	22	1.00
91500-2			80	30	1.87	0.04	0.18	0.00	5.57	0.12	0.08	0.00	0.05	0.00	1064	22	0.99
91500-3			81	30	1.84	0.04	0.18	0.00	5.60	0.12	0.07	0.00	0.05	0.00	1060	22	1.00
91500-4			80	30	1.86	0.04	0.18	0.00	5.57	0.12	0.08	0.00	0.05	0.00	1064	22	1.00
91500-5			80	30	1.85	0.04	0.18	0.00	5.58	0.11	0.07	0.00	0.05	0.00	1063	21	1.00
91500-6			80	30	1.85	0.04	0.18	0.00	5.60	0.13	0.07	0.00	0.05	0.00	1059	23	1.00
91500-8			81	30	1.85	0.04	0.18	0.00	5.59	0.12	0.07	0.00	0.05	0.00	1061	22	1.00
91500-9			80	30	1.85	0.04	0.18	0.00	5.57	0.12	0.07	0.00	0.05	0.00	1065	23	1.00
91500-10			80	30	1.85	0.04	0.18	0.00	5.57	0.12	0.08	0.00	0.05	0.00	1065	22	1.00
91500-17			81	30	1.85	0.04	0.18	0.00	5.60	0.12	0.07	0.00	0.05	0.00	1060	22	1.00
91500-11			79	30	1.86	0.05	0.18	0.00	5.57	0.13	0.07	0.00	0.05	0.00	1064	24	1.00
91500-14			81	30	1.85	0.04	0.18	0.00	5.58	0.12	0.07	0.00	0.05	0.00	1062	23	1.00
91500-12			80	30	1.85	0.04	0.18	0.00	5.59	0.13	0.07	0.00	0.05	0.00	1061	23	1.00
91500-13			80	30	1.86	0.04	0.18	0.00	5.55	0.12	0.07	0.00	0.05	0.00	1068	23	1.00
91500-15			80	30	1.85	0.04	0.18	0.00	5.59	0.12	0.07	0.00	0.05	0.00	1061	23	1.00
91500-16			80	30	1.85	0.05	0.18	0.00	5.60	0.12	0.07	0.00	0.05	0.00	1058	22	1.00
91500-18			80	30	1.85	0.04	0.18	0.00	5.58	0.11	0.07	0.00	0.05	0.00	1063	21	1.00
91500-19			80	30	1.85	0.04	0.18	0.00	5.58	0.11	0.07	0.00	0.05	0.00	1062	21	1.00
91500-20			80	30	1.85	0.04	0.18	0.00	5.58	0.12	0.07	0.00	0.05	0.00	1063	21	1.00
91500-21			80	30	1.85	0.04	0.18	0.00	5.59	0.12	0.07	0.00	0.05	0.00	1061	22	1.00

LASS spot number	Grain fragment	Grain texture	U ppm	Th ppm	$^{207}Pb/^{235}U$	2s	$^{206}Pb/^{238}U$	2s	$^{238}U/^{206}Pb$	2s	$^{207}Pb/^{206}Pb$	2s	$^{208}Pb/^{232}Th$	2s	$^{207}Pb/^{206}Pb$ date	2s	Concordance
91500-22			80	30	1.85	0.04	0.18	0.00	5.58	0.11	0.07	0.00	0.05	0.00	1063	21	1.00
91500-23			80	30	1.85	0.04	0.18	0.00	5.57	0.12	0.07	0.00	0.05	0.00	1065	21	1.00
91500-24			80	30	1.85	0.04	0.18	0.00	5.61	0.12	0.07	0.00	0.05	0.00	1057	22	1.00
91500-25			80	30	1.85	0.04	0.18	0.00	5.57	0.12	0.07	0.00	0.05	0.00	1065	22	1.00
GJ1-1			263	10	0.81	0.02	0.10	0.00	10.24	0.22	0.06	0.00	0.03	0.00	600	13	1.00
GJ1-2			253	10	0.80	0.02	0.10	0.00	10.27	0.23	0.06	0.00	0.03	0.00	600	13	1.01
GJ1-3			260	10	0.80	0.02	0.10	0.00	10.24	0.22	0.06	0.00	0.03	0.00	601	12	1.01
GJ1-4			261	11	0.80	0.02	0.10	0.00	10.24	0.21	0.06	0.00	0.03	0.00	601	12	1.00
GJ1-5			266	11	0.81	0.02	0.10	0.00	10.20	0.21	0.06	0.00	0.03	0.00	604	12	1.00
GJ1-7			259	10	0.80	0.02	0.10	0.00	10.26	0.21	0.06	0.00	0.03	0.00	600	12	1.00
GJ1-8			258	11	0.80	0.02	0.10	0.00	10.29	0.22	0.06	0.00	0.03	0.00	598	12	1.00
GJ1-9			261	10	0.80	0.02	0.10	0.00	10.25	0.22	0.06	0.00	0.03	0.00	601	13	1.01
GJ1-10			265	10	0.81	0.02	0.10	0.00	10.15	0.22	0.06	0.00	0.03	0.00	606	13	1.01
GJ1-11			260	10	0.79	0.02	0.10	0.00	10.19	0.21	0.06	0.00	0.03	0.00	605	12	1.02
GJ1-12			255	11	0.81	0.02	0.10	0.00	10.21	0.21	0.06	0.00	0.03	0.00	602	12	1.00
GJ1-13			258	11	0.79	0.02	0.10	0.00	10.26	0.22	0.06	0.00	0.03	0.00	600	13	1.01
GJ1-14			261	10	0.80	0.02	0.10	0.00	10.26	0.22	0.06	0.00	0.03	0.00	600	13	1.01
GJ1-15			262	11	0.80	0.02	0.10	0.00	10.25	0.22	0.06	0.00	0.03	0.00	600	13	1.01
GJ1-16			258	10	0.79	0.02	0.10	0.00	10.26	0.21	0.06	0.00	0.03	0.00	600	12	1.01
GJ1-17			255	10	0.79	0.02	0.10	0.00	10.26	0.21	0.06	0.00	0.03	0.00	600	12	1.01
GJ1-18			261	11	0.80	0.02	0.10	0.00	10.26	0.21	0.06	0.00	0.03	0.00	600	12	1.00
GJ1-19			272	11	0.81	0.02	0.10	0.00	10.22	0.21	0.06	0.00	0.03	0.00	602	12	1.00
GJ1-20			270	11	0.80	0.02	0.10	0.00	10.26	0.22	0.06	0.00	0.03	0.00	600	13	1.00
GJ1-21			257	10	0.80	0.02	0.10	0.00	10.24	0.21	0.06	0.00	0.03	0.00	601	12	1.01
GJ1-22			256	10	0.81	0.02	0.10	0.00	10.13	0.21	0.06	0.00	0.03	0.00	607	12	1.01
GJ1-23			265	10	0.80	0.02	0.10	0.00	10.13	0.21	0.06	0.00	0.03	0.00	608	12	1.02
GJ1-24			268	11	0.80	0.02	0.10	0.00	10.23	0.21	0.06	0.00	0.03	0.00	602	12	1.01

Table D5b: LASS zircon analyses of separated grain fragments: trace element data. REE concentrations are reported as chondrite normalized values

LASS spot number	Grain fragment	Grain texture	Ti (ppm)	2s	Y (ppm)	Hf (ppm)	La	Ce	Pr	Nd	Sm	Eu	Gd	Tb	Dy	Ho	Er	Tm	Yb	Lu	Eu*	Lun/Dyn	Th/U
24	PPC15-01-02z1a	rim	12.9	4.3	244	12210	0	25	1	7	53	9	113	132	142	166	211	266	384	533	0.11	3.75	0.72
26	PPC15-01-02z1a	rim	12.2	2.3	175	12670	0	24	1	5	36	18	106	129	122	116	114	118	159	155	0.29	1.27	0.44
45	PPC15-01-02z9b	rim	16.7	3.1	726	12240	0	17	2	8	64	9	219	333	392	452	504	497	542	585	0.07	1.49	0.44
44	PPC15-01-02z9b	rim	22.2	4.1	610	12930	0	19	2	6	84	15	249	363	389	394	356	334	383	331	0.10	0.85	0.19
46	PPC15-01-02z9b	rim	14.3	2.9	616	13230	0	18	3	9	87	17	245	363	382	394	356	359	362	286	0.11	0.75	0.16
47	PPC15-01-02z9c	rim	16.1	3	708	12410	0	19	2	9	93	16	273	368	393	414	405	418	438	415	0.10	1.05	0.24
53	PPC15-01-02z10a	rim	14.5	4.4	166.5	13370	0	33	2	6	55	14	121	142	131	105	94	91	124	154	0.17	1.17	0.42
52	PPC15-01-02z10b	outer core	9.9	2.7	763	9800	0	5	0	1	12	5	68	136	265	493	760	1166	1770	2341	0.18	8.82	0.17
55	PPC15-01-02z10b	rim	15.3	4.2	218.7	12970	0	32	2	7	51	17	140	137	140	139	139	162	215	238	0.19	1.70	0.50
50	PPC15-01-02z10e	rim	13.6	2.3	214.7	12600	0	23	1	5	55	21	164	192	162	137	123	110	138	153	0.22	0.94	0.38
14	PPC15-01-02z17a	rim	9.9	3	162.3	12080	0	28	1	4	43	11	93	102	102	105	98	104	127	176	0.17	1.73	0.44
17	PPC15-01-02z18a	rim	16.5	6.4	265.7	12780	0	26	2	11	83	12	167	181	171	155	162	155	175	204	0.10	1.20	0.43
59	PPC15-01-02z25a	rim	15.7	2.9	183.5	12390	0	32	3	6	68	14	109	122	115	126	105	106	130	148	0.16	1.29	0.58
60	PPC15-01-02z25a	rim	17.2	4.6	346	12270	0	20	2	6	66	7	146	194	203	203	245	287	337	439	0.07	2.16	0.44
58	PPC15-01-02z25b	rim	10.9	2.7	192	12620	0	34	3	11	72	11	143	137	137	121	104	111	135	134	0.11	0.98	0.71
80	PPC15-01-02z29a	rim	15.3	4.4	401	12880	0	16	3	6	46	25	102	146	186	242	318	457	582	695	0.36	3.74	0.28
79	PPC15-01-02z29b	rim	16	3.9	244.4	12630	0	29	2	11	84	11	144	155	146	150	171	188	225	290	0.10	1.99	0.58
77	PPC15-01-02z29c	core	15.7	5.3	721	9570	0	19	0	2	20	13	59	134	234	447	691	984	1373	1793	0.38	7.67	0.83
113	PPC15-01-02z33a	whole grain	25.8	2.6	589	13640	0	16	2	5	80	13	230	340	343	344	344	342	327	257	0.10	0.75	0.11
93	PPC15-01-02z34a	rim	12	2.4	177.5	12980	0	31	2	7	53	10	110	123	112	100	100	128	175	157	0.14	1.40	0.59
94	PPC15-01-02z34a	rim	14.9	2.7	256	12150	0	33	3	8	74	12	133	135	147	175	189	247	285	372	0.12	2.54	0.74
95	PPC15-01-02z34a	rim	17.2	5.2	246	12470	0	36	6	13	92	21	136	160	154	152	164	184	224	266	0.19	1.73	0.62
171	PPC15-01-01z5a	whole grain	24.3	4.6	774	14440	1	20	4	8	99	39	278	453	467	491	486	437	472	427	0.24	0.91	0.10
172	PPC15-01-01z5a	whole grain	16.4	6.8	522	14030	0	17	1	4	51	12	203	310	325	359	306	336	311	286	0.12	0.88	0.10
174	PPC15-01-01z5a	whole grain	20.5	4.6	564	14360	0	16	2	5	64	16	230	308	333	350	355	336	337	333	0.13	1.00	0.08
173	PPC15-01-01z5b	whole grain	17.2	4.5	546	14220	0	15	1	8	87	15	198	329	330	326	331	317	355	305	0.12	0.92	0.11
166	PPC15-01-01z7a	whole grain	24.2	3.9	841	12790	0	23	2	9	93	19	279	411	513	516	588	568	609	532	0.12	1.04	0.31
164	PPC15-01-01z7a	whole grain	19.9	3.8	657	11950	0	18	2	7	48	10	185	310	379	449	460	445	489	519	0.11	1.37	0.58

LASS spot number	Grain fragment	Grain texture	Ti (ppm)	2s	Y (ppm)	Hf (ppm)	La	Ce	Pr	Nd	Sm	Eu	Gd	Tb	Dy	Ho	Er	Tm	Yb	Lu	Eu*	Lun/Dyn	Th/U
126	PPC15-01-01z15a	rim	10.6	2.2	509	12470	0	23	4	7	57	12	139	247	299	306	314	347	368	346	0.14	1.15	0.46
123	PPC15-01-01z15b	rim	18.3	5.2	684	12660	0	16	1	6	68	6	180	316	410	440	474	460	518	524	0.05	1.28	0.49
124	PPC15-01-01z15b	core	10	4.2	536	12990	0	8	0	0	5	16	121	219	270	302	289	281	312	305	0.68	1.13	0.04
122	PPC15-01-01z15c	rim	22.7	3.3	653	11660	0	17	1	5	61	10	204	313	348	414	449	490	465	497	0.09	1.43	0.38
125	PPC15-01-01z15d	core	15.6	3.7	722	13080	0	5	0	0	21	15	123	256	386	443	466	482	532	496	0.30	1.28	0.03
156	PPC15-01-01z16a	whole grain	19.1	2.7	487	14390	0	15	1	4	49	11	179	250	306	269	318	293	298	229	0.12	0.75	0.07
153	PPC15-01-01z16b	whole grain	18.9	2.3	848	14270	0	20	3	6	93	29	303	429	489	540	480	481	493	443	0.17	0.91	0.08
154	PPC15-01-01z16c	whole grain	19.7	2.8	496	14250	0	14	2	5	68	13	185	258	305	302	278	309	300	282	0.12	0.92	0.07
155	PPC15-01-01z16d	whole grain	20.6	4.7	919	14060	0	10	1	5	68	20	255	474	545	617	598	602	579	593	0.15	1.09	0.02
Standards																							
91500-1			7.6	4.4	135.7	5440	0	4	0	1	2	4	11	23	46	86	135	254	415	539	0.9	1.17	0.31
91500-2			5.4	2	131.6	5400	0	5	0	0	3	4	17	22	43	88	148	236	422	548	0.5	1.28	0.30
91500-3			2.3	1.8	131.7	5580	0	4	0	1	3	1	15	22	45	90	148	239	398	542	0.2	1.20	0.34
91500-4			1.6	1.9	137.6	5430	0	4	0	0	1	5	14	24	42	87	150	243	435	581	1.3	1.39	0.33
91500-5			1	3.2	131.5	5220	0	4	0	1	0	5	9	24	44	82	139	236	402	510	0.0	1.17	0.31
91500-6			3.3	2.6	134.4	5230	0	5	0	0	1	3	13	20	39	92	138	221	391	577	0.7	1.48	0.30
91500-8			4.9	2.3	138.1	5650	0	4	0	0	2	7	11	21	53	88	149	242	416	517	1.4	0.97	0.31
91500-9			4.5	3.7	137.9	5650	0	4	0	0	2	4	9	27	48	86	149	286	408	581	0.9	1.22	0.32
91500-10			6.1	3.7	135.6	5310	0	4	0	0	2	6	10	29	42	77	166	251	411	528	1.5	1.26	0.32
91500-17			5.9	3.2	132.2	5370	0	4	0	0	1	6	12	25	38	75	158	251	381	550	2.5	1.44	0.32
91500-11			2.9	2.3	135.7	5410	0	4	0	0	0	2	11	20	55	92	144	219	416	573	0.0	1.05	0.32
91500-14			5.8	3.3	142.6	5430	0	3	0	1	9	4	12	17	44	79	148	235	440	565	0.4	1.28	0.33
91500-12			6.7	4	136.6	5350	0	4	0	0	3	3	7	22	47	77	158	248	396	533	0.7	1.13	0.33
91500-13			1.9	1.7	136.4	5380	0	4	0	1	0	2	10	23	39	83	159	227	410	504	0.0	1.28	0.32
91500-15			4.3	2.8	133.6	5530	0	3	0	0	3	3	10	25	44	71	146	221	389	541	0.5	1.23	0.32
91500-16			1.3	2	134	5660	0	4	0	0	5	5	15	19	49	88	146	224	395	549	0.6	1.13	0.35
91500-18			3.7	2.2	131.5	5360	0	4	0	0	1	7	14	25	39	82	141	239	406	508	2.1	1.29	0.35
91500-19			3.2	2	136	5500	0	4	0	0	1	3	13	22	49	94	155	270	412	552	0.6	1.13	0.34
91500-20			6.7	1.8	134.9	5340	0	5	0	0	3	7	8	22	41	92	153	238	383	476	1.3	1.17	0.35

LASS spot number	Grain fragment	Grain texture	Ti (ppm)	2s	Y (ppm)	Hf (ppm)	La	Ce	Pr	Nd	Sm	Eu	Gd	Tb	Dy	Ho	Er	Tm	Yb	Lu	Eu*	Lun/Dyn	Th/U
91500-21			5.3	3.1	137.6	5430	0	4	0	1	0	6	17	25	38	97	156	253	399	533	0.0	1.41	0.33
91500-22			6.6	5.4	131.6	5320	0	3	0	0	8	5	5	16	32	89	156	243	407	500	0.8	1.56	0.36
91500-23			4.3	2	132.4	5490	0	4	0	0	3	5	7	19	43	77	158	265	393	569	0.9	1.33	0.34
91500-24			5.2	2.1	137.8	5600	0	4	0	1	5	6	13	16	44	79	146	283	388	516	0.7	1.17	0.34
91500-25			1.9	2	135.1	5650	0	5	1	1	1	3	9	25	46	76	153	286	404	488	1.2	1.06	0.34
GJ1-1			3.4	2.6	251.1	6830	0	27	0	1	13	24	36	52	83	130	196	255	380	569	1.1	0.68	0.03
GJ1-2			2.5	2.4	239.4	6370	0	25	0	2	17	19	40	43	85	124	177	249	384	537	0.7	0.63	0.03
GJ1-3			2.6	3.1	248.3	6690	0	25	1	2	12	13	34	58	81	130	167	266	397	550	0.7	0.68	0.03
GJ1-4			0.2	2.8	248.9	6620	0	27	1	2	14	22	31	56	77	129	193	233	418	565	1.1	0.74	0.03
GJ1-5			2	2.7	243.1	6510	0	25	0	1	13	18	32	55	84	116	199	242	383	516	0.9	0.61	0.04
GJ1-7			2.1	3	242.7	6650	0	27	0	1	4	16	33	58	75	124	177	248	375	536	1.4	0.71	0.04
GJ1-8			2.1	1.6	240.1	6500	0	27	0	2	10	23	30	49	80	120	188	266	393	497	1.3	0.62	0.03
GJ1-9			5.7	1.5	245.1	6520	0	27	0	1	13	16	42	52	73	120	174	279	367	524	0.7	0.72	0.04
GJ1-10			4.9	1.5	241	6570	0	27	0	1	10	15	36	65	78	116	178	248	370	553	0.8	0.71	0.04
GJ1-11			4.4	1.6	245	6280	0	27	0	1	14	25	30	52	81	122	184	268	366	570	1.2	0.70	0.03
GJ1-12			3.6	2.2	252.2	6730	0	26	0	1	11	10	34	57	78	131	183	243	402	547	0.5	0.70	0.03
GJ1-13			3.1	2.5	251	6700	0	27	0	1	10	20	29	64	76	131	201	245	391	581	1.1	0.76	0.04
GJ1-14			7.4	3.1	253.6	6550	0	29	0	1	12	17	48	60	81	126	186	234	411	573	0.7	0.71	0.03
GJ1-15			5.6	2.5	245.8	6890	0	26	1	1	8	22	36	49	85	133	187	270	377	557	1.3	0.65	0.03
GJ1-16			2.6	2.6	239.8	6410	0	26	0	1	9	16	41	52	84	113	184	237	353	541	0.8	0.65	0.03
GJ1-17			3.9	4.1	253.1	6600	0	28	0	2	12	16	34	55	78	120	195	234	411	554	0.8	0.71	0.04
GJ1-18			4	2	250.7	6820	0	26	0	2	11	12	40	52	88	120	188	276	381	513	0.6	0.58	0.03
GJ1-19			5.6	2.3	239.4	6450	0	26	0	2	5	20	24	48	80	124	166	289	384	500	1.8	0.62	0.03
GJ1-20			3.3	3	243.9	6700	0	25	0	2	12	17	39	64	83	129	190	279	415	524	0.8	0.63	0.04
GJ1-21			3.3	3.2	246	6750	0	26	0	1	12	20	35	63	67	116	186	249	397	543	1.0	0.81	0.04
GJ1-22			1.1	2.3	242	6530	0	29	0	1	14	15	30	50	80	126	169	266	369	484	0.8	0.60	0.04
GJ1-23			5.1	2.1	245.5	6450	0	24	0	1	10	16	31	54	80	123	186	296	395	528	0.9	0.66	0.04
GJ1-24			0.3	2.2	244.5	6930	0	24	0	1	18	17	30	53	83	143	181	261	396	541	0.7	0.66	0.03

Table D6: All ID-TIMS monazite analyses: isotopic data

Fragment	207Pb/206Pb date	2s	%disc	Th/U	Pb* (pg)	Pbc (pg)	206Pb/204Pb	206Pb/238U	2s (%)	207Pb/235U	2s (%)	207Pb/206Pb	2s (%)
PPC15-01-m1a	2666.5	1.2	-0.01	122	33700	11.64	6018	0.51238	0.15	12.822	0.18	0.18157	0.063
PPC15-01-m1b	2665.4	1.1	0.97	152	206000	13.3	26039	0.506	0.29	12.653	0.31	0.18145	0.061
PPC15-01-m1c	2674.68	0.9	0.86	131	138000	5.14	52007	0.50882	0.16	12.796	0.19	0.182467	0.043
PPC15-01-m1c 2	2672.52	0.94	0.89	131	138000	5.71	46764	0.50818	0.12	12.763	0.15	0.182229	0.047
PPC15-01-m2a dt 41.2	2639.3	1.1	-1.05	63	19000	11.72	6282	0.51243	0.12	12.614	0.14	0.17861	0.058
PPC15-01-m2a dt 46	2629.12	0.99	-2.02	64	19100	11.74	6314	0.51599	0.11	12.624	0.14	0.177523	0.05
PPC15-01-m2d	2643.56	0.9	-0.68	31	10900	5.2	15563	0.51116	0.13	12.615	0.15	0.179074	0.043
PPC15-01-m2e	2635.3	1	-2.02	42	9140	9.13	5758	0.5175	0.078	12.708	0.12	0.178183	0.05
PPC15-01-m2f	2674.1	1.2	0.12	28	2500	2.7	7666	0.5133	0.22	12.904	0.22	0.1824	0.066
PPC15-01-m3a	2639.11	0.91	0.62	16	2060	1.04	26099	0.50209	0.062	12.358	0.1	0.178594	0.044
PPC15-01-m3b	2665.5	2.4	-0.03	101	9650	6.72	3582	0.51226	0.12	12.811	0.15	0.18146	0.14
PPC15-01-m3c	2620.99	0.93	0.72	65	10500	4.73	8433	0.49726	0.087	12.107	0.12	0.176657	0.046
PPC15-01-m3d	2616.1	1.1	1.34	99	15100	7.75	4907	0.49239	0.1	11.953	0.13	0.176143	0.054
PPC15-01-m3e	2660.36	0.92	0.49	63	11300	3.71	11928	0.50785	0.059	12.661	0.099	0.180897	0.045
PPC15-01-m4a	2655.9	1	0.59	61	6030	4.66	5175	0.50619	0.062	12.586	0.11	0.180409	0.052

Table D7a: LASS monazite analyses of separated grain fragments m1a and m3b: isotopic data

Analysis Name	U ppm	Th ppm	$^{207}Pb/^{235}U$	2s	$^{206}Pb/^{238}U$	2s	$^{238}U/^{206}Pb$	2s	$^{207}Pb/^{206}Pb$	2s	$^{208}Pb/^{232}Th$	2s	$^{207}Pb/^{206}Pb$ date	2s	Concordance
Grain m1a															
PPC15-01mnzmt-g1-51	398	57000	12.59	0.29	0.51	0.01	1.95	0.04	0.18	0.00	0.14	0.00	2621	38	1.01
PPC15-01mnzmt-g1-53	429	69700	12.63	0.31	0.51	0.01	1.95	0.04	0.18	0.00	0.14	0.00	2630	41	1.00
PPC15-01mnzmt-g1-52	421	56200	12.91	0.30	0.52	0.01	1.93	0.04	0.18	0.00	0.14	0.00	2649	39	1.01
PPC15-01mnzmt-g1-47	1022	38900	12.95	0.27	0.53	0.01	1.89	0.04	0.18	0.00	0.14	0.00	2613	35	1.02
PPC15-01mnzmt-g1-56	383	70900	15.77	0.44	0.64	0.01	1.57	0.03	0.18	0.01	0.13	0.00	2633	47	1.11
PPC15-01mnzmt-g1-54	998	39600	15.98	0.35	0.64	0.01	1.55	0.03	0.18	0.00	0.13	0.00	2642	35	1.12
PPC15-01mnzmt-g1-57	403	69300	15.61	0.48	0.63	0.01	1.58	0.03	0.18	0.01	0.12	0.00	2642	49	1.11
PPC15-01mnzmt-g1-45	770	40300	14.70	0.34	0.60	0.01	1.66	0.04	0.18	0.00	0.14	0.00	2615	35	1.09
PPC15-01mnzmt-g1-46	1008	43100	13.70	0.28	0.56	0.01	1.79	0.04	0.18	0.00	0.14	0.00	2623	35	1.05
PPC15-01mnzmt-g1-48	546	68800	12.68	0.28	0.52	0.01	1.91	0.04	0.17	0.00	0.14	0.00	2596	37	1.02
PPC15-01mnzmt-g1-59	495	65000	13.69	0.38	0.58	0.01	1.71	0.04	0.17	0.00	0.13	0.00	2559	47	1.09
PPC15-01mnzmt-g1-58	394	75800	15.94	0.47	0.65	0.01	1.54	0.03	0.18	0.00	0.12	0.00	2645	44	1.12
PPC15-01mnzmt-g1-55	433	59000	16.80	1.15	0.69	0.02	1.45	0.03	0.18	0.01	0.13	0.00	2616	118	1.16
Grain m3b															
PPC15-01mnzmt-g3-40	1780	12980	11.62	0.24	0.49	0.01	2.06	0.04	0.17	0.00	0.13	0.00	2572	34	0.99
PPC15-01mnzmt-g3-39	1503	14570	12.09	0.25	0.50	0.01	2.01	0.04	0.18	0.00	0.13	0.00	2607	34	1.00
PPC15-01mnzmt-g3-38	597	27700	11.90	0.27	0.50	0.01	2.02	0.04	0.17	0.00	0.13	0.00	2588	37	1.00
PPC15-01mnzmt-g3-37	428	51000	12.62	0.32	0.50	0.01	1.98	0.04	0.18	0.00	0.13	0.00	2660	42	0.99
PPC15-01mnzmt-g3-36	394	36800	12.12	0.29	0.50	0.01	2.02	0.04	0.18	0.00	0.13	0.00	2615	40	0.99
PPC15-01mnzmt-g3-28	535	34200	11.99	0.27	0.49	0.01	2.02	0.04	0.18	0.00	0.13	0.00	2611	38	0.99
PPC15-01mnzmt-g3-27	650	28600	11.94	0.26	0.49	0.01	2.03	0.04	0.18	0.00	0.13	0.00	2616	36	0.99
PPC15-01mnzmt-g3-26	760	23500	12.44	0.26	0.51	0.01	1.97	0.04	0.18	0.00	0.13	0.00	2643	35	1.00
PPC15-01mnzmt-g3-25	1178	19100	12.17	0.25	0.50	0.01	1.99	0.04	0.18	0.00	0.13	0.00	2626	34	1.00
PPC15-01mnzmt-g3-24	598	29300	12.26	0.27	0.50	0.01	2.00	0.04	0.18	0.00	0.13	0.00	2643	37	1.00

Table D7b: LASS monazite analyses of separated grain fragments m1a and m3b: trace element data. REE concentrations are reported as chondrite normalized values

Analysis Name	Ca ppm	Sr ppm	Y ppm	La	Ce	Pr	Nd	Sm	Eu	Gd	Tb	Dy	Ho	Er	Tm	Yb	Lu	Eu/Eu*	Th/U	Gdn/Ybn
Grain m1a																				
PPC15-01mnzmt-g1-51	2820	2	1026	470464	440457	375000	291904	115946	5471	25276	6870	2195	698	459	243	93	35	0.10	143	273
PPC15-01mnzmt-g1-53	2720	2	677	443038	448613	383621	315098	100405	4920	20452	5540	1362	493	305	119	38	5	0.11	162	540
PPC15-01mnzmt-g1-52	3010	2	780	468776	440457	357759	291028	108784	5435	21508	6066	1626	491	331	126	60	45	0.11	133	361
PPC15-01mnzmt-g1-47	4580	7	1155	421857	380098	321121	267615	128378	8632	30402	8753	2541	786	450	219	96	51	0.14	38	316
PPC15-01mnzmt-g1-56	3000	28	696	453586	429038	401940	310722	112500	5844	22362	5734	1589	518	366	87	58	81	0.12	185	387
PPC15-01mnzmt-g1-54	4540	37	1371	470042	446982	375000	312910	163514	10391	34121	10000	2841	1077	594	219	106	114	0.14	40	321
PPC15-01mnzmt-g1-57	3130	52	1000	518987	468189	462284	378556	144595	9041	27889	7230	2114	711	391	138	41	0	0.14	172	680
PPC15-01mnzmt-g1-45	4600	24	1231	443460	409462	340517	279650	146622	10462	32211	9501	2663	919	486	202	93	48	0.15	52	348
PPC15-01mnzmt-g1-46	4420	14	1251	488608	460033	392241	295624	164189	10124	33618	9917	2902	919	489	239	107	77	0.14	43	315
PPC15-01mnzmt-g1-48	3400	3	727	447257	466558	414871	323851	116216	5648	23970	6150	1618	540	373	110	61	4	0.11	126	394
PPC15-01mnzmt-g1-59	3740	30	827	458228	471452	390086	310722	118243	7584	27186	6676	2012	711	375	178	68	20	0.13	131	402
PPC15-01mnzmt-g1-58	3600	23	815	472574	433931	429957	334792	128378	6075	23216	7147	1923	643	344	162	19	73	0.11	192	1246
PPC15-01mnzmt-g1-55	3870	21	829	507173	424144	404095	336980	131757	6643	24070	6399	2081	650	488	178	73	89	0.12	136	328
Grain m3b																				
PPC15-01mnzmt-g3-40	2400	2	4350	520675	424144	329741	256674	165541	20071	61206	23850	9024	3390	1163	538	213	224	0.20	7	287
PPC15-01mnzmt-g3-39	2610	4	3910	502954	401305	338362	253829	154054	18757	55578	22078	7967	2745	1063	409	260	110	0.20	10	214
PPC15-01mnzmt-g3-38	3210	4	3140	468354	412724	354526	276368	141892	12131	47588	17507	6122	2491	926	308	142	150	0.15	46	335
PPC15-01mnzmt-g3-37	5380	5	3920	463291	398042	355496	286652	147838	10444	54774	22438	7707	3278	1313	579	248	264	0.12	119	220
PPC15-01mnzmt-g3-36	4100	4	3170	455696	402936	344828	267834	136757	11528	49598	18726	6276	2584	906	457	209	102	0.14	93	238
PPC15-01mnzmt-g3-28	3970	3	3300	443882	399674	348060	271335	141892	10941	49347	18199	6260	2582	1031	348	185	122	0.13	64	267
PPC15-01mnzmt-g3-27	4140	10	3350	488186	411093	348060	270022	152568	12345	48342	18920	6098	2527	1037	437	186	171	0.14	44	259
PPC15-01mnzmt-g3-26	3440	4	3070	497890	426101	333190	272867	146622	14263	48894	19058	6301	2509	919	332	157	146	0.17	31	311
PPC15-01mnzmt-g3-25	3100	4	3610	494093	415987	344828	265208	144662	17300	54070	18532	6789	2674	950	462	199	138	0.20	16	271
PPC15-01mnzmt-g3-24	3370	4	3090	475949	415987	338362	264770	133108	11528	48543	18864	6098	2326	956	300	208	138	0.14	49	233